ACS SYMPOSIUM SERIES 1117

Ionic Liquids: Science and Applications

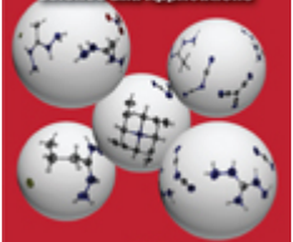

EDITED BY

Ann E. Visser, Nicholas J. Bridges, and
Robin D. Rogers

Downloaded by DALHOUSIE UNIV on December 19, 2012 | http://pubs.acs.org
Publication Date (Web): December 18, 2012 | doi: 10.1021/bk-2012-1117.fw001

Ionic Liquids: Science and Applications

In Ionic Liquids: Science and Applications; Visser, A., et al.;
ACS Symposium Series; American Chemical Society: Washington, DC, 2012.

Downloaded by DALHOUSIE UNIV on December 19, 2012 | http://pubs.acs.org
Publication Date (Web): December 18, 2012 | doi: 10.1021/bk-2012-1117.fw001

ACS SYMPOSIUM SERIES **1117**

Ionic Liquids: Science and Applications

Ann E. Visser, Editor
Savannah River National Laboratory
Aiken, South Carolina

Nicholas J. Bridges, Editor
Savannah River National Laboratory
Aiken, South Carolina

Robin D. Rogers, Editor
The University of Alabama
Tuscaloosa, Alabama

Sponsored by the
ACS Division of Industrial and Engineering Chemistry

American Chemical Society, Washington, DC

Distributed in print by Oxford University Press, Inc.

Downloaded by DALHOUSIE UNIV on December 19, 2012 | http://pubs.acs.org
Publication Date (Web): December 18, 2012 | doi: 10.1021/bk-2012-1117.fw001

Downloaded by DALHOUSIE UNIV on December 19, 2012 | http://pubs.acs.org
Publication Date (Web): December 18, 2012 | doi: 10.1021/bk-2012-1117.fw001

Library of Congress Cataloging-in-Publication Data

Ionic liquids : science and applications / Ann E. Visser, editor, Savannah River National Laboratory, Aiken, South Carolina, Nicholas J. Bridges, editor, Savannah River National Laboratory, Aiken, South Carolina, Robin D. Rogers, editor, The University of Alabama, Tuscaloosa, Alabama ; sponsored by the ACS Division of Industrial and Engineering Chemistry.
pages cm. -- (ACS symposium series ; 1117)
Includes bibliographical references and index.
ISBN 978-0-8412-2763-7 (alk. paper)
1. Ionic solutions--Congresses. I. Visser, Ann E. II. Bridges, Nicholas J. III. Rogers, Robin D. IV. American Chemical Society. Division of Industrial and Engineering Chemistry.
QD565.I5875 2012
541′.3723--dc23
2012042799

The paper used in this publication meets the minimum requirements of American National Standard for Information Sciences—Permanence of Paper for Printed Library Materials, ANSI Z39.48n1984.

Copyright © 2012 American Chemical Society

Distributed in print by Oxford University Press, Inc.

All Rights Reserved. Reprographic copying beyond that permitted by Sections 107 or 108 of the U.S. Copyright Act is allowed for internal use only, provided that a per-chapter fee of $40.25 plus $0.75 per page is paid to the Copyright Clearance Center, Inc., 222 Rosewood Drive, Danvers, MA 01923, USA. Republication or reproduction for sale of pages in this book is permitted only under license from ACS. Direct these and other permission requests to ACS Copyright Office, Publications Division, 1155 16th Street, N.W., Washington, DC 20036.

The citation of trade names and/or names of manufacturers in this publication is not to be construed as an endorsement or as approval by ACS of the commercial products or services referenced herein; nor should the mere reference herein to any drawing, specification, chemical process, or other data be regarded as a license or as a conveyance of any right or permission to the holder, reader, or any other person or corporation, to manufacture, reproduce, use, or sell any patented invention or copyrighted work that may in any way be related thereto. Registered names, trademarks, etc., used in this publication, even without specific indication thereof, are not to be considered unprotected by law.

PRINTED IN THE UNITED STATES OF AMERICA

Downloaded by DALHOUSIE UNIV on December 19, 2012 | http://pubs.acs.org
Publication Date (Web): December 18, 2012 | doi: 10.1021/bk-2012-1117.fw001

Foreword

The ACS Symposium Series was first published in 1974 to provide a mechanism for publishing symposia quickly in book form. The purpose of the series is to publish timely, comprehensive books developed from the ACS sponsored symposia based on current scientific research. Occasionally, books are developed from symposia sponsored by other organizations when the topic is of keen interest to the chemistry audience.

Before agreeing to publish a book, the proposed table of contents is reviewed for appropriate and comprehensive coverage and for interest to the audience. Some papers may be excluded to better focus the book; others may be added to provide comprehensiveness. When appropriate, overview or introductory chapters are added. Drafts of chapters are peer-reviewed prior to final acceptance or rejection, and manuscripts are prepared in camera-ready format.

As a rule, only original research papers and original review papers are included in the volumes. Verbatim reproductions of previous published papers are not accepted.

ACS Books Department

Downloaded by DALHOUSIE UNIV on December 19, 2012 | http://pubs.acs.org
Publication Date (Web): December 18, 2012 | doi: 10.1021/bk-2012-1117.pr001

Preface

A decade has passed since the first American Chemical Society (ACS) Symposium Series was published on ionic liquids (*Ionic Liquids: Industrial Applications for Green Chemistry*, Vol. 818, 2002). Then, as is the case now, ionic liquids were finding application in a wide range of science and engineering disciplines. Since 1987, the annual number of publications in the field of ionic liquids continues to increase (Figure 1). The number of patents and books in the field of ILs has also experienced a similar surge in numbers.

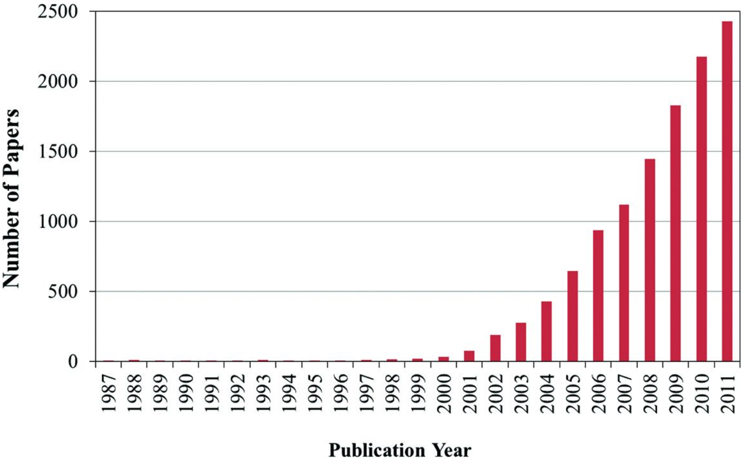

Figure 1. Annual Number of Publications on Ionic Liquids (Search performed on SciFinder using "ionic liquid" and limiting publication types to commentary, letter, journal, report, and review. Search performed on 9/4/2012).

It has been a few years since a full week of ionic liquids talks has been organized at an ACS meeting in a cohesive symposium, and we were motivated to highlight many of the emerging themes that are becoming quite important worldwide. The symposium organizers also believed that these many new areas of impact needed to be brought to the attention of the scientific community and an ACS Symposium Series publication would be the optimal means to communicate the science in a timely fashion.

This book contains some of the papers presented at the ACS meeting symposium *Ionic Liquids: Science and Applications*, held at the 243rd National ACS meeting in San Diego, California, March 25–29, 2012. The symposium contained nine sessions (Energetic Ionic Liquids; Physical Properties/Physical Chemistry; Ionic Liquids for Fuel, Energy, and Chemical Production; Biomass and Renewables; Advanced Electrolytes; Molecular Modeling; Nanomaterials; New Materials; and Biotechnology) running from Sunday through Monday morning and Tuesday morning through Thursday afternoon. More than 75 presentations were given. The symposium organizers are grateful to the session organizers, T. Hawkins, S. Schneider, J. Wishart, E. Castner, E. Fox, W. M. Reichert, W. Henderson, E. Maginn, A. Mudring, J. Davis, and D. MacFarlane, for assembling a diverse and interesting program.

The overarching theme of this symposium was the science and applications of ionic liquids. No longer are ionic liquids interesting simply because they could be considered part of the next generation of “green” solvents, but their unique physical and chemical properties make them a wholly unique class of solvents. As shown in the presentations, the fundamental science gleaned from physical chemistry, molecular modeling, and characterization of ionic liquids facilitates the proliferation of ionic liquid applications in biotechnology, advanced electrolytes, and nanomaterials, to name but a few areas where ionic liquids are being investigated. We hope that as you read the contributions presented in this book, you will agree that ionic liquids remain a fascinating and fertile field of scientific endeavor.

Downloaded by DALHOUSIE UNIV on December 19, 2012 | http://pubs.acs.org
Publication Date (Web): December 18, 2012 | doi: 10.1021/bk-2012-1117.pr001

Ann E. Visser
National and Homeland Security
Savannah River National Laboratory
Aiken, South Carolina 29808
ann.visser@srnl.doe.gov (e-mail)
803-725-5383 (telephone)

Nicholas J. Bridges
Environmental and Chemical Processing Technology
Savannah River National Laboratory
Aiken, South Carolina 29808
nicholas.bridges@srnl.doe.gov (e-mail)
803-725-7279 (telephone)

Robin D. Rogers
Center for Green Manufacturing and Department of Chemistry
The University of Alabama
Tuscaloosa, Alabama 35487
rdrogers@as.ua.edu (e-mail)
205-348-4323 (telephone)

Editors' Biographies

Dr. Ann E. Visser

Dr. Ann Visser joined the Actinide Technology Section (ATS) of the Savannah River National Laboratory as a chemist in 2003. While in the ATS, her initial work involved support of Savannah River Site facilities for flowsheet development for plutonium- and uranium-containing materials. Since then, she has contributed to several multi-year programs involving the development of ionic liquid technology at the Lab. In 2012, she joined the National and Homeland Security Directorate.

Dr. Nicholas J. Bridges

Dr. Nicholas Bridges received his B.S. in chemistry from Tennessee Technological University in 2002 and was awarded his Ph.D. from The University of Alabama under the mentoring of Prof. Robin Rogers in 2007. At The University of Alabama, he focused on understanding the interactions of ionic liquids in aqueous systems and f-element chemistry. Nicholas conducted a post-doctoral at Washington State University before starting at Savannah River National Laboratory. Working in the Separation and Actinide Science Division, he has been able to continue investigating ionic liquids in various energy-related fields.

Dr. Robin D. Rogers

Dr. Robin D. Rogers obtained both his B.S. in Chemistry (1978, Summa Cum Laude) and his Ph.D. in Chemistry (1982) at The University of Alabama and currently serves as Distinguished Research Professor, Robert Ramsay Chair of Chemistry, and Director of the Center for Green Manufacturing at UA. His research interests cover the use of ionic liquids and green chemistry for sustainable technology through innovation and include materials, separations, energy, and medicine. Rogers is the founding Editor-in-Chief of the American Chemical Society journal *Crystal Growth & Design* and serves on the editorial boards of several international journals. He has been named a Fellow of the American Chemical Society, the Royal Society of Chemistry, and the American Association for the Advancement of Science.

In Ionic Liquids: Science and Applications; Visser, A., et al.;
ACS Symposium Series; American Chemical Society: Washington, DC, 2012.

Chapter 1

Ionic Liquid Fuels for Chemical Propulsion

Stefan Schneider,* Tom Hawkins, Yonis Ahmed,
Stephan Deplazes, and Jeff Mills

Air Force Research Laboratory, 10 E. Saturn Blvd.,
Edwards AFB, California 93524-7680
***E-mail: stefan.schneider@edwards.af.mil**

Downloaded by FORDHAM UNIV on December 19, 2012 | http://pubs.acs.org
Publication Date (Web): December 18, 2012 | doi: 10.1021/bk-2012-1117.ch001

The ionic liquid (IL) program at the Air Force Research Laboratory is investigating tailored energy-dense liquids to provide a scientific foundation for the advancement of the performance and operability envelopes of current propulsion systems. General efforts focus on the discovery of energetic ILs based on heterocyclic and open-chain cations in combination with reactive anions. A major goal has been the development of IL fuels which undergo hypergolic ignition upon contact with common propulsion oxidizers. This account discusses the combination of some azolium, ammonium, hydrazinium, guanidinium and hydrazidinium cations with dicyanamide, nitrocyanamide, cyanoureate, nitrate, azide and tricyanomethanide anions. Their synthesis and characterization are described along with results of simple hypergolicity drop tests. The utility and reproducibility of these tests and possible mechanistic scenarios for these reactions are also discussed.

Introduction

Despite early mention in the propellant literature (*1*), energetic ILs are only now receiving increasing consideration as practical rocket propellants. Understanding this trend requires reflection upon the historical context in which our current state-of-the-art propellants were chosen and developed.

The urgency of the Cold War and the race for the moon led to an explosion in resources devoted to rocket propulsion. In these “glory days” large regions of the chemical landscape were explored in the quest for the competitive edge in chemical propulsion. Accounts of this time remain an important

In Ionic Liquids: Science and Applications; Visser, A., et al.;
ACS Symposium Series; American Chemical Society: Washington, DC, 2012.

resource for today's propellant chemist. In his memoir surveying this work, an American pioneer, John Clark, makes tantalizing mention of ILs in general and ethylammonium nitrate in particular (*1*): "Molten salts are nothing new, but these were the only ones I ever heard of that were liquid at 25°C. I've never found a use for the ethylamine compound, but something with such interesting properties ought to be good for *something!*"

In addition to providing the impetus for ground-breaking chemical research, the objectives of the time demanded that environmental and health considerations be subjugated to raw performance. It is therefore little wonder that at the time of his writing Clark saw a future for the hydrazine/ClF_5 fuel-oxidizer combination. Although nitric acid (in the form of inhibited red fuming nitric acid (IRFNA)) and nitrogen tetroxide were ultimately down-selected as room-temperature oxidizers in preference to the interhalogens, the hydrazines remain the state-of-the-art fuels for non-cryogenic applications.

Another feature that makes hydrazine such a desirable fuel is its hypergolic ignition (the spontaneous ignition upon contact) with most commonly used oxidizers. This type of chemical ignition makes system starts and restarts reliable and minimizes complexity as no additional ignition source is needed. There is a simple, effective method to quickly screen a variety of materials for this desired ignition behavior. The procedure is commonly referred to as a drop test. Typically a drop of fuel is released from a syringe or pipette into a crucible containing an oxidizer and ignition is determined by a high speed video camera, perhaps in combination with measurement of a sudden pressure increase (Figure 1). The ignition delay (ID) time is the interval between the first contact of fuel with oxidizer and ignition. With origins extending back to at least the second world war, this test was the primary initial screening tool in what Clark describes as the "hunt for the hypergol" during the nineteen sixties. It continues despite the wide recognition that its conditions are not perfectly representative of those in a combustion chamber.

Today, well after the Sputnik era, priorities have shifted. Even as ease of ignition is still desirable and higher performance remains a preeminent goal, hazard properties have arisen as more significant drivers of cost and feasibility.

Downloaded by FORDHAM UNIV on December 19, 2012 | http://pubs.acs.org
Publication Date (Web): December 18, 2012 | doi: 10.1021/bk-2012-1117.ch001

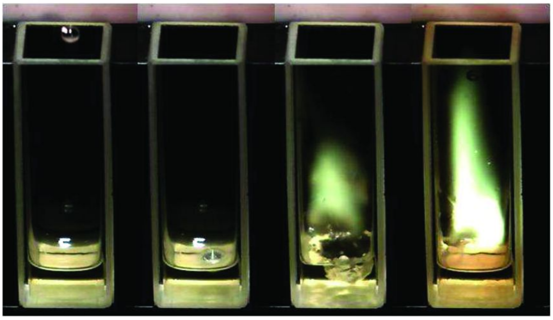

Figure 1. Drop test: A fuel drop is released from a syringe into the oxidizer.

Downloaded by FORDHAM UNIV on December 19, 2012 | http://pubs.acs.org
Publication Date (Web): December 18, 2012 | doi: 10.1021/bk-2012-1117.ch001

Most of the handling difficulties of the noncryogenic fuel/oxidizer combinations are associated with the vapor toxicity of hydrazines. Flammability is also a significant handling and operations issue. Energetic ILs with virtually no vapor pressure and low flammability would seem ideally suited as potential hydrazine replacements.

Ethylammonium nitrate is generally regarded as the first reported room temperature ionic liquid (RTIL). Since it is a nitrate salt, it certainly carries a significant amount of energy and might even be thought of as a promising prototype of a monopropellant. These single component propellants carry the advantages of engineering simplicity associated with the fuel and oxidizer residing in a single tank. However, by itself, ethylammonium nitrate lacks sufficient oxygen to assure balanced combustion to CO, CO_2, H_2O and N_2. The work of Christe (*2*) and Shreeve (*3*) begins to overcome this difficulty by introducing multiple nitrato- functionalities into a single molecule. Chemical stability is often sacrificed by this approach and the Air Force's current monopropellant development program (not otherwise discussed in this work) seeks a suitable candidate by partitioning the fuel and oxidizer into separate molecules or ions in a single solution.

In contrast, the present work is primarily concerned with what are referred to as bipropellants in which safety and stability are enhanced by segregating fuel and oxidizer into separate working fluids. Indeed the substantial history of underoxidized energetic ILs (like ethylammonium nitrate) of varying energy content seemed to promise ILs of sufficient energy to undergo hypergolic ignition with common propellant oxidizers. Nevertheless, initial tests with some easily prepared nitrate (NO_3^-), dinitramide ($N(NO_2)_2^-$), and perchlorate (ClO_4^-) salts were disappointing. None yielded a visible flame in drop tests. Even multiple drops in the same test were insufficient to lead to ignition.

At this point, it became clear that new design work would need to be conducted targeting fuel-rich materials with sufficient propensity toward oxidation to support facile ignition. The first class of compounds considered were ILs incorporating the azide anion, based on the known, exothermic reactivity of simple azides with nitrogen tetroxide (NTO) (Scheme 1). Various liquid IL azides were prepared but, while exhibiting significant reactivity, they did not undergo hypergolic ignition (*4*). Therefore, we considered the investigations unsuccessful.

$$\begin{array}{lcl} N_2O_4 & \rightleftharpoons & NO_3^- + NO^+ \\ N_3^- + NO^+ & \rightleftharpoons & N_3NO \longrightarrow N_2 + N_2O \\ \hline N_2O_4 + N_3^- & \longrightarrow & NO_3^- + N_2 + N_2O \end{array}$$

Scheme 1. Reaction of ionic azides with N_2O_4.

The breakthrough in this research resulted from a serendipitous effort to enhance the physical properties of the ILs. While we recognized that the dicyanamide (dca) anion provides a combustible organic structure, we primarily sought to take advantage of the fact that the dca anion is known to produce

ILs with low viscosities and a large liquidus range. Even though dca could not be considered a very high-energy anion, these ILs were subjected to drop test experiments. This resulted in the discovery of the first hypergolic IL family (*5*, *6*). Ever since, many hypergolic ILs have been developed, in our laboratory and elsewhere (*7–13*), but the majority of these are based on the dca anion.

Our laboratory is continuing to pursue the interesting class of hypergolic ILs, both by themselves and in combination with other materials including nanoparticles (*14*). This work is a summary account of our efforts to devise chemical strategies to discover ILs with reduced IDs and improved performance characteristics.

Downloaded by FORDHAM UNIV on December 19, 2012 | http://pubs.acs.org
Publication Date (Web): December 18, 2012 | doi: 10.1021/bk-2012-1117.ch001

Results and Discussion

Ammonium-Based IL Dicyanamides

If we follow the accepted definition of an IL, a salt with a melting point below 100°C, the literature provides us with an interesting timeline leading to the development of the first RTIL. One of the first ILs produced was probably hydroxyethylammonium nitrate (mp. 52-55°C) in 1888 (*15*), followed by hydrazinium azide (mp. 75°C) in 1891 (*16*) and finally the first RTIL, ethylammonium nitrate (mp. 9°C) in 1914 (*17*). There are two noteworthy features: all of these first generation ILs are based on open-chain amine cations and all are energetic ILs. Many neutral, open-chain amines have also been considered as potential propellant fuels and their hypergolic reactivity decreases as tertiary > secondary > primary (*1*).

We chose to study a narrow set of protic and aprotic cations based on commercial availability, and therefore ease of preparation, as well as the presence of potentially reactive substituents (Scheme 2).

A total of seven protic, ammonium-based IL dcas were investigated: four monoalkylated (*18*), one dialkylated (*18*, *19*) and two trialkylated. An additional eleven were tetraalkyl-ammonium dca salts, six with two different substituents, four with three different substituents and tetrapropargyl-ammonium dca. Their physical properties are listed in Table 1.

These studies substantiate the difficulty of *a priori* prediction of IL physical properties. Ethylammonium nitrate is well established as an RTIL. Therefore, it was expected that **1** would also be an RTIL, since dcas generally possess lower melting points than their nitrate counterparts. As can be seen from Figure 2 and Table 1, **1** is a solid with a surprisingly high melting point of 46°C. The X-ray crystal structure reveals a strong hydrogen-bond network (Figure 3) but it is not obvious why the general trend is reversed in this case.

About half of the materials were obtained as RTILs with melting points ranging between -4°C and 28°C (Table 1). Furthermore, the liquids manifested acceptably low viscosities between 26cP and 120cP. While the melting points and viscosities appear to be attractive for the protic IL dcas, their low decomposition onsets render them impractical for propellant applications. In contrast, the fully quarternized ammonium dcas generally showed excellent thermal stability.

Downloaded by FORDHAM UNIV on December 19, 2012 | http://pubs.acs.org
Publication Date (Web): December 18, 2012 | doi: 10.1021/bk-2012-1117.ch001

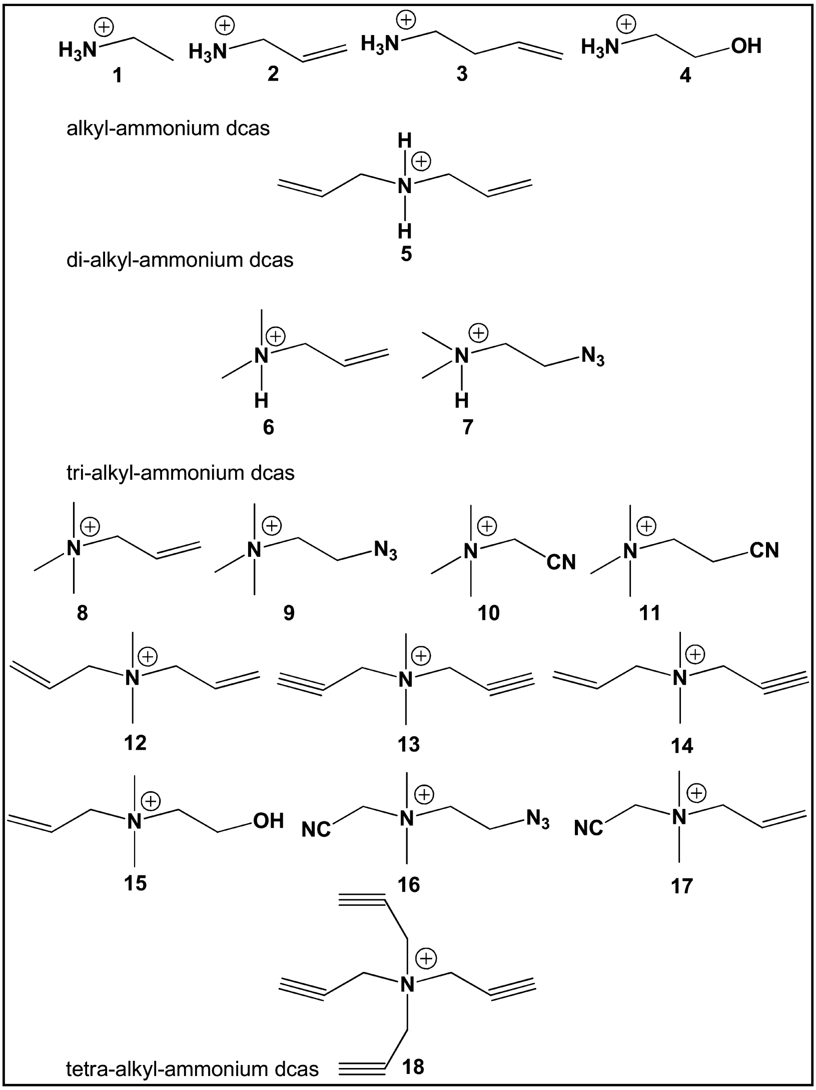
1
2
3
4
alkyl-ammonium dcas
5
di-alkyl-ammonium dcas
6
7
tri-alkyl-ammonium dcas
8
9
10
11
12
13
14
15
16
17
18
tetra-alkyl-ammonium dcas

Scheme 2. Substituted ammonium dicyanamides investigated.

Downloaded by FORDHAM UNIV on December 19, 2012 | http://pubs.acs.org
Publication Date (Web): December 18, 2012 | doi: 10.1021/bk-2012-1117.ch001

Table 1. Physical properties of the ammonium IL dcas

Compound dicyanamide	*melting point [°C]*	*decomp. onset [°C]*	*Viscosity 25°C [cP]*
1	46	86	[a]
2	11	78	95
3	[b]	75	120
4	14	[c]	106
5	37	71	37[b]
6	[b]	108	[c]
7	16	95	74
8	28	229	26[b]
9	16	187	81
10	122	176	[a]
11	79	113	[a]
12	[b]	200	37
13	74	155	[a]
14	23	172	111
15	-4	193	87
16	[d]	100	[a]
17	35	144	[a]
18	113	147	[a]

[a] solid. [b] supercooled liquid. [c] not determined. [d] not observed.

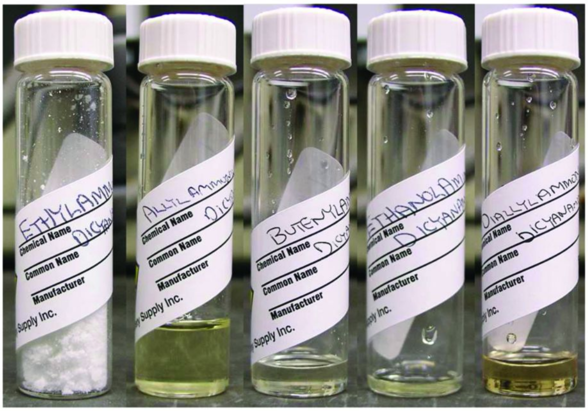
ETHYLAMM
DICYAN
ALLYLAMMON
DICYA
BUTENYLAM
DICYA
ETHANOLAM
DICYANAM
DIALLYLAMMON
DICYANA
Chemical Name
Common Name
Manufacturer
Supply Inc.

*Figure 2. Protic IL dcas **1**, **2**, **3**, **4** and **5**.*

Downloaded by FORDHAM UNIV on December 19, 2012 | http://pubs.acs.org
Publication Date (Web): December 18, 2012 | doi: 10.1021/bk-2012-1117.ch001

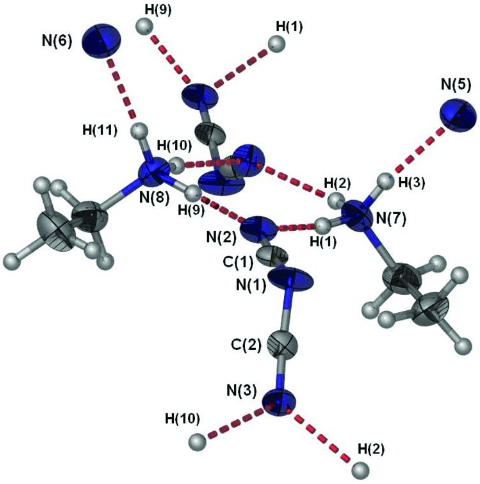

Figure 3. Molecular structure and hydrogen-bond network in ***1****. (Thermal ellipsoids shown at 50% probability level).*

Represented by compounds **7** and **9**, the intrinsic thermal stabilities of protic and aprotic IL dcas are illustrated in Figure 4. The TGA study on **9** (isothermal at 75°C) revealed a weight loss of less than 0.2% after 100h compared to over 30% after only 48h for **7**. Compounds **7** and **9** were prepared from the same parent amine, dimethylazidoethyl amine (DMAZ) (**9** was also investigated by Shreeve (*10*)). This amine was considered for a time as a replacement for hydrazine in bipropellant applications (*20*) and, therefore, it seemed ideally suited as a starting point for ammonium ILs.

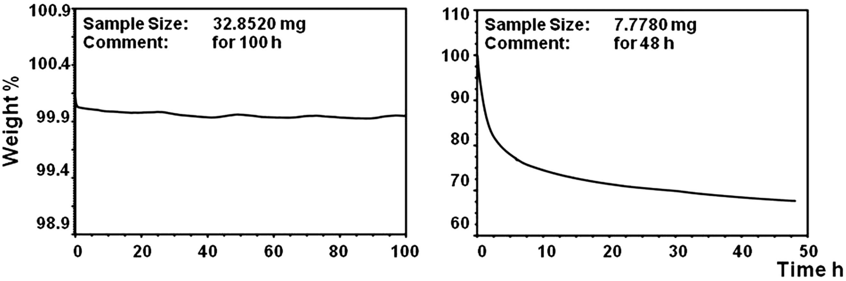

Figure 4. TGA isothermal at 75°C of ***9*** *(left) and 7 (right).*

Downloaded by FORDHAM UNIV on December 19, 2012 | http://pubs.acs.org
Publication Date (Web): December 18, 2012 | doi: 10.1021/bk-2012-1117.ch001

Reactivity of Protic and Aprotic IL dcas with WFNA

The next step was to test the reactivity of the ILs towards white fuming nitric acid (WFNA) and measure approximate ID times. Tests with other oxidizers, *i.e.* N_2O_4 (NTO) and 93% H_2O_2 did not produce ignition. Only RTILs **2**, **5**, **8**, **9**, **12**, **14** and **15** were tested because the initial quantities of **3**, **4** and **7** were consumed in characterization. Solids were not tested. The results are presented in Table 2.

Table 2. Hypergolic ignition of ammonium IL dcas with WFNA

Compound dca	*1st test ID time [ms]*	*2nd test* ID time [ms]*	*3rd test* ID time [ms]*
2	NI[a]	88	97
5	NI	149	185[b]
8	40		
9	34		
12	69		
14	50		
15	NI	198	
19	NI	NI	155[b]

* freshly prepared sample. [a] NI = No ignition. [b] ignition on second drop.

The first test series might lead to the conclusion that protic IL dcas and those containing hydroxyl functionalities are not hypergolic. Protic dca salts are known to undergo cyclization upon heating which could explain the initial drop test results, as otherwise reactive species are diverted from ignition. Examples in the literature are ammonium and guanidinium dcas forming melamine (*21*, *22*) and hydrazinium dca cyclizing to guanazole (*23*) (Scheme 3).

Although these cyclization reactions are exothermic and can lead to explosions, the end products have high melting and decomposition points and are not hypergolic with WFNA (*23*). Cyclization may compete with condensed phase pre-ignition chemistry of the dca anion. In fact, cyclization products have been found in the residue of the reaction of some IL dcas with WFNA (*24*).

In an effort to substantiate the hypothesis concerning inhibition of ignition by a hydroxyl group, a new IL was prepared, 1-(2-hydroxyethyl)-4-amino-1,2,4-triazolium dca, **19** (Scheme 4). It has a decomposition onset of 154°C and a viscosity of 747cP at 25°C.

An initial test produced a violent reaction but no ignition with WFNA (Table 2). Two more batches were freshly prepared and gave the same negative result. During the third experiment a second drop was inadvertently released from the needle and hit the oxidizer 3016 ms after the first drop. Ignition followed after an additional 155 ms. This might have occurred because of exothermic events following the addition of the first drop.

Downloaded by FORDHAM UNIV on December 19, 2012 | http://pubs.acs.org
Publication Date (Web): December 18, 2012 | doi: 10.1021/bk-2012-1117.ch001

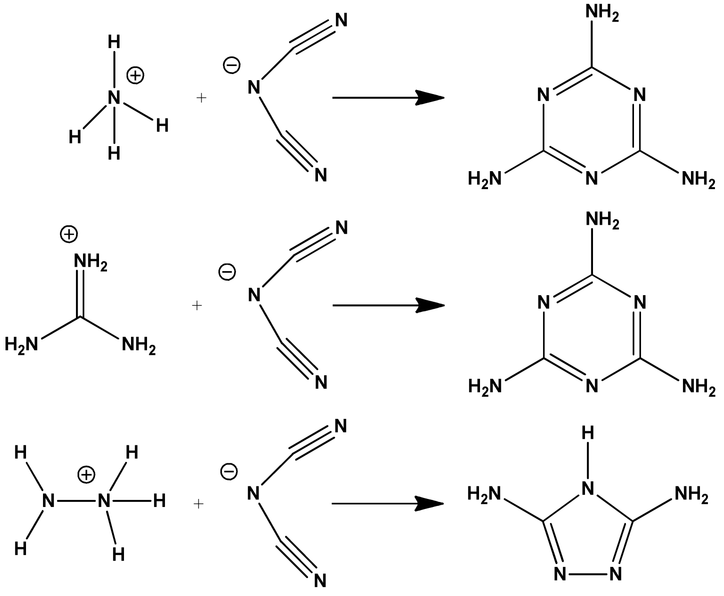

Scheme 3. Known cyclization reactions of some dicyanamides.

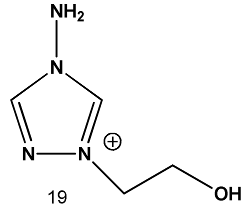

Scheme 4. 1-(2-hydroxyethyl)-4-amino-1,2,4-triazolium dicyanamide.

These results prompted us to reinvestigate ILs **2**, **5**, and **15** which previously gave negative drop test responses. While the initial samples had been stored at ambient conditions for a few weeks before the drop tests (and may have undergone some preliminary cyclization), freshly prepared samples were immediately subjected to drop tests. All three samples ignited with the first drop (Table 2). A third sample of **2** gave the same result as the second, but for **5** a second drop (arriving 3892 ms after the initial drop) was necessary, with ignition following after 185 ms.

Before we continue to discuss drop tests in more detail, the prevalence of dca cyclization reactions is illustrated by our investigation of hydroxyl-ammonium dca, **20**. The thermally induced cyclization product was reported to be 3,5-diamino-1,2,4-oxadiazole, **21** (Scheme 5) (*25*). After preparing **20** at ambient temperature, the NMR spectra indicated contamination with **21**. The ring structure was confirmed by a single-crystal X-ray determination (Figure 5).

Downloaded by FORDHAM UNIV on December 19, 2012 | http://pubs.acs.org
Publication Date (Web): December 18, 2012 | doi: 10.1021/bk-2012-1117.ch001

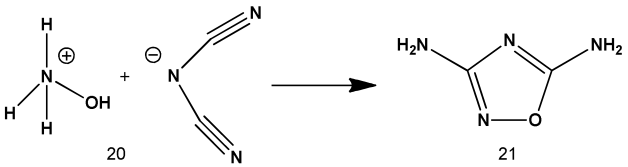

Scheme 5. Cyclization of hydroxylammonium dicyanamide.

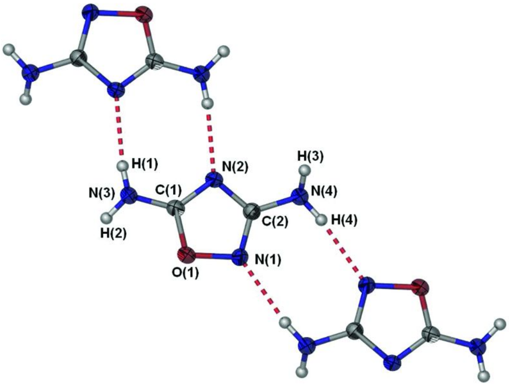

*Figure 5. Molecular structure and hydrogen-bond network of **21**. (Thermal ellipsoids shown at 50% probability level).*

To further explore the reactivity of this barely investigated diamino-oxadiazole, a simple protonation (*26*) with HCl as well as reaction with a transition metal salt, $Cu(NO_3)_2{\bullet}H_2O$, were carried out. The X-ray structures of the obtained materials, **22** and **23**, are shown in Figure 6 and 7.

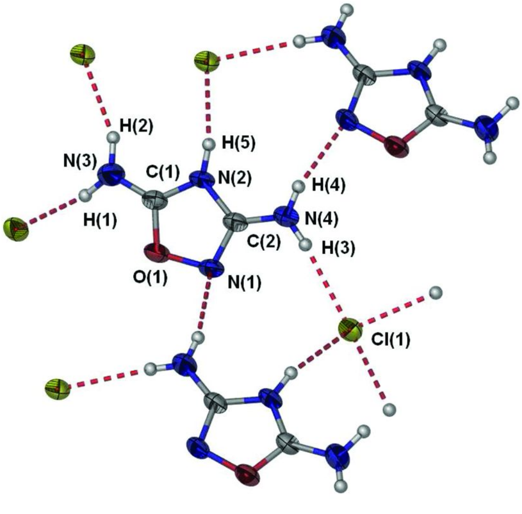

*Figure 6. Molecular structure and hydrogen-bond network of **22**. (Thermal ellipsoids shown at 50% probability level).*

Downloaded by FORDHAM UNIV on December 19, 2012 | http://pubs.acs.org
Publication Date (Web): December 18, 2012 | doi: 10.1021/bk-2012-1117.ch001

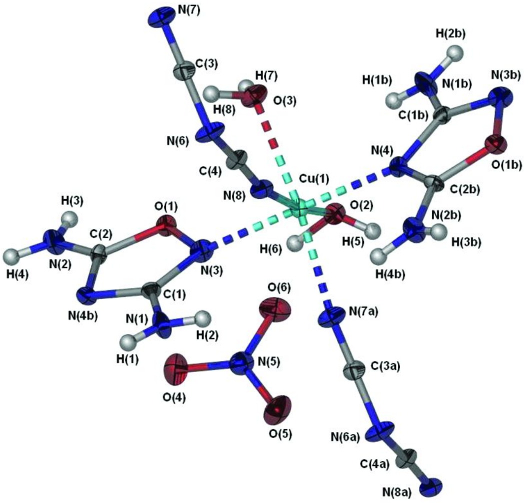

Figure 7. Molecular structure of ***23****. (Thermal ellipsoids shown at 50% probability level).*

Figure 7 illustrates that in **23** the heterocycle coordinates through both ring nitrogens. Contamination with dca is apparent as the Cu complexes dca anions as well.

Drop Test Reliability and Reproducibility

At this stage it seems appropriate to make some more general remarks about drop tests. In most cases ignition occurred with a marked "pop" sound. Popping phenomena are known in many hypergolic systems where they have been characterized as explosions. Systematic studies have been undertaken to minimize their occurrence in the hydrazine-NTO system (*27*, *28*).

With regard to ID times, different laboratories rarely report the same ID time for the same compound, but they generally agree on the rankings of propellant combinations (*1*). Being so simple, quick and inexpensive, these tests and the rankings obtained from them are an indispensable resource for the propellant chemist, even if they do not definitively measure the intrinsic ID. They are certainly no substitute for subsequent small engine tests to solve "popping" and other potential hard-start issues.

Nevertheless, some simple actions can enhance their reliability and reproducibility and increase confidence in the rankings of IDs determined. In our laboratory the apparatus has been moved into a dedicated drybox with inert nitrogen atmosphere to eliminate interference from atmospheric oxygen and to more reliably assess the reactivity of moisture-sensitive materials. Also the fuel is dropped into a cuvette with a standard 250µL volume of the oxidizer. Hypergolic reactions which require multiple drops for the same oxidizer aliquot do not provide ID data which we regard as significant. Furthermore, a remote-controlled syringe is used to keep the flow rate, height and drop sizes constant for each fuel and a standard IL, **9**, is employed to confirm the quality of the WFNA used for each day's tests. The details of this test and the importance of WFNA purity are discussed later in the chapter.

Many variables influence these drop test results. For example, drop sizes are determined by surface tension, viscosity, etc. Fuel and oxidizer temperature are major factors. In addition, each drop test provides different speed and efficiency of mixing and a variation of the local oxidizer-to-fuel ratio. Whether the fuel or the oxidizer is dispensed from the syringe is also important. In the case of IL dcas, ID times were recorded as short as 15 ms if the fuel is dropped into a pool of oxidizer (*5*), but upon reverse addition the ID time can be greater than 1 second (*13*). An even more subtle effect was observed in the class of IL nitrocyanamides (nca) exemplified by trimethylazidoethyl nca, **24** (Scheme 6). This material was reported to ignite within 8 ms with WFNA (*10*), but with our test using a 21-gauge syringe needle, no ignition was observed. Only upon changing to a larger 18-gauge needle, from which presumably a larger drop was released, were we able to observe ignition with an ID time of 156 ms.

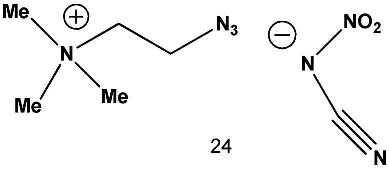

24

Scheme 6. Trimethylazidoethyl nitrocyanamide.

Clearly, not all of these effects can be isolated in such simple tests but the data are informative nonetheless. Our results would seem to caution against over-interpreting single tests. This nearly resulted in mischaracterization of the WFNA hypergolicity of **2**, **5**, **15** and **19**. Similarly misplaced confidence in a single positive result can lead to unwarranted development efforts.

IL Mixtures as Fuels

Some ammonium dcas (Table 1) are solids and therefore did not meet our initial criteria to be subjected to drop tests. Although liquids can be obtained by melting salts, room temperature liquids are preferred as propellants. The cation of **18** would not be expected to form a RTIL because of its relatively high symmetry. In fact, **18** is a solid at room temperature with a melting point of 113°C and a density of 1.18 g/cm^3 (Table 1). Its X-ray structure is shown in Figure 8.

Downloaded by FORDHAM UNIV on December 19, 2012 | http://pubs.acs.org
Publication Date (Web): December 18, 2012 | doi: 10.1021/bk-2012-1117.ch001

Downloaded by FORDHAM UNIV on December 19, 2012 | http://pubs.acs.org
Publication Date (Web): December 18, 2012 | doi: 10.1021/bk-2012-1117.ch001

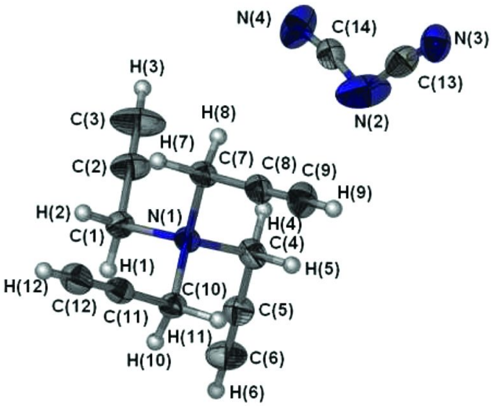

*Figure 8. X-ray crystal structure of **18**. (Thermal ellipsoids shown at 50% probability level).*

Roughly twenty-five weight percent of **18** was dissolved in **9** in the hope, based on the degree of unsaturation, that this mixture would ignite with NTO in addition to WFNA. While the mixture ignited with WFNA, the NTO test was negative. This strategy of optimizing properties by mixing only partially satisfactory ILs and also the goal of enlarging the range of oxidizers led us to investigate the next class of ILs in an effort to overcome some of the shortcomings of IL dcas.

Higher Density Dicyanamides

High propellant density is often desirable, especially for small vehicles or spacecraft, improving tank size, overall vehicle weight, cost and system lifetime. Typical IL dcas possess densities between 1.1 and 1.2 g/cm^3. A literature review shows that unsubstituted ammonium (*21*) and guanidinium dcas (*22*, *29*) can possess densities of 1.3 g/cm^3 or greater (Scheme 7).

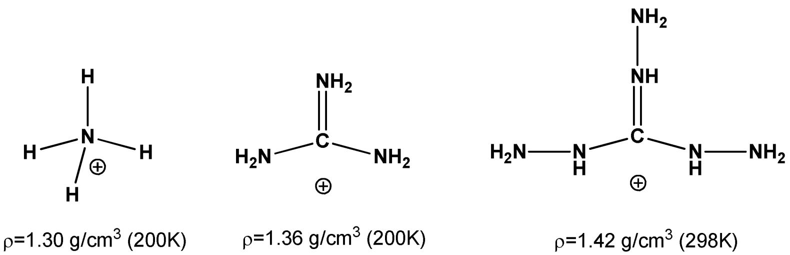

Scheme 7. Higher density dicyanamides.

The substituted ammonium IL dcas have just been addressed, and in this connection we investigated the X-ray structure of the unsubstituted hydrazinium dicyanamide, **25** (*18*, *30*). The material showed a melting point (decomposition/transformation onset) of 84°C, within the regime of an IL, and the crystal density is 1.48 g/cm^3 (173K). Among the simple ammonium-,

Downloaded by FORDHAM UNIV on December 19, 2012 | http://pubs.acs.org
Publication Date (Web): December 18, 2012 | doi: 10.1021/bk-2012-1117.ch001

hydrazinium- and guanidinium-dcas, **25** has the highest density. Unfortunately, it easily undergoes thermal cyclization to guanazole (Scheme 3), either in solution or in the solid state (*23*).

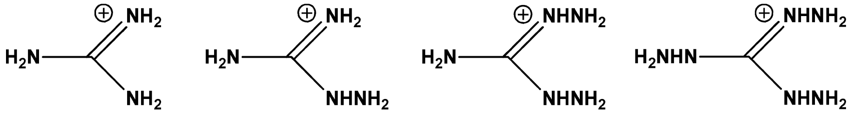
⊕ NH2
H2N
NH2
⊕ NH2
H2N
NHNH2
⊕ NHNH2
H2N
NHNH2
⊕ NHNH2
H2NHN
NHNH2

26 28 29 27

Scheme 8. Guanidinium and aminated guanidinium dicyanamides.

Guanidinium dca, **26** (*22*, *31*, *32*) and triaminoguanidinium (TAG) dca, **27** (*29*, *33*) have been reported previously. The missing links in the chain of aminated guanidinium dcas are aminoguanidinium, **28** and diaminoguanidinium (DAG), **29** dcas (Scheme 8). Their single-crystal X-ray structures are given in Figure 9.

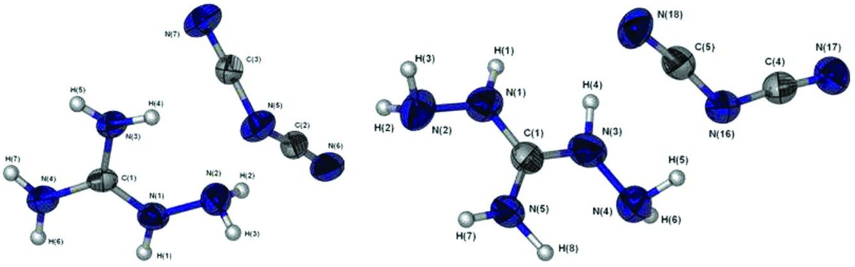
N(7)
C(3)
N(5)
C(2)
N(6)
H(5)
H(4)
N(3)
H(7)
N(4)
C(1)
N(1)
N(2)
H(2)
H(6)
H(1)
H(3)
N(18)
C(5)
C(4)
N(17)
H(3)
H(1)
N(1)
H(4)
H(2)
N(2)
C(1)
N(3)
N(16)
H(5)
N(5)
N(4)
H(6)
H(7)
H(8)

*Figure 9. X-ray crystal structure of **28** (left) and **29** (right) (Thermal ellipsoids shown at 50% probability level).*

As can be seen from Table 3 all the guanidinium dcas are solids at room temperature. Furthermore, like the protic ammonium dcas, they show only marginal thermal stability as is evidenced by low decomposition onsets.

Table 3. Physical properties of guanidinium dcas

Compound dca	*melting point [°C]*	*decomp. onset [°C]*	*Density ρ [gcm⁻³]*
26[a]	57	145	1.38
28	55	120	1.41
29	61	112	1.36
27[b]	124	150	1.42

[a] ref (*21*). [b] ref (*28*).

Downloaded by FORDHAM UNIV on December 19, 2012 | http://pubs.acs.org
Publication Date (Web): December 18, 2012 | doi: 10.1021/bk-2012-1117.ch001

Since three of the four salts have melting points considerably below 100°C we decided to subject them to drop tests (Table 4). The salts were heated until clear liquids were obtained. Ignition was observed between NTO and **29** but not **26** and **28**. **26** is known to undergo cyclization upon heating which might have been partially responsible for its negative results (Scheme 3). Repeating these tests with the solid guanidinium salts did not yield ignition. Therefore, preheating possibly lowered the activation barrier toward ignition. In the context of our drop test caveats, we do not intend to label the ignition of melted salts as hypergolic (and refrain from giving misleading ID times). Nevertheless we present them as justification for seeking hypergolic RTIL mixtures with these ILs as additives. Accordingly, a mixture of **29** and **9** (0.57 : 1.00 molar ratio) was prepared. The solution had a viscosity of 139cp and ignited with NTO, but the ID time was too long to justify further propellant development (Table 4).

Table 4. Ignition tests of melted guanidinium dcas towards WFNA and NTO

Compound Dca	*WFNA*	*NTO*
26	NI[a]	NI
28	NI	NI
29	I[b]	I
9/29 1.00 : 0.57[c]	I	I

[a] NI = no ignition. [b] I = ignition. [c] liquid mixture.

Given the encouraging test results, the question of whether DAG might be a "trigger" for ignition with different oxidizers was addressed by preparing two other salts, DAG tricyanomethanide (tcm), **30** and DAG azide, **31**. The tcm anion was chosen because TAG tcm has been reported as being hypergolic with NTO (*34*), while **31** was previously mentioned in the context of explosives and propellants (*35–38*). **30** has a melting point of 90°C and a decomposition onset of 189°C. **31** is a high-nitrogen compound (84.8 wt%) with a melting point of 109°C and its excellent thermal stability (decomposition onset 187°C) can be explained by the extensive hydrogen bonding observed in the crystal structure (Figure 10). To avoid the use of silver azide in the production of **31**, DAG tetrafluoroborate, **32** was prepared and treated with potassium azide in isopropyl alcohol according to Scheme 9. Both DAG salts were heated to clear liquids and drop tests were performed (Table 5).

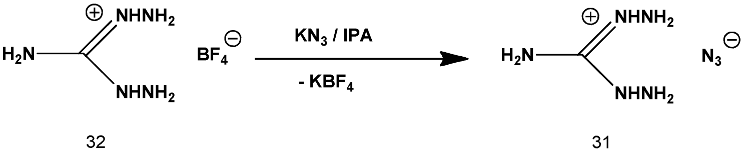

Scheme 9. Silver-free synthesis of diaminoguanidinium azide.

Table 5. Ignition tests of melted DAG salts 29, 30 and 31

Compound	*WFNA*	*NTO*
29	I[a]	I
30	NI[b]	I
31	NI	NI

[a] I = ignition. [b] NI = no ignition.

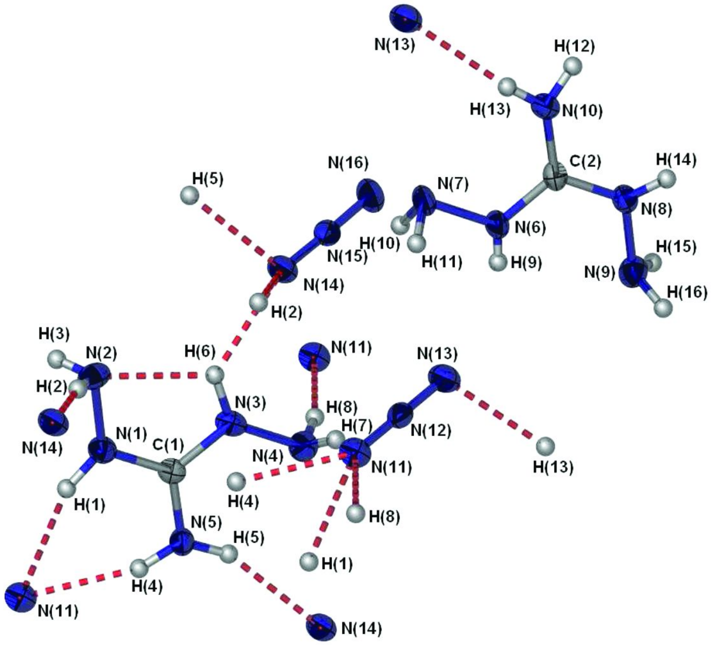

Figure 10. Molecular structure and hydrogen-bond network of ***31*** *(Thermal ellipsoids shown at 50% probability level).*

Downloaded by FORDHAM UNIV on December 19, 2012 | http://pubs.acs.org
Publication Date (Web): December 18, 2012 | doi: 10.1021/bk-2012-1117.ch001

Given the many examples reported, it is reasonable to suppose that it is the dca anion which is responsible for the ignition of IL dcas with WFNA and that the cation plays only a secondary role, influencing the ID time. Our investigations so far suggest that ignition with NTO might be more complex, explaining why only a few hypergolic salts have been found. A successful design path may require particular features on both the cation and anion.

The hydrazidinium cation not only bears a similarity to the DAG cation but it also opens design space by substitution of the central carbon (Scheme 10).

Hydrazidinium chloride **33** (*39*), nitrate **34**, dca **35** and tcm **36** salts were prepared and their X-ray crystal structures are depicted in Figures 11 and 12. These are not RTILs, but they were also subjected to drop tests, either as solids or heated liquids (Table 6).

Downloaded by FORDHAM UNIV on December 19, 2012 | http://pubs.acs.org
Publication Date (Web): December 18, 2012 | doi: 10.1021/bk-2012-1117.ch001

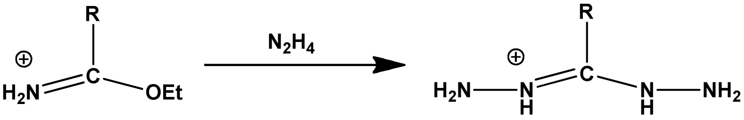
R
⊕
H₂N
C
OEt
N₂H₄
R
⊕
H₂N
N
H
C
N
H
NH₂

Scheme 10. *Synthesis route to hydrazidinium cations.*

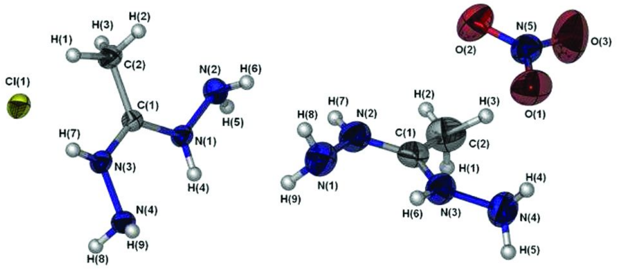
Cl(1)
H(1)
H(3)
H(2)
C(2)
C(1)
N(2)
H(6)
H(5)
H(7)
N(3)
N(1)
H(4)
N(4)
H(9)
H(8)
O(2)
N(5)
O(3)
O(1)
H(8)
H(7)
N(2)
C(1)
H(2)
H(3)
C(2)
N(1)
H(9)
H(1)
H(6)
N(3)
H(4)
N(4)
H(5)

Figure 11. X-ray crystal structures of ***33*** *and* ***34****. (Thermal ellipsoids shown at 50% probability level).*

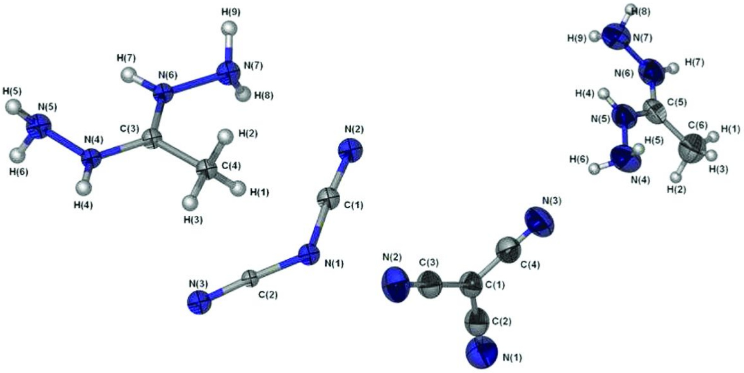
H(9)
H(7)
N(6)
N(7)
H(8)
H(5)
N(5)
N(4)
C(3)
H(2)
C(4)
H(6)
H(4)
H(1)
H(3)
N(2)
C(1)
N(1)
N(3)
C(2)
H(8)
H(9)
N(7)
N(6)
H(7)
H(4)
C(5)
N(5)
C(6)
H(1)
H(5)
H(6)
N(4)
H(2)
H(3)
N(3)
N(2)
C(3)
C(4)
C(1)
C(2)
N(1)

Figure 12. X-ray crystal structures of ***35*** *and* ***36****. (Thermal ellipsoids shown at 50% probability level).*

The reactivity of the hydrazidine salts is quite similar to that observed for the DAG salts. While tests of the chloride and nitrate were negative, molten samples of **35** and **36** ignited with NTO. Unfortunately, preliminary investigations showed that longer alkyl chains lead to decreased thermal stability. The crystal structure of butyrhydrazidinium chloride, **37** is shown in Figure 13 (*39*).

Downloaded by FORDHAM UNIV on December 19, 2012 | http://pubs.acs.org
Publication Date (Web): December 18, 2012 | doi: 10.1021/bk-2012-1117.ch001

Table 6. Ignition tests of liquid or solid 33, 34, 35 and 36

Compound	*WFNA*	*NTO solid salt*	*NTO liquid salt*
33	NI[a]	NI	ND[b]
34	NI	NI	NI
35	I[c]	NI	I
36	NI	NI	I

[a] NI = no ignition. [b] ND = not determined. [c] I = ignition.

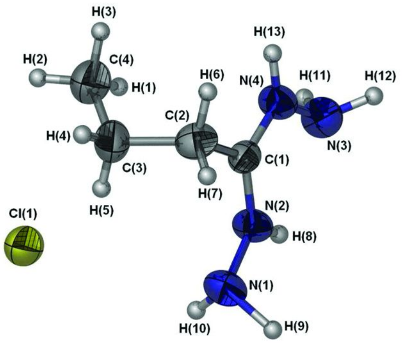

*Figure 13. X-ray crystal structures of **37**. (Thermal ellipsoids shown at 50% probability level).*

Some Mechanistic Considerations

The initial discovery of the hypergolic reactivity of IL dcas with WFNA generated some interest in the pre-ignition reaction chemistry. Inspired by some studies on mono- and dinitrobiuret by Thiele (*40*) and later Klapötke (*41*), a mechanism was proposed in which the first step is nucleophilic attack of the nitrate anion on the triple-bound carbon (*6*). Initial mechanistic experiments were based on two assumptions: that the nitric acid used is indeed 100% nitric acid and that the ionic liquids tested are free of dissolved impurities.

100% nitric acid is a highly complicated system. Nominally nonaqueous nitric acid autodissociates to form small amounts of $H_2NO_3^+$ which, itself, decomposes into its anhydride and water, further shifting the equilibrium to the right (Scheme 11). Thus nitric acid always contains some water and the water leads to formation of additional ions (Scheme 12).

$$\begin{array}{lcl} 2HNO_3 & \rightleftharpoons & H_2NO_3^+ + NO_3^- \\ H_2NO_3^+ & \rightleftharpoons & H_2O + NO_2^+ \\ \hline 2HNO_3 & \rightleftharpoons & NO_2^+ + NO_3^- + H_2O \end{array}$$

Scheme 11. Autodissociation of 100% nitric acid.

Purity is a major issue in IL research, since it is well established that impurities dramatically change physical properties. While we were satisfied with the purity of our ILs, we became interested in the effect of diluting the oxidizer or fuel with water or other solvents. As a practical matter the addition of water to a fuel has been used to decrease the combustion temperature.

Two IL hypergols, 1-butyl-3-methyl imidazolium (BMIM) dca and **9**, were diluted with either water or methanol. **9** continued to ignite with water dilution beyond 20 wt% and below a diluent concentration of 14 wt% there was no noticeable effect on the ID (Figure 14).

$$H_2O + HNO_3 \rightleftharpoons H_3O^+ + NO_3^-$$

$$3HNO_3 \rightleftharpoons H_3O^+ + NO_2^+ + 2NO_3^-$$

Scheme 12. Further ion formation in 100% nitric acid via water.

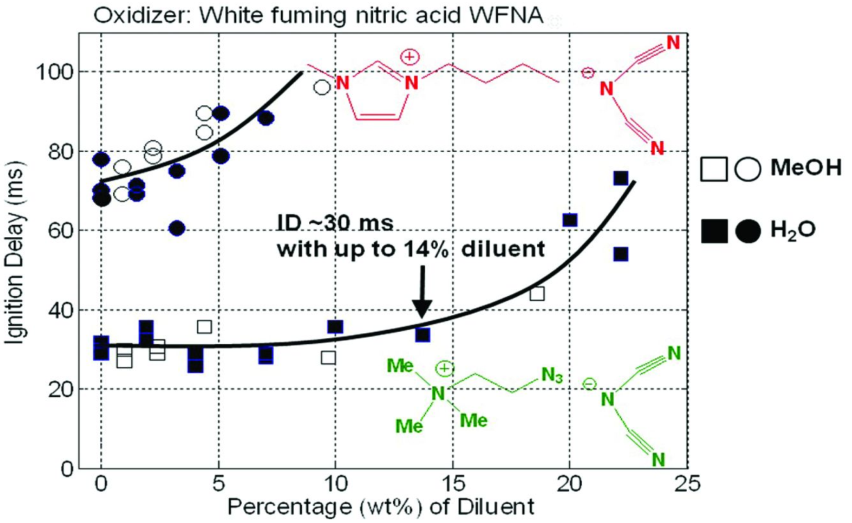

*Figure 14. Influence of dilution on WFNA ID time for BMIM dca and **9**.*

However, when the oxidizer was diluted with water, ignition depended more strongly on which IL was used. A commercial sample of BMIM dca showed no ignition with 96% nitric acid whereas **9** still ignited with 90% nitric acid.

That the quality of the WFNA is of crucial importance for the ID time was already understood in the 1950's (*1*). This justifies our daily check of WFNA quality using **9**. With this material we have accumulated over 100 ID times varying between 20 and 40 ms. An ID outside of this interval (we have recorded delays of up to 300 ms) necessitated replacement of the oxidizer with a fresh sample. We suspect acid quality as a main culprit for the varying ID times reported by different laboratories. We further think it might be advisable for future nitric-acid work to focus on stabilized IRFNA rather than WFNA, especially since IRFNA is the preferred nitric acid for propellant applications.

Downloaded by FORDHAM UNIV on December 19, 2012 | http://pubs.acs.org
Publication Date (Web): December 18, 2012 | doi: 10.1021/bk-2012-1117.ch001

Downloaded by FORDHAM UNIV on December 19, 2012 | http://pubs.acs.org
Publication Date (Web): December 18, 2012 | doi: 10.1021/bk-2012-1117.ch001

Since IL dcas maintain their hypergolicity towards WFNA with substantial dilution, it seems reasonable that water may play a more active role in the ignition mechanism. An investigation of nitrocyanamide decomposition in strong mineral acids established that the acid-catalyzed decomposition involves the cyano group (*42*). The formal addition of H_2O across the CN triple bond was observed with formation of nitrourea (Scheme 13).

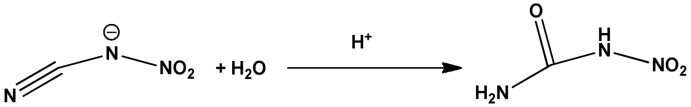

Scheme 13. Reaction of nitrocyanamide with aqueous mineral acids.

Additionally alkyldicyanamides selectively add water across the CN triple bond in both 1.4N and 12.3N sulfuric acid (Scheme 14) (*43*, *44*).

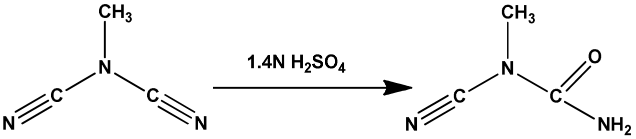

Scheme 14. Reaction of alkyldicyanmides in aqueous sulfuric acid.

Furthermore, it has been demonstrated that sodium dca reacts with HCl, HBr and HI in aequeous solutions to give cyanourea and biuret, while in alcoholic solutions O-ethyl-N-cyanourea is formed (Scheme 15) (*45*).

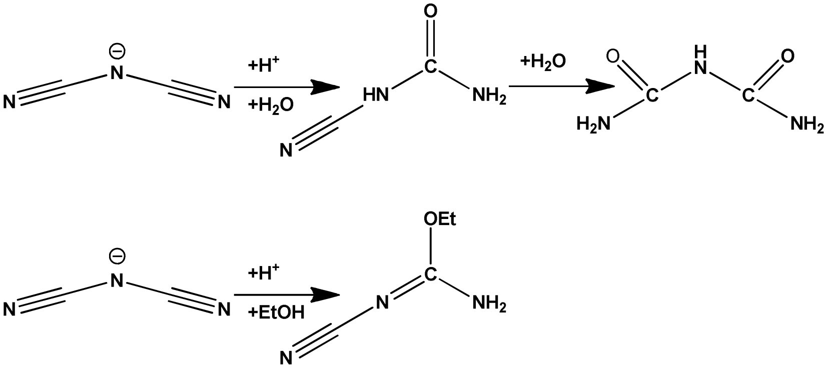

Scheme 15. Reaction of dicyanamide in aqueous or alcoholic acidic solutions.

In one of our IL dca samples we found an impurity that was identified as O-methyl-N-cyanourea, **38**, (*c.f.* Figure 15) which formed by the addition of a solvent molecule (methanol) across one of the triple bonds.

Downloaded by FORDHAM UNIV on December 19, 2012 | http://pubs.acs.org
Publication Date (Web): December 18, 2012 | doi: 10.1021/bk-2012-1117.ch001

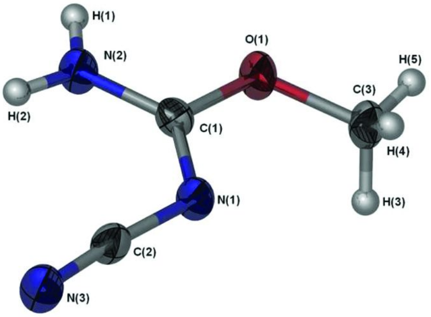

*Figure 15. X-ray crystal structure of **38**. (Thermal ellipsoids shown at 50% probability level).*

Thus, based on our dilution results and literature reactions we propose the mechanism shown in Scheme 16. The action of water leads to the formation of the proposed products cyanourea, biuret, isocyanic acid, cyanamide and urea. Corresponding biuret derivatives have also been observed in the reaction of alkyldicyanamides with sulfuric acid (*44*). The formation of the end products previously identified (*6*), like the nitrobiurets, N_2O and CO_2, may also arise by further reaction of these intermediates with nitric acid.

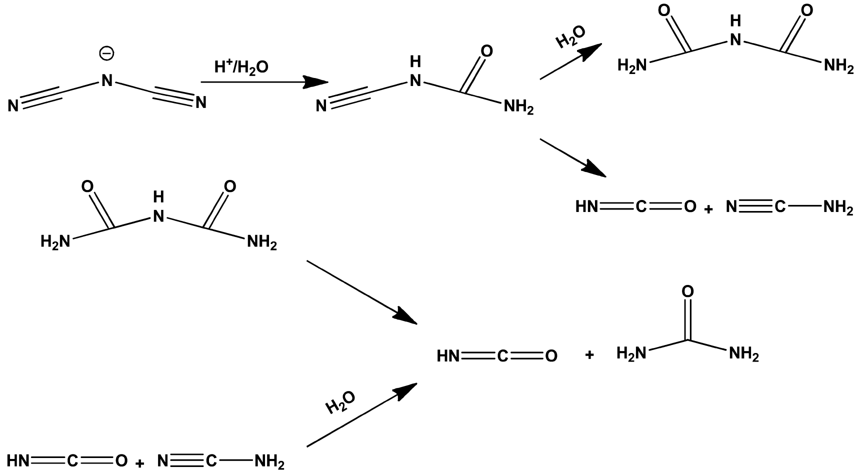

Scheme 16. Proposed reaction mechanism between dicyanamides and nitric acid based on dilution results.

One of the anions which could initially be formed during an acid-catalyzed addition of water to the dicyanamide anion is the cyanoureate anion (cu) (Scheme 17).

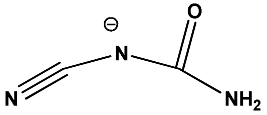

Scheme 17. Cyanoureate anion.

BMIM cu, **39** was prepared and obtained as a highly viscous liquid. Drop tests with WFNA revealed no hypergolic properties and so it seems that the hypergolic reactivity of dca has been tamed by the addition of water across the CN triple bond. In the hope of obtaining a more suitable liquid, trimethylazidoethyl ammonium cu, **40** was prepared but was obtained as a solid with a melting point of 105°C (Figure 16) (*c.f.* its corresponding dca, **9**, an RTIL with a melting point of 16°C, Table 1).

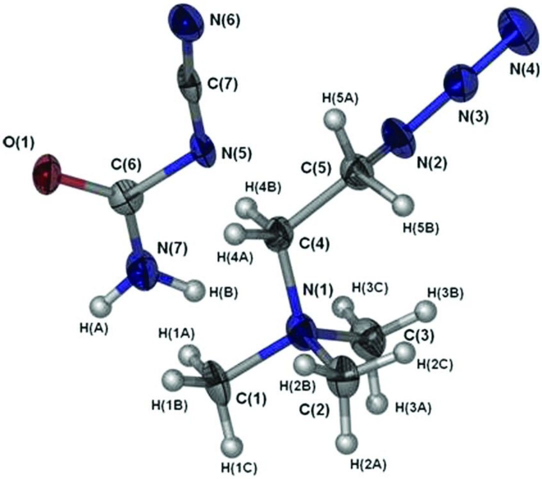

*Figure 16. X-ray crystal structure of **40**. (Thermal ellipsoids shown at 50% probability level).*

Current and Future Directions

Our "hunt for the hypergol" (*1*) continues to be a rollercoaster ride with flaming surprises as well as disappointing splashes. Designing ILs which fulfill all the other requirements for propellants is, in itself, a difficult task; adding the requirement of hypergolicity only compounds the problem. This should not be too surprising when one compares some of the products of previous searches. For example, there appears to be little structural similarity between hydrazine and furfuryl alcohol (Scheme 18), yet both are hypergolic with several oxidizers.

Especially puzzling is the fact that many other materials containing directly bound nitrogens or furans with various pendant groups show no hypergolicity. While our discovery of hypergolicity in a new class of single-component RTILs opened new regions of the chemical landscape, a great deal of work remains to satisfy the additional requirements of physical properties, stability, and energy density.

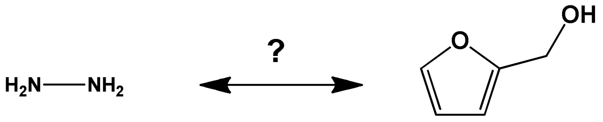

Scheme 18. Two hypergolic fuels with no obvious structural similarity.

Downloaded by FORDHAM UNIV on December 19, 2012 | http://pubs.acs.org
Publication Date (Web): December 18, 2012 | doi: 10.1021/bk-2012-1117.ch001

Downloaded by FORDHAM UNIV on December 19, 2012 | http://pubs.acs.org
Publication Date (Web): December 18, 2012 | doi: 10.1021/bk-2012-1117.ch001

Hydrogen peroxide in concentrated aqueous solution might be an alternative hypergolic oxidizer for some systems. It is attractive for its environmentally benign decomposition products and relatively small ambient vapor pressure. A large part of our current effort focuses on ILs incorporating boro-aluminum hydride scaffolds, but we continue to pursue systems limited to C, H, N and O atoms because many applications require particle-free combustion.

Constrained to this part of the periodic table we are still working to overcome the current limitations of most known hypergols to nitric acid. Relatively few have been found to be hypergolic with higher performing N_2O_4. Although N_2O_4 is highly toxic it is much less corrosive than nitric acid, and therefore easier to handle, and we hope to find more IL partners for this oxidizer. We expect fuel mixtures to play a prominent role, not only in tuning the material properties, but also in surmounting the difficult ignition barrier.

In pressing our quest to fulfill the promise of ILs as unique, energy-dense fuels, we draw on chemical propellant history while maintaining a healthy respect and skepticism for the value and limitations of simple drop tests. We expect that the route to practical fuels lies not so much in the discovery of a definitive "magic trigger group" but in the careful combination of particular structural features on both the cation and the anion, perhaps in solutions. Our experience with NTO hypergolicity indicates that the cation cannot be completely ignored, but anions may be more determinative of hypergolicity and higher energy content.

Experimental

Starting materials were purchased from either the Aldrich Chemical Company, Inc. or TCI America and were used without further purification. Noncommercial ammonium halide salts were prepared by standard alkylation procedures from the free amine and appropriate alkylhalide following the methods described in (*46*). Metathesis reactions were carried out according to the general procedure of (*5*) using silver salts of the anions. When nitrate salts are prepared exact stoichiometry is essential. **20** was prepared according to (*25*). **21** was prepared by passing gaseous HCl through a methanol solution of **20**. **22** was prepared according to (*47*), but using **20** instead of DAF. The hydrazidinium halides were prepared according to (*39*). The purity of all materials was confirmed by NMR spectroscopy.

Nonvolatile solids and liquids were handled in the dry-nitrogen atmosphere of a glovebox. The ^{1}H and ^{13}C spectra were recorded on a 400 MHz Ultrashield™ spectrometer at room temperature using 5mm NMR tubes. Glass transition temperatures, melting points and decomposition onsets were determined by differential scanning calorimetry using a Thermal Analyst 200, Dupont 910 Differential Scanning Calorimeter. Measurements were carried out at a heating rate of 10°C/min in sealed aluminum pans with a nitrogen flow rate of 20mL/min starting at -100°C. Thermal gravimetric analysis was carried out using a TA TGA Q5000 instrument holding the sample in a nitrogen atmosphere isothermally at 75°C for 48h or 100h. The single-crystal X-ray diffraction data were collected on a Bruker 3-circle-platform diffractometer equipped with a SMART APEX 2 detector with the χ-axis fixed at 54.74° and using CuK_α or MoK_α radiation from a fine-focus tube. The goniometer head, equipped with a nylon Cryoloop and magnetic base, was used to mount the crystals using perfluoropolyether oil. The data collection as well as structure solution and refinement were carried out using standard procedures with the APEX2 V.2.1-4, SMART V.5.622, SAINT 7.24A, SADABS, and SHELXTL software packages and programs (*48*). CCDC-878949, **1**; CCDC-878950, **18**; CCDC-878951, **21**; CCDC-878952, **22**; CCDC-878953, **23**; CCDC-878954, **28**; CCDC-878955, **29**; CCDC-878956, **31**; CCDC-878957, **33**; CCDC-878958, **34**; CCDC-878959, **35**; CCDC-878960, **36**; CCDC-878961, **37**; CCDC-878962, **38**; CCDC-878963, **40** comprise the supplementary crystallographic data for this paper. They can be obtained free of charge from the Cambridge Crystallographic Data Centre via http://www.ccdc.cam.ac.uk/data_request/cif.

Downloaded by FORDHAM UNIV on December 19, 2012 | http://pubs.acs.org
Publication Date (Web): December 18, 2012 | doi: 10.1021/bk-2012-1117.ch001

Acknowledgments

The authors would like to thank Michael Berman from the Air Force Office of Scientific Research (AFOSR) for supporting this work under AFOSR Award No. FA9300-06-C-0023. The authors are also grateful to Erik Dambach who worked as a Ph.D. student researcher (under Prof. Stephen Heister, Purdue Univ.) at AFRL from April 2008 – July 2008 on the dilution experiments.

References

1. Clark, J. D. *Ignition!*: Rutgers University Press: New Brunswick, NJ, 1972.
2. Jones, C. B.; Haiges, R.; Schroer, T.; Christe, K. O. *Angew. Chem. Int. Ed.* **2006**, *45*, 4981.
3. Tao, G-H.; Huang, Y.; Boatz, J. A.; Shreeve, J. M. *Chem. Eur. J.* **2008**, *14*, 11167.
4. Schneider, S.; Hawkins, T.; Rosander, M.; Mills, J.; Vaghjiani, G.; Chambreau, S. *Inorg. Chem.* **2008**, *47*, 6082.
5. Schneider, S.; Hawkins, T.; Rosander, M.; Vaghjiani, G.; Chambreau, S.; Drake, G. *Energy Fuels* **2008**, *22*, 2871.
6. Chambreau, S.; Schneider, S.; Rosander, M.; Hawkins, T.; Gallegos, C. J.; Pastewait, M. F.; Vaghjiani, G. L. *J. Phys. Chem. A* **2008**, *112*, 7816.
7. Gao, H.; Joo, Y.-H.; Twamley, B.; Zhou, Z.; Shreeve, J. M. *Angew. Chem., Int. Ed.* **2009**, *48*, 2792.
8. Zhang, Y.; Gao, H.; Guo, Y.; Joo, Y.-H.; Shreeve, J. M. *Chem. Eur. J.* **2010**, *16*, 3114.
9. He, L.; Tao, G.; Parrish, D. A.; Shreeve, J. M. *Chem. Eur. J.* **2010**, *16*, 5736.
10. Joo, Y. H.; Gao, H.; Zhang, Y.; Shreeve, J. M. *Inorg. Chem.* **2010**, *49*, 3282.
11. Zhang, Y.; Shreeve, J. M. *Angew. Chem., Int. Ed.* **2011**, *50*, 935.
12. Zhang, Y.; Gao, H.; Joo, Y-H.; Shreeve, J. M. *Angew. Chem., Int. Ed.* **2011**, *50*, 9554.
13. Schneider, S.; Hawkins, T.; Ahmed, Y.; Rosander, M.; Hudgens, L.; Mills, J. *Angew. Chem., Int. Ed.* **2011**, *50*, 5886.

14. McCrary, P. D.; Beasley, P. A.; Cojocaru, O. A.; Schneider, S.; Hawkins, T. W.; Perez, J. P.; McMahon, B. W.; Pfeil, M.; Boatz, J. A.; Anderson, S. L.; Son, S. F.; Rogers, R. D. *Chem. Commun.* **2012**, *48*, 4311.
15. Gabriel, S. *Ber. Dtsch. Chem. Ges.* **1888**, *21*, 2664.
16. Curtius, T. *Ber. Dtsch. Chem. Ges.* **1891**, *24*, 3341.
17. Walden, P. *Bull. Acad. Imp. Sci.* **1914**, 1800.
18. Rosander, M.; Schneider, S.; Hawkins, T.; Mills, J.; Vaghjiani, G.; Chambreau, S. *Prepr. Symp. - Am. Chem. Soc., Div. Fuel Chem.* **2009**, *54*, 167.
19. Kikuta, M.; Hatakeyama, A. E. EP Patent 1619742, 2006.
20. Mellor, B. *Eur. Space Agency* **2004**, *SP-557*, 130.
21. Jürgens, B.; Höppe, H. A.; Irran, E.; Schnick, W. *Inorg. Chem.* **2002**, *41*, 4849.
22. Lotsch, B. V.; Schnick, W. *New J. Chem.* **2004**, *28*, 1129.
23. Frankel, M. B.; Burns, E. A.; Butler, J. C.; Wilson, E. R. *J. Org. Chem.* **1963**, *28*, 2428.
24. Chingin, K.; Perry, R. H.; Chambreau, S. D.; Vaghjiani, G. L.; Zare, R. N. *Angew. Chem., Int. Ed.* **2011**, *50*, 8634.
25. Roemer, J. J.; Kaiser, D. W. U.S. Patent 2648669, 1953.
26. Huttunen, K. M.; Leppanen, J.; Kemppainen, E.; Palonen, P.; Rautio, J.; Jarvinen, T.; Vepsalainen, J. *Synthesis* **2008**, *22*, 3619.
27. Houseman, J.; Lee, A. *J. Spacecraft Rockets* **1972**, *9*, 678.
28. Daimon, W.; Gotoh, Y.; Kimura, I. *J. Propul. Power* **1991**, *7*, 946.
29. Carvalho, D. A.; Stafiej, S. F. U.S. Patent 3405175, 1968.
30. Hooper, J. B.; Borodin, O.; Schneider, S. *J. Phys. Chem. B* **2011**, *115*, 13578.
31. Gast, E.; Schmid, B.; Semmler, P. WO Patent 9948843, 1999.
32. Zhao, Z.; Ueno, K.; Angell, C. A. *J. Phys. Chem. B* **2011**, *115*, 13467.
33. Dixon, S. J; Tunick, B. R.; Brown, E. D. U.S. Patent 20040094250, 2004
34. Frankel, M. B.; Dickinson, L. A. U.S. Patent. 3981899, 1976.
35. Audrieth, L. F.; Hale, G. C. U.S. Patent 2929698, 1960.
36. Niles, E. T. Seaman, B. H. U.S. Patent 3288660, 1966.
37. Oja, P. D. U.S. Patent 3338762, 1967.
38. Oja, P. D.; Niles, E. T. U.S. Patent 3375230, 1968.
39. Neunhoeffer, H.; Degen, H. J.; Koehler, J. J. *Liebigs Ann. Chem.* **1975**, *6*, 1120.
40. Thiele, J.; Uhlfelder, E. *Liebigs Ann. Chem.* **1898**, *303*, 93.
41. Geith, J.; Holl, G.; Klapotke, T. M.; Weigand, J. J. *Combust. Flame* **2004**, *139*, 358.
42. Astrat'ev, A. A.; Kuznetsov, L. L. *Russ. J. Org. Chem.* **2002**, *38*, 1252.
43. Benders, P. H. *Tetrahedron Lett.* **1973**, *37*, 3653.
44. Benders, P. H. *Recl. Trav. Chim. Pays-Bas* **1976**, *95*, 217.
45. Allenstein, E. *Z. Anorg. Allg. Chem.* **1963**, *322*, 265.
46. Schneider, S.; Drake, G.; Hall, L.; Hawkins, T.; Rosander, M. *Z. Anorg. Allg. Chem.* **2007**, *633*, 1701.
47. Stoner, C. E., Jr.; Rheingold, A. L.; Brill, T. B. *Inorg. Chem.* **1991**, *30*, 360.
48. *APEX2 V.2.1-4, SMART V.5.622, SAINT 7.24A, SADABS, SHELXTL*; Bruker-AXS, Inc.: Madison, WI, 2007.

Downloaded by FORDHAM UNIV on December 19, 2012 | http://pubs.acs.org
Publication Date (Web): December 18, 2012 | doi: 10.1021/bk-2012-1117.ch001

Chapter 2

Ionic Liquids in Electrospray Propulsion Systems

Benjamin D. Prince,*,[1] Bruce A. Fritz,[2] and Yu-Hui Chiu[3,4]

[1]Air Force Research Laboratory, Space Vehicles Directorate,
Kirtland AFB, New Mexico 87117
[2]Space and Missile Systems Center, Defense Weather Systems Directorate,
Los Angeles AFB, California 90245
[3]Air Force Research Laboratory, Space Vehicles Directorate,
Hanscom AFB, Massachusetts 01731
[4]Current address: Busek Co., Inc., 11 Tech Circle,
Natick, Massachusetts 01760
*E-mail: benjamin.prince@kirtland.af.mil

This chapter provides a brief introduction to the use of ionic liquids in electric space propulsion systems. Pertinent performance parameters and recent advances in the use of ionic liquids in electrospray propulsion applications are described. Future use and development of these systems requires a combination of experimental investigation and modeling efforts. A theoretical investigation using atomistic molecular dynamics for an ionic liquid, 1-ethyl-3-methylimidazolium bis(trifluoromethylsulfonyl)imide, is presented. A mass spectrometric study of 2-hydroxyethylhydrazinium nitrate energetic ionic liquid emitted from an externally wetted titanium emitter is presented.

Introduction

Modern space vehicles employ a variety of space propulsion systems to meet their mission requirements. These tasks may include lift-off and escape from a planetary surface, orbit-transfer, deorbiting, station-keeping, and attitude control. Each of these maneuvers has uniquely different thrust requirements ranging from escaping Earth's gravitational pull (high thrust) to countering the solar

Not subject to U.S. Copyright. Published 2012 by American Chemical Society

radiation pressure (extremely low thrust). Example propulsion systems include chemical thrusters which produce hot, gaseous molecular products ejected from the spacecraft, electrostatic plasma-based thrusters which efficiently accelerate ionized species, and electrospray thrusters which utilize high electric fields to form and accelerate charged particles from conductive liquids. Comparisons of various space propulsion systems were discussed in a previous ACS publication and interested readers may find this reference insightful (*1*).

Ionic liquids (IL or ILs) constitute salts with melting points below 100 °C while room temperature ionic liquids are those salts which are liquid at room temperature. ILs are composed of cations and anions and the charged composition generally results in relatively high electrical conductivities and low volatility. ILs exhibit thermal stability over wide temperature ranges and many remain liquids allowing their use in applications at elevated temperatures. In general, they cannot reach their boiling point before thermally decomposing at these elevated temperatures. As the temperature is increased the viscosities of these liquids decrease and non-negligible amounts of vapor (though still very low) are observed enabling gas-phase experiments to probe the structures of the IL pairs (*2*). A great deal of flexibility exists in pairing cation and anion combinations to tune the physical properties of ILs for various applications including, briefly, generation of heavy mass ion beams (*3*), CO_2 sequestration (*4*), electrochemistry (*5*), and catalysis/synthesis (*6*, *7*). According to a recent review on the industrial uses of ionic liquids, nearly 10^{18} combinations of cation/anions are possible (*8*). As of 2009, ionic liquid use had become so ubiquitous that it is reported in over 1000 publications per year (*9*).

The use of ionic liquids for electrospray space propulsion (described below) has been suggested in the literature as far back as 2003 (*10*). The use of mixtures of electrolyte and low vapor pressure solvent, such as NaI in formamide, preceded the use of ILs for electrospray propulsion applications (*11*, *12*). From these investigations it became apparent that the properties of IL such as the negligible vapor pressure, high electrical conductivity, and low viscosity provided unique advantages over the conventional salt-solvent system. The successful application of ionic liquids has been demonstrated in a number of laboratory investigations for vacuum electrospray applications (*13–16*). Electrospray thruster technology using IL as propellants has advanced beyond the laboratory and is on the verge of undergoing its first outer-space mission in the Jet Propulsion Laboratory ST7 Disturbance Reduction System (*17*). In the ST7 mission, two electric thrusters are being examined for the follow-on LISA (Laser Interferometer Space Antenna) mission discussed below, a joint effort between NASA and the European Space Agency (ESA). While both systems are based on vacuum electrospray technology, the electrospray/colloid thruster uses an IL propellant (1-ethyl-3-methylimidazolium bis(trifluoromethylsulfonyl)imide) while a separate field emission thruster uses liquid metal propellants (*18–20*). The LISA mission proposes to measure extra-galactic gravity waves by using three spacecraft separated by ~5 million km from one another as an interferometer. Like all interferometers, the careful control of position is essential to the measurements. As such, the propulsion system must counter the ~10 uN/m^2 (near Earth) solar radiation pressure as well as provide exceptional control of positioning on the order of the wavelength of the laser light used. Electrospray thrusters are ideal for this mission owing to their ability to produce constant and consistent thrusts with precision throttling. Although NASA's role in the LISA mission has been scaled back due to funding constraints, the ESA has proposed a mission derived from the LISA proposal (*21*).

Today, IL's are being investigated for use in high thrust chemical propulsion systems owing to the discovery of energetic IL's. Energetic IL's are high energy density materials, some of which are hypergolic (ignite) upon the addition of an oxidizer (*22*). Of particular advantage to the use of IL's in chemical propulsion systems is that their volatility, and thus vapor toxicity, are considerably lower than hydrazine yielding significant safety benefits for ground crews involved in mission preparation (*23*). Since these ILs can be used both chemically and in electrospray thrusters, energetic ionic liquids have the potential to be utilized in multi-mode propulsion. In the chemical application, interaction with the oxidizer results in a fast combustion process that chemically decomposes the propellant and generates hot, gaseous products used to propel the spacecraft. In the electrospray application, the ionic liquid is left unreacted but is field evaporated. Since the same propellant can be used for very different velocity change (ΔV) maneuvers, it reduces the need for additional propellant storage and adds flexibility in mission planning.

This chapter will focus on the application of ILs in electrospray thruster systems with a focus on those systems employing needle-type emitters. The use of ILs in chemical thrusters will only be briefly discussed and the interested reader will find discussion of IL use in chemical combustion in other chapters of this book. In this chapter, we will review pertinent technical parameters associated with using ILs on needle and capillary emitter systems, and recent developments on theoretical and experimental approaches to gain insights into the stability of charge species produced and their relevance in electrospray propulsion applications. Specific examples will include molecular dynamics studies of a nanometer size 1-ethyl-3-methylimidazolium bis(trifluoromethylsulfonyl)imide droplet subject to high electric fields and mass spectrometric characterization of an energetic IL 2-hydroxyethylhydrazinium nitrate emitted from a titanium emitter.

Electrospray Space Propulsion

Space propulsion systems are characterized by three important parameters: thrust, F, specific impulse, I_{sp}, and efficiency, η. Thrust is a measure of the force a propulsion system exerts in order to propel the vehicle in a specified direction. I_{sp} measures the thrust per unit mass flow and provides an estimate of how efficiently the propulsion system uses its mass. η is determined by the ratio of power output to the power input of the propulsion system. These parameters are often tuned to the velocity change, ΔV, required to accomplish a maneuver or task. While it is ideal to have all three parameters maximized, practical requirements and the fundamental physics of each type of propulsion system prevent the generation of a high thrust, high efficiency propulsion system.

Electric propulsion systems are a diverse subset of space propulsion systems. Probably the most well known electric propulsion system is the Hall Effect thruster (HET). These plasma-based thrusters operate by ionizing an inert gas propellant, typically xenon, and electrostatically accelerating the charged species to high velocities to generate thrust through the use of crossed electric and magnetic fields. HETs have seen a significant increase in use over the last decade, particularly for geosynchronous Earth orbit (GEO)-based satellites (*24*). The main advantage is their high specific impulses which are roughly an order of magnitude greater than chemical propulsion systems.

Electrospray thrusters apply strong electric fields to conductive liquids and electrostatically accelerate charged species to generate thrust. The advantage of electrospray thrusters over HETs is most evident for miniaturized satellites. Miniaturization of HETs is complicated by the fact that the magnetic field scales inversely with length of the thruster channel size. As the surface-to-volume ratio increases, damage to the discharge channel due to erosion from the acceleration process also shortens the lifetime of the HET. Research and engineering efforts are currently underway to mitigate these concerns (*25*). The electrospray thruster, on the other hand, does not employ any magnetic fields in the emission process. Liquid is delivered to the tip of a capillary or needle where a strong electric field at the tip induces formation of a Taylor cone-jet and ejection of charged species.

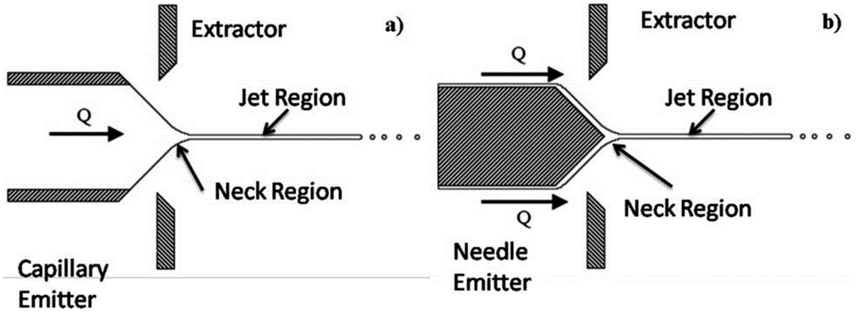

Figure 1. a) Schematic of a capillary emitter. The flow of propellant is internal as a result of a reservoir pressure. b) Schematic of a needle emitter. The flow occurs on the outer surface of the emitter. In both cases, when the effective electric field strength, via voltage applied to both the extractor and emitter, reaches a critical value, emission of charged species from the propellant occurs.

The general operation of the two types of electrospray emitters is shown in Figure 1. In the case of a capillary system, liquid is driven from a reservoir via an applied pressure, akin to the electrospray process most well understood in mass spectrometry. As the liquid reaches the tip of the capillary it is subjected to a strong electric field induced by a combination of voltages applied separately to the emitter and extractor. In the case of an externally wetted emitter system, liquid is drawn from a reservoir to the tip of a sharp needle by a combination of electric field and capillary action. When the critical field strength for ion-field emission is reached (>1 V/nm) and emission of charged species occurs, two particular regions are emphasized. The effective electric field is strongest near the neck region, where ions are typically emitted at large angles and with kinetic energies near the bias potential on the emitter (*13*). The jet region is the region downstream where the liquid has left the emitter surface but not yet fully evaporated. Species emitted in this region are typically centered about the middle of the emitter axis and have lower kinetic energies than those emitted from the neck region. This loss of kinetic energy is due to ohmic losses stemming from the formation of the cone-jet (*11*).

The thrust, F, and specific impulse, I_{sp}, for an individual, accelerated particle, i, in electric propulsion are given by:

$$F = \dot{m}_i v_i = I_i\left(\frac{m_i}{q}\right)\sqrt{2V_{acc}\left(\frac{q}{m_i}\right)} \propto \sqrt{m_i/q} \qquad (1)$$

$$I_{sp} = \frac{F}{\dot{m}_i g} = \left(\frac{1}{g}\right)\sqrt{2V_{acc}\left(\frac{q}{m_i}\right)} \propto \sqrt{q/m_i} \qquad (2)$$

where I_i is the current associated with the charged particle, m_i is the mass of the charged particle, $|q|$ is the charge of the particle, V_{acc} is the electrostatic acceleration, and g is the acceleration due to gravity. For electric propulsion systems, these two equations posit that for systems with high thrust, the specific impulse will be low and vice versa. For a constant applied acceleration voltage, heavier, singly charged species will have greater thrusts but lower specific impulses than lighter, singly charged species.

The link between the physical properties of the conducting liquid and the current emitted (I_{em}) by a Taylor cone was established in the theoretical and experimental treatment of Fernández de la Mora and Loscertales in eqn. 3 (*26*).

$$I_{em} \propto \left(\frac{\gamma K Q}{\varepsilon}\right)^{1/2} \qquad (3)$$

The total current emitted is proportional to the liquid conductivity, K, the surface tension γ, and the volume flow rate, Q while inversely proportional to the dielectric constant, ε. Experimentally the flow rate is the easiest to tune and early investigations confirmed this relationship until very low flow rates were sampled. Gamero-Castaño and Fernández de la Mora found a precipitous rise in current as the flow rate was decreased while studying highly conducting NaI/Formamide solutions (*11*). This observation was additionally confirmed in the work of Romero-Sanz *et al* using the ionic liquid 1-ethyl-3methyl imidazolium tetrafluoroborate (EMIM-BF_4) (*10*). From these investigations, the specific charge of an emitted species (q/m) was linked to the parameters in eqn 3 and recast as (*27*):

$$\frac{q}{m} \propto \frac{I}{\rho Q} \propto \frac{1}{\rho}\sqrt{\frac{\gamma K}{\varepsilon Q}} \qquad (4)$$

where ρ is the liquid density. The q/m value can thus be tuned to result in small q/m values (large charged droplets) resulting in high thrust (eqn. 1) or large q/m values (small ions) resulting in high I_{sp} by means of the volume flow rate, Q. The flow rate is controlled in capillary systems by modification of the reservoir pressure (*10*) while the flow rate is fixed for the externally wetted emitters, although geometry (*14*, *28*), emitter surface material (*29*, *30*), electric field control and tip curvature dimensions (*31*, *32*) influence the observed flow rate. The flow rate for liquids on needle emitters is typically very low, owing to the use of only capillary action and electric fields, and emission of larger q/m values results.

Three modes of operation are used to describe the emission from an electrospray thruster. The first is termed droplet mode where q/m is very small and the emission process is dominated by large charged droplets (100-1000's of molecules per net charge). This mode results in the most thrust per emitter but least efficient use of mass (low I_{sp}). The second mode of operation is the purely ionic regime where q/m is very large and the emission process is dominated by small ions and ion-clusters. While small thrusts per emitter are realized, nearly every molecule is efficiently utilized (high I_{sp}). Between these two operational modes is the mixed ion-droplet mode where both small ions and large droplets coexist and the thrust and specific impulse slide between the two extremes. The purely ionic mode is of particular interest because while the thrust can be scaled by the addition of more emitters, the specific impulse cannot be improved by the same addition. Using MEM fabrication techniques, emitters with dimensions on the order of 30-500 μm are packaged at high densities into small surface areas (*32*). Characterization of such arrays has already been reported and shows significant promise in high specific impulse (~4500 s) and scalable thrust operation (2.8 μN to 4.0 μN for a 21 and 44 emitter linear array, respectively) (*32–34*).

Operating in the purely ionic regime rarely yields emission products that are purely a single cation or single anion. Typically cluster ions are observed which pair a cation or anion with charge-neutral ion pairs. The consequence of emitting clusters larger than bare ions results in a net decrease in the specific impulse of the propellant. These small clusters are observed even at extremely low flow rates. This experimental finding has sparked an effort to use theoretical tools to determine the origin microscopically for the presence of these small clusters.

The sheer size of the molecular systems undergoing emission in the presence of electric fields makes quantum mechanical treatment prohibitively expensive. A droplet emitting in the jet region of a needle emitter is estimated to be less than 10 nm in size (*11*). As a result, molecular dynamics (MD) simulations have been the workhorse of the theoretical investigations. Both atomistic, where each atom has unique force field parameters, and coarse-grained, where groups of atoms are parameterized, force fields have been employed with some specific examples applied to electrospray propulsion applications discussed below. MD simulations conserve the Newtonian nature of the physics providing realistic momentum and time-dynamics experienced by the simulated particles. Observables such as electric field effects on internal energies, determination of observed emission products after electric field application, the effect of varying electric field strengths on observed products and dissociation dynamics of small clusters can all be probed by using MD techniques. Generally, an MD simulation consists of initializing a system using a pre-configured force field, generating a system of desired size, equilibrating the system, and, finally, performing a production run consisting of a large number of timesteps in which the system is free to evolve within the constraints, such as constant energy/constant molecules, where the observables of interest are calculated.

In a pioneering application of MD simulations to the electrospray propulsion application, Luedtke *et al* provided accurate prediction of field-emitted species and relative ratios in a NaI/formamide system (*35*). In a followup investigation probing only the dielectric solvent component of the system, high electric field strengths were found to result in electro-crystallization at the tip of an elongated droplet (*36*). Takahashi and Lozano subjected a droplet of the IL 1-ethyl-3-methylimidazolium tetrafluoroborate (EMIM-BF_4) in the gas phase and on a tungsten surface to electric fields. They found emission of small ionic species n = 0 through n = 2, where n indicates the number of neutral pairs attached to the ion, (i.e. $EMIM^+$-[EMIM-BF_4]$_2$ for n = 2) at field strengths above 1.2 V/nm, although the field strength required to generate emission was much higher from a simulated tungsten surface (*37*, *38*). Very recently, the same ionic liquid was simulated while contained within a capillary of diameter ~100 Å and length ~225 Å and subjected to electric fields of varying strength. Emission was dominated by n = 0 species with smaller contributions from larger n = 1 and 2 species at fields above 1.2 V/nm (*39*). Alternatively, small clusters may be formed from the field-induced dissociation of larger droplets still in the region between the emitter and extractor (i.e. acceleration region) or the evaporation of species from metastable droplets at longer times after emission (*40*). Daily investigated the effects of electric fields on charged droplets in the acceleration region for EMIM-BF_4 and determined that the thermal motion of the molecules within the droplet influences the emission process, especially at low field strengths (*41*).

Presented throughout the remainder of this chapter is a theoretical investigation into a well-known IL 1-ethyl-3-methylimidazolium ($EMIM^+$) bis(trifluoromethylsulfonyl)imide (Tf_2N^-) and experimental research on an energetic ionic liquid 2-hydroxyethylhydrazinium (HEH^+) nitrate (NO_3^-) on a titanium needle emitter. The experiment example demonstrates a nearly purely ionic operational mode.

Theoretical Investigation of Ions Field Evaporated from 1-Ethyl-3-methylimidazolium bis(trifluoromethylsulfonyl)imide

Theoretical Methods

Atomistic molecular dynamics simulations were carried out using the Large-scale Atomic/Molecular Massively Parallel Simulator (LAMMPS) for systems of various sizes composed of the IL EMIM-Tf_2N (*42*). The structure of this IL is shown in Figure 2. The force field parameters were taken from the work of Kelkar and Maginn (*43*) for the cation and Lopes and Padua (*44*) for the anion and used without modification.

To probe the effects of electric fields on ionic liquid droplets, a 125 neutral pair (125 cations, 125 anions, 4250 total atoms) droplet was initially equilibrated in the gas phase for subsequent production runs at 300 K using electric fields of 1.2 V/nm. This equilibration used shrink-wrapped boundary conditions under the NVT (constant molecules, volume, and temperature) ensemble. Equilibrium was confirmed by monitoring the temperature and other key observables under an NVE (constant molecules, volume, and energy) ensemble. The equilibrated droplet was found to be quasi-spherical with an isotropic distribution of cations and anions throughout the droplet. The equilibrated droplet was then subjected to an electric field of 1.2 V/nm applied along the Cartesian x-axis of the simulation box.

An electric field strength of 1.2 V/nm was selected as a balance between generating enough emission events and depletion/breakup of the parent droplet over the 1.5 ns duration of a simulation. In these simulations, a critical field for ion-emission was found to be roughly 1.0 V/nm for this ionic liquid while fields above 1.5 V/nm resulted in rapid droplet breakdown. Generally, the (average) number of small ionic species emitted increased quasi-linearly as a function of electric field strength over the range of 1.0 – 1.4 V/nm over a fixed simulation duration. Emission of species from the droplet was recorded for 1.5 ns or until the droplet fractured into multiple individual droplets. The identity of the species was recorded 10 Å from either edge of the droplet to avoid further dissociation effects resulting from the electric field. This process was repeated for 20 unique simulations to generate statistically meaningful results.

In addition to the electric field studies, simulations of small ionic clusters were also pursued. Investigating smaller ion-clusters ($X^{\pm}$-[EMIM-Tf_2N]$_n$) provides insight into the thermal stability of emission products. The presence or absence of clusters in the mass spectrum is tied to the thermodynamic stability of the particular ion-cluster and the fundamental physics of the emission process. In the case of metastable clusters, insight into the preferred dissociation pathway can be determined. To perform these simulations, cluster ions were first equilibrated at the desired temperature similar as described above and then allowed to evolve under an NVE ensemble for 40 ns or until a trajectory dissociated. 96-200 trajectories per temperature per cluster were performed to generate statistically meaningful results. Only the first dissociation event was recorded and subsequent dissociation was ignored (*45*).

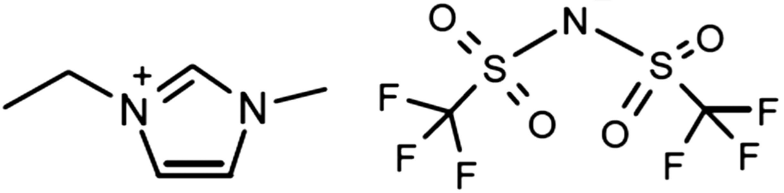

Figure 2. Chemical structure of 1-ethyl-3-methylimidazolium (left) bis(trifluormethylsulfonyl) imide (right).

Results

The application of an electric field to the 125 neutral pair droplet along the x-axis results in the transition from a nearly spherical shape to a droplet elongated along the x-axis. At 1.2 V/nm, the field strength is sufficient to induce emission of pure ions, small ionic species, and neutral pairs from the outer regions of the droplet along the electric field axis. A summary of the electric field MD simulations is presented in Figure 3a. The emission products observed are predominately n = 0 species (pure cations and anions), smaller quantities of n = 1 species (EMIM$^+$-[EMIM-Tf$_2$N] and Tf$_2$N$^-$-[EMIM-Tf$_2$N]) and even smaller quantities of the n = 2 species. Emission of neutral species is also observed in these simulations, totaling approximately 5% of the emission products.

In Figure 3b the MD simulations are compared against two experimental reports. Similar to the MD simulation results, the experimental findings using this IL suggest that small species dominate the emitted products. The experiments in both cases find the most prevalent product to be the n = 1 ion cluster while the MD simulations clearly show a preference for the n = 0 cation. However, excellent agreement between the identity of the species is observed with the only products above 1% emission in all cases being the n = 0 through n = 2 species. The experimental methods were insensitive to the detection of neutral species so no direct comparison was possible.

MD simulations of small ion clusters were performed in the absence of electric fields. The trajectories were initially equilibrated at constant temperature before being allowed to evolve under the NVE ensemble. The resulting cation temperature profiles are shown for n = 1 through n = 4 in Figure 4. The n = 1 cluster does not begin dissociating until nearly 700 K with a 50% dissociation temperature of ~830 K. The n = 2 cluster 50% dissociation temperature decreases considerably to ~640 K. The n = 3 cluster has the lowest observed 50% dissociation temperature (~590 K) for clusters between n = 1 and n = 5. These investigations suggest that all sampled ion-clusters dissociate well above the experimental temperature of 300 K.

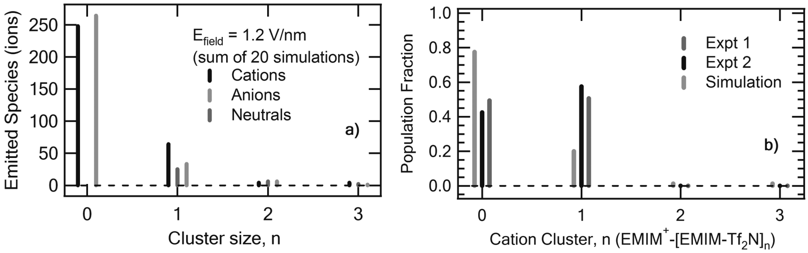

Figure 3. a) Summation of emitted species after 20 E-field simulations at 1.2 V/nm field strengths. n = 0 clusters are pure anions and cations, while larger n clusters are cations and anions paired with n neutral pairs. For the neutrals, n = 1 indicates a single neutral pair. b) Comparison of the MD results to two separate experiments using this IL on externally wetted emitter sources. Expt. 1 is from ref. (13) and Expt. 2 is from ref. (40).

The dissociation pathways for the n = 1 to n = 5 cation clusters are presented in Figure 5. The branching percentage was determined by tabulating the species resulting after the initial dissociation. Trajectories that dissociated between the 25% and 75% range of the temperature profiles shown in figure 4 were the only trajectories included in this analysis. We believe this election more accurately reflects the dissociation pathways and prevents bias from those clusters that were studied at temperatures where 100% of the clusters had dissociated. Dissociation events in these temperature ranges always involve the loss of some number of neutral pairs since the MD simulations were not capable of observing fragmentation due to the fixed bond connectivity requirement within a molecule. The only possible pathway for an n =1 cluster is the loss of a single neutral pair, denoted in Figure 5 as an n – 1 loss pathway, while an n = 2 cluster can lose a single neutral pair or a dimer of neutral pairs (n – 2). For n = 1 and 2 it is clear that the preferred loss pathway is the n – 1 path. The n = 3 cluster shows a slight preference for loss of a dimer, but the n – 1 pathway remains an important path. As cluster size is increased, more dissociation events at higher values of neutral pair loss occur.

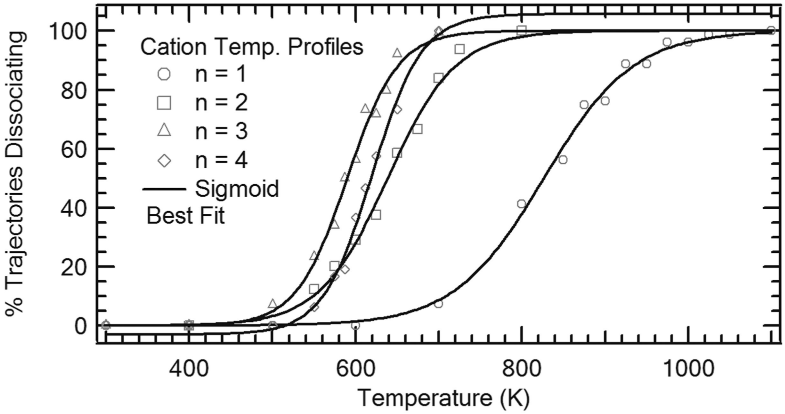

Figure 4. The % of trajectories dissociating at a given temperature is recorded for small cation clusters from n = 1 to n = 4. A sigmoidal best fit function is applied to the data.

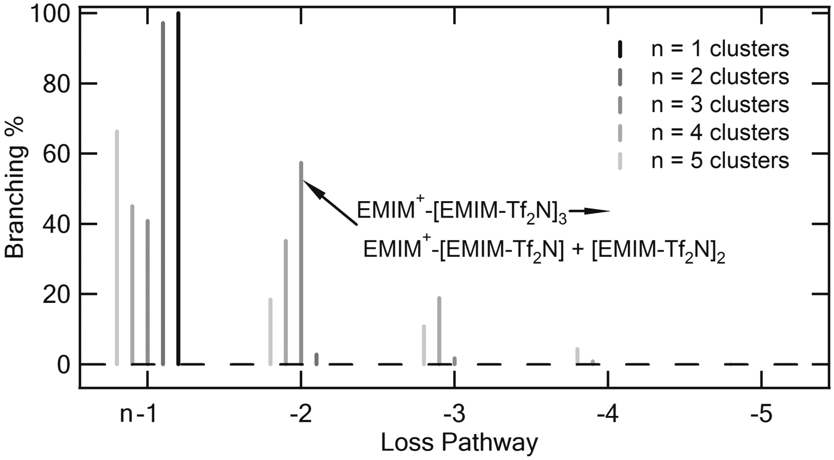

Figure 5. Dissociation pathways for the n = 1 to n = 5 clusters. The n = 1 clusters are always the rightmost bar and n = 5 the leftmost. A value at n – 2 means a cluster has shed two neutral pairs. The branching % has been fixed to sum to 100% over the entire parent cluster. Only dissociating trajectories were counted.

Discussion

The molecular dynamics investigations on small cation clusters determined that the dissociation temperature of clusters greater than n = 2 was well above the temperatures of the experimental comparisons. In one set of reported experimental results, performed at 298 K and 373 K, no difference in the ratios or identities of species was observed (*13*). The MD small cluster-ion results presented here indicate that the experimental temperature would need to be greatly increased to dissociate even the n = 2 cluster observed in the mass spectrum of EMIM-Tf_2N operated on a tungsten emitter electrospray source. The absence of larger cluster emission from the 125 neutral pair droplet in the electric field MD simulations then suggests that the emitted species are not hindered from a thermodynamic instability but instead modified by some feature of the droplet such as its size and perturbation as a result of interaction with the electric field.

The small cluster investigations also highlighted the dissociation pathways expected for small ion-clusters. While n – 1 dissociation was the preferred mechanism for the smallest clusters, n = 3 through n = 5 included dissociation pathways that generally involved more than a single neutral pair. This information provides insight into how larger cluster ions may dissociate which is particularly relevant for the case of a mixed ion-droplet operational mode. In the case of mixed ion-droplet mode, small ions emit at large angles but now include droplets down the center axis. Additional small ions are also observed in conjunction with observing large m/q droplets along the center axis. These ions may result from the dissociation/evaporation of species from a larger parent droplet and can be observed experimentally through an energy analysis of the cluster ions as will be shown in the next section.

Even though quantitative agreement was not observed in the electric field simulations of the 125 neutral pair droplet when compared to experiment, qualitative agreement was observed. The experimental results clearly indicated a preference for n = 1 species where as the simulations predicted n = 0 preference. The same emission species were observed in both simulation and experiment suggesting that the MD methodology is at least generally reflective of the microscopic origin of the electrospray process. The agreement between EMIM-BF_4 and EMIM-Tf_2N MD simulations as to the prediction of emitted species and critical electric field strengths when compared to experiment suggests these theoretical tools can be a useful complement in elucidating the fundamental physics of the electrospray emission process.

Mass Spectrometric Measurements of Ions Field Evaporated from 2-Hydroxyethylhydrazinium Nitrate

Mass Spectrometric Experiment

In the electrospray experiments using an externally wetted emitter, an ionic liquid propellant flows from a reservoir to the tip of a titanium emitter with a radius of curvature of ~20 μm. Capillary action as well as surface characteristics of the emitter drive this flow aided by the application of electric fields to the emitter and an extractor placed near the tip of the emitter. When the total extraction voltage ($V_{ext} = V_{needle} - V_{extractor}$) reaches a critical value, field emission of ions is observed and a Taylor cone (*46*) is formed. This cone is formed at large angles and can contain pure ions, small charged ion-clusters, as well as large charged droplets. In contrast to conventional mass spectrometers using electrospray ionization, these emitted species have hundreds to thousands of eV kinetic energies. These energies are determined largely by the emitter potential but large distributions have been observed particularly for those species emitted in the jet region and the center emission axis. As a result, a detection system relatively insensitive to differing kinetic energies is required to collect all species occurring in the thruster plume. Quadrupole mass spectrometers provide this benefit although the mass resolution decreases for higher kinetic energy particles. In practice, a bias potential of ±500 V on the emitter provides a balance of both mass resolution and ion transmission through the quadrupole mass spectrometer.

The instrumental apparatus employed in these investigations has been presented previously (*1*). Briefly, a sharp titanium emitter is mounted on a temperature controlled rotatable mount. The rotatable source allows investigation of angles ranging from +40 degrees to -40 degrees and temperatures from room temperature to 373 K. The temperature of these investigations was 303 K. A drop of 2-hydroxyethylhydrazinium nitrate (HEH^+, NO_3^-, HEHN, Figure 6) is externally applied to the emitter outside of vacuum on a crossbar fused onto the emitter a small distance from the tip. The source is introduced into vacuum and the chamber is pumped down to ~1 x 10^{-7} torr. Extraction voltages of ±1900 V are used and operated in alternating polarity (AC) mode. AC mode is employed at 1 Hz to suppress the formation of an electrochemical double layer that degrades the IL (*13*, *47*).

The emitted ion beam is sampled in the near-field by means of a translation stage mounted orthogonally to the beam axis. This stage contains a quartz crystal microbalance (QCM: XTM/2 , Inficon) , Faraday cup (FC) and a cylindrical lens element allowing the beam to pass through into the quadrupole. The FC and QCM both have 6 mm entrance apertures. The FC and QCM monitor the current and mass flow respectively as a function of the source angle. These near-field measurements provide a baseline estimation of the average mass per charge (m/q) encountered at a specific angle. The cylindrical lens element allows the beam to pass through a 3mm aperture with a solid angle of acceptance of ~6 degrees. The passed ion beam is focused and extracted into the quadrupole mass spectrometer for m/q identification. All ions are detected by means of an off-axis channeltron operated with the requisite polarities and voltage settings needed to detect cations and anions respectively. The kinetic energies of a mass selected species are determined by monitoring the ion count depletion as a function of the voltage applied to a set of retarding grids.

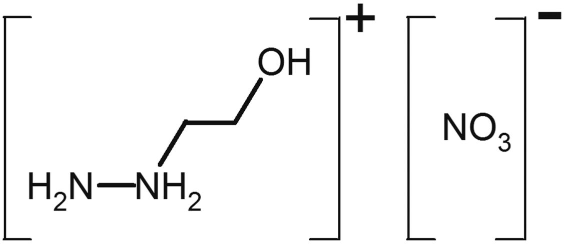

Figure 6. Chemical structure of the HEH$^+$ cation (left) and NO$_3^-$ anion (right).

Results

Near-Field Measurements

Figure 7 depicts the Faraday cup and QCM measurements made in AC mode as a function of thruster angle. The current at a specific angle is represented by the black circles and squares for cations and anions respectively while the mass flow is expressed by gray triangles. The mass flow measurements are tabulated as a combination of both polarities. The positive current readings are made as the total positive emission current is ~220 nA while the negative current readings are made as the emission current is ~210 nA. The spray is roughly symmetric for both polarities although contains a slight broadening to the positive angle side. Measureable current extends from +25 to -25 degrees on either center of the center. The negative polarity maximum current detected by the FC is -80 nA (~ -2.8 nA/mm^2) while the corresponding positive polarity value is 63 nA (~2.2 nA/mm^2). The QCM results indicate negative mass flow from -25 to -5 degrees before becoming slightly positive in the center region. Negative mass flow is again recorded from +5 to 25 degrees. Negative mass flow measurements are not physically meaningful and will be discussed below.

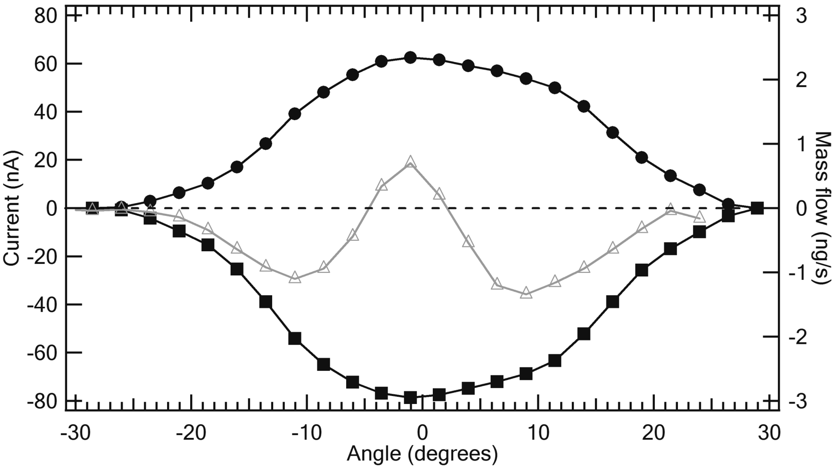

Figure 7. Angular dependence of ion current density (left) and mass flow (right). The black circles and black squares are the positive and negative currents measured by the FC. The gray triangles are the mass flow measurements obtained on the QCM. Both the QCM and Faraday cup have apertures of 6mm.

Mass Spectra

Figure 8 shows the cation mass spectra obtained as a function of thruster spray angle at an extraction voltage of 1900 V and a total emission current of 190 nA. The observed cation mass values encompass the entire scannable range of the quadrupole employed in this experiment up to 1100 amu/q. The mass resolution is +/- 4 amu and listed mass values are the center mass of the spectral feature. The spectra are dominated by large spectral features centered at 77, 120, 153, and 214 amu with smaller features spread throughout the entire mass range. As seen in the left graph of Figure 8, the angular spread of the species is about -25 to +25 degrees consistent with the near field measurements. A small baseline is observed between -10 and 10 degrees and assigned to species with m/q values exceeding the upper range of the quadrupole mass filter (*1*, *13*, *29*). The assignments of all of the peaks are made assuming a single positive charge. The 77 amu peak appears to be of equal intensity at all angles between -20 and 20 degrees while the 120, 153, and 216 amu components peak near -10 and +10 degrees. All peaks observed above 300 amu peak about the center axis.

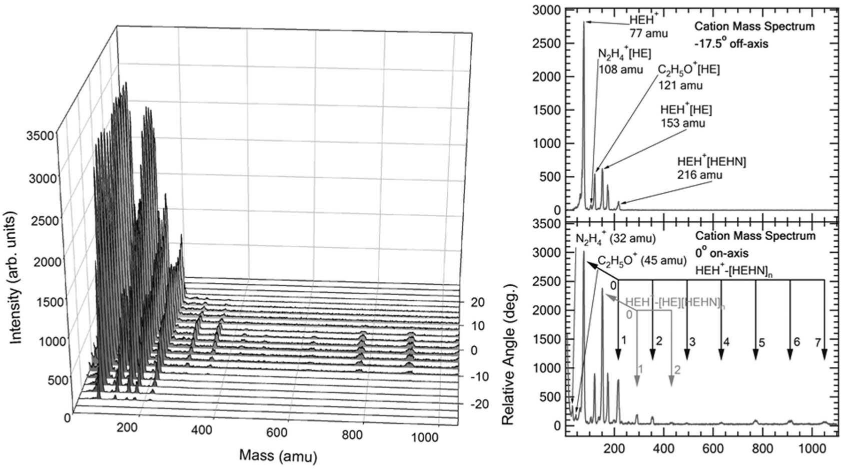

Figure 8. Left: Cation mass spectra as a function of thruster angle for the range 10 amu 1100 amu. Right: Cation mass spectrum at -17.5 degrees(top) and on axis (bottom).

The two graphs at the right of Figure 8 depict the mass spectra taken on- and off-axis. The on-axis spectrum (bottom) depicts two major sequences of ion-clusters. Both sequences contain the 2-hydroxyethylhydrazinium (HEH^+) cation, with the first sequence pairing it with “n” neutral pair 2-hydroxyethylhydrazinium nitrates (HEHN) where “n” denotes the number of neutral pairs attached. This sequence is observed all the way up to n = 7 (HEH^+-$[HEHN]_7$) at 1050 amu. The second sequence is similar in nature, but adds a 2-hydroxyethylhydrazine (HE) inside the sequence forming HEH^+-$[HE][HEHN]_n$. This sequence is observed for n = 0 through 2 in these experiments. The HE species is formed by proton transfer from the cation to the anion and will be discussed below. Fragmentation of the cation is also observed at low mass values where the HEH^+ cation has fragmented along the interior N-C bond resulting in formation of $N_2H_4^+$ and $C_2H_5O^+$ and their associated neutral species. The $N_2H_4^+$ species is observed at 32 amu as well as 108 amu where it is paired with an HE. The $C_2H_5O^+$ fragment is observed at 45 amu and paired with an HE at 121 amu. It was not possible to distinguish $N_2H_4^+$[HE] from $HEH^+[N_2H_4]$ (108/109 amu) or $C_2H_5O^+$ [HE] from $HEH^+[C_2H_5O]$ (121/122 amu) in these experiments although a justification for the assignment will be discussed later. With these assignments all observed peaks had been assigned with exception of a peak at 175 amu which currently remains unassigned.

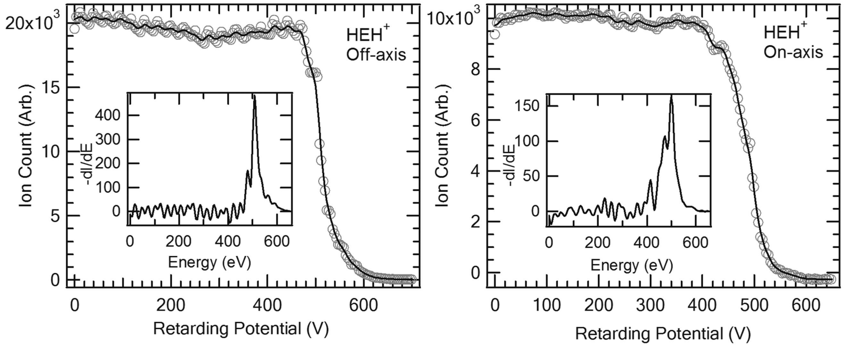

Figure 9. Retarding potential curve for the HEH$^+$ cation at -20 degrees (left) and at 0 degrees (right). The inset is the corresponding energy distribution of the ions.

Figure 9 displays the retarding potential curves measured for the mass-selected HEH$^+$ ion at 77 amu. The curves are generated by averaging 3 separate scans and subtracting out the contribution from species not rejected by the quadrupole. The subtraction is accomplished by collecting signal with the quadrupole mass spectrometer set in an rf-only mode set to only pass high m/q particles. The solid lines are generated by applying a 7-point boxcar smoothing function to the raw data. The inset is generated by taking the negative differential of this smoothed data. The needle potential was +500 V and total extraction voltage was 1900 V. The left graph depicts the HEH$^+$ retarding potential for those mass selected species emitted at -20 degrees relative to the center axis. The energy distribution of these off-axis ions is a sharp, narrow profile centered near the needle potential. The right graph is identical to the left graph except these species were detected along the center axis (on-axis). The profile is similar with the exception that the energy distribution appears slightly broader and a small contribution at 400 eV is observed.

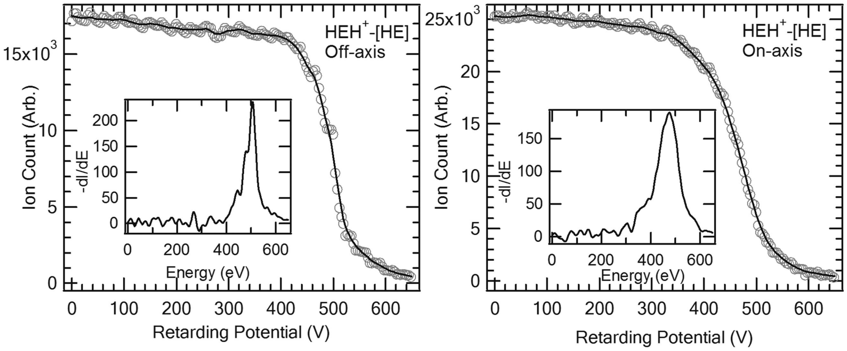

Figure 10. Retarding potential curves for HEH$^+$-[HEHN] (216 amu) at -20 degrees (left) and 0 degrees (right). The inset is the corresponding energy distribution of the ions.

Figure 10 shows the retarding potential curves measured for the mass selected HEH$^+$-HEHN ion at 216 amu. Similar to the n = 0 species shown in Figure 9, the on- and off-axis retarding potentials show distinct differences. The off-axis n = 1 species shows a sharp, narrow energy distribution centered at 507 eV very near the needle of potential of +500 V. The off-axis contains species at the same energy but also considerable population at much lower energies as presented in the inset on the right graph of Figure 10. The distribution appears to begin near 350 eV and continues until ~500 eV. This broadening of the on-axis species is observed for all other cations observed in these measurements.

Discussion

2-hydroxyethylhydrazinium nitrate was successfully field evaporated from an externally wetted titanium emitter. In the example presented above, near field measurements were made to determine the angular dependence of current and mass flow after emission off the needle with extraction voltages of 1900 V. Charged ions and ion-clusters were identified in the 10 – 1100 amu mass range for the cations using a quadrupole mass spectrometer. An ion energy analysis was performed for mass-selected ions both on- and off-axis. No evidence of electrochemical reactions was observed between HEHN and the titanium emitter.

The near-field measurements suggest that HEHN on this titanium emitter was operating in a mixed ion-droplet mode. The slight asymmetry observed in the FC measurements is ascribed to small defects in the tip of the emitter due to fabrication using electrochemical techniques. Emission of nearly pure ions is determined at angles > 10 degrees by the negative mass flow observed on the QCM. Negative QCM deposition readings indicate the reduction of material deposited on the sensor as a result of ion-sputtering off of the surface of the crystal. The ion-energy analysis of the off-axis species clearly indicates that these ion species are emitted at near needle potentials. The off-axis mass spectrum shown in Figuer 8 contains only masses below 250 amu. Although the QCM results present negative going mass flow, large droplets do not contribute to the signal at large angles. As a result, the mass spectra taken can supply the average m/q values under the assumption that undetected neutral species do not contribute to the real mass flow emitted at these angles. Within this assumption, the average mass of off-axis cations is 104 amu/q. The positive QCM deposition about the center angles indicates that some larger species are emitted in this region. These larger masses were observed in Figure 8 as the baseline under the ±15 degree data as well as the larger masses from larger “n” clusters. The QCM result in this region is a combination of mass deposition and mass removal because small, highly energetic ions coexist along the center axis with the slower, larger droplets and ion-clusters. As such, a lower limit of the droplet amu/q along the center axis is 1080 amu/q for cations.

In the mixed ion-droplet mode, the droplets emitted along the center axis are produced in the jet region of the Taylor cone while ions are emitted at large angles from the neck region where the electric field strength is at its nominal maximum (*13*). This results, generally, in the emission of the smallest species off-center, typically 10-20 degrees offset from the center axis and the largest species along the center axis. While the smallest m/q values were in fact maximized at large angles, the depletion down the center was less than was expected when compared to other systems we have studied. The on-axis mass spectrum clearly indicated a large number of small ions along with larger mass species and a background offset indicative of large droplets. The presence of small ions along the center can be explained in a couple of ways. The first is that some ions are formed at the tip of the cone-jet where the jet of conducting liquid pinches off to form droplets and emits ions near and below the needle potential. The second is that larger masses may be emitted that are not necessarily thermodynamically stable and resulting evaporation/dissociation generates smaller charged species. The dissociation has been examined in previous studies of EMIM-BF_4 where it was determined that ~10% of the emitted ions rapidly underwent mass loss in the acceleration region after emission (*40*). These dissociated species provided additional structure to the observed energy profiles. Because the angular distributions of dissociated ions produced by either of these mechanisms may be isotropic, the origin of the ions cannot be determined from the mass intensity results alone. The ion energy distributions measured as a function of angle can assist in making this determination.

In the top graph of Figure 8 only the smallest ion masses were observed with no indication of large "n" ion-clusters or background associated with droplets. The off-axis energy distributions that typify these ions were shown in the left graphs of Figure 9 and 10. In each case, the ion energy distribution was symmetrically centered near the needle potential. These results are consistent with the expectation of ion formation in the neck region of the cone-jet where the maximum electric field occurs. In contrast, the on-axis measurements of these small ions (right graphs of 9 and 10) typically exhibited near-needle potential and additional structure to the lower energy side. These low energy components of these ions could be dissociated from droplets but the near needle components could not be. As a result, the high energy ions are thought to originate from close to the neck region while the lower energy components from either dissociation of droplets or ohmic losses as a result of emitting from the end of the jet region.

The observation of cation mass peaks at 32, 45, 108 and 121 amu indicates fragmentation of the parent HEH^+ molecule occurs to an appreciable extent. The 108 and 121 amu off-axis energy scans indicate kinetic energies at the needle potential. This suggests that these species do not result from fragmentation in large droplets but that they exist in the nascent liquid flow in this form. It is not possible to definitively assign the 121 amu band to $C_2H_5O^+[HE]$ as opposed to $HEH^+[C_2H_5O]$ because the mass resolution of the quadrupole is on the order of 4 amu. However, the electron impact mass spectrum of the neutral 2-hydroxyethylhydrazine molecule (HE) indicates a roughly 10 to 1 preference for formation of $C_2H_5O^+$ to the $N_2H_3^+$ ion (*48*). Since electron impact does not occur in the emission process studied here and the parent cation is HEH^+ as opposed to the neutral HE, we speculate that HEH^+ fragmentation would also reflect the preference of localizing the charge on the ethanolic constituent. This speculation is supported by the intensity ratio of the two bands. When the total signal for both bands is integrated the resulting ratio is 7.5 to 1 in this work. With this ratio in reasonable agreement with the HE electron impact ratio, we believe that the correct assignment of the 108 amu species is to $N_2H_4^+$[HE] and the 121 amu to $C_2H_5O^+$[HE]. If the assignment were HEH^+[fragment] for both bands, under our assumption of the HE mass spectrum acting as a proxy for the HEH^+ fragmentation pattern, we would expect to see the intensity profiles reversed.

In addition to fragmentation in the mass spectra, species that have undergone proton transfer are also observed. The cation species at 153 amu, assigned to the HEH^+[HE] species, and the anion species at 125/188 amu, assigned to the $NO_3^-[HNO_3]$ and $NO_3^-[HNO_3]_2$ species (not shown) respectively, can only be the result of transfer of a single proton from the hydrazinium cation to the nitrate anion neutralizing both species. These species could either reflect chemistry (proton transfer) that occurs post emission in large droplets or reflect chemistry that occurs in the liquid propellant pre-emission. The appearance of ions complexed to proton transferred and fragmented species is unusual for ionic liquid propellants on needle emitters. Fragmentation and chemical reactions are generally the sphere of combustion based propulsion systems where such changes provide the output energy required to generate thrust. Fragmentation of ILs has only been observed previously when IL propellants are operated at high flow rates. The emitted species are typically composed of fragments and large droplets (*49*). The occurrence of these phenomena on needle emitters may reflect the energetic nature of this chemical system. Further investigations into the fragmentation and proton transfer energetics of HEHN are underway using a variety of computational tools.

Finally, the presence of fragments and proton transferred species acts in a beneficial way with respect to the use of HEHN in a high specific impulse electrospray thruster. In the absence of pure n = 0 emission, the mass of the neutral pair has a significant impact on the average mass of the emitted species. Charged fragments, both bare and complexed, result in higher q/m values than the parent ion which improves the mass utilization (specific impulse) of the thruster. Additionally, proton transfer, particularly for the anions, results in masses that increase only 63 amu for clusters complexing HNO_3. If proton transfer does not occur, the only pairing possible with NO_3^- would be the 139 amu HEHN neutral pair. The net effect of both processes is to raise the average cation/anion q/m values emitted at all angles thus increasing the specific impulse. While droplets were observed along the center axis, their apparent contribution, as judged from the magnitude of the baseline along the center axis, is minor. The droplet size, as estimated from the near field measurements, is in the range of 1000-10000 amu/q in contrast to the 50000-300000 amu/q typical of capillary emitters. After integration of the entire set of mass spectra, the average m/q value of the cations is 141 amu/q while the anions is 159 amu/q after exclusion of the contribution from any mass over 1100 amu. This work demonstrates that an energetic IL, HEHN, can also be a suitable propellant candidate for high specific impulse electrospray thrusters.

Conclusions

Significant progress has been made over the last several years with respect to the use of ionic liquids as propellants for space propulsion systems. These liquids, due to ideal physical properties, are exceptional propellants for high-specific-impulse electrospray propulsion systems. Energetic ionic liquids have shown promise in both the high specific impulse application as well as high thrust chemical propulsion systems. An IL electrospray propulsion system using a cluster of capillary emitters is nearing actual space testing. Arrays of needle emitters have been fabricated and characterized in the laboratory with promising performance.

The use of theoretical methods to glean a microscopic understanding of the emission process has seen some initial successes. While the number of reports is not large, excellent agreement between simulation and experimental observables for EMIM-BF_4 and EMIM-Tf_2N has been demonstrated. These reports indicate, at least in the low flow rate regime, that the emission process may not be controlled only by the thermodynamic stability of clusters. The early successes of these theoretical investigations will likely continue to provide insights into regions difficult to probe experimentally.

A mass spectrometric investigation of an energetic ionic liquid was reported for HEHN operating on a titanium emitter operated in a mixed ion-droplet mode. In this liquid, in contrast to a variety of other ionic liquids investigated, proton transfer products were observed in the various mass spectra. Small ions and ion-clusters, at the needle potential, were observed below 216 amu at larger angles while a progression of larger clusters was observed along the center axis. This study shows that HEHN can be operated in a near pure ion mode and is a propellant candidate for high specific impulse electrospray thruster applications.

Acknowledgments

This work has been supported by AFOSR through task 2303EP02 (Program Manager: Michael Berman). The authors thank P. Tiruppathi and E. J. Maginn for their contributions to the MD investigations for this chapter.

References

1. Chiu, Y.-H.; Dressler, R. A. Ionic Liquids for Space Propulsion. In *Ionic Liquids IV: Not Just Solvents Anymore*; Brennecke, J. F., Rogers, R. D., Seddon, K. R., Eds.; ACS Symposium Series 975; American Chemical Society: Washington, DC, 2007; p 138.
2. Chambreau, S. D.; Boatz, J. A.; Vaghjiani, G.; Koh, C.; Kostko, O.; Golan, A.; Leone, S. R. *J. Phys. Chem. A* **2012**, *116* (24), 5867–5876.
3. Larriba, C.; Castro, S.; Fernandez de la More, J.; Lozano, P. *J. Appl. Phys.* **2007**, *101*, 084303.
4. Bates, E. D.; Mayton, R. D.; Ntai, I.; Davis, J. A., Jr. *J. Am. Chem. Soc.* **2002**, *124* (6), 926–927.

5. Endres, F. *ChemPhysChem* **2002**, *3* (2), 144–154.
6. Ding, J.; Desikan, V.; Han, X.; Xiao, T. L.; Ding, R.; Jenks, W. S.; Armstrong, D. W. *Org. Lett.* **2005**, *7*, 335–337.
7. Dyson, P. J.; Geldbach, T. J. *Metal Catalysed Reactions in Ionic Liquids*; Springer: Dordrecht, The Netherlands, 2005; p 246.
8. Plechkova, N. V.; Seddon, K. R. *Chem. Soc. Rev.* **2008**, *37* (1), 123–150.
9. Maginn, E. J. Atomistic Simulations of Ionic Liquids. In *Reviews in Computational Chemistry*; Lipkowitz, K. B., Cundari, T. R., Eds.; John Wiley & Sons, Inc.: Hoboken, NJ, 2009; Vol. 26.
10. Romero-Sanz, I.; Bocanegra, R.; Fernandez de la Mora, J.; Gamero-Castano, M. *J. Appl. Phys.* **2003**, *94*, 3599.
11. Gamero-Castano, M.; Fernandez de la Mora, J. *J. Chem. Phys.* **2000**, *113* (2).
12. Chiu, Y.-H.; Levandier, D. J.; Austin, B. L.; Dressler, R. A.; Murray, P. T.; Lozano, P. Mass Spectrometic Analysis of Ion Emission for Selected Colloid Thruster Fuels. In 39th AIAA/ASME/SAE/ASEE Joint Propulsion Conference and Exhibit, Huntsville, AL, 2003; Vol. AIAA-2003-4848.
13. Chiu, Y.-H.; Gaeta, G.; Levandier, D. J.; Dressler, R. A.; Boatz, J. A. *Int. J. Mass Spectrom.* **2007**, *265*.
14. Ticknor, B. W.; Anderson, J.; Fritz, B. A.; Chiu, Y.-H. Effect of Aspect Ratio on the Wettability and Electrospray Properties of Porous Tungsten Emitters with the Ionic Liquid [EMIM][IM]. In 46th AIAA/ASME/SAE/ASEE Joint Propulsion Conference and Exhibit, Nashville, TN, 2010; Vol. AIAA-2010-6618.
15. Lozano, P.; Martinez-Sanchez, M. *J. Colloid Interface Sci.* **2005**, *282*, 415–421.
16. Legge, R. S., Jr.; Lozano, P.; Martinez-Sanchez, M. In Fabrication and Characterization of Porous Metal Emitters for Electrospray Thrusters, 30th International Electric Propulsion Conference, Florence, Italy, 2007.
17. Ziemer, J.; Gamero-Castano, M.; Hruby, V.; Spence, D.; Demmons, N.; McCormick, R.; Roy, T.; Gasdaska, C.; Young, J.; Connolly, B. In Colloid Micro-Newton Thruster Development for the ST7-DRS and LISA Mission, 41st AIAA/ASME/SAE/ASEE Joint Propulsion Conference and Exhibit, 2005.
18. Ziemer, J. K. Sub-Micronewton Thrust Measurements of Indium Field Emission Thrusters. In 28th International Electric Propulsion Conference, Toulouse, France, 2003; Vol. IEPC-03-247.
19. Demmons, N.; Hruby, V.; Spence, D.; Roy, T.; Ehrbar, E.; Zwahlen, J.; Martin, R.; Ziemer, J. K.; Randolph, T. ST7-DRS Mission Colloid Thruster Development. In 44th AIAA/ASME/SAE/ASEE Joint Propulsion Conference and Exhibit, AIAA: Hartford, CT, 2008; Vol. AIAA-2008-4823.
20. Ziemer, J. K.; Randolph, T. M.; Franklin, G. W.; Hruby, V.; Spence, D.; Demmons, N.; Roy, T.; Ehrbar, E.; Zwahlen, J.; Martin, R.; Connolly, W. Delivery of Colloid Micro-Newton Thrusters for the Space Technology 7 Mission. In 44th AIAA/ASME/SAE/ASEE Joint Propulsion Conference and Exhibit, AIAA: Hartford, CT, 2008; Vol. AIAA-2008-4826.

21. Racca, G. *L1 Mission Reformulation: NGO - New Gravitational Wave Observer*; LISA-EST-RP-1018; ESA: 2012; p 14.
22. Chambreau, S. D.; Schneider, S.; Rosander, M.; Hawkins, T.; Gallegos, C. J.; Pastewait, M. F.; Vaghjiani, G. *J. Phys. Chem. A* **2008**, *112*, 7816–7824.
23. Hawkins, T. W.; Brand, A. J.; McKay, M. B.; Tinnirello, M. In Reduced Toxicity, High Performance Monopropellant at the US Air Force Research Laboratory, 4th International Association for the Advancement of Space Safety Conference, Huntsville, AL, Huntsville, AL, 2010.
24. Hofer, R. R. *Development and Characterization of High-Efficiency, High-Specific Impuse Xenon Hall Thrusters*; NASA: 2004; Vol. CR-2004-213099.
25. Smirnov, A.; Raitses, Y.; Fisch, N. J. In The Effect of Magnetic Field on the Performance of Low-Power Cylindrical Hall Thrusters, 29th International Electric Propulsion Conference, Princeton University, Princeton University, 2005.
26. Fernandez de la Mora, J.; Loscertales, I. G. *J. Fluid Mech.* **1994**, *260*, 155–184.
27. Lozano, P. *Studies on the Ion-Droplet Mixed Regime in Colloid Thrusters*. Ph.D. Thesis, Massachussetts Institute of Technology, 2003.
28. Ticknor, B. W.; Miller, S.; Chiu, Y.-H. Mass Spectrometic Analysis of the Electrospray Plume from an Externally Wetted Tungsten Ribbon Emitter. In 45th AIAA/ASME/SAE/ASEE Joint Propulsion Conference and Exhibit, Denver, CO, 2009; Vol. AIAA-2009-5088.
29. Chiu, Y.-H.; Gaeta, G.; Heine, T.; Dressler, R. A.; Levandier, D. J. Analysis of the Electrospray Plume from the EMI-Im Propellant Externally Wetted on a Tungsten Needle. In 42nd AIAA/ASME/SAE/ASEE Joint Propulsion Conference and Exhibit, Sacremento, CA, 2006; Vol. AIAA-2006-5010.
30. Garza, T. C. *Optimizing Wettability of Externally Wetted Microfabricated Silicon Electrospray Thrusters*; Massachusetts Institute of Technology, 2007.
31. Courtney, D. G.; Lozano, P. C. In Porous Ionic Liquid Ion Source Fabrication Refinements and Variable Beam Energy Experiments, 45th AIAA/ASME/SAE/ASEE Joint Propulsion Conference and Exhibit, AIAA-2009-5087, Denver, CO, AIAA: Denver, CO, 2009; p 11.
32. Legge, R. S., Jr.; Lozano, P. C. *J. Propul. Power* **2011**, *27* (2), 485–495.
33. Le Gac, S.; Arscott, S.; Cren-Olive, C.; Rolando, C. *J. Mass Spectrom.* **2003**, *38*, 1259–1264.
34. Coffman, C. S.; Courtney, D. G.; Hicks, F. M.; Jamil, S.; Li, H.; Lozano, P. C. Progress toward a Variable Specific Impulse Electrospray Propulsion System. In 47th AIAA/ASME/SAE/ASEE Joint Propulsion Conference and Exhibit, AIAA: San Diego, CA, 2011; Vol. AIAA-2011-5591.
35. Luedtke, W. D.; Landman, U.; Chiu, Y.-H.; Levandier, D. J.; Dressler, R. A.; Sok, S.; Gordon, M. S. *J. Phys. Chem. A* **2008**, *112*.
36. Luedtke, W. D.; Gao, J.; Landman, U. *J. Phys. Chem. C* **2011**, *115*, 20343–20358.
37. Takahashi, N.; Lozano, P. Computational Investigation of Molecular Ion Evaporation in Electrospray Thruster. In 44th AIAA/ASME/SAE/ASEE Joint Propulsion Conference and Exhibit, 2008; Vol. AIAA-2008-4533.

38. Takahashi, N.; Lozano, P. Atomistic Numerical Approach to Ion Evaporation from a tungsten Surface for Electrospray Thrusters. In 45th AIAA/ASME/SAE/ASEE Joint Propulsion Conference and Exhibit, Denver, CO, 2009; Vol. AIAA-2009-5089.
39. Borner, A.; Li, Z.; Levin, D. A. Modeling of an ionic liquid electrospray using molecular dynamics with constraints. *J. Chem. Phys.* **2012**, *136*, 124507.
40. Lozano, P. *J. Phys. D: Appl. Phys.* **2006**, *39*, 126–134.
41. Daily, J. W. *J. Propul. Power* **2008**, *24* (5).
42. Plimpton, S. J. *J. Comput. Phys.* **1995**, *117*, 1–19.
43. Kelkar, M. S.; Maginn, E. J. *J. Phys. Chem. B* **2007**, *111*, 4867.
44. Lopes, J. N.; Padua, A. A. *J. Phys. Chem. B* **2004**, *108*, 16893.
45. Prince, B. D.; Tiruppathi, P.; Chiu, Y.-H.; Maginn, E. J. Theoretical Investigation of Ions Field Evaporated from 1-Ethyl-3-methylimidazolium bis(trifluoromethylsulfonyl)imide. *J. Phys. Chem. A* **2012**, in prep..
46. Taylor, G. I. Disintegration of water drops in an electric field. *Proc. R. Soc., A* **1964**, *280*.
47. Lozano, P.; Martinez-Sanchez, M. Ionic Liquid Ion Sources. *J. Colloid Interface Sci.* **2004**, *208*, 149.
48. Mass Spectrum (electron ionization) of 2-Hydrozinoethanol. In *NIST Standard Reference Database*, 2011 ed.; National Institute of Standards and Technology: 2011; Vol. 69, p NIST MS 341054.
49. Miller, S. W.; Prince, B. D.; Rovey, J. L. Capillary Extraction of the Ionic Liquid [BMIM][DCA] for Variable Flow Rate Operations. In 48th AIAA/ASME/SAE/ASEE Joint Propulsion Conference and Exhibit; AIAA: Atlanta, GA, 2012; Vol. AIAA-2012-3738.

Chapter 3

Decomposition and Combustion of Ionic Liquid Compound Synthesized from *N,N,N′,N′*-Tetramethylethylenediamine and Nitric Acid

Shiqing Wang and Stefan T. Thynell[*]

Department of Mechanical and Nuclear Engineering,
The Pennsylvania State University,
University Park, Pennsylvania 16802, USA
[*]E-mail: Thynell@psu.edu. Phone 814-863-0977. Fax 814-863-4848.

A nitrate-based ionic liquid compound, TMEDA•8HNO_3, was synthesized from hypergolic bipropellants *N,N,N′,N′*-tetramethylethylenediamine (TMEDA) and nitric acid by premixing them carefully at a stoichiometric molar ratio of 1:8. The overall ignition and combustion behaviors of this liquid propellant were examined by using a high-pressure strand burner with optical access, coupled with a high-speed video camera for capturing and analyzing the liquid- and gas-phase processes as well as measuring the regression rates of the liquid strands. TMEDA•8HNO_3 has a pressure deflagration limit (PDL) of approximately 300 psi, below which the liquid strand regresses without a luminous flame. Burn rates of this liquid propellant were measured from 400 to 1000 psi. Thermal decomposition of TMEDA•8HNO_3 was investigated by a confined rapid thermolysis setup with heating rates on the order of 2,000 K/s coupled to rapid-scan Fourier transform infrared (FTIR) spectroscopy of the evolved gases. Over the temperature range from 50 to 80°C, the major IR-active gaseous species evolved from the condensed-phase decomposition are HNO_3, NO_2, H_2O, CO_2, HCOOH, and glyoxylic acid (HOCCOOH). At higher temperatures, additional species such as CH_2O, $(CH_3)_2NNO$, NO and N_2O also evolved. Possible

In Ionic Liquids: Science and Applications; Visser, A., et al.;
ACS Symposium Series; American Chemical Society: Washington, DC, 2012.

decomposition pathways of TMEDA•8HNO_3 are discussed based on the rapid thermolysis studies.

Introduction

N,N,N′,N′-Tetramethylethylenediamine[$(CH_3)_2NCH_2CH_2N(CH_3)_2$, TMEDA or TEMED], the molecular structure of which is shown in Figure 1, is widely used as a bidentate ligand that forms stable complexes with many metal halides (*1*). This tertiary amine is of interest as a potential hypergolic propellant with red fuming nitric acid (RFNA) or white fuming nitric acid (WFNA) as the oxidizer (*2–4*). TMEDA as well as its mixtures with dimethylaminoethylazide (DMAZ) are considered to be some of the most promising lower toxicity alternatives (*2*, *5*) for highly toxic hydrazine-based propellants, which have been successfully deployed for decades in rockets and spacecraft (*6*).

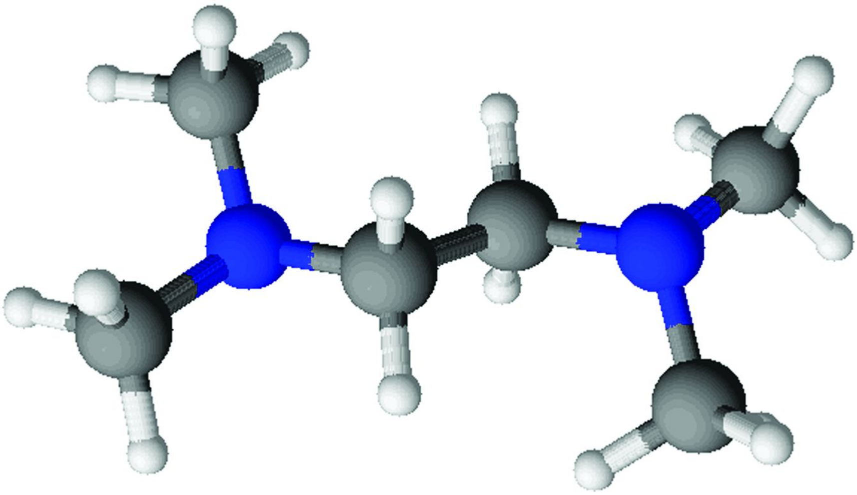

Figure 1. Molecular structure of TMEDA.

Hypergolic propellants are pairs of liquid fuels and oxidizers in which ignition occurs spontaneously upon contact between the two liquids, thereby eliminating the need for a complex ignition system (*7*). Figure 2 are some selected images showing the hypergolic ignition processes when a TMEDA drop falls into a pool of 80μL WFNA. This test was conducted based on a drop-test setup developed and used in earlier works (*8*, *9*) to study the drop-on-pool impingement interaction between various hypergolic pairs. Ignition delay of TMEDA/WFNA measured by this setup is approximately 14 ms. As part of an effort to improve the TMEDA/RFNA mechanism developed by the U.S. Army Research Laboratory (*4*), pre-ignition reactions of TMEDA/HNO_3 were investigated in an early work by using a confined-interaction setup coupled with Fourier transform infrared (FTIR) spectroscopy and time-of-flight mass (ToFMS) spectroscopy (*9*). It was found that the formation of TMEDA dinitrate is the initiation reaction which provides heat to evaporate the reactants as well as to initiate secondary reactions that lead to ignition. The calculated exothermicity of TMEDA•$2HNO_3$ formation is about 45 kcal/mol (*10*).

$$\text{TMEDA} + 2HNO_3 \rightarrow \text{TMEDA}\bullet 2HNO_3$$

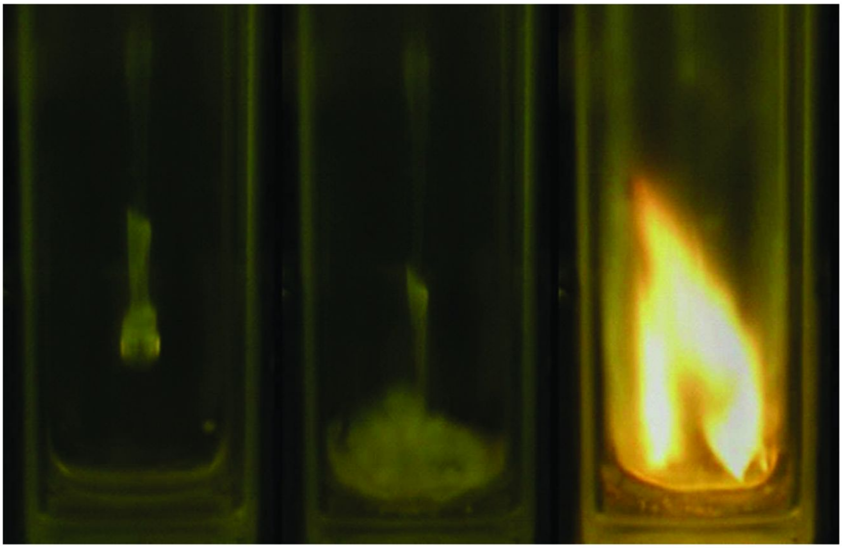

Figure 2. Hypergolic droplet-on-pool impingement of TMEDA/WFNA.

TMEDA•$2HNO_3$ can be synthesized through carefully designed procedures in which the heat from the salt formation reaction is removed rapidly to prevent subsequent secondary reactions from occurring. TMEDA•$2HNO_3$, which can also be written as $C_6H_{18}O_6N_4$, is extremely oxidizer lean, and therefore this nitrate itself can not be considered as a monopropellant. A liquid compound with an improved stoichiometric F/O ratio was synthesized by adding 6 moles of HNO_3 to 1 mole of TMEDA•$2HNO_3$. This is written as TMEDA•$8HNO_3$ or $C_6H_{24}O_{24}N_{10}$. Strictly speaking, TMEDA•$8HNO_3$ is not an ionic liquid. It is a liquid monopropellant comprised of both ions (TMEDA cation, H^+, NO_3^-) and neutral molecules (HNO_3). Complete combustion of this ionic liquid propellant can be written as follows:

$$C_6H_{24}O_{24}N_{10} \rightarrow 6\ CO_2 + 12\ H_2O + 5\ N_2$$

One objective of this work is to conduct combustion and thermal decomposition studies of this novel monopropellant in order to obtain first-hand data such as pressure deflagration limit (PDL), burn rate, decomposition paths, etc. Another motivation of this work is to treat this liquid compound as a premixed system of hypergolic pair TMEDA/HNO_3. Therefore, the experimental data (i.e., burn rate) obtained from this experimental study can be used in future works to compare with computational results from a premixed combustion modeling using the TMEDA/HNO_3 mechanism which was developed by the U.S. Army Research Laboratory (*4*).

Preparation of TMEDA•8HNO$_3$

Warning statement: TMEDA dinitrate (TMEDA•2HNO$_3$) and the liquid monopropellant TMEDA•8HNO$_3$ are energetic compounds which might be sensitive to heat, impact and friction. Special precautions should be taken when preparing and testing these compounds.

TMEDA and nitric acid were purchased from Sigma–Aldrich and used without further purification. Both TMEDA and nitric acid have a purity greater than 99.5% by weight. 7.5 ml TMEDA (0.05 mol) and 4.2 ml HNO$_3$ (0.1 mol) were diluted by 50 ml distilled H_2O, respectively. Both solutions were cooled by contact with an ice bath before mixing. The HNO$_3$ solution was loaded in a burette and dropped into the TMEDA solution in a beaker. During the mixing process, the temperature of the TMEDA solution increased slightly due to the heat generated by neutralization reactions. In order to prevent secondary reactions from occurring, the temperature of the solution was not allowed to increase to levels above 30°C, which can be easily achieved by adjusting the rate at which drops were released. The product from the titration is a clear and colorless solution of TMEDA dinitrate. H_2O was then slowly removed at room temperature under vacuum conditions (boiling point of H_2O is 22°C at about 20 torr). The crystallized salt was then further dried by the vacuum dryer (<1 torr) for 24 hours. The collected TMEDA•2HNO$_3$, which is a white powder as shown in Figure 3a, is about 11.5 g which is quite close to the calculate mass (12.1 g). The mass loss can be explained by a small part of the powder that remains on the beaker wall.

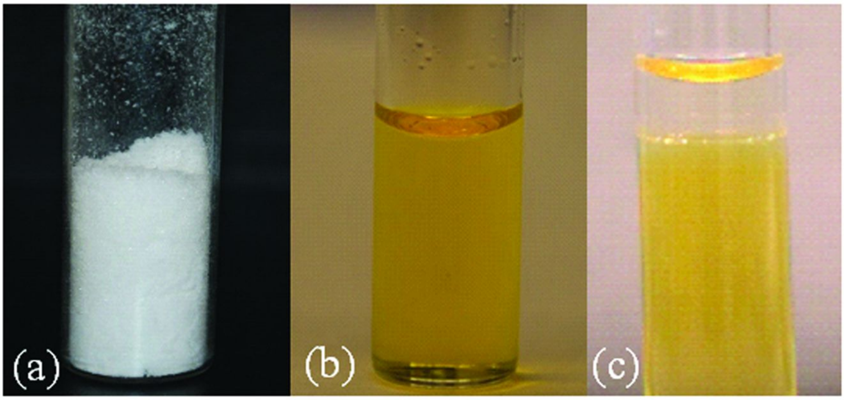

Figure 3. a) TMEDA•2HNO3; b) TMEDA•8HNO3; and c) TMEDA / TMEDA•8HNO3.

The density of TMEDA•2HNO_3 is about 1.67 g/cm^3, which is estimated by observing a volume increase of 0.3 ml after dispersing 0.5 g of this salt into its saturated aqueous solution. TMEDA•2HNO_3 is quite thermally stable similar to ammonium nitrate (*11*) and many alkylammonium nitrates (*12*). In our fast thermolysis experiments with heating rates of 2,000K/s, it starts to melt and decompose rapidly at around 290°C. TMEDA•2HNO_3 is very soluble in both water and WFNA, but almost insoluble in TMEDA. At room temperature, the solubility is about 0.72 g/ml in H_2O and 1.13 g/ml in WFNA. The dissolution of TMEDA·2HNO_3 in H_2O is endothermic, which is similar to ammonium nitrate (*13*). The energy released by solvation of the ions is less than the energy absorbed in breaking up the ionic lattice. However, the dissolution of TMEDA•2HNO_3 in WFNA is exothermic due to the formation of solute-solvent attractions (*14*).

TMEDA•2HNO_3 is extremely oxidizer lean, and therefore this nitrate itself can not be considered as a monopropellant. Instead, an energetic ionic liquid monopropellant was prepared by dissolving TMEDA•2HNO_3 in WFNA at a stoichiometric molar ratio: TMEDA•2HNO_3 / 6HNO_3. This liquid propellant (TMEDA•8HNO_3), shown in Figure 3b, is a viscous yellow liquid with a density of 1.49 g/ml, which is almost the same as that of WFNA. The dissolution process was conducted by adding TMEDA•2HNO_3 to WFNA slowly to avoid potential chemical reactions caused by heat of solvation. Although a major constituent of this liquid propellant is the solvent WFNA which can react with TMEDA violently to cause a hypergolic ignition within a few milliseconds, it is interesting to note that the reactivity of TMEDA•8HNO_3 with TMEDA is unexpectedly slow. These two liquids can be placed together for quite a long time as shown in Figure 3c where the clear liquid on the top is TMEDA and the yellow liquid is TMEDA•8HNO_3 (the two liquids are immiscible). This phenomenon might be explained by the following two reasons: 1) the reactivity of solvent (HNO_3) is reduced due to the formation of solvent-solute attractions during the exothermic solvation process; and 2) the concentration of TMEDA cation is nearly saturated in this liquid propellant, and therefore the salt formation reactions between TMEDA and the solvent HNO_3 are inhibited according to the chemical equilibrium theory.

TMEDA•8HNO_3 is, however, a chemically unstable liquid and will decompose rapidly after about 7 hours even when it is stored at room temperature. The self-accelerating decomposition process of this liquid was recorded by a camera and selected images are shown in Figure 4. During the first 5 hours, this liquid propellant appears to be quite stable and no noticeable changes were observed. After about 6.5 hours, gas bubbles begin to emerge from the liquid due to decomposition reactions. After about 7 hours, the decomposition reactions become very violent and the release of gas bubbles becomes very rapid. Such self-accelerating decomposition phenomena were also reported for hydroxylammonium nitrate (HAN)/nitric acid solutions (*15*). It is important to note that one should not store TMEDA•8HNO_3 in capped vessels in order to avoid potential explosive hazards due to the pressure buildup.

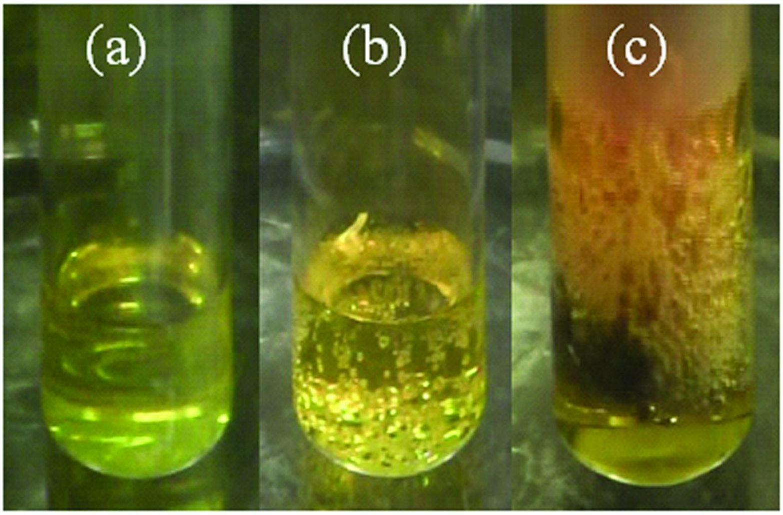

Figure 4. Self-accelerating decomposition of TMEDA•8HNO3 at room temperature: a) 0-5 hours; b) after 6.5 hours; c) after 7 hours.

Experimental Setup

Strand Burner

Strand burners are widely used in combustion studies to obtain burn-rate data of liquid monopropellants (*16–18*). A schematic diagram of the strand burner used for studying the combustion of TMEDA•8HNO_3 liquid strand is shown in Figure 5. The burner is composed of two major portions which are connected by flanges. The bottom portion is a cubic (4×4×4 inches) stainless-steel block with an inner diameter of 1 inch. The top portion is a much larger stainless-steel cylindrical chamber with an inner diameter of 5 inches and a height of inches. The liquid strand, which is held by a glass insert with a diameter of 8 mm and length of 20 mm, is ignited and burned in the bottom chamber. The top chamber functions as a pressure buffer zone for the combustion exhaust gases so that the chamber pressure is kept nearly constant during the combustion. Both the bottom and top chambers are pressurized by nitrogen. The purge-gas flow is kept running through the chamber from the bottom inlet to the top outlet during the test so that the exhaust gases can be carried away from the top portion of the liquid strand and keep a reasonably clean view of the flame zone. The soot of carbon particles (smoke) from incomplete combustion is also effectively carried away from the viewing area. The purge-gas flow is evenly distributed across the chamber by running though many small holes (diameter of 0.8 mm) punched on a round plastic piece. This strand burner also has optical access to a beam from a 100 W CO_2 laser which is used to ignite solid propellants. However, it was found that a liquid strand is difficult to ignite by the CO_2 laser due to a largely in-depth absorption in the liquid of the infrared laser energy at 10.6μm and an inadequate absorption by the evolved gases. The liquid was simply boiled off when the laser was turned on. In this work, the liquid strand was ignited by using a 0.1 mm thick nichrome wire which was connected to two copper rods and positioned at or slightly below the liquid surface. A constant electric current of 1 A, which is slightly lower than the maximum allowable current (1.27 A) above which the nichrome wire will melt and break apart, is provided by a DC power supply through a high-pressure connector. The current needs to be increased slightly due to the increased heat loss when conducting tests at higher pressures with a purge-gas flow. The ignition and combustion processes were recorded by a Phantom V710 high-speed camera, through a glass window with a dimension of 0.75 (width) ×1.75 (height) × 1.0 (thickness) in inches. A printed ruler is placed along the liquid strand to measure the regression rates.

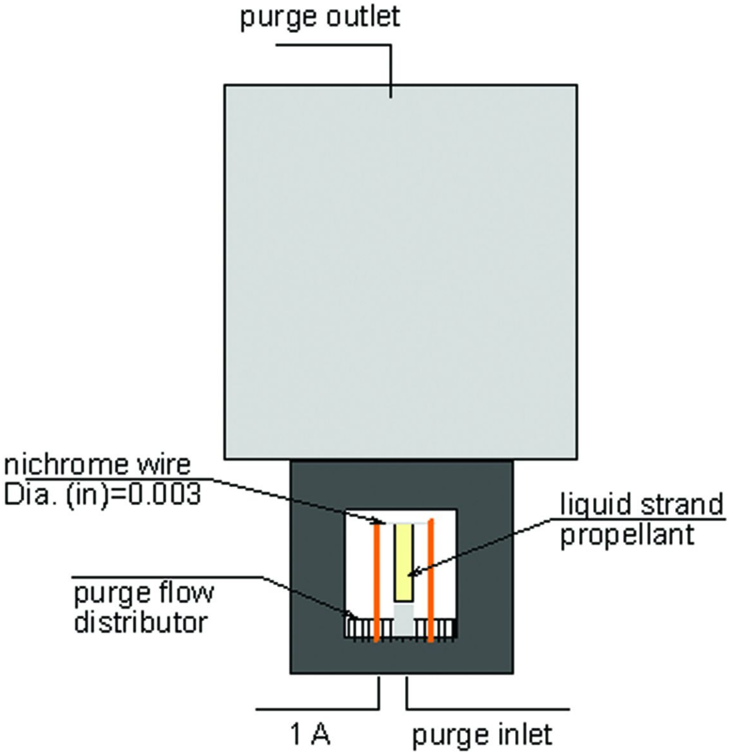

Figure 5. Schematic diagram of strand burner.

Confined Rapid Thermolysis (CRT)/FTIR Setup

The experimental technique utilized to study the rapid thermal decomposition of the energetic materials is known as confined rapid thermolysis (CRT). Detailed discussion of this technique and the associated data-reduction techniques are available in earlier works (*19–21*). A short summary of the process is as follows. A small quantity of the energetic compounds, typically 0.5 mg of a solid or 0.5

μl of a liquid, is confined and heated rapidly between two heated, parallel, and isothermal surfaces in a constant pressure chamber purged by N_2. The heated surfaces are achieved by a stationary top heater and a mobile bottom heater, both of which are fitted with a cartridge heater, while temperature control is maintained by proportional-integral-derivative (PID) controllers. The use of a small sample volume enclosed in a confined space, roughly 300 μm in height, produces heating rates on the order of 2000 K/s. The IR-active gaseous species emerging from the condensed phase are quenched by the relatively cooler atmosphere, and detected in real-time by the modulated beam of a Bruker IFS66/S FTIR spectrometer in the rapid scanning mode, operating at 2 cm^{-1} spectral resolution with a temporal resolution of 50 ms. In each test, a total of 150 spectra are collected, requiring a sampling time of 7.5 s.

Results and Discussion

Combustion of TMEDA•8HNO_3

Liquid strands of TMEDA•8HNO_3 were ignited and burned in the strand burner at various pressures ranging from atmospheric pressure (14.7 psi) to 1000 psi. Figure 6 contains images from combustion tests at several pressures, showing typical gas- and liquid-phase processes as well as flame structures during the combustion and regression of the liquid strands. At one atmosphere, the liquid strand began to decompose when its surface was heated by the hot nichrome wire, but it failed to be ignited. A bubbling zone was formed above the liquid surface due to the release of gases. The thermal decomposition and secondary reactions of TMEDA•8HNO_3 are exothermic and a self-sustained regression of the liquid strand, with a rate of approximately 0.3 mm/s, is observed. Self-sustained decomposition (SSD), in which a locally initiated decomposition will spread throughout the mass of material, is a well-known hazard of ammonium nitrate (AN) based fertilizers (*22*). At 100 and 200 psi, a similar non-luminous self-sustained liquid strand regression was observed. At 300 psi and higher pressures, the liquid strands were ignited by the hot nichrome wire and a bright luminous flame was observed above the liquid surface. At 300 psi, the flame positions itself quite far away from the liquid surface, with a foam layer (approximately 6 mm) and a dark zone (approximately 1 mm) sitting between the flame and the liquid. The foam layer is a two-phase region that is composed of liquid and gas bubbles which are formed by decomposition and evaporation. The dark zone is a gas-phase region where relatively slow reactions occur, usually involving the formation of NO, N_2O and HCN (*23*, *24*). The temperature increases from the liquid's boiling point (or decomposition temperature) to its adiabatic flame temperature in this transition zone (foam layer and dark zone). At this pressure, the flame is not quite stable. It moves up and down frequently with respect to the bubbling surface of the foam layer. When the pressure is increased to 400 psi, the foam layer and dark zone are substantially reduced. A stable flame stays close to and regresses with the liquid surface at an almost constant rate. It should be noted that the regression rate increases slightly with time because the liquid strand becomes preheated by the glass wall, which is heated by the foam layer and hot combustion gases. At higher pressures, such as 600 – 1000 psi, the foam layer is further reduced in size and the flame is almost in contact with the liquid surface. At these pressures, the dark zone is almost undetectable. The glass tube cracked after each test due to the heat transfer from the very hot combustion products.

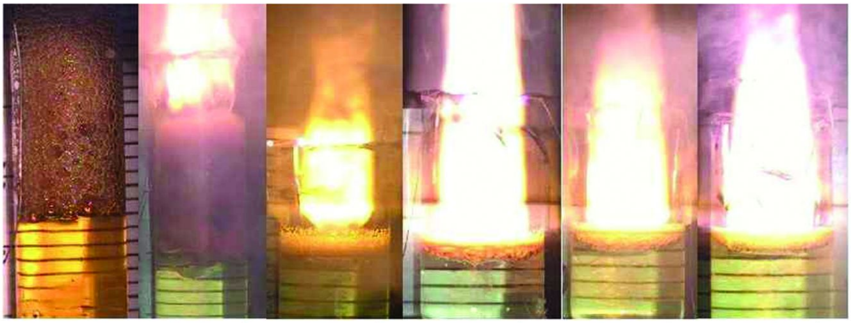

Figure 6. Combustion of TMEDA•8HNO3 strand at various pressures.

As shown in Figure 7, a few selected images from a strand burner test conducted at 400 psi are presented sequentially, showing the temporal processes during the ignition and combustion of the strand. At t = 0, the surface of the strand is heated by the glowing wire and the liquid propellant decomposes to release dark-brown fumes near the surface. The brown color of these fumes is most probably due to the presence of condensed gases of NO_2. At t = 0.3 s, the liquid surface regresses slightly and the volume of the dark-brown fumes keep increasing due to the self-sustained decomposition. A foam layer with gas bubbles is formed between the liquid surface and the fumes above the strand. At t = 0.5 s, the previously accumulated fumes disappear due to further reactions and a luminous flame is observed about 5 mm above the liquid surface. The flame then rapidly propagates towards the liquid surface until a stable flame is formed above the surface, as shown from t = 0.5 to 1.8 s. At t = 0.6 s, the nichrome wire melts and breaks apart due to the high adiabatic flame temperature, and therefore the combustion is self-sustained without further external energy supplied by the nichrome wire. At 400 psi, the flame as well as the strand surface regresses at a rate of about 2 mm/s.

The burn rates of $TMEDA \cdot 8HNO_3$ strands from 400 to 1000 psi are plotted in Figure 8. The data represent average values of three tests at each pressure and the error bars indicate that the burn-rate measurements are quite repeatable. At these pressures, the burn rate increases with pressure almost linearly. The burn rate of $TMEDA \cdot 8HNO_3$ is slower than that of hydroxylammonium nitrate based liquid propellants (*25*).

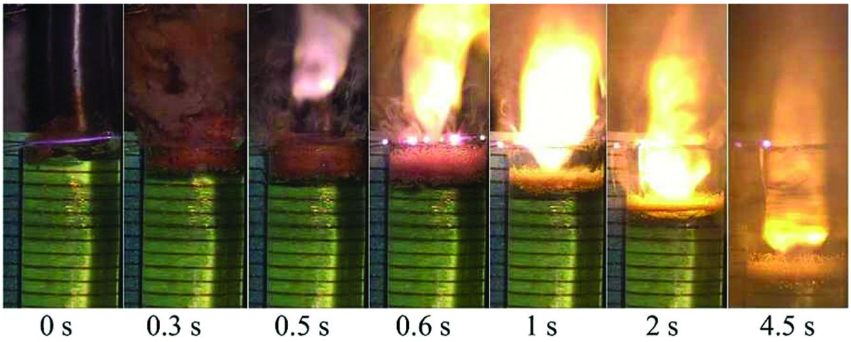

Figure 7. Ignition and combustion of TMEDA•8HNO3 at 400 psi.

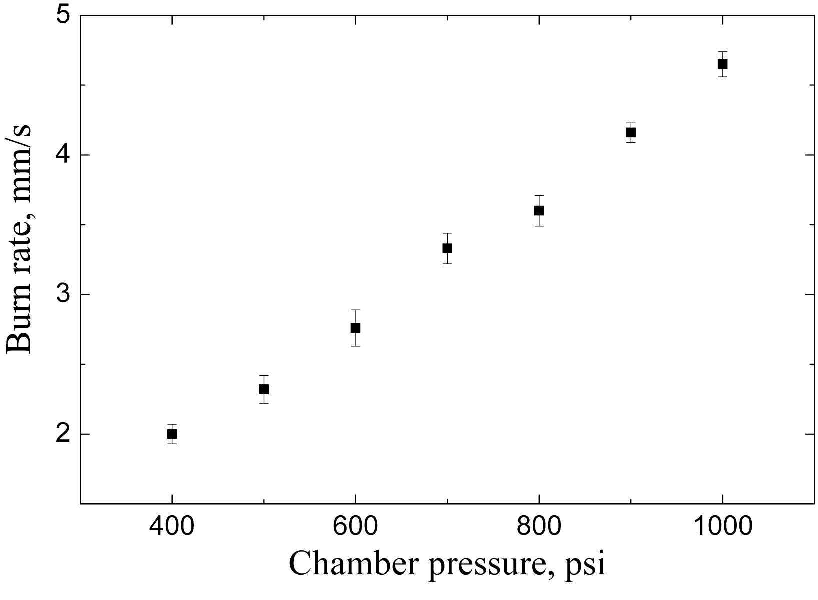

Figure 8. Burn rate of TMEDA•8HNO3.

Rapid Thermolysis of TMEDA•8HNO$_3$

The decomposition of TMEDA•8HNO$_3$ was investigated by conducting confined rapid thermolysis experiments at various temperatures from room temperature to 120°C with a step of 10°C. In each test, only a very small amount of TMEDA•8HNO$_3$ (5 μL) was used so that it can be heated to the preset temperature rapidly. Figure 9 shows the infrared spectra of gaseous IR-active species evolved from the decomposition of TMEDA•8HNO_3 at three selected temperatures (40, 80 and 120°C). The spectrum in each plot is an average of 150 spectra from one test. At 40°C and lower temperatures, the dominant species is nitric acid vapor (HNO_3) which is due to the evaporation of nitric acid, which is a major constituent of this liquid propellant. Small amounts of NO_2 and H_2O, which are typical products from the decomposition of nitric acid (*26*), were also detected, as shown in Figure 9a. At 50-80°C, the major IR-active species evolved from the condensed-phase decomposition include NO_2, H_2O, HNO_3, HCOOH, CO_2 and glyoxylic acid (HOCCOOH) which has infrared absorption bands at 1798 and 1748 cm^{-1} due to the carbonyl and carboxylic groups (*27*), as shown in Figure 9b. The formation of carbon containing species indicates that the TMEDA cation, $(CH_3)_2NH^+CH_2CH_2NH^+(CH_3)_2$, is involved in the reactions and decomposes at these temperatures. At 90-120°C, additional species such as CH_2O, N_2O, NO and a small amount of dimethylnitrosamine $(CH_3)_2NNO$ (1015, 1292 and 1488 cm^{-1}) (*9*) are also detected, as shown in Figure 9c. TMEDA•8HNO_3 decomposes at much lower temperatures than TMEDA dinitrate (TMEDA•2HNO_3) which requires quite high temperatures (around 290°C) to overcome the lattice energy to form TMEDA and HNO_3, TMEDA·2HNO_3 $\rightarrow$ TMEDA + 2HNO_3 (*9*). Decomposition and reaction of TMEDA•8HNO_3, however, is much easier because the TMEDA cation can be directly oxidized by the existing HNO_3 in this liquid.

The temporal evolution of IR-active gaseous species at 80°C is shown in Figure 10. The species concentrations of various species, such as H_2O, HNO_3, NO_2, CO_2 and HCOOH are extracted by a non-linear, least-squares method by comparison with theoretical transmittance. The radiative properties, such as partition function, half-width of spectral lines, and its temperature exponent, are determined from HITRAN database (*28*). A more detailed introduction of this data reduction technique is available in an earlier work (*19*). It should be note that glyoxylic acid (HOCCOOH) has not been quantified due to the lack of its theoretical transmittance in the HITRAN database. As indicated by the temporal species profiles in Figure 10, HNO_3 and NO_2 evolve rapidly as soon as TMEDA·8HNO_3 is heated (t = 0). Meanwhile, H_2O and glyoxylic acid evolve slowly due to slow decomposition in the condensed phase. The rapid decrease of concentrations of species in this plot is caused by the purge-gas flow of N_2. At t = 1.7 s, rapid condensed-phase decomposition release large amounts of NO_2 and H_2O. Glyoxylic acid, formic acid and CO_2 also evolve rapidly. Compared to other species, HNO_3 only increases slightly at t = 1.7 s because it rapidly reacts to form other species. The evolution of large amounts of NO_2 and H_2O indicates the condensed-phase decomposition of nitric acid is of great importance in the decomposition mechanism. Nitric acid and its aqueous solutions decompose to form NO_2, O_2 and H_2O as the final products. The global reaction can be written as follows (*26*):

$$4HNO_3 \rightarrow 4NO_2 + 2H_2O + O_2$$

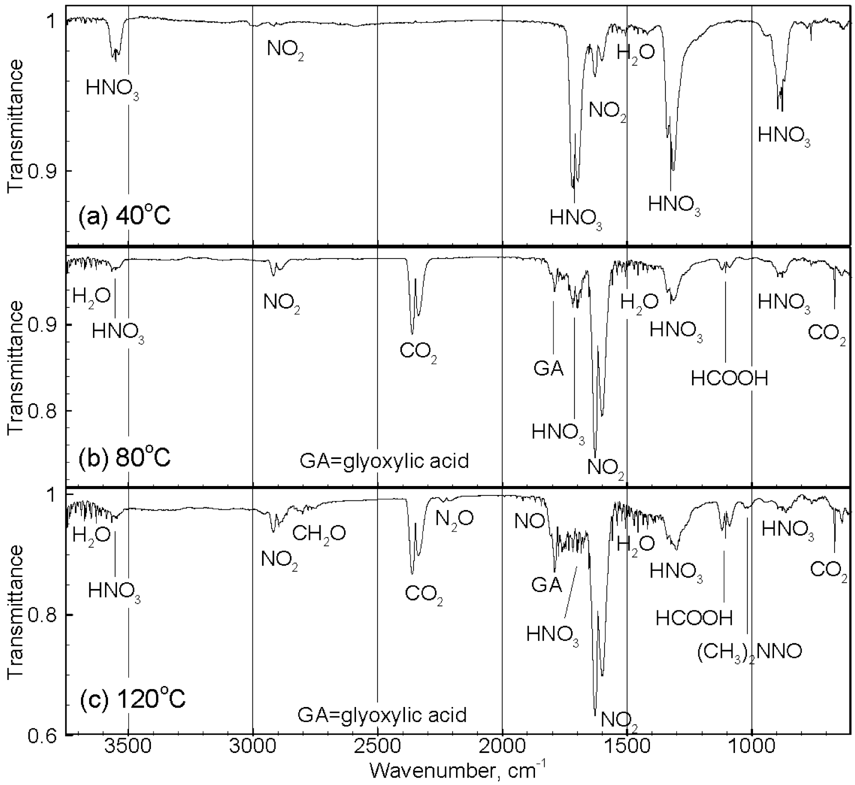

Figure 9. IR spectra of gaseous species evolved from rapid thermolysis of TMEDA•8HNO3 at various temperatures.

The formation of HCOOH and glyoxylic acid has been reported in the oxidation of many aliphatic alkylamines (*29*). The oxidation paths of TMEDA cation $(CH_3)_2NH^+CH_2CH_2NH^+(CH_3)_2$ by nitric acid are proposed in Figure 11. Oxidation of alkyl groups generally follows two steps: 1) oxidation of alkyl groups to carbonyl groups such as aldehydes (-CHO); and 2) further oxidation of carbonyl groups to carboxylic groups (-COOH). Reactions R1-R4 show the paths through which the TMEDA cation is oxidized by HNO_3 to form aldehyde intermediates such as $(CH_3)_2NHCH_2CHO$ and HOC-CHO, involving the elimination of H_2O and the formation of an unstable nitrite (-ONO) intermediate. The remaining part is converted to dimethylnitrosamine $(CH_3)_2NNO$ which has a relative high boiling point (153°C) and tends to stay in the condensed phase, and therefore only very a very small amount of $(CH_3)_2NNO$ was detected at these temperatures. Reactions

R5 and R6 involve the further oxidation of glyoxal (HOC-CHO) to glyoxylic acid (HOC-COOH) which was observed in the experiments. Reactions R7 and R8 represent the further oxidation of glyoxylic acid (HOC-COOH) to oxalic acid (HOOC-COOH), through the same paths as R5-R6, involving the formation of a nitrite intermediate and $ONONO_2$ which is the isomer of dinitrogen tetroxide (N_2O_4). $ONONO_2$ will decompose to NO_2 through the equilibrium reactions R9 and R10 (*30*). Reaction R11 is the decomposition of oxalic acid, which was reported (*31*, *32*) to form formic acid HCOOH and CO_2 which were observed in the experiments. Reaction R12 is the decomposition of glyoxylic acid to form formaldehyde CH_2O and CO_2 (*33*). These reactions (R1-R12) are exothermic from a global reaction point of view, and can cause a self-sustained regression of the liquid strand at atmosphere conditions as discussed in Figures 4 and 6.

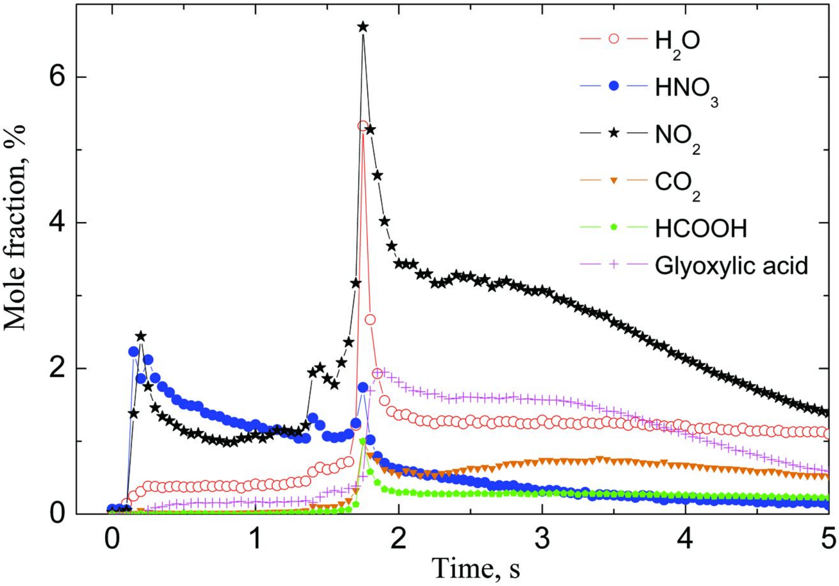

Figure 10. Temporal evolution of species from rapid thermolysis of TMEDA•8HNO3 at 80°C and 1 atm N3.

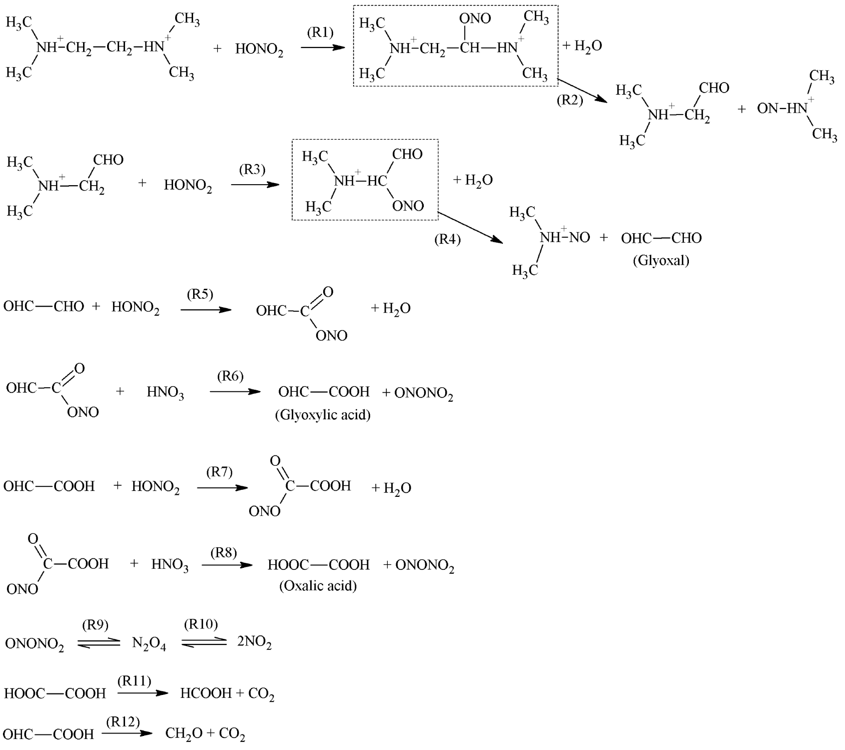

Figure 11. Oxidation of TMEDA cation by HNO3.

Conclusions

TMEDA•8HNO3, an ionic liquid monopropellant with a stoichiometric F/O ratio, was synthesized from the hypergolic pair TMEDA and HNO3 through two steps: 1) synthesis of TMEDA dinitrate TMEDA•2HNO3; and 2) dissolution of TMEDA•2HNO3 in WFNA. TMEDA•8HNO3 can be ignited and burned at pressures above 300 psi, and the burn rate increases linearly with pressure from 400 to 1000 psi. At pressures below 300 psi, the liquid strands decomposed and regressed without a luminous flame. TMEDA•8HNO3 is thermally unstable and can only be kept for a short period of time under atmospheric conditions; if kept longer, it will decompose through a self-accelerating decomposition process. The gaseous products from the decomposition of TMEDA•8HNO3 were analyzed by rapid thermolysis studies from room temperature to 120°C. The major reactions include: 1) decomposition of nitric acid to form NO2 and H2O; 2) the oxidation of TMEDA cation by nitric acid to form carboxylic acids HOC-COOH and HCOOH; and 3) further oxidation of these carboxylic acids to form CO2. Due to its poor thermal stability, TMEDA•8HNO3 can not be considered as a practical monopropellant. However, the combustion studies on this compound provided first-hand burn rate data for future use in premixed combustion modeling of the hypergolic pair TMEDA/HNO_3. The oxidation reactions of TMEDA cation by nitric acid investigated in this study should also be considered as an important part of the TMEDA/RFNA mechanism.

Acknowledgments

This material is based upon work supported by, or in part by, the U.S. Army Research Laboratory and the U.S. Army Research Office under grant number W911NF-08-1-0124.

References

1. Paquette, L. *Encyclopedia of Reagents for Organic Synthesis*; J. Wiley & Sons: New York, 2004.
2. Stevenson, W. H. Hypergolic Liquid or Gel Fuel Mixtures. United States Patent No. 0127551, 2008.
3. McQuaid, M. J.; Stevenson, W. H.; Thompson, D. M. *Computationally Based Design and Screening of Hypergolic Multiamines*; NTIS No. ADA433347; U.S. Army Research Laboratory, Aberdeen Proving Ground, MD, 2004.
4. Chen, C.-C.; Nusca, M. J.; McQuaid, M. J. *Modeling Combustion Chamber Dynamics of Impinging Stream Vortex Engines Fueled with Hydrazine-Alternative Hypergols*; NTIS-ADA503941; U.S. Army Research Laboratory, Aberdeen Proving Ground, MD, 2008.
5. Reddy, G.; Song, J.; Mecchi, M. S.; Johnson, M. S. *Mutat. Res.* **2010**, *700*, 26.
6. Sutton, G. P. *History of Liquid Propellant Rocket Engines*; American Institute of Aeronautics and Astronautics: Alexandria, VA, 2006.
7. Clark, J. D. *Ignition! An Informal History of Liquid Rocket Propellants*; Rutgers University Press: New Brunswick, NJ, 1972.
8. Wang, S. Q.; Thynell, S. T. *Combust. Flame* **2012**, *159*, 438.
9. Wang, S.; Thynell, S. T.; Chowdhury, A. *Energy Fuels* **2010**, *24*, 5320.
10. Liu, W.-g.; Dasgupta, S.; Zybin, S. V.; Goddard, W. A. *J. Phys. Chem. A* **2011**, *115*, 5221.
11. Brower, K. R.; Oxley, J. C.; Tewari, M. *J. Phys. Chem.* **1989**, *93*, 4029.
12. Jain, S. R.; Rao, M. V.; Pai Verneker, V. R. *Propellants, Explos., Pyrotech.* **1978**, *3*, 83.
13. Kauffman, G. B.; Ferguson, C. A. *J. Chem. Educ.* **1988**, *65*, 267.
14. Siegel, G. G.; Huyskens, P. L.; Vanderheyden, L. *Ber. Bunsengesellschaft Phys. Chem.* **1990**, *94*, 549.
15. Harlow, D. G.; Felt, R. E.; Agnew, S.; Barney, G. S.; McKibben, J. M.; Garber, R.; Lewis, M. *Technical Report on Hydroxylamine Nitrate*; U.S. Department of Energy, 1998.
16. Boyer, J. E. Combustion Characteristics and Flame Structure of Nitromethane Liquid Monopropellant. Ph.D. Thesis, The Pennsylvania State University, 2005.

17. Vosen, S. R. *Symp. (Int.) Combust.* **1989**, *22*, 1817.
18. Katsumi, T.; Kodama, H.; Matsuo, T.; Ogawa, H.; Tsuboi, N.; Hori, K. *Combust., Explos., Shock Waves* **2009**, *45*, 442.
19. Mallery, C. F.; Thynell, S. T. *Combust. Sci. Technol.* **1997**, *122*, 113.
20. Kim, E. S.; Lee, H. S.; Mallery, C. F.; Thynell, S. T. *Combust. Flame* **1997**, *110*, 239.
21. Chowdhury, A.; Thynell, S. T. *Thermochim. Acta* **2006**, *443*, 159.
22. Hadden, R.; Jervis, F.; Rein, G. *Fire Saf. Sci.* **2008**, *9*, 1091.
23. Kumbhakarna, N.; Thynell, S. T.; Chowdhury, A.; Lin, P. *Combust. Theory Modell.* **2011**, *15*, 933.
24. Anderson, W. R.; Meagher, N. E.; Vanderhoff, J. A. *Combust. Flame* **2011**, *158*, 1228.
25. Kondrikov, B.; Annikov, V.; Egorshev, V.; De Luca, L. *Combust., Explos., Shock Waves* **2000**, *36*, 135.
26. Stern, S. A.; Mullhaupt, J. T.; Kay, W. B. *Chem. Rev.* **1960**, *60*, 185.
27. Redington, R. L.; Liang, C.-K. J. *J. Mol. Spectrosc.* **1984**, *104*, 25.
28. Rothman, L. S.; Jacquemart, D.; Barbe, A.; Chris Benner, D.; Birk, M.; Brown, L. R.; Carleer, M. R.; Chackerian, J. C.; Chance, K.; Coudert, L. H.; Dana, V.; Devi, V. M.; Flaud, J. M.; Gamache, R. R.; Goldman, A.; Hartmann, J. M.; Jucks, K. W.; Maki, A. G.; Mandin, J. Y.; Massie, S. T.; Orphal, J.; Perrin, A.; Rinsland, C. P.; Smith, M. A. H.; Tennyson, J.; Tolchenov, R. N.; Toth, R. A.; Vander Auwera, J.; Varanasi, P.; Wagner, G. *J. Quant. Spectrosc. Radiat. Transfer* **2009**, *110*, 533.
29. Takasaki, M.; Harada, K. *Tetrahedron* **1985**, *41*, 4463.
30. Pimentel, A. S.; Lima, F. C. A.; da Silva, A. B. F. *J. Phys. Chem. A* **2007**, *111*, 2913.
31. Kakumoto, T.; Saito, K.; Imamura, A. *J. Phys. Chem.* **1987**, *91*, 2366.
32. Higgins, J.; Zhou, X.; Liu, R.; Huang, T. T. S. *J. Phys. Chem. A* **1997**, *101*, 2702.
33. Back, R. A.; Yamamoto, S. *Can. J. Chem.* **1985**, *63*, 542.

Chapter 4

Ionic Liquid-Based Electrolytes for High Energy, Safer Lithium Batteries

G. B. Appetecchi,*,[1] M. Montanino,[1] and S. Passerini*,[2]

[1]ENEA (Italian National Agency for New Technologies, Energy and Sustainable Economic Development) UTRINN-IFC C.R. Casaccia,
Via Anguillarese 301, 00123 Rome, Italy
[2]Westfälische Wilhelm Universität Muenster,
Institute of Physical Chemistry, Corrensstrasse 28/30, MEET,
Corrensstrasse 46, D-48149 Muenster, Germany
***E-mail: stefano.passerini@uni-muenster.de (S.P.);**
gianni.appetecchi@enea.it (G.B.A)

Ionic Liquids (ILs), salts molten at room temperature, have very interesting properties such as high chemical, thermal and electrochemical stability, high conductivity, no measurable vapor pressure and non-flammability. Because of these characteristics, ILs were proposed as electrolyte components for replacing the hazardous and volatile organic solvents used in commercial electrochemical devices, particularly rechargeable lithium batteries. In the last ten years ionic liquid-based electrolytes in combination with lithium battery electrodes were extensively investigated with the aim to realize safer devices without hindering their electrochemical performance. Here, a review of best promising uses of ionic liquid-based electrolytes in lithium batteries is reported.

In Ionic Liquids: Science and Applications; Visser, A., et al.;
ACS Symposium Series; American Chemical Society: Washington, DC, 2012.

Ionic Liquid Electrolytes for Lithium Batteries

Lithium Batteries

Rechargeable lithium batteries are excellent candidates for the next generation power sources (*1*, *2*) because of their high gravimetric and volumetric energy with respect to other cell chemistries as reported in Figure 1 (left panel).

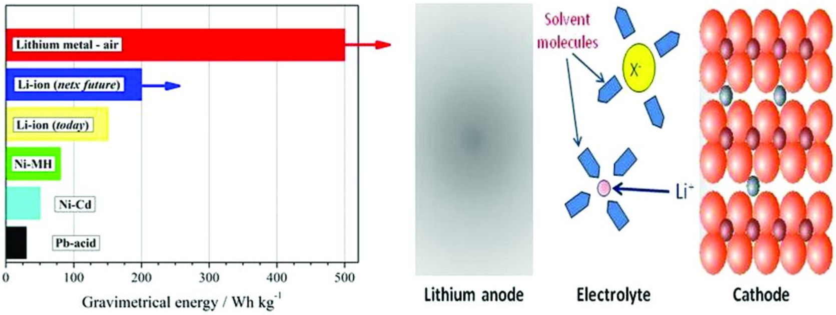

Figure 1. Gravimetrical energy of different cell chemistries. Schematic illustration of a lithium battery.

The lithium battery technology (Figure 1, right panel) is based on the use of electrode materials able to reversibly intercalate lithium cations. Lithium metal is used for the negative electrode (anode), whereas a lithium transition metal oxide (LiMO) is used for the positive electrode (cathode). During the discharge step, electrons are generated at the anode to do external work whereas positive ions migrate to the cathode through the electrolyte. The electrode reactions during discharge are:

$$\begin{array}{rlll} & x\,\mathrm{Li}^{\circ} \rightarrow & x\,\mathrm{Li}^{+} + x\,\mathrm{e}^{-} & \text{(negative electrode)} \\ x\,\mathrm{Li}^{+} + x\,\mathrm{e}^{-} + & \mathrm{Li_yMO_z} \rightarrow & \mathrm{Li}_{(y+x)}\mathrm{MO_z} & \text{(positive electrode)} \end{array}$$

However, lithium metal cells exhibit poor safety because of the high reactivity of Li anode towards the electrolyte, this leading to the growth of a porous passive layer (which is sensible to mechanical, thermal and electrical abuse) and/or dendrites (which might lead to internal short-circuit) onto the lithium electrode. Therefore, the lithium anode has been replaced with a negative electrode (generally a carbonaceous material) able to reversibly intercalate Li^+ cations:

$$x\,\mathrm{Li}^{+} + 6\,\mathrm{C} \rightarrow \mathrm{Li}_x\mathrm{C}_6 \quad \text{(graphite anode)}$$

The graphite/Li_yMO cell system is called "*lithium-ion*" since the lithium is present just as a cation. The overall electrochemical process may be schematized as the following:

$$6\,\mathrm{C} + \mathrm{Li_yMO_z} \rightarrow \mathrm{Li}_x\mathrm{C}_6 + \mathrm{Li_{y-x}MO_z}.$$

Safety Drawbacks in Lithium Batteries

Rechargeable lithium battery systems commonly use small amount of electrolytes based on suitable lithium salts (generally $LiPF_6$) and organic solvents (generally alkylcarbonates as EC, DEC, DMC), volatile and flammable, which represent a major problem for device safety (*2–4*).

The lithium-ion battery configuration improves the safety of lithium batteries because lithium is only contained within a host structure, both at the anode and at the cathode. During charge and discharge, lithium is simply transferred between one host structure and the other, with concomitant oxidation and reduction processes occurring at the two electrodes. However, in their charged state, the lithium-ion cells are inherently unsafe. The lithiated graphite electrode is strongly reducing as it operates close to the potential of metallic lithium. The interface between lithiated graphite and the electrolyte is stable only because of the formation of a solid electrolyte interphase (also called SEI) that is generated during the first charge of the battery. It is typically formed by the electrolyte decomposition products and has a mixed organic-inorganic nature. The SEI is a pure Li^+ ion conductor, and, once formed, prevents the electrolyte from being further reduced. However, if the SEI is degraded then the electrolyte is further degraded with heat release and generation of flammable gases, such as H_2, CO, C_2H_4 and C_2H_6. A delithiated $Li_{1-x}MO_2$ electrode is, on the other hand, an extremely strong oxidant. The presence of flammable and volatile organics (even if trapped in polymeric hosts as in a few commercial lithium-ion polymer batteries), dangerous events such as heat generation, thermal runaway, cell venting, fire, and rapid disassembly may occur. Therefore, whereas lithium-ion batteries are rapidly replacing NiMH batteries in consumer market devices (e.g., portable and hand-held devices), the main drawback for their large introduction in automotive products (electric and hybrid vehicles) continues to be the safety related to thermal effects.

As is well known, the safety (but also the performance and life) of lithium-ion batteries is affected by their storage and operative temperatures (*5*). If heat developed during the charge step is not effectively dissipated, the battery internal temperature increases rapidly which triggers heat-generating exothermic reactions, such as the SEI breakdown, which, in turn, raise the temperature further and triggers more deleterious reactions, often leading to destructive results. Such a process, considered as a sort of uncontrolled positive feedback, is known as "*thermal runaway*" (Figure 2, left panel).

Rechargeable lithium batteries can experience thermal runaway, especially when handled improperly (overcharged) or manufactured defectively. Several stages are involved in the build up to thermal runaway, each one resulting in progressively more permanent damage to the cell:

i) The first stage is the breakdown of the thin passive SEI layer on the (graphite) anode due to overheating or physical penetration. The initial overheating may be caused by excessive current flow, overcharging or high external ambient temperature. The SEI film (which normally protects the lithiated graphite from further reaction with the organic electrolyte) contains both stable and metastable compounds, the latter decomposing exothermically when the temperature rises to a value between 85°C and 120°C (*6*, *7*). Once breaching the SEI layer, the organic electrolyte begins to exothermically react (around 100°C) with the negative electrode just as it did during the formation process, but driving the temperature up to much higher and uncontrolled values (near 200°C).

ii) As the temperature builds up, heat from the anode reaction causes the breakdown of the organic solvents used in the electrolyte this releasing flammable hydrocarbon gases (ethane, methane and others) but no oxygen. This typically starts at 110°C, but with some electrolytes it can occur as low as 70°C. The gas generation due to the breakdown of the electrolyte causes pressure to build up inside the cell. Although the temperature increases to beyond the flashpoint of the vapors released by the electrolyte decomposition, the gases do not burn because there is no free oxygen in the cell to sustain a fire. The cells are normally fitted with a safety vent which allows the controlled release of the gases to relieve the internal pressure in the cell avoiding the possibility of an uncontrolled rupture of the cell - otherwise known as an explosion or more euphemistically "rapid disassembly" of the cell. Once the hot gases are released into the atmosphere, they can, of course, burn in air.

iii) At around 135°C the polymer separator melts, allowing the electrodes to short circuit.

iv) Heat from short circuits causes breakdown of the metal oxide cathode material, which releases oxygen, thus enabling the combustion burning of both the electrolyte and the gases inside the cell. Also, the cathode breakdown is highly exothermic, thus further increasing the internal temperature and pressure. This reaction starts above 180°C (*8*), e.g., around 200°C for LCO cells but at higher temperatures for other cathode chemistries such as LFP (*9*) and $LiNi_{0.8}Co_{0.15}Al_{0.05}O_2$ (*7*).

v) By this time the internal pressure is extremely high, thus leading to the violent explosion of the cell if safety vents are overwhelmed or nonfunctional.

A similar pathway was proposed by Yang at al. (*7*) for thermal runaway in lithium-ion batteries. Once the SEI layer begins to exothermally decompose (T > 85°C), a secondary film starts to form, which is successively decomposed if the temperature increases above 110°C. The thermal energy released at this stage may be absorbed through electrolyte vaporization (about 140°C) or separator melting (130 - 190°C). Hazardously, the organic electrolyte can readily combust once vaporized if oxygen is available (e.g., from the delithiated positive electrode). In addition, the separator melting could cause short circuit of the battery electrodes, leading to additional heating. The negative graphite electrode begins to react at 330°C, releasing some additional heat. Eventually, the aluminum current collector can melt at 660°C, if catastrophic events (explosion) do not occur first. In addition, it is noteworthy that the electrolyte burning causes the decomposition of the $LiPF_6$ salt, leading to the development of highly toxic HF gas.

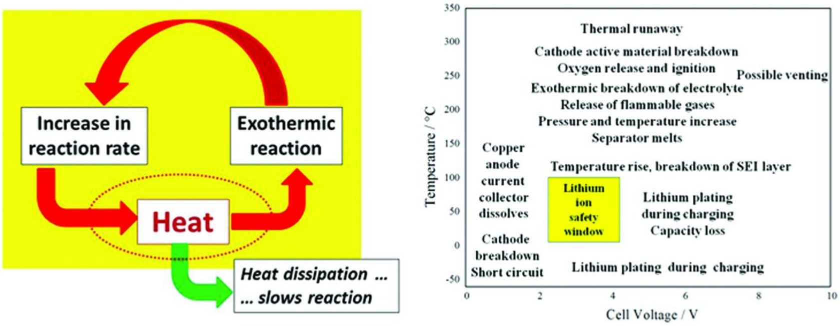
Increase in reaction rate
Exothermic reaction
Heat
Heat dissipation …
… slows reaction
Thermal runaway
Cathode active material breakdown
Oxygen release and ignition
Possible venting
Exothermic breakdown of electrolyte
Release of flammable gases
Pressure and temperature increase
Separator melts
Copper anode current collector dissolves
Temperature rise, breakdown of SEI layer
Lithium ion safety window
Lithium plating during charging
Capacity loss
Cathode breakdown
Short circuit
Lithium plating during charging
Temperature / °C
350
300
250
200
150
100
50
0
-50
0
2
4
6
8
10
Cell Voltage / V

Figure 2. Left panel: diagram of thermal runaway. Right panel: Lithium-ion cell operating window. Data from refs. (10, 11).

To summarize, heat is a major danger for lithium-ion batteries. The effect of decreasing the operating temperature is to reduce the rate at which the active chemicals are transformed. This leads to a reduction in the current carrying capacity of the cell both for charging and discharging. Moreover, the operating voltage can affect the battery performance. If the charging voltage is increased beyond the recommended upper cell voltage (typically 4.2 V), excessive current flows giving rise to two problems, e.g., lithium plating and overheating. The diagram reported in the right panel of Figure 2 shows that the cell operating voltage and temperature must be kept within the limits indicated by the yellow box or permanent damage to the cell will be initiated.

Obviously, this scenario can be quite dangerous for lithium-ion batteries, especially for large systems. Therefore, large efforts are currently aimed to increase battery safety. Air and/or liquid cooling can improve the cell temperature uniformity, even if poor thermal conductivity does not allow fast heat dissipation from the battery. For anodes, LTO results much safer than graphite since no growth passive layer occurs at interface with the electrolyte. For cathodes, LCO starts to break just above 150°C releasing very large amount of thermal energy whereas LFP breaks down with oxygen release a much higher temperature (> 225°C) since oxygen has a much stronger valence bond to phosphorous, resulting also in smaller exothermic heat release (*9*). The addition of flame-retardants, as aromatic phosphorous-containing esters, to the electrolyte was found to remarkably inhibit the thermal runaway, thus preventing potential fire and explosion (*12*). Finally, an appealing and very promising approach, which currently knows a true blowing-up, is represented by the replacement of organic hazardous solvents with non-volatile, non-flammable, thermally stable fluids known as "*ionic liquids*".

Viable Ionic Liquids for Lithium Batteries

"Ionic liquid" (IL) is the commonly accepted term for low-melting salts, typically below 100°C (*13*). If molten at room temperature, they are called room temperature ionic liquids (RTILs). ILs, constituted by an organic cation and an inorganic/organic anion, represent a new class of room temperature fluids with very interesting properties including non-flammability, negligible vapor pressure in conjunction with a ambient or sub-ambient melting point (*14*, *15*), remarkable ionic conductivity, high thermal, chemical end electrochemical stabilities, low heat capacity, ability to dissolve inorganic (including lithium salts), organic and polymeric materials and, in some cases, hydrophobicity (*16*, *17*). Because of these unique properties, the ILs have attracted growing attention as electrolyte components to replace organic solvents currently used not only for lithium batteries, but also in other electrochemical devices such as fuel cells, double-layer capacitors, hybrid supercapacitors, photoelectrochemical cells, and applications such as electrodeposition of electropositive metals (*18*–*24*), resulting in improved safety in case of overheating/overcharging (e.g., such as some spectacular flaming/explosions have occurred with conventional lithium-ion batteries in recent years).

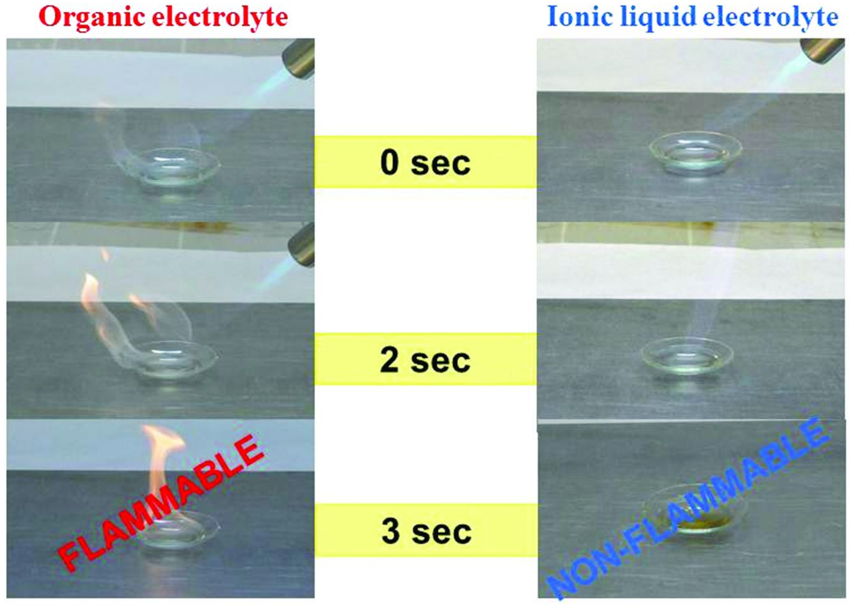

Figure 3. Flammability tests performed on organic solvent mixture (EC-DMC, left panel) and IL (PYR$_{14}$TFSI, right panel) for lithium conducting electrolytes.

Flammability and volatility tests have evidenced the remarkably improved behavior of IL electrolytes with respect to organic ones. As shown in Figure 3, no flammability is observed for the IL material even upon prolonged exposition to fire. Figure 4 evidences the internal pressure increase of an organic electrolyte pouch cell (panel A) due to solvent evaporation after heating the electrochemical device up to medium-high temperature (≥ 50°C). Conversely, no volume change was exhibited by the IL-containing cell (panel B), which evidenced a very good vacuum retention.

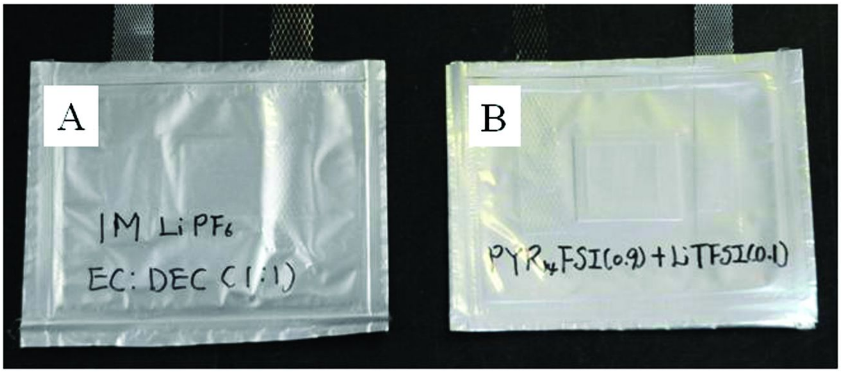

Figure 4. Heating tests performed on vacuum-sealed cells based on organic- (A) and IL- (B) based electrolytes.

An IL-lithium salt mixture needs to meet a few requirements to find application as an electrolyte component in lithium batteries:

- High ionic conductivity ($\geq 10^{-3}$ S cm^{-1}), even at sub-ambient temperature in order to assure sufficiently high Li^+ transport properties through the electrolyte;
- Wide electrochemical stability to allow Li^+ reversible intercalation, even at high voltages, without any relevant degradation;
- High thermal stability to allow safe utilization at high-temperature;
- No hydrolysis, thus minimizing the generation of protons;
- Hydrophobicity, minimizing the water incorporation into the battery.

Such properties are mainly satisfied by ILs formed by di- or trialkyl-imidazolium, saturated cyclic aliphatic quaternary ammonium as *N*-methyl-*N*-alkylpyrrolidinium (PYR_{1A} where the subscripts indicate the number of carbon atoms in the alkyl side chains) or *N*-methyl-*N*-alkylpiperidinium (PIP_{1A}), tetraalkylammonium (A_4N) cations in combination with hydrophobic perfluoroalkylsulfonylimide anions, e.g., FSI, TFSI, BETI, IM_{14} (where the subscripts indicate the number of carbon atoms in the fluorine-containing side chains).

Figure 5 depicts the chemical structure of the most common IL cations and anions used as electrolyte components for lithium batteries, while their physicochemical properties are summarized in Table 1. The room or sub-ambient melting point is addressed to cation/anion bulkiness and asymmetry, which hinder the crystal packing of the ions (*13*, *15–17*). In particular, highly asymmetric anions such as IM_{14} do not allow the IL material to crystallize even in presence of symmetric cation (i.e., PYR_{11}), resulting in a very low melting point, e.g., lower than -40°C (*25*). Also, the introduction of an oxygen atom in the side aliphatic chain was seen to sharply decrease the melting temperature as a result of the enhanced flexibility of the ether group, this further reducing the ion packing (*26*, *27*) but also affecting the thermal and electrochemical stability of the IL (*25*, *28*).

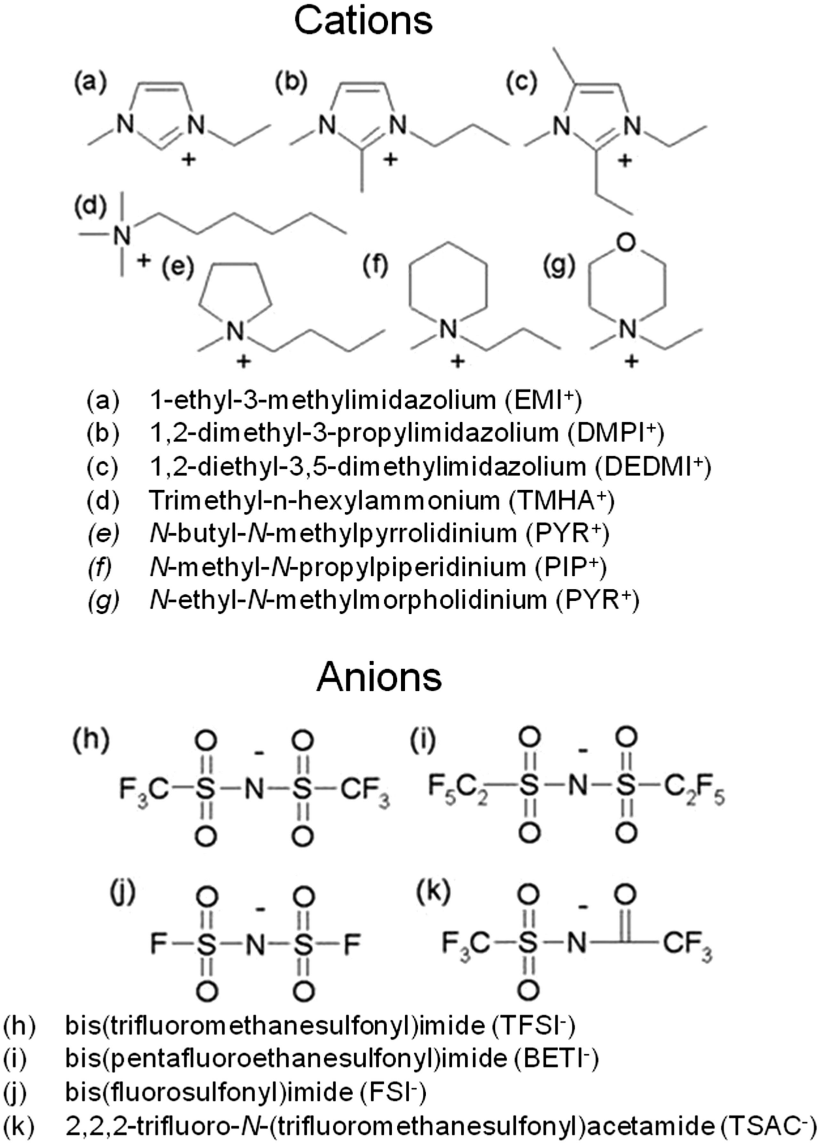

(a) 1-ethyl-3-methylimidazolium (EMI^+)
(b) 1,2-dimethyl-3-propylimidazolium ($DMPI^+$)
(c) 1,2-diethyl-3,5-dimethylimidazolium ($DEDMI^+$)
(d) Trimethyl-n-hexylammonium ($TMHA^+$)
(e) *N*-butyl-*N*-methylpyrrolidinium (PYR^+)
(f) *N*-methyl-*N*-propylpiperidinium (PIP^+)
(g) *N*-ethyl-*N*-methylmorpholidinium (PYR^+)

(h) bis(trifluoromethanesulfonyl)imide ($TFSI^-$)
(i) bis(pentafluoroethanesulfonyl)imide ($BETI^-$)
(j) bis(fluorosulfonyl)imide (FSI^-)
(k) 2,2,2-trifluoro-*N*-(trifluoromethanesulfonyl)acetamide ($TSAC^-$)

Figure 5. Chemical structure of the most common IL cations and anions used as electrolyte components for lithium batteries.

Table 1. Physicochemical properties of various ILs for lithium battery applications. Melting point: m.p.; thermal stability: ther. stab.; viscosity: η. Data from refs. (*25*, *28–30*)

Ionic Liquid	*m.p./°C*	*Ther. stab. / °C*		*η / mPa s*		*σ / mS cm^{-1}*		*ESW / V*
		N$_2$	*Air*	*20°C*	*60°C*	*- 10°C*	*20°C*	*20°C*
PYR$_{11}$TFSI	131.0	405.1	390.0	solid	solid	$< 10^{-5}$	2×10^{-5}	solid
PYR$_{12}$TFSI	91.8	----	----	solid	solid	$< 10^{-5}$	----	solid
PYR$_{13}$TFSI	11.4	----	----	72	17	$< 10^{-5}$	2.7	5.84
PYR$_{1iso3}$TFSI	6.0	----	----	solid	solid	$< 10^{-5}$	$< 10^{-5}$	solid
PYR$_{1n4}$TFSI	-6.5	392.2	381.1	95	21	6.2×10^{-4}	1.8	5.83
PYR$_{1isO4}$TFSI	6.0	----	----	----	----	4.0×10^{-4}	2.3	6.09
PYR$_{1sec4}$TFSI	10.1	----	----	79	18	1.5×10^{-5}	1.8	3.61
PYR$_{15}$TFSI	13.6	----	----	103	23	$< 10^{-5}$	1.3	5.91
PYR$_{16}$TFSI	2.2	----	----	125	24	$< 10^{-5}$	1.0	5.95
PYR$_{17}$TFSI	16.7	389.3	373.4	131	28	$< 10^{-5}$	0.8	5.96
PYR$_{18}$TFSI	-13.7	----	----	149	28	7.4×10^{-2}	0.54	5.83
PYR$_{1,10}$TFSI	9.6	----	----	210	37	$< 10^{-5}$	0.33	5.63
PYR$_{1(2O1)}$TFSI	< -40°C	414.8	416.4	71	19	0.47	2.4	4.84
PYR$_{1(2O2)}$TFSI	< -40°C	----	----	62	17	0.41	2.1	4.38
PIP$_{11}$TFSI	127.0	443.5	439.4	solid	solid	$< 10^{-5}$	2.2×10^{-5}	solid

Continued on next page.

Table 1. (Continued). Physicochemical properties of various ILs for lithium battery applications. Melting point: m.p.; thermal stability: ther. stab.; viscosity: η.

Ionic Liquid	*m.p./°C*	*Ther. stab. / °C*		*η / mPa s*		*σ / mS cm⁻¹*		*ESW / V*
		N_2	*Air*	*20°C*	*60°C*	*- 10°C*	*20°C*	*20°C*
$PIP_{12}TFSI$	89.9	----	----	solid	solid	3.1×10^{-5}	3.7×10^{-4}	solid
$PIP_{13}TFSI$	12.3	----	----	190	33	$< 10^{-5}$	0.92	5.82
$PIP_{14}TFSI$	-10.0	427.8	420.5	240	37	2.4×10^{-4}	0.64	5.80
$PIP_{15}TFSI$	-3.5	----	----	280	41	1.5×10^{-5}	0.54	5.85
$PIP_{16}TFSI$	21.7	----	----	270	39	$< 10^{-5}$	2.0×10^{-4}	5.91
$PIP_{17}TFSI$	6.2	423.6	408.5	330	47	$< 10^{-5}$	0.26	5.89
$PIP_{18}TFSI$	-12.4	----	----	370	52	8.0×10^{-5}	0.22	5.89
$PIP_{23}TFSI$	46.8	----	----	solid	----	$< 10^{-5}$	2.0×10^{-5}	solid
$PIP_{24}TFSI$	7.5	----	----	275	37	$< 10^{-5}$	0.53	5.00
$PIP_{25}TFSI$	3.7	----	----	285	40	$< 10^{-5}$	0.35	5.06
EMITFSI	-9.7	----	390	36	12	2.4×10^{-3}	4.7	3.98
TEATFSI	103.5	----	----	solid	solid	$< 10^{-5}$	4.3×10^{-5}	solid
$PYR_{11}BETI$	133.3	----	----	solid	solid	$< 10^{-5}$	1.7×10^{-5}	solid
$PYR_{13}BETI$	6.5	----	----	204	34	$< 10^{-5}$	0.53	5.52
$PYR_{14}BETI$	8.9	----	----	348	52	$< 10^{-5}$	0.42	5.68
EMIBETI	-1.3	----	----	98	22	$< 10^{-5}$	2.0	3.72

Ionic Liquid	*m.p./°C*	*Ther. stab. / °C*		*η / mPa s*		*σ / mS cm^{-1}*		*ESW / V*
		N_2	*Air*	*20°C*	*60°C*	*- 10°C*	*20°C*	*20°C*
TEABETI	83.4	----	----	solid	solid	$< 10^{-5}$	1.9×10^{-5}	solid
PYR$_{11}$Im$_{14}$	< -40°C	----	----	720	97	0.01	0.18	5.39
PYR$_{13}$Im$_{14}$	< -40°C	----	----	306	54	0.024	0.30	4.79
PYR$_{14}$Im$_{14}$	< -40°C	----	----	556	65	0.025	0.28	5.51
EMIIm$_{14}$	< -40°C	----	----	150	30	0.15	1.1	3.69
TEAIm$_{14}$	< -40°C	----	----	790	84	4.3×10^{-3}	0.13	5.30
PYR$_{13}$FSI	-13.6	240	240	45	17	0.08	5.6	5.48
PYR$_{14}$FSI	-20.0	230	230	66	21	1.3	4.1	5.50
PYR$_{1(2O2)}$FSI	-26.3	200	200	179	36	1.3	4.1	4.97

Aliphatic quaternary ammonium (or imidazolium) perfluorosulfonylimide ILs show high thermal stability (Table 1). However, accelerating rate calorimetry measurements, reported by Dahn and co-workers (*31*), have shown that not all ILs are safer than standard organic solvents used in lithium battery electrolytes. In particular, the imidazolium FSI behaves worse than conventional carbonate-based electrolytes. Otherwise, TFSI-based ILs have been found to be much safer.

Imidazolium-based electrolytes show higher conductivities than those of aliphatic quaternary ammonium since their quasi-planar, two-dimensional structure (compare with the three-dimensional one of tetraalkylammonium cations (*13*, *16*, *17*)) leads to lower viscous drags (*25*). Conversely, ILs based on pyrrolidinium and piperidinium cations, having the nitrogen in a ring, exhibit a much wider cathodic stability (e.g., exceeding 5 V) than non-cyclic quaternary ammonium cations (*25*) and, especially, unsaturated cyclic cations (*32*, *33*) because of the absence of acidic protons and double bounds in the cation ring. Nevertheless, several cyclic tetraalkylammonium-based ILs exhibit a molten state conductivity around 10^{-3} S cm^{-1} (or higher) at room temperature. It is noteworthy how the ionic conductivity is in good relationship with the viscosity values.

Perfluoroalkylanions were successfully proposed as anion for lithium battery electrolytes (*21*, *34–36*). Among them, TFSI was found to be among the best because of its high anodic potential stability, good conductivity and thermal stability, hydrophobicity, e.g., acting as non hydrogen-bonding anion (*36*). In particular, McFarlane et al. (*37–40*), Passerini et al. (*41–44*) and Tatsumi et al. (*27*, *45*) have demonstrated the feasibility of pyrrolidinium-TFSI ILs as lithium battery electrolyte components, improving the performance, cyclability and long-term stability of electrochemical storage devices. Comparable behavior with TFSI was displayed by the TSAC anion as reported by Tatsumi at al. (*45*). A remarkable interest has been progressively attracted by the FSI anion since its reduced steric hindrance guarantees lower viscosities and, therefore, higher conductivities (*28*, *46*, *47*). In addition, FSI-based ILs exhibit remarkably lower melting point than corresponding TFSI-based materials, resulting in large ionic conductivity even at sub-ambient temperatures, e.g., 1.3 mS cm^{-1} at -10°C for $PYR_{14}FSI$ (*47*). On the other hand, the FSI anion leads to a reduction of the electrochemical and, especially, thermal stability since the reactivity of the fluorine atoms directly bound to the sulfonyl groups (*48*, *49*).

Lithium batteries need high purity ILs for achieving good long-term cycling ability. Recently, suitable procedure routes (*50*) were developed to obtain hydrophobic ILs with impurities and moisture content below 100 ppm and 1 ppm, respectively, which, in addition, do not require the use of hazardous solvents such as dichloromethane, acetonitrile and acetone (*50*). Figure 6 shows schematized a synthesis route to obtain highly pure, anhydrous, colorless, hydrophobic ILs (Figure 7).

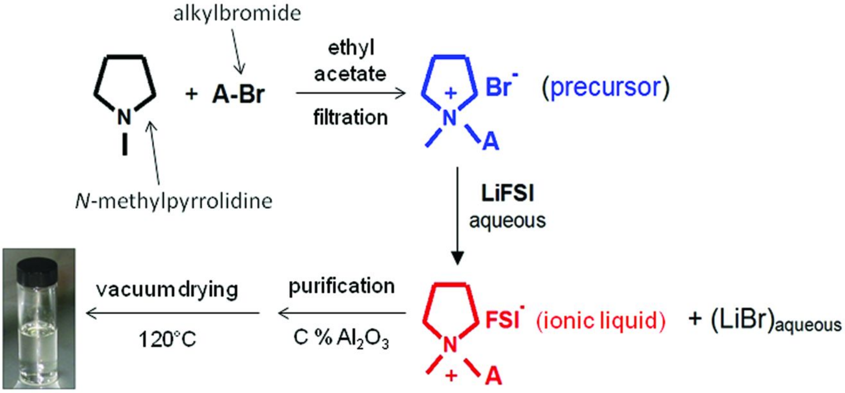
alkylbromide
+ A-Br
N-methylpyrrolidine
ethyl acetate
filtration
Br⁻ (precursor)
A
LiFSI aqueous
FSI⁻ (ionic liquid) + (LiBr)aqueous
purification
C % Al2O3
vacuum drying
120°C

Figure 6. Scheme of the synthesis route of hydrophobic ILs. Data from ref. (50).

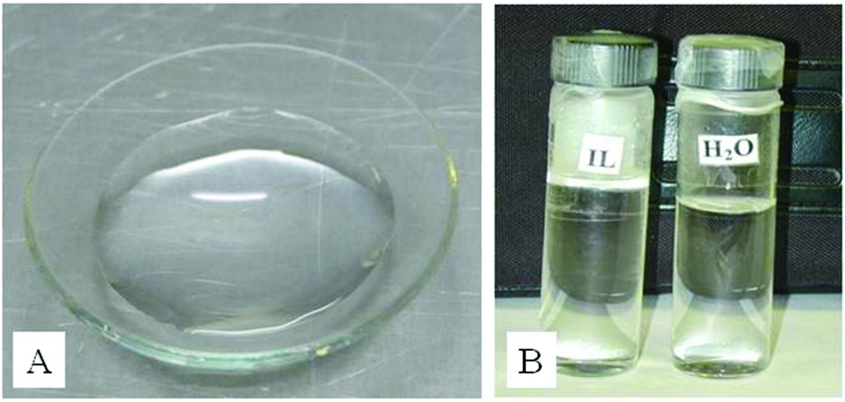

Figure 7. Left panel: $PYR_{13}FSI$. Right panel: visual comparison of $PYR_{14}TFSI$ and deionized water.

Ionic Liquid Electrolytes for Lithium Batteries

The possibility to combine a large variety of cations with several anions opens up the design of the most suitable ILs for matching the requirements of different electrochemical devices. Therefore, numerous IL-lithium salt mixtures as electrolytes for lithium batteries were investigated.

In spite of their apparent low dielectric constant, ILs are able to dissolve lithium salts (*16*, *17*, *36*). Angell et al. (*51–53*) have extensively studied a series of lithium molten salts, particularly focusing on the "ionicity" concept (*54*, *55*), for lithium battery applications. NMR measurements, performed by Castriota e al. (*56*) in LiTFSI-PYR_{13}TFSI mixtures, have evidenced that the TFSI anions have only very weak interactions with the pyrrolidinium cations (which appear sterically well shielded), but strong coordination to the Li^+ cations. In addition, the existence of multiple ionic aggregates (Li·····TFSI) was detected in mixed lithium salt-IL crystalline complexes, exhibiting a change of coordination in the molten state. This is in agreement with the molecular dynamics simulation results reported by Borodin el al. (*57*, *58*), showing that a relevant Li^+ fraction (about 60%) forms aggregates where lithium ions are bridged by sulfonyl groups ($\cdots SO_2 \cdots$) through ionic bonds. Li^+ cations are coordinated by 3.75-3.9 TFSI oxygen atoms (each TFSI contributing only one oxygen atom to the lithium coordination shell). The remarkable interactions between lithium and TFSI ions support for a conductivity decrease in ILs upon addition of lithium salts as clearly evidenced from Figure 8 (*25*), even if favorable transport properties (e.g., good conductivity) are still exhibited in the molten state. As expected, further addition of lithium salt leads to a progressive decay in conductivity as reported in panel B of Figure 8 (*28*, *47*) and Table 2. It is noteworthy the higher conductivity of FSI-based IL electrolytes (due the small steric hindrance of the FSI anion, which enhances the fluidity of the resulting electrolyte) with respect to analogous TFSI-based materials as reported by various authors (*28*, *46*, *47*) and in Table 2.

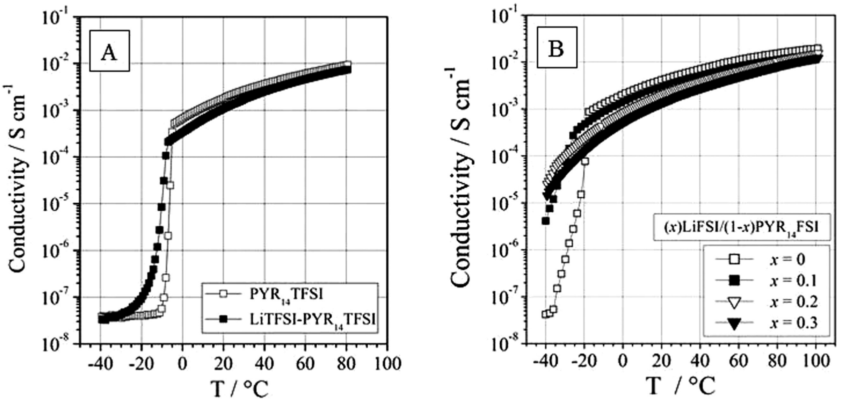

Figure 8. Ionic conductivity vs. temperature dependence of LiTFSI-PYR_{14}TFSI (panel A) and LiFSI-PYR_{14}FSI (panel B) electrolyte mixtures. Data from ref. (25).

According to the results of a few researcher (*58*) the Li^+ transport is due to two different contributions: *i*) exchange of TFSI anions in the lithium first coordination shell (about 70% of total) and *ii*) diffusion with the lithium coordination shell. Kunze et al. (*59*) have reported that pyrrolidinium cations containing an oxygen atom in the alkyl side chain, $PYR_{1(2OA)}^+$, are able to coordinate Li^+ ions even if this does not result in any enhanced lithium mobility. Variable-temperature measurements of the self-diffusion coefficients, performed by Castiglione et al. (*60*), have shown selective and unexpected enhancement of Li^+ mobility with temperature, probably related to the diffusion mechanism in ILs involving the continuous disruption and formation of the TFSI coordination shell of Li^+.

Henderson et al. (*44*) have observed that (x)LiTFSI-(1-x)$PYR_{1A}TFSI$ (A = 2,3,4) electrolyte mixtures exhibit a crystalline phase (solid at room temperature) with a molar fraction composition (x) equal to 0.33. This behavior, once more indicating rigid coordination between Li^+ and $TFSI^-$, may drastically affect the high rate battery performance if LiTFSI-$PYR_{1A}TFSI$ blends are used as electrolytes. For instance, concentration gradients originating in IL-based electrolytes during the operation of the device may lead to the formation of crystalline (if $x \geq 0.33$) LiTFSI-rich phases which exhibit very poor Li^+ transport properties. Different behavior was shown from lithium salt-rich LiFSI-$PYR_{14}FSI$ mixtures (*47*), which, despite numerous attempts to crystallize them, remained completely amorphous, thus showing an extended liquid range down to the glass transition (T_g) temperature.

Incorporation of small molar fractions of lithium salts into ILs lowers their melting point (as clearly observed in Figure 8 and Table 2) this resulting in good ionic conductivity even at low temperatures (*28*, *44*, *47*). In particular, 10^{-3} S cm^{-1} is approached at -20°C by LiFSI-$PYR_{14}FSI$ mixtures, which appear to be very appealing electrolytes for low temperature devices. It is noteworthy that the transport properties of lithium salt-IL electrolytes are in good agreement with their thermal and rheological properties (*16*, *17*, *25*, *29*). Panel A of Figure 9 shows how the solid-liquid transition of 0.1LiFSI-0.9$PYR_{14}FSI$ (*28*, *47*) is evidenced by a slope change of the conductivity vs. temperature plot and an endothermic feature in the DSC trace, both occurring around -20°C. Below -20°C, the conductivity was seen to linearly increase with the temperature, suggesting continuous solid-solid phase transitions prior the melting. This is also highlighted from the broad shape of the melting peak observed in the DSC trace. The IL conductivity dependence on the viscous drag is evidenced from panel B of Figure 9, which reports an analogous temperature trend for viscosity and resistivity of 0.1LiFSI-0.9$PYR_{14}FSI$ (*28*, *47*).

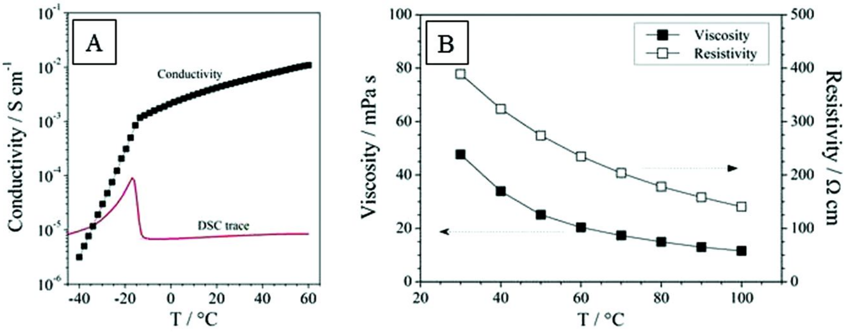

Figure 9. Thermal behavior of 0.1LiFSI-0.9$PYR_{14}FSI$. Panel A: ionic conductivity as a function of temperature and DSC trace. Panel B: viscosity and resistivity as function of the temperature. Data from refs. (28, 46, 47).

A successful approach for improving the transport properties, especially at low temperatures, is represented by mixing ILs in the electrolytes. The main idea is to combine different IL species, e.g., ILs constituted by bulky and/or asymmetric ions with those formed by light ions, which generally exhibit, respectively, low melting points and high conductivity (*25*), to obtain electrolytes with improved performance. Recent studies reported by Appetecchi et al. (*61*, *62*), Zhou at al. (*63*) and Montanino at al. (*64*) have demonstrated that the use of mixed ILs hinders the electrolyte crystalization. In particular, LiTFSI (or $LiPF_6$)-$PYR_{14}TFSI$-$PYR_{13}FSI$ ternary mixtures have shown much lower melting points with respect to the single IL electrolytes, this resulting in conductivity values approaching 10^{-4} S cm^{-1} at very low temperatures (-30°C). The synergistic effect due to IL blending has been also observed in terms of electrochemical stability (*61*, *63*).

Despite their undoubtedly favorable characteristics, the conductivity of IL electrolytes is, however, still lower than that of conventional, organic solvent-based electrolytes, with a negative effect on the high rate performance of electrochemical devices based on ILs. Therefore, large efforts are in progress with the aim to improve the transport properties of the IL electrolytes. In this scenario, mixtures of ILs in combination with organic compounds have been proposed as electrolyte components for lithium batteries. Such an approach represents a very good compromise between high ionic conductivity (low viscosity) and high safety (low flammability) of the resulting electrolyte. Guerfi et al. (*65*) and Kühnel et al. (*66*) have focused on $LiPF_6$-EMITFSI-EC-DEC-VC and LiTFSI-$PYR_{14}TFSI$-PC mixtures, respectively, as lithium battery electrolytes. The results of such investigations are reported in Table 2, which summarizes the physicochemical properties of several kinds of IL-based electrolytes. A general improvement of the transport properties of the electrolyte mixtures is observed with the addition of organic compounds but, unexpectedly, the conductivity vs. organic solvent content dependence shows a bell-shape behavior with a maximum at intermediate compositions, whereas the viscosity exhibits a linear trend. This is ascribed to the different interactions between the molecular solvents and the ILs, which are by themselves salts. It is also noteworthy that mixed IL-organic solvent based electrolyte are not flammable up to an organic compound content equal to 60 wt.% (*65*, *66*).

Wide thermal stability range is a very important requirement for electrolytes in lithium battery operating at medium-high temperatures or subjected at continuous thermal shocks. FSI-based IL electrolytes were found to be less thermally stable than the TFSI electrolytes (*25*, *28*, *46*, *47*), whereas the introduction of an oxygen atom in the cation alkyl side chain was seen to promote the thermal decomposition, as clearly evidenced from Figure 10. In the literature, thermal stabilities of IL-based electrolytes ranging from 200°C to above 400°C, depending on the nature of the cation and the anion, are widely reported. However, long-term thermal stability results on IL electrolytes are not easily available or often not reported. Variable-temperature TGA measurements, performed on LiFSI-$PYR_{1A}FSI$ electrolytes and illustrated in panel A of Figure 10, show a thermal stability ranging from 200°C to above 250°C (*28*, *47*). Conversely, isothermal TGA curves, reported in panel B, indicates thermal decomposition of the IL electrolytes even after two hour storage at 100°C (*28*, *47*). This supports the validity of the latter approach for a careful evaluation of the thermal stability in IL-based electrolyte systems.

Finally, an extended electrochemical stability window (ESW) allows whatever electrolyte to be used in combination with high voltage cathodes and low voltage anodes for high energy lithium batteries without any relevant degradation process. IL electrolytes based on unsaturated, cyclic, quaternary ammonium cations such as pyrrolidinium and piperidinium, are found to be more electrochemically stable with respect to those based on imidazolium and non-cyclic, tetraalkylammonium cathodes (*25*) as shown in Table 1. Analogously, TFSI was found to confer a better electrochemical stability than other perfluorosulfonylimide anions (*25*). For instance, LiTFSI-PYR$_{14}$TFSI electrolyte have displayed an ESW exceeding 5 V (panel A of Figure 11), this allowing lithium plating prior to cathodic decomposition, while no reduction of the anodic potential limit was observed with respect to pure PYR$_{14}$TFSI (*50*). The absence of relevant features prior to anodic or cathodic decompositio indicates that no parasitic reaction occurs prior to the oxidation or reduction processes, also supports for a high purity of the IL electrolyte. Panel B of Figure 11 compares sweep voltammetry traces obtained on different LiFSI-PYR$_{1A}$FSI electrolytes. Once more, it is evidenced that the replacement of the TFSI anion with FSI, as well as the incorporation of an oxygen atom in the cation aliphatic side chain, leads to a less wide ESW, but one that is still close to 5 V (Table 2).

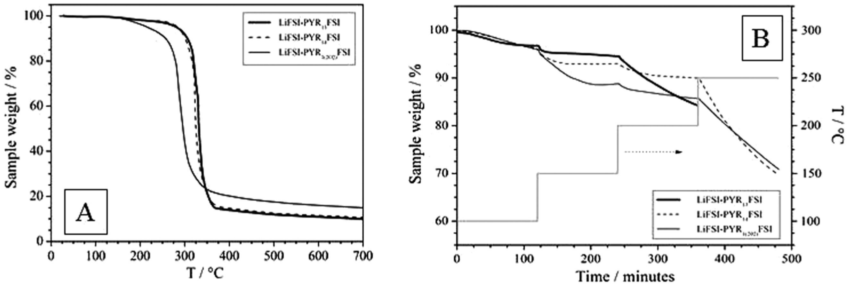

Figure 10. Variable temperature (panel A) and isothermal (panel B) TGA traces of different LiFSI-PYR$_{1A}$FSI electrolytes in nitrogen atmosphere. The grey solid step curve in panel B refers to different temperature intervals. Scan rate: 10°C min^{-1}. Data from refs. (28, 47, 61).

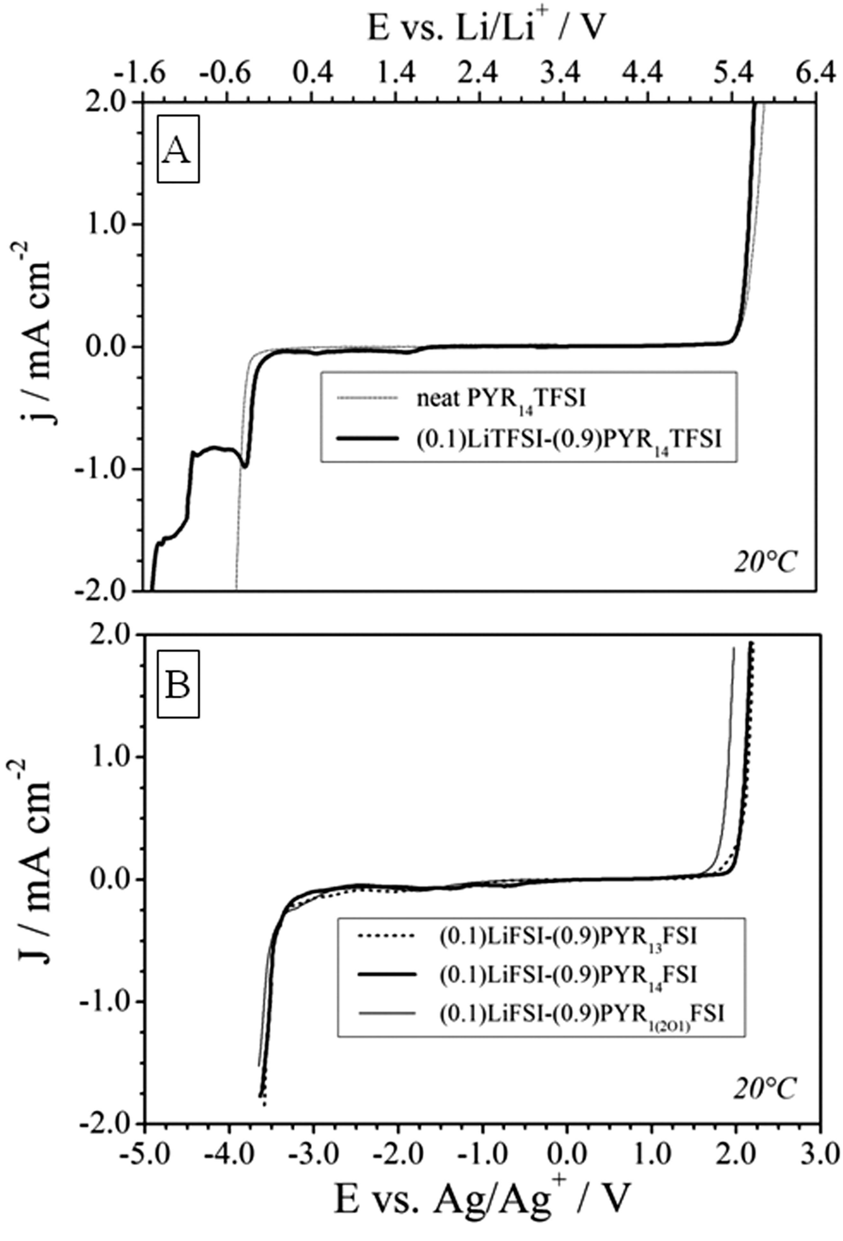

Figure 11. Panel A: ESW of neat PYR$_{14}$TFSI and (0.1)LiFSI-(0.9)PYR$_{14}$TFSI electrolyte. Panel B: ESW of different (0.1)LiFSI-(0.9)PYR$_{1A}$FSI electrolytes. Platinum as working and counter electrodes. The reference electrode is a silver wire immersed in a 0.01 M solution of AgCF$_3$SO$_3$ in PYR$_{14}$TFSI. Scan rate: 5 mV s^{-1}. T = 20°C. Data from refs. (25, 47, 50).

Table 2. Physicochemical properties of various lithium salt - IL electrolytes for lithium battery systems. (a) = lithium salt concentration in mole fraction; (b) = lithium salt concentration in mole dm^{-3}; (c) = IL mole fraction; (d) = IL and organic compound volume fraction. Data from refs. (*28*, *47*, *61*, *65–69*)

Ionic liquid electrolyte	*m.p. / °C*	*η / mPa s*	*σ / S cm^{-1}*
(0.1)LiTFSI-(0.9)PYR$_{14}$TFSI (a)	-10.6	---	1.1×10^{-3}
(0.1)LiTFSI-(0.9)PYR$_{(2O1)}$TFSI (a)	---	104	1.8×10^{-3}
(0.1)LiBETI-(0.9)PYR$_{14}$BETI (a)	---	414	2.9×10^{-4}
(0.1)LiIM$_{14}$-(0.9)PYR$_{14}$IM$_{14}$ (a)	---	758	1.6×10^{-4}
(0.1)LiFSI-(0.9)PYR$_{13}$FSI (a)	-16.6	60	5.5×10^{-3}
(0.1)LiFSI-(0.9)PYR$_{14}$FSI (a)	-25.1	93	3.2×10^{-3}
(0.2)LiFSI-(0.8)PYR$_{14}$FSI (a)	-35.3	132	2.1×10^{-3}
(0.3)LiFSI-(0.7)PYR$_{14}$FSI (a)	n. d.	194	1.3×10^{-3}
(0.1)LiFSI-(0.9)PYR$_{1(2O2)}$FSI (a)	-24.9	---	3.1×10^{-3}
(0.1)LiTFSI-(0.9)PYR$_{14}$FSI (a)	---	80	3.2×10^{-3}

(0.3M)LiTFSI-EMITFSI (b)	---	55	5.1×10^{-3}
(0.3M)LiTFSI-PYR$_{13}$TFSI (b)	---	130	2.0×10^{-3}
(0.3M)LiTFSI-PIP$_{13}$TFSI (b)	---	330	7.3×10^{-4}
(0.3M)LiTFSI-EMIFSI (b)	---	24	1.1×10^{-2}
(0.3M)LiTFSI-PYR$_{13}$FSI (b)	---	51	5.5×10^{-3}

Continued on next page.

Table 2. (Continued). Physicochemical properties of various lithium salt - IL electrolytes for lithium battery systems. (a) = lithium salt concentration in mole fraction; (b) = lithium salt concentration in mole dm^{-3}; (c) = IL mole fraction; (d) = IL and organic compound volume fraction.

Ionic liquid electrolyte	*m.p. / °C*	*η / mPa s*	*σ / S cm^{-1}*
(0.3M)LiTFSI-PIP$_{13}$FSI (b)	---	124	2.5×10^{-3}
(0.7M)LiFSI-EMIFSI (b)	---	25	1.1×10^{-2}
(0.2M)LiTFSI-CTMATFSI (b)	---	---	2.0×10^{-4}
(0.2M)LiTFSI-BTMATFSI (b)	---	---	1.1×10^{-3}
(0.3M)LiTFSI-PYR$_{13}$FSI (b)	-9.0	---	4.9×10^{-3}
(0.3M)LiTFSI-(0.75)PYR$_{14}$TFSI-(0.25PYR$_{13}$FSI (b,c)	-36.0	---	1.5×10^{-3}
(0.3M)LiTFSI-(0.42)PYR$_{14}$TFSI-(0.58)PYR$_{13}$FSI (b,c)	n. d.	---	2.5×10^{-3}
(0.3M)LiPF$_6$-PYR$_{14}$TFSI (b)	-6.0	---	6.2×10^{-3}
(0.3M)LiPF$_6$-PYR$_{13}$FSI (b)	-9.0	---	4.6×10^{-3}
(0.3M)LiPF$_6$-(0.75)PYR$_{14}$TFSI-(0.25)PYR$_{13}$FSI (b,c)	n. d.	---	1.4×10^{-3}
(0.3M)LiPF$_6$-(0.42)PYR$_{14}$TFSI-(0.58)PYR$_{13}$FSI (b,c)	n. d.	---	2.6×10^{-3}
(1M)LiPF$_6$-EMITFSI (b)	inflammable	36.3	8.6×10^{-3}
(1M)LiPF$_6$-(0.9)EMITFSI-(0.1)EC/DEC/VC (b,d)	inflammable	30.5	9.8×10^{-3}

Ionic liquid electrolyte	*m.p. / °C*	*η / mPa s*	*σ / S cm^{-1}*
(1M)$LiPF_6$-(0.4)EMITFSI-(0.6)EC/DEC/VC (b,d)	inflammable	14.9	1.0×10^{-2}
(1M)$LiPF_6$-(0.3)EMITFSI-(0.7)EC/DEC/VC (b,d)	flammable	14.1	9.4×10^{-3}
(1M)$LiPF_6$-(0.1)EMITFSI-(0.9)EC/DEC/VC (b,d)	flammable	12.7	9.4×10^{-3}
(0.3M)LiTFSI-(0.48)PYR_{14}TFSI-(0.52)PC (b,c)	inflammable	39	2.9×10^{-3}
(0.3M)LiTFSI-(0.19)PYR_{14}TFSI-(0.81)PC (b,c)	flammable	11	5.3×10^{-3}
(0.3M)LiTFSI-(0.05)PYR_{14}TFSI-(0.95)PC (b,c)	flammable	7	3.8×10^{-3}

Use of Ionic Liquid Electrolytes in Lithium Batteries

Lithium battery active materials (Table 3) so far investigated in IL-based electrolytes include graphite, LTO and Li-alloys for negative electrodes (characterized by potential below 1 V and a capacity from 400 to about 4,000 mA h kg^{-1}) and LCO, LMO and LFP for the positive electrodes (characterized by potential above 4 V and a specific capacity up to 200-300 mA h kg^{-1}).

Several ILs in various combinations have been investigated as feasible electrolyte components in lithium batteries, depending both on the physicochemical properties of the IL material and on requirements of the electrochemical device. The applications here reported can be roughly divided into three main branches:

i) IL + lithium salt
ii) IL + lithium salt + additive
iii) IL + lithium salt + organic compound

In the following is presented an overview of:

- negative electrodes in IL electrolytes
- positive electrodes in IL electrolytes and
- lithium-ion cells in IL electrolytes

Table 3. Potential and capacity of active materials for lithium batteries. Data from ref. (*70*)

Anode materials	*Specific capacity / mA h g^{-1}*	*Potential vs. Li/Li$^+$ / V*
Graphite	330-410	0.15-0.40
Sn-Li-alloys	350-670	0.50-0.75
Sn oxide	400-720	0.70-1.00
Carbon	450-800	0.25-0.60
Nitrides LiM_xN_2	800-1000	0.45-0.60
3D Metal oxide	660-1000	1.0-1.3
Li Metal	3500-4000	0-0.15
Silicon	4000-4600	0.15-0.45
$Li_4Ti_5O_{12}$	145-170	1.4-1.7

Cathode materials	*Specific Capacity / mAhg^{-1}*	*Potential vs. Li/Li$^+$ / V*
MnO_2	170-210	2.8-3.2
V_2O_5, LiV_3O_8	240-260	2.8-3.5
$Li_xMn_{1-y}M_yO_2$	200-210	3.0-4.5

Continued on next page.

Table 3. (Continued). Potential and capacity of active materials for lithium batteries.

Cathode materials	*Specific Capacity / mAhg^{-1}*	*Potential vs. Li/Li$^+$ / V*
$LiFePO_4$, Li_xVOPO_4	170-200	3.1-3.9
$Li_{1-x}Ni_{1-y-z}Co_yM_zO_4$	145-210	3.7-4.0
$Li_{1-x}Co_{1-y}M_yO_4$	150-200	4.0-4.3
$Li_{1-x}Mn_{2-y}MO_4$	145-180	4.3-4.5

Negative Electrodes in Ionic Liquid Electrolytes

Lithium Metal

Lithium metal anodes are of particular interest since their very large capacity (3,800 mA h g^{-1}, e.g., the largest one among the anodic materials) in conjunction with their low potential (Table 3) enables the highest gravimetric energy value for any battery. Nevertheless, they suffer a major drawback resulting from their poor compatibility with respect to electrolytes, in particular the organic solvent-based ones, which depletes the performance and the safety of the battery.

Non-cyclic, tetraalkylammonium (e.g., TMBA and CTMA) TFSI IL electrolytes have exhibited modest compatibility towards the lithium anode, resulting in an initial Li/electrolyte interfacial resistance of about 300 Ω cm^2 that levels to 30 kΩ cm^2 after a few days of storage even in open circuit conditions (*67*).

Koch at al. (*33*) have found that DMPITFSI electrolytes initially react with the Li anode to progressively achieve a stable interfacial resistance at 1,500 Ω cm^2 after 60 days of storage due to the protective passive layer formed on the lithium electrode (Figure 12, left panel). TFSI-based ILs with saturated, cyclic, tetraalkyl ammonium cations (PYR_{1A} and PIP_{1A}) were found to exhibit a better compatibility towards lithium anodes (Figure 12, left panel), because of the absence of acidic protons and double bounds in the cation ring (*32*, *33*), which are present in imidazolium cations. This advantage, in conjunction with their cathodic decomposition limit well below the Li$^+$ plating potential (*59*), makes pyrrolidinium- and piperidinium-TFSI ILs more appealing as electrolyte components for lithium metal batteries. Lewandowsky at al. (*71*) have observed that the Li$^+$ charge transfer process occurs at a solid/solid SEI/Li anode interface, this having a grain-like structure.

A remarkable improvement in the stability towards lithium metal anodes was obtained in FSI-based pyrrolidinium IL electrolytes, particularly in LiFSI-PYR_{14}FSI mixtures, as reported by Kim et al. (*72*). Apart from an initial increase (due to the SEI formation on the lithium anode), the Li/LiFSI-PYR_{14}FSI interface displayed stable resistance values around 300 Ω cm^2, e.g., five times lower than that of the analogous TFSI-based IL electrolytes, even after prolonged storage time (Figure 12, left panel). This performance indicates the ability of the

FSI anion to form a protective SEI passive layer on the lithium anode (as well as observed in graphite electrodes) without any further major decomposition, even at medium-high temperatures. For instance, excellent long-term stability was observed even at 40°C (30 Ω cm^{2}) and 80°C (3 Ω cm^{2}) (Figure 12, right panel), leading to one of the lowest and, at the same time, most time-stable interfacial resistances ever reported for any kind of room temperature, highly conductive electrolyte.

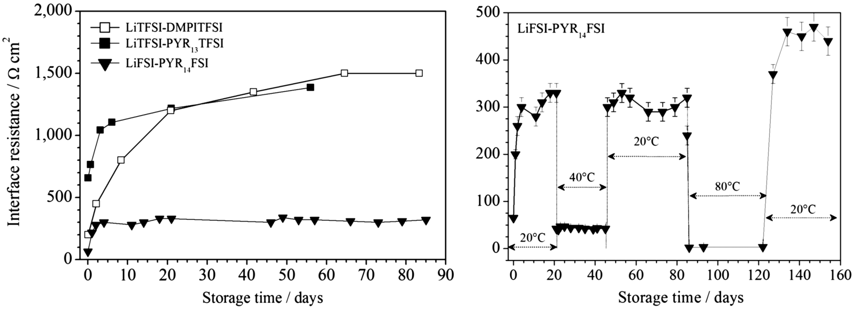

Figure 12. Time evolution of the interfacial resistance at lithium metal anodes in contact with different lithium salt/IL electrolytes at 20°C (left panel) and LiFSI (0.1)-PYR_{14}FSI (0.9) at different temperatures (right panel). Data from refs. (33, 72).

The lithium plating-stripping behavior in lithium salt-IL electrolytes was initially limited to a few dozen cycles with low efficiency values, especially for ILs based on cathodically unstable cations such as quaternary alkyl ammonium (*67*) and imidazolium (*73*, *74*). Improved lithium cycling performance was observed in cyclic and saturated tetraalkylammonium-based ILs even at medium temperatures. Sakaebe (*74*) and Howlett (*40*) have reported LiTFSI-PIP_{13}TFSI and LiTFSI-PYR_{13}TFSI electrolytes to display average Li plating/stripping coulombic efficiency above 96% and 99%, respectively. The nature of the plating substrate as well as the plating/stripping history was found to affect the lithium deposition (*40*). For instance, high cycling efficiencies (> 99%) were achieved on platinum substrate even at 1.0 mA cm^{-2} whereas on copper nice plating was observed only at relatively low current density (0.1 mA cm^{-2}). Above 1.75 mA cm^{-2} the deposits became dendritic and coulombic efficiency decayed.

Excellent lithium cycling behavior was observed in LiFSI-PYR_{14}FSI electrolyte (*47*, *72*). Stripping/plating tests performed on Li/Ni cells, showed an initial slight decrease of the cell overvoltage followed by a substantial stability for more than 1,200 cycles around values lower than 10 mV (Table 4). The sudden overvoltage increase after 1,300 cycles indicates complete disappearance of lithium from the nickel electrode (cell failure), even if the IL-based electrolyte is still able to supply lithium ions for lithium plating (as indicated by the regular cell overvoltage detected at the end of the 1301st plating step). This cycling performance corresponded to a lithium plating-stripping efficiency of 0.9923, which is one of the highest, if not the highest, lithium plating-stripping value ever obtained for lithium electrodes in any kind of electrolyte.

It is important to highlight that a good compatibility with respect to Li anodes requires high purity ILs (still not easily available). Even very low contents in I^-, Br^- and, especially, H_2O strongly deplete the lithium coulombic cycling efficiency, e.g., 100 ppm of water lead to a decrease of the Li plating-stripping efficiency in LiTFSI-PIP_{13}TFSI from 97% down to 10% (*74*). However, opposite results concerning water contamination were found in EMI-based ILs, e.g., a 0.04 M H_2O concentration in $EMIBF_4$ enables the reversible Li cycling on Pt (*68*).

Table 4. Plating/stripping overvoltage value recorded, at the end of selected half-cycles, during cycling tests performed on Li/PYR_{14}FSI-LiFSI/Ni cell at 20°C. Current density: 0.26 mA cm^{-2}. Data from ref. (*72*)

Cycle	*1st*	*10th*	*100th*	*500th*	*1000th*	*1298th*	*1299th*	*1300th*	*1301th*
η (Ni) / mV	10.3	9.8	6.5	4.8	6.8	10.6	13.7	16.6	2,002
η (Li) / mV	-10.4	-10.2	-6.9	-6.9	-7.3	-7.0	-6.8	-6.9	-7.9

Graphite

Most of commercial lithium-ion batteries use graphite as the anode material due to its good capacity (370 mA h g^{-1}), favorable cyclability, and low cost. The very low lithium intercalation potential in graphite, close to 0 V vs. Li/Li^+, allows the realization of cells with operating voltages up to 4 V, this leading to high battery energy. The lithium intercalation process into graphite electrodes in IL-based electrolytes has been extensively investigated in the last ten years.Poor cycling efficiency was initially observed due the reduction of the IL cation. For instance, EMI was found to reduce at potentials well above the Li^+ intercalation potential, e.g., 1.4 V vs. Li^+/Li (*25*). Intercalation of the EMI cation into graphite anodes was also reported to occur below 1 V vs. Li/Li^+ (*75*, *76*), thus causing graphite exfoliation. *In-situ* Raman measurements have also evidenced the intercalation of the TFSI anion above 4.65 V vs. Li/Li^+ (*76*), which opens up the possibility of using graphite as a positive electrode. Trulove et al. (*75*) have investigated the IL anion and cation intercalation into graphite, showing that it is theoretically possible to realize rechargeable electrochemical cells using graphite as the anode and cathode (Table 5). This work has been further developed by Winter et al. (*77*), however, the overall energy of the system is limited by the high molecular weight of the IL anion.

In the use of graphite as an anode, however, progress was made by adding organic additives to form a SEI at the graphite/electrolyte interface (occurring at 300 mV vs. Li^+/Li), which, by prevent the electrolyte cation intercalation, avoids the graphite exfoliation and, therefore, allows the reversible intercalation of Li^+

cations (*78–84*). EMITFSI was found to reversibly permit lithium intercalation into graphite when VC is used in small amounts as an additive. The best performance was obtained when 5 wt.% of VC was added to a 1 M solution of $LiPF_6$ in EMITFSI (Table 5). Intercalation of lithium close to 95% of the theoretical value was demonstrated over prolonged cycling (150 cycles) without noticeable capacity fading (e.g., more than 95% of the initial capacity) and with a coulombic efficiency close to 100%. Additives such as ethylene sulphite and acrylonitrile have also shown a smaller, but still positive, effect (Table 6). Other researchers (*61*, *85*, *86*) have reported that the use of VC as an additive appears to be indispensable in TFSI-based pyrrolidinium IL electrolytes for the formation of the SEI layer on graphite anodes whereas it is not strictly required in electrolytes containing FSI-based ILs. For instance, the addition of VC into $PYR_{13}FSI$-based electrolytes decreases slightly the irreversible capacity while the reversible capacity was comparable to that of the VC-free solutions.

Table 5. Discharge intercalation potential (referred to Al° in 1.5/1.0 chloroaluminate melt) of IL cations and anions. (*) = 90°C. Data from ref. (*75*)

Ionic Liquid	*EMI^+*	*$DMPI^+$*	*$AlCl_4^-$*	*BF_4^-*	*PF_6^-*	*$CF_3SO_3^-$*
$EMI\text{-}AlCl_4$	-1.47	---	+ 1.60	---	---	---
$DMPI\text{-}AlCl_4$	---	-1.25	+1.50	---	---	---
$EMI\text{-}BF_4$	-1.30	---	---	+1.50	---	---
(*) $EMI\text{-}PF_6$	-1.40	---	---	---	+1.30	---
$EMI\text{-}CF_3SO_3$	n.a.	---	---	---	---	+1.30

Table 6. Graphite reversible capacity in a 1 M $LiPF_6$ in EMITFSI electrolytes containing different additives. Data from ref. (*78*)

Additive	*Reversible capacity / mA h g^{-1}*
additive-free	< 50
acrylonitrile	100
ethylene sulphite	200
vinylene carbonate	350

Also, addition of chloroethylenene carbonate, Cl-EC (20% in volume), was found to promote the formation of a thin and homogenous SEI on the graphite surface due to the mild reduction of solvated Cl-EC molecules at the graphite/IL liquid electrolyte interface (*84*).

The feasibility of reversibly inserting Li^+ cations into graphite without any additive was successfully investigated by Appetecchi et al. (*61*), Ishikawa et al. (*87–89*), Zaghib et al. (*90*, *91*), Best et al. (*92*) and Dominko et al. (*93*) using LiTFSI or LiFSI as the lithium salt and FSI-based ILs with EMI, PYR_{13}, or PYR_{14} cations. These authors have demonstrated the beneficial effect of the FSI anion on the graphite performance. Cyclic voltammograms (Figure 13, upper panel) performed in LiTFSI-PYR_{13}FSI electrolyte (*61*) have revealed a broad peak at about 1.1 V vs. Li/Li^+ in the first cathodic sweep whereas no current flow was recorded above 0.4 V vs. Li/Li^+ in the following cycles. The presence of this peak indicates that an irreversible reaction takes place only in the first (cathodic) cycle. Completely different is the behavior in LiTFSI-PYR_{14}TFSI (Figure 13, lower panel) where the features displayed in the 0.8-0.25 V vs. Li/Li^+ range are most likely correlated with the PYR_{14} cation insertion (*61*, *85*) leading to graphite exfoliation and no reversible peak due the lithium intercalation is observed at lower potentials.

Unexpectedly, the reason for such different behavior resides in the lower cathodic stability of PYR_{13}FSI (*28*, *46*), which decomposes on the graphite anode forming a Li^+ ion-conducting SEI layer that prevents the IL-cation intercalation. In fact, performance comparable to that exhibited in $LiPF_6$ (1M) EC-DEC and LiFSI-EC-DEC electrolytes was observed in LiTFSI-EMIFSI, LiFSI-EMIFSI and LiFSI-PYR_{13}FSI electrolytes upon prolonged cycling tests at current rates ranging from C/20 to C/5 (e.g., more than 94% of the initial capacity, which was close to the theoretical value, was delivered after 30 consecutive cycles) (*61*, *85–92*). On the other hand, only a pseudo-plateau of about 4 mA h g^{-1}, addressed to an irreversible intercalation of the EMI cation (*87*), was observed at around 0.5 V during the first discharge (corresponding to 6 mA h g^{-1}) of graphite in an LiTFSI-EMITFSI electrolyte. These results, illustrated in Table 7, demonstrate that the FSI anion, in contrast to TFSI, can form a stable SEI passivation layer even in presence of cathodically unstable cations such as the EMI cation. The IL cation is, therefore, prevented from being inserted or reductively decomposed because, analogously to conventional lithium-ion cells, only Li^+-ions can cross the formed SEI and no electrons are available at the SEI-electrolyte interface for electrolyte decomposition to take place. For instance, no irreversible cathodic peak is seen for LiTFSI-EMIFSI and LiTFSI-PYR_{13}FSI (*87*, *89*) while it is detected for LiTFSI-EMITFSI at ca. 0.6 V vs. Li/Li^+. Impedance measurements of fully intercalated graphite anodes have revealed smaller interfacial resistances in IL electrolytes than in organic compound-based electrolytes (Table 7). This suggests that not only the interfacial resistance (due to a thinner layer generated by FSI) but also the Li^+ intercalation resistance into graphite (due to lower energy for Li^+ to transfer into the graphite interlayers) results much lower in FSI-based IL electrolytes.

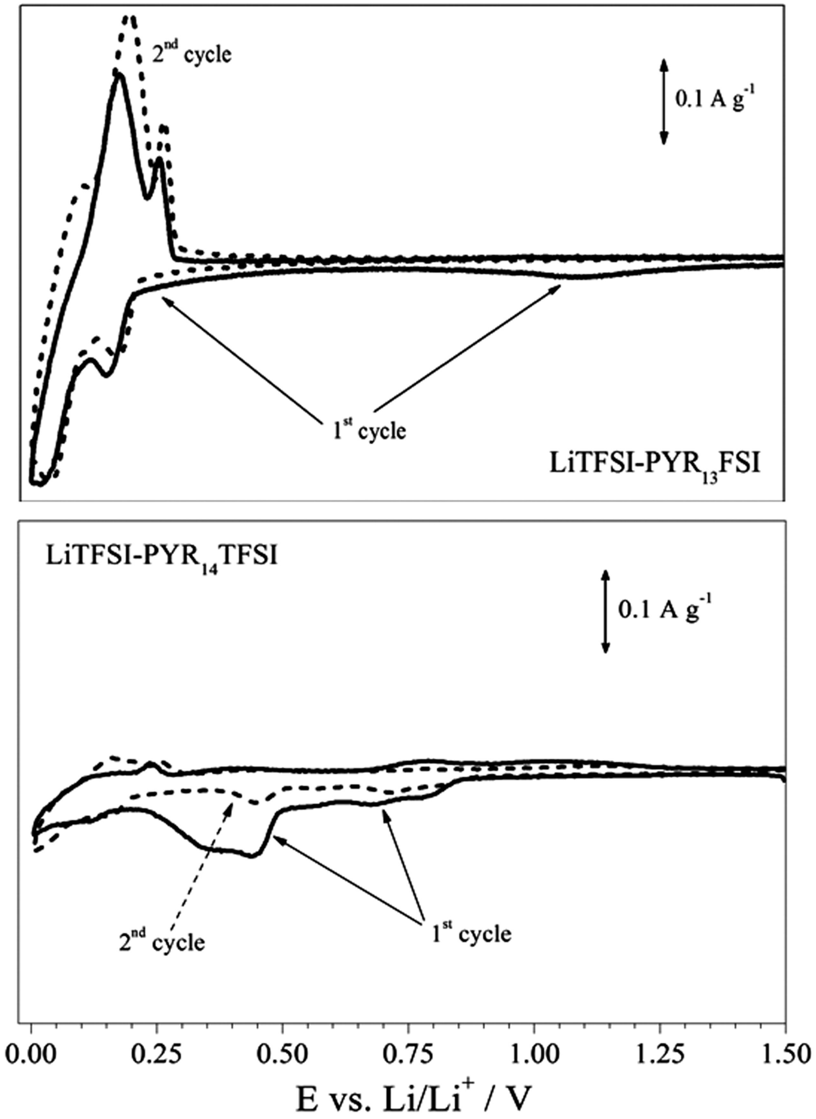

Figure 13. Cyclic voltammetries of graphite (KS-6) electrodes in LiTFSI-PYR$_{14}$TFSI (upper panel) and LiTFSI-PYR$_{13}$FSI (lower panel) electrolytes. Data from ref. (61).

Table 7. Reversible capacity and efficiency values of natural graphite electrodes in different electrolytes. The graphite/electrolyte interfacial resistance is also reported. T = 20°C. Data from refs. (*87*, *89*, *91*)

Electrolyte	*1st cycle / mA h g^{-1}*	*30th cycle / mA h g^{-1}*	*1st cycle efficiency / %*	*Resistance / /Ω cm^2*
$LiPF_6$-EC/DEC	370	340	93	30
LiFSI-EC/DEC	369	350	97	25
LiTFSI-EMITFSI	< 1	< 1	17	n.a.
LiTFSI-EMIFSI	370	350	85	10
LiFSI-EMIFSI	348	340	81	20
LiFSI-PYR_{13}FSI	367	350	80	15

A different approach was followed by Dominko et al. (*93*) while investigating the LiFSI-PYR_{14}TFSI electrolyte. The purpose here, was to combine the high electrochemical and thermal stabilities and cycling behavior of PYR_{14}TFSI with the SEI-forming capability of FSI in order to obtain good performance with graphite anodes even at medium temperatures. In addition, a reduced amount of FSI anion, which represents the most expensive electrolyte component, was used. Cycling tests performed on different carbonaceous anodes at 55°C (Table 8) have shown a high nominal capacity (e.g., 96-98% of the theoretical value) in conjunction with very good capacity retention and coulombic efficiency (both close to 100%), which are appealing for medium temperature lithium-ion battery systems.

Table 8. Charge (deintercalation process) capacity and coulombic efficiency values of different graphite anodes in a LiFSI-PYR_{14}TFSI electrolyte at 55°C. Current rate: C/10. Data from ref. (*99*)

Cycle Number	*graphite KS6L*		*graphite SLP30*	
	Capacity / mA h g^{-1}	*Efficiency / %*	*Capacity / mA h g^{-1}*	*Efficiency / %*
1st cycle	360	72.3	364	84.2
2nd cycle	362	96.3	364	97.9
3rd cycle	361	97.9	363	98.5
50th cycle	350	99.5	317	99.8

The IL/lithium salt couple plays a key role in the performance of graphite anodes. For instance, the replacement of LiTFSI with $LiPF_6$ (*61*, *85*, *86*) leads to a remarkable increase in capacity (300 mA h g^{-1}), e.g., more than twice that in $PYR_{13}FSI$-based electrolytes, in conjunction with a reduction of the irreversibility of the Li^+ intercalation process (Table 8). Matsuda et al. (*94*) also reported the good film-forming ability of $LiPF_6$ on carbonaceous anodes. However, a much lower cycling stability with respect to LiTFSI-based electrolytes, in particular those containing $PYR_{14}TFSI$, is observed.

In order to combine the good electrochemical stability and cycling behavior of $PYR_{14}TFSI$ with the SEI-forming ability and high ionic conductivity (Table 1) of $PYR_{13}FSI$, ternary mixtures of these two ILs with LiTFSI or $LiPF_6$ salt were proposed by Appetecchi et al. as electrolytes for graphite anodes (*61*, *85*, *86*). The LiTFSI-based ternary mixtures have displayed an intrinsic film-forming ability, resulting in capacity values more than two times higher than those obtained in single-IL electrolytes (Table 9) and a very good capacity retention upon prolonged cycling tests at high current rates. For instance, practically 100% of the initial capacity was delivered after 50 consecutive discharge/charge cycles. Otherwise, analogous $LiPF_6$-based ternary electrolytes have shown a much worse cycling behavior (10-15 cycles), which was strongly affected by the $PYR_{13}FSI$ content, once more highlighting the interaction between this IL and the $LiPF_6$ salt.

Table 9. Reversible capacity and coulombic efficiency referred to the 1st discharge/charge cycle of graphite (KS-6) electrodes in different single-IL and mixed-IL electrolytes. The mole fraction is only referred to the IL components. Current rate: 1C. T = 20°C. Data from refs. (*61*, *85*, *86*)

	Single-IL electrolytes				*Mixed-IL electrolytes*			
LiTFSI / mole dm^{-3}	0.3	0.3	---	---	0.3	0.3	---	---
$LiPF_6$ / mole dm^{-3}	---	---	0.3	0.3	---	---	0.3	0.3
$PYR_{13}FSI$ / mole fraction	1.00	---	1.00	---	0.25	0.58	0.25	0.58
$PYR_{14}TFSI$ / mole fraction	---	1.00	---	1.00	0.75	0.42	0.75	0.42

Continued on next page.

Table 9. (Continued). Reversible capacity and coulombic efficiency referred to the 1st discharge/charge cycle of graphite (KS-6) electrodes in different single-IL and mixed-IL electrolytes. The mole fraction is only referred to the IL components. Current rate: 1C. T = 20°C.

	Single-IL electrolytes				*Mixed-IL electrolytes*			
Capacity / mA h g^{-1}	130	130	300	180	300	270	230	260
Efficiency / %	89.8	74.5	96.5	92.1	74.9	37.1	89.0	47.8

Additive-free, ternary LiTFSI-EMITFSI-PYR_{13}TFSI electrolyte mixtures were found to well behave in hard carbon-graphite blend anodes (*95*) showing a capacity that stabilized at 275 mA h g^{-1} after an initial value of 300 mA h g^{-1} (with a coulombic efficiency equal to 70%).

The electrochemical characteristics of graphite anodes were investigated in mixed electrolytes based on ILs and the organic solvents used in commercial lithium-ion batteries with the purpose of determining the optimal compromise among conductivity and non-flammability of the mixed electrolyte and, on the other hand, cell performance. Guerfi et al. (*65*) have focused on $LiPF_6$-EMITFSI-EC-DEC-VC electrolyte mixtures, which have displayed the ability to form a stable SEI layer (not previously obtained in TFSI-based ILs). The best results in terms of reversible capacity were obtained for an IL content (EMITFSI) equal to 20 wt.%, whereas the coulombic efficiency was seen to increase with the organic solvent amount (Table 10).

Table 10. Reversible capacity and coulombic efficiency values, referred to the 1st and 2nd cycles, for graphite anodes in $LiPF_6$-EMITFSI-EC-DEC-VC electrolytes at different EMITFSI content. Room temperature. Data from ref. (*65*)

EMITFSI content / wt.%	*1st cycle*		*2nd cycle*	
	Rev. Cap. / mA h g^{-1}	*Efficiency / %*	*Rev. Cap. / mA h g^{-1}*	*Efficiency / %*
0	316	92	312	100
10	329	91	302	99
20	337	87	331	100
30	315	85	312	99
50	250	80	248	97
100	96	68	79	84

Titanium Oxides

The interest in lithium titanium oxide, LTO, as an anode material is due to its structural *zero* strain upon lithium intercalation that leads to an exceptional cycling stability (*96*). In addition, LTO exhibits several advantages including large capacity (175 mA h g^{-1}), high stability (i.e., the material operates within the electrochemical stability window of the electrolyte, no passive layer growth occurs at the interface with the electrolyte), very flat charge and discharge plateaus, coulombic efficiency close to 100%, low cost and environmental impact, but poor electronic conductivity.

The intercalation potential of lithium in LTO is relatively high (e.g., around 1.5 V vs. Li/Li^+), limiting the cell voltage of lithium-ion cells to 2.5 V, even if coupled with 4 V cathodes. This issue lowers the battery energy but, at the same time, results in higher safety. The use of IL electrolytes in conjunction with lithium titanate electrodes is very welcome because of their non-flammable nature which increases the safety of LTO-based cells even further. Kim et al. (*97*) and Lux et al. (*98*) have investigated LTO anodes in an LiTFSI-PYR_{14}FSI electrolyte, which represents the right compromise between the higher electrochemical and thermal stabilities of LiTFSI-PYR_{14}TFSI and the higher ionic conductivity of LiFSI-PYR_{14}FSI (Figure 8 and Table 2). It is important to highlight that the LTO anode electrodes were fabricated using a natural and water-soluble binder rather than the conventional and more expensive poly(vinylidenedifluoride) (PVdF), thus allowing for cheaper and environmentally friendly production processes and easier recyclability at the end of life of the electrodes. More than 220 mA h g^{-1} were displayed during the first intercalation step with a decrease to 165 mA h g^{-1} in the third cycle, remaining stable around this value for at least 250 cycles (Figure 14, left panel). Such a performance is comparable, if not better, to that showed from PVdF-based LTO anodes in organic electrolytes (Figure 14, right panel). Some irreversibility was detected in the 1_{st} intercalation-deintercalation step, likely due to modifications with the electrolyte, but the electrodes behaved very reversibly in the following cycles.

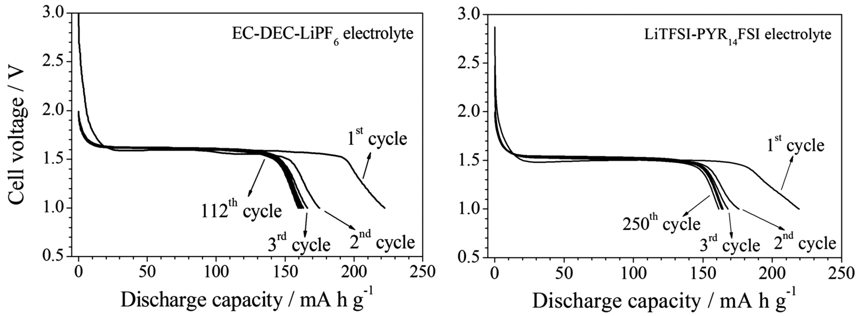

Figure 14. Voltage vs. capacity profile of selected discharge steps for a LTO anode in EC-DEC $LiPF_6$ (left panel) and LiTFSI-PYR_{14}FSI (right panel) electrolytes. Current rate: C/10. T = 20°C. Data from refs. (97, 98).

Promising performance of LTO electrodes was also found in ternary, lithium salt-ILs electrolytes, e.g., LiTFSI-EMITFSI-PYR_{13}TFSI (*95*), which allowed reversible cycling with a stable capacity of 130 mA h g^{-1} and a coulombic efficiency above 99%.

Recently, titanium oxide, TiO_2, has also been investigated as an anode material since its intercalation potential, e.g., 1.4-1.6 V vs. Li/Li^+, falls within the electrochemical stability window of most common ILs. Mun at al. (*99*) have reported the results obtained using TiO_2 anodes in EMITFSI, PYR_{13}TFSI and PIP_{13}TFSI based electrolytes with LiTFSI as the lithium salt. In all of these LiTFSI-IL electrolytes, the TiO_2 electrodes showed capacity and cycling performances comparable to those observed in EC/DEC electrolytes (Table 11), when the cathodic cut-off was set to 1.2 V. Nevertheless, if the cut-off was extended down to 0.6 V, where electrochemical reduction of imidazolium takes place, the Li/TiO_2 cell displays rapid capacity fading in the EMITFSI-based electrolyte. However, TiO_2 electrodes tested in the cathodically stable IL electrolytes based on PYR_{13}TFSI and PIP13TFSI show very reasonable performance, which is even better than that observed in EC/DEC.

Table 11. Deintercalation capacity exhibited from TiO_2 anodes in various electrolytes at a different cathodic cut-off. T = 25°C. I = 70 mA g^{-1}. Data from ref. (*99*)

Cathodic cut-off = 1.2 V	*Capacity / mA h g^{-1}*			
Electrolyte	*1st cycle*	*3rd cycle*	*10th cycle*	*50th cycle*
LiTFSI-EC/DEC	150	146	135	125
LiTFSI-EMITFSI	150	147	142	138
LiTFSI-PYR_{13}TFSI	136	136	135	131
LiTFSI-PIP_{13}TFSI	143	143	137	134

Cathodic cut-off = 0.6 V				
LiTFSI-EC/DEC	275	184	150	108
LiTFSI-EMITFSI	275	220	50	12
LiTFSI-PYR_{13}TFSI	215	173	162	150
LiTFSI-PIP_{13}TFSI	215	173	162	133

Very interesting behavior is observed in Li/TiO_2 cells cycled at high temperatures. After a few cycles at room temperature, the cells are subjected to one cycle at high temperature (120°C) and then cycled again at room temperature (Table 12). From the table it is observed that the cells containing the conventional electrolyte (EC/DEC-based) and the IL electrolyte (EMI-based) did not withstand the high temperature cycle. SEM images and impedance measurements demonstrated that the capacity fading detected in the EMITFSI electrolyte was likely associated with the growth of a very thick passive layer on the TiO_2 anode as a result of the electrolyte decomposition (EMI cation reduction). X-ray photoelectron spectroscopy results indicate that EMITFSI, as well as EC/DEC, decomposed at high temperatures (*28*).

Table 12. Deintercalation capacity exhibited from TiO_2 anodes in various electrolytes at 25°C (70 mA g^{-1}), at 120°C (250 mA g^{-1}) and again at 25°C. Voltage range: 1.2 – 2.5 V. Data from ref. (*99*)

	Capacity / mA h g^{-1}		
Electrolyte	*25°C*	*120°C*	*25°C*
LiTFSI-EC/DEC	135	85	20
LiTFSI-EMITFSI	142	> 300	20
LiTFSI-PYR_{13}TFSI	125	225	110
LiTFSI-PIP_{13}TFSI	125	215	110

Lithium-Alloys

Metals such as tin (Sn), antimonium (Sb) and aluminum (Al) have been proposed as anodes for lithium-ion batteries since their capability to form reversible alloys with lithium metal resulting in capacities approaching or overcoming 2 A h g^{-1}. However, these materials suffer from a large volume increase (up to 300%) during the Li insertion, leading to particle disintegration and fast anode degradation.

A few articles are present in the literature on the cycling performance of Li-alloys in IL electrolytes. Scrosati at al. (*100–102*) have reported a detailed impedance investigation on Li/Sn-C half cells in LiTFSI-PYR_{24}TFSI, showing that the nanostructured Sn-C composites exhibit a much more stable interface with the electrolyte than Li anodes, as a result of the growth of a passive layer that prevents the continuous decomposition of the IL electrolyte. For instance, cathodic scans performed on Li/Sn-C carbon half-cells displayed only a broad peak in the 0.1-0.7 potential range, likely ascribed to Sn-Li alloying which occurs at a nominal voltage of 0.4 V. Katayama et al. (*102*) have observed that LiTFSI-PYR_{14}TFSI electrolytes allow reversible Li alloying/de-alloying of Sn anodes, showing comparable performance with respect to organic electrolytes (Table 13). This issue highlights the ability of PYR_{BA}TFSI-based electrolytes to well behave with tin electrodes. The resistance at the electrolyte/Sn interface was found to decrease upon the addition of 0.2 M glymes (e.g., from 250 Ω cm^2 to 45 Ω cm^2), likely due to their coordination with Li^+ (Table 14).

Table 13. Specific capacity referred to the initial cycles of Li/Sn-C anodic half-cells in different electrolytes. Current rate: C/5. T = 25°C. Data from ref. (*102*)

Electrolyte	*Specific capacity / mA h g^{-1}*			
	1st discharge	*1st charge*	*2nd discharge*	*2nd charge*
$LiClO_4$-EC-DMC	1,060	457	868	537
LiTFSI-PYR_{14}TFSI	1,062	496	765	496

Table 14. Resistance of Sn anodes in LiTFSI-PYR_{14}TFSI electrolytes containing different additives (0.2 M concentration). T = 25°C. Data from ref. (*102*)

Additive	*additive-free*	*monoglyme*	*diglyme*	*triglyme*	*tetraglyme*
Ω cm^2	250	45	100	150	125

The most appealing property of silicon is the high lithiation capacity (4,200 mA h g^{-1} not considering the weight of alloyed lithium) at low redox potentials that makes them very appealing for rechargeable lithium batteries.

Thin silicon anodes, prepared by sputtering (*103*) on stainless steel substrates, showed good performance with a stable capacity of 3,000 mA h g^{-1} and a relatively low irreversible capacity in LiTFSI-PIP_{13}TFSI electrolytes. Si-Ni-carbon composite anodes, investigated by Ishikawa et al. (*104*), have exhibited a very stable reversible capacity in FSI-based electrolytes, comparable to that observed in standard organic electrolytes, whereas no reversible capacity was presented in TFSI-based electrolytes. The silicon anodes in the FSI-based electrolyte delivered an initial capacity of 800 mA h g^{-1} while 790 mA h g^{-1} were still discharged at the 50th cycle, corresponding to a 98.8 % capacity retention. AC measurements have evidenced very low charge-transfer resistances at the Si/electrolyte interface in FSI-based electrolytes.

Lee et al. (*105*) have plated a $FeSi_{2.7}$ thin film onto a Cu substrate by RF magnetron sputtering from a Fe-Si alloy target. The $FeSi_{2.7}$ anode was able to deliver an initial discharge capacity of 756 mA h g^{-1} with a very good capacity retention (92% of the initial value) after 100 cycles, in a PYR_{14}TFSI based electrolyte, due to the formation of a stable SEI at the $FeSi_{2.7}$/electrolyte interface (promoted by PYR_{14}TFSI). The influence of the Si/electrolyte stability and the SEI composition in pyrrolidinium-based electrolytes was also demonstrated by Song et al (*106*) on $SiO_{1.3}$ electrodes made by pulsed laser deposition. IR and XPS analyses have indicated the growth of a passive layer constituted by the decomposition products of PYR_3TFSI on the oxygen abundant, silicon oxide anode surface. This significantly enhanced the cycling stability even with respect to a commercial organic solvent-based electrolyte (Table 15). For instance, 88% of the initial capacity (1,058 mA h g^{-1}) was delivered after 200 consecutive cycles in LiTFSI-PYR_3TFSI.

Table 15. Capacity delivered at selected discharge half-cycles from $SiO_{1.3}$ anodes in organic and LiTFSI-PYR_3TFSI electrolytes. Data from ref. (*106*)

Electrolyte	*Delivered capacity / mA h g^{-1}*				
	1st	*50th*	*100th*	*150th*	*200th*
Organic-based	1,100	400	250	150	100
LiTFSI- PYR_3TFSI	1,090	1,000	950	950	945

Positive Electrodes in Ionic Liquid Electrolytes

Lithium Cobalt Oxide

Most of commercial lithium-ion batteries use lithium cobalt oxide, LCO, as the cathodic material. LCO exhibits a good capacity (140 mA h g^{-1}) and on intercalation potential close to 4 V, but it is based on toxic and expensive cobalt.

Matsumoto et al. (*68*, *74*, *107*, *108*) have extensively studied the cycling behavior of LCO in electrolytes (LiTFSI as the lithium salt) based on room temperature ILs composed of different cations, e.g., imidazolium, $(Am)_4N$, $(Et)_4N$, pyrrolidinium and piperidinium, and different anions, e.g., FSI, TFSI, TPSI, and TSAC. The results, summarized in Table 16 and Figure 156, evidence how PIP_{13}TFSI is a rather promising candidate as an electrolyte component for Li/LCO cells, e.g., 88% of the theoretical capacity was discharged after 50 consecutive charge/discharge cycles at a C/10 current rate. Interesting capacity retention values were also obtained in FSI-based electrolytes, e.g., more than 92% of the initial capacity (135 mA h g^{-1}) was delivered after 50 cycles in LiTFSI-PYR_{13}FSI (C/10). The highest rate capabilities were observed in FSI-based IL electrolytes, e.g., about 85% of capacity discharged at C/10 was delivered at 3C in LiTFSI-EMIFSI (Figure 15) whereas at a current rate of 1C the electrolyte LiTFSI-EMITFSI only retained of just 42% of the capacity recovered at C/10.

Table 16. Discharge capacity values delivered from LCO cathodes in various IL-LiTFSI electrolytes at room temperature. Current rate: C/10. Data from refs. (*68*, *74*, *107*, *108*)

Ionic liquid Component	*Discharge capacity / mA h g^{-1}*				
	1st cycle	*2nd cycle*	*4th cycle*	*30th cycle*	*50th cycle*
EMITFSI	132	131	130	102	---
EMITSAC	110	115	115	90	---
EMIFSI	130	---	---	115	100
PYR_{13}TFSI	113	122	118	90	---
PYR_{13}FSI	135	---	---	130	125

Continued on next page.

Table 16. (Continued). Discharge capacity values delivered from LCO cathodes in various IL-LiTFSI electrolytes at room temperature. Current rate: C/10.

Ionic liquid Component	*Discharge capacity / mA h g^{-1}*				
	1st cycle	*2nd cycle*	*4th cycle*	*30th cycle*	*50th cycle*
$PIP_{13}TFSI$	142	141	140	130	125
$PIP_{13}TSAC$	132	131	130	120	110
$PIP_{13}TPSI$	109	110	110	110	110
TMPITFSI	117	120	80	---	---
$(Am)_4NTFSI$	113	117	119	125	120
$(Et_4)NTSAC$	119	117	115	40	---

To summarize, it is noteworthy that the use of ILs as electrolyte component for lithium metal battery systems is mainly fixed by its stability at the Li interface (*68*, *74*). The rate properties of the Li/LCO cells were dominated by the IL viscosity rather than by the introduction of asymmetric anions into the IL architecture, even if the conductivity resulted to be improved. Therefore, the cycling performance of lithium cobalt oxide in IL-based electrolytes depends on the nature of the IL cation and anion according to the following sequence (*68*, *74*, *107*, *108*):

cation: $PIP_{13} > PYR_{13} > EMI > TMPI > (Am)_4N > (Et)_4N$

anion: FSI > TFSI > TSAC > TPSI

Hayashi et al. (*109*) focused their attention on ILs based on the 1,2-diethyl-3,4(5)-dimethyl imidazolium (DEDMI) cation. In particular, DEDMITFSI, which shows a melting point of -35 °C and higher conductivity than $DEDMIBF_4$, allowed reversible cycling of LCO cathodes with a capacity of about 100 mA h g^{-1}.

The temperature dependence of the LCO electrochemical performance in IL electrolytes was also investigated. Ogumi at al. (*110*) focused on a TMHATFSI mixture with LiTFSI, which has a wide liquid phase temperature range. However, the optimal operating temperature was found to be around 35°C as a compromise between capacity retention and initial coulombic efficiency (Table 17). It is to noteworthy that the room temperature high internal resistance of the Li/LCO cells, deriving from the relatively high viscosity of the TMHATFSI-based electrolyte (*110*) and its poor wettability of the electrode material (evidenced from AC measurements), resulted in serious voltage hysteresis, this accounting for the moderate electrode capacity at low temperatures. Higher temperatures promoted the electrolyte conduction (lower viscosity) and the wettability with LCO cathodes, but led to irreversible structural variation of LCO, even if the Li^+ extraction/insertion was facilitated.

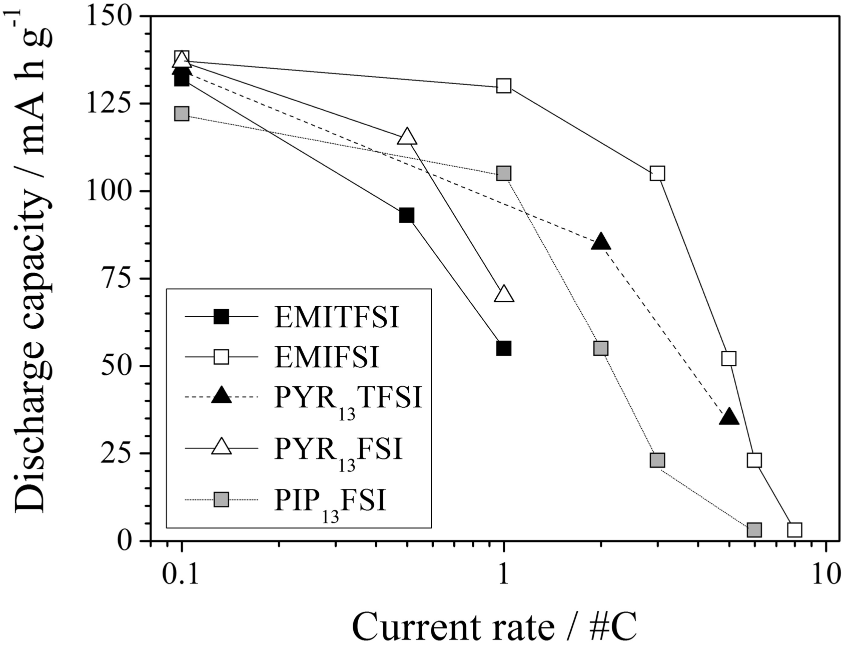

Figure 15. Discharge capacity vs. current rate dependence of LCO cathodes in different LiTFSI-IL electrolytes. Room temperature. Data from refs. (68, 74, 107).

Table 17. Capacity values delivered from LCO cathodes in LiTFSI-TMHATFSI electrolytes at different temperatures. The coulombic efficiency in the 1st charge/discharge cycle is also reported. Data from ref. (*110*)

Cycle	*Delivered capacity / mA h g^{-1}*		
	20°C	*35°C*	*50°C*
1st	111 (*88.6**)	129 (*95.6**)	122 (*75.6**)
2nd	112	127	120
5th	114	115	100
10th	111	107	70

A different approach for improving the thermal stability of LCO electrodes was followed by Lee at al. (*111*), which was based on the surface treatment of LCO with BDMIPF$_6$ (e.g., incorporated during the electrode preparation). DSC measurements showed an enhanced thermal stability with respect to the pristine electrodes, resulting from a strong reduction of the exothermic features displayed in the DSC traces between 200-250°C, which are due to: *i*) surface reaction of delithiated LCO with the IL electrolyte and *ii*) decomposition of layered LCO which, in addition, generates oxygen, which further reacts with the IL electrolyte (*112*, *113*). The improved performance (Table 18) of the $BDMIPF_6$-modified LCO cathodes was attributed to the preferential localization of the IL onto the electrode surface, which decreased the local surface concentration of electrolyte and, therefore, suppressed the exothermal reaction with the electrode.

Table 18. Discharge capacity of pristine and $BDMIPF_6$-modified LCO cathodes (with respect to carbon anodes) at different current rates. Data from ref. (*111*)

LCO cathode	*Discharge capacity / mA h*		
	C/5	*C/2*	*1C*
Pristine	670	650	570
$BDMIPF_6$-modified	735	730	725

Lithium Manganese Oxide

Spinel-like structure, lithium manganese oxide (LMO), was proposed as cathode active material for lithium-ion batteries due to its good capacity (above 140 mA h g^{-1}) and high intercalation potential (above 4 V) in conjunction with low cost and environmental impact. Unfortunately, in practice, LMO exhibits moderate capacity retention due to degradation phenomena.

Ogumi et al. (*114*) focused on the physicochemical characteristics vs. temperature dependence of spinel LMO in TMHATFSI-LiTFSI electrolytes. Li/LMO cells exhibited room temperature discharge capacities of about 110 mA h g^{-1} with an initial coulombic efficiency equal to 91.4%. At sub-ambient temperature, a reversible capacity decay was observed due to the increase of the cell internal resistance and the high activation energy for lithium ion transfer through the electrode/electrolyte interface. Conversely, an anodic electrolyte oxidation and coulombic efficiency decrease occurred with increasing temperature. Ogumi et al. (*114*) attributed the cycling performance decay of LMO to irreversible structural conversion of LMO in the IL electrolyte possibly associated with the formation of TMHA-intercalated compounds and/or Jahn-Teller distortion (*115*).

Xu at al. (*116*) have revealed that, unlike EMITFSI, a small addition (5 wt.%) of a dication, such as $MIEM_3N$, based IL to the conventional $LiPF_6$-EC-DMC electrolyte improves the discharge capacity and cycle durability of LMO cathodes (Table 19).

Similarly, Lewandowski at al. (*117*) have found an enhanced capacity retention (e.g., from 68% to 94% after 25 consecutive charge/discharge cycles at 100% depth of discharge) and coulombic efficiency in $LiTFSI-PIP_{13}TFSI$ electrolytes upon the incorporation of 10 wt.% VC (Table 20). A linear capacity vs. current rate behavior (Figure 16) was observed up to C/2, e.g., about 70% of capacity value delivered at C/10 is discharged at C/2.

Table 19. Capacity values delivered from LMO cathodes, at selected discharge half-cycles, upon 5 wt.% addition of different ILs in the $LiPF_6$-EC-DMC electrolyte. Current range: 1C. Room temperature. Data from ref. (*116*)

	Discharge capacity / mA h g^{-1}			
	1st cycle	*10th cycle*	*50th cycle*	*100th cycle*
Additive-free	150	148	146	140
EMITFSI	140	130	125	120
$MIEM_3NTFSI$	160	158	154	154

Table 20. Capacity delivered by LMO cathodes in $LiTFSI-PIP_{13}TFSI$ electrolyte upon addition of different VC content. Current range: 1C. Room temperature. Data from ref. (*117*)

VC content / wt. %	*Discharge capacity / mA h g^{-1}*			
	1st cycle	*5th cycle*	*10th cycle*	*25th cycle*
0	95	89	85	65
10	125	120	120	118

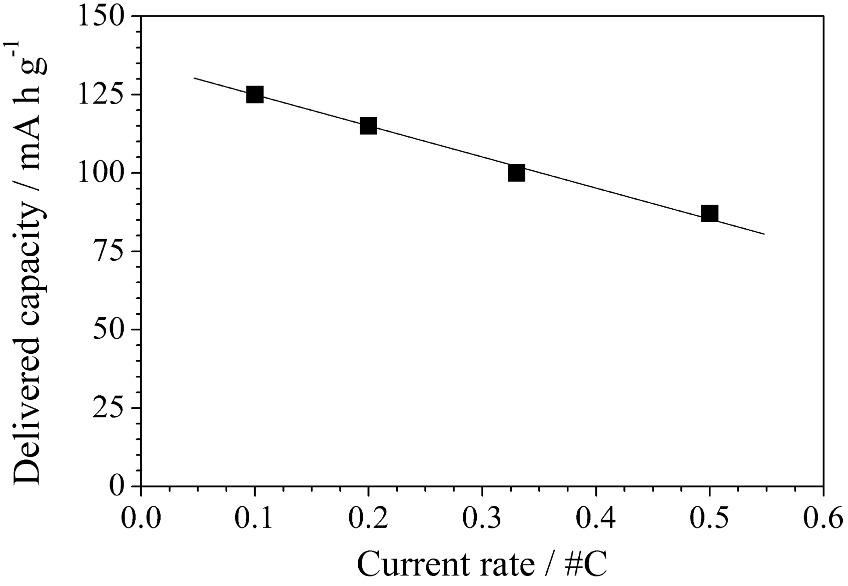

Figure 16. Discharge capacity vs. current rate dependence of LMO cathodes in $LiTFSI-PIP_{13}TFSI$ + 10 wt.% VC electrolyte at room temperature. Data from ref. (117).

Doping with Ni and/or Co was seen to increase both the specific capacity (above 200 mA h g^{-1}) and the operating voltage (up to 5 V) of lithium manganese oxide. However, electrolytes with anodic stability exceeding 5 V are not easily available. Nevertheless, IL electrolytes allow high voltage, Mn-based cathodes to be cycled with a relatively low parasitic process extent (during the charge step). In particular, Li/$LiNi_{0.5}Mn_{1.5}O_4$ cells have exhibited better behavior (in terms of capacity and coulombic efficiency) in pyrrolidinium- and, especially, piperidinium- TFSI based electrolytes than in conventional, organic solvent-based electrolytes (Table 21). Borgel at al. (*118*) have addressed this issue to the high anodic stability of the TFSI anion. In addition, the reduction of TFSI in the presence of Li^+ cations generates insoluble lithium compounds, thus leading to the growth of a protective passive layer on the lithium anode. Conversely, poor cyclability was displayed in imidazolium electrolytes since the reduction products formed on the lithium anode migrate, according to a shuttle mechanism due to insufficient Li passivation, to the cathode to be oxidized upon charge at high voltages.

Table 21. Specific capacity in selected charge/discharge cycles of Li/$LiNi_{0.5}Mn_{1.5}O_4$ cells in different organic and IL electrolytes. Current rate: C/16. T = 20°C. Data from ref. (*118*)

Electrolyte	*Specific capacity / mA h g^{-1}*									
	1st cycle		*2nd cycle*		*5th cycle*		*20th cycle*		*50th cycle*	
	Ch	*Dis*	*Ch*	*Dis*	*Ch*	*Dis*	*Ch*	*Dis*	*Ch*	*Dis*
$LiPF_6$-EC-DMC	390	107	205	130	164	143	164	136	160	130
LiTFSI-PYR_{14}TFSI	200	105	130	114	125	114	118	114	107	105
LiTFSI-PIP_{13}TFSI	182	150	164	143	157	150	150	147	143	140

Very promising results, even better than those found in organic solutions, were displayed by $Li(Li_{0.2}Mn_{0.56}Ni_{0.16}Co_{0.08})O_2$ cathodes in LiTFSI-PYR_{14}FSI electrolytes. At 40°C, Passerini et al. (*119*) have observed an initial capacity close to 300 mA h g^{-1} (near to the value exhibited in $LiPF_6$-EC-DMC) to leveling at 220 mA h g^{-1} after 50 cycles at C/2, e.g., more than 210 mA h g^{-1} were delivered upon 100 cycles whereas just 150 mA h g^{-1} in $LiPF_6$-EC-DMC, with a coulombic efficiency progressively achieving 100% (Figure 17). A very good capacity retention was evidenced at near room temperature (Figure 18), e.g., 74% of the capacity delivered at C/10 (270 mA h g^{-1}) was discharged at 2C (200 mA h g^{-1}), whereas a further increase of the current rate up to 5C leads to a capacity decrease down to 95 mA h g^{-1}. At 20°C, a relatively moderate decay in capacity was recorded up to 1C (185 mA h g^{-1}). However, still acceptable capacity values were obtained at higher current rates (100 mA h g^{-1} discharged at 2C).

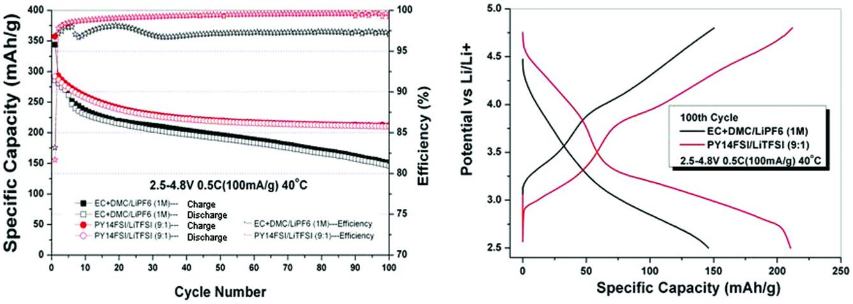

Figure 17. Cycling performance (left panel) and 100th cycle voltage vs. capacity profile (right panel) of $Li(Li_{0.2}Mn_{0.56}Ni_{0.16}Co_{0.08})O_2$ cathodes in LiTFSI-$PYR_{14}FSI$ (red data markers) and $LiPF_6$-EC-DMC (black data markers) at 40°C and C/2 rate. Data from ref. (119).

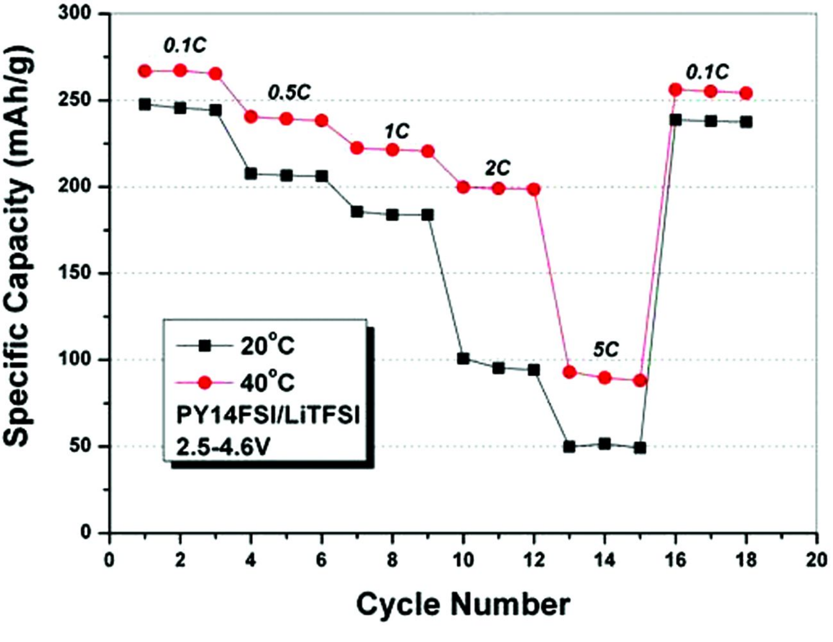

Figure 18. Cycling performance at different current rates for $Li(Li_{0.2}Mn_{0.56}Ni_{0.16}Co_{0.08})O_2$ cathodes in LiTFSI-$PYR_{14}FSI$ electrolyte at 20°C and 40°C. Data from ref. (119).

Saint at al. (*120*) have compared the performance of layered $LiMnO_2$ cathodes in LiTFSI-$PYR_{13}TFSI$ and LiTFSI-$PYR_{13}FSI$ electrolytes with respect to $LiPF_6$-EC:DMC solutions. The results (Table 22) have shown lower capacity retention and rate capability in the lithium salt-IL mixtures with respect to the conventional electrolyte, likely due to their higher viscosity (and, consequently, lower conductivity). In addition, Raman and FTIR measurements carried out by Hardwick et al. (*121*), have addressed the capacity fading observed in $LiMnO_2$ to surface decomposition and/or partial phase transformation of lithium manganese oxide, which, in conjunction with electrolyte oxidation at the cathode side, promotes the growth of thick, insulating (ionically and electronically) passive layers (especially during cycling). However, this phenomenon is remarkably decreased upon doping the $LiMnO_2$ with titanium. For instance, $Li_xTi_yMn_{(1-y)}O_2$ (y = 0.11) has exhibited much better cycling performance than undoped Li_xMnO_2 (Table 22).

Table 22. Capacities delivered, at selected cycles (A) and current rates (B), by Li_xMnO_2 cathodes in conventional and IL-based electrolytes. Capacity values discharged (C) by Li_xMnO_2 and $Li_xTi_{0.11}Mn_{0.89}O_2$ cathodes at selected cycles in LiTFSI-PYR_{13}FSI electrolyte. Current rate: C/15. Data from refs. (*120*, *121*)

	Discharge capacity of Li_xMnO_2 / mA h g^{-1}			
(A) Electrolyte	*1st cycle*	*5th cycle*	*10th cycle*	*30th cycle*
$LiPF_6$-EC-DMC	120	120	110	115
LiTFSI-PYR_{13}FSI	107	105	90	50
LiTFSI-PYR_{13}TFSI	120	115	110	95

(B) Electrolyte	*C/50*	*C/10*	*C/2*	*1C*
$LiPF_6$-EC-DMC	120	110	100	80
LiTFSI-PYR_{13}FSI	120	100	60	1

	Discharge capacity in LiTFSI-PYR_{13}FSI / mA h g^{-1}				
(C) Cathode	*1st cycle*	*5th cycle*	*20th cycle*	*50th cycle*	*160th cycle*
Li_xMnO_2	95	93	100	73	---
$Li_xTi_{0.11}Mn_{0.89}O_2$	78	83	85	90	85

Lithium Iron Phosphate

The adoption of lithium iron phosphate (LFP), LFP, as a cathode material has attracted much interest for lithium-ion batteries, especially due to its structural *zero* strain during lithium intercalation, which results in an exceptional cycling stability. As for LTO, LFP exhibits several advantages including a high capacity (170 mA h g^{-1}), high safety (e.g., no oxygen release upon overcharge), very flat charge and discharge plateaus, coulombic efficiency close to 100%, low cost and environmental impact, but poor electronic conductivity.

Room temperature IL-based electrolytes, consisting of the FSI anion and EMI or PYR_{13} cations, have been investigated with LFP cathodes, Guerfi et al.

(*69*, *91*). Obtained reversible capacities of 143 and 155 mA h g^{-1} was detected in LiFSI-PYR$_{13}$FSI and LiFSI-EMIFSI electrolytes, respectively, which are comparable with the capacity obtained in LiFSI-EC-DEC (Table 23). An increase of the temperature up to 60°C boosted the LFP capacity above 160 mA h g^{-1}. Conversely, a lower initial coulombic efficiency was found in IL electrolytes (80%) with respect to that obtained with a conventional electrolyte (93%). AC measurements showed electrolyte diffusion resistances varied in the order:

$$\text{LiFSI-EC-DEC} < \text{EC-DEC-LiPF}_6 < \text{LiFSI-PYR}_{13}\text{FSI} = \text{LiFSI-EMIFSI}$$

Acceptable cycling performance, although at a current rate of C/20, was also found in LiTFSI-PIP$_{14}$TFSI by Jin et al. (*122*), as reported in Table 23. The lower capacity observed in the piperidinium electrolyte is due to the higher viscosity of this IL (*30*). The addition of VC (5 wt.%) was found to increase the cycling behavior of the LFP cathodes, mostly due to the formation of a stable SEI, which decreases the resistance at the electrolyte/electrode interface and, at the same time, protects the lithium anode from corrosion.

Table 23. Delivered capacity, at selected cycles, of LFP cathodes in LiFSI-PYR$_{13}$FSI, LiTFSI-PIP$_{14}$TFSI and LiTFSI-PIP$_{14}$TFSI + 5 wt.% VC electrolytes. Current rates: C/4 (PYR$_{13}$FSI) and C/20 (PIP$_{14}$TFSI). Room temperature. Data from refs. (*59*, *69*, *122*)

Electrolyte	*Discharge capacity / mA h g^{-1}*				
	1st cycle	*10th cycle*	*20th cycle*	*50th cycle*	*90th cycle*
LiFSI-PYR$_{13}$FSI	149	149	150	150	149
LiTFSI-PIP$_{14}$TFSI	90	100	105	105	---
LiTFSI-PIP$_{14}$TFSI + 5 wt.% VC	127	130	130	120	---

The slight increase of the cell testing temperature was found to enhance the Li$^+$ diffusion kinetics through both LFP and the IL-based electrolyte, as well as the charge transfer at electrolyte/electrode interface. Lewandowsky et al. (*123*) have obtained very good behavior in LiTFSI-PYR$_{14}$FSI and, especially, LiTFSI-PYR$_{13}$FSI electrolytes in terms of rate capability and cycling ability (Table 24). At 50°C, a capacity of 110 mA h g^{-1} was delivered at 4C rate in LiTFSI-PYR$_{13}$FSI, which corresponds to 72% of the capacity delivered at C/10 (153 mA h g^{-1}). Also, a capacity higher than 140 mA h g^{-1} was retained upon 250 consecutive charge/discharge cycles at C/2, corresponding to a capacity fading of 0.011% per cycle, with a coulombic efficiency close to 99.8%. These results, comparable if not better than those obtained in LiPF$_6$-EC-DMC solutions (Table 24), suggest that a very good long-term cycling behavior of LFP cathodes and lithium metal anodes is possible in IL-based electrolytes.

Table 24. Upper: discharge capacity vs. current rate behavior of LFP cathodes in LiTFSI-PYR_{13}FSI electrolyte at 50°C. Lower: Cycling performance of LFP cathodes in $LiPF_6$-EC-DMC and LiTFSI-PYR_{13}FSI electrolytes at 50°C and different current rates. Data from ref. (*123*)

Discharge capacity / mA h g^{-1}					
C/10	*C/5*	*C/2*	*1C*	*2C*	*4C*
153	150	144	137	131	110

Electrolyte	*Discharge capacity / mA h g^{-1}*				
	1st cycle	*10th cycle*	*20th cycle*	*30th cycle*	*40th cycle*
$LiPF_6$-EC-DMC (C/10)	155	155	153	152	150
LiTFSI-PYR_{13}FSI (C/10)	157	158	158	159	159

Electrolyte	*Discharge capacity / mA h g^{-1}*				
	1st cycle	*10th cycle*	*50th cycle*	*100th cycle*	*250th cycle*
LiTFSI-PYR_{13}FSI (C/2)	150	147	145	143	140

Li/LFP cells were also tested with 1-alkyl-2,3-dimethylimidazolium TFSI electrolytes by Yan et al. (*124*). In particular, the best cycling behavior and reversibility were shown in ADMI-TFSI, which, due to its relatively low viscosity, showed an initial discharge capacity of about 153 mA h g^{-1}. The lowest capacity was observed in IODMI-TFSI (8.1 mA h g^{-1}), but the addition of 10% propylene carbonate was found to increase this value up to 127 mA h g^{-1}. Also, the incorporation of VC was found to improve the compatibility of the 1-alkyl-2,3-dimethylimidazolium TFSI electrolytes towards LFP cathodes and to promote SEI formation and thus protection from lithium anode corrosion.

Kim et al. (*97*) and Lux et al. (*98*) have focused on LFP cathodes in LiTFSI-PYR_{14}FSI electrolyte using natural, water-soluble binders, e.g., carboxymethylcellulose sodium salt (CMC), with the aim to develop greener, safer and easily recyclable lithium batteries. As reported in Table 25, a performance comparable, if not superior, to that exhibited by standard PVdF-based electrodes was recorded even at high rates, e.g., above 74% of the capacity delivered at C/10 (148 mA h g^{-1}) was delivered by CMC-based, LFP cathodes at 5C (110 mA h g^{-1}). This exceptional rate capability is accomplished by a high capacity retention, e.g., 75% of the initial capacity (140 mA h g^{-1}) was delivered after 1,000 cycles (105 mA h g^{-1}) at medium-high rates (1C), corresponding to a fading of 0.025% per cycle, with a coulombic efficiency leveling at 100% after a few cycles. Figure 19 illustrates the voltage vs. capacity profile of selected charge/discharge cycles obtained at C/10 and 20°C, which display very flat plateaus during the lithium insertion/deinsertion process. The slight increase in capacity upon cycling is ascribed to the modest wettability of the porous cathode with respect to the IL electrolyte.

Table 25. Discharge capacity vs. current rate dependence (upper) and prolonged cycling (current rate of 1C) performance (lower) of different binder-based LFP cathodes in LiTFSI-PYR$_{14}$FSI electrolyte. Room temperature. Data from refs. (*97*, *98*)

Discharge capacity / mA h g^{-1}								
Binder	*C/10*	*C/5*	*C/3*	*C/2*	*1C*	*2C*	*3C*	*4C*	*5C*
PVdF	160	158	155	152	147	140	125	107	68
CMC	148	147	147	145	140	130	125	118	110

Binder	*C/rate*	*1st*	*5th*	*20th*	*50th*	*100th*	*240th*	*500th*	*1000th*
CMC	C/10	160	163	165	165	164	163	---	---
CMC	1C	140	142	141	140	135	130	120	105
PVdF	1C	155	150	145	140	---	---	---	---

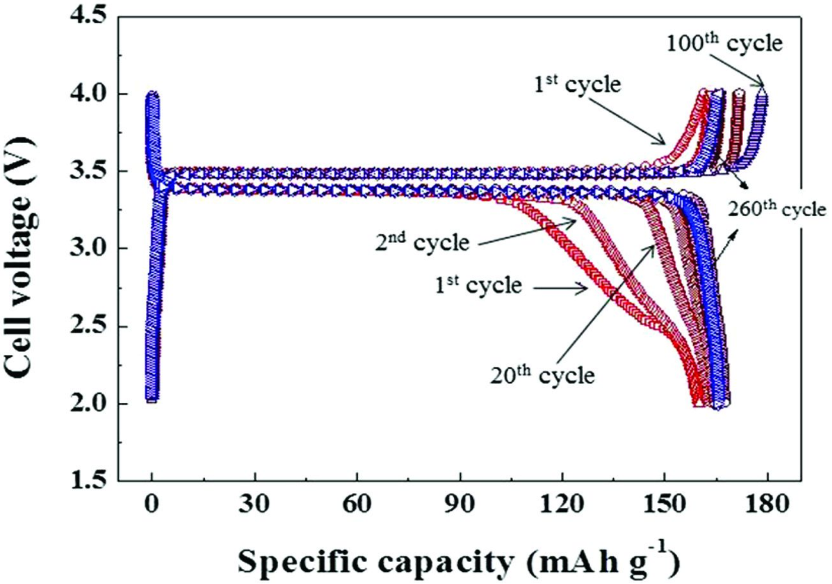

Figure 19. Selected voltage vs. capacity profiles of LFP cathodes in LiTFSI-PYR$_{14}$FSI electrolyte. Current rate: C/10. Temperature: 20°C. Data from ref. (97).

LFP cathodes were also tested in mixtures of organic solvent and IL based electrolytes with the aim to improve the transport properties without depleting the cell safety. Guerfi et al. (*65*) have investigated the behavior of LFP cathodes in $LiPF_6$-EMITFSI-EC-DEC-VC electrolytes. As reported in Table 26, no practical decay in terms of capacity and coulombic efficiency was observed up to an EMITFSI content equal to 50 wt.%. Larger IL amounts resulted in performance decay due to the high viscosity of the IL component and the low wettability of the carbon-coated LFP. Only a moderate reduction in capacity, for IL amounts ranging for 0 to 50 wt.%, was detected up to a current rate of 4C (Table 27), thus resembling the behavior of the pure organic electrolyte. The high rate performance (≥ 20C) has highlighted a bell-shape behavior with a maximum in capacity at IL content equal to 20 wt.%.

Table 26. Specific capacities and coulombic efficiencies detected during the 1st charge/discharge cycle of LFP cathodes in $LiPF_6$-EMITFSI-EC-DEC-VC electrolytes at different EMITFSI content. Current rate: C/12. Room temperature. Data from ref. (*65*)

IL content / wt.%	*Specific capacity / mA h g^{-1}*		*Efficiency / %*
	Charge	*Discharge*	
0	156	156	100
10	154	154	100
20	154	152	99
30	154	154	100
50	154	153	99
100	150	123	82

Table 27. Discharge capacity vs. current rate of LFP cathodes in $LiPF_6$-EMITFSI-EC-DEC-VC electrolytes at different EMITFSI content. Room temperature. Data from ref. (*65*)

IL / wt.%	*Discharge capacity / mA h g^{-1}*							
	C/12	*C/3*	*1C*	*2C*	*4C*	*10C*	*20C*	*30C*
0	156	152	141	135	123	90	2	1
10	154	151	140	132	120	90	60	1
20	152	150	140	130	118	88	70	12
30	154	148	138	130	117	85	30	8

Continued on next page.

Table 27. (Continued). Discharge capacity vs. current rate of LFP cathodes in $LiPF_6$-EMITFSI-EC-DEC-VC electrolytes at different EMITFSI content. Room temperature.

IL / wt.%	*Discharge capacity / mA h g^{-1}*							
	C/12	*C/3*	*1C*	*2C*	*4C*	*10C*	*20C*	*30C*
50	153	143	135	125	105	50	15	1
100	123	65	5	3	2	1	---	---

Kühnel et al. (*66*) have reported very interesting cycling results obtained in ternary LiTFSI-PYR_{14}TFSI-PC electrolyte mixtures. Table 28 illustrates the discharge capacity vs. current rate values delivered by different LiTFSI-(*x* wt.%)PYR_{14}TFSI-(100-*x* wt.%)PC electrolytes at room temperature. The optimal PYR_{14}TFSI-PC weight composition was found to be equal to 1:1, which represents the best compromise among high ionic conductivity, wide electrochemical stability, low flammability and, on the other side, large specific capacity and rate capability. With such an electrolyte composition, 50 mA h g^{-1}, which corresponded to about 36% (50 mA h g^{-1}) of the capacity delivered at C/10 rate, were discharged at a 5C rate. Also, excellent capacity retention was observed upon prolonged cycling tests even at medium temperatures and high rates as evidenced in Table 27, e.g., 94.4% (85 mA h g^{-1}) and 92.3% (120 mA h g^{-1}) of the initial capacity values (90 and 130 mA h g^{-1}) were discharged after 150 and 550 consecutive cycles run, respectively, at 60°C and 10C and 20°C and C/2 with coulombic efficiencies close to 100%. These results make ternary lithium salt - IL - organic solvent mixtures very appealing electrolytes for high power, safe lithium batteries.

Table 28. Discharge capacity vs. current rate behavior at 20°C (A), discharge capacity performance at 20°C for different current rates (B), percent of the initial capacity at 60°C and 5C (C) and discharge capacity performance at 60°C for different current rates (D) of LFP cathodes in LiTFSI-PYR_{14}TFSI-PC electrolytes. Data from ref. (*66*)

(A) PYR_{14}FSI wt.%	*Discharge capacity (20°C) / mA h g^{-1}*								
	C/10	*C/5*	*C/3*	*C/2*	*1C*	*2C*	*3C*	*4C*	*5C*
0	156	147	145	135	125	110	100	91	85
20	146	143	144	134	124	105	80	62	55
50	135	130	125	115	103	75	60	53	45
80	115	106	100	85	65	50	40	35	30

Continued on next page.

Table 28. (Continued). Discharge capacity vs. current rate behavior at 20°C (A), discharge capacity performance at 20°C for different current rates (B), percent of the initial capacity at 60°C and 5C (C) and discharge capacity performance at 60°C for different current rates (D) of LFP cathodes in LiTFSI-PYR$_{14}$TFSI-PC electrolytes.

(A) PYR$_{14}$FSI wt.%	*Discharge capacity (20°C) / mA h g^{-1}*								
	C/10	*C/5*	*C/3*	*C/2*	*1C*	*2C*	*3C*	*4C*	*5C*
100	102	80	65	55	37	25	22	18	15

(B) PYR$_{14}$FSI wt.%	*Discharge capacity (20°C) / mA h g^{-1}*								
	1st cycle		*20th cycle*		*50th cycle*		*100th cycle*		*550th cycle*
	C/2	*3C*	*C/2*	*3C*	*C/2*	*3C*	*C/2*	*3C*	*C/2*
0	141	---	140	---	140	---	138	---	---
20	137	108	135	105	134	104	132	102	---
50	135	102	133	100	132	100	130	98	120
80	128	100	127	97	126	95	125	95	---
100	42	---	42	---	38	---	38	---	---

(C) PYR$_{14}$FSI wt.%	*Percent of the initial capacity (60°C and 5C) / %*				
	1st cycle	*50th cycle*	*100th cycle*	*200th cycle*	*500th cycle*
0	100	97	95	93	80
20	100	97	95	92	84
50	100	98	96	93	85
80	100	100	98	97	92

(D) PYR$_{14}$FSI wt.%	*Discharge capacity (60°C) / mA h g^{-1}*				
	1st cycle	*50th cycle*	*120th cycle*	*250th cycle*	*500th cycle*
3C	143	142	140	---	---
5C	135	132	130	125	115
10C	90	87	85	----	---

Finally, ILs were also used as electrolyte media to synthesize LFP. Tarascon et al. (*125*) have reported the electrochemically-assisted preparation route of lithium iron phosphate in EMITFSI, obtaining electrochemically active lithium iron phosphate with a particle size of 500 nm.

Lithium-Ion Cells with Ionic Liquid Electrolytes

Several research groups have investigated the behavior of complete lithium-ion cells in IL electrolytes, which differed in electrode chemistry. Table 29 summarizes the performance of the various electrode (anode and cathode) active materials in different IL-based electrolytes.

Table 29. Summary of performance of various lithium-ion battery electrode materials in different IL-based electrolytes. (*) = referred to the 1st cycle. The operating voltage value is reported near the active material acronym. Data from refs. (*61*, *65*, *68*, *69*, *74*, *78*, *86*, *89*, *91*, *93*, *95*, *97–99*, *102–104*, *107*, *108*, *110*, *114*, *117*, *121–123*)

Electrode material	*Electrolyte*	*T / °C*	*mA h g^{-1}*	*Eff. / %*
Graphite (0.2 V)	LiTFSI-EMIFSI	20	370	85 (*)
	LiFSI-EMIFSI	20	348	81 (*)
	LiFSI-PYR$_{13}$FSI	20	367	80 (*)
	LiFSI-PYR$_{14}$TFSI	55	360	84 (*)
	LiPF$_6$-PYR$_{13}$FSI-PYR$_{14}$TFSI	20	300	75 (*)
	LiPF$_6$-EMITFSI-EC-DEC-VC	RT	337	87 (*)
LTO (1.5 V)	LiTFSI-PYR$_{14}$FSI	20	170	99
	LiTFSI-EMITFSI-PYR$_{13}$TFSI	20	130	99
TiO$_2$ (1.5 V)	LiTFSI-EMITFSI	25	275	99
	LiTFSI-PYR$_{13}$TFSI	25	215	99
	LiTFSI-PIP$_{13}$TFSI	25	215	99
Sn (0.4 V)	LiTFSI-PYR$_{14}$TFSI	25	496	47 (*)
Si (0.5 V)	LiTFSI-PIP$_{13}$TFSI	RT	3,000	n.a.
SiO$_{1.3}$ (0.5 V)	LiTFSI-PYR$_{13}$TFSI	RT	1,090	n.a.
LCO (3.8 V)	LiTFSI-PYR$_{13}$FSI	RT	135	n.a.
	LiTFSI-PIP$_{13}$TFSI	RT	142	n.a.
	LiTFSI-TMHATFSI	20	111	89 (*)
LMO (4.0 V)	LiTFSI-TMHATFSI	RT	110	91 (*)
	LiTFSI-PIP$_{13}$TFSI	RT	95	n.a.

Continued on next page.

Table 29. (Continued). Summary of performance of various lithium-ion battery electrode materials in different IL-based electrolytes. (*) = referred to the 1st cycle. The operating voltage value is reported near the active material acronym.

Electrode material	*Electrolyte*	*T / °C*	*mA h g^{-1}*	*Eff. / %*
LiNi$_{0.5}$Mn$_{1.5}$O$_4$ (4.8 V)	LiTFSI-PYR$_{14}$TFSI	20	105	51 (*)
	LiTFSI-PIP$_{13}$TFSI	20	150	82 (*)
Li$_{1.2}$Mn$_{0.56}$Ni$_{0.16}$Co$_{0.08}$O$_2$ (4.8 V)	LiTFSI-PYR$_{14}$FSI	20	250	82 (*)
Li$_x$MnO$_2$ (3.5 V)	LiTFSI-PYR$_{13}$TFSI	RT	120	n.a.
LFP (3.5 V)	LiFSI-EMIFSI	RT	155	80 (*)
	LiFSI-PYR$_{13}$FSI	RT	149	n.a.
	LiTFSI-PYR$_{13}$FSI	50	157	n.a.
	LiTFSI-PYR$_{14}$FSI	RT	160	n.a.
	LiPF$_6$-EMITFSI-EC-DEC-VC	RT	154	99
	LiTFSI-PYR$_{14}$FSI-PC	20	146	92

Holzapfel et al. (*79*) have investigated the cycling behavior of graphite/LCO cells in LiPF$_6$(1M)-EMITFSI electrolyte, observing good charge capacity retention over more than 30 consecutive charge/discharge cycles. The graphite electrode delivered a capacity from 370 mA h g^{-1} (5th cycle) to about 320 mA h g^{-1} (30th cycle) with a coulombic efficiency of 62% in the 1st cycle, but approaching 100% from the 2nd cycle (Table 30). A VC additive was incorporated into the IL-based electrolyte because of its SEI forming ability on the graphite anode. An analogous behavior was observed in ammonium-based ILs, e.g., MTOTFSI, showing interesting cycling performance when VC was used as an additive, but only at slightly more elevated temperatures.

Table 30. Discharge capacity and coulombic efficiency values, obtained at selected cycles, for a graphite/LCO cell in LiPF$_6$-EMITFSI-5wt.%VC electrolyte at room temperature. The capacity values are referred to the graphite active material weight. Data from ref. (*79*)

	1st cycle	*2nd cycle*	*5th cycle*	*10th cycle*	*33th cycle*
Capacity / mA h g^{-1}	330	350	370	360	320
Efficiency / %	62	98	99	99	99

Preliminary results on Si/LCO (cathode rich) cells using LiTFSI-PIP$_{13}$TFSI electrolyte have been presented by Aurbach et al. (*103*), showing an initial capacity (referred to the Si weight) of 2,500 mA h g^{-1}, but with a fading of 2%

per cycle in conjunction with an initial coulombic efficiency of only 48% (Table 31). Therefore, a further optimization of this cell chemistry, in terms of active material balancing and cycling conditions, is required.

Table 31. Discharge capacity and coulombic efficiency values, obtained at selected cycles, for a Si/LCO cell in LiTFSI-PIP_{13}TFSI electrolyte at 30°C and C/10. The capacity values are referred to the silicon active material weight. Data from ref. (*103*)

	1st cycle	*2nd cycle*	*5th cycle*	*10th cycle*	*32th cycle*
Capacity / mA h g^{-1}	2,500	2,400	2,200	2,000	1,200
Efficiency / %	48	97	98	98	98

A combination of a Sn-C anode with a LFP cathode was investigated by Scrosati et al. (*100*) in a LiTFSI-PYR_{24}TFSI electrolyte. The Sn-C/LFP cells have exhibited promising performance in terms of cycle life and rate capability. An initial capacity of 140 mA h g^{-1} (referred to the LFP weight) was delivered at C/10, slightly decreasing to 112 mA h g^{-1} at C/5, with a good capacity retention and a coulombic efficiency quickly leveling to 100% (Table 32), after an initial value of 77%. Difficulties in obtaining the theoretical capacity may be attributed to the relatively high viscosity of the IL-based electrolyte, which depletes the Li^+ ion transport properties, and the poor wettability of electrodes, preventing the full utilization of the active materials.

Table 32. Discharge capacity and coulombic efficiency at different current rates of a Sn/LFP cell in LiTFSI-PYR_{24}TFSI electrolyte at room temperature. The capacity values are referred to the LFP active material weight. Data from ref. (*100*)

	C/10	*C/7*	*C/5*
Capacity / mA h g^{-1}	140	120	112
Efficiency / %	99	99	99

The combination LTO/LFP is considered a very safe, if not the safest, cell chemistry for lithium-ion batteries. Therefore, this chemistry is appealing for applications having safety as absolute priority. The employment of non-volatile and non-flammable compounds as electrolyte components contributes to remarkably enhance the safety level of this kind of cell chemistry. Passerini and co-workers (*97*) have manufactured LTO/LFP cells using a LiTFSI-PYR_{14}FSI electrolyte. As reported above, both electrodes were fabricated using CMC (instead of PVdF) as the binder, thus allowing the use of only water as a process solvent (considerable reduction of the overall cost, possibility to easy battery recycling, low environmental impact). The so-realized LTO/LFP (cathode rich) cells have shown excellent room temperature, long-term cycleability (Table 33), displaying a stable discharge capacity of 140 mA h g^{-1} with a coulombic efficiency above 99% for at least 160 cycles (corresponding to a fading equal to 0.03% per cycle). As is also found for LTO (Figure 14) and LFP (Figure 19) cells with lithium anodes, very flat plateaus were detected in the voltage profiles (Figure 20) with a slight increase in the first cycles due to the moderate electrode wettability. The room temperature performance was rate limited due to the high viscosity of the IL-based electrolyte. However, a temperature increase to 60°C allowed the cell to deliver large capacities (150 mA h g^{-1}) even at medium rates (C/2) without any relevant degradation (Table 33).

Table 33. Discharge capacity and coulombic efficiency at different cycles performed at 20°C and C/10 rate (A) and at various temperature/current rates, for LTO/LFP cells in LiTFSI-PYR$_{14}$FSI electrolyte. The capacity values are referred to the LTO active material weight. Data from ref. (*97*)

(A) 20°C and C/10	*1st cycle*	*10th cycle*	*50th cycle*	*100th cycle*	*160th cycle*
Capacity / mA h g^{-1}	130	140	140	135	135
Efficiency / %	90	97	100	100	100

(B)	*20°C and C/10*	*40°C and C/5*	*60°C and C/2*
Capacity / mA h g^{-1}	130	155	150
Efficiency / %	100	100	99

Mixtures of ILs in combination with organic compounds were also employed as electrolyte components in lithium-ion batteries. Guerfi et al. (*65*) have manufactured LTO/LFO cells using a LiPF$_6$(1M) - EMITFSI (40 wt.%)-EC-DEC-VC electrolyte, which represents a good compromise between high ionic conductivity and low flammability. Table 34 compares the rate performance of this mixed electrolyte with that of a pure organic solvent solution. No relevant decay in capacity was noticed up to 2C since the delivered capacities of 119 and 109 mAhg^{-1} were detected, respectively, for the mixed electrolyte and the conventional electrolyte. Additionally, a similarly low electrode polarization (40 mV) was observed in the charge and discharge curves with bth electrolytes. At higher rates, however, the discharge capacity of the LTO/LFP cell with the IL-based electrolyte showed a faster decay. Conversely, a better high-rate charge capability was observed up to a current rate of 2C. This behavior is ascribed to the lower concentration of organic solvent molecules, which are available for ion solvation required for high-rate charge and discharge. However, the rates offered by the IL-based electrolyte are still attractive, and the safety of the mixed organic solvent-IL based electrolytes is acceptable for many battery applications.

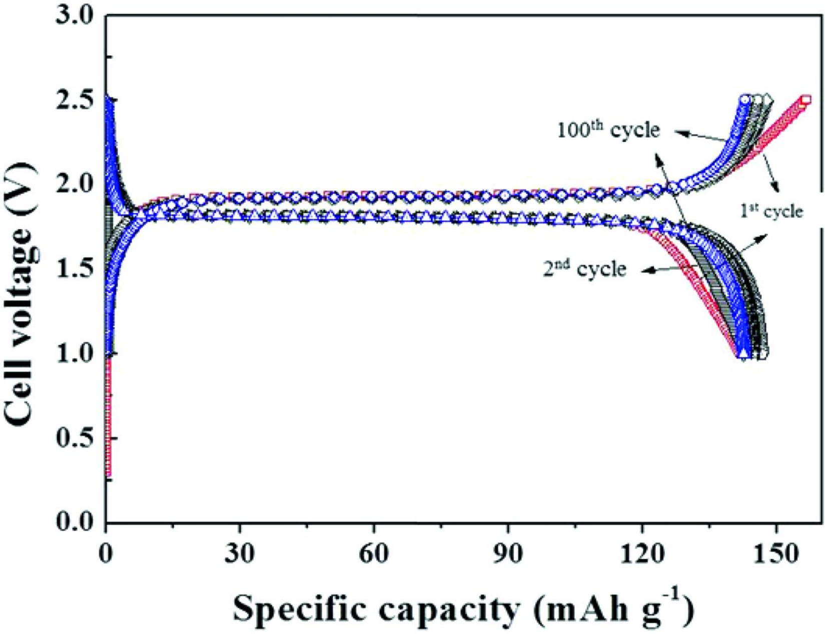

Figure 20. Selected voltage vs. capacity profiles of lithium-ion LTO/LFP cells in LiTFSI-PYR$_{14}$FSI electrolyte. Current rate: C/10. Temperature: 20°C. Data from ref. (97).

Table 34. Discharge capacity vs. current rate values for LTO/LFP cells in LiPF$_6$-EMITFSI-EC-DEC-VC electrolytes at different EMITFSI content. Room temperature. Data from ref. (*65*)

IL / wt.%	*Discharge capacity / mA h g^{-1}*							
	C/24	*C/3*	*1C*	*2C*	*4C*	*10C*	*20C*	*30C*
0	132	130	125	119	115	97	78	57
40	128	125	118	109	90	12	1	---
	Charge capacity / mA h g^{-1}							
0	120	118	103	85	55	40	30	10
40	133	100	83	70	34	10	7	3

A summary of the room temperature or near room temperature electrochemical performance, in terms of capacity and coulombic efficiency, of various lithium-ion cell chemistries in different IL-based electrolytes is reported in Table 35, which presents the state-of-the-art of the IL-based lithium battery technology.

Table 35. Room temperature electrochemical performance of various lithium-ion cell chemistries in different IL-based electrolytes. The capacity values are referred to the weight of the electrode active material indicated in the capacity column. * = referred to 1st cycle. Data from refs. (*65*, *79*, *97*, *100*, *103*)

Cell chemistry (operating voltage)	*Electrolyte*	*T / °C*	*Capacity / mA h g^{-1}*	*Efficiency / %*
Graphite/LCO (3.7 V)	$LiPF_6$-EMITFSI	20	370 (graphite)	62*(99)
Si/LCO (3.2 V)	LiTFSI-PIP_{13}TFSI	30	2,500 (Si)	48*(98)
Sn/LFP (3.0 V)	LiTFSI-PYR_{24}TFSI	RT	140 (LFP)	77*(99)
LTO/LFP (2.0 V)	LiTFSI-PYR_{14}FSI	20	140 (LTO)	90*(100)
LTO/LFP (2.0 V)	$LiPF_6$-EMITFSI-EC-DEC-VC	RT	128	96*(>99)

To demonstrate the feasibility of manufacturing IL-based lithium batteries, rechargeable LTO/LFP cells were scaled-up to fabricate 0.7 A h stacked prototypes (Figure 21, panel A) using innovative CMC-based composite electrodes and LiTFSI-PYR_{14}FSI as the electrolyte. Electrochemical tests, recently reported by Appetecchi et al. (*126*), have evidenced a very good long-term cycling ability, e.g., more than 80% of the initial capacity (close to the theoretical value) was delivered after 800 cycles with a coulombic efficiency close to 100% (Figure 21, panel B). The moderate rate capability, likely addressed to diffusive phenomena occurring within the electrolyte, may be enhanced using more conductive IL-based electrolytes. However, the results evidenced the validity of the organic solvent-free battery chemistry design and the reproducibility of the manufacturing process.

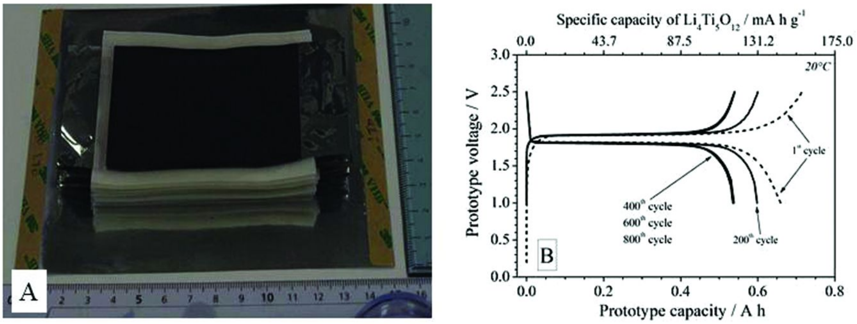

Figure 21. Stack of 0.7 A h, IL-based electrolyte, LTO/LFP prototype cell before vacuum-sealing (panel A) and its voltage vs. capacity profiles at C/20 rate and 20°C (panel B). Data from ref. (126).

Addendum: Glossary

Table A

Cations	*Acronym*
tetraamylammonium	$(Am)_4N$
1-amyl-2,3-dimethylimidazolium	ADMI
1-butyl-2,3-dimethylimidazolium	BDMI
tetrabutylammonium	Bu_4N
cianotetramethylammonium	CTMA
1,2-diethyl-3,4(5)-dimethylimidazolium	DEDMI
1,2-dimethyl-3-propylimidazolium	DMPI
1-ethyl-3-methylimidazolium	EMI
tetraethylammonium	TEA
1-isooctyl-2,3-dimethylimidazolium	IODMI
1-(3-methylthyimidazolium-1-yl)ethane-(trymethylammonium)	$MIEM_3N$
methyltrioctylammonium	MTO
N,*N*-dimethylpiperidinium	PIP_{11}
N-ethyl-*N*-methylpiperidinium	PIP_{12}
N-methyl-*N*-propylpiperidinium	PIP_{13}
N-butyl-*N*-methylpiperidinium	PIP_{14}
N-methyl-*N*-pentylpiperidinium	PIP_{15}
N-hexyl-*N*-methylpiperidinium	PIP_{16}
N-heptyl-*N*-methylpiperidinium	PIP_{17}
N-methyl-*N*-octylpiperidinium	PIP_{18}
N-ethyl-*N*-propylpiperidinium	PIP_{23}
N-butyl-*N*-ethylpiperidinium	PIP_{24}
N-ethyl-*N*-pentylpiperidinium	PIP_{25}
N,*N*-dimethylpyrrolidinium	PYR_{11}
N-ethyl-*N*-methylpyrrolidinium	PYR_{12}
N-methyl-*N*-propylpyrrolidinium	PYR_{13}
N-methyl-*N*-isopropylpyrrolidinium	PYR_{1iso3}
N-butyl-*N*-methylpyrrolidinium	PYR_{14}
N-isobutyl-*N*-methylpyrrolidinium	PYR_{1isO4}
N-secbutyl-*N*-methylpyrrolidinium	PYR_{1sec4}
N-methyl-*N*-pentylpyrrolidinium	PYR_{15}

Continued on next page.

Table A. (Continued)

Cations	*Acronym*
N-hexyl-*N*-methylpyrrolidinium	PYR_{16}
N-heptyl-*N*-methylpyrrolidinium	PYR_{17}
N-methyl-*N*-octylpyrrolidinium	PYR_{18}
N-decyl-*N*-methylpyrrolidinium	PYR_{110}
N-methoxyethyl-*N*-methylpyrrolidinium	$PYR_{1(2O1)}$
N-ethoxyethyl-*N*-methylpyrrolidinium	$PYR_{1(2O2)}$
trimethylbutylammonium	TMBA
trimethylhexylammonium	TMHA

Anions	
bis(pentafluoroethanesulfonyl)imide	BETI
tetrafluoroborate	BF_4
bis(fluorosulfonyl)imide	FSI
(nonafluorobutanesulfonyl) (trifluoromethanesulfonyl)imide	IM_{14}
hexafluorophosphate	PFM_6
(trifluoromethanesulfonyl)(trifluoromethane)acetamide	TSAC
bis(trifluoromethanesulfonyl)imide	TFSI
(pentafluoroethanesulfonyl)(trifluoromethanesulfonyl)imide	TPSI

Electrode materials	
lithium cobalt oxide ($LiCoO_2$)	LCO
lithium iron phosphate ($LiFePO_4$)	LFP
lithium manganese oxide ($LiMn_2O_4$)	LMO
lithium titanium oxide ($Li_4Ti_5O_{12}$)	LTO

Organic Solvents	
ethylene carbonate	EC
diethylcarbonate	DEC
dimethylcarbonate	DMC
vinylene carbonate	VC
propylene carbonate	PC

References

1. Tarascon, J. M.; Armand, M. *Nature* **2001**, *414*, 359.
2. Pistoia G., Eds.; *Lithium Batteries: New Materials, Developments and Perspectives*; Industrial Chemistry Library, Elsevier: New York, 1995; Vol. 5.
3. Scrosati, B. *Nature* **1995**, *373*, 557.
4. Lex-Balducci A.; Henderson, W. A.; Passerini, S. Electrolytes for Lithium Batteries. In *Lithium-Ion Batteries: Advanced Materials and Technologies*; Yuan, J., Liu, X., Zhang, H., Eds.; CRC Press: Boca Raton, FL, 2011; Chapter 4; print ISBN 978-1-4398-4128-0, eBook ISBN 978-1-4398-4129-7.
5. Bandhauer, T. M.; Garimella, S.; Fuller, T. F. *J. Electrochem. Soc.* **2011**, *158*, R1–R25.
6. Spotnitz, R.; Franklin, J. *J. Power Sources* **2003**, *113*, 81.
7. Yang, H.; Amiruddin, S.; Bang, H. J.; Sun, Y. K.; Prakash, J. *J. Ind. Eng. Chem.* **2006**, *12*, 12.
8. Abraham, D. P.; Roth, E. P.; Kostecky, R.; McCarthy, K.; MacLaren, S.; Doughty, D. H. *J. Power Sources* **2006**, *161*, 648.
9. Joachin, H.; Kaun, T. D.; Zaghib, K.; Prakash, J. *J. Electrochem. Soc.* **2009**, *156*, A401.
10. Thermal Runaway, Wikipedia. http://en.wikipedia.org/wiki/thermal_runaway.
11. Battery and Energy Tecnologies, Electropaedia. http://www.mpoweruk.com/lithium_failures.htm.
12. Mandal, B. K.; Padhi, A. K.; Shi, Z.; Chakraborty, S.; Filler, R. *J. Power Sources* **2006**, *161*, 1341.
13. Chiappe, C.; Pieraccini, D. *J. Phys. Org. Chem.* **2005**, *18*, 275.
14. Zhou, Z.-B.; Matsumoto, H.; Tatsumi, K. *Chem. Eur. J.* **2005**, *11*, 752.
15. Xu, W.; Cooper, E. I.; Angell, A. A. *J. Phys. Chem. B* **2003**, *107*, 6170.
16. Rogers, J. R. D.; Seddon, K. R., Eds.; *Ionic Liquids: Industrial Application to Green Chemistry*; ACS Symposium Series 818; American Chemical Society: Washington, DC, 2002.
17. Ohno, H., Ed.; *Electrochemical Aspects of Ionic Liquids*; John Wiley & Sons Inc.: Hoboken, NJ, 2005.
18. Bhatt, A. I.; May, I.; Volkovich, V. A.; Hetherington, M. E.; Lewin, B.; Thied, R. C.; Ertok, N. *J. Chem. Soc. Dalton Trans.* **2002**, 4532.
19. Panozzo, S.; Armand, M.; Stephan, O. *Appl. Phys. Lett.* **2002**, *80*, 679.
20. Wang, P.; Zakeeruddin, S. M.; Exnar, I.; Gratzel, M. *Chem. Comm.* **2002**, 2972.
21. Fuller, J.; Breda, A. C.; Carlin, R. T. *J. Electroanal. Chem.* **1998**, *29*, 459.
22. Nakagawa, H.; Izuchi, S.; Kunawa, K.; Nukuda, T.; Aihara, Y. *J. Electrochem. Soc.* **2003**, *150*, A695.
23. Noda, A.; Susan, M. A. B. H.; Kudo, K.; Mitsushima, S.; Hayamizu, K.; Watanabe, M. *J. Phys. Chem. B* **2003**, *107*, 4024.
24. Balducci, A.; Henderson, W. A.; Mastragostino, M.; Passerini, S.; Simon, P.; Soavi, F. *Electrochim. Acta* **2005**, *50*, 2233.

25. Appetecchi, G. B.; Montanino, M.; Carewska, M.; Moreno, M.; Alessandrini, F.; Passerini, S. *Electrochim. Acta* **2011**, *58*, 1300.
26. Dearden, J. C. *Sci. Total Environ.* **1991**, *109*, 59.
27. Zhou, Z. -B.; Matsumoto, H.; Tatsumi, K. *Chem. Eur. J.* **2006**, *12*, 2196.
28. Appetecchi, G. B.; Montanino, M.; Carewska, M.; Alessandrini, F.; Passerini, S. *ECS Trans.* **2010**, *25*, 49.
29. Appetecchi, G. B.; Montanino, M.; Zane, D.; Carewska, M.; Alessandrini, F.; Passerini, S. *Electrochim. Acta* **2009**, *54*, 1325.
30. Appetecchi, G. B.; Montanino, M.; Carewska, M.; Alessandrini, F.; Passerini, S. *Electrochim. Acta* **2011**, *57*, 153.
31. Wang, Y.; Zaghib, K.; Guerfi, A.; Bazito, F. F. C.; Torresi, R. T.; Dahn, J. R. *Electrochim. Acta* **2007**, *52*, 6346.
32. Zhou, Z. -B.; Matsumoto, H.; Tatsumi, K. *Chem. Eur. J.* **2006**, *12*, 2196.
33. Koch, V. R.; Nanjundiah, C.; Appetecchi, G. B.; Scrosati, B. *J. Electrochem. Soc.* **1995**, *142*, L116.
34. Carlin, R. T.; Fuller, J. U.S. Patent 5,552,238, September 3, 1996.
35. Carlin, R. T.; Fuller, J. In *Molten Salts*; Carlin, R. T.; Deki, S., Matsunaga, M., Newman, D. S., Selman, J. R., Stafford G. R., Eds.; The Electrochemical Society: Pennington, NJ, 1996; Vol. 96−97, p 362.
36. Bonhote, P.; Dias, A.-P.; Papageorgiou, N.; Kalyanasundaram, K.; Grätzel, M. *Inorg. Chem.* **1996**, *35*, 1168.
37. Sun, J.; Forsyth, M.; MacFarlane, D. R. *J. Phys. Chem. B* **1998**, *102*, 8858.
38. MacFarlane, D. R.; Huang, J.; Forsyth, M. *Nature* **1999**, *402*, 792.
39. MacFarlane, D. R.; Meakin, P.; Sun, J.; Amini, N.; Forsyth, M. *J. Phys. Chem. B* **1999**, *103*, 4164.
40. Howlett, P. C.; MacFarlane, D. R.; Hollenkamp, A. F. *Electrochem. Solid-State Lett.* **2004**, *7*, A97.
41. Shin, J.-H; Henderson, W. A.; Passerini, S. *Electrochem. Commun.* **2003**, *5*, 1016.
42. Shin, J.-H; Henderson, W. A.; Passerini, S. *Electrochem. Solid-State Lett.* **2005**, *8*, A125.
43. Shin, J.-H; Henderson, W. A.; Passerini, S. *J. Electrochem. Soc.* **2005**, *152*, A978.
44. Henderson, W. A.; Passerini, S. *Chem. Mater.* **2004**, *16*, 2881.
45. Matsumoto, H.; Sakaebe, H.; Tatsumi, K. *J. Power Sources* **2006**, *12*, 2196.
46. Zhou, Q.; Henderson, W. A.; Appetecchi, G. B.; Montanino, M.; Passerini, S. *J. Phys. Chem. B* **2008**, *112*, 13580.
47. Paillard, E.; Zhou, Q.; Henderson, W. A.; Appetecchi, G. B.; Montanino, M.; Passerini, S. *J. Electrochem. Soc.* **2009**, *156*, A891.
48. Conte, L.; Gambaretto, G.; Caporiccio, G.; Alessandrini, F.; Passerini, S. *J. Fluorine Chem.* **2004**, *125*, 243.
49. Toulgoat, F.; Langlois, B. R.; Medebielle, M.; Sanchez, J.-Y. *J. Org. Chem.* **2007**, *72*, 9046.
50. Appetecchi, G. B.; Scaccia, S.; Tizzani, C.; Alessandrini, F.; Passerini, S. *J. Electrochem. Soc.* **2006**, *153*, A1685.
51. Cooper, E. I.; Angell, C. A. *Solid State Ionics* **1983**, *9−10*, 617.
52. Cooper, E. I.; Angell, C. A. *Solid State Ionics* **1986**, *18−19*, 570.

53. Liu, C.; Angell, C. A. *Solid State Ionics* **1996**, *86−88*, 467.
54. Xu, W.; Cooper, E. I.; Angell, C. A. *J. Phys. Chem. B* **2003**, *107*, 6170.
55. Xu, W.; Wang, L. M.; Nieman, R. A.; Angell, C. A. *J. Phys. Chem. B* **2003**, *107*, 11749.
56. Nicotera, I.; Oliviero, C.; Henderson, W. A.; Appetecchi, G. B.; Passerini, S. *J. Phys. Chem. B* **2005**, *109*, 22184.
57. Borodin, O.; Smith, G. D. *J. Phys. Chem. B* **2006**, *110*, 11481.
58. Borodin, O.; Smith, G. D.; Henderson, W. A. *J. Phys. Chem. B* **2006**, *110*, 16879.
59. Kunze, M.; Paillard, E.; Jeong, S. S.; Appetecchi, G. B.; Schönhoff, M.; Winter, M.; Passerini, S. *J. Phys. Chem. C* **2011**, *115*, 19431.
60. Castiglione, F.; Ragg, E.; Mele, A.; Appetecchi, G. B.; Montanino, M.; Passerini, S. *J. Phys. Chem. Lett.* **2011**, *2*, 153.
61. Appetecchi, G. B.; Montanino, M.; Balducci, A.; Lux, S. F.; Winter, M.; Passerini, S. *J. Power Sources* **2009**, *192*, 599.
62. Appetecchi, G. B.; Montanino, M.; Carewska, M.; Alessandrini, F.; Passerini, S. *Adv. Sci. Technol.* **2010**, *72*, 315.
63. Zhou, Q.; Henderson, W. A.; Appetecchi, G. B.; Passerini, S. *J. Phys. Chem. C* **2010**, *114*, 6201.
64. Montanino, M.; Moreno, M.; Alessandrini, F.; Appetecchi, G. B.; Passerini, S.; Zhou, Q.; Henderson, W. A. *Electrochim. Acta* **2012**, *60*, 163.
65. Guerfi, A.; Dontigny, M.; Charest, P.; Petitclerc, M.; Lagacé, M.; Vijh, A.; Zaghib, K. *J. Power Sources* **2010**, *195*, 845.
66. Kuhnel, R. -S.; Böckenfeld, N.; Passerini, S.; Winter, M; Balducci, A. *Electrochim. Acta* **2011**, *56*, 4092.
67. Egashira, M.; Okada, S.; Yamaki, J.–I.; Dri, D. A.; Bonadies, F.; Scrosati, B. *J. Power Sources* **2004**, *138*, 240.
68. Matsumoto, H.; Sakaebe, H.; Tatsumi, K.; Kikuta, M.; Ishiko, E.; Kono, M. *J. Power Sources* **2006**, *160*, 1313.
69. Guerfi, A.; Dontigny, M.; Kobayashi, Y.; Vijh, A.; Zaghib, K. *J. Solid State Electrochem.* **2009**, *13*, 1003.
70. *Basic Research Needs for Electrochemical Energy Storage*; Report of the Basic Energy Sciences Workshop on Electrical Energy Storage, April 2−4, 2007; Office of Basic Energy Science: Department of Energy, July 2007.
71. Lewandosky, A.; Bieguin, M.; Galinski, M. *Electrochim. Acta* **2012**, *63*, 204.
72. Kim, G. -T.; Appetecchi, G. B.; Montanino, M.; Alessandrini, F.; Passerini, P. *ECS Transactions* **2010**, *25*, 127.
73. Fuller, J.; Carlin, R. T.; Osteryoung, R. A. *J. Electrochem. Soc.* **1997**, *144*, 3881.
74. Sakaebe, H.; Matsumoto, H.; Tatsumi, K. *Electrochim. Acta* **2007**, *53*, 1048.
75. Carlin, R. T.; De Long, H.; Fuller, J.; Trulove, P. C. *J. Electrochem. Soc.* **1994**, *141*, L73.
76. Hardwick, L. J.; Ruch, P. W.; Hahn, M.; Scheifele, W.; Koetz, R.; Novak, P. *J. Phys. Chem. Solids* **2008**, *69*, 1232.
77. Placke, T.; Bieker, P.; Lux, S. F.; Fromm, O.; Meyer, H. W.; Passerini, S.; Winter, M. *Z. Phys. Chem.* **2012**, DOI:10.1524/zpch.2012.0222.
78. Holzapfel, M.; Jost, C.; Novak, P. *Chem. Commun.* **2004**, *10*, 2098.

79. Holzapfel, M.; Jost, C.; Prodi-Schwab, A.; Krumeich, F.; Wuersig, A.; Buqa, H.; Novak, P. *Carbon* **2005**, *43*, 1488.
80. Lewandowsky, A. P.; Sviderska-Mocek, A. *J. Power Sources* **2009**, *194*, 502.
81. Lane, G. H.; Best, A. S.; MacFarlane, D. R.; Forsyth, M.; Hollenkamp, A. H. *Electrochim. Acta* **2010**, *55*, 2210.
82. Fu, Y. B.; Chen, C. C.; Qju, C. C.; Ma, X. H. *J. Appl. Electrochem.* **2009**, *39*, 2597.
83. Zheng, H.; Li, B.; Fu, Y.; Abe, T.; Ogumi, Z. *Electrochim. Acta* **2006**, *52*, 1556.
84. Zheng, H.; Jiang, K.; Abe, T.; Ogumi, Z. *Carbon* **2006**, *44*, 203.
85. Lux, S. F.; Schmuck, M.; Appetecchi, G. B.; Passerini, S.; Winter, M.; Balducci, A. *J. Power Sources* **2009**, *192*, 606.
86. Lux, S. F.; Schmuck, M.; Rupp, B.; Kern, W.; Appetecchi, G. B.; Passerini, S.; Winter, M. *ECS Trans.* **2009**, *16*, 45.
87. Ishikawa, M.; Sugimoto, T.; Kikuta, M.; Ishiko, E.; Kono, M. *J. Power Sources* **2006**, *162*, 658.
88. Sugimoto, T.; Kikuta, M.; Ishiko, E.; Kono, M.; Ishikawa, M. *J. Power Sources* **2008**, *183*, 436.
89. Sugimoto, T.; Atsumi, Y.; Kikuta, M.; Ishiko, E.; Kono, M.; Ishikawa, M. *J. Power Sources* **2009**, *189*, 802.
90. Sebi, S.; Kobayashi, Y.; Miayshiro, H.; Ohno, Y.; Mita, Y.; Terada, N.; Charest, P.; Guerfi, A.; Zaghib, Z. *J. Phys.Chem. C* **2008**, *112*, 16708.
91. Guerfi, A.; Duchesne, S.; Kobayashi, Y.; Vijh, A.; Zaghib, Z. *J. Power Sources* **2008**, *175*, 866.
92. Lewandowsky, A. P.; Hollenkamp, A. H.; Donne, S. W.; Best, A. S. *J. Power Sources* **2010**, *195*, 2029.
93. Madherna, M.; Reiter, J.; Moskon, J.; Dominko, R. *J. Power Sources* **2011**, *196*, 7700.
94. Masayuki, M.; Ishikawa, M.; Matsuda, Y. In *Lithium Ion Batteries*; Wakihara, M.; Yamamoto O., Eds.; Wiley-VCH: Weinheim, Germany, 1998.
95. An, Y.; Zuo, P.; Cheng, X.; Liao, L.; Yin, G. *Int. J. Electrochem. Sci.* **2011**, *6*, 2398.
96. Kawamura, K.; Umegaki, T.; Naito, H.; Takehara, Z.; Yao, T. *J. Appl. Electrochem.* **2001**, *31*, 73.
97. Kim, G. -T.; Jeong, S. S.; Joost, M.; Rocca, E.; Winter, M.; Passerini, S.; Balducci, A. *J. Power Sources* **2011**, *196*, 2187.
98. Lux, S. F.; Schappacher, F.; Balducci, A.; Passerini, S.; Winter, M. *J. Electrochem. Soc.* **2010**, *157*, A320.
99. Mun, J.; Jung, Y. S.; Yim, T.; Lee, H. Y.; Kim, H.-J.; Kim, Y. G.; Oh, S. M. *J. Power Sources* **2009**, *194*, 1068.
100. Hassoun, J.; Fernicola, A.; Navarra, M. A.; Panero, S.; Scrosati, B. *J. Power Sources* **2010**, *195*, 574.
101. Scrosati, B.; Hassoun, J.; Sun, Y. K. *Energy Environ. Sci.* **2011**, *4*, 3287.
102. Katayama, Y.; Miyashita, S.; Miura, T. *J. Power Sources* **2010**, *195*, 6162.
103. Baranchugov, V.; Markevich, E.; Pollak, E.; Salitra, G.; Aurbach, D. *Electrochem. Commun.* **2007**, *9*, 796.

104. Sugimoto, T.; Atsumi, Y.; Kono, M.; Kikuta, M.; Ishiko, E.; Yamagata, M.; Ishikawa, M. *J. Power Sources* **2010**, *195*, 6153.
105. Choi, J.; Kim, D.-W.; Bae, Y. S.; Song, S. W.; Hong, S.-H.; Lee, S.-M. *Electrochim. Acta* **2011**, *56*, 9818.
106. Song, J.-W.; Nguyen, C. C.; Song, S.-W. *RSC Adv.* **2012**, *2*, 2003.
107. Sakaebe, H.; Matsumoto, H. *Electrochem. Commun.* **2003**, *5*, 594.
108. Sakaebe, H.; Matsumoto, H.; Tatsumi, K. *J. Power Sources* **2005**, *146*, 693.
109. Hayashi, K.; Nemoto, Y.; Akuto, K.; Sakurai, Y. *J. Power Sources* **2005**, *146*, 689.
110. Zheng, H.; Qin, J.; Zhao, Y.; Abe, T.; Ogumi, Z. *Solid State Ionics* **2005**, *176*, 2219.
111. Lee, S.-Y.; Yong, H. H.; Kim, S. K.; Kim, J. Y.; Ahn, S. *J. Power Sources* **2005**, *146*, 689.
112. Maleki, H.; Geng, G.; Anani, A.; Howard, J. *J. Electrochem. Soc.* **1999**, *146*, 3224.
113. Baba, Y.; Okada, S.; Yamaki, J. *Solid State Ionics* **2000**, *148*, 311.
114. Zheng, H.; Zhang, H.; Fu, Y.; Abe, T.; Ogumi, Z. *J. Phys. Chem. B* **2005**, *109*, 13676.
115. Yamada, A.; Tanaka, M. *Mater. Res. Bull.* **1995**, *6*, 715.
116. Zhang, Z.; Zhou, H.; Yang, L.; Tachibana, K.; Kamijima, K.; Xu, J. *Electrochim. Acta* **2008**, *53*, 4833.
117. Lewandowski, A.; Świderska-Mocek, A.; Acznik, I. *Electrochim. Acta* **2010**, *55*, 1990.
118. Borgel, L.; Markevich, E.; Aurbach, D.; Semrau, G.; Schmidt, M. *J. Power Source* **2009**, *189*, 331.
119. Li, J.; Jeong, S. S.; Winter, M.; Passerini, S. *Power Our Future Workshop*, March 19−21, 2012, Vitoria, Spain.
120. Saint, J.; Best, A. S.; Hollenkamp, A. F.; Kerr, J.; Shin, J.-H.; Doeff, M. M. *J. Electrochem. Soc.* **2008**, *155*, A172.
121. Hardwick, L. J.; Saint, J. A.; Lucas, I. T.; Doeff, M. M.; Kostecki, R. *J. Electrochem. Soc.* **2009**, *156*, A120.
122. Jin, J.; Li, H. H.; Wei, J. P.; Zhou, Z.; Yan, J. *Electrochem. Commun.* **2009**, *11*, 1500.
123. Lewandowsky, A. P.; Hollenkamp, A. F.; Donne, S. W.; Best, A. S. *J. Power Sources* **2010**, *195*, 2029.
124. Yan, C.; Zaijun, L.; Hailang, Z.; Yinjun, F.; Xu, F.; Junkang, L. *Electrochim. Acta* **2010**, *55*, 4728.
125. Chen, Y.; Tarascon, J.-M.; Guéry, C. *Electrochem. Commun.* **2011**, *13*, 673.
126. Kim, G. -T.; Jeong, S. S.; Xue, M.-Z.; Balducci, A.; Winter, M.; Passerini, S.; Alessandrini, F.; Appetecchi, G. B. *J. Power Sources* **2012**, *199*, 239.

Chapter 5

Development and Selection of Ionic Liquid Electrolytes for Hydroxide Conducting Polybenzimidazole Membranes in Alkaline Fuel Cells

Elise B. Fox,*,[1] Héctor R. Colón-Mercado,[1]
Yuanxin Chen,[2] and W. S. Winston Ho[2]

[1]Savannah River National Laboratory, Aiken, South Carolina 29808
[2]Ohio State University, 2041 College Road, Columbus, Ohio 43210
***E-mail: elise.fox@srnl.doe.gov. Phone: (803) 507-8560.**

Alkaline fuel cell (AFC) operation is currently limited to specialty applications such as low temperatures and pure H_2/O_2 due to the corrosive nature of the electrolyte and formation of carbonates. AFCs are the cheapest and potentially most efficient (approaching 70%) fuel cells. The fact that non-Pt catalysts can be used, makes them an ideal low cost alternative for power production with respect to proton exchange membrane fuel cells. The anode and cathode are separated by a solid electrolyte or alkaline porous media saturated with KOH. However, CO_2 from the atmosphere or fuel feed severely poisons the electrolyte by forming insoluble carbonates in the porous electrode. The corrosivity of KOH (electrolyte) limits operating temperatures to no more than 80°C. This chapter examines the development of ionic liquids electrolytes that are less corrosive, have higher operating temperatures, do not chemically bond to CO_2, and enable alternative fuels. Work is detailed on the IL selection and characterization as well as casting methods of the polybenzimidazole based solid membrane. This approach is novel as it targets the root of the problem (the electrolyte) unlike other current work in alkaline fuel cells which focus on making the fuel cell hardware more durable.

In Ionic Liquids: Science and Applications; Visser, A., et al.;
ACS Symposium Series; American Chemical Society: Washington, DC, 2012.

Introduction

Alkaline Fuel Cells (AFCs) differ from typical Proton Exchange Membrane Fuel Cells (PEMFCs) in that the reactions occur in a basic environment. Because the electrolyte is basic, oxygen at the cathode is reduced to hydroxide ions that are transported through the cell to the anode where they combine with hydrogen to produce water. The schematic of an AFC is found in Figure 1. Under these conditions, slow reactions, such as those at the cathode can occur at faster rates, eliminating kinetic limitations that typically affect PEMFCs. This fact enables the use of alternative electrocatalysts to Pt at the cathode electrode. Typically AFCs operate at low temperatures due to the corrosive nature of the electrolyte, which could be dissolved KOH or solid polymer hydroxide ions conductors. The use of new solid conductors has created renewed interest in AFCs. AFCs enable the use of air, instead of pure oxygen, without the detrimental effects typically seen from the binding of CO_2 present in air with the hydroxide salts forming insoluble carbonates. However, solid proton conductors still have major limitations in temperatures, stabilities, conductivities, and manufacturability. In this work we began studying a new and un-explored alternative route to solving all of the issues plaguing AFCs, which consists on the use of stable easy to manufacture polymers impregnated with ionic liquids.

AFCs are the highest performing fuel cell systems even though on-going issues with the electrolyte and electrode degradation has hindered their advancement. For optimal operation, it is necessary to maintain high hydroxyl conductivity and maintain stability in a high pH environment (*1*). The formation of insoluable carbonates (CO_3^{2-}) and/or bicarbonates (HCO_3^-), which are formed by the reaction of OH^- (from aqueous NaOH or KOH) ion with CO_2 (contamination from the oxidation stream) is one of the largest hinderances of widescale implementation. The formation of these insoluble carbonates/bicarbonates creates the largest problem in the electrodes because they cause blockages within the electrolyte-filled pores that destroy the active layers.

One of the benefits of imidazolium IL electrolytes is that they do not form these insoluble carbonates in large quantities (*2*, *3*). While the choice of anion can largely influence the solubility and adsorption ability of the IL for CO_2, the side chain length of the anion, such as imidazoliums, did not play as large of a role (*4*). In addition to CO_2 solubility, the large electrochemical window of ILs makes them favorable as fuel cell electrolytes (*5*).

Anion exchange membranes based on quaternized polymers have been used for Alkaline fuel cells (AFCs) (*6*, *7*), however the polymer has proved unstable at high temperatures due to the nucleophilic displacement through the Hofmann elimination reaction (*8*). To overcome these limitations, polybenzimidazole (PBI) membranes have been used as separator. PBI membranes are well known for their excellent chemical stability at high temperatures, low permeability and high ionic conductivity when doped with phosphoric acid or sulfuric acid (*9*). While acid doped PBI membranes have been used in Phosphoric Acid fuel cells (PAFCs) for many years, their performance is limited by the strong anion adsorption on the Pt catalysts. Hydroxide doped PBI has been studied and shown to possess both endurance in alkali medium and high temperatures (*6*, *9*). It has been shown to have high ionic conductivity and comparable performance to PEMFC. However, the use of hydroxide salts constrains the oxidant gas feed to only low carbon dioxide oxidant feeds, as the presence of CO_2 will react with the hydroxide salts and form carbonate precipitates (*10*).

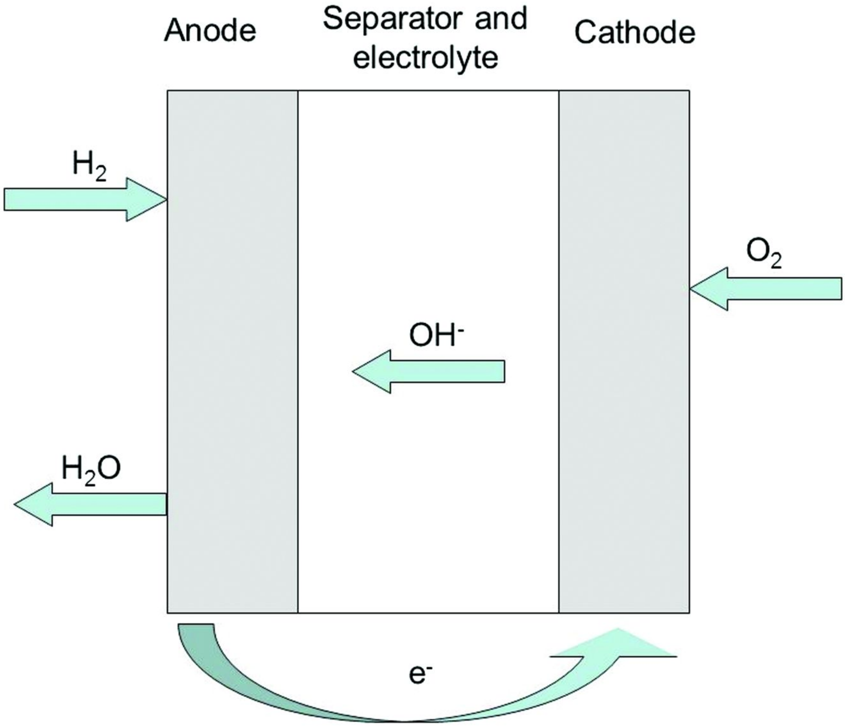

Figure 1. Schematic of an AFC during operation.

Protic-ILs have been proposed and studied as proton conduction enhancers for PEMFC either by doping the membranes with IL (*11–14*) or by polymerizing the ionic liquid into membranes (*15*). The purpose of the use of IL for PEMFC has mostly focused on the extension of PEMFC to operate at high temperatures higher than 120°C where the humidity levels are low and the effect of impurities in the fuel streams are minimal. Nakamoto et al. showed that with the right combination of IL acid and bases the high temperature electrochemical performance for the hydrogen oxidation reaction (HOR) and the oxygen reduction reaction (ORR) at the Pt electrode can be facilitated and even surpassed the performance of a phosphoric acid or sulfuric acid solutions (*12*). The performance improvement has been attributed to the higher proton activities and lower negative adsorption of ions on to the electrode surface. While significant progress has been made during the last few years, improvements on ionic conductivity and high performance under load must continue.

Ionic Liquid Characterization

Experimental

All ionic liquids described here-in were purchased off- the shelf from Ionic Liquid Technologies, with the exception of 1-butyl-3-methylimidazolium bis(perfluoroethylsulonyl)imide [C_4mim][BETI] and 1-butyl-3-methylimidazolium hydroxide [C_4mim][OH] which are described below.

Ionic Liquid Synthesis

[C_4mim][BETI]

A 1:1 molar ratio of 1-butyl-3-metylidizolium chloride (Aldrich) and Li bis(perfluoroethylsulfonyl)imide (3M) were mixed together and covered in 300mL of deionized water. The mixture was allowed to stir for 30 minutes after all salts were dissolved. The solution was allowed to settle into two phases. The organic phase was washed with DI water and allowed to settle for thirty minutes. This process was repeated three times. The washed organic phase was then bubbled with dry N_2 for 24 hours to help dry the resulting ionic liquid. The water content by Karl Fisher titration was 200ppm, which is sufficient for applications where the electrolyte will be humidified, as in this case. The chloride content was undetectable by IC anion analysis.

[C_4mim][OH]

1-butyl-3-methylimidazolium hydroxide was made from a procedure derived from Refs. (*16*) and (*17*). 0.2 mol of [C_4mim][Cl] was added to 150 mL of tetrahydrofuran and stirred for 30 minutes until dissolved. An excess of NaOH (0.25 mol) was added and stirred for 22 hours. Gravity filtration was used to remove NaCl solids that were formed. THF was removed from the filtered solution via rotoevaporator to obtain a bright yellow liquid. The rotoevaporator conditions were changed to remove any residual water and left for 90 minutes. The remaining ionic liquid was washed three times with 50 mL of diethylether and rotoevaporated at 80°C. The remain IL was now a dark viscous solution. Composition was confirmed by FT-IR, see Figure 2, and a bulk conductivity of 102 μS/cm was measured for the product. FT-IR peaks are similar in location to those reported by Ranu and Banerjee (*17*).

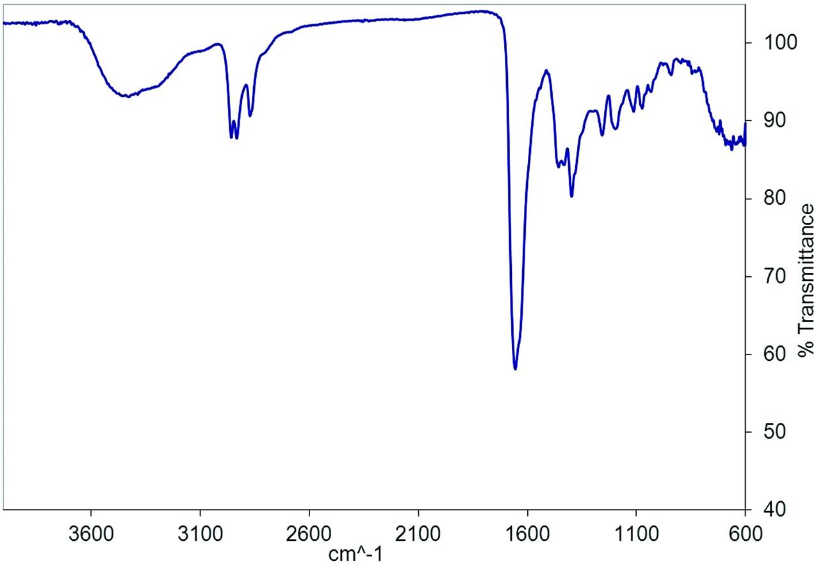

Figure 2. FT-IR spectra of [C_4mim][OH].

Bulk IL Conductivity

Bulk conductivity was measured on a Fisher Scientific Accumet Excek XL60 Meter using a two prong K-type ion conductivity probe with 1cm^2 active area at a controlled temperature of 25°C. The probe was calibrated with conductivity standards at 10,000 µS/cm, 1,000 µS/cm and 100 µS/cm before measurement of the ILs. Figure 3 shows the effect of cation on conductivity. All ionic liquids have the common anion bis(trifluorpmethylsulfonyl)imide. The imidazolium cations have the highest conductivity. The high ion conductivity of the imidazole has been attributed to the fact that it has both proton donor and acceptor groups within the molecule (*18*). This is reduced when a methyl group is substituted for the C-2 proton. The lowest conductivity is seen with the 1,1,1,-trimetylammonium 1-butyric acid cation. It is also important to note that the ion conductivity decreases with increasing viscocity of the IL in the case of the common anion. This trend is not followed when there is a common cation.

The effect on conductivity by changing the anion is seen in Figure 4. All ILs examined have the common cation 1-butyl-1-methyl imidazolium. The [Tf_2N] had the highest conductivity, followed by [BF_4] and [triflate]. [BF_4] would be a poor candidate for this application due to ability to strongly hydrogen bonf to water (*19*, *20*). [triflate] has been investigated for use in fuel cells and has seen some success (*21*, *22*).

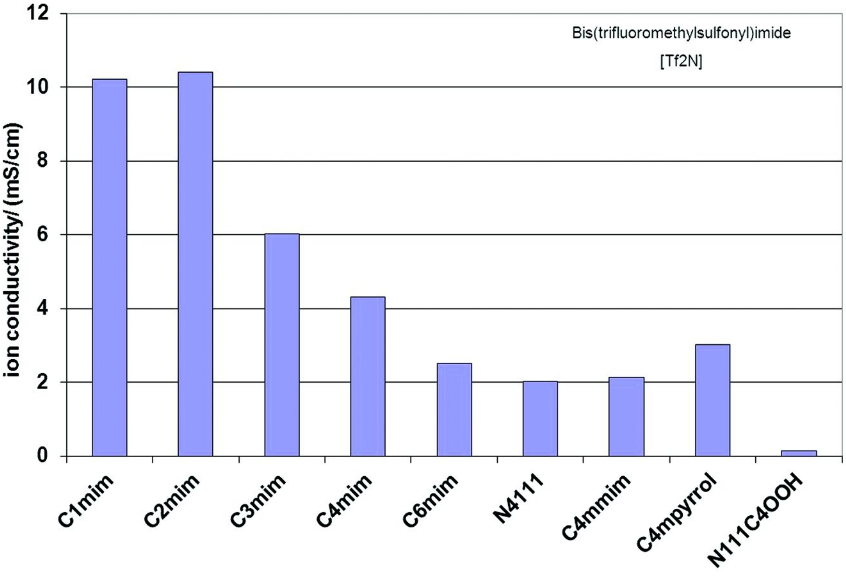

Figure 3. Bulk conductivity of ionic liquids with the common anion [Tf$_2$N].

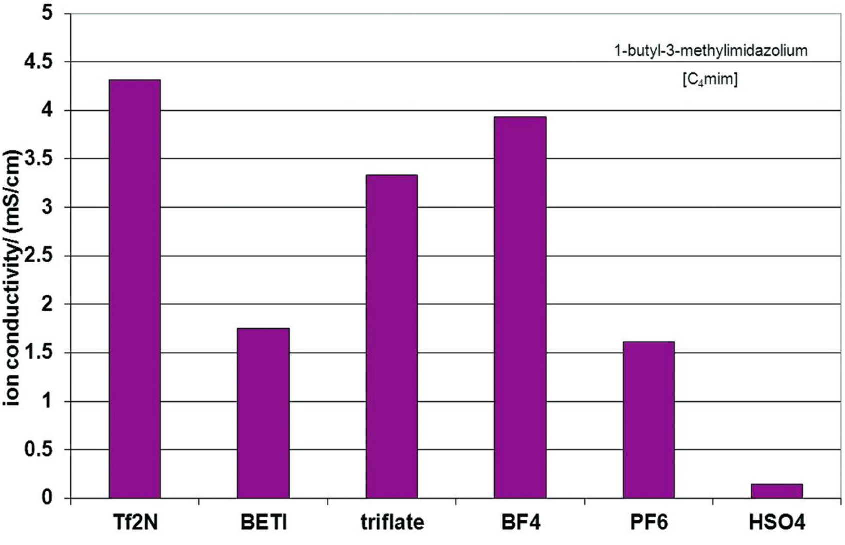

Figure 4. Bulk conductivity of ionic liquids with the common cation [C$_4$mim].

Thermogravimetric Analysis

An important component of extending the operating range of AFCs relies not only on conductivity of the electrolyte, but also thermal stability. If an electrolyte can operate at higher temperature ranges, the operating window for the cell can be extended and total efficiencies can be increased. Thermogravimetic analysis (TGA) was utilized to determine the relative thermal stability of all ILs described here-in. All TGA experiments were conducted under a N_2 atmosphere using a Netzsch 209 F1 thermal gravimetric analyzer with single use Al crucibles at a ramp rate of 10°C/minute. The thermal analysis software (Proteus V5.2.0) calculates the thermal onset temperature based on the intersection of the baseline with the tangent, at the inflection point, of the decomposition rate.

Figure 5 shows the how the side chain length on the imidazole effects decomposition. All defined temperatures are also reported in Table 1. As the length of the chain increases, the thermal stability of the IL decreases. A thrity degree decrease in stabily can be found between a C_6 substituted imidazole and a C_1 substituted imidazole. This indicates that as the side chain lengthens, it is more easily cleaved from the cation during heating. By keeping a common anion and changing the cation from 1,1,1-trimethylammonium 1-butionic acid [N111C_4OOH] to dimetthylimidazolium [C_1mim], there is a 94 degree increase in thermal stability.

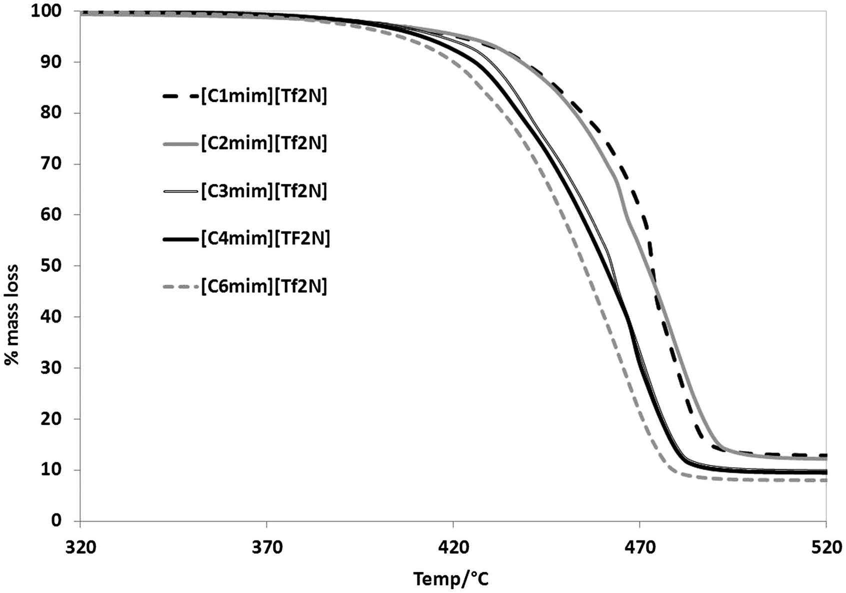

Figure 5. Effect of side chain length on [1-N-3-methylimidazolium][Tf_2N] on thermal stability of IL.

Alternatively, changes in the anion do not necessarily effect the thermal stability as dramatically as changing the cation does. As seen in Figure 6, there is only a thirty degree difference between common IL cations. However, when the cation is in hydroxide form, we see a significant decrease in the thermal stability, a drop to 203°C. This is an important indicator of complex molecules that will be present within an AFC membrane operating with IL electrolytes, so it will limit the operating window at 200°C for the system.

Table 1. Summary of decomposition temperatures and bulk conductivity of all ILs screened in this work

Ionic Liquid	Decomposition Temperature/°C	Conductivity/ mS/cm
[mim][Tf_2N]	402.0	Solid at room temp.
[C_1mim][Tf_2N]	472.5	10.21
[C_2mim][Tf_2N]	463.5	10.40
[C_3mim][Tf_2N]	460.2	6.014
[C_4mim][Tf_2N]	443.2	4.313
[C_6mim][Tf_2N]	429.2	2.504
[C_4mmim][Tf_2N]	459.0	2.124
[N_{4111}][Tf_2N]	435.0	2.022
[C_4mpyrr][Tf_2N]	435.7	3.009
[C_4N_{11}pyr][Tf_2N]	465.3	2.500
[$N_{111}C_4$OOH][Tf_2N]	379.1	0.149
[C_4mim][PF_6]	425.1	1.616
[C_4mim][BF_4]	389.8	3.936
[C_4mim][BETI]	417.9	1.748
[C_4mim][triflate]	394.1	3.332
[C_4mim][OH]	203.2	0.102
[C_4mim][HSO_4]	388.5	0.149
Benzalkonium chloride	187.7	Solid at room temp.

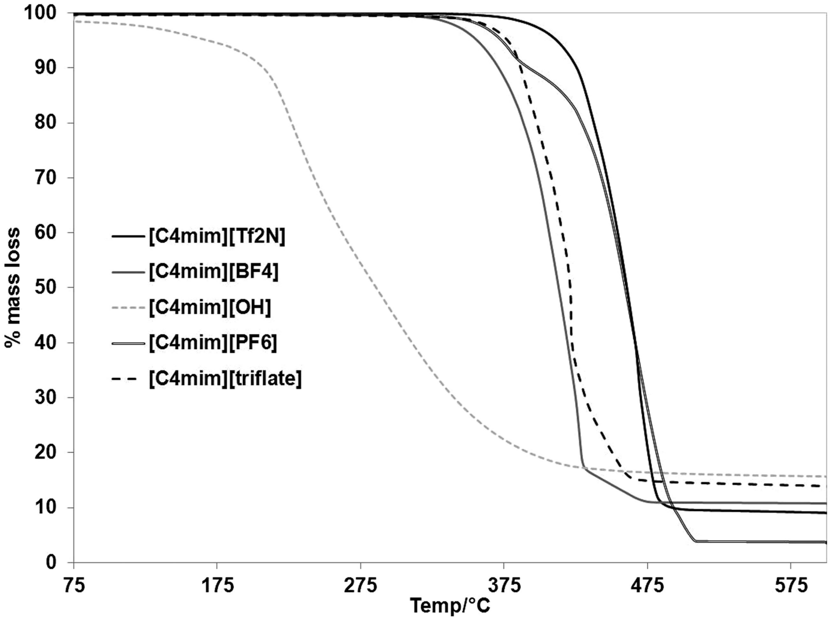

Figure 6. Effect of anion on thermal stability of IL with common [C_4mim] cation.

IL Incorporation into Alkaline Fuel Cell Membranes

In order to improve the conductivity and stability of the AFC membranes, we expect to incorporate ILs to a very stable polymer matrix. The polymers we used were polybenzimidazole (PBI) and crosslinked polyvinyl alcohol (PVA).

Difficulty of Incorporating ILs into PBI and Crosslinked PVA Membranes

In our initial attempts to incorporate ILs in to polymer membranes, we used 1-butyl-3-methyl-imidazolium bis(trifluoromethylsulfonyl) imide as the IL and tried to incorporate it into the PBI or crosslinked PVA membranes. However, this IL had a very low solubility in both PBI/dimethyl sulfoxide (DMSO) solution and crosslinked PVA/H_2O solution. Phase separation occurred after solvent evaporation, which indicated that the IL was not compatible with PBI or PVA. Therefore, we used another IL (benzalkonium chloride) and KOH to replace the previously used IL, and we were able to prepare some homogeneous membranes.

Synthesis of PBI Polymer

PBI polymer was synthesized using a one-step high temperature polymerization method from 3,3′-diaminobenzidine (DABD) and 4,4′-oxybis(benzoic acid) (OBBA), using polyphosphoric acid (PPA) as the solvent

(*23–25*). Figure 7 shows the schematic of the PBI synthesis. The reaction took place under nitrogen purge at 80 °C for 2 h and at 200 °C for 3 h. The yield of PBI was more than 99%. The PBI polymer synthesized generally showed high viscosity with 3.0 – 5.0 wt.% solutions in DMSO, indicating that high molecular weight polymer was synthesized (we did not measure the molecular weight of the PBI polymer).

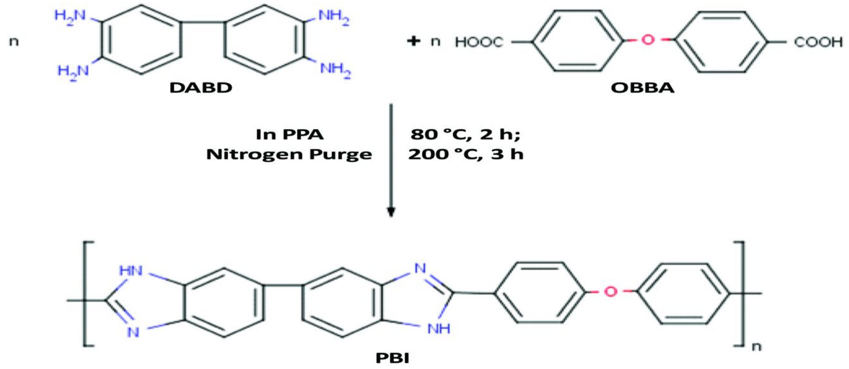

Figure 7. Schematic of the polybenzimidazole (PBI) synthesis.

Membrane Preparation

Preparation of PBI Polymer/Benzalkonium-OH Membrane

The powder-like PBI polymer was dissolved in DMSO to form a homogeneous solution. To the PBI solution, certain amount of benzalkonium chloride was added. Then, the solution was poured onto a clean glass plate and cast into a membrane. The membrane was dried in an oven at 80 °C for 6 h and at 120 °C for 12 h. Finally, it was soaked in 1.0 M KOH solutions for the purpose of hydroxide exchange treatment at room temperature for 24 h. The resulting membrane in hydroxide form was washed with de-ionized water and dried at 90 °C overnight. The final membrane had a thickness of 40 µm.

Preparation of PBI/KOH Membrane

PBI polymer was first dissolved in DMSO and cast into a membrane. The pure PBI membrane was soaked in 6M KOH solution for more than 24 h. After drying, the membrane was soaked in de-ionized water to release KOH into water. Then, hydrochloric acid solution was used for titration, using methyl orange as the indicator. The result showed that the PBI membrane successfully absorbed KOH. The weight ratio of PBI/KOH was about 80/20. The final membrane had a thickness of around 25 µm.

Preparation of Crosslinked PVA/KOH Membrane

PVA was first dissolved in water under stirring at room temperature overnight and then at 80 °C for 80 min. Then a stoichiometric amount of glutaraldehyde and a certain amount of KOH solution were added into the solution. The PVA/glutaric dialdehyde/KOH solution was stirred at 80 °C for 2 h (*26–28*).

Then, the solution was cast on a clean glass plate to obtain a membrane. The membrane was dried in a hood at room temperature overnight. Then, it was dried at 120 °C in a furnace for 6 h. After drying, the final membranes was flexible and had a thickness of approximately 50 μm.

Ex-Situ Electrochemical Testing of the ILs

Cyclic voltammetry was used to verify the stability of the ionic liquids and to ensure the ILs support H_2 oxidation and O_2 reduction on the electrode Pt surface by studying the current responses on the different electrolytes. The experimentes were carried out in a three electrode setup that consisted of a reversible hydrogen electrode (RHE, Hydroflex™, Gaskatel GmbH), a platinum wire counter electrode and a mirror polished Pt disk working electrode (1.6 mm diameter, Bioanalytical Systems, Inc.). The potentials was scaned from -120 mV to 1850 mV vs. RHE at a rate of 5mV/s. In typical experiments, the cell was filled with the ionic liquid electrolyte and allowed to saturate with the gas of interest by bubbling the electrolyte. A minimum of 30 minutes was waited to ensure complete saturation. While we intended to test different ILs, the high viscocity at room temperature and stong adsorption on the Pt surface prevented electrochemical testing. The CVs under nitrogen atmosphere represents the electrochemical stability range of the ILs. For the IL [C_4mim][Tf_2N] the electrochemical stable window is from approximatety -100 mV to 1,800 mV. The nitrogen sparged curve shows no electrochemical activity except for a redox peak at around 0.9 V which is also can be seen through out the experiments with other gases, as seen in Figure 8. This peak can be attributed to the interaction of the Pt disk with traces of water present in the IL with the Pt[14]. When the IL is sparged with H_2, the hydrogen adsorption/desorption on the Pt surface can be seen at the expected potentials between 0-100 mV. In the case of oxygen sparging, we observe a negative current increase at around 850 mV. This low potential can be expected as imide base ILs show low kinetics due to the strong adsorptions of the IL on to the electrode surface. The slow reduction reaction has been observed by other reserachers in aprotic ILs (*29*) and basic ILs (*30*).

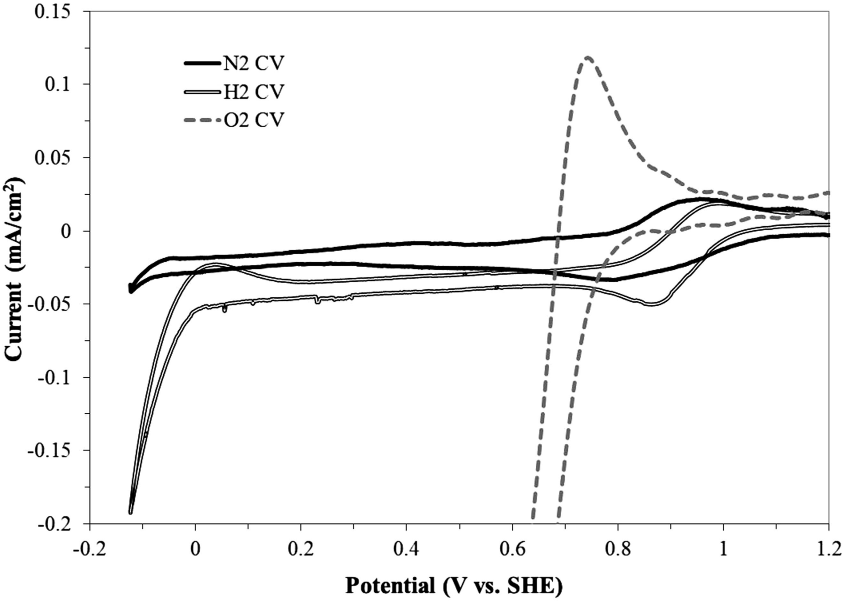

Figure 8. room temperature cyclic voltammetry of Pt disk in [C_4mim][Tf_2N] as a function of different sparged gases at a scan rate of 5 mV/s.

Conductivity Testing of the Membrane Samples

The conductivity of the membranes was tested using a BekkTech LLC in-plane conductivity cell. Sample preparation and testing protocols were acquired from the BekkTech LLC procedures document (*31*). In brief, samples with dimensions of 5 mm x25 mm were cut and fixed into the four electrode system cell. Once in the cell, a ParStat 2273 was used to sweep the voltage from -0.1 to 0.1V at a scan rate of 20 mV/s. The membranes were then tested in a hydrogen atmosphere at different RH (0, 30, 70 and 100 RH) and cell temperatures of 80 and 120 °C. Figure 9 depicts the effect of the different doping levels and operating condition on the ionic conductivity. As expected the conductivity increases as a function of relative humidity, however in some instances such as PVA at 120 °C, the conductivity declines. This effect can be attributed to the degradation of the membrane composite. At a given doping level we observe the overall conductivity of the PVA doped with KOH far superior to that of PBI doped with benzalkonium hydroxide. In the case of PVA, a relative humidity higher than 70 degraded the membrane. This result is believed to mainly be caused by a combination of loss off the doping substance by water condenstaion and loss of mechanical stability of the membrane and chemical attack from the hydroxy ions (*32*). On the other hand the PBI samples showed higher degree of stability at higher relative humidities at which their ionic conductivity begins to approach that of the hydroxide based PVA membranes.

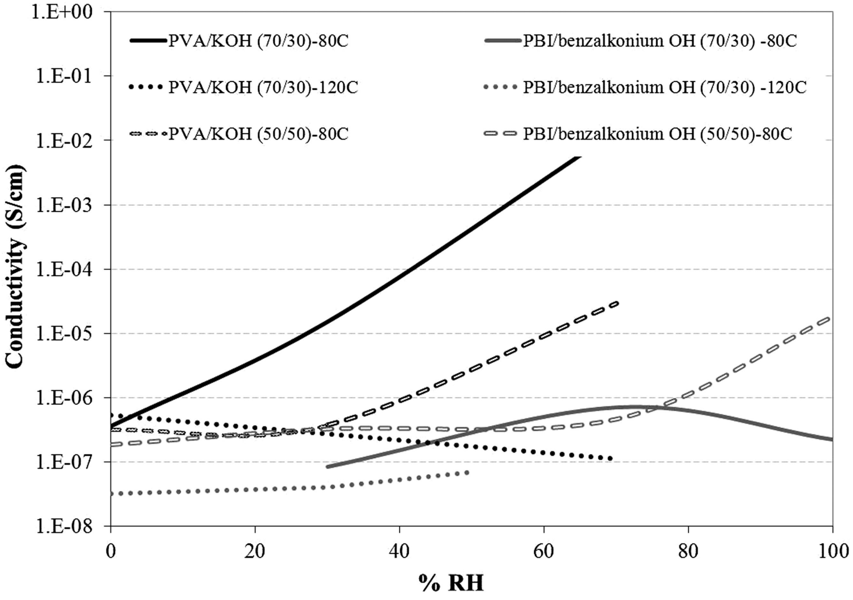

Figure 9. Membrane conductivity as a function of relative humidity and temperature.

Conclusions

Ionic liquids have been investigated for their application in PBI-based membranes in alkaline fuel cells. Although ILs show promise in terms of conductivity and thermal stability, significant work needs to be continued on the incorporation of the IL into solid polymer membranes in order to achieve validation of their operational performance in a fuel cell.

Acknowledgments

Funding for this work is greatfully acknowledged from SRNL’s DOE funded Laboratory Directed Research and Development (LDRD) Program. The authors wish to thank Ann E. Visser and Nicholas J. Bridges for their discussion and insight on ionic liquids. Savannah River National Laboratory is operated by Savannah River Nuclear Solutions. This document was prepared in conjunction with work accomplished under Contract No. DEAC09-08SR22470 with the U.S. Department of Energy.

References

1. Kim, Y. S. In *Resonance-Stabilized Anion Exchange Polymer Electrolytes*; DOE Annual Merit Review; Washington, D.C., 2010.
2. Cadena, C.; Anthony, J. L.; Shah, J. K.; Morrow, T. I.; Brennecke, J. F.; Maginn, E. J. Why is CO_2 so soluble in imidazolium-based ionic liquids? *J. Am. Chem. Soc.* **2004**, *126* (16), 5300–5308.
3. Bates, E. D.; Mayton, R. D.; Ntai, I.; Davis, J. H. CO_2 capture by a task-specific ionic liquid. *J. Am. Chem. Soc.* **2002**, *124* (6), 926–927.
4. Aki, S. N. V. K.; Mellein, B. R.; Saurer, E. M.; Brennecke, J. F. High-pressure phase behavior of carbon dioxide with imidazolium-based ionic liquids. *J. Phys. Chem. B* **2004**, *108* (52), 20355–20365.
5. Wilkes, J. S.; Levisky, J. A.; Wilson, R. A.; Hussey, C. L. Dialkylimidazolium chloroaluminate melts: A new class of room-temperature ionic liquids for electrochemistry, spectroscopy and synthesis. *Inorg. Chem.* **1982**, *21* (3), 1263–1264.
6. Hou, H.; Sun, G.; He, R.; Wu, Z.; Sun, B. Alkali doped polybenzimidazole membrane for high performance alkaline direct ethanol fuel cell. *J. Power Sources* **2008**, *182*, 95–99.
7. Varcoe, J. R.; Slade, R. C. T. *Fuel Cells* **2005**, *5*, 187–200.
8. Wang, A.; Li, A.; Zhang, S. *Macromolecules* **2010**, *43*, 3890–3896.
9. Xing, B.; Savadogo, O. Hydrogen/oxygen polymer electrolyte membrane fuel cells (pemfcs) based on alkaline-doped polybenzimidazol (pbi). *Electrochem. Commun.* **2000**, *2*, 697–702.
10. McLean, G. F.; Niet, T.; Prince-Richard, S.; Djilali, N. *Int. J. Hydro. Energy* **2002**, *27*, 507–526.
11. Lee, S.-Y.; Yasuda, T.; Watanabe, M. *J. Power Sources* **2010**, *195*, 5909–5914.
12. Nakamoto, H.; Watanabe, M. *Chem. Commun.* **2007**, 2539–2541.
13. Belieres, J.-P.; Gervasio, D.; Angell, C. A. *Chem. Commun.* **2006**, 4799–4801.
14. Rollins, J. B.; Conboy, J. C. *J. Electrochem. Soc.* **2009**, *156*, B943–B954.
15. Yan, F.; Yu, S.; Zhang, X.; Qiu, L.; You, J.; Lu, J. *Chem. Mater.* **2009**, 1480–1487.
16. Peng, Y.; Li, G.; Li, J.; Yu, S. Convenient syntheisi of various ionic liquids from onium hydroxides and ammonium salts. *Tetrahedron Lett.* **2009**, *50*, 4286–4288.
17. Ranu, B. C.; Banerjee, S. Ionic liquid as catalyst and reaction medium. The dramatic influence of task-specific ionic liquid, [bmim][oh], in michael addition of active methylene compounds to conjugated ketones, carboxylic esters, and nitriles. *Org. Lett.* **2005**, *7* (14), 3049–3052.
18. Yoshizawa, M.; Ohno, H. Fuel Cell. In *Electrochemical Aspects of Ionic Liquids*; Ohno, H., Ed. John Wiley & Sons, Inc.: New York, 2005; pp 199−203.
19. Danten, Y.; Cabaço, M. I.; Besnard, M. Interaction of water highly diluted in 1-alkyl-3-methyl imidazolium ionic liquids with the pf6− and bf4−anions. *J. Phys. Chem. A* **2009**, *113* (12), 2873–2889.

20. Rivera-Rubero, S.; Baldelli, S. Influence of water on the surface of hydrophilic and hydrophobic room-temperature ionic liquids. *J. Am. Chem. Soc.* **2004**, *126* (38), 11788–11789.
21. Li, Q.; He, R.; Jensen, J. O.; Bjerrum, N. J. Approaches and recent development of polymer electrolyte membranes for fuel cells operating above 100 °C. *Chem. Mater.* **2003**, *15* (26), 4896–4915.
22. Lee, S.-Y.; Ogawa, A.; Kanno, M.; Nakamoto, H.; Yasuda, T.; Watanabe, M. Nonhumidified intermediate temperature fuel cells using protic ionic liquids. *J. Am. Chem. Soc.* **2010**, *132* (28), 9764–9773.
23. Bai, H.; Ho, W. S. W. New sulfonated polybenzimidazole (spbi) copolymer-based proton-exchange membranes for fuel cells. *J. Taiwan Inst. Chem. Eng.* **2009**, *43* (3), 260–267.
24. Bai, H.; Ho, W. S. W. New carbon dioxide-selective membranes based on sulfonated polybenzimidazole (spbi) copolymer matrix for fuel cell applications. *Ind. Eng. Chem. Res.* **2009**, *48* (5), 2344–2354.
25. Bai, H.; Ho, W. S. W. *Polym. Int.* **2011**, *60*, 26–41.
26. Zou, J.; Ho, W. S. W. *J. Membr. Sci.* **2006**, *286*, 310–321.
27. Bai, H.; Ho, W. S. W. *Ind. Eng. Chem. Res.* **2011**, *50*, 12152–12161.
28. Xing, R.; Ho, W. S. W. *J. Membr. Sci.* **2011**, *367*, 91–102.
29. Nakamoto, H.; Watanabe, M. *Chem. Commun.* **2007**, 2539–2541.
30. deSouza, R. F.; Padilha, J. C.; Goncalves, R. S.; Dupont, J. *Electrochem. Comm.* **2003**, *5*, 728.
31. BekkTech's Procedures for Performing In-Plane Membrane Conductivity Testing. U.S. Department of Energy, 2008. http://www1.eere.energy.gov/hydrogenandfuelcells/pdfs/htmwg_may09_conductivity_testing.pdf.
32. Merle, G.; Schwan Hosseiny, S.; Wessling, M.; Nijmeijer, K. *J. Membr. Sci.* **2012**, *409−410*, 191–199.

Chapter 6

Natural Fiber Welding: Ionic Liquid Facilitated Biopolymer Mobilization and Reorganization

**Luke M. Haverhals,[1] Matthew P. Foley,[1] E. Kate Brown,[1]
Douglas M. Fox,[2] Hugh C. De Long,[3] and Paul C. Trulove*,[1]**

**[1]Department of Chemistry, U. S. Naval Academy,
Annapolis, Maryland 21402
[2]Department of Chemistry, American University, Washington, DC 20016
[3]Directorate of Mathematics and Life Sciences,
Air Force Office of Scientific Research, Arlington, Virginia 22203
*E-mail: trulove@usna.edu**

In this report, we discuss "natural fiber welding" - an ionic liquid-based methodology that enables the generation of complex, functionalized composites from natural fibrous materials. A unique feature of fiber welding is the ability to selectively open and mobilize biopolymer structures while simultaneously preserving a portion of the biopolymer (micro and meso structures) in the native state. By precisely regulating process variables such as the purity, type, amount, and placement of ionic liquid solvent as well as the duration and temperature of treatment, controlled reorganization of natural material hydrogen bonding networks is achieved. The end result is often dramatic enhancement and modification of physical and chemical properties without disruption to many desirable properties intrinsic to natural materials.

In Ionic Liquids: Science and Applications; Visser, A., et al.;
ACS Symposium Series; American Chemical Society: Washington, DC, 2012.

Introduction

The extensive diversity of life presents a remarkable variety of biopolymers, each with distinctive chemical and physical functionalities. From prehistoric times until the modern age, mankind has utilized natural materials for survival and to improve our standard of living. Silk, for example, has been the subject of investigation and manipulation for thousands of years. It is noteworthy, that even in the present day, the mechanical properties of many natural materials rival and even exceed those of the most advanced synthetic polymers, Table 1 (*1*, *2*). Despite our history with biopolymers, humans have been unable to fully exploit these extraordinary properties in the development of high performance materials. This is chiefly due to our relative inability to manipulate, preserve, and replicate the complex motifs found in natural materials, Figures 1 and 2 (*3*–*5*). The dissolution and reconstitution of silk proteins, for example, is still often as much an art as science (*6*). (Many scientists would argue that silk proteins are only considered "silk" provided certain key micro and meso scale structures are present (*4*).)

Table 1. Properties comparison between natural and synthetic materials

Polymer Type	*Modulus*	*Strength to Break*	*Strain to Break*	*Toughness to Break*
	GPa	*GPa*	*%*	*J/g*
Cellulose [a]	6-11	0.3-0.7	6-7	5-15
Silk [b]	4-6	0.6-0.7	15-35	60-80
Silk [c]	9-14	1.5-1.9	30-70	200-500
Nylon-66	5	0.9	18	80
Kevlar-49	124	2.8	2.5	15
Steel	200	2.0	8	2

[a] Cotton. [b] *Bombyx Mori*, Cocoon Silk. [c] *Caerostris Darwini*, Dragline Silk.

Ionic liquids (ILs) represent a unique class of solvents that offer extraordinary versatility and tenability (*7*, *8*). Within the last decade, researchers have developed ILs that are potent solvents for processing biopolymers such as cellulose (*9*–*15*), lignin (*16*, *17*), chitin (*18*), keratin (*19*), and silk (*20*, *21*). Generally speaking, the efficacy of ILs as solvents for biopolymers appears to be largely due to the interactions between IL anions and biopolymers. Anions are typically adept at accepting hydrogen bonds and this results in the efficient interruption of hydrogen bonding networks between biopolymers (*22*). Cations also play important roles in interacting with and stabilizing biopolymers as they peel away from the bulk material (*23*). Synergies of anion and cation activities have been shown to be particularly relevant in the dissolution of materials containing cellulose (*24*).

When natural materials are dissolved, intramolecular and intermolecular hydrogen bonding networks are disrupted as the native material structure is deconstructed. Figures 1 and 2 illustrate hierarchies of material order from the macro, meso, and micro scale perspectives for silk and cotton fibers, respectively (*3–5*, *25*). Note that the over simplified diagrams do not capture the full scope of the complex structural motifs that are known. Despite this, the figures are intend to convey a sense of what is lost during full dissolution of biomaterials. Given this structural information and some basic knowledge of the complex life processes that produce such materials, it is readily apparent why such structural motifs are difficult, if not impossible, to reproduce upon bulk reconstitution of dissolved biomaterials. In so far as native functionality and physical properties are desired, the loss of key micro and meso structures is detrimental to processes that aim to utilize natural materials. In this chapter, we shall consider processes that preserve vital native structure while simultaneously transforming and repurposing natural materials for innovative applications.

Very recently we have demonstrated an IL-based biopolymer processing technique that we call "natural fiber welding" (NFW), Figure 3 (*26–30*). The overarching intention of NFW is to generate composite materials from fibrous natural materials (i.e., cotton, hemp, silk, wool, et cetera) while simultaneously retaining many of the native materials characteristics (micro and meso structures). Process control is achieved by carefully regulating the type, purity, amount, and placement of IL solvent as well as precisely managing the duration and temperature of treatment. Additionally, subtle process variables such as the reconstitution solvent utilized and the drying conditions (i.e., whether or not materials are constrained during drying) can play important roles in process outcomes. When properly executed, the welding process reproducibly reorganizes hydrogen bonding networks to fuse individual fibers. The fiber-matrix composites generated are observed to possess consistent physical and chemical properties that maintain certain aspects of the original natural material while also displaying new and unique functionalities.

Figure 3 details basic NFW process steps utilizing four generalized illustrations (Panels A – D). Panel A depicts a controlled (limited) amount of an IL-based solvent added to a fibrous material. Upon introduction, the IL disrupts hydrogen bonding between polymers as it moves into individual fibers. Polymers at fiber surfaces swell and are mobilized to permit interactions between material from adjacent fibers, Panel B. (Polymer motifs within fiber cores may be largely undisturbed.) Panel C shows the introduction of an anti-solvent, often water and/or alcohols, that removes IL from the fiber matrix (reconstitution). After reconstitution, the anti-solvent is removed by drying. The drying process reveals the extension of hydrogen networks between adjacent fibers as materials noticeably contract, Panel D.

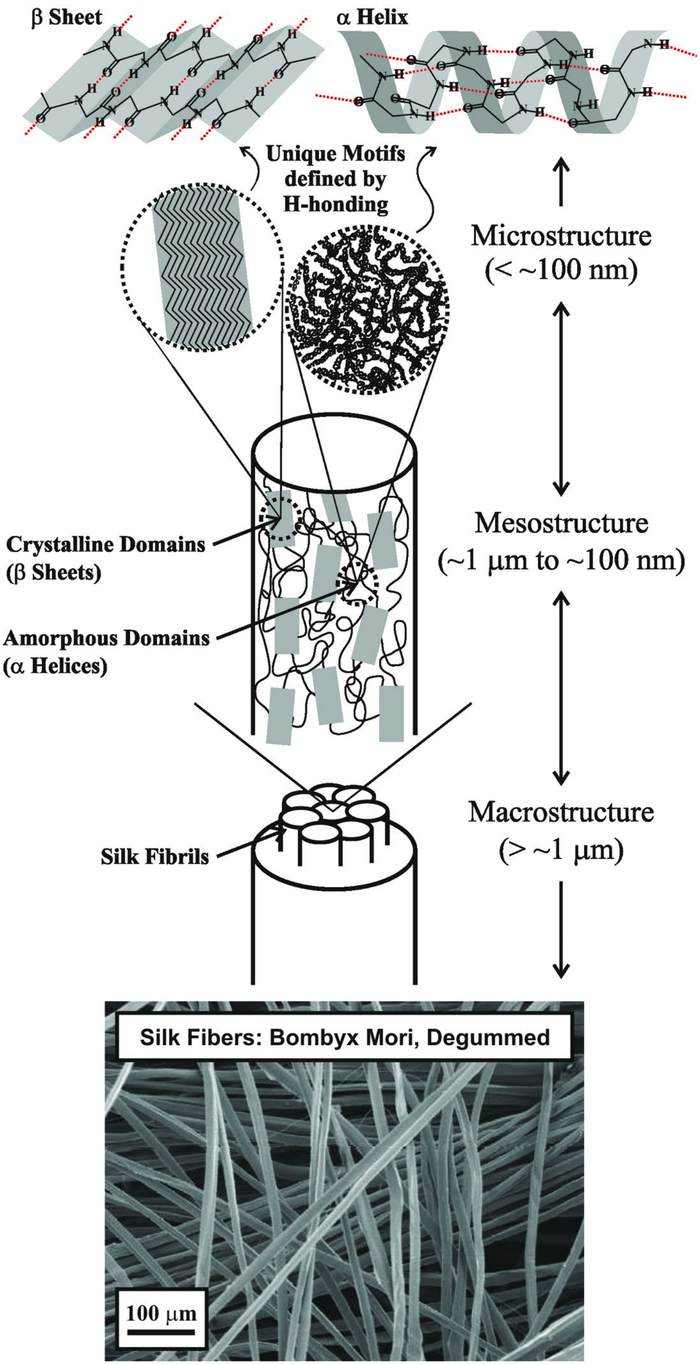
β Sheet
α Helix
Unique Motifs defined by H-honding
Microstructure (< ~100 nm)
Crystalline Domains (β Sheets)
Amorphous Domains (α Helices)
Mesostructure (~1 µm to ~100 nm)
Silk Fibrils
Macrostructure (> ~1 µm)
Silk Fibers: Bombyx Mori, Degummed
100 µm

Figure 1. Generalized diagrams and an SEM image of silk (fibers).

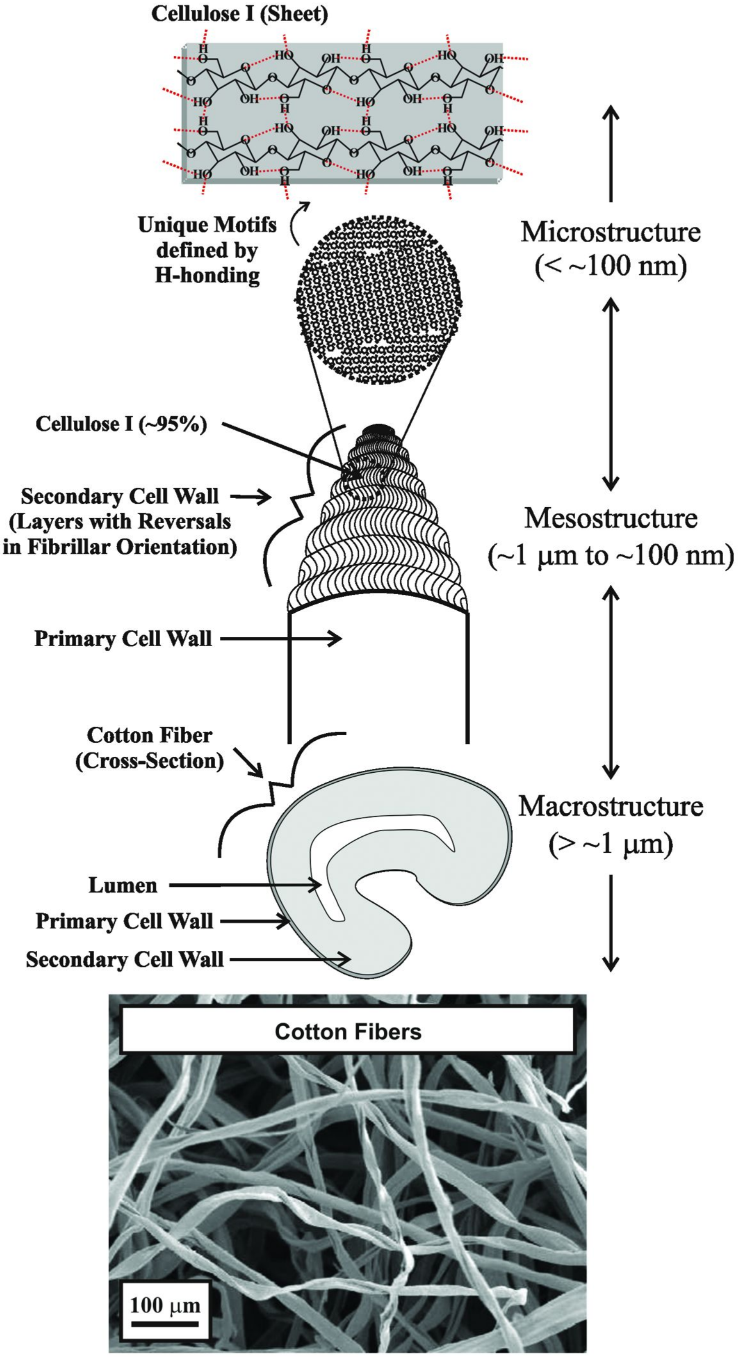
Cellulose I (Sheet)
Unique Motifs defined by H-honding
Microstructure (< ~100 nm)
Cellulose I (~95%)
Secondary Cell Wall (Layers with Reversals in Fibrillar Orientation)
Mesostructure (~1 μm to ~100 nm)
Primary Cell Wall
Cotton Fiber (Cross-Section)
Macrostructure (> ~1 μm)
Lumen
Primary Cell Wall
Secondary Cell Wall
Cotton Fibers
100 μm

Figure 2. Generalized diagrams and an SEM image of cotton (fibers).

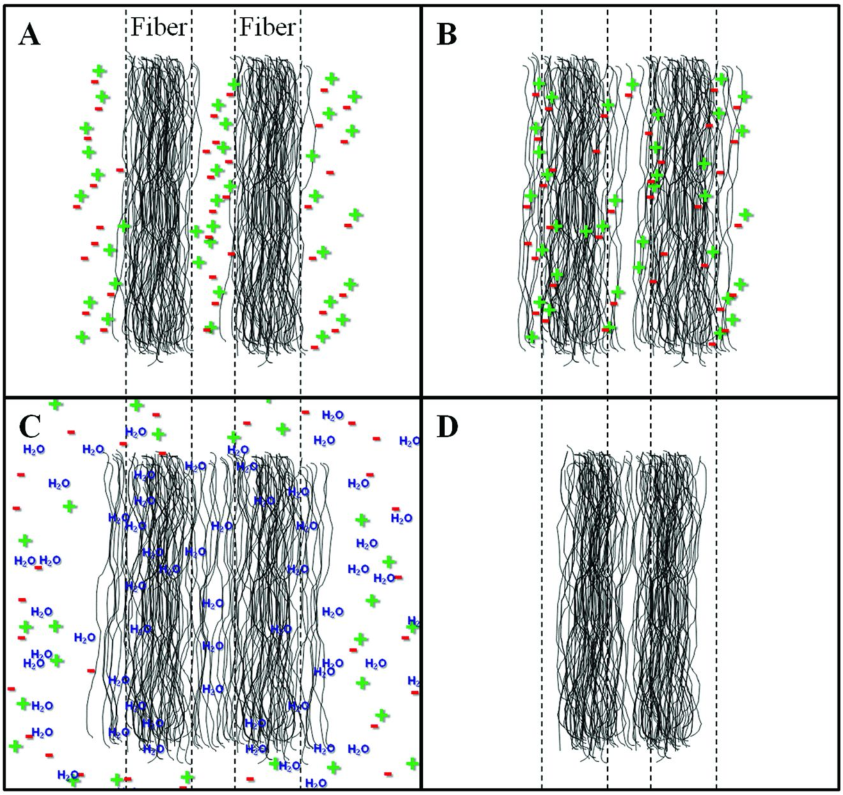

Figure 3. Generalized schematics of NFW. (Illustrations not to scale).

In addition to efficient biopolymer solvation, ionic liquids are known to significantly enhance the interaction of nanoscale clays and carbon nanotubes with polymeric materials (*31*, *32*). Previous research has clearly demonstrated the introduction of nanoscale materials into polymers can dramatically enhance the inherent properties and confer unique functionalities to many types of systems. The integration of clays, for example, has potential to impart significant improvements in mechanical, thermal, barrier, and flame-retardant properties over the parent polymer (*33–38*). Unfortunately, the wealth of new materials that could be generated by integrating nanoscale materials into, for example, silk have yet to be realized due to the limited processing abilities previously mentioned. While detailed data are not discussed here, we would be remiss not to mention that NFW is easily adapted to include strategies for nano and micron sized material incorporation into functional biocomposites.

Experimental

General, limited experimental details are provide below. Please see our previous reports on NFW for additional information (*26–30*).

Materials and NFW Protocols

Silk and cotton based materials (yarns and cloth) were purchase from a local fabric store. Care was taken to utilize materials that were clean of dyes and other additives. Yarns were dyed using fluorescent coumarin- and fluorescein-based dyes utilizing standard protocols from literature (*39*). Cloth and yarns were treated with 1-ethyl-3-methylimidizolium acetate (C_2MIm OAc, Sigma Aldrich) which had been analyzed for adventitious water (by Karl Fischer titrations) and residual acetic acid (by acid/base titrations). Concentrations vary somewhat between vendor lots but are typically 1-2 mg water/g solvent and 8-10 mg acetic acid/g solvent, respectively. IL solvents (as well as dried biopolymer substrates) are fairly hydroscopic so that welding experiments are typically carried under a dry atmosphere. We have found it convenient to perform experiments in a glove box on a large, preheated aluminum block "oven" (typically heated to 40 - 80 °C). ILs may be applied to substrates by any number of techniques (i.e., dip coating, dropwise addition from a syringe, inkjet printing, et cetera). Cloth substrates are typically dip coated with IL. Yarn junctions are often treated with a small (2.0 µL) dropwise addition of IL. After IL application, substrates are placed on the Al block oven for a prescribed length of time. IL is removed by reconstitution in either methanol (silk substrates) or water (cellulosic substrates) immediately after heat treatment. After thorough removal of IL (samples are spectroscopically clean of IL), welded composites are gently dried in an oven (typically at ~60 °C) overnight prior to chemical analysis and imaging characterizations.

Instrumentation and Composite Characterization Protocols

SEM Imaging

Cotton yarn junctions were imaged by scanning electron microscopy (SEM) utilizing a JEOL JSM-6360LV instrument. Prior to imaging, samples were each junction was sputter coated with several nm of gold.

Confocal Fluorescent Microscopy

Cotton and silk yarn junctions were imaged by confocal fluorescent microscopy (CFM) utilizing a Nikon C2 confocal microscope outfitted with a spectral detector. Cross-sectional images were obtained by potting junctions in epoxy and microtoming with a RMC Powertome fitted with a diamond knife. (Due to size and geometric considerations, yarn junctions are not transparent to visible light and cannot, therefore, be optically sectioned.) Spectromicroscopic images were collected by sequential illumination with 408 nm and 488 nm lasers, respectively. During illumination, the spectral region from 440 nm to 600 nm was monitored at 5 nm resolution. Fluorescence from 7-diethylaminocoumarin-3-carboxylic acid, hydrazide (DCCH) and 5-([4,6-dichlorotriazin-2-yl]amino)fluorescein hydrochloride (DTAF) chromophores was distinguished and quantified by linearly unmixing spectral data. (Individual data channels are thus free of cross talk and bleed through fluorescence.) The unmixing process utilized reference spectra collected for each chromophore/laser combination separate control experiments.

Physical Properties Testing

Cotton cloth samples were mechanically (tensile) tested utilizing an ADMET eXpert Universal Testing Machine. Dog-bone shaped samples had 20.0 mm gauge lengths and 5.0 mm widths. Samples were cut in two different orientations with respect to the aida-weave cloth. The aida-weave pattern was either in-line with, or was 45° with respect to the strain axis. The test speed (of strain application) was 3.0 mm•min^{-1}.

ATR-FTIR Spectroscopy

Cotton cloth samples were analyzed by Fourier transform infrared (FT-IR) spectroscopy utilizing a Thermo Scientific 380 spectrometer fitted with a diamond ATR crystal.

Powder XRD

Cotton cloth samples were analyzed by powder X-ray diffraction (XRD) utilizing a Philips PW 1729 diffractometer equipped with a Cu X-ray source: $CuK_{\alpha1}$ = 1.54056 Å and $CuK_{\alpha2}$ = 1.54439 Å ($CuK_{\alpha2}/CuK_{\alpha1}$ = 0.5). The goniometer operated with a scan step size: $2\theta = 0.025°$.

Results and Discussion

The characterization of NFW materials provides feedback to improve process design as well as give insight to specific applications and uses. The discussion that follows focuses on characterizations of materials with this idea in mind.

Characterizations of Physical Transformations

Data that follow highlight several methods to characterize physical alterations imparted to natural substrates by NFW. Physical characterizations at relatively small scales are discussed first. Later, information distilled from small scale analyses is utilized to understand and contextualize analyses of bulk physical properties.

Microscopic characterizations of NFW yarn junctions are "simple" yet extremely informative demonstrations of polymer mobilization and reorganization that results from processing. Figures 4 and 5 show comparisons of cotton yarn junctions in orthogonal and parallel configurations, respectively. In each figure, unprocessed junctions (i.e., not exposed to IL) are imaged by SEM (panel A) and CFM (panel B). Panels C and D (Figures 4 and 5) show yarn junctions treated with a 2 μL drop of C_2MIm OAc for 5 minutes at 60 °C. Panels E and F (Figures 4 and 5) show yarn junctions treated with a 2 μL drop of C_2MIm OAc for 15 minutes at 60 °C. (NFW junctions have been reconstituted in water and dried prior to imaging.) Each junction contains one yarn that was covalently labeled with a fluorescent coumarin-based dye, DCCH, and the other yarn covalently labeled with a fluorescein-based dye, DTAF. (Dye attachment procedures were performed prior to NFW.) Fluorescence from DCCH is false colored purple, while fluorescence from DTAF is green. Note that while both SEM and CFM images display excellent depth of field with valuable topographical data, CFM images additionally differentiate individual fibers that originate from different yarns.

Data in Figures 4 and 5 highlight several transformations often observed for fibrous materials. Notice first the significant decrease in the diameters of individual yarns that have been exposed to IL. Substantial consolidation of loose fibers around the periphery of each yarn junction is also evident. Given the time of treatment (5 min for junctions shown in panels C and D), both of these phenomena indicate that biopolymer from individual fibers promptly interacts (hydrogen bonds) with neighboring fibers upon introduction of IL. It is also apparent that fiber fusion via extended hydrogen bonding does not require the full solubilization of individual fibers. As the time of interaction between IL and substrate is increased, however, some individual fibers appear to be fully solubilized, panels E and F. After 15 minutes (of exposure to IL), individual yarns are joined by noteworthy amounts of fully solubilized, mobile polymer (especially evident for the orthogonal junction). The origin of fully solubilized materials appears to be fibers at the outermost regions of individual yarns and is supported by the lack of loose fibers and the apparent smoothing of yarn surfaces.

Despite the observation of material movement on the macroscopic scale, it is remarkable that a very distinct interface exists between individual yarns. Note for example, that while SEM data in Figure 5E provide little distinction between what were originally two distinct yarns, CFM data in 5F indicate a definite interface between materials that originated from different yarns. Data in Figure 6 show that restricted polymer mobility is observed in other systems as well (*30*). The figure shows low and high resolution images of a cross-sectioned (by microtome) parallel silk yarn junction that was treated with a 2 μL drop of C_2MIm OAc for 60 minutes at 60 °C. (Reconstituted in methanol.) Prior to NFW, yarns were covalently labeled with DCCH (blue) and DTAF (green), respectively. In, particular, the high resolution image clearly demonstrates a sharp boundary between silk from different yarns. This indicates that biopolymers are highly constrained (within yarn cores) due to the limited amount of IL applied.

Generally speaking, the mass ratio of IL applied relative to biopolymer substrate is a critical consideration that determines process outcomes. In other work we have shown extensive fusion and consolidation of cotton fibers can be achieved with less than one part by mass C_2MIm OAc added to one part cotton (degree of polymerization ~ 2000 cellobiose units) (*29*). In contrast with solution-based processes where biopolymers are fully dissolved, 20% by mass of micro crystalline cellulose (MCC, degree of polymerization ~ 500 cellobiose units) in C_2MIm OAc is the upper limit that can be practically realized. (Note that solution viscosities are extremely high, even at elevated temperatures.) In present context, we believe the data in Figures 4-6 demonstrate that relatively small amounts of IL can significantly transform and modify fibrous, high molecular weight substrates into interesting and potential useful composite materials.

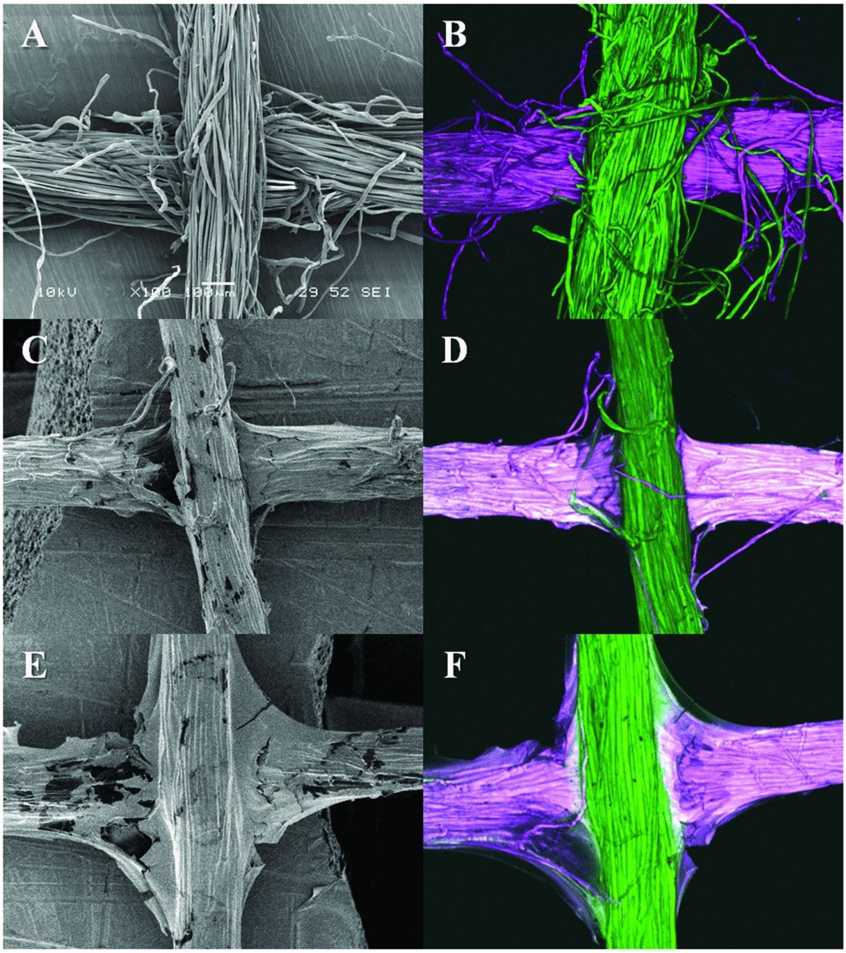

Figure 4. Orthogonal cotton yarns: SEM and CFM imaging. (see color insert)

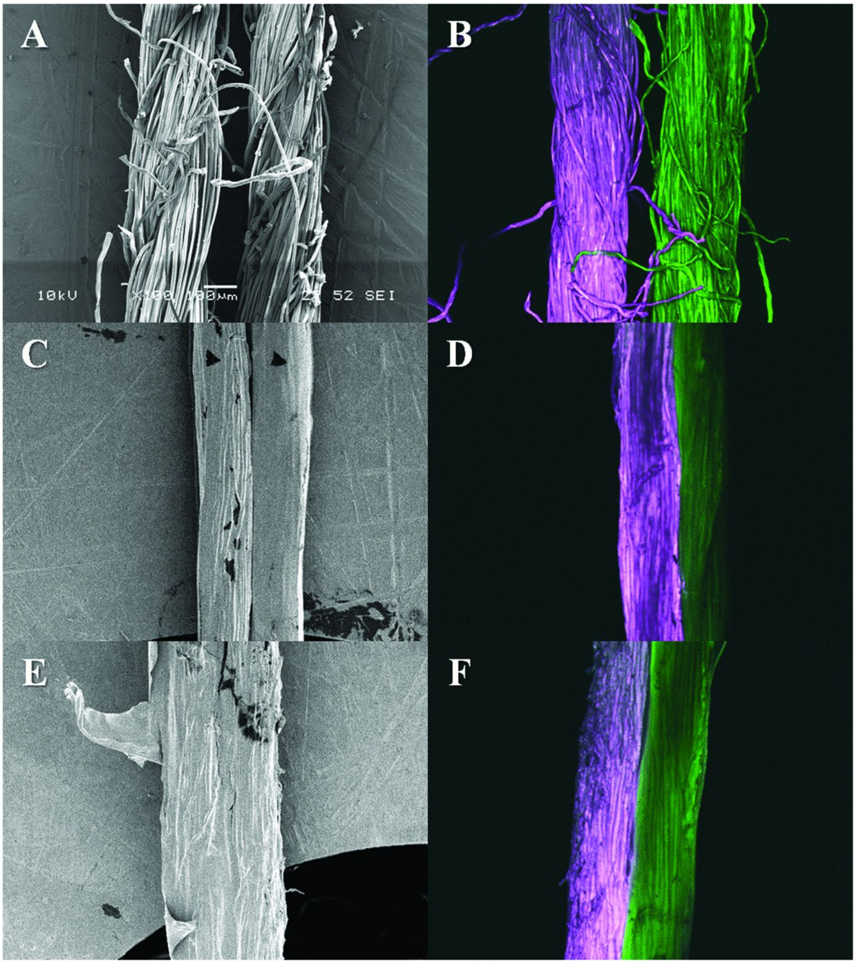
A
B
C
D
E
F
10kV X100 100μm 52 SEI

Figure 5. Parallel cotton yarns: SEM and CFM imaging. (see color insert)

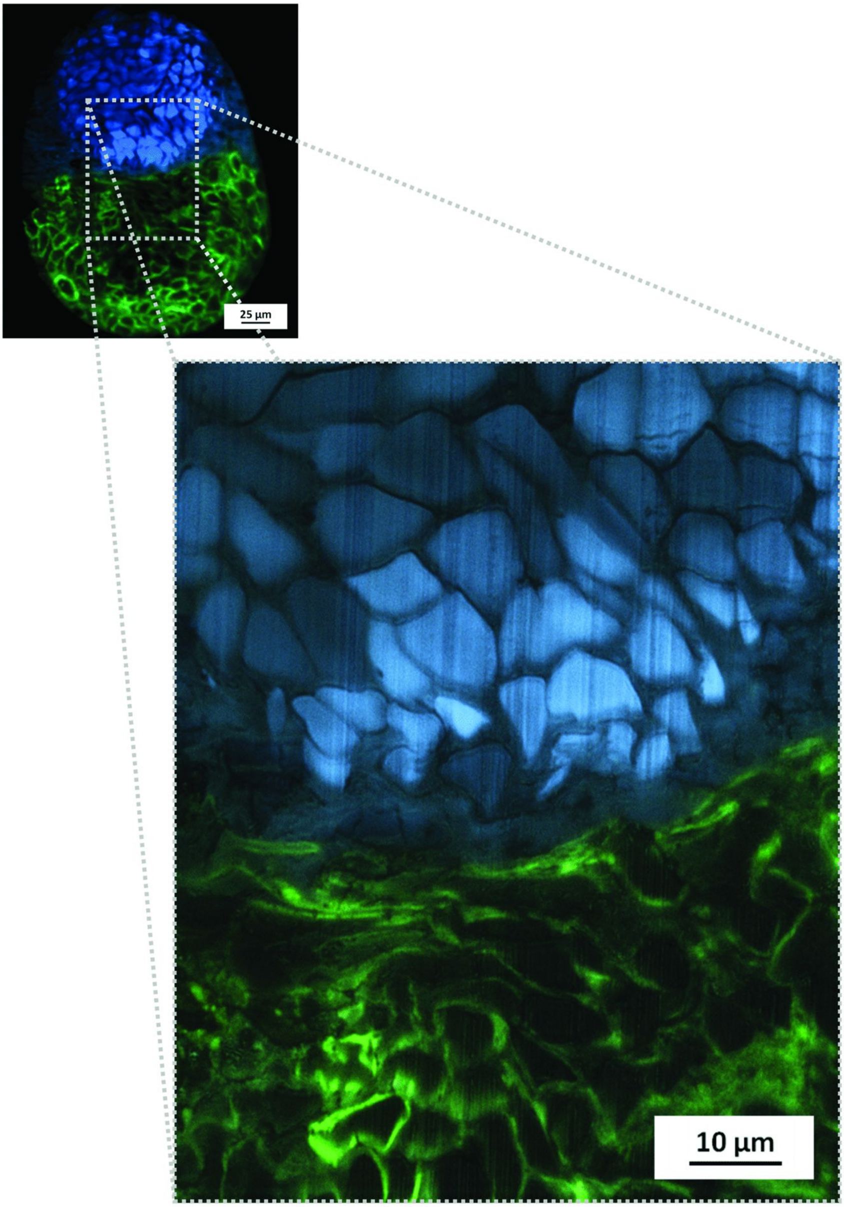

Figure 6. Cross-section of a parallel silk yarn junction: CFM imaging. Reproduced with permission from reference (30). Copyright 2012, The Royal Society of Chemistry. (see color insert)

Bulk Mechanical Properties

Bulk mechanical properties are significantly impacted by the level of the polymer mobilization and reorganization. For example, as the individual fibers that make up a yarn are fused by extended hydrogen bonding networks, the overall mechanical properties of the yarn are altered (*26*). In particular, yarns may become considerably stiffer (increased modulus) because welded fibers that make up the yarn cannot slide past one another as freely as before NFW. That said, the overall breaking strength (max stress at break) and toughness (energy to break) of the yarn are not greatly altered provided samples are not severely denatured (especially relevant for silk). Generally speaking for the single yarn scenario, NFW does not greatly increase the amount of load bearing material that resists the strain. (Only short and/or loose, non-load bearing fibers may be converted to load bearing components.) When yarns are utilized in woven samples, however, hydrogen bonding networks can be extended across orthogonal yarns. (Revisit Figure 4E and 4F.) Directionally dependant load bearing capacities can thus be greatly increased.

When properly executed, NFW can produce tremendous changes to the strength and toughness of woven materials. Figure 7 presents example mechanical testing data to illustrate this point. The data are the energy to break for dog-bone shaped specimens cut from cotton cloth (unprocessed and NWF). The cotton cloth is an aida-weave, which is an open (warp threads do not come together) and even-weave (the warp and weft yarns are of the same size and count). Dog-bones are cut either in-line with (panel A) or at 45° with respect to the aida-weave (panel B). The cloth samples from which the dog-bones are cut were processed with roughly 1 g of IL per g of cotton cloth substrate for either 5, 10, or 30 minutes at either 20 °C or 80 °C. Reconstitution was conducted in water and samples were dried at 60 °C prior to testing. Toughness data for tensile testing conducted in-line with the weave show no significant difference between unprocessed and NFW cloths. This result is not surprising because stress applied in-line with the aida-weave only tests the yarns that run parallel with the strain axis. Such a scenario is very similar to that previously discussed for a single yarn. Data for stress applied at 45° relative to the weave show dramatic (approximately 40-fold) increases in toughness for samples processed at 80 °C. In this mode of testing, individual yarns do not run the full gauge length of the strain axis. In the native cloth, therefore, strain can only be resisted by the weak frictional forces present between intersecting yarns. It is obvious that strong hydrogen bonding between orthogonal yarns do not exist in samples processed at 20 °C as well. It is interesting to note, however, that cloths processed at 20 °C and tested in-line with the weave (data not presented here) do show an increase in the modulus which indicates significant hydrogen bonding between the fibers of individual yarns.

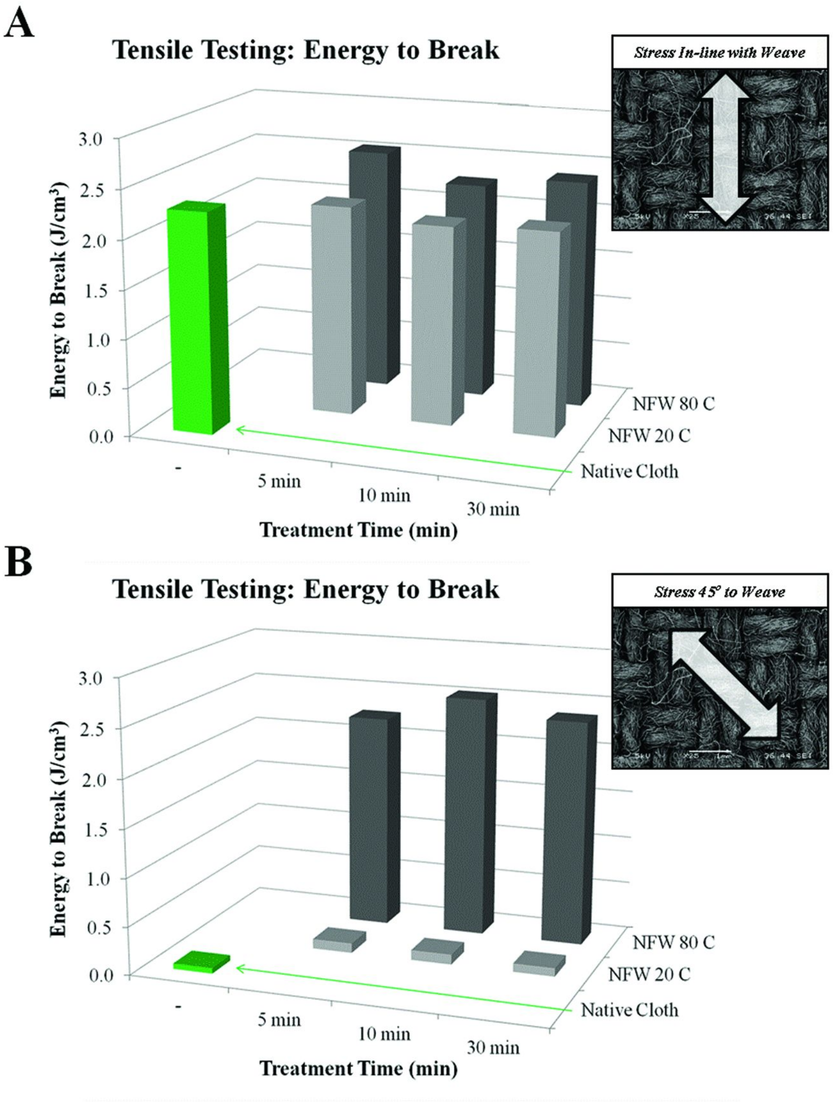

Figure 7. Mechanical testing data for unprocessed and NFW cotton cloth.

Characterizations of Chemical Transformations

Mechanical properties are often indicative of structural changes caused by the NFW process. These data do not, however, directly provide chemical information. The discussion turns its focus to analyses that characterize chemical (micro and meso structures) alterations imparted to natural substrates by NFW (i.e., surface analyses by FTIR and bulk characterizations by XRD).

Surface Characterizations

While SEM and CFM provide data to decipher how and where biopolymers move and interact, various other spectroscopic techniques may be utilized to provide chemical information of altered biopolymers. Specifically, ATR-IR and Raman spectroscopies (and associated spectromicroscopies) have been utilized to obtain detailed information on the chemical changes imparted to NFW composites. Figure 8 contains ATR-FTIR surface analyses of unprocessed and processed cotton cloth (*29*). Curve A is IR data for the untreated cotton cloth and is characteristic for relatively crystalline cellulose I (*40–42*). Curves B, C, and D are for cotton cloth treated with C_2MIm OAc at 40 °C for 0.5, 2.0, and 24.0 hr, respectively. The ratios of the mass of IL applied versus mass of cotton substrate were similar for each sample: 1.6 (B), 1.5 (C), 1.5 (D) g IL/g cotton. Curve E is IR data for fully dissolved and reconstituted cotton cloth and is characteristic for cellulose II (and much less crystalline than cellulose I) (*40–42*).

Before discussing the data further, it should be reiterated that the ATR-FTIR experiments presented characterize the outer surface of cotton yarns that make up the cloth. (Here, cloth samples are clamped against the ATR crystal for analysis.) Equation 1 provides a basis to estimate the penetration depth, d, of the evanescent wave:

$$d = \lambda / \{2\pi n_1[\sin^2 \theta - (n_2 / n_1)^2]^{1/2}\}$$

where λ is the wavelength of (IR) light, θ is the angle of incidence, and n_1 and n_2 are the refractive indices of the ATR crystal and the sample (*43*, *44*). Given the experimental parameters, the penetration depth is no more than approximately two microns into the surface of individual fibers (at the perimeter of the cotton yarns) (*43*, *44*). Curves A and E form “bookends” which span the range of cloth from undisturbed cellulose I to fully “denatured” cellulose II. Curves B, C, and D show characteristics of both cellulose I and II, with increased cellulose II character observed with increasing time of treatment (*40–42*). In particular, notice that as treatment time increases, O–H stretching at 2,600–3,500 cm^{-1} broadens. Additionally, peaks associated with C–O and C–O-C stretching, COH and CCH vibrations, and CH_2 wagging in the 1,000–1,300 cm^{-1} range are less well defined. In context, these data suggest that the NFW process can be finely tuned to yield micron level control over surface-specific alterations of individual fibers.

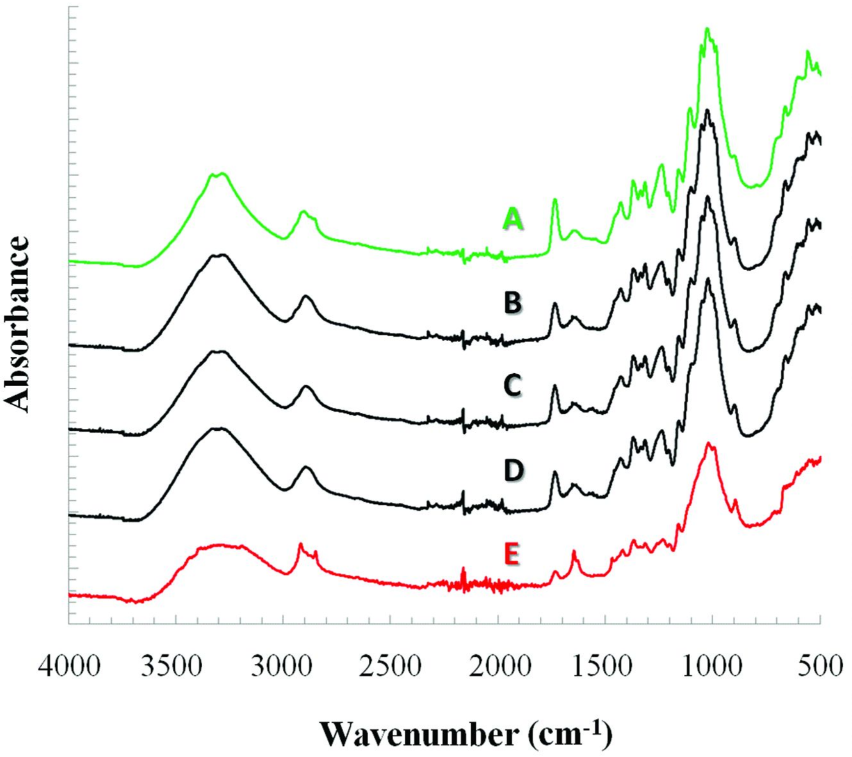

Figure 8. ATR-FTIR analysis of cotton cloth samples. Reproduced with permission from reference (29). Copyright 2011 Springer Science+Business Media B.V.

Bulk Characterizations

Powder XRD is a technique useful in determining the bulk composition of materials before, during, and after NFW processing. XRD data thus provide valuable insight into both process design and material properties that may impact composite functionality (*42*). Figure 9 is an example that shows powder XRD data for cotton cloth as well as a modeled fit to example data. (Curve intensities are offset for clarity.) Data represented by curve A is typical for cotton fibers (that are >95% cellulose I). A doublet at 2θ = 15° and 16.5°, a sharp peak at 22.5°, and a broad peak at 34° are attributable to cellulose I 101, 101, 002, and 040, respectively (*42*, *45*, *46*). Fully dissolved and then reconstituted cotton cloth (curve B) is typical of cellulose II with a broad 021 reflection centered at 2θ = 21° (*42*, *45*, *46*). Together, these data bracket the spectrum from fully "natured" (untreated) cotton cloth to fully denatured cotton cloth. XRD characterization of treated (NFW) materials are expected to yield diffraction patterns somewhere between these extremes. Curve C are data derived from curves A and B according to the following equation:

$$C = (x)(A) + (1-x)(B)$$

where x is within the range $0 \leq x \leq 1$. For this particular example, $x = 0.82$ such that the model (curve C) closely matches curve D which is actual data for cloth treated with a solution of 90% by mass C_2MIm OAc/10% methanol for 2 hrs at 80 °C. The best value for x was deduced by iteratively varying x at 0.01 increments and comparing the differences between curves C and D. The best fit is defined as the value in x that yields the minimum differences between curves C and D. (Data fits are determined by an automated algorithm written in Visual Basic © for Excel ©.) The processed cloth (represented by curve D) is thus determined to retain about 82% of its native character. Note that this data analysis method does not strictly quantify cellulose I content nor does it attempt to assign a crystallinity index. However, this data treatment does provide a practical and relatively robust way to quantify the effect of various process control variables.

Figure 10 shows the percentage of native character calculated for cotton cloths treated with various amount of IL for a range of temperatures and times. Within the error of these experiments, the amount of cellulose I to II conversion process occurs at time scales faster than the shortest (thirty minutes) observation. This is consistent with imaging data from SEM and CFM . Figure 10 data also suggest that in the limit of low IL loading (< 1 g of IL applied per g of cotton substrate), the amount of cellulose I transformed into cellulose II is correlated with the amount of IL applied.

Data in Figure 10 are noteworthy, however, there are some important experimental parameters that warrant further discussion. One consideration is that IL was delivered with a co-solvent (methanol) in order to achieve even incorporation of IL on the cloth substrates at relatively low IL loading. Up until this point, we have discussed NFW processes that utilized "neat" IL, either by dropwise addition (yarn junctions) or dip coating (cloth analyzed by ATR-FTIR and tensile testing). ("Neat" C_2MIm OAc does contain adventitious water and acetic acid.) The presence of co-solvents in IL-based solutions, be them either adventitious impurities or deliberate additions, can significantly modify the efficacy and rheology of the base IL solvent (*15*). In this example, methanol was chosen as a co-solvent because of its vapor pressure and its ability to participate in hydrogen bonding. The volatility of methanol provides a means to selectively remove it from the substrate (while leaving the IL behind). Additionally, methanol's hydrogen bond donor/acceptor abilities, reduce the efficacy of the C_2MIm OAc-based solvent and limit any NFW that may occur during the removal process. After dip coating cloth in the IL/methanol solution but prior to heat treatment, samples were exposed to vacuum conditions for 30 minutes at room temperature to remove most of the methanol. (IL is removed after heat treatment by reconstitution in water.) So, while data do suggest that biopolymer dissolution can be restricted by strictly controlling and limiting the amount of IL applied, we are hesitant to make broad generalizations based solely on these data (experiments). (Future work for our group includes the evaluation of NFW methods that utilize ILs and co-solvents.)

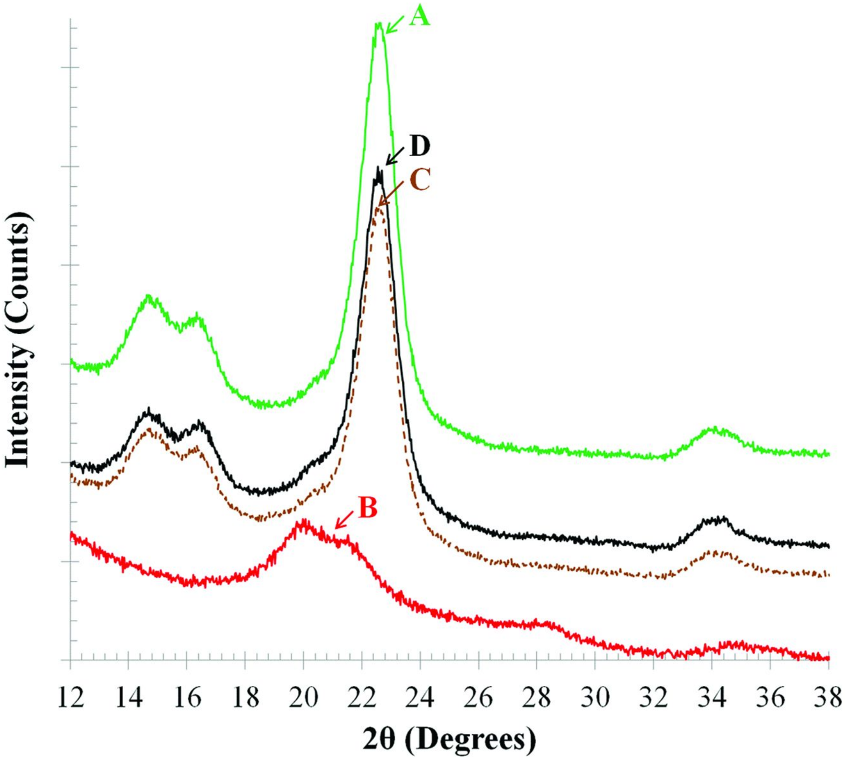

Figure 9. Examples of powder XRD data and modeling. Reproduced with permission from reference (29). Copyright 2011 Springer Science+Business Media B.V.

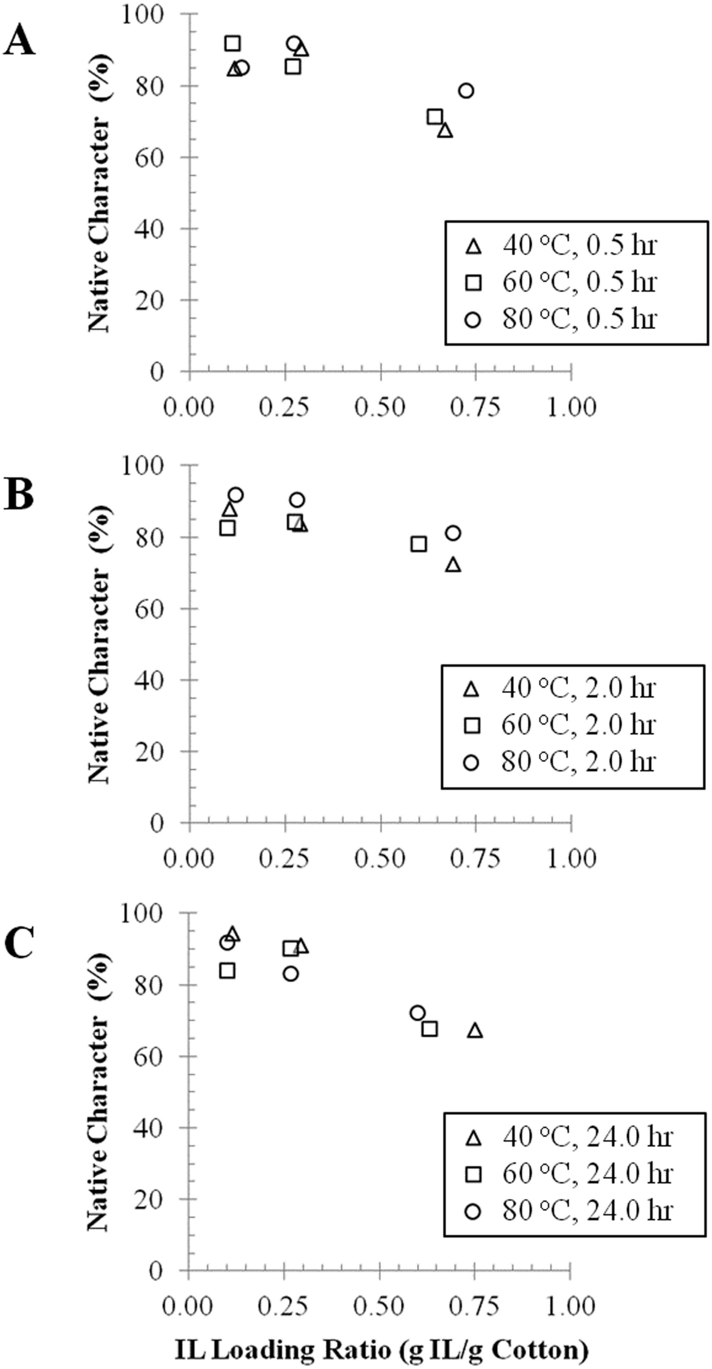

Figure 10. XRD characterizations of NFW cotton cloth.

Conclusions

The controlled mobilization and reorganization of biopolymer substrates has been demonstrated. The judicious choices of solvent and application methods transforms fibrous natural materials into fiber matrix composites useful for any number of potential applications. In this process, natural materials are rendered open to derivatization and new chemistries while simultaneously preserving important native micro and meso structures. We believe NFW to be a versatile suite of techniques that are also quite "green" in that methods utilize fairly small amounts of IL solvents in order to repurpose natural materials.

Acknowledgments

We are grateful to the US Air Force Office of Scientific Research and US Naval Academy for funding portions of this work. Any opinions, findings, conclusions, or recommendations expressed in this work are those of the authors and do not necessarily reflect the views of the US Air Force or the US Navy.

References

1. Kaplan, D. L.; Lombardi, S. J.; Muller, W.; Fossey, S. In *Biomaterials: Novel Materials from Biological Sources*; Byrom, D., Ed.; Stockton Press: New York, 1991.
2. Agnarsson, I.; Kuntner, M.; Blackledge, T. A. *PLoS ONE* **2010**, *5*, e11234.
3. Vollrath, F. *Rev. Mol. Biotechnol.* **2000**, *74*, 67–83.
4. Porter, D.; Vollrath, F. *Adv. Mater.* **2009**, *21*, 487–492.
5. Wakelyn, P. J.; et al. *Int. Fiber Sci. Technol. Ser.* **1998**, *15*, 577–724.
6. Vollrath, F.; Porter, D.; Holland, C. *Soft Matter* **2011**, *7*, 9595–9600.
7. Rogers, R. D.; Seddon, K. R. *Science* **2003**, *302*, 792–793.
8. *Ionic Liquids in Synthesis*; Wasserscheid, P., Welton, T., Eds.; Wiley-VCH: Weinheim, Germany, 2003.
9. Swatloski, R. P.; Spear, S. K.; Holbrey, J. D.; Rogers, R. D. *J. Am. Chem. Soc.* **2002**, *124*, 4974–4975.
10. Remsing, R. C.; Swatloski, R. P.; Rogers, R. D.; Moyna, G. *Chem. Commun.* **2006**, 1271–1273.
11. Moulthrop, J. S.; Swatloski, R. P.; Moyna, G.; Rogers, R. D. *Chem. Commun.* **2005**, 1557–1559.
12. Turner, M. B.; Spear, S. K.; Holbrey, J. D.; Rogers, R. D. *Biomacromolecules* **2004**, *5*, 1379–1384.
13. Turner, M. B.; Spear, S. K.; Holbrey, J. D.; Daly, D. T.; Rogers, R. D. *Biomacromolecules* **2005**, *6*, 2497–2502.
14. Viswanathan, G.; et al. *Biomacromolecules* **2006**, *7* (2), 415–418.
15. Rinaldi, R. *Chem. Commun.* **2010**, *47*, 511–513.
16. Pu, Y.; Jiang, N.; Ragauskas, A. J. *J. Wood Chem. Technol.* **2007**, *27*, 23–33.
17. Brandt, A.; Hallett, J. P.; Leak, D. J.; Murphy, R. J.; Welton, T. *Green Chem.* **2010**, *12*, 672–679.
18. Xie, H.; Zhang, S.; Li, S. *Green Chem.* **2006**, *7*, 630–633.

19. Xie, H.; Li, S.; Zhang, S. *Green Chem.* **2005**, *7*, 606–608.
20. Phillips, D. M.; Drummy, L. F.; Conrady, D. G.; Fox, D. M.; Naik, R. R.; Stone, M. O.; Trulove, P. C.; DeLong, H. C.; Mantz, R. A. *J. Am. Chem. Soc.* **2004**, *126* (44), 14350–14351.
21. Phillips, D. M.; Drummy, L. F.; Naik, R. R.; De Long, H. C.; Fox, D. M.; Trulove, P. C.; Mantz, R. A. *J. Mat. Chem.* **2005**, *15*, 4206–4208.
22. Remsing, R. C.; Swatloski, R. P.; Rogers, R. D.; Moyna, G. *Chem. Commun.* **2006**, *12*, 1271–1273.
23. Zhang, J.; Zhang, H.; Wu, J.; Zhang, J.; He, J.; Xiang, J. *Phys. Chem. Chem. Phys.* **2010**, *12*, 1941–1947.
24. Xu, H.; Pan, W.; Wang, R.; Zhang, D.; Liu, C. *J. Comput-Aided Mol. Des.* **2012**, *26*, 329–337.
25. Keten, S.; Xu, Z.; Ihle, B.; Buehler, M. J. *Nat. Mater.* **2010**, *9*, 359–367.
26. Haverhals, L. M.; Reichert, W. M.; De Long, H. C.; Trulove, P. C. *Macromol. Mater. Eng.* **2010**, *295*, 425–430.
27. Haverhals, L. M.; Sulpizio, H. M.; Fayos, Z. A.; Trulove, M. A.; Reichert, W. M.; Foley, M. P.; De Long, H. C.; Trulove, P. C. *ECS Trans.* **2010**, *33*, 79–90.
28. Haverhals, L. M.; Sulpizio, H. M.; Fayos, Z. A.; Trulove, M. A.; Reichert, W. M.; Foley, M. P.; De Long, H. C.; Trulove, P. C. *ECS Trans.* **2010**, *33*, 91–98.
29. Haverhals, L. M.; Sulpizio, H. M.; Fayos, Z. A.; Trulove, M. A.; Reichert, W. M.; Foley, M. P.; De Long, H. C.; Trulove, P. C. *Cellulose* **2011**, *19*, 13–22.
30. Haverhals, L. M.; Nevin, L. M.; Foley, M. P.; Brown, E. K.; De Long, H. C.; Trulove, P C *Chem. Commun.* **2012**, *48*, 6417–6419.
31. Bellayer, S.; Gilman, J. W.; Eidelman, N.; Bourbigot, S.; Flambard, X.; Fox, D. M.; De Long, H. C.; Trulove, P. C. *Adv. Funct. Mater.* **2005**, *15*, 910–916.
32. Gilman, J. W.; Awad, W. H.; Davis, R. D.; Shields, J.; Harris, R. H., Jr.; Davis, C.; Morgan, A. B.; Sutto, T. E.; Callahan, J.; Trulove, P. C.; De Long, H. C. *Chem. Mater.* **2002**, *14*, 3776–3785.
33. Usuki, A.; Kojima, Y.; Kawasumi, M.; Okada, A.; Fukushima, Y.; Kurauchi, T.; Kamigaito, O. *J. Mater. Res.* **1993**, *8*, 1179–1183.
34. Tyan, H. L.; Liu, Y. C.; Wei, K. H. *Chem. Mater.* **1999**, *11*, 1942–1947.
35. Messersmith, P.; Giannelis, E. P. *J. Polym. Sci. A: Polym. Chem.* **1995**, *33*, 1047–1057.
36. Gilman, J. W.; Kashiwagi, T.; Lichtenhan, J. D. *SAMPE J.* **1997**, *33*, 40–46.
37. Gilman, J. W. *App. Clay Sci.* **1999**, *15*, 31–49.
38. Gilman, J. W.; Jackson, C. L.; Morgan, A. B.; Harris, R., Jr. *Chem. Mater.* **2000**, *12*, 1866–1873.
39. Thomson, C. I.; Lowe, R. M.; Ragauskas, A. J. *Carbohyd. Polym.* **2007**, *69*, 799–804.
40. Zhang, J.; Lin, L.; Sun, Y.; Peng, H.; Pang, C.; He, B.; Liu, S.; Li, J.; Ouyang, P. *J. Biobased Mater. Bioenergy* **2009**, *3*, 69–74.
41. Proniewicz, L. M.; Paluszkiewicza, C.; Weseucha-Birczyska, A.; Majcherczyk, H.; Baraskia, A.; Konieczna, A. *J. Mol. Struct.* **2001**, *596*, 163–169.
42. Oh, S. Y.; Yoo, D. I.; Shin, Y.; Kim, H. C.; Kim, H. Y.; Chung, Y. S.; Park, W. H.; Youk, J. H. *Carbohydr. Res.* **2005**, *340*, 2376–2391.

43. Edwards, D. F.; Ochoa, E. *J. Opt. Soc. Am.* **1981**, *71*, 607–608.
44. Hind, A. R.; Bhargava, S. K.; McKinnon, A. *Adv. Colloid Interface Sci.* **2001**, *93*, 91–114.
45. Garvey, C.; Parker, I.; Simon, G. *Macromol. Chem. Phys.* **2005**, *206*, 1568–1575.
46. Pinkert, A.; Marsh, K.; Pang, S.; Staiger, M. *Chem. Rev.* **2009**, *109*, 6712–6728.

Chapter 7

Advanced Biopolymer Composite Materials from Ionic Liquid Solutions

Mirela L. Maxim,[1] Jacqueline F. White,[1,†] Leah E. Block,[1]
Gabriela Gurau,[1,2] and Robin D. Rogers[*,1]

[1]Center for Green Manufacturing and Department of Chemistry,
The University of Alabama, Tuscaloosa, Alabama 35487
[2]525 Solutions, Inc., 720 2nd Street, Box 861426, Tuscaloosa, Alabama 35486
[†]Current affiliation: Southview Middle School, 2605 Southview Drive,
Tuscaloosa, Alabama 35405
[*]E-mail: rdrogers@as.ua.edu

Advanced biocomposite materials from microcrystalline cellulose (MCC) and alginic acid (AA) were produced using 1-butyl-3-methylimidazolium chloride ([C_4mim]Cl) as the biopolymers' solvent. The effect of factors such as the mass ratio of cellulose and alginic acid in the materials as well as the soaking agent used for the removal of residual ionic liquid (IL) from them were evaluated. While the physical properties of the biopolymer blends (surface morphology, thermal properties, absorption capacity) were not affected by the increase in the AA content, the materials exhibited significant changes when aqueous 4.8 wt% $CaCl_2$ solution was used as soaking agent. Firstly, the surface morphology imaged by SEM showed increased porosity. The materials showed better thermal stability mainly due to the presence of Ca^{2+} ions in the blend. The mechanical properties of the composite fibers extruded by the dry-jet wet spinning process showed an increase in strain, but exhibited a significant decrease in strength. The soaking agent affected also the absorption capacity of the materials. The hydrophilic nature of the Ca^{2+} ions improved the absorption capacity significantly.

In Ionic Liquids: Science and Applications; Visser, A., et al.;
ACS Symposium Series; American Chemical Society: Washington, DC, 2012.

Introduction

There are a significant number of natural biopolymers available in nature (both on land (*1*) and in the marine environment (*2*)) that are currently underutilized due to their recalcitrance to dissolution in traditional solvents without derivatization or degradation. Ionic liquids (ILs), which by definition are salts with melting points below 100 °C, have been found to dissolve many of these natural biopolymers (e.g., silk fibroin (*3*), wool keratin (*4*), starch (*5*), chitin (*6*–*8*) wood (*9*) and konjac glucomannan (*10*), to name only a few).

The medical textiles field, specifically wound management products sector, is continuously growing, and new emerging technologies allow access to advanced or well-known materials with improved properties. There is a constant need to design fibers and dressings with improved efficacy, while still retaining key properties such as being highly absorbent, hemostatic, biocompatible, and having good mechanical behavior (*11*). Biopolymers that have some or all of these characteristics are naturally occurring, but they are either difficult to process in their natural form, or once processed lack some of the crucial properties needed in wound care (e.g., strength or high absorbency) due to their molecular degradation. One of these biopolymers, alginic acid, is widely used as a gel dressing in wound care (*12*).

During the last two decades, alginate fibers have been used as high-tech wound dressings (*13*, *14*), not only because they provide an ideal moist healing environment (*15*) (proven by clinical trials), but also they promote wound healing (*16*). Alginic acid (Figure 1) is obtained from brown seaweed that consists of residues of β-1,4-D-mannuronic acid and α-1,4-L-guluronic acid (*17*) The technological process to obtain the alginate fibers is relatively expensive requiring multiple processing steps (*12*) Since alginic acid is not soluble in water and most organic solvents, the large scale production of the alginate fibers involves the use of alginate metal salts, most commonly sodium, calcium, and silver.

Alginate fibers are non-toxic, non-carcinogenic, non-allergic, hemostatic, biocompatible, of reasonable strength, capable of being sterilized, and can be easily manipulated to incorporate medications (*11*, *18*, *19*). The major limitation for wider use in medical wound management is their poor mechanical properties. Cellulose, as a structurally sound biopolymer and highly biocompatible (Figure 1), if blended with alginic acid could help reinforce the alginate fibers.

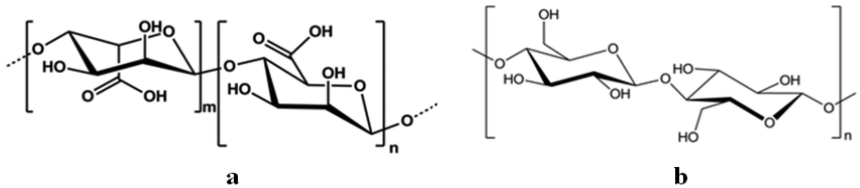

Figure 1. Chemical structure of alginic acid with its residues (1-4)-linked β-D-mannuronate (M) and (1-4)-linked α-L-guluronate (G) (a) and cellulose (b).

In our quest to develop cellulose/alginate biocomposite materials suitable for the wound care sector, we have chosen to take advantage of the ability of ILs to dissolve almost any type of biomass. ILs offer a unique opportunity for controlled processing of natural and synthetic polymers (*20*) and facilitate dispersion of various additives – particles with magnetic (*21*) or antimicrobial properties (*22*), enzymes (*23*), molecular sensors (*24*), or macromolecular inclusions (*25*) that increase the functionality and value of the final product. Another example of cellulose bioactive composite fibers obtained via IL route is heparin (anticoagulant) blended with cellulose with applications in human blood dialysis (*26*, *27*).

Here we discuss our work to utilize 1-butyl-3-methylimidazolium chloride ([C_4mim]Cl, Figure 2), to co-dissolve and process cellulose and alginic acid blended fibers. The continuing goal is to develop highly absorbent cellulose-alginic acid blends that retain the gel-swelling ability of the alginic acid and at the same time have good mechanical properties conferred by the cellulose structural polymer matrix.

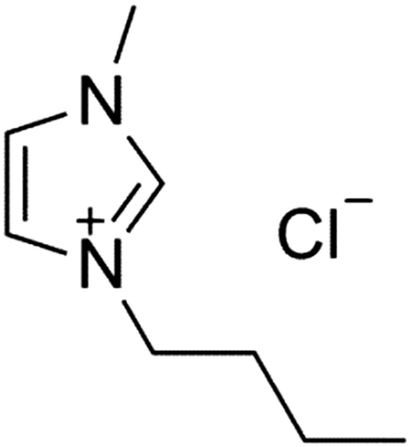

Figure 2. Chemical structure of 1-butyl-3-methylimidazolium chloride ([C_4mim]Cl).

Experimental

Materials

The ionic liquid, 1-butyl-3-methylimidazolium chloride ([C_4mim]Cl) with more than 90% purity was provided by BASF (Florham Park, NJ) and used as solvent for biopolymers. Microcrystalline cellulose (MCC) and alginic acid (AA) with 61% mannuronic and 39% guluronic residues were purchased from Aldrich (Milwaukee, WI) and dried in vacuum oven at 70 °C for 12 h prior to use.

Deionized (DI) water from an in-house water purifier (Culligan, Northbrook, IL) was used for the fibers regeneration bath. The removal of residual IL was made by soaking the regenerated fibers overnight in DI water or 4.8 wt% aqueous solution of $CaCl_2$ (solid pellets of ACS certified grade with 75.9% purity purchased from Fisher Scientific, Pittsburgh, PA). DI water and aqueous solution of 0.9 wt% NaCl with 98.6% purity (Fisher Scientific, Pittsburgh, PA) were used to evaluate the absorption capacity of the fibers.

All the chemicals used for washing or purification of the materials were commercial grade and used as received from the chemicals suppliers.

Standard Powder Mixture

A total mass of 1 g of alginic acid and microcrystalline cellulose powders with MCC:AA mass ratios of 95:5, 90:10, 85:15, 75:25, and 50:50 were mixed in plastic 20 mL vials using the vortex. The mixtures were characterized by FTIR spectroscopy to identify the changes in the mixture structure with increasing alginic acid load and their thermal behavior was studied using thermogravimetric analysis.

Solubility of Alginic Acid in Ionic Liquid

The IL, $[C_4mim]Cl$, which is solid at room temperature, was firstly melted at 90 °C for 30 min in a Precision Scientific Econotherm Laboratory Oven, Model 1025 (Winchester, VA). The alginic acid powder was added in small increments (0.1 g) to the melted ionic liquid (10 g) and stirred vigorously. The mixture was heated repeatedly using microwave irradiation with 3 s pulses until complete dissolution was achieved (monitored by optical microscopy). The process was repeated until the solution became saturated with alginic acid. **[CAUTION: Care must be taken as the IL/biopolymer solution overheating can cause degradation and burning of the cellulose. Special heat gloves need to be used when handling glass vials with solutions heated in the microwave].**

Preparation of the Spinning Solution

The preparation steps of the spinning solution for plain and composite materials are shown in Figure 3. The biopolymer/IL solution concentrations are reported throughout the paper as the mass ratio (as a percent) of the biopolymers in 10 g of IL, while the MCC:AA ratios are referred as mass ratios. Microcrystalline cellulose powder (10%) was added to the melted IL and the mixture was vortexed for one minute to ensure uniform dispersion of cellulose powder in the solvent. The resulting mixture was heated by means of microwave irradiation for ca. 1.5 min with 3 s pulses and manual stirring in between pulses until complete dissolution.

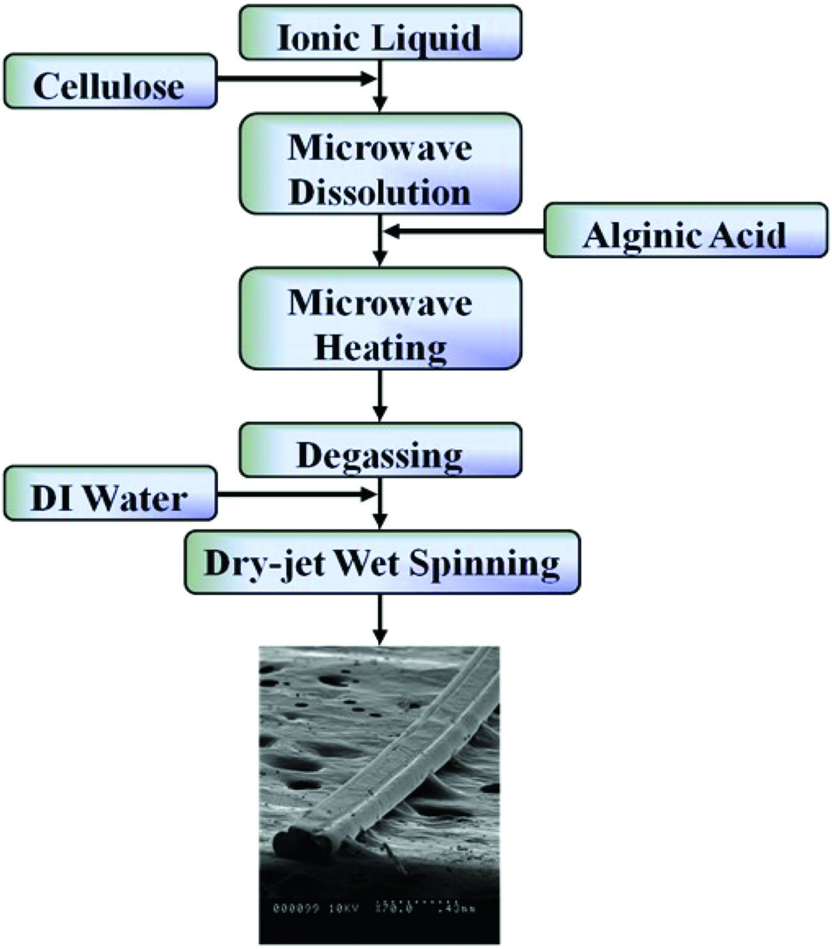
Ionic Liquid
Cellulose
Microwave Dissolution
Alginic Acid
Microwave Heating
Degassing
DI Water
Dry-jet Wet Spinning

Figure 3. Schematic representation of the MCC:AA preparation process.

For the biopolymer composite solutions, the alginic acid powder was added to the MCC/IL solution in different ratios relative to the MCC load after complete dissolution of cellulose was achieved. The solution was homogenized by vigorous mixing and heating in the microwave for ca. 1 min using 3 s pulses (to avoid overheating of the mixture). The final compositions of the prepared solutions of cellulose to alginic acid (MCC:AA mass ratio) were: 100:0, 90:10, and 75:25 for films, and 100:0, 95:5, 90:10, and 85:15 for fibers. The solution was then degassed by centrifugation for 3-5 min using a Clay Adams Brand, Dynac Centrifuge, Model 420101/2, Becton Dickinson & Co. (Sparks, MD) at a speed of approximately 2900 rpm.

]

Preparation of the Composite Materials

All fibers were spun using a dry-jet wet spinning experimental apparatus we have previously used to prepare cellulose and cellulose composite fibers (*21*, *22*). The MCC:AA:IL solutions were poured into a 20 mL plastic syringe. The syringe was wrapped in a heating jacket (with controlled temperature – 70 °C – to ensure uniform fluidity of the solution) and placed on the syringe pump. The syringe tip was at 5 cm distance from the DI water bath to facilitate the proper extrusion of the fiber before regeneration. Godets were used for fiber stretching, guidance, and washing in the DI water bath, and a take-up spool was used to collect the regenerated fiber. The parameters of the fiber extrusion set-up were adjusted based on previous studies (*21*, *22*) to ensure the production of thin continuous fibers (godets voltage – 3.4 V; spooler voltage – 3.2 V; extrusion rate – 0.8 mL/min). After extrusion, the fibers were soaked overnight in water or aqueous 4.8 wt% $CaCl_2$ solution and air dried at room temperature for two days.

The composite films were prepared from MCC:AA solutions obtained using the same method as for the fibers. After degassing, the solutions were poured on a glass plate and the films were cast using a metal rod size RDS 20. The thickness of the film was controlled by guiding the casting rod on a metal frame placed on top of the glass plate. The films were regenerated on the glass plate using water or aqueous 4.8 wt% $CaCl_2$ solution and soaked in the regeneration solvent overnight to remove the residual ionic liquid.

Characterization Methods

Scanning Electron Microscopy (SEM)

The surface morphology and the cross-section of the fibers was analyzed by SEM using a Hitachi S-2500 SEM (Hitachi High-Technologies Pte Ltd, Singapore) operated at 10 kV accelerating voltage. The samples were mounted on aluminum stubs and then sputter-coated with silver and palladium to make them conductive, thus avoiding charge build-up and degradation.

Fourier Transform Infrared Spectroscopy (FTIR)

Infrared spectroscopy was used to qualitatively evaluate the interactions between the biopolymers before and after their dissolution in ionic liquid. Standard powder mixtures of cellulose and alginic acid were prepared with MCC:AA mass ratios of 0:100, 50:50, 75:25, 85:15, 90:10, 95:5, and 100:0. The powder mixtures were dried, homogenized, placed on the sample holder and pressure was applied to record the spectra of each sample. The films were cut in 0.5 cm pieces and analyzed using a PerkinElmer Spectrum 100 FTIR spectrometer (Waltham, MA) equipped with an attenuated total reflectance (ATR) cell with 4 scans at 2 cm^{-1} resolution.

Thermal Analysis (TGA)

The thermal stability of the standard powder mixtures and the fibers was studied using a 2950 Thermogravimetric Analyzer from TA Instruments (New Castle, DE). The standard powder mixtures were dried in a vacuum oven (12 h at 70 °C) prior to thermal analysis. Fibers were air dried and cut into approximately 1 mm pieces. The samples were loaded into an aluminum pan and subjected to 5 °C/min temperature ramp over a range from room temperature up to 600 °C. An isothermal step of 30 min at 90 °C was used to remove all the moisture from the samples. The furnace chamber was continuously purged with air during the analyses.

Mechanical Properties

A minimum of four test samples of uniform cross section from each category of fibers were visually screened for defects and measured at five different sections of the fiber to calculate the average diameter of each individual fiber sample. An MTS Q-Test 25 machine (MTS, Eden Prairie, MN) was used to determine the tensile properties of the fibers. The fibers were placed in a specially designed pneumatic grip with the gauge length of 7.62 cm that was suitable for testing thin and flexible fibers. The fibers were subjected to a gradual increase of load at a crosshead speed of 0.05 in/min using a 5 lb capacity load cell. The measurement data were recorded using a data acquisition system for stress and strain.

Absorption Capacity

A known amount of alginic acid (0.5 g) was mixed with 20 mL of DI water in a vial and mixed well by vortexing. The mixture was left to sit for an hour and then centrifuged for 15 min at the highest speed. The water layer was decanted (using a pipette), and the amount of the swollen alginic acid was determined gravimetrically. The absorption capacity of alginic acid was calculated using eq. (1) and represents the ratio of absorbed water to dry alginic acid powder weight multiplied by 100%.

$$\%\ \text{absorption capacity} = \{(\text{wet weight} - \text{dry weight})/\text{dry weight}\} \times 100\% \qquad (1)$$

The absorption capacity (*17*) for the plain cellulose and composite materials was determined according to the standard protocol from British Pharmacopoeia Monograph for Alginate Dressings and Packings (*28*). A known dry amount of composite material was placed in a flat bottom Petri dish (Φ = 90 mm) that contained a swelling agent (DI water or 0.9 wt% NaCl) of a quantity 40 times the weight of the material. The sample was allowed to sit in the swelling agent for 30 min at room temperature and then it was lifted by one end and held in air for 30 s before the weight was measured. Percent absorption capacity was calculated using eq. (1) and represents the ratio of absorbed water to dry fiber weight multiplied by 100%.

Results and Discussion

Characterization Methods

Scanning Electron Microscopy (SEM)

The surface morphology of the plain and composite fibers was analyzed by SEM. All the fibers retain the circular shape of the syringe tip and are uniform in thickness. Figures 4 and 5 show fibers regenerated and soaked overnight in DI water (to remove the residual IL), or soaked in aqueous 4.8 wt% $CaCl_2$ solution after regeneration in DI water. After regeneration and overnight soaking in DI water, only some fine surface defects were observed over the length of the plain fiber (Figure 4a, b) which are most probably due to the roughness on the inside of the syringe tip. By increasing the AA concentration (Figure 5a, b), apart from defects caused by the syringe tip, the surface of the fibers are fairly smooth, probably due to AA's gel-like appearance after swelling.

The surface morphology of the plain and composite fibers changes when 4.8 wt% $CaCl_2$ is added to the final washing solution. The surface of the fibers becomes rough and small cracks are visible, although it does not seem to affect the integrity of the fibers (Figure 4a′, b′). The composite fibers (Figure 5a′, b′) have a slightly rougher surface and increase in surface area most likely due to the overnight treatment of the fibers with $CaCl_2$ solution and possible alkali metal coordination with carboxyl groups from carbohydrates forming 'pseudo bridged' unidentate arrangements, as reported by others (*29–31*).

Fourier Transform Infrared Spectroscopy (FTIR)

Infrared spectroscopy (IR) was used to identify the interactions between cellulose and alginic acid before and after dissolution in the IL. Standard powder mixtures were prepared using different ratios of MCC:AA, in order to better visualize the appearance of the IR frequency bands with increase of alginic acid concentration. As expected, the C=O stretch at 1728 cm^{-1} characteristic of a carboxylic acid is can be seen increasing in intensity with addition of alginic acid to the mixture (Figure 6).

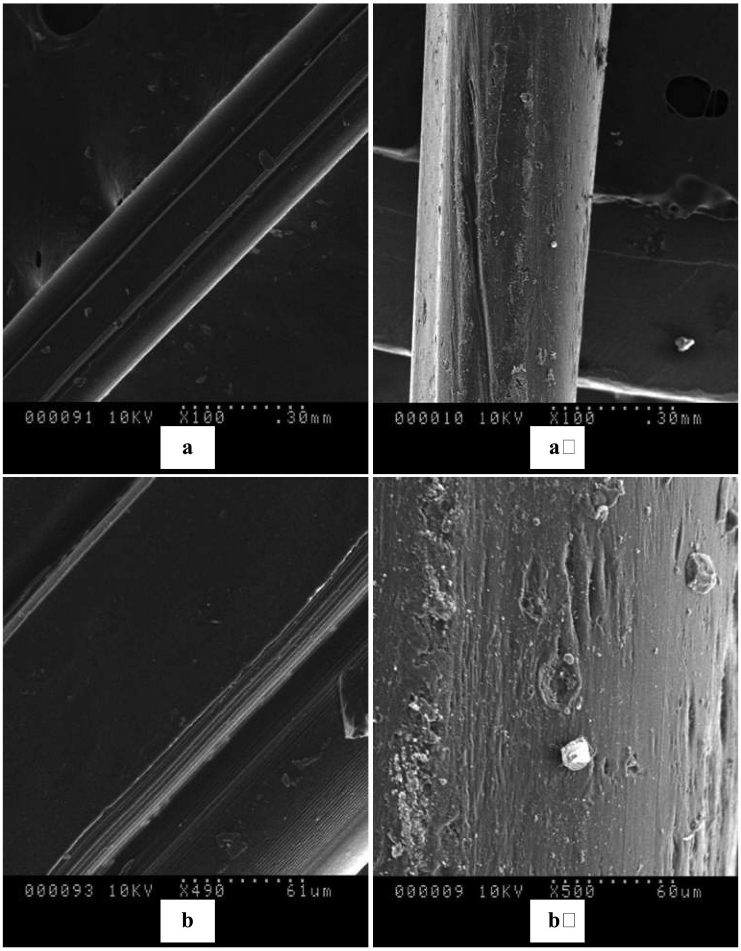
000091 10KV X100 .30mm
a
000010 10KV X100 .30mm
a□
000093 10KV X490 61um
b
000009 10KV X500 60um
b□

Figure 4. SEM images of pure MCC fibers soaked in DI water (left) and aqueous 4.8 wt% $CaCl_2$ (right).

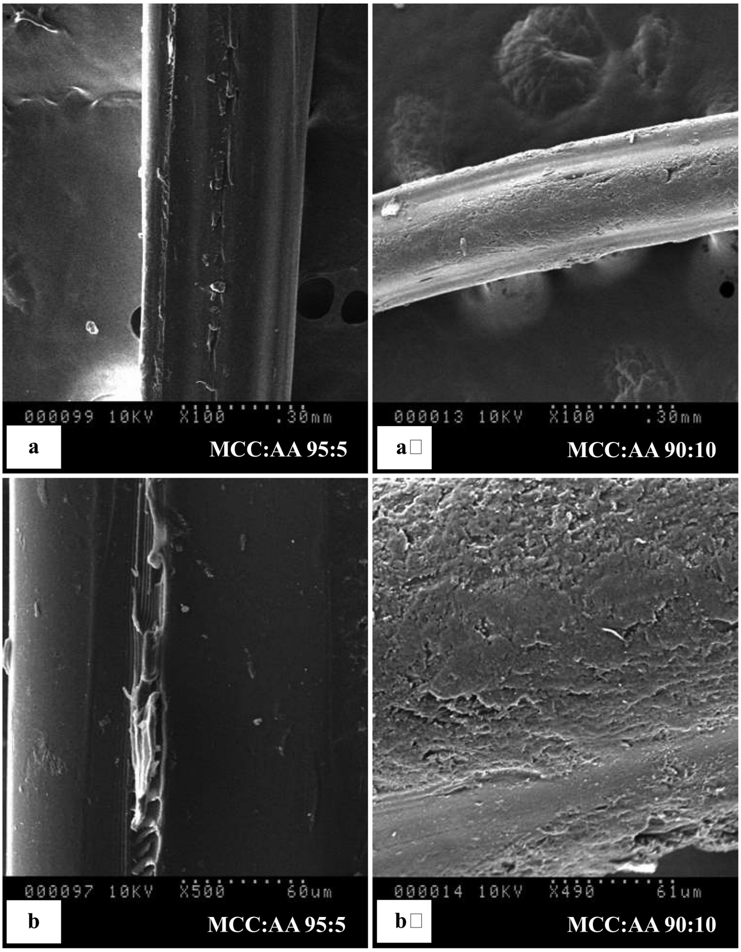
000099 10KV X100 .30mm
a
MCC:AA 95:5
000013 10KV X100 .30mm
a□
MCC:AA 90:10
000097 10KV X500 60um
b
MCC:AA 95:5
000014 10KV X490 61um
b□
MCC:AA 90:10

Figure 5. SEM images of MCC:AA fibers soaked in DI water (left) and aqueous 4.8 wt% $CaCl_2$ (right).

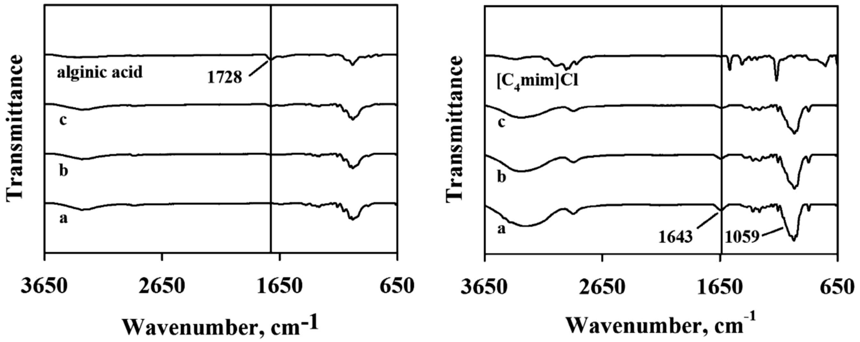

Figure 6. FTIR spectra for MCC:AA standard powder mixtures (left) and films soaked in DI water (right); MCC:AA ratios: (a) 100:0; (b) 90:10; (c) 75:25.

A comparison with the IR of the pure IL shows no residual IL left in the MCC:AA films. The representative cellulose band around 1059 cm^{-1} is very intense for each composite sample and its intensity is consistent with the concentration of MCC in the fiber composite. This peak represents the C-O-C pyranose ring skeletal vibration (*32*) and the C-O stretching vibration found in cellulose and hemicelluloses (*33*).

The MCC:AA films regenerated and soaked in aqueous 4.8 wt% $CaCl_2$ solution were also analyzed by FTIR and compared with the calcium alginate salt (Figure 7). The 1728 cm^{-1} C=O stretch characteristic of the carboxylic group in alginate acid has shifted to lower wavelength, that might indicate an interaction between the alginic acid and the calcium salt, similar to what has been observed by Papageorgiou *et al.* (*29*).

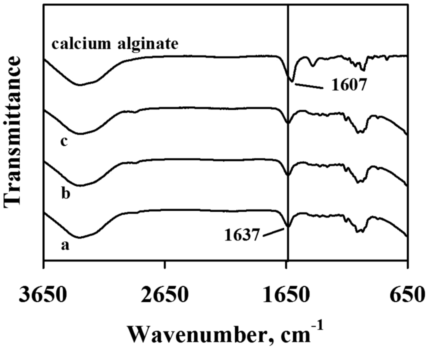

Figure 7. FTIR spectra for MCC:AA films soaked in 4.8 wt% $CaCl_2$ solution; MCC:AA ratios: (a) 100:0; (b) 90:10; (c) 75:25.

Thermal Analysis (TGA)

The thermal stability of the standard powder mixtures in known MCC:AA ratios and that of the starting materials were studied by thermogravimetric analysis to determine any changes in the decomposition temperature due to the interactions between the two biopolymers. There is an obvious temperature and slope difference between the starting materials – microcrystalline cellulose and alginic acid powders, as depicted in Figure 8a. While cellulose has a very steep decomposition around 300 °C, pure alginic acid has a lower decomposition point around 150 °C which confirms the results from Soares *et al.* (*34*) where these authors studied alginic acid and its sodium salt under atmospheric pressure and showed a small slope decomposition curve over a large temperature range from 150 to 450 °C.

The different standard powder mixtures partially retain the behavior of cellulose and alginic acid under heating conditions based on the different ratios of the biopolymer contained by the mixture. Therefore, it is not surprising that the decomposition temperature decreases with higher content of alginic acid and also the steepness of the slope decreases gradually.

A similar change in the thermal behavior of the composite fibers (MCC:AA 85:15) regenerated and soaked in DI water, compared to the plain cellulose fibers is observed (Figure 8b). There is a slight decrease in the decomposition temperature of the composite and also a slope attenuation of the decomposition curve with increasing temperature. The change is very similar to the thermal behavior of the standard powder mixture for MCC:AA 75:25 ratio and the small difference between the decomposition temperatures for the plain and composite materials may be attributed to the low concentration of alginic acid in the composite material.

The thermal behavior for the fibers regenerated in DI water and soaked overnight in 4.8 wt% $CaCl_2$ solution are shown in Figure 8c as typical decomposition curves for the calcium alginate salts, complementing our IR results which indicate that Ca^{2+} ions interact with alginic acid. According to the literature, the calcium alginate materials have a two step decomposition curve over a wide range of temperatures from 200 to 545 °C (*35*). Specifically calcium alginate has a decomposition curve with less weight loss over the temperature range compared to alginic acid and its sodium salt. Our data (Figure 8c) show that both plain cellulose and composite fibers have similar behavior in weight loss and decomposition. The obvious conclusion is that the content of calcium in the fiber prevents its fast pyrolysis even though it has high cellulose content. Therefore, the fibers with or without alginic acid soaked in $CaCl_2$ aqueous solution exhibit stable thermal behavior over a wide temperature range with low weight loss and thick residues that can successfully inhibit the heat transfer within the fiber (*36*).

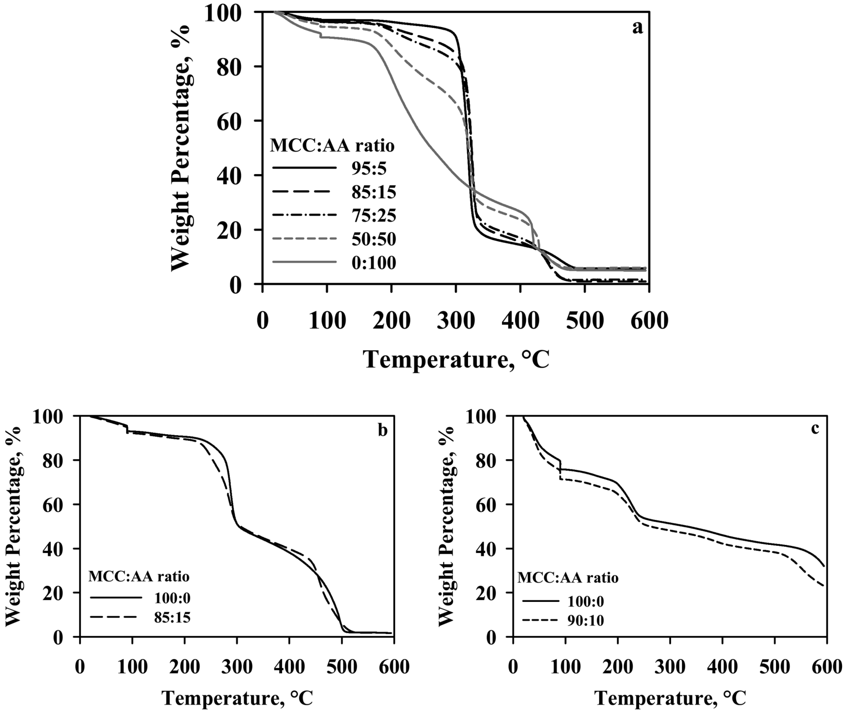

Figure 8. Thermal analysis of (a) MCC:AA standard powder mixtures, (b) fibers soaked in DI water, and (c) fibers soaked in 4.8 wt% $CaCl_2$.

Mechanical Properties

The mechanical properties of the MCC:AA fibers were tested to evaluate if the incorporation of alginic acid in the cellulose matrix allowed interaction between the two biopolymers and provided any enhancement of the material strength or strain.

The MCC:AA fibers were tested for ultimate tensile strength, which is the maximum stress that a material can undertake before it breaks. The tensile strength measures the applied force at which a material can no longer maintain its structural reliability. At the same time the strain of the materials was measured to determine the maximum elongation at break, expressed in percent strain of the gauge length. Fibers with various MCC:AA ratios that were regenerated and soaked in DI water were tested and the representative stress-strain curves are shown in Figure 9. By varying the MCC:AA ratio the cellulose content in the fibers was gradually decreased which means that for an accurate comparison control fibers with the same cellulose content were needed.

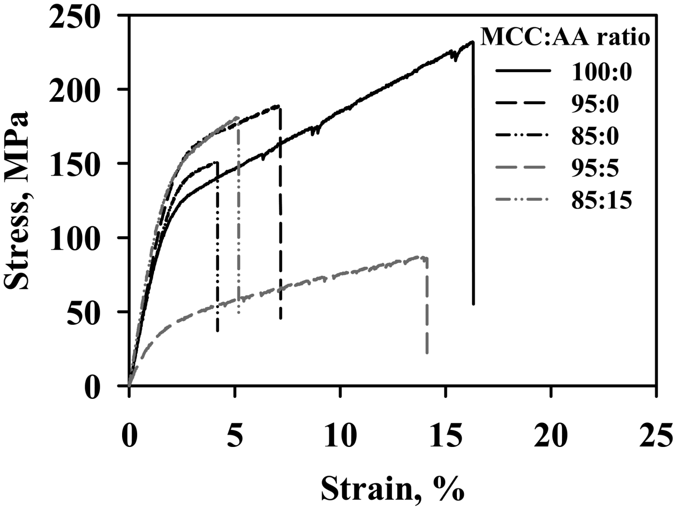

Figure 9. Stress-strain representative curves for MCC:AA fibers soaked in DI water.

It can be observed that the plain cellulose fibers decrease in strength and strain with decreasing cellulose concentration. Since cellulose is a structural polymer it is important to have enough cellulose content to regenerate the polymer chains and create the structure of the fiber. For the composite fibers, it was expected that some interaction would occur between cellulose chains and alginic acid residues. It can be seen in Figure 9 that the fibers with MCC:AA 85:15 ratio exhibit the same ultimate stress as the plain cellulose fibers MCC:AA 95:0. At the same time, they are stronger than the plain fibers with the same cellulose concentration (MCC:AA 85:0). These results suggest that the alginic acid residues in the fiber with the highest alginic acid content interact at a molecular level with cellulose and form a stronger structure. In order to understand the behavior of the polymer composite during the tensile testing, SEM imaging was used at the fracture point of the fiber for the fibers with MCC:AA ratios of 100:0, 95:5, and 85:15 (Figure 10).

The polymer layers converge to the breaking point (as indicated by the two arrows) at both ends of the fiber as can be observed in Figure 10a and a′. The fiber in the image is a plain cellulose fiber with MCC:AA ratio of 100:0. The layers are very tight and homogeneous, but this is not only a factor of polymer capacity to homogeneously regenerate, but also depends on the blend preparation and degassification before fiber extrusion.

The images in Figure 10b, b′, c, and c′ show the neck formation when the fibers are subjected to a constant load increase. It seems that during testing the polymer layers slipped on top of each other until they broke, suggesting that the polymer blend was not homogeneous and failure points were created. Neck formation is expected in the deformation of the polymers, this being one of their characteristics.

The stress-strain curves shown in Figure 9 indicate that the 95:5 MCC:AA fiber almost reaches the strain percentage observed for the plain 100:0 cellulose fiber, but its stress is much lower compared to all the other fibers. This suggests that the failure and permanent deformation of the fiber occurred very early in the testing process for this particular fiber.

The images in Figure 10 were taken at different magnifications in order to better observe the separation of the layers and the breaking point of the fiber. In Figure 10c and c′ the two matching ends of a broken fiber (MCC:AA 85:15) can be recreated like a puzzle. This fiber could sustain almost as much stress as the fiber with higher cellulose content (85:15 MCC:AA fiber *vs.* 95:0 MCC:AA fiber), but its elongation was visibly affected probably due to the lack in structural polymer chains from the cellulose.

The representative stress-strain curves for the MCC:AA fibers regenerated in water and soaked overnight in 4.8 wt% $CaCl_2$ solution are shown in Figure 11. These fibers' mechanical properties are quite different to the fibers soaked in DI water. Their strength significantly decreased and remained relatively constant for all fiber concentrations, but they have higher strain compared to all the fibers soaked in DI water. Specifically the plain MCC fiber soaked in aqueous $CaCl_2$ has a high percentage strain and during testing it formed the characteristic necking of the polymers. It underwent a lot of stretching and thinning before the breaking finally occurred. The other fibers with MCC:AA ratios of 95:5 and 90:10 can sustain little stress and the percentage strain is better than for fibers soaked in DI water.

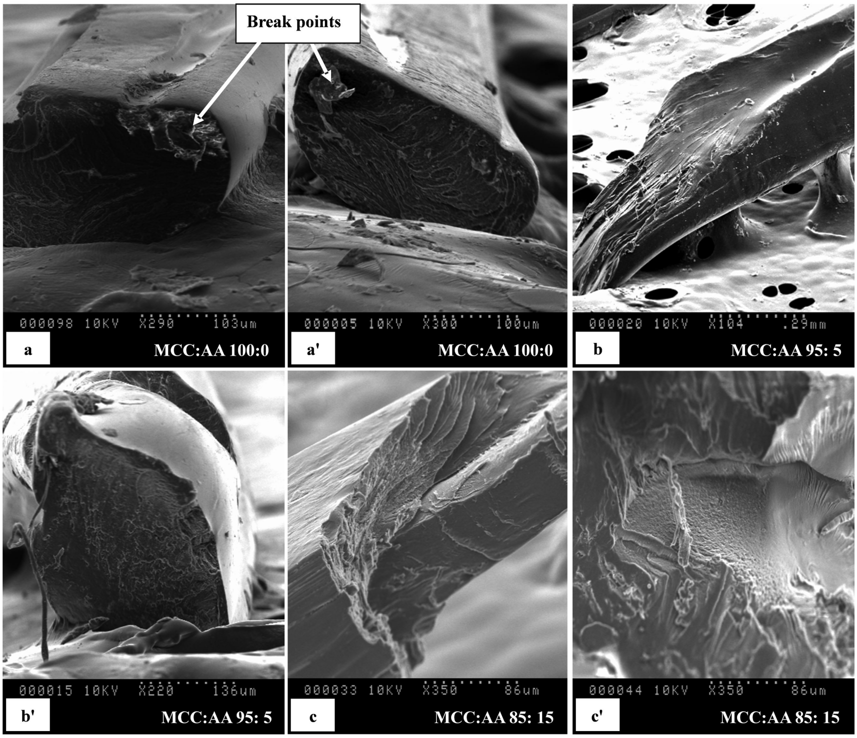
Break points
000098 10KV X290 103um
a
MCC:AA 100:0
000005 10KV X300 100um
a'
MCC:AA 100:0
000020 10KV X104 .29mm
b
MCC:AA 95: 5
000015 10KV X220 136um
b'
MCC:AA 95: 5
000033 10KV X350 86um
c
MCC:AA 85: 15
000044 10KV X350 86um
c'
MCC:AA 85: 15

Figure 10. SEM images of the cross-section at the fracture point for MCC:AA fibers soaked in DI water.

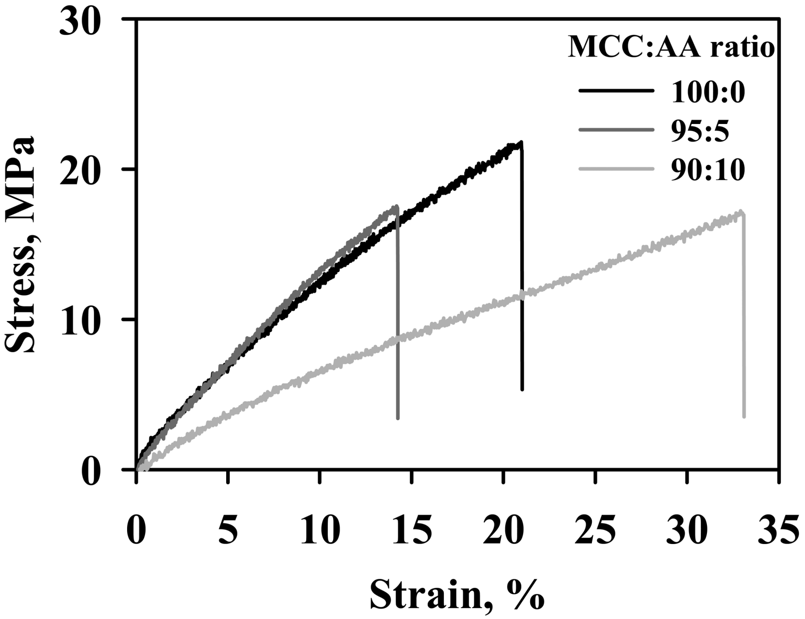

Figure 11. Representative stress-strain curves for MCC:AA fibers soaked in aqueous 4.8 wt% $CaCl_2$.

Images representing the cross-section of the failure point for the MCC:AA fibers washed in an aqueous 4.8 wt% $CaCl_2$ are illustrated in Figure 12. The composite fibers with MCC:AA ratios of 95:5 and 90:10 show a slight separation of the layers that can be interpreted as a non-homogeneous blend. Qin (*17*) and others (*37*, *38*) found that the alginic acid rich in mannuronic (M) residues are most likely to self-associate rather than coordinate with a metal or with another polymer chain to form a complex. In our case, alginic acid has a majority of M residues (61%), which can lead to the formation of the non-homogeneous regions within the cellulose matrix and also contribute to the increase in the fibers strain.

The average values for the stress and strain of all fibers tested with corresponding standard deviations expressed by error bars are presented in Figure 13. The fibers soaked overnight in DI water have higher stress than the fibers soaked in $CaCl_2$ solution, while the latter exhibit higher strain. At the same time, it seems that each type of fibers has an optimal MCC:AA ratio (85:15 for fibers soaked in DI water and 90:10 for fibers soaked in aqueous $CaCl_2$) that show improvement in strength and strain respectively, compared to the fibers with other ratios.

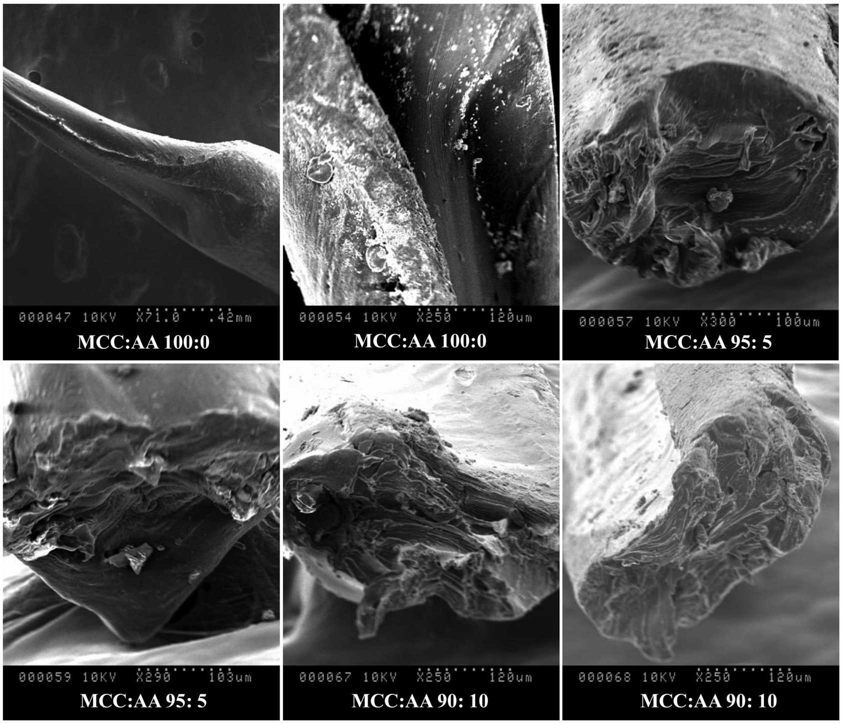
000047 10KV X71.0 .42mm
MCC:AA 100:0
000054 10KV X250 120um
MCC:AA 100:0
000057 10KV X300 100um
MCC:AA 95: 5
000059 10KV X290 103um
MCC:AA 95: 5
000067 10KV X250 120um
MCC:AA 90: 10
000068 10KV X250 120um
MCC:AA 90: 10

Figure 12. SEM images of the cross-section at the fracture point for MCC:AA fibers soaked in aqueous 4.8 wt% $CaCl_2$.

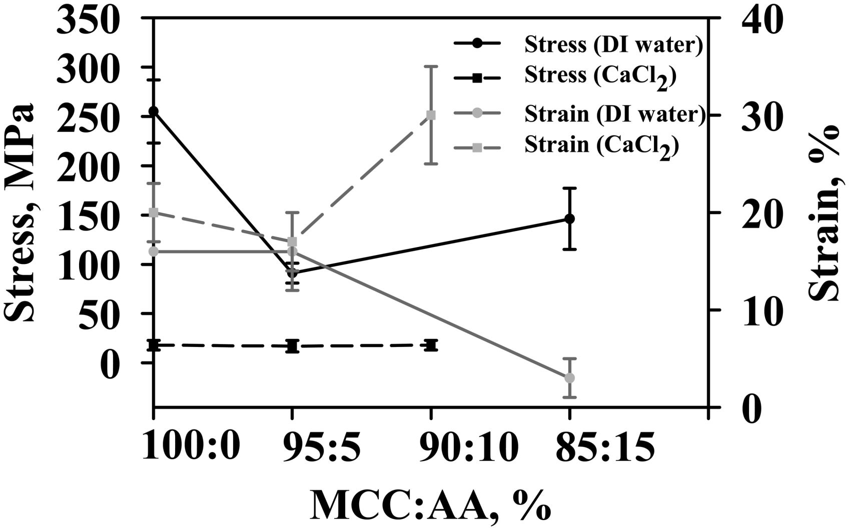

Figure 13. Average stress (black line) and strain (grey line) values for the MCC:AA fibers soaked in DI water (solid line) and aqueous 4.8 wt% $CaCl_2$ (dashed line) for various MCC:AA ratios.

Absorption Capacity

The absorption capacity for the original alginic acid powder was determined using the same method as for the films and fibers; calculated as the ratio between absorbed water to dry alginic acid powder multiplied by 100%. The absorption capacity of the alginic acid powder was 482% for 0.5 g starting material. The literature (*39*) reports that the absorption capacity exceeds 300% depending mostly on the composition of the polymer (mannuronic and guluronic residues).

The absorption capacities for the plain and composite films and fibers do not show a specific trend based on the alginic acid content in the materials. However, a significant difference is observed between materials that were soaked in DI water *vs.* those soaked in $CaCl_2$ solution after regeneration. Due to the strong hygroscopic nature of $CaCl_2$ all materials that have been in contact with $CaCl_2$ show a high absorption capacity regardless of their theoretical alginic acid content (Table 1). The swelling agent used for absorption measurements was either DI water or 0.9 wt% NaCl solution (to mimic the body exudates that are normally found in wounds).

Table 1. Absorption capacity for MCC:AA films and fibers

	FILMS				FIBERS	
	Absorption capacity for DI water,%		Absorption capacity for 0.9 wt% NaCl,%		Absorption capacity for DI water,%	
MCC:AA mass ratio, % / Regeneration Solvent	DI water	4.8 wt% $CaCl_2$	DI water	4.8 wt% $CaCl_2$	DI water	4.8 wt% $CaCl_2$
100:0	35	231	-	132	99	232
95:5	33	398	45	169	63	170
90:10	62	305	-	176	-	240
85:15	49	182	91	166	73	-

According to the literature (*17*), the absorption capacity of the calcium alginate materials varies depending on their content of mannuronic and guluronic residues. The materials with high mannuronic content tend to form weaker and softer gels when in contact with body exudates (which contain Na+ ions) and have a higher Ca^{2+} – Na^+ ion exchange capacity compared to materials with high guluronic content. This is attributed to the ability of mannuronic residues to weakly bind calcium, facilitating the ion exchange between Ca^{2+} and Na^+ (*17*).

The alginic acid powder used in this study has high mannuronic (61%) and low guluronic residues (39%), which confers it the ability to weakly bind calcium ions. The MCC:AA films and fibers soaked in water after regeneration have relatively low absorption values for both swelling agents (DI water or 0.9 wt% NaCl). The change in absorption values is not consistent with the increase of alginic acid content in the material which indicates that some of the alginic acid may have been washed out of the material during the processing and soaking steps.

On the contrary, the films soaked in aqueous $CaCl_2$ solution after regeneration showed large absorption values for both swelling agents, although a certain affinity for DI water as the swelling agent is observed. As mentioned before, this selectivity can be attributed to the hygroscopic nature of $CaCl_2$, but because the fact that the absorption capacity of the films decreases as the content of alginic acid increases might suggest that there is an interaction between alginic acid and calcium ions. On the other hand, when NaCl is used as a swelling agent for the plain cellulose film (MCC:AA 100:0) the absorption capacity is relatively low compared to the films that were swelled with DI water. However, with increased content of alginic acid the absorption values increase slightly and remain constant for the MCC:AA composite films with different ratios. This result may reflect the ion exchange between the Ca and Na ions which reaches equilibrium and hinders a significant increase of the absorption capacity.

The absorption capacity results for MCC:AA fibers swelled in DI water were slightly higher compared to the results for the films. No specific trend was observed for the fibers with various MCC:AA ratios. The effect of the soaking agent was seen for the fibers as well: the absorption values were small for the fibers soaked in DI water and high for the ones soaked in aqueous $CaCl_2$ solution.

Conclusions

Cellulose/alginic acid materials were successfully prepared as films and fibers from [C_4mim]Cl solution. The materials soaked in aqueous $CaCl_2$ solution show very good absorption capacity, but there was no clear connection between the alginic acid content and the absorption values. In addition, the thermal stability of the materials soaked in $CaCl_2$ solution were close to the flame-retardant materials, which gives them additional value. It was found that there is an optimal MCC:AA ratio at which the materials exhibit good mechanical properties. Future research is directed toward the preparation of composite materials of alginic acid in combination with other natural biopolymers (*e.g.* chitin), with the optimal chitin to alginic acid ratio where the materials exhibit prime mechanical, physical and biological properties. In order for these materials to be accepted by the wound care sector as wet dressings, biocompatibility and efficacy studies would need to be performed. In addition, further analysis needs to be conducted regarding the ion exchange ability between the materials and body exudates, as well as the improved homogeneity of the biopolymer blend.

Acknowledgments

This work was partially supported by Alabama EPSCoR Research Infrastructure Improvement Project (EPS-0814103), and 525 (NSF SBIR award No. IIP-1143278). Jacqueline F. White was funded in part by an NSF REU award (CHE 0647789) to the Department of Chemistry at The University of Alabama. We also thank Dr. Kim Lackey, Manager Coordinator/Instructor at Optical Analysis Facility, Department of Biological Sciences, The University of Alabama for assistance with SEM imaging.

References

1. French, A. D.; Bertoniere, N. R.; Brown, M. R.; Chanzy, H.; Gray, D.; Hattori, K.; Glasser, W. In *Kirk-Othmer Encyclopedia of Chemical Technology*; Kroschwitz, J. I., Ed.; Wiley: New York, 2001; Vol. 5, pp 360−394.
2. Bartlett, D. H.; Azam, F. *Science* **2005**, *310*, 1775–1777.
3. Phillips, D. M.; Drummy, L. F.; Conrady, D. F.; Fox, D. M.; Naik, R. R.; Stone, M. O.; Trulove, P. C.; De Long, H. C.; Mantz, R. A. *J. Am. Chem. Soc.* **2004**, *126*, 14350–14351.
4. Xie, H.; Li, S.; Zhang, S. *Green Chem.* **2005**, *7*, 606–608.
5. Biswas, A.; Shogren, R. L.; Stevenson, D. G.; Willett, J. L.; Bhowmik, P. K. *Carbohydr. Polym.* **2006**, *66*, 546–550.
6. Xie, H.; Zhang, S.; Li, S. *Green Chem.* **2006**, *8*, 630–633.
7. Wu, Y.; Sasaki, T.; Irie, S.; Sakurai, K. *Polymer* **2008**, *49*, 2321–2327.
8. Qin, Y.; Lu, X.; Sun, N.; Rogers, R. D. *Green Chem.* **2010**, *12*, 968–971.
9. Sun, N.; Rahman, M.; Qin, Y.; Maxim, M. L.; Rodríguez, H.; Rogers, R. D. *Green Chem.* **2009**, *11*, 646–655.
10. Chen, Z. G.; Zong, M. H.; Li, G. J. *Chem. Technol. Biotechnol.* **2006**, *81*, 1225–1231.
11. Petrulyte, S. *Danish Medical Bull.* **2008**, *55*, 72–77.
12. Qin, Y. *Polym. Adv. Technol.* **2008**, *19*, 6–14.
13. Qin, Y; Gilding, D. K. *Med. Device Technol.* **1996**, *7*, 32–41.
14. Thomas, S. *J. Wound Care* **2000**, *9*, 56–60.
15. Thomas, S. *Wound Management and Dressings*; The Pharmaceutical Press: London, 1990.
16. Jeter, K. F.; Tintle, T. E. *Ostomy Wound Manage.* **1990**, *28*, 75–81.
17. Qin, Y. *J. Appl. Polym. Sci.* **2004**, *91*, 1641–1645.
18. Muri, J. M.; Brown, P. J. In *Biodegradable and Sustainable Fibers: Alginate Fibers*; Blackburn, R. S., Ed.; Woodhead Publishing: Cambridge, UK, 2005; pp 89−109.
19. Le, Y.; Anand, S. C.; Horrocs, A. R. In *Using Alginate Fibre as a Drug Carrier for Wound Healing*; Anand, S. C., Ed.; Medical Textiles 96; Woodhead Publishing: Cambridge, UK; 1997; pp 21−26.
20. Holbrey, J. D.; Chen, J.; Turner, M. B.; Swatloski, R. P.; Spear, S. K.; Rogers, R. D. In *Ionic Liquids in Polymer Systems: Solvents, Additives, and Novel Applications*; Brazel, C. S., Rogers, R. D., Eds.; ACS Symposium Series 913; American Chemical Society: Washington, DC, 2005; pp 71.
21. Sun, N.; Swatloski, R. P.; Maxim, M. L.; Rahman, M.; Harland, A. G.; Haque, A.; Spear, S. K.; Daly, D. T.; Rogers, R. D. *J. Mater. Chem.* **2008**, *18*, 283–290.

22. Maxim, M. L.; Sun, N.; Swatloski, R. P.; Rahman, M.; Harland, A. G.; Haque, A.; Spear, S. K.; Daly, D. T.; Rogers, R. D. In *Cellulose Solvents: For Analysis, Shaping and Chemical Modification*; Liebert, T. F., Heinze, T. J., Edgar, K. J., Eds.; ACS Symposium Series 1033; American Chemical Society: Washington, DC, 2010; pp 261−274.
23. Turner, M. B.; Spear, S. K.; Holbrey, J. D.; Daly, D. T.; Rogers, R. D. *Biomacromolecules* **2005**, *6*, 2497–2502.
24. Hines, J. H.; Wanigasekara, E.; Rudkevich, D. M.; Rogers, R. D. *J. Mater. Chem.* **2008**, *18*, 4050–4055.
25. Poplin, J. H.; Swatloski, R. P.; Holbrey, J. D.; Spear, S. K.; Metlen, A.; Grätzel, M.; Nazeeruddin, M. K.; Rogers, R. D. *Chem. Commun.* **2007**, 2025–2027.
26. Viswanathan, G.; Murugesan, S.; Pushparaj, V.; Nalamasu, O.; Ajayan, P. M.; Linhardt, R. J. *Biomacromol.* **2006**, *7*, 415–418.
27. Murugesan, S.; Mousa, S.; Vijayaraghavan, A.; Ajayan, P. M.; Linhardt, R. J. *J. Biomed. Mater. Res., Part B* **2006**, *79B*, 298–304.
28. British Pharmacopoeia Monograph for Alginate Dressings and Packings, 1994.
29. Papageorgiou, S. K.; Kouvelos, E. P.; Favvas, E. P.; Sapalidis, A. A.; Romanos, G. E.; Katsaros, F. K. *Carbohydr. Res.* **2010**, *345*, 469–473.
30. Yang, G; Zhang, L.; Peng, T.; Zhong, W. *J. Membr. Sci.* **2000**, *175*, 53–60.
31. Tokuyasu, K.; Tabuse, M.; Miyamoto, M.; Matsuki, J.; Yoza, K. *Carbohydr. Res.* **2008**, *343*, 1232–1236.
32. Liu, C. F; Sun, R. C.; Zhang, A. P.; Ren, J. L. *Carbohydr. Polym.* **2007**, *68*, 17–25.
33. Labbe, N.; Rials, T. G.; Kelley, S. S.; Cheng, Z. M.; Kim, J-Y.; Li, Y. *Wood Sci. Technol.* **2005**, *39*, 61–76.
34. Soares, J. P.; Santos, J. E.; Chierice, G. O.; Cavalheiro, E. T. G. *Ecletica. Quim.* **2004**, *29*, 53–56.
35. Ross, A. B.; Hall, C.; Anastasakis, K.; Westwood, A.; Jones, J. M.; Crewe, R. J. *J. Anal. Appl. Pyrolysis* **2011**, *91*, 344–351.
36. Zhang, J.; Ji, Q.; Shen, X.; Xia, Y.; Tan, L.; Kong, Q. *Polym. Degrad. Stab.* **2011**, *96*, 936–942.
37. Chen, X.; Wells, G.; Woods, D. M. In *Medical Textiles: Proceedings of the International Conference*, August 24−25, 1999, Bolton, UK; Anand, S. C., Ed.; Woodhead Publishing Limited: Cambridge, UK, 1999; pp 20−29.
38. Miraftab, M.; Qiao, Q.; Kennedy, J. F.; Anand, S.; Collyer, G. In *Medical Textiles: Proceedings of the International Conference*, August 24−25, 1999, Bolton, UK; Anand, S., Ed.; Woodhead Publishing Limited: Cambridge, UK, 1999; pp 164−172.
39. Rowe, R. C., Sheskey, P. J., Quinn, M. E., Eds.; In *Handbook of Pharmaceutical Excipients*, 6th ed.; Pharmaceutical Press: London, 2009; pp 11–12.

Chapter 8

Degradation of Chitin Utilizing Acid Functionalized Ionic Liquids Technology

W. Matthew Reichert,* Arsalan Mirjafari,§ James H. Davis Jr., Taylor Goodie, Nathan G. Williams, Vivian Ho, Matthew Yoder, and Maelynn La

Department of Chemistry, University of South Alabama,
Mobile, Alabama 36688, USA
§Current Address: Department of Chemistry and Mathematics,
Florida Gulf Coast University, Fort Myers, Florida 33965, USA
***E-mail: reichert@southalabama.edu**

Biopolymers are a new source of feedstock chemicals for chemical reactions and polymeric materials. Currently biopolymer utilization is low due to their insolubility in common molecular solvents. The use of ionic liquids for the dissolution of chitin has enabled new processing methods for it, as well as other biopolymers. Recent results demonstrate that chitin can be depolymerized in ionic liquids. The present research concerns the use of ionic liquids and various acid catalysts for the depolymerization of chitin into its monomer units. Further, it addresses the effects of temperature, the nature of the catalyst, and solvent effects on the depolymerization of chitin.

Introduction

Biopolymers are potential sources for new advanced materials as well as sources of energy and feedstock chemicals. There have been many hurdles to the processing of these biopolymers for applications. The main hurdle has been the insolubility of the biopolymers in common solvents without degradation or derivatization. The application of ionic liquids (ILs) to this problem has

In Ionic Liquids: Science and Applications; Visser, A., et al.;
ACS Symposium Series; American Chemical Society: Washington, DC, 2012.

resulted in new solvents for biopolymers without the drawbacks of previous solvents (*1*, *2*). Ionic liquids provide a medium for the dissolution of biopolymers that is non-derivatizing and non-degrading. This allows for the processing and manipulation of the native polymer.

The two most abundant biopolymers that are both available in large quantities and are renewable are cellulose and chitin. There have been numerous publications on utilizing cellulose and chitin for new materials (*3*), and increasing interest in utilizing these materials as starting sources for fuel and chemicals through degradation. Chitin and cellulose have great potential to provide inexpensive and renewable sources of feedstock chemicals for the production of new polymers.

Chitin, in particular, is the focus of the present study. It is the second most abundant biopolymer and several sources of it are available, i.e. crustaceans, fungi, and insect exoskeletons. Chitin has a similar structure to cellulose in that it is a polymer based on a saccharide. Where cellulose is comprised of glucose units linked through β-1,4 linkages, chitin is comprised of *N*-acetyl-D-glucosamine (NAG) units using the same linkage motif. It is the cleavage of these linkages to form NAG that is of interest in this study. Currently, chitin is broken down into its monomer unit through hydrolysis of the ether linkage using enzymes or acid catalysts (*4*–*6*) shown in Figure 1. While these methods are effective at the hydrolysis of chitin there are drawbacks, very specific reaction requirements and produce unwanted byproducts. IL solvents and catalysts can be advantageous in depolymerizing chitin by providing a homogeneous environment and control of the hydrolysis reaction.

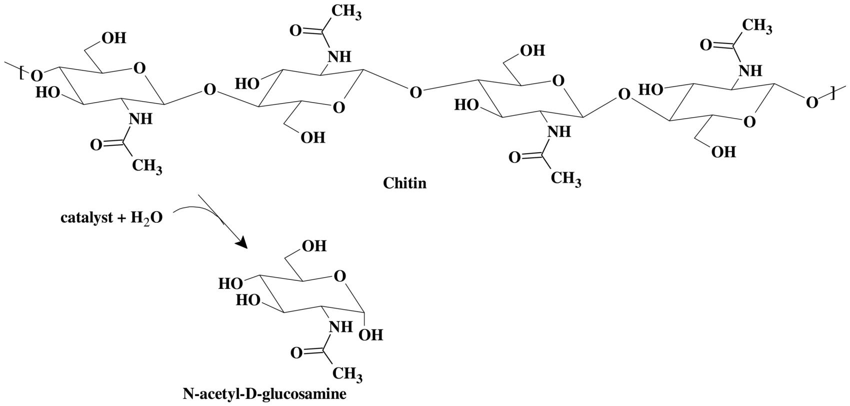

Figure 1. Hydrolysis of chitin into N-acetyl-D-glucosamine.

Ionic liquids have grown from being just a new solvent system of intellectual interest to finding a role in applications outside the laboratory in real world industrial problems. The current definition of an ionic liquid is that of a material composed entirely of ions that melts at or below 100 °C. The Coulombic nature of these materials imbues them with valuable properties such as low volatility, high thermal stability and unique solvent properties. The unique properties of interest in the present research are the unique (find a synonym! Too many 'uniques!) dissolution abilities and the ability to incorporate functionality into the ionic liquid (*7*, *8*). ILs have been shown to dissolve a number of biopolymers such as silk fibers, wool, cellulose, and chitin (*1*, *2*, *9–12*). The previous studies lead to the utilization of ILs has a solvent for the hydrolysis of cellulose using several different types of catalyst, mineral acids (*13*), solid acid catalysts (*14*), and metal chloride catalysts (*15*). These methods illustrate how IL solvents can facilitate the hydrolysis of cellulose. Yet there are drawbacks to the lack of control of the strength of the acid catalysts such as further degradation of the products into unwanted chemicals. ILs can provide an answer to this problem by incorporating acid functionality into either the cation or anion. Since the cation and anion can possess their own unique properties, one can develop an IL for a very specific process or application. The literature shows a variety of processes incorporating tailored ILs (*16*, *17*). By incorporating the functionality into the cation, one can gain a measure of control over the acidity of the IL catalyst and thus gain improved control of the hydrolysis reaction. The focus of this research will be on alkane sulfonic acid functionalized ionic liquids. The combination of IL solvent and IL acid catalyst has been applied to the hydrolysis of cellulose and found to be effective at the hydrolysis (*18*).

A recent development is the use of thiol-ene chemical in the field of ILs, and this has opened up new avenues to longer chain sulfonic acid ILs. Over the past decade, functionalized or "task-specific" ionic liquids (TSILs) have found utility in a wide array of applications, ranging from catalysis to separations. Typically, functional groups in TSILs have been heteroatom-based, and their synthesis complicated by unwanted byproducts.

The thiol-ene coupling reaction can be considered as a "click" reaction and has proven to be a versatile and useful synthetic tool to synthesize a wide range polymers and biomaterials. Thiol–ene reactions proceed *via* the sequential propagation of a thiyl radical through a vinyl functional group and subsequent chain transfer of hydrogen from the thiol, which regenerates the thiyl radical (*19*). For the first time, the thiol-ene reaction was employed in order to synthesize new polyhydroxylated TSILs by Davis and his co-workers (*20*). In that study, different *ene*-functionalized ionic liquids (ILs) were reacted photochemically with 1-thioglycerol, yielding polyhydroxylated ILs in a single step. Imidazolium and quaternary ammonium-based cations with either *N*-vinyl or *N*-allyl appendages were chosen to assess the effect, if any, of having the alkene moiety connected directly to the center of the cationic charge versus being separated from it by one carbon unit. Thioglycerol was chosen in order to demonstrate the incorporation of a desirable functional group (-OH) into an IL by way of the orthogonal reaction of *ene*-bearing IL ions.

Herein, we use a four-step synthesis route including thiol-ene, deprotection and oxidation in order to prepare Brønsted acidic IL with an alkane sulfonic acid group covalently tethered to the IL cation (Figure 2). In this research, we have focused the effects of temperature and IL acid catalyst composition on the hydrolysis of chitin.

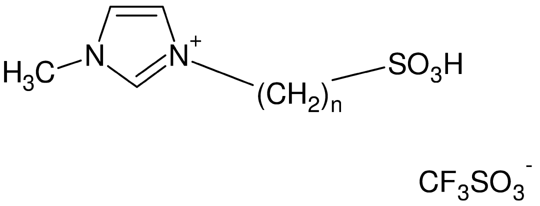

Figure 2. Structure of ionic liquid catalyst, [C_nSO_3H][TfO].

Experimental

Materials

1-methylimidazole was purchased from Fisher Scientific (Pittsburgh, PA) and vacuum distilled to increase purity. Unbleached practical grade chitin (MW: 770.8) was also purchased from Fisher Scientific (Pittsburgh, PA) and demineralized and deproteinated with 3 M HCl and 3 M NaOH, respectively. After treatment, the appearance of the chitin changed from a reddish brown to off white. Utilization of ATR FT-IR spectroscopy showed no change in the chemical structure of the chitin. 1-butyl-3-methylimidazolium chloride ([C_4mim][Cl]), ≥ 95% purity, and *N*-acetyl-D-glucosamine, ≥ 95% purity, was purchased from Sigma Aldrich (Milwaukee, WI). All other chemicals used were obtained from Fisher Scientific (Pittsburgh, PA) and used has received.

Synthesis of Ionic Liquids Acid Catalysts

The ionic liquid catalysts, 1-methyl-3-(alkylsulfonic acid)imidazolium triflate, [C_nSO_3H][TfO], were synthesized using literature techniques (*17*, *21*). Redistilled 1-methylimidazole was dissolved in 50 mL of acetone in a round bottom flask. An equal molar amount of 1,3-propane sultone was dissolved in acetone and added drop wise to the 1-methylimidazole solution at room temperature. The solution stirred for two days. The reactions formed a white precipitate. A washed with ethyl acetate removed any unreacted starting materials from the precipitate. Solvent was removed *in vacuo* to produce a dried solid. The zwitterion product was then reacted with triflic acid and stirred for eight hours. The resulting [C_3SO_3H][TfO] ionic liquid was a yellow viscous liquid.

Recently, the authors have synthesized longer alkyl chain sulfonic acid ionic liquids (*22*). Here the authors present a general synthesis of these IL acid catalysts. The first part is addition of thioacetic acid to the ILs containing double bond **I** *via* thiol-ene reaction. A mixture of **I** (0.0022 mol), 2,2-dimethoxy-2-phenylacetophenone (0.0022mol), thioacetic acid (0.0044mol), methanol (8 mL) and chloroform (2 mL) was added to a quartz tube and stirred until a homogenous mixture was observed. It is worth mentioning that dimethoxy-2-phenylacetophenone served as photoinitiator in order to start radical-based addition reaction. The system was purged with nitrogen for 2 minutes. The contents were irradiated without stirring at ambient temperature for 8 hours. The solvents were removed from the crude product via evaporation. The residue was then washed with hexane (5 × 20 mL). Removal of residual solvent *in vacuo* yielded **II**.

In the second step (deprotection reaction), a mixture of **II** (0.002 mol), acetyl chloride (0.2 mol), and methanol (10 mL) were stirred at room temperature for 36 h. After completion of the reaction, the reaction mixture was extracted CH_2Cl_2 (3 × 15 mL) and saturated $NaHCO_3$ solution was added dropwise until the reaction attained pH 7.0. The organic layer was washed with water (3 × 10 mL) and dried over anhydrous sodium sulphate. Removal of residual solvent *in vacuo* yielded **III**.

The last step is oxidation. To a stirred solution of **III** (0.002 mol) in CH_2Cl_2 (10 mL) was slowly added, dropwise, a solution of *m*-CPBA (meta-chloro peroxybenzoic acid, 0.002 mol) in CH_2Cl_2 (4 mL) at 0 °C and stirred for 24 h. At the end of the reaction the solvent was removed *in vacuo* without heating, the residue was suspended in brine and neutralized with a saturated solution of sodium carbonate. The mixture was washed with ether (3 × 20 mL) and was dried *in vacuo* to obtain **IV** as final product in high yields (Figure 3).

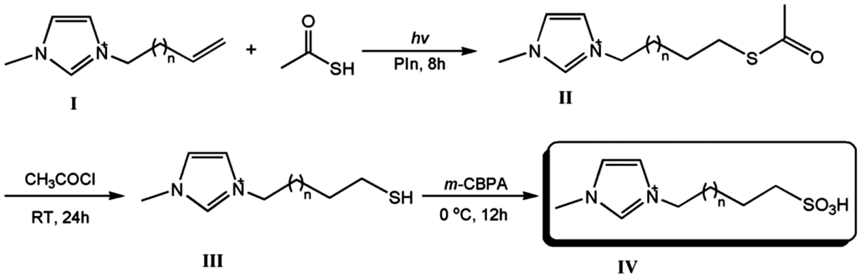

Figure 3. General synthesis of 1-methyl-3-(alkylsulfonic acid)imidazolium acid catalysts.

Reaction Experiment

The chitin solutions used were 1% chitin (w/w) in [C_4mim][Cl]. The chitin solutions were produced by placing 0.15g of chitin and 14.85g of ionic liquid in a glass jar and microwave irradiated for 5 minutes at 100 °C at 300W. This process was repeated until complete dissolution was observed.

The depolymerization reaction was performed on 15g of the 1% chitin (w/w) in ionic liquid solution. The reaction solution was placed in 60 mL glass jars and heated to the reaction temperature being investigated. At this point 1g of catalyst and 0.035g of water were added to the reaction solution to initiate the depolymerization reaction. The reaction was stirred and reaction temperature maintained. Two samples of the reaction solution weighting 0.25g each were removed periodically starting at time 0 sec then every 10 minutes for the first hour and then every 30 minutes to the 6 hour mark. The aliquots were placed in separate 20 mL glass vials. One vial was used for UV/Vis analysis and the other for HPLC analysis.

Benedict's Test

The aliquots to be analyzed by UV/Vis used a modified Benedict's test for reducing sugars used by Trulove, *et al.* for the detection of glucose (*18*) and was used to detect NAG in the reaction solutions. The following is an example of the modified Benedict's test procedure. To each 0.25 g sample, 1 mL of Benedict's reagent (*23*, *24*) and the samples were heated to 100 °C for 30 minutes. The vials were removed and allowed to cool to room temperature. Next, 1 mL of a 0.024 M solution of neocuproine in ethanol was added to the samples and they were again heated to 100 °C for an additional 30 minutes. The samples were removed from heat and allowed to cool to room temperature. The solutions were then diluted and placed in 20 mL scintillation vials. UV/Vis data was obtained for each diluted sample using a Shimadzu model UV-2501PC with a CPS240A temperature controller.

HPLC Measurements

A Shimadzu HPLC with an evaporative light scattering detector (ELSD) was used to analyze the reaction samples. The column used is a 3 cm Phenomenex Luna-NH_2 column which was thermostated at 40 °C. Prior to analysis on the HPLC, the samples were filter through a Whatman PTFE 0.45 μm syringe filter and placed in glass autosampler vials. The mobile phase of the HPLC was 95% acetonitrile and 5% water. The flow rate was set to 1.5 mL/min. The UV/Vis detector was set to 254 nm. The ELSD parameters were drying column set to 60 °C, N_2 carrier gas set to 350 psi. Calibration standards were prepared using *N*-acetyl-D-glucosamine. The samples were analyzed for *N*-acetyl-D-glucosamine.

Results and Discussion

The effects of ionic liquid acid catalysts on the depolymerization of chitin into *N*-acetyl-D-glucosamine and other products were investigated and evaluated using a UV/Vis and HPLC. The choice of solvent IL for these experiments was [C_4mim][Cl]. Preliminary work by Trulove and co-workers (*18*) and the authors showed that the acetate anion, a common choice in IL used in the dissolution of biopolymers, deactivate the catalyst resulting in no hydrolysis of biomass. Therefore the less effective solvent of chitin, [C_4mim][Cl], was chosen in order to perform the hydrolysis reaction. The analysis of the reaction samples was carried out using UV/Vis and the modified Benedict's test. The Benedict's test detects the presence of reducing sugars like glucose and fructose. Since the hydrolysis of chitin results in NAG, a derivative of glucose, the Benedict's test should detect the presence of NAG in the reaction solutions. The concentration of reducing sugar in the reaction samples provides an indication of the level of depolymerization of chitin, but no information on the identity of the products. The data presented in Figure 4 is the UV/Vis evaluation of the reaction products.

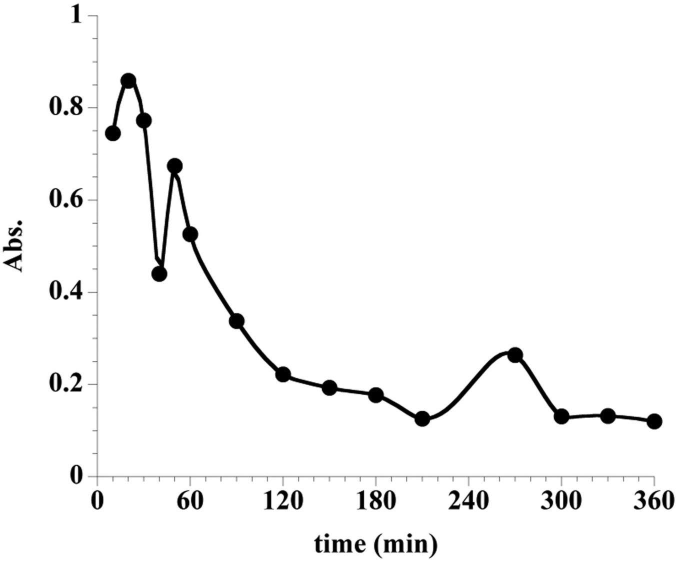

Figure 4. Conversion of chitin into reducing sugars using [C_3SO_3H][TfO] catalyst at100°C from UV/Vis data.

The data presented above is still in absorbance units due to our inability to get consistent standards in order to calculate concentration of reducing sugars. Still the results demonstrate that the IL catalyst is effective at the hydrolysis of chitin. The data shows that initially the concentration of reducing sugars increases in the first 30 minutes of the reaction then rapidly decreases. This rapid decrease is due to a secondary reaction. The IL acid catalyst further degrades the reducing sugars products into a currently unknown product. An increase in the alkyl group of the sulfonic acid functionality leads to a decrease in the amount of NAG produced and an increase in the conversion to the secondary product, as shown in Figure 5. The anion could also play a role in the acid of the catalyst and that effect is currently being investigated.

In order to gain better insight into the product stream of the reaction, HPLC with UV/Vis and ELSD analysis were performed on the reaction solutions. These analyses confirmed the presence of NAG as one of the products and allowed the calculation of percent conversion of chitin into NAG. Based on this analysis, a study of the effects of temperature and IL acid catalyst composition on chitin hydrolysis was conducted. In addition, the analysis observed an unknown product by UV/Vis at 254 nm, which is most likely a dehydration product of the NAG.

The catalyst [C_3SO_3H][TfO] was evaluated at 100 °C and 120 °C and is shown in Figure 6. Analysis of the reaction solutions confirmed the present of N-acetyl-

D-glucosamine (NAG). The depolymerization reaction at 100 °C shows very little production of NAG over time, a little over 6%. The fluctuation in the production is due to the further degradation of the NAG into another product. The concentration of this secondary product is below the detection limit for the UV-Vis and ELSD at this temperature. By increases the reaction temperature from 100 °C to 120 °C, the production of NAG increases from a maximum of 6% to 15%. The increase in temperature also increases the degradation of the NAG. According to this data, a new compound is being produced by the degradation of the NAG. In a similar study by Trulove, *et al.* using cellulose, the authors found that the IL acid catalyst could degrade the glucose further into hydromethylfurfural (*18*). This data supports the degradation of the NAG by the IL acid catalyst into a new compound. Changing the catalyst to [C_7SO_3H][NTf_2] had a dramatic effect on the product of NAG in the reaction. The concentration of NAG dropped to below detectable limits at all the data points. This suggests that the catalyst effective converts the NAG into the secondary product extremely quickly. The authors are currently trying to identify the compound through NMR and LC/MS techniques.

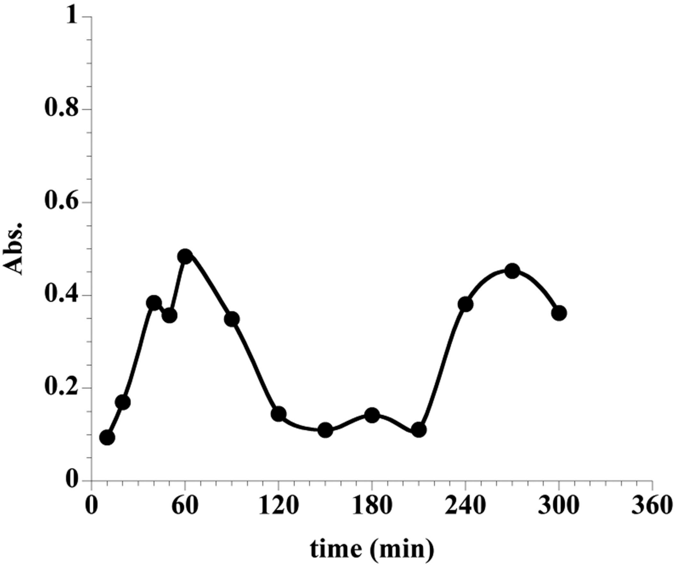

Figure 5. Conversion of chitin into reducing sugars using [C_7SO_3H][NTf_2] catalyst at100°C from UV/Vis data.

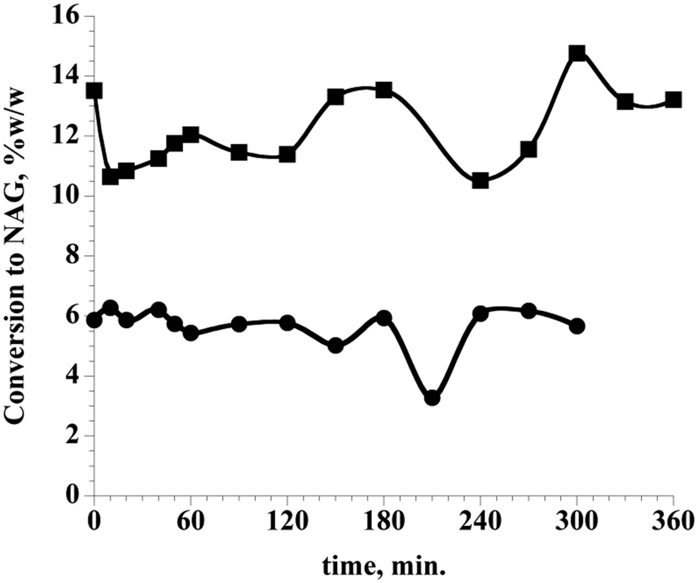

Figure 6. HPLC data showing the percent conversion of chitin into NAG at 100 °C (□) and 120 °C (■).

Conclusions

In summary, IL acid catalyst hydrolyzes chitin into NAG and other compounds. Currently, traditional methods of chitin hydrolysis have higher yields of NAG compared to the use of IL technology. The advantage to employing IL technology is the amount of control one has on the acid catalyst. This data illustrates the effect of temperature on the system but that is not the only reaction variable available to IL researchers. Currently, research into the effects of alkyl chain length on the acid catalyst is under investigation. In addition, LC/MS analysis of the degradation products is underway. As well, the authors will pursue further study of the effects of various acid functionality, catalyst loading, and co-catalyst.

Acknowledgments

Acknowledgements go to the Air Force Office of Scientific Research for funding through the Investigators Program, grant number FA9550-11-1-0053. Also the authors would like to acknowledge the University of South Alabama for facilities and personnel.

References

1. Swatloski, R. P.; Spear, S. K.; Holbrey, J. D.; Rogers, R. D. *J. Am. Chem. Soc.* **2002**, *124*, 4974.
2. Qin, Y.; Lu, X.; Sun, N.; Rogers, R. D. *Green Chem.* **2010**, *12*, 968.
3. Zhang, X. Z.; Jin; Liu, X. *Macromol. Res.* **2012**, *20*, 703.
4. Cosio, I. G.; Fisher, R. A.; Carroad, P. A. *J. Food Sci.* **1982**, *47*, 901.
5. No, H. K.; Meyers, S. P. *J. Aquat. Food Prod. Technol.* **1995**, *4*, 27.
6. Sashiwa, H.; Fujishima, S.; Yamano, N.; Kawasaki, N.; Nakayama, A.; Muraki, E.; Hiraga, K.; Oda, K.; Aiba, S.-i. *Carbohydr. Res.* **2002**, *337*, 761.
7. *Ionic Liquids in Synthesis*; 2nd ed.; Wiley-VCH Verlag GmbH & Co.: Wienheim, Germany, 2008.
8. Welton, T. *Chem. Rev.* **1999**, *99*, 2071.
9. Mantz, R. A.; Fox, D. M.; Green, J. M., III; Fylstra, P. A.; De Long, H. C.; Trulove, P. C. *Z. Naturforsch., A: Phys. Sci.* **2007**, *62*, 275.
10. Phillips, D. M.; Drummy, L. F.; Conrady, D. G.; Fox, D. M.; Naik, R. R.; Stone, M. O.; Trulove, P. C.; De Long, H. C.; Mantz, R. A. *J. Am. Chem. Soc.* **2004**, *126*, 14350.
11. Xie, H.; Zhang, S.; Li, S. *Green Chem.* **2006**, *8*, 630.
12. Wu, Y.; Sasaki, T.; Irie, S.; Sakurai, K. *Polymer* **2008**, *49*, 2321.
13. Li, C.; Wang, Q.; Zhao, Z. K. *Green Chem.* **2008**, *10*, 177.
14. Rinaldi, R.; Palkovits, R.; Schuth, F. *Angew. Chem,. Int. Ed.* **2008**, *47*, 8047.
15. Su, Y.; Brown, H. M.; Huang, X.; Zhou, X.-d.; Amonette, J. E.; Zhang, Z. C. *Appl. Catal., A* **2009**, *361*, 117.
16. Gu, Y.; Ogawa, C.; Kobayashi, J.; Mori, Y.; Kobayashi, S. *Ange. Chem., Int. Ed.* **2006**, *45*, 7217.
17. Cole, A. C.; Jensen, J. L.; Ntai, I.; Tran, K. L. T.; Weaver, K. J.; Forbes, D. C.; Davis, J. H., Jr. *J. Am. Chem. Soc.* **2002**, *124*, 5962.
18. McIlvaine, W. B.; Foley, M. P.; Reichert, W. M.; Mandia, J. J.; Haverhals, L. M.; O'Sullivan, D. W.; De Long, H. C.; Trulove, P. C. *ECS Trans.* **2010**, *33*, 109.
19. Kade, M. J.; Burke, D. J.; Hawker, C. J. *J. Polym. Sci., Part A: Polym. Chem.* **2010**, *48*, 743.
20. O'Brien, R. A.; Mirjafari, A.; Jajam, V.; Capley, E. N.; Stenson, A. C.; West, K. N.; Davis, J. H., Jr *Tetrahedron Lett.* **2011**, *52*, 5173.
21. Yoshizawa, M.; Hirao, M.; Ito-Akita, K.; Ohno, H. *J. Mater. Chem.* **2001**, *11*, 1057.
22. Reichert, W. M.; Davis, J. H., Jr; Mirjafari, A.; Goode, T.; Williams, N.; La, M.; Ho, V.; Yoder, M. *ECS Trans.* **2012**, in press.
23. Benedict, S. R. *J. Bio. Chem.* **1908**, *5*, 485.
24. Gahler, A. R. *Anal. Chem.* **1954**, *26*, 577.

Chapter 9

Lipid-Inspired Ionic Liquids Containing Long-Chain Appendages: Novel Class of Biomaterials with Attractive Properties and Applications

Arsalan Mirjafari,*,[1,3] Richard A. O'Brien,[1] Samuel M. Murray,[2]
Kaila M. Mattson,[1] Niloufar Mobarrez,[1] Kevin N. West,[2]
and James H. Davis Jr.*,[1]

[1]Department of Chemistry, University of South Alabama,
Mobile, Alabama 36688, USA
[2]Department of Chemical and Biomolecular Engineering,
University of South Alabama, Mobile, Alabama 36688, USA
[3]Department of Chemistry and Mathematics,
Florida Gulf Coast University, Fort Myers, Florida 33965, USA
***E-mails: amirjafari@fgcu.edu (A.M.);**
jdavis@southalabama.edu (J.H.D., Jr.)

Lipid-inspired ionic liquids, first described by our group in a symposium in 2007, and more extensively in recent publications, are a class of ionic liquids that utilize structural features similar to those of natural lipids to allow the incorporation of long alkyl chains in ionic liquids while preserving low melting points. Such compounds are of interest as potential separation agents, because of their higher solubility of non-polar compounds relative to other ionic liquids, lubrication applications and as models for lipid membranes. In addition, ionic liquids of cations bearing two lipid-like aliphatic tails are shown to have values of T_m that can be very low, and that can be tunable by the addition, deletion, or combination of dipolar modules and side-chain double bonds. Furthermore, ILs with multiple hydroxyl and thioether functional groups are readily prepared by the photoinitiated radical coupling of 1-thioglycerol and salts of imidazolium and quaternary ammonium cations bearing tethered allyl and/or

In Ionic Liquids: Science and Applications; Visser, A., et al.;
ACS Symposium Series; American Chemical Society: Washington, DC, 2012.

vinyl groups. The results of this research indicate that the construction of functionalized ILs using the thiol-ene reaction offers considerable promise as an easy methods to create structurally elaborated IL ions.

Introduction

Nature is an infinite source of inspiration for developing novel functional materials, which are gaining more interest because of their unique chemical and biological properties. In recent decades, bio-inspired materials have found many real-world applications in biosensing, biomedical engineering, bionanotechnology, smart biomaterials, and biologically-based materials for self-assembly (*1*). Central to many of these technologies is the notion of bio-inspiration in which biological concepts, mechanisms, function, and design features lead to novel synthetic bio-based materials with advanced structures and functions (*2*).

Ionic liquids (ILs) containing the imidazolium moiety have found dramatic increasing interest within the past decade due to their unique physicochemical properties (*3*). These organic salts have been utilized in a multitude of diverse applications, from organic catalysis (*4*) to biofuel preparation (*5*) as well as novel biological applications (*6*). The focus of the first generation of ILs was mainly on their unique intrinsic physical properties, such as density, viscosity, conductivity, solubility, and high thermochemical stability. The second generation of ILs offered the potential to tune these physical and chemical properties by way of "task-specific ionic liquids" which have utility as lubricants, gas absorption, and as more environmentally-friendly reaction media (*7*). Task-specific ionic liquids (TSILs) or functionalized ionic liquids are a unique subclass of ionic liquids which possess a potential spectrum of utility extending far beyond that likely for more conventional ionic liquids. The incorporation of functionality into an ionic liquid is usually accomplished by the grafting of preexisting groups onto one of the ion structures and the number of applications is likely to continue to increase (*8*).

Amino acids derivatives, alkaloids, terpenes and natural hydroxyl acids represent an excellent class of starting materials for the construction of bio-based TSILs, especially chiral ones, because of their availability (often in both enantiomeric forms) at a reasonable cost (*9*). Amino acids and their simple derivatives can be easily used to design chiral cations and anions in order to synthesize chiral TSILs. These bio-based ILs can be constructed without amino acid residues, with modification of side chains and preservation of the amino and acid moieties, with alteration of either the acidic or basic functionality, or by polyfunctional modification of both the amine and acid functions. Several lines of research have been carried out by using such approaches to make either the chiral cation, the chiral anion or both in the structure of bio-based ionic liquids. The main advantage of this strategy is the chirality arising from the starting materials, chiral α-amino acids, is kept in the structure of ionic liquids (*10*, *11*).

The growing global environmental awareness and social concern, concept of sustainability and, the increasing demand to use new bio-based materials have led us to now expand this search to novel lipid-inspired ionic liquids, making use of a category (fatty acids and their derivatives) which have not heretofore been widely used as elements of IL formulations.

Lipid-Inspired Ionic Liquids Based on Fatty Acids: Synthesis, Physical Properties, and Potential Applications

The development for the formulation of poorly water-soluble or water-insoluble active pharmaceutical ingredients (APIs) has been an important challenging issue for the pharmaceutical industries over the past decades (*12*). The interest for the lipid-based formulation has increased and novel drug delivery systems have been developed using lipids and fatty acids as the bio-based precursors (*13*). Fatty acids are the main ingredients of oils and fats which have been important, renewable feedstocks for the chemical industry, especially for biofuel production. The advances have made during the last decade in organic synthesis, catalysis, and biotechnology using plant oils and basic oleochemicals derived from them are truly remarkable (*14*).

The fluid mosaic model was first proposed by S. J. Singer and G. L. Nicolson in 1972 to describe the structure of cell membranes (*15*). This model holds that the phospholipid bilayer is a dynamic two dimensional liquid membrane. Its proper function is strongly related to its "fluidity", and that is often quantified by reference to the melting point, T_m (increased fluidity corresponds to a lower T_m value). The basic concept of the fluid mosaic model of a biological membrane is that the membrane proteins are floating in a sea of excess lipid molecules organized in a bilayer. According to this model, lipids are mainly responsible for isolating the cell interior from the outside world and providing the environment for membrane proteins that regulate the exchange of substances between the cell and its surroundings (*16*). The fliud-mosaic model could be the heart of many desirable solvent characteristics and physical properties of ionic liquids (*17*). According to this model, the function of phospholipid bilayers is tied to the T_m value of ILs. While ILs often have low T_m values despite being composed of charged species with aliphatic appendages, the fluidity of ILs generally declines when progressively longer aliphatic appendages are used. In other words, as the length of the alkyl chain increases, the nonpolar domains become larger and more connected and cause swelling of the ionic network, in a manner analogous to systems exhibiting microphase separation (*18*).

Synthesis of hydrophobic ionic liquids by incorporation of more lipophilic structural elements while keeping their melting points sufficiently below room temperature remains still challenging. In fact, the T_m values of these ILs begin to increase significantly once an appended *N*-alkyl group exceeds six or seven carbon atoms in length (Figure 1). By using a method modeled on homeoviscous adaptation (HVA) (*19*), ILs with very long alkyl appendages and very low T_m values can be prepared. By studying the melting points of natural fatty acids, we realized that low-melting fats (oils) often contain a *cis* configured double bond in the alkyl chain. This “kink”, as it is often called, leads to a lower packing efficiency and thus to an increased fluidity- most probably as an entropy-dominated effect.

A series of lipid-inspired ILs were synthesized which containing a long alkyl appendage identical to that in a natural fatty acid such as stearic and oleic acids (Scheme 1). This new class of ionic liquids (ILs) can potentially creates a new and facile means of separating biomolecules such as proteins and fat-soluble vitamins that is faster than chromatography and other well established methods. This is also a major advance in that the new ILs should provide a platform to investigate enzyme catalyzed reactions in ionic liquids and should serve as model systems for cell membranes for thermodynamic and transport processes. The development of these new ILs could result in more environmentally benign and economical processes. Furthermore, this discovery may have significant implications for IL use in lubricants, heat-transfer fluids, and gas storage and separation, among other applications.

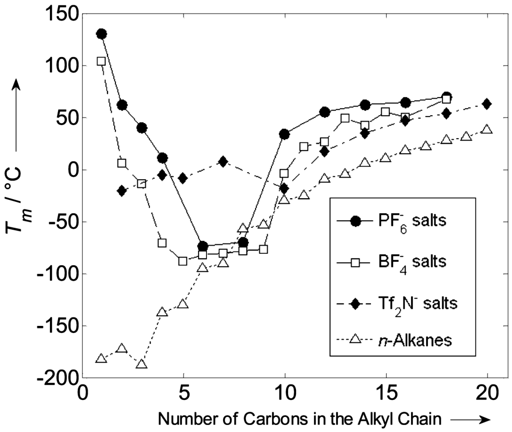

Figure 1. The influence of alkyl chain length on T_m in N-methyl-N-alkyl imidazolium salts and corresponding n-alkanes. Includes data from the literature (18) and newly synthesized ionic liquids (20). Reproduced with permission from reference (20). Copyright 2010 John Wiley and Sons.

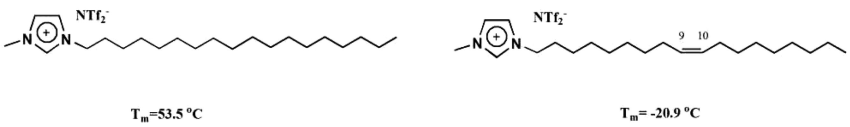

*Scheme 1. Fatty acid-derivative-based ILs using stearic acid **1** (left) and oleic acid **4** (right) (20).*

Based on the HVA mechanism, the melting temperature of cell membranes depends on the degree of saturation of a fatty acid which affects particularly the fatty acid melting point. Double bonds do not permit rotation and introduces "kinks" (rigid bends) in the hydrocarbon tails. Ideally, fully saturated fatty acid chains pack into nearly crystalline arrays, stabilized by many *van der Waals* interactions; however, the presence of double bond interferes with this tight packing and results in high fluidity, which decreases the melting point of fatty acids (*19*). A comparison of the T_m value of distearoylphosphatidylcholine with that of dioleylphosphatidylcholine shows the dramatic impact of the presence of double bond on the melting points of these phospholipids. The saturated C_{18} tails yielded a T_m value of 58 °C but the "kinked" C_{18} tails contain *cis* double bond have a T_m value of -22 °C. This effect is also at the heart of the T_m difference between the solid triacyl glycerols called fats, and those that are liquid at room temperature known as oils. In both instances, the effect is probably entropic in nature, as in the case of anthracene ("linear", T_m =217 °C) and phenanthrene ("kinked", T_m = 99 °C) (*21*). Accordingly, our research has assured a progressive direction in the development of the ILs with long, unsaturated, aliphatic tail structures which are generally similar to the corresponding phospholipids and have significantly lower T_m values than their counterparts with saturated appendages (*20*).

These lipidic ionic liquids were prepared in good yields using a multi-step procedure involving high-purity fatty alcohols and 1-methylimidazole as starting materials (Scheme 2). Each of the synthesized ILs has a long saturated or unsaturated alkyl appendage which is identical to the natural fatty acids (Table 1). Compounds **1**, **3** and **8** feature fully saturated C_{16}, C_{18}, and C_{20} side chains, respectively. Compound **2**, the unsaturated counterpart of **1**, is *cis*-unsaturated between C9 and C10. Similarly, **4**-**7** are analogs of **3** that bear C_{18} side chains, albeit ones in which there are one or more double bonds. These further differ on the basis of the latter being either *cis*- (**4**, **5**, and **7**) or *trans*- (**6**) in nature, and in terms of their location along the C_{18} backbone. *cis*-Unsaturated between C11 and C12, **9** is the "kinked" analog of C_{20} IL **8**.

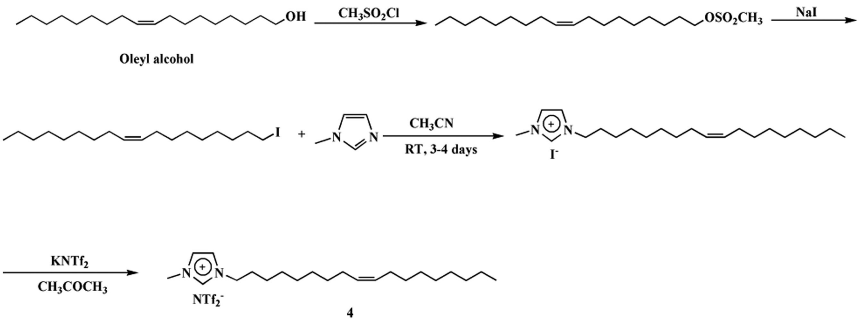

*Scheme 2. Multi-step synthesis procedure of oleic acid-based IL **4** (20).*

Table 1. T_m value of lipid-inspired ILs and related fatty acids and fatty acid methyl esters (*20*)

IL	Alkyl group[a]	Lipidic IL	T_m (IL) °C	T_m (FA) °C[b]	T_m (ME) °C[c]
1	$C_{16}(0)$	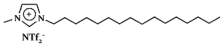	46.9	63.5	33.5
2	$C_{16}(1[9])$	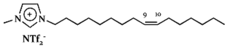	-22.0	0.5	-33.9
3	$C_{18}(0)$	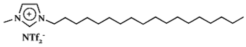	53.5	69.6	38.9
4	$C_{18}(1[9])$	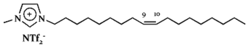	-20.9	16.2	-19.6
5	$C_{18}(1[11])$	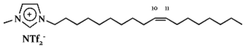	-9.8	12.0	-
6	$C_{18}(1[9t])$	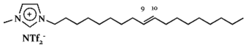	16.0	43.7	10.3
7	$C_{18}(2[9,12])$	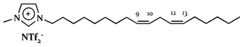	-46.8	-6.5	-35.0
8	$C_{20}(0)$	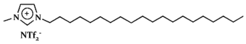	62.5	75.5	54.0
9	$C_{20}(1[11])$	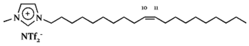	4.2	23.5	-34.5
10	$C_{10}(0)$	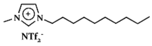	-18.9	31.0	-12.5
11	$C_{10}(1[4])$	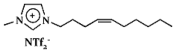	-37.0	-	-

[a] *(x[y]): x= number of double bonds in the alkyl appendage; y= position of double bond; t = trans olefin.*
[b] *T_m of corresponding fatty acids (22). Common name of fatty acids (top to bottom): palmitic, palmitoleic, stearic, oleic, cis-vaccenic, elaidic, linoleic, arachidic, gandoic, capric, obtusilic.*
[c] *T_m of corresponding methyl ester of fatty acids (22).*

The T_m of each of the synthesized lipid-inspired ILs is listed in Table 1, along with reported T_m values for their native fatty acid and fatty acid methyl ester counterparts. Clearly, when *cis*-double bonds ("kinked" structure) are introduced into the long aliphatic tails of these salts, their fluidity increases in a fashion that closely parallels that of their molecular relatives and their melting points decrease (Table 1). In fact, compared to the relevent saturated IL standards **1**, **3** or **8**, unsaturation brings about a significant T_m decrease on a same-chain-length basis. Specifically, ΔT_m for the saturated/unsaturated ILs such as **1**/**2**, **3**/**4** and **8**/**9** are 68.9° C, 74.4° C and 58.3° C, respectively. For instance, T_m of oleic acid-based IL **4** (C_{18} unsaturated) is significantly lower than stearic acid-based IL **3** (C_{18} saturated) because of the presence of double bond with *cis* conformation (Scheme 1). Interestingly, the lowest overall T_m values are those of ILs **2**, **7** and **11**. Compound **11** has an unsaturated C_{10} group, **2** has a C_{16} unsaturated side chain, while **7** has a C_{18} side chain incorporating two *cis* olefin groups (Figure 2).

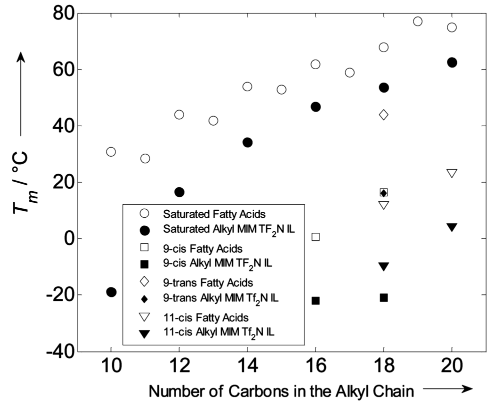

Figure 2. T_m of saturated C_{10}-C_{20} [Alkylmim][Tf_2N] ILs, the new lipid-inspired unsaturated ILs (20), and the corresponding saturated fatty acids (22), versus alkyl chain length. Reproduced with permission from reference (20). Copyright 2010 John Wiley and Sons.

According to the obtained data from the C_{18} series, *cis* double bond position in the side chain has a relatively small difference in the T_m compared to the effect of introducing unsaturation at the either position in the side chain. ΔT_m for the C9-C10, (**4**), and C11-C12 (**5**) is 11.1 °C which suggests that the position of double bond is less effective at decreasing T_m in contrast to double bond incorporation. In addition, the effect of double bond geometry (*cis-* or *trans-*) causes substantial differences. While the *cis-* double bond of **4** imparts a T_m decrease of 74.4° C relative to saturated IL **3**, the T_m decrease induced by the same-position *trans* geometry in **6** is only 37.5° C. This behavior closely tracks that exhibited by the analogous C_{18} fatty acids and their methyl esters. For example, the ΔT_m between stearic and oleic acids is 53.4° C, while that between stearic and elaidic acids is 25.9° C. In the case of the corresponding methyl esters, these values are 58.5° C and 28.6° C, respectively. The consistently smaller T_m differences imparted by *trans-* versus *cis-* unsaturation across this series of related compounds is most likely because of a smaller packing-disruption effect being imposed by *trans-*olefinic features.

As described by Rotherberg *et al.* in regard to *N*-methyl-*N*-alkyl imidazolium salts, the *N*-alkyl groups impart to the cations the symmetry reduction responsible for poor ion packing and low melting points (*18*). The influence of alkyl chain length on the melting point of the IL has to be subdivided into two parts, namely the "symmetry breaking region" ranging from C2–C8, where decreased melting points are observed, and the "hydrophobic region" ≥ C10, where melting points are drastically raised due to increasing dispersive forces between the alkyl chains. The latter phenomenon is also responsible for determining the viscosity and the solubility characteristics of the material (*18*). Seeking greater insight into these issues, **11** was synthesized for comparison with **10** because the site of unsaturation in **11**, unlike those in **2**, **4**-**7** and **9**, is in the "symmetry breaking region" of the imidazolium cation. However, the T_m of such salts are commonly observed to increase once the alkyl group exceeds six or seven carbons in length, due to the increasing cohesion from *van der Waals* forces in the "hydrophobic region". Significantly, the comparative T_m of **10** and **11** indicate that the effects of side-chain unsaturation are operative whether the double bond is in the symmetry breaking or hydrophobic region. However, the impact of unsaturation within the former (18° C in this case) is substantially less than when it occurs in the hydrophobic region in **2**, **4**, **5**, **7**, and **9**. Overall, we interpret this data as follows: (a) the T_m effect of the symmetry breaking region can be intensified by structural modifications and (b) the incorporation of structural and geometrical irregularities in the hydrophobic region can lead to T_m increasing and normally occurring as *van der Waals* forces accumulate in this part of the ion.

This new class of lipid-inspired ILs would be suitable as non-polar solvents that permit desirable dissolution of lipophilic biomolecules such as cholesterol which is an essential structural component of mammalian cell membranes. Generally, ILs readily dissolving moderately-polar and polar solutes (like-dissolves-like) but often being poor solvents for non-polar compounds which limits the applicability of ILs for chemical reactions and separations processes that involve non-polar compounds, including those of biological origin such as fatty acids, steroids and prostaglandins. While very small amount of cholesterol can be dissolved into classical ILs such as [bmim][Tf_2N] (*23*), we have observed the dissolution of up to 30 mass percent in **4** at room temperature. This result can be the potential starting point to suggest that these new lipophilic ILs are prospectively useful solvents for biomolecules that are membrane localized, or drug molecules which act on membrane components or passively diffuse across the phospholipid bilayer into the cell. Furthermore, the lipophilic behavior of these ILs may also prove important for reactions catalyzed using (normally) membrane-localized enzymes, where they are associated with the ability to enhance enzyme stability and selectivity, and reduce side reactions. Although the majority of enzymes reported to be active in ILs are lipases, other biocatalysts have been investigated in ILs with improved results compared to water (*23*). It seems reasonable to propose that IL-as-solvent environments more akin to those in which such enzymes naturally function may offer advantages over those which are somehow less similar.

Lipidic Ionic Liquids from Gene Transfection Agents (Lipofection)

A number of methods have been developed to facilitate the delivery of functional DNA into the eukaryotic cells for the study of gene regulation and gene expression. One of the most important of these is cationic liposome-mediated transfection (lipofection). In a seminal 1987 paper, Felgner *et al.* described the self-assembly in water of lipidic amphiphiles (liposomes) that "interact with DNA spontaneously, fuse with tissue culture cells, and facilitate the delivery of functional DNA into the cell" (*24*). Describing this transfection process as "simple, highly reproducible, and more efficient than some other, commonly-used procedures," it has been extended to the delivery DNA siRNA, oligonucleotides, ribonucleoproteins, proteins and also other therapeutic payloads into the eukaryotic cell (*25*). Enabling this now standard technology are commercially available cationic lipids such as *N*-[1-(2,3-dioleyloxy)propyl)-*N,N,N*-trimethyl ammonium chloride (DOTMA), *N*-[1-(2,3-dioleoyloxy)propyl)-*N,N,N*-trimethyl ammonium chloride (DOTAP), and *N*-[1-(2,3-diolyloxy)propyl)-*N,N,N*-trimethyl ammonium chloride (TAP) and other closely related salts (Scheme 3).

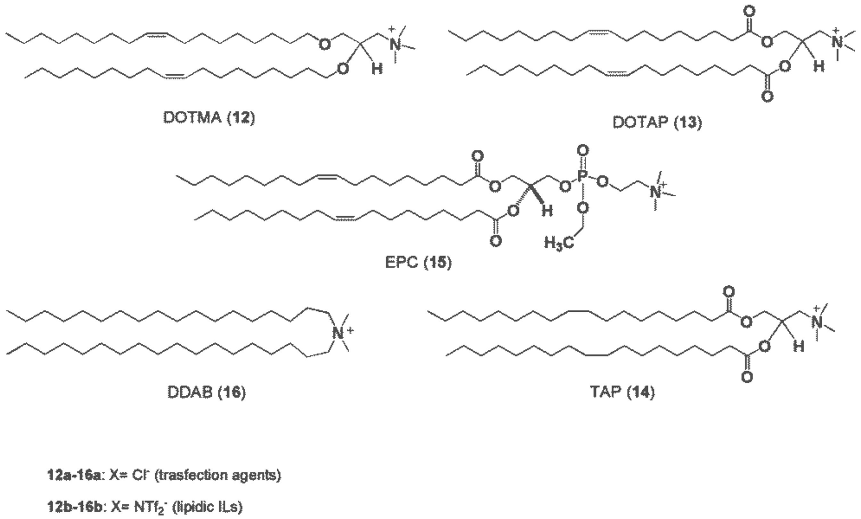
DOTMA (12)
DOTAP (13)
EPC (15)
DDAB (16)
TAP (14)
12a-16a: X= Cl⁻ (trasfection agents)
12b-16b: X= NTf2⁻ (lipidic ILs)

Scheme 3. Cation structures in ***12a-16a*** *(Cl^- salts) and* ***12b-16b*** *(Tf_2N^- salts).*

Strikingly similar to the structures of many cell membrane lipids, the cations of DOTMA, DOTAP, and their congeners consist of three structural subcomponents. The first is a quaternary ammonium head group which provides a locus of cationic charge. It, unlike the internally charge compensated zwitterionic head groups of natural lipids such as dioleylphosphatidylcholine (DOPC), facilitates the electrostatic binding of DNA and RNA, both of which are anionic polymers (*26*). Its cationic character also helps ensure that the self-assembled liposomes will be soluble in water, an attribute further enhanced by the commonly hard, hydrophilic nature of the counter ions (*e.g.,* Cl^-) associated with them (*27*). A glyceryl moiety is the second subcomponent, its role being to provide a covalent bridge between the headgroup and the final substructure, a lipidic tail section. The latter consists of two long aliphatic chains which each of them is tethered to the glyceryl moiety *via* an ether or ester link. It is commonly accepted that the hydrophobic association of these tails leads to the self-assembly of the liposome. Furthermore, it has been observed that the precise nature (length, saturation/unsaturation, *etc.*) of these tails plays a key role in modulating the 'fluidity' of the liposomes of which they are elements, paralleling the relationship between natural lipid structures and membrane fluidity (*28*).

Despite the global structural congruence that exists between DOTMA-type transfection agents and first generation lipidic ILs (cationic head groups tethered to long aliphatic tails), there are stark differences which might profoundly impact their comparative liquefaction behaviors (*29*, *30*). Whereas the ILs have highly charge-diffuse cationic head groups (generally thought to favor lower liquefaction temperatures), those in the DOTMA-type cations are compact and more charge localized. Second, the ILs for which the low T_m double-bond effect were described have a single long aliphatic tail, not two as in the transfection agents. Finally, the transfection agents have a branch point in their cation structure but the ILs do not, and branching is known to influence the physical properties of organic molecules, including lipids. Indeed, there are numerous organisms that utilize lipid branching to depress T_m and modulate cell membrane fluidity (*31*).

In light of these considerations, it seemed worthwhile to prepare fully hydrophobic Tf_2N^- versions of the DOTMA-type cations, from the commercially available and characteristically amphiphilic chloride salts **12a-16a** (Scheme 3). It was our hypothesis that these might prove to be versatile and convenient 'tutors' of lipidic IL cation design, providing valuable insights on structural elements that are consistent with simultaneous low-temperature fluidity and high IL lipophilicity (*32*).

Transfection agents **12a-16a** are invariably paired with hydrophilic anions that enhance liposome interactions with water, and as pure materials often manifest liquid crystalline phases (*27*). Since our interests expressly involve lipophilic ILs (not amphiphilic salts) that transition to isotropic liquid phases at low temperatures, it was clear that the predisposition of the head groups to interact with water needed to be 'switched off,' as did their (likely) chloride-facilitated organization into liquid crystalline phases. The anion $(CF_3SO_2)_2N^-$ (Tf_2N^-) is well-known for its capacity to induce both changes. For instance, Dai *et al.* have successfully demonstrated its capacity to induce the conversion of water soluble, macromolecular polycations with charges as high as +137 (evocative of liposome self-assemblies) into hydrophobic ILs (*33*). In turn, Hardacre and co-workers have shown that while imidazolium halide salts with long, saturated side chains are prone to form liquid crystalline phases, the same cations do not tend to do so when Tf_2N^- is the anion (*34*).

Experimentally, liposome collapse into macroscopically hydrophobic phases is visibly apparent, signaled by the instantaneous formation of water-immiscible materials when clear aqueous solutions of liposomes of **12a-16a** are combined with aqueous KTf_2N (Figure 3). Once isolated, the DSC-determined value of T_m for each of the new Tf_2N^- salts (**12b-16b**) provided a solid basis for its description as an IL. With T_m values ranging from *ca* 65 °C down to -42 °C, all fall below the customary benchmark of 100 °C used to categorize salts as ILs. As expected, comparison of the T_m values of **12b-16b** and **3**, **4**, **7** (representative first-generation lipidic ILs) versus the structural differences between them allows for the ready identification of key structure-property (T_m) relationships (Table 2).

As noted, our earlier study provided compelling evidence that the incorporation of one or more double bonds in the long, lipidic side-chains of imidazolium ILs brings about sharp decrease in T_m versus saturated analogs (Table 1, Figure 2). Significantly, the same phenomenon is operative in the new lipidic ILs, as can be ascertained by comparing the T_m values of **13b** (14.6 °C) and **14b** (54.8 °C), which are structurally identical save for the presence in the former of a *cis* double bond between C9-C10 in each of the two lipidic appendages. While the 40.2 °C drop in T_m that results from the formal addition of a single double bond to each side chain of **14b** is less than that (74.4 °C) which results from the addition of a single double bond to the side chain of **3**, the impact is still profound. Indeed, the T_m of **13b** –with its two long aliphatic appendages, two dipolar carbonyl moieties, and a small head group with its highly localized charge – is still low for a large-ion salt, and comparable to that (16.7 °C) of an imidazolium IL that differs from **4** only by way of having a *trans* (versus *cis*) C9-C10 double bond (Figure 4).

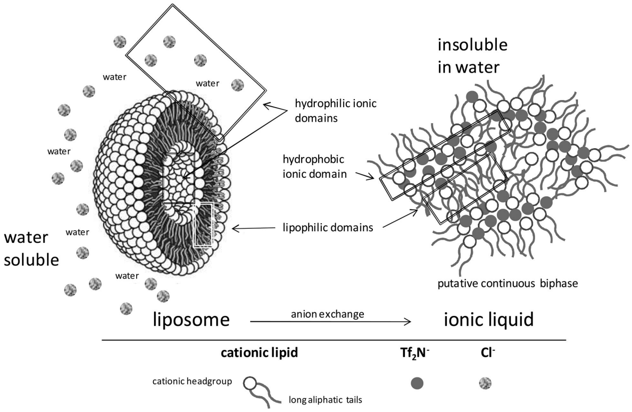
water
water
water
water
water
water soluble
hydrophilic ionic domains
hydrophobic ionic domain
lipophilic domains
insoluble in water
putative continuous biphase
liposome
anion exchange
ionic liquid
cationic lipid
Tf_2N^-
Cl^-
cationic headgroup
long aliphatic tails

Figure 3. Idealized depiction of the putative anion-induced transformation of water-soluble liposomes (left) (reproduced from reference (35)) into macroscopically hydrophobic IL phases (right).

Table 2. T_m values of cationic-lipid derived ILs (*32*)

ILs	T_m *(°C)*	±
12b	-42.2	0.5
13b	14.6	0.5
14b	54.8	0.5
15b	38.1	0.5
16b	65.3	0.5
3	53.5	1.0
4	-20.9	1.0
7	-46.8	1.0

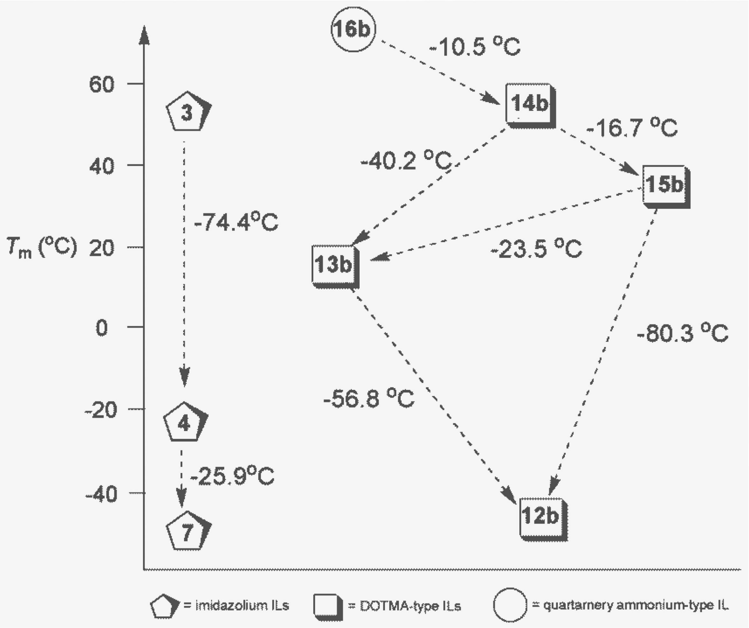

*Figure 4. ΔT_m relationships in ILs **12b-16b** and **3**, **4** and **7** (32).*

Equally apparent from the comparative T_m values of **12b-15b** is the impact of having dipolar functional groups present near the head group of the molecule. For example, the ΔT_m between **12b** and **13b** is quite large (56.8 °C), and the sole structural difference between them is the presence in the latter of two C=O groups at the glyceryl linker moiety. Even more dramatic is the 80.3 °C ΔT_m between **15b** and **12b**. Note that **15b** has a third linker-situated polar entity, specifically a phosphate group. The progressive increases in T_m arising from incorporation of dipolar entities (*e.g.,* **12b** → **13b** → **15b**) make sense, given the increasing inter-ionic cohesion that would be expected to result from dipole-dipole interactions (Figure 4).

Side-chain branching is another structural feature of the new ILs that appears to have an important impact upon T_m (*33*). Inspection of the structures of **12b-15b** reveals that the glyceryl linker in each contains a branch point from which the head group and each of the two lipidic appendages diverge. However, the uniformity of branching in **12b-15b** leaves only **16b** as a reference against which any effect can be gauged. Fortunately, like **12b-15b**, **16b** has a compact quaternary ammonium head group linked to two C_{18} appendages, making it a passable benchmark for assessing the effect of branching, especially in comparison to **14b** which, like it, has saturated alkyl appendages.

Although the measured ΔT_m between **14b** and **16b** is modest (10.5 °C), **14b** has two polar ester groups near its head a difference that is singularly responsible for **13b** having a T_m value 56.8 °C higher than **12b**. Hence, the 10.5 °C T_m gap between **16b** and **14b** is likely a net effect; viewed alongside the behaviors of

12b versus **13b**, it can be inferred that the intrinsic impact of the branching in these cations may actually be much greater, but that it is largely masked by the countervailing influence of the ester groups in **14b**.

Collectively, the forgoing data indicate that there is considerable structural latitude possible when designing highly lipophilic ILs that exhibit low (or relatively low) values of T_m. In the present examples, the inclusion of *cis* double bonds in the side chains appears to be the most powerful downward driver of T_m. However, side-chain branching also has a demonstrable effect, and might prove (pending further investigation) to be similarly efficacious. The utilization of quaternary ammonium head groups, with their more highly localized charge, appears to have little or no intrinsic T_m -increasing impact in these lipidic materials. Note that the T_m of **12b** (the 'best' of the transfection-agent based ILs) with its two side-chain double bonds and quaternary ammonium headgroup is a scant 5 °C higher that that of **7** (the 'best' first-generation lipidic IL), with its two side-chain double bonds and more charge-diffuse imidazolium head group. In contrast, the presence of dipolar functional groups (esters) in the head group/linker region of the cations consistently results in higher T_m values, although sub-ambient T_m values (*e.g.,* **13b**, 14.6 °C) can still be achieved.

Synthesis of Structurally Diverse Thiol Substituents Lipid-Inspired Ionic Liquids *via* Thiol-ene "Click" Chemistry

As noted, in the first generation of lipidic ionic liquids, bio-derived fatty alcohols were used to generate the side chains of 1-methyl-3-alkylimidazolium ions to show the dramatic melting point decrease observed for the bistriflimide salts (NTf_2) when simple structural features such as a single *cis*-double bond were introduced into the alkyl chain. In the second generation of these compounds, we demonstrated similar effects with other natural and synthetic asymmetric structural features that introduce either "kinks", "bumps", or both in the alkyl chain structure. However, these alkene-induced reductions in T_m are accomplished by an increase in the chemical fragility of the ionic liquid like edible oils containing unsaturated lipids, the former are subject to slow oxidative cleavage of their alkyl side chains at the site of unsaturation. In order to minimize this effect, the thiol-ene reaction (*36*) was utilized with different *ene*-functionalized ionic liquids by reacting them photochemically with alkyl thiols, yielding third generation of lipidic ILs with a thioether linkage.

In the third generation of these materials, we utilized the "click" chemistry of thiol-ene reaction to generate synthetic analogs of the naturally derived side chains. Asymmetric features are introduced through the inclusion of sulfur atoms and branches in the alkyl chain, both easily facilitated through the use of thiol-ene chemistry. This synthetic motif has also allowed us to examine the effect of the location of the heteroatom and branches in the alkyl chain on the thermophysical properties of the species providing valuable structure/property information which informs molecular design. In this work, we focused on the synthesis of a new class of functionalized ionic liquids and provide insights which may be useful for designing novel TSILs.

Addition of sulfurs to alkenes is certainly not a recent discovery. The vulcanization of natural rubber, poly(*cis*-isoprene), by sulfur moieties was patented in the mid-19th century by Charles Goodyear (*38*). This process was the start of thiol-ene chemistry. Its mechanism is mostly the radical addition of thiols across unactivated carbon–carbon double bonds. In some cases, reaction can take place by a mixed mechanism, including the classical radical addition but also Michael-type nucleophilic addition (*37*, *39*). Thiol-ene showed unique properties, which allowed them to have variety of commercial products such as high molecular weight polymers. Resurgence over the past decades has occurred in response to the many benefits thiol-ene coupling presents for polymer synthesis in different reaction conditions/solvents, clearly defined reaction pathways/products, and facile synthetic strategies from a range of easily obtained starting materials. These qualities, mostly resulting from the high efficiency and orthogonality of the reaction, have led to thiol-ene chemistry being used increasingly in polymer functionalization, macromolecular synthesis and functionalized biomaterials (*36*, *37*).

Impressed by the click paradigm, using thiol-ene "click" reaction on *ene*-functionalized ionic liquids to assess its potential utility in TSIL synthesis has been reported by our group for the first time (*40*). A series of novel TSILs with highly polar polyhydroxylated appendages containg sulfur moieties was prepared *via* radical-based thiol-ene addition (Scheme 4). In this strategy, construction of functionalized ILs using the thiol-ene click reaction offers considerable promise as an easy means by which to create structurally elaborated IL ions. **17T-20T** (T= thioglycerol addition product) ILs with multiple hydroxyl and thioether functional groups were readily prepared by the radical addition of 1-thioglycerol and salts of imidazolium and quaternary ammonium cations bearing tethered allyl and/or vinyl groups. Neither the proximity of the unsaturated appendage to the charge locus (*cf.*, vinylic vs allylic), the nature of the cation as aromatic (imidazolium) or nonaromatic (quaternary ammonium), or the nature of the anion appears to have a material effect on the ease with which the couplings can be accomplished. The incorporation of two hydroxyl groups per cation per tethered *ene* moiety gives the resulting ions richly polar appendages with multiple H-bond donor and acceptor sites, features which have a significant, temperature-dependent impact on the viscosity of these ILs.

As shown in Scheme 4, four different ILs (**17-20**) were selected as *ene* substrates for this study. Imidazolium and quaternary ammonium-based cations with either *N*-vinyl or *N*-allyl appendages were chosen to assess the effect, if any, of having the alkene moieties connected directly to the center of the cationic charge versus being separated from it by one carbon unit. In addition, two different anions were employed to detect any control over the course of the thiol-ene reaction (Br^- and NTf_2^-). 1-thioglycerol used for initial study in order to demonstrate the incorporation of a thioether and multiple hydroxyl functional groups into an IL by way of the orthogonal reaction of *ene*-bearing IL ions and a building block bearing both the functional group of interest and necessary thiol moiety (Scheme 4).

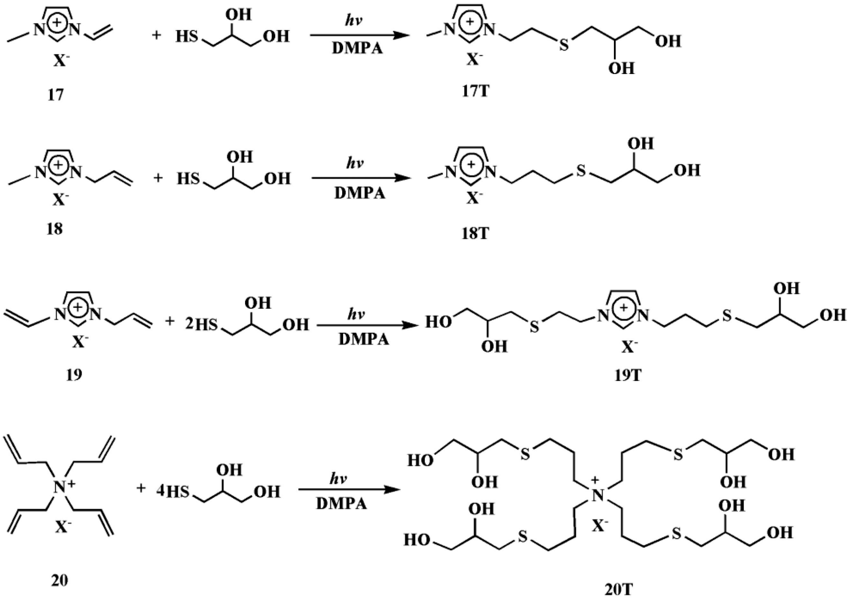

X= Br$^-$ and NTf$_2^-$
DMPA= 2,2-dimethoxy-2-phenylacetophenone

*Scheme 4. Synthesis of polyhydroxylated TSILs (**17T-20T**) via thiol-ene reaction of ene-functionalized ILs and 1-thioglycerol (40).*

The coupling reaction of thioglycerol to **17-20** was carried out using an approach modeled on that used by Hawker, *et al.* for the thiol-ene based assembly of functionalized dendrimers (*37*). The reactions proceed quickly and cleanly, and usually give acceptable yields of products without optimization (64-83%). The use of small amount of DMPA (2,2-dimethoxy-2-phenyl) acetophenone) relative to alkene (mol/mol) resulted erratic results under air or N_2, prompting us to significantly increase the amount this photocatalyst used in each reaction. While the mechanistic basis for this apparent diminution in catalyst efficiency from that normally observed is unclear, our use of larger quantities did not complicate the workup and isolation of the products. Indeed, the photocatalyst is readily removed by washing the reaction residue with hexane, in which none of the starting or product ILs is soluble. Likewise, in the case of the Tf_2N^- salts, any residual/excess thioglycerol was easily removed by washing with water, with which those ILs were immiscible. All of the new ILs **17T-20T** were isolated as yellow liquids at room temperture.

Given the ease with which **17** and **18** were functionalized, we expanded the scope of the study to ILs with ions bearing more than one *ene* group (Scheme 4). ILs **19** and **20** were used as multiple *ene*-functionalized starting materials for the thiol-ene reaction using standard approaches. When combined with 1-thioglycerol and irradiated under the same conditions, the anticipated polyaddition products were formed quantitatively and isolated in good yields. Not surprisingly, the viscosities of the **19T** and **20T** ILs tangibly greater than **17T** and **18T,** likely because of the more omni-directional H-bonding potential inherent in the cations of the former.

In order to expand this study, oleyl-based ionic liquid **4** was selected as *ene* substates for the thiol-ene recation. The IL cation was imidazolium-based and bore an appended *N*-oleyl group which was prepared by the *N*-alkylation reaction of 1-methylimidazole and oleiodide (Scheme 2).

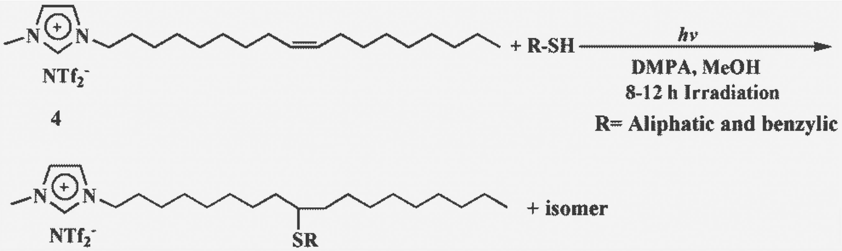

*Scheme 5. Thiol-ene reaction on oleyl-based ILs **4**.*

The thiol-ene reactions were carried out under mild conditions utilizing two equivalents of thiol per alkene in MeOH and irradiated at room temperature. Isolated yields varied from 63-89% (Scheme 5). All of synthesized ILs were viscous liquids at ambient temperature. The thiol-ene reaction allows for the incorporation of short alkyl chains (propyl); sterically hindered molecules (*tert*-butyl); long alkyl chains (octyl); aromatic (benzyl) and long fluorinated chains. It is important to note, however, that the thiol-ene addition to the oleyl side chain is not regioselective, and produces equal amounts (NMR) of two products – one from addition of the RS radical to C9 and the other from addition of the RS radical to C10. Accordingly, the physical state and properties of these materials are those of the mixture, not those of either pure product. While it should be possible, in principle, to separate the two isomers, we do not view such an effort as being especially practical or necessary. Note that a key objective in our work with lipid-inspired ionic liquids is to develop materials that are highly lipophilic while being low melting. With regard to the former attribute, both isomers of any given addition product have equal contents of aliphatic structural units. Insofar as maintaining or achieving low melting points, having a mixture of isomers likely enforces lower phase transition temperatures than those which would be observed for the individual isomers.

Conclusion

In conclusion, our studies show that ILs with long alkyl appendages respond to side-chain modification –specifically unsaturation and branching– in a fashion that mimics that underlying homeoviscous adaptation in living organisms. Further, a family of low-melting, highly lipophilic thiol-functionlized lipid-inspired ILs were synthesized *via* thiol-ene reaction. It is a phenomenon that is eminently exploitable from a utilitarian standpoint, and which we believe creates new opportunities for manipulating the properties of ILs and other synthetic soft biomaterials. Studies aimed at assessing an array of such possibilities are already in progress.

Despite a certain degree of maturity, the synthsis of functionlized bio-based ionic liquids still faces complicated issues. There are challenges, and still many new ILs with low T_m remain to be discovered. There will be many opportunities, and also much need, for continuously expanding the scope of lipid-based TSILs.

Acknowledgments

The corresponding authors would like to thank the National Science Foundation (Grant No. CBET-1133101) and Chevron for support of this research.

References

1. Dujardin, E.; Mann, S. *Adv. Mater.* **2002**, *14*, 1–14.
2. Xia, F.; Jiang, L. *Adv. Mater.* **2008**, *20*, 2842–2858.
3. For a comprehensive review of the history, properties, and applications of ionic liquids, see: Wasserscheid, P.; Welton, T. *Ionic Liquids in Synthesis*, 2nd ed.; Wiley-VCH: Weinheim, 2008.
4. Hallett, J. P.; Welton, T. *Chem. Rev.* **2011**, *111*, 3508–3576.
5. Sun, N.; Rodriguez, H.; Rahman, M.; Rogers, R. D. *Chem. Commun.* **2011**, *47*, 1405–1421.
6. Hough, W. L.; Smiglak, M.; Rodriguez, H.; Swatloski, R. P.; Spear, S. K.; Daly, D. T.; Pernak, J.; Grisel, J. E.; Carliss, R. D.; Soutullo, M. D.; Davis, J. H., Jr.; Rogers, R. D. *New J. Chem.* **2007**, *31*, 1429–1436.
7. Tang, S.; Baker, G. A.; Zhao, H. *Chem. Soc. Rev.* **2012**, *41*, 4030–4066.
8. Davis, J. H., Jr. *Chem. Lett.* **2004**, *33*, 1072–1077.
9. Bao, W.; Wang, Z.; Li, Y. *J. Org. Chem.* **2003**, *68*, 591–593.
10. Ohno, H.; Fukumoto, K. *Acc. Chem. Res.* **2007**, *40*, 1122–1129.
11. Plaquevent, J. -C.; Levillain, J.; Guillen, F.; Malhiac, C.; Gaumont, A. -C. *Chem. Rev.* **2008**, *108*, 5035–5060.
12. Doktorovova, S; Souto, E. B. *Expert Opin. Drug Delivery* **2009**, *6*, 165–176.
13. Mahato, R. I.; Rolland, A.; Tomlinson, E. *Pharm. Res.* **1997**, *14*, 853–859.
14. Biermann, U.; Bornscheuer, U.; Meier, M. A. R.; Metzger, J. O.; Schäfer, H. J. *Angew. Chem., Int. Ed.* **2011**, *50*, 3854–3871.
15. Singer, S. J.; Nicholson, G. L. *Science* **1972**, *175*, 720–731.
16. Wiśniewska, A.; Draus, J.; Subczynski, W. K. *Cell. Mol. Biol. Lett.* **2003**, *8*, 147–159.
17. Canongia Lopes, J. N. A.; Padua, A. A. H. *J. Phys. Chem. B* **2006**, *110*, 3330–3335.
18. Löpez-Martin, I.; Burello, E.; Davey, P. N.; Seddon, K. R.; Rothenberg, G. *ChemPhysChem* **2007**, *8*, 690–695.
19. Sinensky, M. *Proc. Natl. Acad. Sci. U.S.A.* **1974**, *71*, 522–525.
20. Murray, S. M.; O'Brien, R. A.; Mattson, K. M.; Ceccarell, C.; Sykora, R. E.; West, K. N.; Davis, J. H., Jr. *Angew. Chem., Int. Ed.* **2010**, *49*, 2755–2758.

21. Wei, J. *Ind. Eng. Chem. Res.* **1999**, *38*, 5019–5027.
22. Linstrom, P. J.; Mallard, W. G. NIST Chemistry WebBook, National Institute of Standards and Technology. http://webbook.nist.gov (retrieved October 31, 2009).
23. Van Rantwijk, F.; Sheldon, R. A. *Chem. Rev.* **2007**, *107*, 2757–2785.
24. Felgner, P. L.; Gadek, T. R.; Holm, M.; Roman, R.; Chan, H. W.; Wenz, M.; Northrop, J. P.; Ringold, G. M.; Danielsen, M. *Proc. Nat. Acad. Sci. U.S.A.* **1987**, *84*, 7413–7417.
25. Ewert, K. K.; Zidovska, A.; Ahmad, A.; Bouxsein, N. F.; Evans, H. M.; McAllister, C. S.; Samuel, C. E.; Safinya, C. R. *Top. Curr. Chem.* **2010**, *296*, 191–226.
26. Midoux, P.; Breuzard, G.; Gomez, J. P.; Pichon, C. *Curr. Gene Ther.* **2008**, *8*, 335–352.
27. Siepi, E.; Lutz, S.; Meyer, S.; Panzner, S. *Biophys. J.* **2011**, *100*, 2412–2421.
28. Hart, S. L. *Curr. Drug Delivery* **2005**, *2*, 423–428.
29. Douce et al. have recently reported expressly amphiphilic, double-tailed imidazolium salts as prospective siRNA transfection agents and commented upon their relationship to ILs. See: Dobbs, W.; Heinrich, B.; Bourgogne, C.; Donnio, B.; Terazzi, E.; Bonnet, M.-E.; Stock, F.; Erbacher, P; Bolcato-Bellemin, A.-L.; Douce, L. *J. Am. Chem. Soc.* **2009**, *131*, 13338–13348.
30. Mudring et al. have recently examined different types of double-tailed imidazolium salts as ionic liquid crystals. See Wang, X.; Heinemann, F. W.; Yang, M.; Melcher, B. U.; Fekete, M.; Mudring, A.-V.; Wasserscheid, P.; Meyer, K. *Chem. Commun.* **2009**, 7405–7407.
31. Beranova, J.; Jemiola-Rzeminska, M.; Elhottova, D.; Strzalka, K.; Konopasek, I. *Biochim. Biophys. Acta* **2008**, *1782*, 445–453.
32. Mirjafari, A.; Murray, S. M.; O'Brien, R. A.; Stenson, A. C.; West, K. N.; Davis, J. H., Jr. *Chem. Commun.* **2012**, *48*, 7522–7524.
33. Huang, J.-F.; Luo, H.; Liang, C.; Sun, I.-W.; Baker, G. A.; Dai, S. *J. Am. Chem. Soc.* **2005**, *127*, 12784–12785.
34. Bradley, A. E.; Hardacre, C.; Holbrey, J. D.; Johnston, S.; McMath, S. E. J.; Nieuwenhuyzen, M. *Chem. Mater.* **2002**, *14*, 629–635.
35. Copyright-free liposome graphic by Villarreal, M. R. http://schools-wikipedia.org/images/623/62382.png.htm.
36. Bowman, C. N.; Hoyle, C. E. *Angew. Chem. Int. Ed.* **2010**, *49*, 1540–1573.
37. Kade, M. J.; Burke, D. J.; Hawker, C. J. *J. Polym. Sci., Part A: Polym. Chem.* **2010**, *48*, 743–750.
38. Posner, T. *Chem. Ber.* **1905**, *38*, 646–657.
39. Lowe, A. B. *Polym. Chem.* **2010**, *1*, 17–36.
40. O'Brien, R. A.; Mirjafari, A.; Jajam, V.; Capley, E. N.; Stenson, A. C.; West, K. N.; Davis, J. H., Jr. *Tetrahedron Lett.* **2011**, *52*, 5173–5175.

Chapter 10

Gas Solubility in Ionic Liquids: Mixed Gases in Pure Ionic Liquids and Single Gases in Binary Liquid Mixtures

Dirk Tuma[1,2] and Gerd Maurer[*,1]

[1]Department of Mechanical and Process Engineering,
University of Kaiserslautern, P. O. Box 3049,
D-67653 Kaiserslautern, Germany
[2]Current address: BAM Federal Institute for Materials Research and Testing, D-12200 Berlin, Germany
[*]E-mail: gerd.maurer@mv.uni-kl.de

In the last two decades, the solubility of gases in ionic liquids has attracted a lot of attention. While at the beginning most publications dealt with the solubility of a single gas in a pure ionic liquid, recently the interest starts to shift to the – from an application-oriented point of view – more challenging area of the simultaneous solubility of several gases in an ionic liquid and/or the solubility of a single gas in solvent mixtures with ionic liquids. The current state of information on experimental data (and the phenomena encountered) in such systems is summarized and discussed.

Introduction

Accurate experimental data for the solubility of gases in liquids are required in many applications of ionic liquids. While most scientific publications in that area deal with the solubility of a single gas in a pure ionic liquid (*1*, *2*), most applications deal with either gas mixtures and/or liquid mixtures with ionic liquid components (*3*–*5*). The main focus of this chapter is a) on the simultaneous solubility of two gases in a pure ionic liquid and b) on the solubility of a single gas in a binary liquid mixture where one of the solvent components is an ionic liquid. The presence

In Ionic Liquids: Science and Applications; Visser, A., et al.;
ACS Symposium Series; American Chemical Society: Washington, DC, 2012.

of a large amount of a gas in a liquid often results in a volume expansion of the solvent (that phenomenon is commonly called "gas-expanded liquid") and causes a decrease (increase) of the viscosity (intrinsic diffusivity of solutes) (*6*). Experimental data for the volume expansion are sometimes obtained as a side product from gas solubility measurements (see, for example, Kumełan et al. (*7*)). Therefore, the volume expansion caused by the presence of a gaseous solute in an ionic liquid (or a solvent mixture with an ionic liquid component) is also discussed briefly.

Simultaneous Solubility of Two Gases in a Pure Ionic Liquid

The solubility of a gas G in a pure ionic liquid IL is here described by the extended Henry's law on the molality scale assuming that the saturation pressure of the ionic liquid is negligible:

$$k_{\mathrm{H,G,IL}}^{(m,0)}(T)\exp\left(\frac{v_{\mathrm{G,IL}}\,p}{R\,T}\right)\frac{m_{\mathrm{G}}}{m^{\mathrm{o}}}\gamma_{\mathrm{G}}^{(m)}=f_{\mathrm{G}}=p\,y_{\mathrm{G}}\,\varphi_{\mathrm{G}} \tag{1}$$

$k_{\mathrm{H}}^{(m,0)}(\mathrm{G,IL})\,(T)$ is Henry's constant of G in the ionic liquid IL on the molality scale at zero pressure, $v_{\mathrm{G,IL}}$ is the partial molar volume of G in the ionic liquid IL, p is the pressure, R is the universal gas constant, T is the thermodynamic temperature, m_{G} is the molality of G (i.e., the number of moles of G per kilogram of IL), m^{o} = 1 mol/kg IL, and $\gamma_{\mathrm{G}}^{(m)}$ is the activity coefficient of G (normalized according to Henry's law on the molality scale) in the ionic liquid IL; f_{G}, y_{G}, and φ_{G} are the fugacity, the mole fraction, and the fugacity coefficient, respectively, of G in the vapor phase. $k_{\mathrm{H}}^{(m,0)}(\mathrm{G,IL})\,(T)$ depends only on temperature.

The volume of the liquid phase is:

$$V_{\mathrm{liq}}=\sum_{i} n_i v_{i,\mathrm{liq}} \tag{2}$$

where n_i and $v_{i,\mathrm{liq}}$ are the number of moles and the partial molar volume of component i in the liquid phase, respectively. In connection with gas solubility phenomena, it is often sufficient to replace the partial molar volume of the solvent by the molar volume of the pure solvent $v_{\mathrm{IL,liq}} = v_{\mathrm{IL,pure\ liq}}$ and the partial molar volume of a dissolved gas G by its partial molar volume at infinite dilution in the particular ionic liquid $v_{\mathrm{G,liq}} = v^{\infty}_{\mathrm{G,IL}}$.

Furthermore, the influence of pressure on the volumetric properties is in most cases negligible.

Therefore, when two non-reacting gases G_1 and G_2 are simultaneously dissolved in an ionic liquid at a constant temperature, the phase equilibrium condition becomes:

$$k_{\mathrm{H,G,IL}}^{(m,0)}(T)\exp\left(\frac{v_{\mathrm{G,IL}}^{\infty}\,p}{R\,T}\right)\frac{m_{\mathrm{G}}}{m^{\mathrm{o}}}\gamma_{\mathrm{G}}^{(m)}=p\,y_{\mathrm{G}}\,\varphi_{\mathrm{G}}\quad(\mathrm{G}=\mathrm{G}_1,\mathrm{G}_2) \tag{1a}$$

and the volume of the liquid phase is:

$$V_{\text{liq}} = n_{\text{IL}}\ v_{\text{IL,pure liq}}(T) + n_{G_1}\ v^{\infty}_{G_1,\text{IL}} + n_{G_2}\ v^{\infty}_{G_2,\text{IL}} \tag{2a}$$

Three cases should be distinguished.

Case I: Both Gases Are Only Sparsely Soluble in the Ionic Liquid

In such cases, the zero-pressure Henry's constant on the molality scale $k_H^{(m,0)}$(G,IL) (T) is typically larger than about 50 MPa (for example, for H_2 and CO in 1-*n*-butyl-3-methylimidazolium methyl sulfate ([bmim][CH_3SO_4]) at 300 K: $k_H^{(m,0)}$(H_2,[bmim][CH_3SO_4]) = 160 MPa and $k_H^{(m,0)}$(CO,[bmim][CH_3SO_4]) = 93 MPa (*8*)), and the molality of the dissolved gas at a partial pressure of 10 MPa is typically below 0.2 mol/kg IL. Then, the activity coefficients of both gases can be neglected, and consequently the solubility of the gases in the ionic liquid can be calculated by superimposing the solubilities of both single gases in the ionic liquid with small corrections due to, first, the influence of pressure in the exponential term on the left-hand side of eq 1a (i.e., the so-called Krichevsky-Kasarnovsky correction) and, second, the influence of pressure and vapor phase composition on the fugacity coefficients of both gases. However, both corrections are often very small, and the deviation from the described superimposition can hardly be detected in experimental work.

To the best of our knowledge, no experimental data for the solubility of two sparsely soluble gases in a single ionic liquid are available in the open literature yet.

The partial molar volume of a gas at infinite dilution in an ionic liquid is typically about 20 cm^3/mol (for example, at 300 K: v^{∞}(H_2,[bmim][CH_3SO_4]) = 20 cm^3/mol and v^{∞}(CO,[bmim][CH_3SO_4]) = 18 cm^3/mol (*8*)), and the molar volume of a pure ionic liquid is typically about 200 cm^3/mol (for example, at 300 K: v([bmim][CH_3SO_4],liq) = 208 cm^3/mol (*9*)). Therefore, the volume expansion caused by the dissolved gases is also small. For example, when an equimolar mixture of H_2 and CO is dissolved in one kilogram of [bmim][CH_3SO_4] at 300 K and 10 MPa, the volume expansion caused by the dissolved gases is about 0.2 % (*7*).

Case II: One Gas Is Well Soluble, but the Other One Is Sparsely Soluble in the Ionic Liquid

For a rough distinction between a "well soluble" gas on the one hand and a "sparsely soluble" gas on the other hand, it is sufficient to discuss the Henry's constants of both gases. As in case I, we characterize here a "sparsely soluble" gas by a Henry's constant $k_H^{(m,0)}$(G,IL) > 50 MPa, whereas Henry's constant of a "well soluble" gas is typically smaller by a factor of more than 10, i.e., $k_H^{(m,0)}$(G,IL) < 5 MPa. Several examples have been reported for this combination in the literature. In the following cases, CO_2 was the well soluble gas and either H_2 (*10*, *11*), O_2 (*12*), N_2 (*13*), or CH_4 (*12*) was the sparsely soluble gas. Such experimental data are of interest, for example, for chemical reactions in CO_2-expanded solvents. In most publications (*11–13*), 1-*n*-hexyl-3-methylimidazolium bis(trifluoromethylsulfonyl) amide ([hmim][Tf_2N]) was the solvent. All experimental results revealed that the presence of CO_2 increases the solubility of a sparsely soluble gas (i.e., CO_2 acts as a cosolvent for a sparsely soluble gas). A similar finding, however, occurred in a study on SO_2 solubility in the presence of N_2 (10 mol % SO_2 in N_2) in five different ionic liquids (*14*). The experimental results reveal that dissolved SO_2 is a cosolvent for nitrogen which – as a pure gas – is nearly insoluble in those ionic liquids. Heintz et al. (*15*) reported experimental results for the solubility of H_2S and N_2 in an ionic liquid with a polymeric ammonium polyether-based cation and chloride anion.

Although in principle, a well soluble gas might also act as an antisolvent for the sparsely soluble gas, no such experimental findings have been reported so far.

The experimental results by Kumełan et al. (*11*) for the simultaneous solubility of CO_2 and H_2 in [hmim][Tf_2N] are discussed here as a typical example for the solubility of a binary gas mixture in a pure ionic liquid.

Figure 1 shows the experimental data for the pressure that is required to simultaneously dissolve about 0.018 (0.037) moles of H_2 and between 0.35 and 3.8 moles of CO_2 in one kilogram of [hmim][Tf_2N] at 293 K in comparison with prediction results.

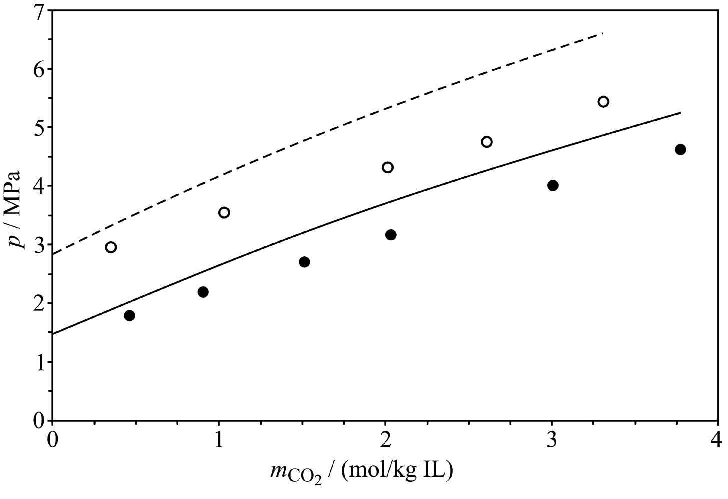

Figure 1. Pressure required to simultaneously dissolve CO_2 and H_2 in [hmim][Tf_2N] at 293 K. Experimental results: (●) $m_{H_2} \approx 0.018$ mol/kg IL; (○) $m_{H_2} \approx 0.037$ mol/kg IL. Lines represent predictions neglecting interactions between CO_2 and H_2 in the liquid phase.

The predictions are based on a simple model that combines the truncated virial equation of state for describing the fugacity coefficients in the vapor phase and an osmotic virial equation (based on the molality scale) for the excess Gibbs energy of the liquid phase. The corresponding activity coefficient of a dissolved gas G_i is:

$$\ln \gamma_{G_i}^{(m)} = 2\sum_{J} \frac{m_J}{m^o}\cdot \beta_{G_i,J} + 3\sum_{J}\sum_{K}\left(\frac{m_J}{m^o}\right)\cdot\left(\frac{m_K}{m^o}\right)\cdot \mu_{G_i,J,K} \qquad (3)$$

where J and K represent a dissolved gas. $\beta_{G_i,J}$ and $\mu_{G_i,J,K}$ are parameters that describe the strength of binary and ternary interactions, respectively, between gas molecules in the ionic liquid. These parameters depend on temperature. They are symmetric (for example, $\beta_{G_i,J} = \beta_{J,G_i}$ and $\mu_{G_i,J,K} = \mu_{J,G_i,K} = \mu_{J,K,G_i}$). Parameters for interactions between the same gaseous solutes in [hmim][Tf_2N] were taken from the correlations by Kumełan et al. (*7*). Neglecting all parameters for interactions between hydrogen on the one hand and carbon dioxide on the other hand (i.e., setting $\beta_{H_2,CO_2} = \mu_{H_2,CO_2,CO_2} = \mu_{H_2,H_2,CO_2} = 0$) allows to predict the simultaneous solubility of H_2 and CO_2 in [hmim][Tf_2N]. The predicted values for the solubility pressure are higher than the experimental results. The differences increase with increasing amounts of dissolved gases. For the comparison shown in Figure 1, the standard deviation between the experimental results and the prediction results for the total pressure is 0.76 MPa (18 %). The differences decrease when parameters for interactions between H_2 on the one hand and CO_2 on the other hand in the liquid phase are considered in eq 3. For example, when the two parameters β_{H_2,CO_2} and μ_{H_2,CO_2,CO_2} were fitted to the experimental results for the solubility pressure at given temperature and composition of the liquid phase at 293 K, the standard deviation decreases to 0.049 MPa (0.4 %) (Kumełan et al. (*11*)). From eq 1, one can estimate the influence of gas G_1 on the solubility of gas G_2 at constant temperature and constant fugacity of gas G_2 in the vapor phase f_{G_2} to:

$$\left(\frac{\Delta m_{G_2}}{m_{G_2}}\right)_{T,f_{G_2}} \cong -2\cdot \beta_{G_2,G_1}\cdot \frac{\Delta m_{G_1}}{m^o} \qquad (4)$$

As for 293 K, the correlation yields $\beta_{H_2,CO_2} \cong -0.16$ (cf. Kumełan et al. (*11*)), and one mole of CO_2 (corresponding to $f_{CO_2} \approx 1.2$ MPa) increases the solubility of H_2 in the ionic liquid [hmim][Tf_2N] at 293 K by about 30 %. Vice versa, there is also an influence of H_2 on the solubility of CO_2 in [hmim][Tf_2N]. However, as the molality-based Henry's constants of H_2 and CO_2 in [hmim][Tf_2N] differ considerably at 293 K ($k_H^{(m,0)}(H_2,[hmim][Tf_2N]) = 86.2$ MPa (*7*); $k_H^{(m,0)}(CO_2,[hmim][Tf_2N]) = 1.24$ MPa (*16*)), at $f_{H_2} = 1.2$ MPa, the molality of H_2 in [hmim][Tf_2N] is only 0.014 mol/kg IL, and the increase in the molality of dissolved CO_2 is only about 0.4 %. This effect is so small that it is very difficult to determine it experimentally.

In most cases, the volume expansion of an ionic liquid (for example, [hmim][Tf_2N]) caused by the simultaneous solubility of a well soluble and a sparsely soluble gas (for example, CO_2 and H_2) is dominated by the amount of the well soluble gas that is dissolved in the ionic liquid. In particular, the changes that are due to the increase of the solubility of the sparsely soluble gas (caused by the presence of a well soluble gas) are often smaller than the uncertainty of the experimental results for the volumetric properties (cf. Kumełan et al. (*7*)).

Case III: Both Gases Are Well Soluble in the Ionic Liquid

Experimental investigations on the simultaneous solubility of two well soluble, non-reacting gases are rarely found in the literature, although in recent years an increasing interest for applications of ionic liquids in gas separation technology has been observed. Most published experimental data originate from the group of Shiflett who investigated the solubility of (CO_2 + SO_2) in [hmim][Tf_2N] (*17*) and [bmim][CH_3SO_4] (*18*), of (CO_2 + H_2S) in [bmim][CH_3SO_4] (*19*) and [bmim][PF_6] (*20*), and of (CO_2 + N_2O) in [bmim][BF_4] (*21*) in the temperature range from 295 K to 323 K and at pressures between 0.1 MPa and 0.5 MPa in the (CO_2 + SO_2 + IL) systems, between 0.2 MPa and 0.8 MPa in the (CO_2 + H_2S + IL) systems, and ultimately between 0.47 MPa and 0.65 MPa in the (CO_2 + N_2O + [bmim][BF_4]) system. Kim et al. (*13*) presented a few experimental data points for the solubility of (CO_2 + propane) in [hmim][Tf_2N] at 298 K; Jalili et al. (*22*) reported experimental results for the solubility of (CO_2 + H_2S) in [C_8mim][Tf_2N] at temperatures from 303 to 343 K and at pressures from 0.17 MPa to 1.2 MPa.

The primary objective of those publications by Shiflett and co-workers is not on gas solubility but on the application of an ionic liquid for the separation of mixtures of liquefied gases by extractive distillation – with an IL additive – at ambient (and at a slightly elevated) pressure. Therefore, they use the gaseous absorption selectivity S_{G_2/G_1} to describe the influence of an ionic liquid on a vapor-liquid equilibrium:

$$S_{G_2/G_1} = \left(\frac{y_{G_1}}{x_{G_1}}\right) \Bigg/ \left(\frac{y_{G_2}}{x_{G_2}}\right) \tag{5}$$

where y_{G_i} and x_{G_i} are the mole fractions of gas G_i in the vapor and liquid phases, respectively. In particular, they discuss the influences of the mole fraction of an ionic liquid and the molar ratio of G_1/G_2 in a ternary feed solution (G_1 + G_2 + IL) on S_{G_2/G_1}. For example, their experimental results for the ionic liquid [bmim][CH_3SO_4] show that the addition of an ionic liquid to the binary system (G_1 (= CO_2) + G_2 (= SO_2)) results in a strong increase of S_{G_2/G_1} (at constant temperature and pressure) (*18*). That increase of S_{G_2/G_1} becomes more pronounced when the molar ratio of CO_2/SO_2 decreases. For the same ionic liquid, however, there appears a maximum in a plot of S_{G_2/G_1} versus the amount of added ionic liquid at lower temperatures and pressures (at temperature, pressure, and molar ratio of CO_2/SO_2 being constant).

Jalili et al. (*22*) used a similar method as Kumełan et al. (*11*) to describe the activities of solute species in an ionic liquid. They also used eq 3 to calculate the activity coefficient of a solute species, but they did not apply the common assumption on the symmetry of the binary parameters $\beta_{G_1,G_2} = \beta_{G_2,G_1}$. The authors fitted two binary parameters $\beta_{CO_2,H_2S} \neq \beta_{H_2S,CO_2}$ (together with a ternary parameter μ_{H_2S,CO_2,H_2S}) to their experimental results for the simultaneous solubility of CO_2 and H_2S in [C_8mim][Tf_2N] instead. According to eq 4, different numbers for β_{CO_2,H_2S} and β_{H_2S,CO_2} were required to account for the difference in the influence of H_2S on the solubility of CO_2 on the one hand, and of CO_2 on the solubility of H_2S on the other hand. The correlation of Jalili et al. results in very large and negative numbers of both binary parameters for interactions between the dissolved gases (for example, at 300 K: $\beta_{CO_2,H_2S} = -1.525$ and $\beta_{H_2S,CO_2} = -2.610$). As can be seen from eq 4, the gases act as mutual cosolvents in [C8mim][Tf2N] (i.e., CO_2 is a cosolvent for H_2S, and vice versa H_2S is a cosolvent for CO_2). As the Henry's constants of both gases differ by a factor between about 2.5 and 3 (at 300 K (350 K) $k_H^{(m,0)}(CO_2,[C_8mim][Tf_2N])$ = 0.56 MPa (0.96 MPa) and $k_H^{(m,0)}(H_2S,[C_8mim][Tf_2N])$ = 0.21 MPa (0.42 MPa) (*22*)) and the absolute numbers of both binary interaction parameters β_{CO_2,H_2S} and β_{H_2S,CO_2} are extremely large, eq 4 gives unreasonable numbers for the cosolvency effects. Furthermore, the correlation by Jalili et al. also gives large and negative numbers for the partial molar volumes of both gases in [C8mim][Tf2N]. Jalili explained that the applied model had been optimized for the best correlation performance. To maintain a rigorous physical meaning was not strictly intended in that study (*23*). A recent reevaluation of the experimental results for the solubility of the single gases CO_2 and H_2S as well as their mixtures in [C8mim][Tf2N] showed that a correlation with a more rigorous physical meaning is possible and that a single binary parameter β_{CO_2,H_2S} is sufficient to describe the cosolvency effect of one gas on the solubility of the other gas (*24*). Furthermore, that parameter is of the same order of magnitude as the corresponding binary parameter for the simultaneous solubility of CO_2 and H_2 in [hmim][Tf2N].

No reliable volumetric data for ternary liquid mixtures of an ionic liquid and two well soluble gases are available. Therefore, using eq 2a is the only way to estimate the volume expansion caused by the simultaneous solubility of two gases in a single ionic liquid.

Solubility of a Single Gas in a Binary Liquid Mixture of an Ionic Liquid

All published experimental results in this area consider CO_2 as the dissolved gas. The main reason for investigations in that field is the observation that CO_2 can act as an antisolvent for liquid solutions, i.e., pressurizing a liquid mixture with CO_2 can result in a liquid-liquid (or liquid-solid) phase split. Such a phase split might be applied for separation purposes. Scurto et al. (*25*) reported for the first time that – similar to aqueous solutions of hydrophilic organic solvents – a homogeneous liquid solution of an ionic liquid ([bmim][PF6]) and an organic solvent (methanol) can be forced to split into two liquid phases at 313 K when CO_2 is dissolved in the solvent mixture at pressures between 7 and 8 MPa. This phenomenon is commonly called "Salting Out by a Nearcritical Gas" (SONG). The first observations of the SONG phenomenon (in aqueous solutions of hydrophilic organic solvents) were reported by Elgin and Weinstock in 1959 (*26*). That particular phenomenon is often observed at temperatures around the critical temperature of the gas when at least one of the solvent components is a good solvent for that gas (*27*). The corresponding phase behavior is explained in Figures 2 and 3. Figure 2 shows three qualitative triangular composition diagrams for the ternary system (CO_2 + methanol + [bmim][PF6]) at a (constant) temperature slightly above the critical temperature of CO_2. As already mentioned, the saturation pressure of [bmim][PF_6] is negligible. Therefore, in Figure 2, the evanescent solubility of [bmim][PF_6] in the vapor phase V is not exactly drawn to scale for a better legibility. In the diagram on the left-hand side of Figure 2, the pressure is low, and the phase diagram is dominated by a large liquid-vapor (LV) region. At higher pressure (i.e., at pressures beyond the pressure at the "lower critical endpoint" (LCEP)), the dissolved gas induces a liquid-liquid phase split resulting in a liquid-liquid-vapor (L_1L_2V) phase equilibrium that is bordered by regions of two vapor-liquid phase equilibria as well as a liquid-liquid phase equilibrium (cf. the diagram in the center of Figure 2). When the pressure increases further, one of the vapor-liquid regions gets smaller and finally disappears (together with the three-phase liquid-liquid-vapor region) at the "upper critical endpoint" (UCEP). The diagram on the right-hand side of Figure 2 shows the phase behavior at a pressure beyond the upper critical endpoint. In that region, the phases L_2 and V have merged and display a fluid-like density. Therefore, the three-phase liquid-liquid-vapor (L_1L_2V) equilibrium only exists between the lower critical endpoint pressure (where both liquid phases reveal a critical behavior, i.e., at ($L_1 = L_2$) V) and the upper critical endpoint pressure, where the vapor phase and one of the liquid phases become critical, i.e., at L_1 ($L_2 = V$).

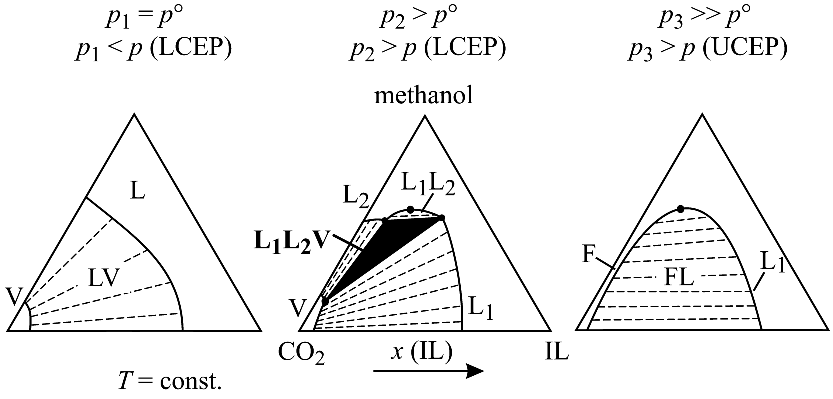

Figure 2. Qualitative composition diagrams showing the phase behavior in the ternary system (CO_2 + methanol + [bmim][PF_6]) at different pressures. Here, $p° = 0.1$ MPa.

Figure 3 shows a schematic of the phase behavior of the ternary system (CO_2 + methanol + [bmim][PF_6]) together with the phase behavior of the corresponding binary subsystems in a pressure versus temperature plot. At temperatures below the critical temperature of CO_2, the binary system (CO_2 + [bmim][PF_6]) exhibits a three-phase L_1L_2V equilibrium (*28*). The three-phase line L_1L_2V of this binary phase equilibrium is the upper critical endpoint line for the L_1L_2V equilibrium of the ternary system (CO_2 + methanol + [bmim][PF_6]) at temperatures below the critical point of CO_2. The branch of the critical line for the vapor-liquid equilibrium (L = V) of the binary system (CO_2 + [bmim][PF_6]) that starts from the critical point of CO_2 ends in the upper endpoint CEP of the binary L_1L_2V line of that binary system. The upper critical endpoint line L_1 (L_2 = V) starts at that CEP and ends in a tricritical point TCP ($L_1 = L_2 = V$) of the ternary mixture. In the real system (cf. Figure 5 for experimental data), the three-phase L_1L_2V line of the binary system (CO_2 + [bmim][PF_6]) and the vapor pressure curve of pure CO_2 almost coincide, similarly the critical point of CO_2 and the upper endpoint CEP do. In Figure 3, the differences are again scaled up to become distinguishable for the reader. Both critical endpoint lines (which border the three-phase L_1L_2V equilibrium) converge in a pressure versus temperature plot to the tricritical point TCP which coordinates are a characteristic property of the ternary system. No three-phase region L_1L_2V exists at temperatures and pressures beyond those at the tricritical point.

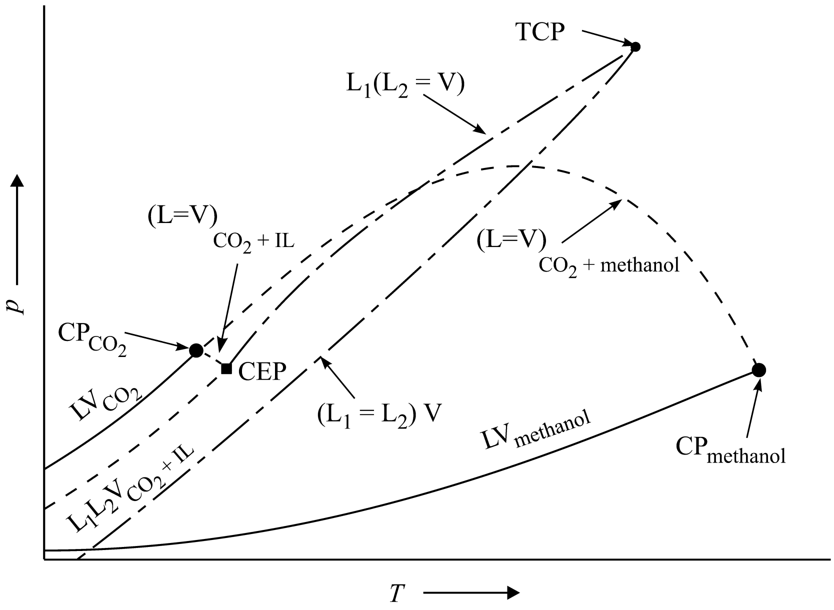

Figure 3. Qualitative pressure vs. temperature projection of phase boundaries for the ternary system (CO_2 + methanol + [bmim][PF_6]), the binary subsystems (CO_2 + [bmim][PF_6]) and (CO_2 + methanol), and for the pure compounds CO_2 and methanol. (——), pure compound; (– – –), binary system; (— — — – —), ternary system.

The three-phase behavior of that system was investigated in more detail by Liu et al. (*29*), Zhang et al. (*30*), Wu et al. (*31*), Aki et al. (*32*), Lim et al. (*33*), and recently by Chobanov et al. (*34*). Figure 4 shows experimental results for the composition of the coexisting liquid phases L_1 and L_2 in the L_1L_2V equilibrium of the system (CO_2 + methanol + [bmim][PF_6]) at 313 K (*30*, *34*). The three-phase equilibrium extends from 7 MPa to about 8 MPa. At the lower critical endpoint (i.e., at ($L_1 = L_2$) V), the mole fractions of CO_2 and [bmim][PF_6] in the critical liquid phases were determined by Aki et al. to $x^{(LCEP)}(CO_2) = 0.40$ and $x^{(LCEP)}([bmim][PF_6]) = 0.05$ (*32*). At the upper critical endpoint (i.e., at L_1 (L_2 = V)), the composition of the coexisting liquid phases can be estimated from the slope of a curve fitted to composition data. With increasing pressure, the mole fraction of [bmim][PF_6] in the liquid phase L_2 decreases to $x^{(L_2,UCEP)}$([bmim][PF_6]) < 0.002 at the upper critical endpoint, and the mole fraction of CO_2 increases to $x^{(L_2,UCEP)}(CO_2) > 0.86$. With increasing pressure, the mole fractions of [bmim][PF_6] and CO_2 in the liquid phase phase L_1 increase to $x^{(L_1,UCEP)}$([bmim][PF_6]) > 0.21 and $x^{(L_1,UCEP)}(CO_2) \approx 0.44$ at the upper critical endpoint pressure.

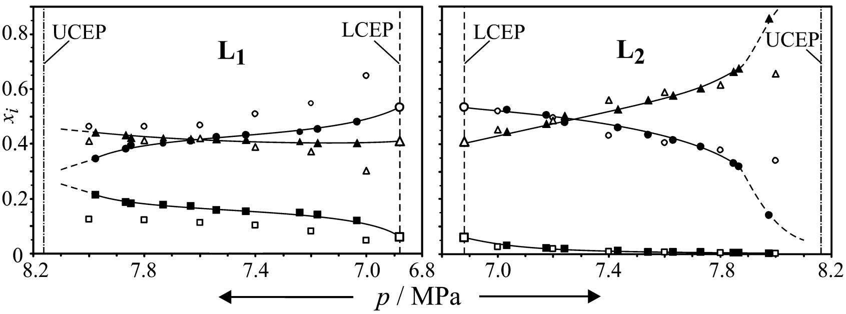

Figure 4. Compositions of the coexisting liquid phases L_1 and L_2 of the L_1L_2V equilibrium in the ternary system (CO_2 + methanol + [bmim][PF_6]) at T = 313 K. (■), [bmim][PF_6] (34); (□), [bmim][PF_6] (30); (large □), [bmim][PF_6], composition at the LCEP (32); (●), methanol (34); (○), methanol (30); (large ○), methanol, composition at the LCEP (32); (▲), CO_2 (34); (△), CO_2 (30); (large △), CO_2, composition at the LCEP (32).

As it is shown in Figure 5, at temperatures above the critical temperature of CO_2, the upper critical endpoint line of the ternary system (CO_2 + methanol + [bmim][PF_6]) coincides within experimental uncertainty with the (p,T) coordinates of the critical line for the vapor-liquid equilibrium of the binary system (CO_2 + methanol). Furthermore, the distance between both critical endpoint lines only slightly decreases with increasing temperature, i.e., the pressure range where a L_1L_2V equilibrium is observed for the ternary system (CO_2 + methanol + [bmim][PF_6]) is almost constant in the (investigated) temperature range from 295 K to 335 K (≈ 1 MPa). As a consequence, both temperature and pressure at the tricritical point are expected to be well beyond the investigated range of state ($T^{(TCP)}(L_1L_2V) > 340$ K; $p^{(TCP)}(L_1L_2V) > 12$ MPa).

Currently, the amount of published experimental three-phase equilibrium data is rather limited. First and at foremost, almost all experimental work was performed with CO_2 as the dissolved gas.

Zhang et al. (*36*) investigated the system (CO_2 + acetone + [bmim][PF_6]) at 313 K. They found a three-phase L_1L_2V equilibrium as described above at pressures between 4.9 and 8.1 MPa. Although that three-phase equilibrium exists over a more extended pressure region than in the system (CO_2 + methanol +

[bmim][PF_6]), the influence of pressure on the composition of the coexisting phases was similar in both systems. In contrast, the three ternary mixtures (CO_2 + 1-propanol + the ionic liquids [emim][Tf_2N], [emim][TfO] (i.e., [emim] triflate), and [C_{10}mim][Tf_2N], respectively) that were investigated by Bogel-Łukasik et al. (*37*) only showed a two-phase liquid-vapor equilibrium at 313 K and in a pressure range from 9 to 12 MPa.

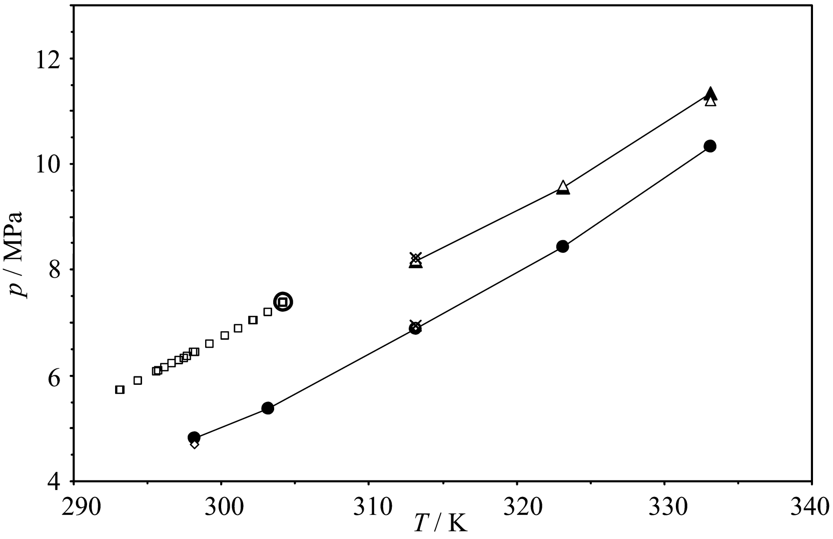

Figure 5. Coordinates of the lower (LCEP) and upper (UCEP) critical endpoint lines of the L_1L_2V equilibrium in the ternary system (CO_2 + methanol + [bmim][PF_6]): (●), LCEP (34); (▲), UCEP (34); (◊), LCEP and UCEP (32); (×), LCEP and UCEP (30); (△), coordinates of the vapor-liquid critical line of the binary subsystem (CO_2 + methanol) (34); (□), coordinates of the liquid-liquid-vapor line of the binary subsystem (CO_2 + [bmim][PF_6]) (28); (large ○), critical point of pure CO_2 (35).

The group of Brennecke investigated a total of 18 ternary systems mostly at 313 K and a few ones also at 298 K (*32*, *38*). They studied the influence of several cations (for example, [bmim], [hmim], and [hmmim]) and anions (for example, [PF_6], [Tf_2N], and [TfO]) in combination with a variety of organic solvents (i.e., among others, acetonitrile (polar aprotic), methanol (protic, hydrogen bond donor and acceptor), acetone (polar, hydrogen bond acceptor)) on the phase behavior. They also employed ethane and N_2 as the dissolved gas (*32*). Their results show that the coordinates of the LCEP strongly depend on the combination of ionic liquid and organic solvent (*25*, *32*, *38*). However, it was later explained by Peters and co-workers that not the critical endpoint (particularly regarding the LCEP data) was reached but the adjacent two-phase region instead (*39*, *40*).

In a series of publications, the group of Peters reported experimental results for the solubility of CO_2 in a binary solvent mixture of (organic solvent + 1-*n*-butyl-3-methylimidazolium tetrafluoroborate [bmim][BF_4]) at temperatures from 280 K to 443 K and pressures up to 14 MPa (*41–46*). In most experimental investigations, they studied a single solvent mixture, i.e., the mole fraction of the organic solvent in the CO_2-free solvent mixture was fixed to a single value. In the first paper of that series (*41*), they studied the influence of three organic compounds on the pressure that is required to dissolve CO_2 (at a fixed molar ratio of CO_2 to [bmim][BF_4]) in a homogeneous (or two-phase) liquid binary solvent mixture. Later publications presented experimental results for the solubility of CO_2 in a single solvent composition (mole fraction of the organic solvent in the binary solvent mixture around 0.05 to 0.10) of a) (4-isobutylacetophenone + [bmim][BF_4]) (*42*), b) (1-phenylethanol + [bmim][BF_4]) as well as (acetophenone + [bmim][BF_4]) (*43*), c) (1-(4-isobutylphenyl)ethanol + [bmim][BF_4]) (*44*), d) (methyl-(Z)-α-acetamido cinnamate (MAAC) + [bmim][BF_4]) (*45*), and e) ((S)-naproxen + [bmim][BF_4]) (*46*). The publications that deal with the organic solvents MAAC and (S)-naproxen also report experimental data for phase equilibria with solid phases. In an extension of their work on (CO_2 + 4-isobutylacetophenone + [bmim][BF_4]), Kühne et al. presented additional results for the vapor-liquid equilibrium and results for the liquid-liquid-vapor equilibrium – including also pressure, temperature, and composition data for the LCEP line (*47*). Two more recent publications from the group of Peters deal with the vapor-liquid equilibrium and the liquid-liquid-vapor equilibrium that are observed when CO_2 is dissolved in a binary solvent mixture of the ionic liquid [hmim][BF_4] and either methanol (*48*) at temperatures from 254 K to 348 K and at a single mole fraction of methanol (0.05) in the binary solvent mixture or 2-propanol (*49*) at temperatures from 253 K to 370 K and at a single mole fraction of 2-propanol (0.05) in the binary solvent mixture.

The three-phase L_1L_2V behavior of the ternary system (CO_2 + 1-butanol + [hmim][Tf_2N]) was investigated by Chobanov et al. between 293 K and 333 K (*34*). As it is shown in Figure 6, a three-phase equilibrium is only observed in a narrow pressure range. Shiflett and Yokozeki (*50*) proved that the binary system (CO_2 + [hmim][Tf_2N]) reveals a L_1L_2V phase equilibrium (similar to that in the system (CO_2 + [bmim][PF_6]), cf. Figure 5) where the second liquid phase consists of nearly pure CO_2: $x^{(L_2)}(CO_2) = 0.999 \pm 0.001$.

Therefore, at temperatures below the critical temperature of CO_2, the bordering pressure of the three-phase L_1L_2V equilibrium of the ternary system (CO_2 + 1-butanol + [hmim][Tf_2N]) can be approximated by the vapor pressure of CO_2, and the pressure difference (at a given temperature) between the lower critical endpoint line and the upper limiting pressure amounts to less than 0.5 MPa. At temperatures above the critical temperature of CO_2, the upper critical endpoint line nearly coincides with the critical line for the vapor-liquid equilibrium of the binary system (CO_2 + 1-butanol), and the difference between both critical endpoint lines of the ternary system decreases with increasing temperature (to 0.13 MPa at 333 K).

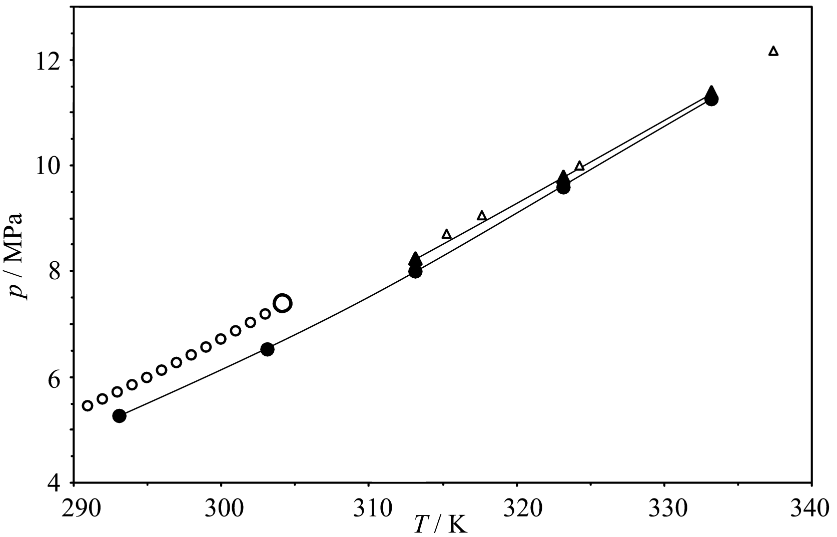

Figure 6. Coordinates of the lower (LCEP) and upper (UCEP) critical endpoint lines of the L_1L_2V equilibrium in the ternary system (CO_2 + 1-butanol + [hmim][Tf_2N]): (●), LCEP (34); (▲), UCEP (34); (△), coordinates of the vapor-liquid critical line of the binary subsystem (CO_2 + 1-butanol) (51); (○), vapor pressure curve of pure CO_2 (35); (large ○), critical point of pure CO_2 (35).

Experimental data for the densities of the coexisting phases in L_1L_2V equilibria are rarely available. Figure 7 shows the densities of the coexisting liquid phases L_1 (IL-rich) and L_2 (IL-depleted) in a three-phase L_1L_2V equilibrium of the ternary systems (CO_2 + methanol + [bmim][PF_6]) at 333 K and (CO_2 + 1-butanol + [hmim][Tf_2N]) at 293 K, respectively (from Chobanov et al. (*34*)). The densities of the coexisting liquid phases are difficult to predict. For example, assuming an ideal liquid mixture behavior (with densities of the pure liquids for CO_2 and methanol from Wagner and Overhoff (*35*) and for [bmim][PF_6] from Li et al. (*52*)) results in densities which are only 70 % (50 %) of the experimental results for the IL-rich (CO_2-rich) liquid phase. This is mainly caused by the density of CO_2 (which as a pure substance is in a supercritical, but nearcritical state). We applied a modification of eq 2a to calculate the molar volume $\tilde{V}_{\text{liq}}$ of the liquid mixture:

$$\tilde{V}_{\text{liq}} = x_{\text{IL}}\ v_{\text{IL,pure liq}}(T) + x_{\text{org. solv}}\ v_{\text{org. solv,pure liq}}(T,p) + x_{\text{CO}_2}\ v^{\infty}_{\text{CO}_2,\text{IL}}(T) \quad \text{(2b)}$$

where x_i is the mole fraction of component i, $v_{\text{IL,pure liq}}$ and $v_{\text{org. solv,pure liq}}$ are the molar volumes of the pure solvent components, and $v^{\infty}(CO_2,\text{IL})$ is the molar volume of CO_2 in the ionic liquid at infinite dilution of CO_2 in the ionic liquid. Replacing the molar volume of pure CO_2 by the molar volume of CO_2 at infinite dilution in the ionic liquid (at 333 K: $v^{\infty}(CO_2,[\text{bmim}][PF_6])$ was estimated to 39 cm^3/mol from the corresponding values of the ionic liquids [bmim][CH_3SO_4] and [hmim][Tf_2N] (*7*)) results in a better agreement with the experimental data for the densities of the coexisting liquid phases. Such estimates for the density of the

CO_2-rich as well as the IL-rich liquid phase of the ternary system (CO_2 + methanol + [bmim][PF_6]) are about 10 % above the experimental results. Similar results are obtained for the densities of the coexisting liquid phases of the system (CO_2 + 1-butanol + [hmim][Tf_2N]). For example, assuming an ideal liquid mixture behavior (with densities for CO_2 from Wagner and Overhoff (*35*), for 1-butanol from Alaoui et al. (*53*), and for [hmim][Tf_2N] from Kato and Gmehling (*54*)) results in densities which are by a factor of 4.0 (butanol-rich phase) and a factor of 3.4 (IL-rich phase) smaller than the experimental results for the densities of the coexisting liquid phases at 293 K. Replacing the molar volume of pure CO_2 by the molar volume of CO_2 at infinite dilution in [hmim][Tf_2N] – from Kumełan et al. (*7*) – improves the predictions essentially, too. The prediction results are except for one point larger than the experimental results for both liquid phases. The deviations amount to about 2 % for the IL-rich phase and between 2 % near the lower critical endpoint line and 15 % near the upper endpoint line (i.e., the three-phase L_1L_2V line of the binary system (CO_2 + [hmim][Tf_2N])) for the butanol-rich liquid phase.

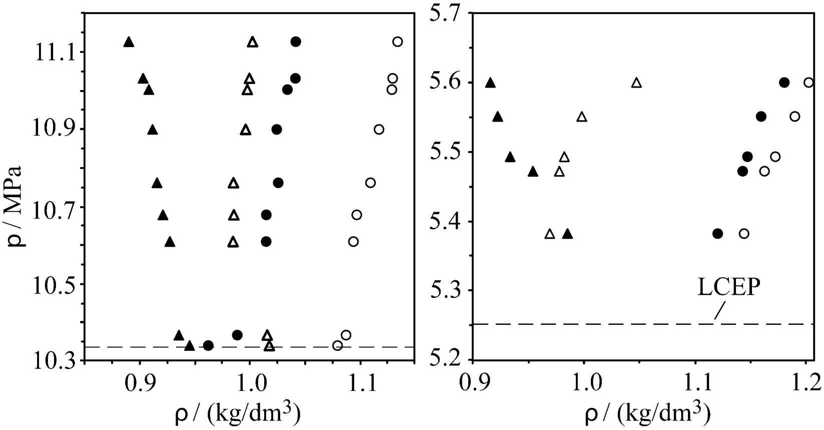

Figure 7. Results for the densities of the coexisting liquid phases L_1 and L_2 in the L_1L_2V equilibrium of the two ternary systems (CO_2 + methanol + [bmim][PF_6]) at 333 K (left-hand side) and (CO_2 + 1-butanol + [hmim][Tf_2N]) at 293 K (right-hand side), respectively. (●), L_1, experimental (34); (▲), L_2, experimental (34); (○), L_1, prediction employing eq 2b; (△), L_2, prediction employing eq 2b.

The SONG phenomenon should also be expected when – like in the “classical” experiments (*26*) – CO_2 pressure is administered on aqueous solutions of hydrophilic ionic liquids. In a 2003 communication, Brennecke’s group was the first to report such a system (*55*). During experiments at temperatures between 288 K and 298 K, the (hydrophilic) ionic liquids [bmim][BF_4] and [bmim][CF_3SO_3] displayed a characteristic three-phase L_1L_2V equilibrium. Later on, Zhang et al. (*56*) systematically investigated the phase behavior in the ternary system (CO_2 + water + [bmim][BF_4]) at temperatures from 278 K to 298 K and pressures up to 16 MPa. At a constant temperature and with increasing pressures, they found a similar behavior as shown in Figure 4.

Chobanov (*57*) further investigated the high-pressure L_1L_2V equilibrium when CO_2 is dissolved in aqueous solutions of some single hydrophilic ionic liquids (which were completely miscible with water at ambient pressure). As the binary system (CO_2 + water) reveals a three-phase L_1L_2V equilibrium at pressures below (but very close to) the vapor pressure of CO_2, such ternary systems reveal also a high-pressure L_1L_2V equilibrium. Chobanov found that for all those hydrophilic ionic liquids investigated the pressure on the lower critical endpoint line is less than 0.05 MPa below the pressure on the upper critical endpoint line (at subcritical temperatures for CO_2, that is the pressure on the three-phase L_1L_2V line of the binary system (CO_2 + water)). Therefore, the pressure region where a liquid-liquid phase split in the ternary system (CO_2 + water + hydrophilic ionic liquid) is observed when CO_2 is dissolved in the liquid mixture at elevated pressures is extremely small, and the phenomenon is certainly not suited for applications (as, for example, in separation technology).

Another high-pressure solubility study was performed by the group of Coutinho (*58*). The solubility of CO_2 in aqueous solutions of different concentrations of tri-iso-butyl(methyl)phosphonium tosylate was measured at temperatures from 275 K to 370 K and pressures up to 100 MPa. A three-phase L_1L_2V equilibrium that appeared within a very narrow pressure region was observed for concentrations higher than 4 mol % of ionic liquid in water when working at pressures between 4 MPa and 8 MPa and temperatures between 280 K and 305 K, respectively.

General features of the high-pressure L_1L_2V phase behavior of ternary systems (well soluble gas + solvent + ionic liquid) are

a) a high-pressure L_1L_2V region is always (but not exclusively) observed when one of the binary subsystems (CO_2 + solvent component) reveals a liquid-liquid-vapor three-phase equilibrium,
b) the amount of the ionic liquid component in the vapor phase of the L_1L_2V equilibrium is extremely small, and consequently the upper critical endpoint line only slightly deviates from that branch of the critical line for the vapor-liquid equilibrium of the binary system (CO_2 + non-ionic solvent component) that starts at the critical point of CO_2,
c) it is not possible to predict the LCEP pressure from information on the solubility of CO_2 in the single solvents alone,
d) the densities of the liquid phases L_1 and L_2 that coexist at elevated pressures can be reasonably estimated (when the compositions are known) from pure-component density data (for both solvents) and the partial molar volume of the dissolved gas in the ionic liquid.

The group of Costa Gomes has published results of experimental investigations on the low-pressure solubility of CO_2 in binary solvent mixtures of the ionic liquid [emim][Tf_2N] where the other solvent component was either acetonitrile (*59*) or water (*60*). Hong et al. (*59*) reported experimental results (and a polynomial correlation) for the solubility of CO_2 at a partial pressure of 0.1 MPa in four different solvent mixtures of (acetonitrile + [emim][Tf_2N]) at temperatures between 293 K and 334 K. With an increasing amount of acetonitrile in the ionic liquid, the solubility of CO_2 decreases. At all investigated temperatures, there is a linear increase of (the logarithm of) Henry's constant of CO_2 with the mole fraction of acetonitrile in the solvent mixture.

The group of Zhao also published ternary phase equilibrium data (*61*, *62*). Liu et al. (*61*) investigated high-pressure phase equilibria of, among other systems, the ternary systems (CO_2 + dibenzothiophene (DBT) + [bmim][CF_3SO_3]) and (CO_2 + naphthalene + [bmim][CF_3SO_3]) at 323 K and up to 15 MPa, whereas Fu et al. (*62*) determined the concentration of naphthalene in the CO_2-rich (i.e., L_2) phase of the system (CO_2 + naphthalene + [bmim][PF_6]) by UV spectroscopy at different naphthalene molalities and within temperature and pressure ranges of 313 K to 333 K and 8 MPa to 20 MPa, respectively.

From another study performed by Bogel-Łukasik et al. (*63*), high-pressure VLE data of the ternary systems (CO_2 + solute + [C_8mim][PF_6] or [C_8mim][$N(CN)_2$]) at 308 K and up to 11 MPa are available. 2-Octanol was one of the solutes investigated.

Most other publications deal with the influence of small amounts of water in an ionic liquid on the solubility of CO_2 or SO_2. Fu et al. (*64*) reported the influence of water concentrations between 0.007 mass % and 1.6 mass % on the solubility of CO_2 in [bmim][PF_6] at 313, 323, and 333 K and pressures up to 25 MPa. At the lower end of the water mass fractions investigated, the experimental results agree with the data for the solubility of CO_2 in water-free [bmim][PF_6] within experimental uncertainty. The solubility of CO_2 (on the mole fraction scale) at $p = 5$ MPa decreases between 6 % (at 313 K) and 9 % (at 333 K) when the mass fraction of water increases from zero to 0.016. Notably, the influence of water impurities on the gas solubility is very likely the main reason for the significant differences among reported data in the past.

Bermejo et al. (*65*) from the group of Peters presented some experimental results for the pressure that is required to dissolve CO_2 in aqueous solutions of the ionic liquid 1-(1-hydroxypropyl)-3-methylimidazolium nitrate ([hopmim][NO_3]) at temperatures between 303 K and 363 K. The mole fraction of water in the CO_2-free solvent mixture was 0.03, 0.13, and 0.36, respectively, and the mole fraction of CO_2 in the ternary liquid mixture was between 0.05 and 0.22. As one might expect, the experimental data show that, when some of the ionic liquid is replaced by water, the pressure required to dissolve a fixed amount of CO_2 (on the mole fraction scale in the liquid mixture) increases considerably with the amount of water in the solvent mixture, while it remains nearly constant when the mole fraction of CO_2 is calculated on a water-free basis. These results indicate that at least for that particular system investigated, at fixed temperature and pressure, the molar ratio of CO_2 to [hopmim][NO_3] in the liquid phase is only slightly influenced by the presence of water in the solvent. These findings were confirmed by the investigations by Ren et al. (*66*) on the influence of a small amount of water in the ionic liquid 1,1,3,3-tetramethylguanidinium lactate on the solubility of SO_2 at temperatures between 293 K and 333 K.

In addition to the previously mentioned work by Costa Gomes, Husson et al. (*60*) observed a similar result in their experimental study on the influence of water on the solubility of CO_2 in [emim][Tf_2N] at low pressures at 303 K and 323 K. The experiments revealed that the Henry's constant of CO_2 (solubility of CO_2) on mole fraction scale in the solvent mixture increases (decreases) by 40 % (28 %) when the mole fraction of water is increased from 0 to 28 mol %. But again, on a water-free basis, the solubility of CO_2 in [emim][Tf_2N] remains unchanged when water is added to the ionic liquid.

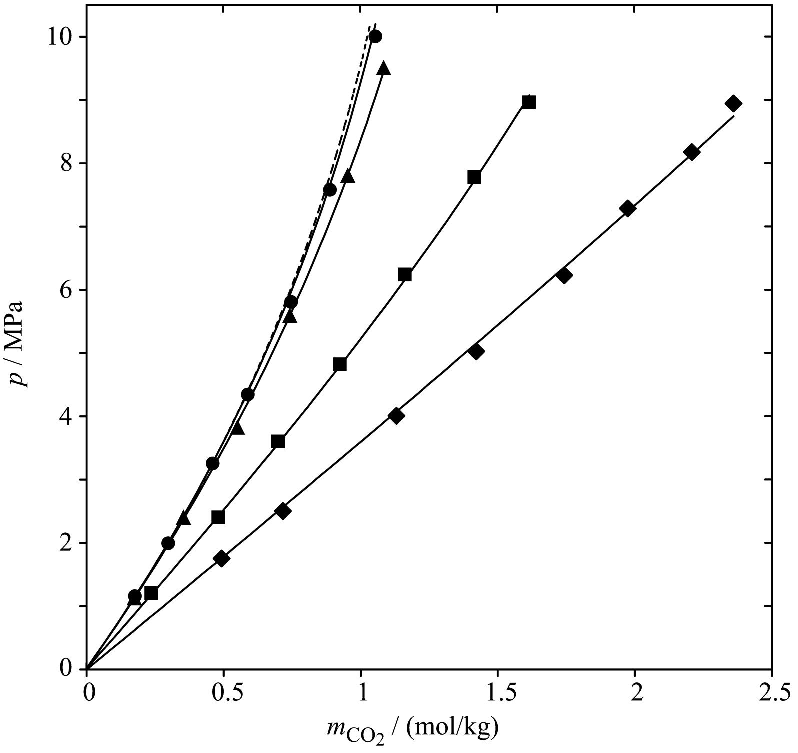

Figure 8. Total pressure above solutions of (CO_2 + water + [bmim][CH_3SO_4]) versus molality of CO_2 in that solution at 333 K (67). Experimental data are represented by full symbols; lines correspond to correlations: (- - - -), pure water solvent; (●), water mass fraction of 0.15; (▲), 0.50; (■), 0.87; (◆), pure ionic liquid solvent.

A comprehensive study on the solubility of CO_2 in aqueous solutions of an ionic liquid was recently performed by Kumełan et al. (*67*). The experimental work covered the solubility of CO_2 in three aqueous solutions of [bmim][CH_3SO_4] with water mass (mole) fractions (in the gas-free solvent mixture) of 0.15 (0.013), 0.50 (0.066), and 0.87 (0.326), respectively, at 293 K, 333 K, and 373 K and pressures up to 10 MPa. The experimental data for 333 K are shown in Figure 8 together with the results of a correlation that is an extension to solvent mixtures of the description given above for the solubility of a gas in a single solvent (cf. Pérez-Salado Kamps (*68*)). The experimental results for the pressure that is required to dissolve a certain amount of CO_2 (expressed as its molality in the solvent mixture) at a constant temperature monotonously increases when water is added to the ionic liquid. Both pure solvents (i.e., water and [bmim][CH_3SO_4]) are poor solvents for

CO_2, but CO_2 is better soluble in [bmim][CH_3SO_4] than in water. At 373 K, the Henry's constant of CO_2 (on the molality scale in the solvent mixture) decreases steadily with increasing mole fraction of the ionic liquid in the solvent mixture $x_{IL,liq}$. However, at 293 K, the Henry's constant at first increases to a maximum at $x_{IL,liq} \approx 0.12$ before it decreases (cf. Figure 9).

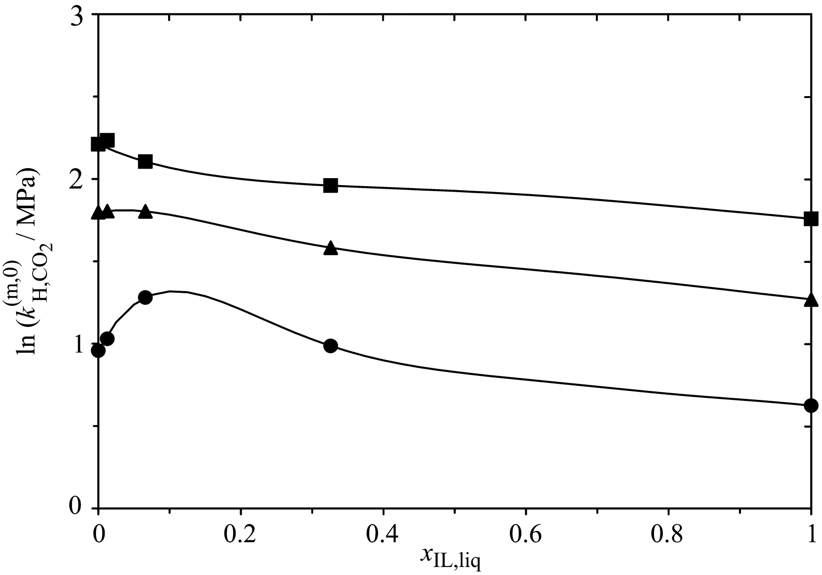

Figure 9. Henry's constant on the molality scale of CO_2 in a binary mixture of (water + [bmim][CH_3SO_4]) plotted versus the gas-free mole fraction of the ionic liquid in the solvent mixture at a constant temperature (67). Full symbols ((●), 293 K; (▲), 333 K; (■), 373 K) represent experimental data, the solid lines are correlation results.

As a side product of the gas solubility experiments, Kumełan et al. (*67*) also reported density data of the liquid mixture at vapor-liquid equilibrium. The data evaluation gave evidence that the experimental results for the partial molar volume of CO_2 at infinite dilution in (water + [bmim][CH_3SO_4]) $v^{\infty}(CO_2,(\text{water} + \text{IL}))$ increase for water mole fractions of about 0.015 onwards, whereas there is no unambiguous trend at lower water mole fractions.

The solubility of a single gas in mixtures of two ionic liquids is another possibility for gas solubility in ionic liquids. The group of Noble (*69*) studied the (low-pressure) solubility of CO_2, CH_4, and N_2 in binary mixtures of [emim][Tf_2N] and [emim][BF_4] at 313 K over the entire composition range (i.e., from pure [emim][BF_4] to pure [emim][Tf_2N]). Higher mole fractions of [emim][Tf_2N] enhance CO_2 solubility, a finding that is in accordance with the expected solubility behavior in the pure ionic liquids (*1*). Ortiz et al. (*70*), however, employed a reactive ionic liquid mixture of Ag[BF_4] dissolved in either [bmim][BF_4] or N-butyl-4-methylpyridinium tetrafluoroborate [bmpy][BF_4] to investigate the solubility of propane and propene. The experiments were carried out between

278 K and 318 K, up to 0.6 MPa, and at different silver ion concentrations. The solubility of propane was found to be approximately the same for all mixture compositions, whereas the solubility of propene was found to increase linearly with silver ion concentration.

Finally, although that area is not directly within the scope of the present publication, replacing amine-based aqueous solvent mixtures by ionic liquid systems for the capture of CO_2 has been discussed by, for example, Noble and co-workers (*71*, *72*). Reaction of CO_2 with amines in ionic liquid solvents was observed to proceed rapidly and efficiently, and mixtures of amines and ionic liquids perform similarly to aqueous amine solutions that are used for CO_2 capture. But the versatility of ionic liquids opens various ways for improvement, for example, regarding solvent volatility or energy efficiency.

Recently, the group of Yusoff and Aroua studied the influence of the ionic liquids guanidinium trifluoromethanesulfonate [gua][TfO] (*73*) and guanidinium tris(pentafluoroethyl)trifluorophosphate [gua][FAP] (*74*) on the solubility of CO_2 in aqueous solutions of N-methyldiethanolamine (MDEA).

Conclusions

The experimental data for the solubility of two gases in a pure ionic liquid and of a single gas in binary solvent mixtures (common solvent + ionic liquid), including the "salting out by a nearcritical gas" phenomenon that is always observed when either one of the binary systems (gas + common solvent) or (gas + ionic liquid) reveal a liquid-liquid-vapor three-phase line, are reviewed and discussed. Furthermore, some volumetric properties of the liquid phases are treated. Although experimental investigations on the solubility of a single gas in a pure ionic liquid have attained a much higher attention by various research groups, experimental results on the simultaneous solubility of two (or even more) gases in an ionic liquid as well as on gas solubility in mixed solvents with an ionic liquid solvent compound are rather limited. However, such information is required both in applications and in theoretical (correlation as well as prediction) work. Therefore, it is of outstanding importance and highly welcome.

References

1. Anderson, J. L.; Anthony, J. L.; Brennecke, J. F.; Maginn, E. J. In *Ionic Liquids in Synthesis*, 2nd ed.; Wasserscheid, P., Welton, T., Eds.; Wiley-VCH: Weinheim, 2008; pp 103–129.
2. Kroon, M. C.; Peters, C. J. In *Applied Thermodynamics of Fluids*; Goodwin, A. R. H., Sengers, J. V., Peters, C. J., Eds.; RSC Publishing: Cambridge, 2010; pp 368–393.
3. Wasserscheid, P.; Schulz, P. In *Ionic Liquids in Synthesis*, 2nd ed.; Wasserscheid, P., Welton, T., Eds.; Wiley-VCH: Weinheim, 2008; pp 369–463.

4. Olivier-Bourbigou, H.; Favre, F. In *Ionic Liquids in Synthesis*, 2nd ed.; Wasserscheid, P., Welton, T., Eds.; Wiley-VCH: Weinheim, 2008; pp 464–488.
5. Hintermair, U.; Leitner, W.; Jessop, P. In *Handbook of Green Chemistry, Volume 4: Supercritical Solvents*; Leitner, W., Jessop, P. G., Eds.; Wiley-VCH: Weinheim, 2010, pp 101–187.
6. Scurto, A. M.; Hutchenson, K.; Subramaniam, B. In *Gas-Expanded Liquids and Near-Critical Media. Green Chemistry and Engineering*; Hutchenson, K. W., Scurto, A. M., Subramaniam, B., Eds.; ACS Symposium Series 1006; American Chemical Society: Washington, DC, 2009, pp 3–37.
7. Kumełan, J.; Tuma, D.; Maurer, G. *Fluid Phase Equilib.* **2009**, *275*, 132–144.
8. Kumełan, J.; Pérez-Salado Kamps, Á.; Tuma, D.; Maurer, G. *Fluid Phase Equilib.* **2007**, *260*, 3–8.
9. Kumełan, J.; Pérez-Salado Kamps, Á.; Tuma, D.; Maurer, G. *J. Chem. Eng. Data* **2006**, *51*, 1802–1807.
10. Solinas, M.; Pfaltz, A.; Cozzi, P. G.; Leitner, W. *J. Am. Chem. Soc.* **2004**, *126*, 16142–16147.
11. Kumełan, J.; Tuma, D.; Maurer, G. *Fluid Phase Equilib.* **2011**, *311*, 9–16; **2012**, *329*, 92.
12. Hert, D. G.; Anderson, J. L.; Aki, S. N. V. K.; Brennecke, J. F. *Chem. Commun.* **2005**, 2603–2605.
13. Kim, Y. S.; Jang, J. H.; Lim, B. D.; Kang, J. W.; Lee, C. S. *Fluid Phase Equilib.* **2007**, *256*, 70–74.
14. Huang, J.; Riisager, A.; Wasserscheid, P.; Fehrmann, R. *Chem. Commun.* **2006**, 4027–4029.
15. Heintz, Y. J.; Sehabiague, L.; Morsi, B. I.; Jones, K. L.; Luebke, D. R.; Pennline, H. W. *Energy Fuels* **2009**, *23*, 4822–4830.
16. Kumełan, J.; Pérez-Salado Kamps, Á.; Tuma, D.; Maurer, G. *J. Chem. Thermodyn.* **2006**, *38*, 1396–1401.
17. Yokozeki, A.; Shiflett, M. B. *Energy Fuels* **2009**, *23*, 4701–4708.
18. Shiflett, M. B.; Yokozeki, A. *Energy Fuels* **2010**, *24*, 1001–1008.
19. Shiflett, M. B.; Niehaus, A. M. S.; Yokozeki, A. *J. Chem. Eng. Data* **2010**, *55*, 4785–4793.
20. Shiflett, M. B.; Yokozeki, A. *Fluid Phase Equilib.* **2010**, *294*, 105–113.
21. Shiflett, M. B.; Niehaus, A. M. S.; Yokozeki, A. *J. Phys. Chem. B* **2011**, *115*, 3478–3487.
22. Jalili, A. H.; Safavi, M.; Ghotbi, C.; Mehdizadeh, A.; Hosseini-Jenab, M.; Taghikhani, V. *J. Phys. Chem. B* **2012**, *116*, 2758–2774.
23. Jalili, A. H. Research Institute of Petroleum Industry (RIPI), Tehran, Iran; private communication, 2012.
24. Pérez-Salado Kamps, Á.; Maurer, G. Comments on ref 22. *J. Phys. Chem. B* **2012**, submitted for publication.
25. Scurto, A. M.; Aki, S. N. V. K.; Brennecke, J. F. *J. Am. Chem. Soc.* **2002**, *124*, 10276–10277.
26. Elgin, J. C.; Weinstock, J. J. *J. Chem. Eng. Data* **1959**, *4*, 3–12.
27. Adrian, T.; Wendland, M.; Hasse, H.; Maurer, G. *J. Supercrit. Fluids* **1998**, *12*, 185–221.

28. Shariati, A.; Gutkowski, K.; Peters, C. J. *AIChE J.* **2005**, *51*, 1532–1540.
29. Liu, Z.; Wu, W.; Han, B.; Dong, Z.; Zhao, G.; Wang, J.; Jiang, T.; Yang, G. *Chem. Eur. J.* **2003**, *9*, 3897–3903.
30. Zhang, Z.; Wu, W.; Liu, Z.; Han, B.; Gao, H.; Jiang, T. *Phys. Chem. Chem. Phys.* **2004**, *6*, 2352–2357.
31. Wu, W.; Li, W.; Han, B.; Jiang, T.; Shen, D.; Zhang, Z.; Sun, D.; Wang, B. *J. Chem. Eng. Data* **2004**, *49*, 1597–1601.
32. Aki, S. N. V. K.; Scurto, A. M.; Brennecke, J. F. *Ind. Eng. Chem. Res.* **2006**, *45*, 5574–5585.
33. Lim, B.-H.; Kim, J.-W.; Paek, S.-M.; Son, B.-K.; Lee, C.-S.; Lee, H.; Ra, C.-S.; Shim, J.-J. *Clean Technol.* **2006**, *12*, 128–137.
34. Chobanov, K.; Tuma, D.; Maurer, G. *Fluid Phase Equilib.* **2010**, *294*, 54–66.
35. Wagner, W.; Overhoff, U. *ThermoFluids*, Version 1.0 (Build 1.0.0); Springer: Berlin, Heidelberg, 2006.
36. Zhang, Z.; Wu, W.; Wang, B.; Chen, J.; Shen, D.; Han, B. *J. Supercrit. Fluids* **2007**, *40*, 1–6.
37. Bogel-Łukasik, R.; Matkowska, D.; Bogel-Łukasik, E.; Hofman, T. *Fluid Phase Equilib.* **2010**, *293*, 168–174.
38. Mellein, B. R.; Brennecke, J. F. *J. Phys. Chem. B* **2007**, *111*, 4837–4843.
39. Kühne, E.; Alfonsín, L. R.; Mota Martinez, M. T.; Witkamp, G.-J.; Peters, C. J. *J. Phys. Chem. B* **2009**, *113*, 6579–6580.
40. Brennecke, J. F.; Scurto, A. M.; Aki, S. N. V. K. *J. Phys. Chem. B* **2009**, *113*, 6581.
41. Kühne, E.; Peters, C. J.; van Spronsen, J.; Witkamp, G.-J. *Green Chem.* **2006**, *8*, 287–291.
42. Kühne, E.; Perez, E.; Witkamp, G. J.; Peters, C. J. *J. Supercrit. Fluids* **2008**, *45*, 27–31.
43. Kühne, E.; Santarossa, S.; Perez, E.; Witkamp, G. J.; Peters, C. J. *J. Supercrit. Fluids* **2008**, *46*, 93–98.
44. Kühne, E.; Saez Calvo, E.; Witkamp, G. J.; Peters, C. J. *J. Supercrit. Fluids* **2008**, *45*, 293–297.
45. Kroon, M. C.; Toussaint, V. A.; Shariati, A.; Florusse, L. J.; van Spronsen, J.; Witkamp, G.-J.; Peters, C. J. *Green Chem.* **2008**, *10*, 333–336.
46. Kühne, E.; Santarossa, S.; Witkamp, G.-J.; Peters, C. J. *Green Chem.* **2008**, *10*, 762–766.
47. Kühne, E.; Witkamp, G.-J.; Peters, C. J. *Green Chem.* **2008**, *10*, 929–933.
48. Kroon, M. C.; Florusse, L. J.; Peters, C. J. *Fluid Phase Equilib.* **2010**, *294*, 84–88.
49. Kroon, M. C.; Florusse, L. J.; Kühne, E.; Witkamp, G.-J.; Peters, C. J. *Ind. Eng. Chem. Res.* **2010**, *49*, 3474–3478.
50. Shiflett, M. B.; Yokozeki, A. *J. Phys. Chem. B* **2007**, *111*, 2070–2074.
51. Yeo, S.-D.; Park, S.-J.; Kim, J.-W.; Kim, J.-C. *J. Chem. Eng. Data* **2000**, *45*, 932–935.
52. Li, W.; Zhang, Z.; Han, B.; Hu, S.; Xie, Y.; Yang, G. *J. Phys. Chem. B* **2007**, *111*, 6452–6456.
53. Alaoui, F.; Montero, E.; Bazile, J. P.; Comuñas, M. J. P.; Galliero, G.; Boned, C. *Fluid Phase Equilib.* **2011**, *301*, 131–136.

54. Kato, R.; Gmehling, J. *J. Chem. Thermodyn.* **2005**, *37*, 603–619.
55. Scurto, A. M.; Aki, S. N. V. K.; Brennecke, J. F. *Chem. Commun.* **2003**, 572–573.
56. Zhang, Z.; Wu, W.; Gao, H.; Han, B.; Wang, B.; Huang, Y. *Phys. Chem. Chem. Phys.* **2004**, *6*, 5051–5055.
57. Chobanov, K. Doctoral Thesis (Doctor of Engineering), University of Kaiserslautern, Kaiserslautern, Germany, 2011.
58. Ventura, S. P. M.; Pauly, J.; Daridon, J. L.; Lopes da Silva, J. A.; Marrucho, I. M.; Dias, A. M. A.; Coutinho, J. A. P. *J. Chem. Thermodyn.* **2008**, *40*, 1187–1192.
59. Hong, G.; Jacquemin, J.; Husson, P.; Costa Gomes, M. F.; Deetlefs, M.; Nieuwenhuyzen, M.; Sheppard, O.; Hardacre, C. *Ind. Eng. Chem. Res.* **2006**, *45*, 8180–8188.
60. Husson, P.; Pison, L.; Jacquemin, J.; Costa Gomes, M. F. *Fluid Phase Equilib.* **2010**, *294*, 98–104.
61. Liu, J.; Sun, X.; Fu, D.; Zhao, S. *Chem. Eng. J.* **2009**, *147*, 63–70.
62. Fu, D.; Sun, X.; Qiu, Y.; Jiang, X.; Zhao, S. *Fluid Phase Equilib.* **2007**, *251*, 114–120.
63. Bogel-Łukasik, R.; Najdanovic-Visak, V.; Barreiros, S.; Nunes da Ponte, M. *Ind. Eng. Chem. Res.* **2008**, *47*, 4473–4480.
64. Fu, D.; Sun, X.; Pu, J.; Zhao, S. *J. Chem. Eng. Data* **2006**, *51*, 371–375.
65. Bermejo, M. D.; Montero, M.; Saez, E.; Florusse, L. J.; Kotlewska, A. J.; Cocero, M. J.; van Rantwijk, F.; Peters, C. J. *J. Phys. Chem. B* **2008**, *112*, 13532–13541.
66. Ren, S.; Hou, Y.; Wu, W.; Chen, X.; Fan, J.; Zhang, J. *Ind. Eng. Chem. Res.* **2009**, *48*, 4928–4932.
67. Kumełan, J.; Pérez-Salado Kamps, Á.; Tuma, D.; Maurer, G. *J. Chem. Eng. Data* **2011**, *56*, 4505–4515.
68. Pérez-Salado Kamps, Á. *Ind. Eng. Chem. Res.* **2005**, *44*, 201–225.
69. Finotello, A.; Bara, J. E.; Narayan, S.; Camper, D.; Noble, R. D. *J. Phys. Chem. B* **2008**, *112*, 2335–2339.
70. Ortiz, A.; Galán, L. M.; Gorri, D.; de Haan, A. B.; Ortiz, I. *Ind. Eng. Chem. Res.* **2010**, *49*, 7227–7233.
71. Camper, D.; Bara, J. E.; Gin, D. L.; Noble, R. D. *Ind. Eng. Chem. Res.* **2008**, *47*, 8496–8498.
72. Bara, J. E.; Carlisle, T. K.; Gabriel, C. J.; Camper, D.; Finotello, A.; Gin, D. L.; Noble, R. D. *Ind. Eng. Chem. Res.* **2009**, *48*, 2739–2751.
73. Sairi, N. A.; Yusoff, R.; Alias, Y.; Aroua, M. K. *Fluid Phase Equilib.* **2011**, *300*, 89–94.
74. Aziz, N.; Yusoff, R.; Aroua, M. K. *Fluid Phase Equilib.* **2012**, *322–323*, 120–125.

Chapter 11

Ionic Liquids in Extractive Distillation of Ethanol/Water: From Laboratory to Pilot Plant

**G. Wytze Meindersma,* Esteban Quijada-Maldonado,
Tim A. M. Aelmans, Juan Pablo Gutierrez Hernandez,
and André B. de Haan**

**Department of Chemical Engineering and Chemistry/SPS,
Eindhoven University of Technology, P.O. Box 513,
5600 MB Eindhoven, The Netherlands
*E-mail: g.w.meindersma@tue.nl**

The ionic liquid 1-ethyl-3-methylimidazolium dicyanamide, $[C_2mim]N(CN)_2$ is a suitable solvent for the extractive distillation of ethanol/water mixtures. This IL has comparable relative ethanol/water volatility as the benchmark solvent ethylene glycol (EG). Pilot plant experiments with both EG and $[C_2mim]N(CN)_2$ as solvent proved that the developed model for the extractive distillation of ethanol/water could well describe the experimental results. The achieved purity of the ethanol in the pilot plant using $[C_2mim]N(CN)_2$ as solvent was 99.91%. A conceptual process was designed for both the benchmark solvent EG and the IL. The process with the IL as solvent required 11% more energy than that with EG as solvent. However, if heat integration is implemented, the extractive distillation with the IL requires 16% less energy than the EG-based process. The key performance points for extractive distillation of ethanol/water mixtures are the recovery of the ionic liquid and the heat integration.

In Ionic Liquids: Science and Applications; Visser, A., et al.;
ACS Symposium Series; American Chemical Society: Washington, DC, 2012.

Introduction

Ethanol is an important base chemical which is produced from petrochemical streams or bioprocesses. It is used as a solvent in the cosmetic and food industries, among others. However, ethanol as a (partial) replacement of gasoline has influenced its worldwide demand (*1*, *2*). Ethanol forms an azeotrope with water at an ethanol content of 95.6 wt.% and its challenging energy-efficient separation has been widely reported (*3*).

Bio-refinery production data are used as a model process. Typical plants have an ethanol production capacity of 150-200 kmol/h, with a molar purity ≥ 99.8% (*4*, *5*). The fermenter produces an aqueous solution containing about 5-12 wt% ethanol. This stream is introduced into an ordinary distillation column (also called pre-concentrator), where the ethanol is purified until 60-90 wt%. Due to the azeotropic composition (95.6 wt% of ethanol), further purification by ordinary distillation becomes unfeasible. Several technologies can carry out the dehydration of ethanol, e.g. azeotropic distillation, extractive distillation, adsorption and membrane separations, among others (*3*). Extractive distillation has several advantages over other technologies: it is operated like a conventional distillation process, uses two key variables such as polarity and boiling point difference and it does not require additional steps to purify products (*6*, *7*). Figure 1 shows a conventional extractive distillation process (*3*, *8*).

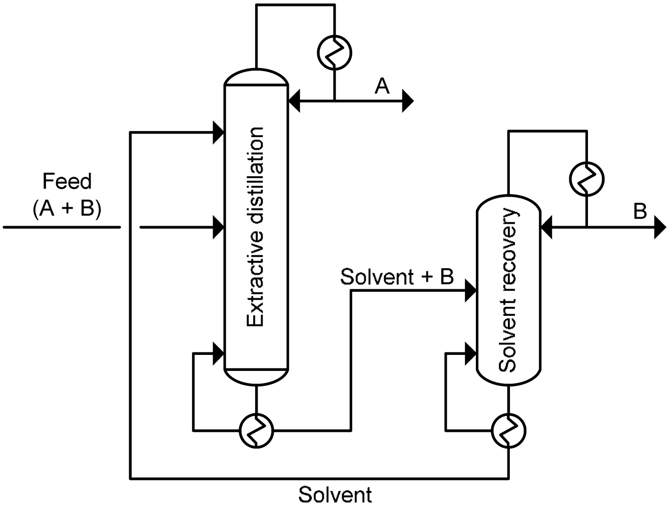

Figure 1. Extractive distillation process.

The feed, ethanol/water, enters the extractive distillation column (EDC) in the middle of the column and the solvent is introduced at the top of the column. Anhydrous ethanol is obtained in the overhead of the EDC and the solvent containing the water exits the column in the bottom. The solvent is then recovered in the solvent recovery column by ordinary distillation of the bottom stream of the EDC and recycled back to the EDC (*8*). The water exits at the top of the solvent recovery column.

Ethylene glycol (EG) is one of the most commonly used extractive solvents for ethanol dehydration (*3*, *8–13*). This solvent increases the relative volatility of the mixture and enhances the separation. Ionic liquids can also be employed as solvents in extractive distillation of ethanol/water mixtures (*3*, *5*, *6*, *14–17*). The extractive solvent interacts with the components of different chemical structure within the mixture. The activity coefficients are modified in such a way that the relative volatility, α_{ij}, (equation 1) is increased.

$$\alpha_{ij} = \frac{y_i/x_i}{y_j/x_j} = \frac{\gamma_i}{\gamma_j}\frac{P_i^0}{P_j^0} \tag{1}$$

Since the ratio of saturation pressures, P_i^0/P_j^0, is constant for isothermal systems, the only way that the relative volatility is affected, is by changing the ratio of the activity coefficients, γ_i/γ_j. This ratio, in the presence of the solvent, is called selectivity, S_{ij}.

$$S_{ij} = \left(\gamma_i/\gamma_j\right)_s \tag{2}$$

The solvent with the highest selectivity is always considered to be the most promising for the separation of the mixture. A rigorous comparison of the candidate solvents requires their selectivities to be determined at a consistent solvent concentration and key components ratio. Generally, the activity coefficient (and thus the selectivity) of each key component is determined at infinite dilution in each of the potential solvents. In most of the cases, the selectivity increases, often almost linearly, with solvent concentration (*11*). Thus, the solvent with the largest selectivity at infinite dilution usually has the largest selectivity at the lower solvent concentrations. Therefore, the selectivity at infinite dilution (equation 3) provides a good estimation of the effectiveness of the solvents (*18*).

$$S_{ij}^{\infty} = \left(\frac{\gamma_i^{\infty}}{\gamma_j^{\infty}}\right)_s \tag{3}$$

The selected solvent for an extractive distillation process should have the following characteristics:

- High boiling point to avoid solvent losses.
- High selectivity and solvency to obtain high purity products and to reduce the quantity of solvent used.
- Easy recovery to increase the efficiency in the solvent recovery process and to reduce the recovery costs.

The objectives of this study are to select one or more suitable ionic liquids for the extractive distillation of ethanol/water, compare the results with the benchmark solvent ethylene glycol, both on laboratory and on pilot plant scale, and to design a conceptual process with both EG and an IL as the extractive solvent.

Materials

Table 1 shows the chemicals used and their density, dynamic viscosity and surface tension.

Table 1. Chemicals used with some physical properties at 25 °C

Compound	*Purity*	*Density g/cm³*	*Viscosity mPa.s*	*Surface tension mN/m*	*Supplier*
Water (*19*)		0.997039	0.89	71.5	
Ethanol (*19*)	>99.5%	0.78507	1.087	22.0	Merck
Ethylene glycol (*20*)	>99.8%	1.10989	16.61	48.6 (*21*)	Sigma-Aldrich
$[C_2mim]N(CN)_2$ (*19*)	> 98%	1.10198	14.9	40.3	IoLiTec

Ionic Liquids in Extractive Distillation

Ionic liquids as solvents combine the advantages of both organic solvents and salts: increasing the relative volatility of one of the components and reducing the solvent-to-feed ratio by the salting-out effect without the disadvantages of a solid salt (*5*, *6*, *22–31*). The more selective the solvent, the more efficient the separation is (*32*).

Figure 2 shows a process scheme of extractive distillation with ionic liquids as solvents. The best option for the regeneration column will probably be a flash column or a multi-effect evaporator, which requires a low amount of energy, possibly followed by a strip column for the removal of last traces of products.

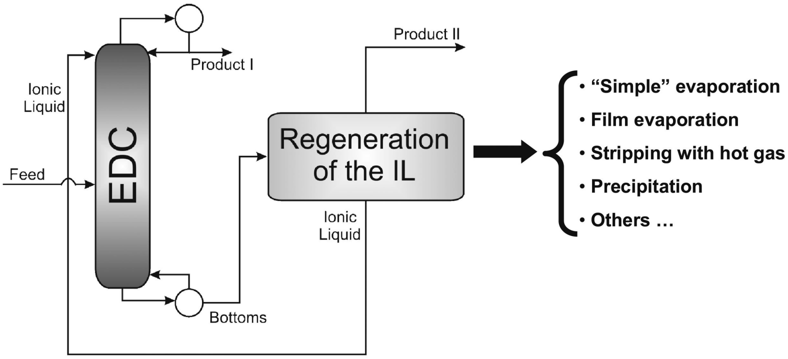
Product II
Product I
Ionic Liquid
Feed
EDC
Regeneration of the IL
Ionic Liquid
Bottoms
• “Simple” evaporation
• Film evaporation
• Stripping with hot gas
• Precipitation
• Others …

Figure 2. Process scheme of extractive distillation with ILs (EDC= extractive distillation column).

Selection of Ionic Liquids

There are several ionic liquids investigated in literature for the extractive distillation of ethanol/water mixtures, for example [C_2mim]Cl (*15*), [C_4mim]Cl (*15*, *33*, *34*), [C_6mim]Cl (*35*, *36*), [C_2mim]BF_4, [C_4mim]BF_4 (*15*), [C_2mim]$C_2H_5SO_4$ (*37*), [C_4mim]CH_3SO_4 (*38*), [C_2-C_1py]$C_2H_5SO_4$ (*39*), [C_2mim][TfO] (*16*), [C_2mim][OAc], [C_4mim][OAc], [C_4mim]$N(CN)_2$ (*15*) and [C_2mim]$N(CN)_2$ (*15*, *17*). According to Ge, the four most suitable ILs are [C_2mim]Cl, [C_2mim][OAc], [C_2mim]$N(CN)_2$ and [C_4mim]BF_4 (*15*). However, the Cl^--containing ILs are corrosive and have a high viscosity ([C_2mim]Cl: η = 65 mPa.s, [C_4mim]Cl: η = 142 mPa.s and [C_6mim]Cl: η = 293 mPa.s, all at 80 °C (*40*)) and are, therefore, not suitable. The IL [C_4mim]BF_4 is not stable at higher temperatures in presence of water and can form HF, which is very corrosive. Therefore, this IL is discarded. Hence, two ILs were selected: 1-ethyl-3-methylimidazolium acetate, [C_2mim][OAc], and 1-ethyl-3-methylimidazolium dicyanamide, [C_2mim]$N(CN)_2$. Orchillés mentions the IL [C_2mim]$N(CN)_2$ as the best IL for the extractive distillation of ethanol/water (*17*).

We have screened a large number of cations and anions with COSMO-RS/ COSMOTherm in order to select suitable combinations for the ethanol/water separation. The results of the COSMO screening were validated by experiments. Figure 3 shows the selected solvents for the ethanol/water separation. The ILs show comparable or slightly higher relative ethanol/water volatilities than EG.

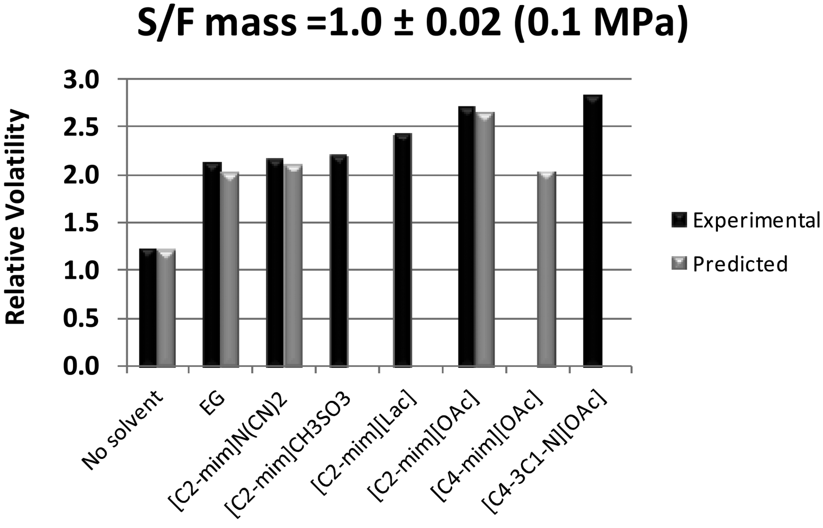

Figure 3. Relative volatilities of ethanol/water with several solvents.

The best ILs for this separation are [C_2mim][OAc] and [C_4-3C_1-N][OAc]. However, the last IL is a solid and is, therefore, not suitable. The IL [C_2mim][Lac] was not suitable because the IL proved to be unstable during our experiments and [C_2mim]CH_3SO_3 was discarded because of its high viscosity: 149.9 mPa.s at 25 °C (*41*). The ILs [C_2mim][OAc] and [C_2mim]$N(CN)_2$ were used in the process simulations. However, due to the strong interactions between water and [C_2mim][OAc], the recovery and purification of this IL appeared to be challenging and energy intensive. Because of the lower thermal stability of the IL [C_2mim][OAc] (*42*), the regeneration of this IL required very low pressures (1×10^{-7} kPa) at the maximum allowable temperature for this IL, 160 °C, and, therefore, the process using this IL becomes unfeasible. Even though the relative volatility of the mixture ethanol/water using [C_2mim]$N(CN)_2$ is lower, this IL is better solvent than [C_2mim][OAc], considering the complete process.

The IL [C_2mim]$N(CN)_2$ has a low viscosity: η = 14.9 mPa.s at 25 °C and 11 mPa.s at 80 °C. Therefore, this IL was selected and evaluated in our extractive distillation pilot plant for the separation of ethanol/water, and compared with the benchmark solvent EG. A conceptual process design with both EG and [C_2mim]$N(CN)_2$ was carried out taking into account the recovery of the solvent and energy requirements (heat integration).

Pilot Plant Experiments (*43*)

Pilot Plant

The extractive distillation pilot plant consists of three packed column sections, a reboiler and a condenser. The packing in the pilot plant is Sulzer Mellapak™ 750Y structured packing, see Figure 4.

Due to the excellent performance in columns with diameters up to 15 meter, the Mellapak™ packing is the most used structured packing worldwide. The minimum load ($u_{l,min}$) of a Sulzer Mellapak™ 750Y packing is 0.2 $m^3/(m^2.h)$ and the minimum liquid flow is 0.28 kg/h for the ethanol-water distillation, 0.33 kg/h for the extractive distillation with EG as solvent, and 0.31 kg/h with the IL as solvent.

The dimensions and other characteristics concerning the column are summarized in Table 2. The column sections and the reboiler are connected to each other by distributors for the redistribution of the liquid over the next section.

Figure 5 shows the pilot plant column during construction and a schematic drawing of the column. The feed enters the column between the first and second section of the column, at a height of 1.04 m, and the solvent enters the column at the top, at 3.12 m. The ethanol is collected from the condenser as distillate and the solvent/water mixture from the bottom. The pilot plant has four tanks of each 100 L for the feed, solvent, distillate (ethanol) and heavy product (solvent and water).

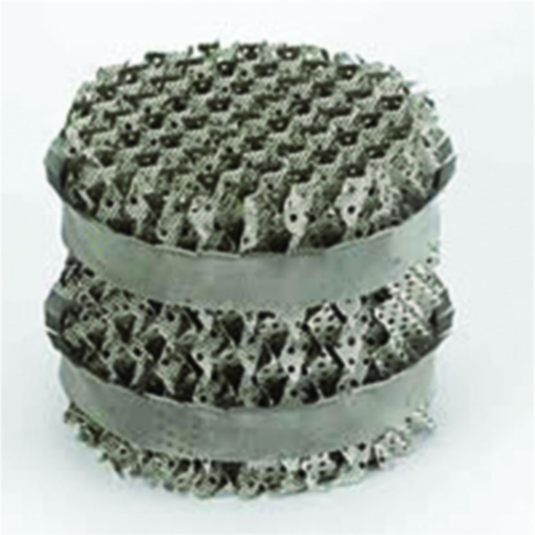

Figure 4. Sulzer Mellapak™ 750 Y. Photo courtesy of ©Sulzer Chemtech Ltd.

Table 2. Pilot plant dimensions and information

Pilot plant column	*Value*	*Unit*
Total height	3.12	meter
Section height	1.04	meter
Section diameter	0.049	meter
Nr. of column sections	3	
Nr. of distributors	3	
Feed entry	1.04	meter
Solvent entry	3.12	meter
Reboiler duty (max.)	2.04	kW
Sampling points	11	
Temp. Indicators	17	
Packing diameter of Sulzer Mellapak™ 750Y Standard material	0.049	meter

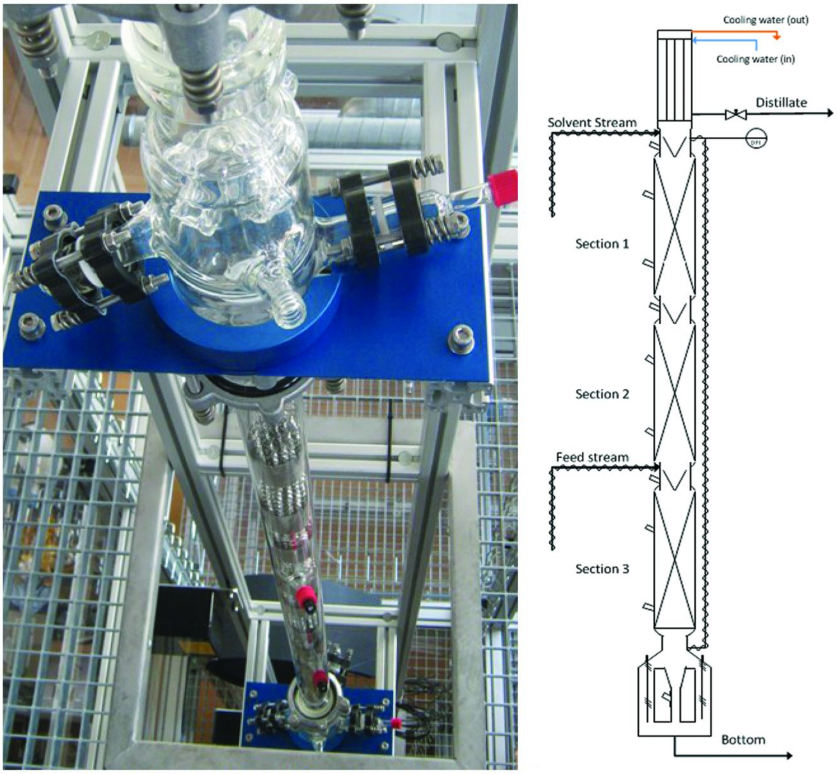

Figure 5. Column section (left) and schematic drawing (right) of the pilot plant column.

Experimental Conditions

The conditions (concentration and temperature) of the feed and solvent streams are kept constant during all experiments. The feed flow remains constant at 3 kg/h throughout the experiment and the solvent stream is dependent on the desired solvent-to-feed (S/F) ratio. The feed composition is 70% water and 30% ethanol. The key part in extractive distillation is the use of the solvent and, therefore, the S/F ratio is an important parameter in the experiments. The solvent will extract the high boiling component from the mixture and, hence, purify the low boiling component. By changing the S/F ratio, the efficiency of the solvent in the stripping section of the column will change. Thus, the capacity of the column can be altered: a higher amount of stages is needed at a lower S/F ratio. However, a higher solvent flow generates more bottom flow and, consequently, a higher capacity is required for the stripping section. During the experiments, the S/F-ratio is set at 2 (6 kg/h solvent).

Determination of feed temperature in a distillation process is also essential for the efficiency of the column itself. The temperature of the feed entering the column does not have to be equal to the temperature inside the column. However, an equality of the temperatures will increase the exergy efficiency (second law of thermodynamics) of the process. Therefore, the feed streams in the pilot plant are preheated in the storage tanks and in the transportation lines. The mixture (ethanol-water) feed is preheated to 50 °C and the solvent feed to 70 °C.

The purity and amount of product can be controlled by changing the distillate rate. The distillate rate influences the reflux ratio and, therewith, the vapor to liquid ratio. A decrease in the distillate rate would result in an increase of the reflux ratio and vice versa. The purity will decrease with decreasing reflux ratios. The distillate rate in these experiments was set at 0.9 kg/h, which is 100% of the introduced ethanol.

Modeling of the Extractive Distillation (*43*)

The extractive distillation was modeled in Aspen V7.2 using a rate-based model, RadFrac, which requires reliable predictions of mass transfer coefficients, interfacial areas and diffusion coefficients to predict the performance of the column. The physical properties of the IL needed to model this process were determined by us (*19*, *20*). Aspen Rate-Based Distillation uses state-of-the-art mass and heat transfer correlations to predict column performance, eliminating the need for efficiency factors or HETPs (Height Equivalent of a Theoretical Plate). The mass transfer correlation depends on the type of packing used in the pilot plant. Aspen gives a few correlations for packed columns to choose from: Bravo and Billet and Schultes. The Billet and Schultes correlation needs additional mass transfer correlation parameters in order to converge and, therefore, only the Bravo correlation is used.

Bravo, Rocha and Fair first developed a generalized correlation for mass transfer in packed distillation columns and later a theoretical model for structured packing (*44–46*). The first method is based on the assumption that the surface is completely wetted and that the interfacial area density is equal to the specific packing surface. The liquid phase mass transfer coefficients are predicted by the penetration model. The generalized correlation is used to model the extractive distillation column.

Extractive Distillation with EG and [C_2mim]N$(CN)_2$

There is one run carried out with ethanol and water only, one with EG and one with [C_2mim]N$(CN)_2$ as the extractive solvent. The operational conditions are summarized in Table 3.

The experiment with ethanol and water was carried out in order to test the pilot plant and to record the performance of the pilot plant. The purity of the product should be higher with the use of the extractive solvents. The experimental performance of the pilot plant is compared with the results of the model of the extractive distillation.

Table 3. Operational conditions of extractive distillation experiments

Experiment	*Solvent*	*Feed flow kg/h*	*Solvent flow kg/h*	*Distillate rate kg/h*
1	–	3	–	0.9
2	EG	3	6	0.9
3	[C$_2$mim]N(CN)$_2$	3	6	0.9

Samples taken from the feed flow, sampling ports, distillate and bottom flows were analyzed. Most samples consist of ternary mixtures of water-ethanol-solvent, and the concentration of ethanol in the mixtures was obtained by GC, using 1-butanol as an internal standard. Water cannot be analyzed in the GC and, therefore, the Karl Fischer method for an accurate analysis of the water content was used. Since the ionic liquid has no vapor pressure, it cannot be analyzed by GC and is collected in a pre-column and a cup-liner. The IL concentration is then calculated by means of a mass balance. The EG concentration was also calculated by means of a mass balance.

The profiles of the concentrations and temperatures over the height of the column of experiment 2, extractive distillation with EG as the solvent, are shown in Figure 6. This Figure shows that the model describes the experiments adequately. The water content decreases from 2.7% at 1.36 m to 0.13% at 3.12 m. The temperature in the upper part of the column is around 90 °C.

The compositions and the temperature profile of an extractive distillation with [C$_2$mim]N(CN)$_2$ as solvent is shown in Figure 7.

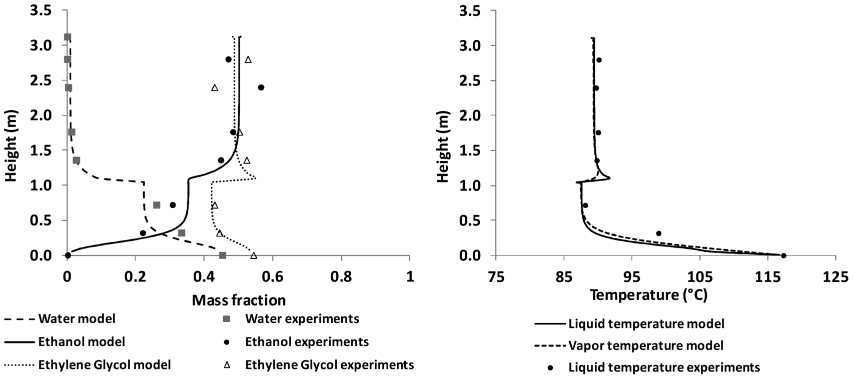

Figure 6. Composition (left) and temperature (right) profiles for ethanol/water distillation with EG as solvent. S/F = 2, distillate rate 0.9 kg/h.

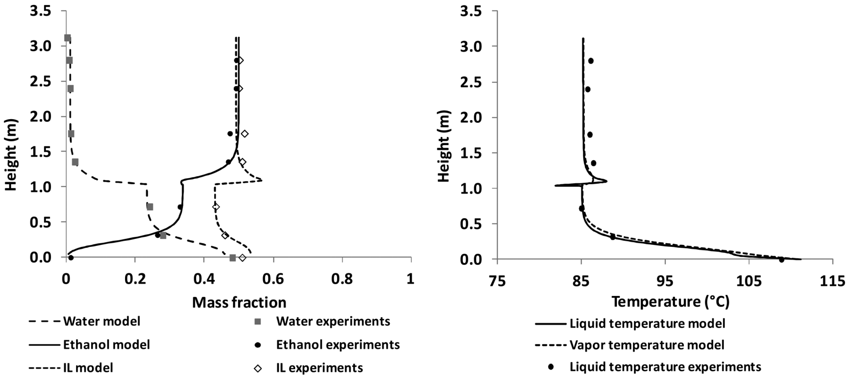

Figure 7. Composition (left) and temperature (right) profiles for ethanol/water distillation with [C_2mim]N(CN)$_2$ as solvent. S/F = 2, distillate rate 0.9 kg/h.

Figure 7 shows that also for [C_2mim]N(CN)$_2$ as solvent the model describes the experiments very well. The water content decreases from 2.3% at 1.36 m to 0.087% at 3.12 m. The temperature in the upper part of the column is around 85 °C. The temperature in the upper part of the column is around 5 °C higher for EG as solvent than for the IL as solvent and this is caused by the higher heat of mixing when EG is used.

The product purity, water content and the reflux ratio of all experiments are given in Table 4. The ethanol content of the distillate of the extractive distillation is calculated via the water content. The analysis of ethanol at high ethanol concentrations, above 95%, was not accurate enough.

Table 4. Product purity, water content and reflux ratio of all experiments

Run	*1*	*2*	*3*
Solvent	–	EG	IL
S/F	–	2	2
Distillate rate, kg/h	0.9	0.9	0.9
Product purity, %	93.5	99.87	99.91
Water content, %	6.5	0.13	0.087
Reflux ratio	7.43	6.34	7.10

The lowest purity is obtained for the normal distillation of ethanol/water mixture, 93.5%, as is to be expected. Extractive distillation of ethanol/water mixtures provides higher purities, up to 99.91% as can be seen in Table 4. The IL [C_2mim]N(CN)$_2$ achieves slightly higher purities than ethylene glycol. The conclusion is that the pilot plant performs well and that a high purity of the ethanol product can be achieved. The developed model describes the extractive distillation experiments with both EG and [C_2mim]N(CN)$_2$ well.

Conceptual Process Design

A model feed mixture of 200 kmol/h composed of 160 kmol/h of ethanol and 40 kmol/ h of water (which corresponds to the outlet concentration of the pre-concentrator, 90 wt%) at 35 °C and 100 kPa is used. These values are based on representative plant capacities for bio-ethanol production (*3–5*). The separation processes simulated are subject to the constraints that the recovered ethanol should have a molar purity $\geq$ 99.8% (*4*, *5*). The condenser and the reboiler are taken into account as equilibrium stages, the condenser being the first stage. The results are based on thermodynamic equilibrium stage modeling using Aspen Plus V7.2, because determination of detailed properties and more complex simulation methods than equilibrium-based methods are not required for the conceptual design of the process. Due to the decomposition temperature, the ionic liquid $[C_2mim]N(CN)_2$ is not allowed to be at temperatures higher than 240 °C (*47–49*).

Extractive Distillation with Ethylene Glycol

The minimum number of stages in the extractive distillation column (EDC) is estimated with the Fenske equation (*50*), using the desired ethanol purity in the distillate and a relative volatility calculated at a molar S/F ratio of unity (arbitrary) at 100 kPa. The reflux ratio and solvent flow are chosen in such a way that the energy requirements of the process are then the lowest. It has been common practice to take two to four times the minimum number of stages (*51*). In our work, thrice the minimum number of stages is taken as the actual number. This means that the actual number of stages for the extractive distillation column using ethylene glycol (EG) is 30. An optimization procedure was implemented to determine the optimal feed stage, solvent feed stage, molar reflux ratio and the molar S/F ratio. The main feed is located at stage 23 and the solvent is fed at the 4th stage to avoid solvent losses in the overhead of the column. An analogous procedure was applied for the solvent recovery column (SRC), resulting in 15 actual stages. Figure 8 depicts the flow sheet of the extractive distillation process with EG as extractive solvent.

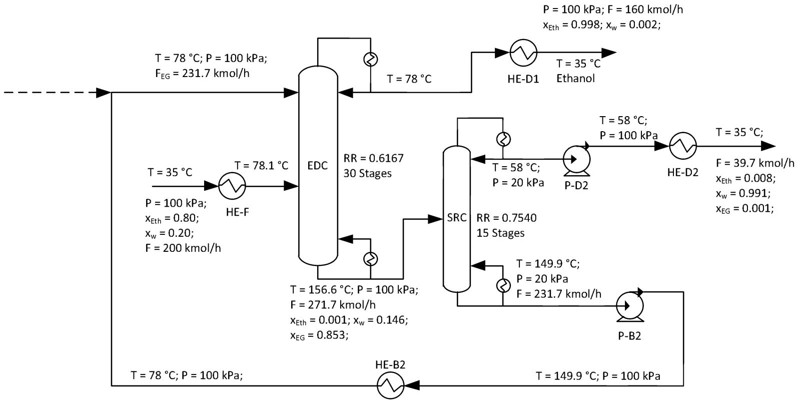
P = 100 kPa; F = 160 kmol/h
x_{Eth} = 0.998; x_w = 0.002;
T = 78 °C; P = 100 kPa;
F_{EG} = 231.7 kmol/h
T = 78 °C
HE-D1
T = 35 °C
Ethanol
T = 58 °C;
P = 100 kPa
T = 35 °C;
T = 35 °C
T = 78.1 °C
EDC
RR = 0.6167
30 Stages
T = 58 °C;
P = 20 kPa
P-D2
HE-D2
F = 39.7 kmol/h
x_{Eth} = 0.008;
x_w = 0.991;
x_{EG} = 0.001;
P = 100 kPa;
x_{Eth} = 0.80;
x_w = 0.20;
F = 200 kmol/h
HE-F
SRC
RR = 0.7540
15 Stages
T = 149.9 °C;
P = 20 kPa
F = 231.7 kmol/h
T = 156.6 °C; P = 100 kPa;
F = 271.7 kmol/h
x_{Eth} = 0.001; x_w = 0.146;
x_{EG} = 0.853;
P-B2
HE-B2
T = 78 °C; P = 100 kPa;
T = 149.9 °C; P = 100 kPa

Figure 8. Conventional extractive distillation process using ethylene glycol.

To avoid solvent losses in the SRC, the maximum ethylene glycol composition allowed in the overhead of the SRC was limited to less than 500 ppm. The feed is located at the 8th stage. A lower pressure in the SRC results in lower energy requirements and it is maintained by the condenser.

However, if the pressure is lower than 20 kPa, the constraint for the EG in the overhead is not satisfied, as the solvent becomes more volatile due to the low pressure. Therefore, a pressure in the SRC of 20 kPa is chosen which gives a temperature in the condenser 58 °C.

The molar S/F ratio of the process is 1.16 (which gives a mass S/F ratio of 1.8) and the reflux ratio of the extractive distillation column and solvent recovery column are 0.6 and 0.8, respectively (Figure 8). About 0.02 kmol/h of ethylene glycol is lost through the overhead of both columns (90% through the SRC).

Extractive Distillation with $[C_2mim]N(CN)_2$

As in the previous case, the minimum number of stages was calculated with the Fenske equation using an arbitrary molar S/F ratio of unity to calculate the relative volatility. Thus, the actual number of stages of the extractive distillation column using ionic liquids is 30. The S/F ratio, reflux ratio and feed stage were determined using a minimization procedure. The ionic liquid can be fed into the column combined with the reflux flow without losing the solvent in the overhead due to its non-volatility. According to the results, the feed should be located at the 23rd stage.

The molar purity of the IL component (the IL including its associated impurities) fed to the extractive distillation column should be 99.8% and the maximum water content should be 0.2%. A lower purity of the IL, which means a higher water content in the stream, results in an increase in the reflux ratio and, consequently, in an increase in the energy requirements or results in a violation of the purity constraint in the overhead product. The energy requirements of the IL recovery technology will be also affected by the purity of the IL fed to the EDC, since a higher required purity of the IL results in higher costs involved in the recovery process.

The molar S/F ratio for the process using $[C_2mim]N(CN)_2$ is 0.54, which is lower than the one obtained for EG (molar ratio of 1.16). However, when mass based S/F ratios are used, the S/F ratio is higher than with EG, 2.38 for $[C_2mim]N(CN)_2$ and 1.8 for EG.

Ionic Liquid Recovery Techniques

Ordinary distillation is not a suitable technology to recover ILs due to their non-volatility. Several technologies have been proposed to recover and recycle the ionic liquids. Evaporation (at high temperature and low pressure) and stripping are potential technologies to recover ionic liquids from volatile compounds (*22*). Membrane-based processes have been analyzed, but, due to their large membrane area needed, these processes are not feasible for IL recovery (*52*). Extraction with supercritical carbon dioxide ($SCCO_2$) of the volatile compounds had been suggested (*52*), but requires 20 times more energy than the conventional process

In Ionic Liquids: Science and Applications; Visser, A., et al.;
ACS Symposium Series; American Chemical Society: Washington, DC, 2012.

using ethylene glycol. Processes like flash vaporization, stripping with N2 and a combination of both technologies are taken into account. All the regeneration technologies analyzed yielded higher energy requirements for the process using the IL than for the process using ethylene glycol.

The process with the lowest energy requirements is flash evaporation of the bottom stream of the EDC. This process consists of a simple evaporation flash drum which will remove the water from the ionic liquid due to the decrease in pressure and simultaneously an increase of temperature. The water is obtained in the vapor outlet of the flash with a high purity and the ionic liquid is obtained in the liquid outlet of the drum with the desired purity, which will be influenced by the pressure and temperature used in this unit. Due to the interactions of the IL and water, high temperatures need to be used. The flash evaporator was operated at their maximum tolerable temperature, 240 °C for $[C_2mim]N(CN)_2$.

Although the TGA analysis of the IL $[C_2mim]N(CN)_2$ indicate that the decomposition temperature is around 240 °C (*47–49*), several studies show that the scanning nature of the experiment, the onset and peak decomposition temperatures obtained from a single temperature ramp experiment, are often overestimations of the long term thermal stability of the ILs (*53*, *54*). Paraknowitsch et al. reported that the IL $[C_2mim]N(CN)_2$ showed no weight loss up to a temperature of 280 °C (*49*). Decomposition then occurs in three distinct steps for this IL and the first decomposition can be found at around 300 °C, probably representing the cleavage of alkyl chains. However, long-term thermal stability tests of the IL $[C_2mim]N(CN)_2$ will be required to show that it is suitable in extractive distillation and for the regeneration at higher temperatures. If the thermal stability tests show that the temperature range of this IL lies below 240 °C, then alternative regeneration techniques must be investigated and evaluated.

Figure 9 shows the complete extractive distillation process with $[C_2mim]N(CN)_2$ as solvent and with flash evaporation of the water.

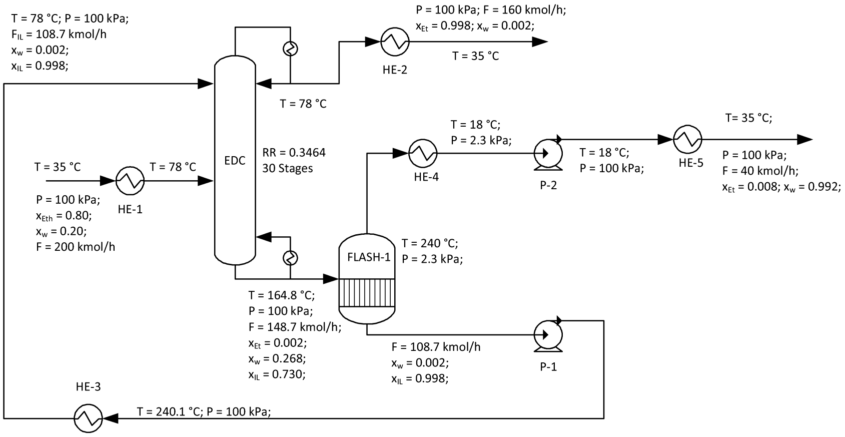
T = 78 °C; P = 100 kPa;
F_{IL} = 108.7 kmol/h
x_w = 0.002;
x_{IL} = 0.998;
P = 100 kPa; F = 160 kmol/h;
x_{Et} = 0.998; x_w = 0.002;
T = 35 °C
HE-2
T = 78 °C
T = 18 °C;
P = 2.3 kPa;
T= 35 °C;
T = 35 °C
T = 78 °C
EDC
RR = 0.3464
30 Stages
HE-4
T = 18 °C;
P = 100 kPa;
HE-5
P = 100 kPa;
F = 40 kmol/h;
x_{Et} = 0.008; x_w = 0.992;
P-2
P = 100 kPa;
x_{Eth} = 0.80;
x_w = 0.20;
F = 200 kmol/h
HE-1
T = 240 °C;
P = 2.3 kPa;
FLASH-1
T = 164.8 °C;
P = 100 kPa;
F = 148.7 kmol/h;
x_{Et} = 0.002;
x_w = 0.268;
x_{IL} = 0.730;
F = 108.7 kmol/h
x_w = 0.002;
x_{IL} = 0.998;
P-1
HE-3
T = 240.1 °C; P = 100 kPa;

Figure 9. ED process using $[C_2mim]N(CN)_2$. Recovery of IL with flash drum at 240 °C.

Energy Requirements

Replacing the conventional solvent EG with [C_2mim]N(CN)$_2$ yields 6.6% lower energy duties in the EDC. However, the recovery of the IL is more energy intensive than the recovery of EG, due to the higher heat capacity of the IL. Therefore, no energy savings are achieved when the conventional solvent is replaced by an IL. Hence, heat integration is an essential requirement for a feasible extractive distillation process with an ionic liquid. Composite curves are used to determine the maximum energy that can be recovered using process-to-process heat exchangers. It also gives information about the minimum energy requirements (minimum usage of heating and cooling utilities, when exchanging heat between hot and cold streams within a process). The composite curves and the heat integration were created with methods proposed in literature (*50*, *55*) and using Aspen Energy Analyzer V7.2, taking a minimum temperature difference (ΔT_{min}) of 10 K. Figure 10 shows the composite curves for the conventional process using ethylene glycol and [C_2mim]N(CN)$_2$.

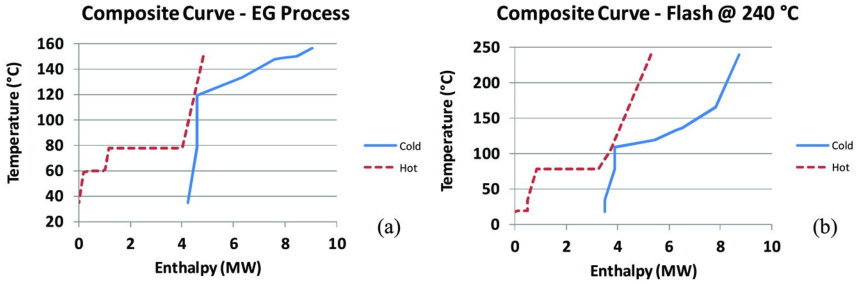

Figure 10. Composite curve for (a) the conventional ED process and (b) the process using [C_2mim]N(CN)$_2$ utilizing a flash drum at 240 °C for IL recovery.

The composite curves for the EG process (Figure 10 (a)) show that the heating and cooling targets (minimum energy input and output to the process) are 4.21 and 4.22 MW, respectively. Performing heat integration, a maximum of 0.61 MW can be recovered with process-to-process heat exchangers, representing 13% of the energy requirements of the process without heat integration. The composite curves for the process using [C_2mim]N(CN)$_2$ (Figure 10 (b)) show that the heating and cooling targets are 3.43 and 3.49 MW, respectively. Some of the energy should be removed with a refrigerant due to the low temperatures reached in this process. Performing the heat integration, a maximum of 1.82 MW can be recovered which results in a total energy requirement of 3.52 MW (34% lower than the process without heat integration). Most of the recovered energy involves the cooling down of the solvent being recycled to the extractive distillation column in both processes. These streams have enough energy to heat up the feed to the extractive distillation column and even some of the energy required in the reboiler of the ED column in both processes. The energy required in the reboiler in the IL process is not only provided by the energy of the recycled IL, but also by the energy from the condensation stream after the water flash. This explains why the energy savings with [C_2mim]N(CN)$_2$ as solvent are higher than for the conventional solvent. The total energy requirements of the recovery technologies combined with the extractive distillation column and including heat integration are summarized in Figure 11.

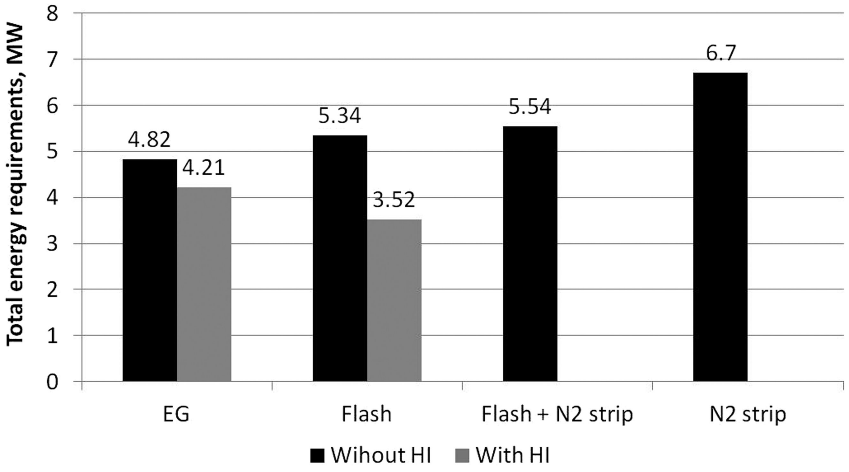

Figure 11. Total energy requirements for the ED process using [C_2mim]N$(CN)_2$, (ED column + recovery technology), including heat integration (HI). Feed 200 kmol/h.

The extractive distillation process without heat integration using [C_2mim]N$(CN)_2$ as solvent requires about 11% more energy than the process using EG as solvent. However, the IL process with heat integration requires 16% less energy than the EG process with heat integration.

Conclusion

The extractive distillation of ethanol/water using the benchmark solvent ethylene glycol and an ionic liquid was investigated. The best ionic liquid for this separation is [C_2mim]N$(CN)_2$, which shows comparable relative ethanol/water volatility as ethylene glycol.

Experiments in the pilot plant showed that the experimental results could very well be described by the developed model. A product purity of 99.91% could be achieved.

Besides the performance in the ED column, the IL should be easily recoverable. All the recovery processes studied yielded higher energy requirements than the benchmark (ED using EG). The recovery of the IL using flash evaporation at 240 °C required the lowest amount of energy, but the extractive distillation process using the IL used 11% more energy than the benchmark. After implementing heat integration, the total energy requirements of both processes can be decreased and the use of the IL becomes more attractive, yielding 16% of energy savings compared with the heat integrated conventional process.

The key performance points in extractive distillation of ethanol/water using ionic liquids as extractive solvents are the recovery of the IL and the heat integration in the whole process.

Acknowledgments

The authors acknowledge AgentschapNL, formerly SenterNovem, for the financial support for this project, project number EOSLT06016 (Energie Onderzoek Subsidie, Lange Termijn).

References

1. Kumar, S.; Singh, N.; Prasad, R. *Renew. Sust. Energy Rev.* **2010**, *14* (7), 1830–1844.
2. McPhail, L. L. *Energy Econ.* **2011**, *33* (6), 1177–1185.
3. Huang, H.-J.; Ramaswamy, S.; Tschirner, U. W.; Ramarao, B. V. *Sep. Purif. Technol.* **2008**, *62* (1), 1–21.
4. Mielenz, J. R. *Curr. Opin. Microbiol.* **2001**, *4* (3), 324–329.
5. Seiler, M.; Jork, C.; Kavarnou, A.; Arlt, W.; Hirsch, R. *AIChE J.* **2004**, *50* (10), 2439–2454.
6. Lei, Z.; Li, C.; Chen, B. *Sep. Purif. Rev.* **2003**, *32* (2), 121–213.
7. Bastidas, P. A.; Gil, I. D.; Rodriguez, G. *Comput.-Aided Chem. Eng.* **2010**, *28*, 1709–1714.
8. Li, G.; Bai, P. *Ind. Eng. Chem. Res.* **2012**, *51* (6), 2723–2729.
9. Gil, I. D.; Uyazan, A. M.; Aguilar, J. L.; Rodriguez, G.; Caicedo, L. A. *Braz. J. Chem. Eng.* **2008**, *25* (1), 207–215.
10. Ramanujam, M.; Laddha, G. S. *Chem. Eng. Sci.* **1960**, *12* (1), 65–68.
11. Doherty, M. F.; Knapp, J. P. Distillation, Azeotropic, and Extractive. In *Kirk-Othmer Encyclopedia of Chemical Technology*; John Wiley & Sons, Inc.: Hoboken, NJ2000.
12. Ravagnani, M. A. S. S.; Reis, M. H. M.; Maciel, F. R.; Wolf-Maciel, M. R. *Process Saf. Environ. Prot.* **2010**, *88* (1), 67–73.
13. Kamihama, N.; Matsuda, H.; Kurihara, K.; Tochigi, K.; Oba, S. *J. Chem. Eng. Data* **2012**, *57* (.2), 339–344.
14. Jork, C.; Seiler, M.; Beste, Y. A.; Arlt, W. *J. Chem. Eng. Data* **2004**, *49* (4), 852–857.
15. Ge, Y.; Zhang, L.; Yuan, X.; Geng, W.; Ji, J. *J. Chem. Thermodyn.* **2008**, *40* (8), 1248–1252.
16. Orchillés, A. V.; Miguel, P. J.; Vercher, E.; Martinez-Andreu, A. *J. Chem. Eng. Data* **2010**, *55* (4), 1669–1674.
17. Orchillés, A. V.; Miguel, P. J.; Llopis, F. J.; Vercher, E.; Martínez-Andreu, A. *J. Chem. Eng. Data* **2011**, *56* (12), 4875–4880.
18. Bastos, J. C.; Soares, M. E.; Medina, A. G. *Ind. Eng. Chem. Proc. Des. Dev.* **1985**, *24* (2), 420–6.
19. Quijada-Maldonado, E.; van der Boogaart, S.; Lijbers, J. H.; Meindersma, G. W.; de Haan, A. B. *J. Chem. Thermodyn.* **2012**, *51* (0), 51–58.

20. Quijada-Maldonado, E.; Meindersma, G. W.; de Haan, A. B. *J. Chem. Thermodyn.* **2012**.
21. Azizian, S.; Hemmati, M. *J. Chem. Eng. Data* **2003**, *48* (3), 662–663.
22. Beste, Y. A.; Schoenmakers, H.; Arlt, W.; Seiler, M.; Jork, C. Recycling of Ionic Liquids with Extractive Distillation. Patent WO2005016484, 2005.
23. Arlt, W.; Seiler, M.; Jork, C.; Schneider, T. Ionic Liquids As Selective Additives for the Separation of Close-Boiling or Azeotropic Mixtures. Patnet WO02074718 A2; also published as WO02074718 (A3), EP1372807 (A3), EP1372807 (A2), 2002.
24. Gmehling, J.; Krummen, M. Einsatz ionischer Flüssigkeiten als selektive Lösungsmittel für die Trennung aromatischer Kohlenwasserstoffe van nichtaromatischen Kohlenwasserstoffe durch extractieve Rektifikation und Extraktion. Patent DE 10154052 A1, 2003.
25. Jork, C.; Seiler, M.; Beste, Y.-A.; Arlt, W. *J. Chem. Eng. Data* **2004**, *49* (4), 852–857.
26. Seiler, M.; Jork, C.; Arlt, W. *Chem. Ing. Tecnol.* **2004**, *76* (6), 735–744.
27. Beste, Y. A.; Schoenmakers, H. Distillative Method for Separating Narrow Boiling or Azeotropic Mixtures Using Ionic Liquids.Patent WO2005016483 (A1), 2005.
28. Beste, Y.; Eggersmann, M.; Schoenmakers, H. *Chem. Ing. Technol.* **2005**, *77* (11), 1800–1808.
29. Beste, Y. A.; Eggersmann, M.; Schoenmakers, H. In *Ionic liquids: Breaking Azeotrops Efficiently by Extractive Distillation*. Sustainable (Bio)Chemical Process Technology, incorporating the 6th Intenational Conference on Process Intensification, Delft, Nl., Jansens P., S. A., Green A., Eds., 2005; pp 5−8.
30. Lei, Z.; Arlt, W.; Wasserscheid, P. *Fluid Phase Equilib.* **2006**, *241* (1−2), 290–299.
31. Zhu, J.; Chen, J.; Li, C.; Fei, W. *Fluid Phase Equilib.* **2006**, *247* (1-2), 102–106.
32. Stratula, C.; Oprea, F.; Mihaescu, D. *Rev. Chim. (Bucharest, Rom.)* **2005**, *56* (5), 544–548.
33. Calvar, N.; González, B.; Gómez, E.; Domínguez, A. *J. Chem. Eng. Data* **2006**, *51* (6), 2178–2181.
34. Geng, W.; Zhang, L. Z.; Deng, D. S.; Ge, Y.; Ji, J. B. *J. Chem. Eng. Data* **2010**, *55* (4), 1679–1683.
35. Calvar, N.; González, B.; Gómez, E.; Domínguez, A. *Fluid Phase Equilib.* **2007**, *259* (1), 51–56.
36. Zhang, L.; Ge, Y.; Ji, D.; Ji, J. *J. Chem. Eng. Data* **2009**, *54* (8), 2322–2329.
37. Calvar, N.; González, B.; Gómez, E.; Domínguez, A. *J. Chem. Eng. Data* **2008**, *53* (3), 820–825.
38. Calvar, N.; González, B.; Gómez, E.; Domínguez, Á. *J. Chem. Eng. Data* **2009**, *54* (3), 1004–1008.
39. Calvar, N.; Gómez, E.; González, B.; Domínguez, Á. *J. Chem. Eng. Data* **2010**, *55* (8), 2786–2791.
40. Fendt, S.; Padmanabhan, S.; Blanch, H. W.; Prausnitz, J. M. *J. Chem. Eng. Data* **2010**, *56* (1), 31–34.

41. Hasse, B.; Lehmann, J.; Assenbaum, D.; Wasserscheid, P.; Leipertz, A.; Fröba, A. P. *J. Chem. Eng. Data* **2009**, *54* (9), 2576–2583.
42. Vagt, U., Cellulose Dissolution and Processing with Ionic Liquids. In *Green Solvents*; Wasserscheid, P., Stark, A., Eds.; Wiley-VCH: Weinheim, Germany, 2010; Vol. 6, Ionic Liquids, pp 123−136.
43. Quijada-Maldonado, E.; Aelmans, T. A. M.; Meindersma, G. W.; de Haan, A. B. Pilot Plant Validation of a Rate-Based Extractive Distillation Model for Water−Ethanol Separation with the Ionic Liquid [EMIM]DCA as Solvent. In *CHISA 2012*, Prague, CZ, 2012; Vol. Paper 160.
44. Bravo, J. L.; Fair, J. R. *Ind. Eng. Chem. Proc. Des. Dev.* **1982**, *21* (1), 162–170.
45. Rocha, J. A.; Bravo, J. L.; Fair, J. R. *Ind. Eng. Chem. Res.* **1993**, *32* (4), 641–651.
46. Rocha, J. A.; Bravo, J. L.; Fair, J. R. *Ind. Eng. Chem. Res.* **1996**, *35* (5), 1660–1667.
47. Yoshida, Y.; Muroi, K.; Otsuka, A.; Saito, G.; Takahashi, M.; Yoko, T. *Inorg. Chem.* **2004**, *43* (4), 1458–1462.
48. Yoshida, Y.; Baba, O.; Saito, G. *J. Phys. Chem. B* **2007**, *111* (18), 4742–4749.
49. Paraknowitsch, J. P.; Zhang, J.; Su, D.; Thomas, A.; Antonietti, M. *Adv. Mater. (Weinheim, Ger.)* **2010**, *22* (1), 87–92.
50. Seider, W. D.; Seader, J. D.; Lewin, D. R. *Product and Process Design Principles: Synthesis, Analysis and Evaluation*, 2nd ed.; Wiley: New York; 2004; p 802.
51. Tiverios, P. G.; Van Brunt, V. *Ind. Eng. Chem. Res.* **2000**, *39* (6), 1614–1623.
52. Haerens, K.; Van Deuren, S.; Matthijs, E.; Van der Bruggen, B. *Green Chem.* **2010**, *12* (12), 2182–2188.
53. Wooster, T. J.; Johanson, K. M.; Fraser, K. J.; MacFarlane, D. R.; Scott, J. L. *Green Chem.* **2006**, *8* (8), 691–696.
54. Liang, R.; Yang, M.; Xuan, X. *Chin. J. Chem. Eng.* **2010**, *18* (5), 736–741.
55. Smith, R. M. *Chemical Process: Design and Integration*; John Wiley & Sons: Chichester, West Sussex, UK, 2005; p 712.

Chapter 12

Al_2O_3-Based Nanoparticle-Enhanced Ionic Liquids (NEILs) for Advanced Heat Transfer Fluids

Ann E. Visser, Nicholas J. Bridges, Brenda L. Garcia-Diaz, Joshua R. Gray, and Elise B. Fox*

Savannah River National Laboratory, Savannah River Site,
Aiken, South Carolina 29808
***E-mail: Elise.Fox@srnl.doe.gov**

Herein we describe the chemical and physical properties of Nanoparticle Enhanced Ionic Liquids (NEILs) and highlight their potential as novel heat transfer fluids. The Ionic Liquids (ILs) contain the bis(trifluoromethylsulfonyl)imide or bis(perfluoroethylsulfonyl)imide anion and a variety of imidazolium cations. Alumina nanoparticles were added to ILs and increased the heat capacity above that for the ILs. This report discusses our current results with characterizing NEILs and evaluating the corrosion behavior of a target IL against common materials.

Introduction

Renewable resources provide a source of domestic energy and foster the development of next-generation energy production, storage and conversion technologies. Solar energy, for example, is a free resource that does not need to be mined, transported, or burned to realize its full potential. While harvesting the sun's energy is not a new idea, solar energy collection is a vastly underutilized source of energy. There are two types of solar energy production: photovoltaics (PV) and concentrating solar power (CSP). PV is more well know an typically uses a Si or organic based semiconductor with a p-n junction to great an electric current. These systems are widespread throughout the U.S. and can have smaller distributed systems on individual rooftops or large-scale power production facilities. CSP is mostly limited to the southwest U.S, although there are

Not subject to U.S. Copyright. Published 2012 by American Chemical Society
In Ionic Liquids: Science and Applications; Visser, A., et al.;
ACS Symposium Series; American Chemical Society: Washington, DC, 2012.

commercial power plants in operation in Florida. CSP has smoother short-term fluctuations than PV and stores energy as thermal energy, which is considerably simpler than electrical energy storage necessary for PV.

Heat Transfer Fluids

Solar parabolic trough systems are one type of CSP technology. In general, solar trough systems consist of many modular parabolic trough collectors that capture and focus solar heat radiation onto a linear receiver tube. A heat transfer fluid (HTF) flows through the receiver tube and transports the thermal energy to, ultimately, drive a steam turbine and generate electricity (*1*). Heat transfer fluids are commonly used in industry and in solar energy collections as a means to exchange energy from one source to another, either to dissipate the energy or convert the thermal energy into power. The physical properties of the thermal fluid greatly affect the overall efficiency of the system. Thus there is always a driving force to design a thermal fluid with better physical properties.

The current generation of organic heat transfer fluids employs molecules that have significant vapor pressure within the temperature range for system operation, thus the systems must operate under pressure. The organic heat transfer fluids also decompose to produce hydrogen (*1*, *2*). Recent observations indicate that the long-term exposure of molecular heat transfer fluids to 400°C can lead to hydrogen pressures that exceed the gas-absorbing capacity of the hydrogen getters, thereby causing the significant heat losses that are currently observed in several solar trough plants (*1*). Improving the thermal stability of HTF can bring dual benefits: operation at higher temperatures to take advantage of the increased thermal-to-electric conversion efficiency, and reductions in the generation of hydrogen gas.

Ionic Liquids as Heat Transfer Fluids

Therminol VP-1® , a eutectic mixture of biphenyl and diphenyl oxide, is made of organics that have low vapor pressures, low viscocity, reasonable heat capacity, and can breakdown into H_2 upon decomposition (*2*). When H_2 is produced in the system is removed by getters, such as Pd-keiselruhr, which can increase the cost of the HTF system by up to 60%. It also has a low boiling temperature and is limited to operational temperatures less than 390°C. It is, therefore, desirable to investigate alternative HTFs that o not breakdown into H_2, have reduced vapor pressure while having low viscosity and high heat capacity. In recent decades, Ionic Liquids (ILs) have attracted significant attention as novel solvent media for separations, synthesis, and electrochemistry. ILs are usually composed of organic cations and organic or inorganic anions and have a unique combination of properties including high density, wide temperature range for liquid phase, and high heat capacity. ILs are sparingly volatile and they can be distilled without decomposition under extreme conditions (*3*). Nonetheless, the vapor pressure of ILs is substantially lower than that for traditional molecular solvents.

ILs have high heat capacities and have been previously investigated as heat transfer and heat storage fluids (*4*). Reddy et al calculated that [C_4mim][Tf_2N] has a sensible heat storage density of greater than 170 MJ/m^3 when the inlet and outlet field temperatures were 210 °C and 310 °C, respectively (*5*). Blake et al found [C_8mim][PF_6] and [C_4mim][Tf_2N] to be promising ILs for thermal storage (*6*). Anouti et al have found ILs containing the alkylammonium cation to have high heat storage capacity (*7*). Van Valkenberg reported [C_4mim][BF_4] to have a heat storage density of 194 MJ/m^3 (*8*). These high heat capacities and storage densities make ILs ideal for HTFs and thermal energy storage media in CSP.

Early research with ILs has shown the wide temperature range for the liquid phase to be a distinct advantage for ILs vs. traditional organic heat transfer fluids and inorganic nitrate-based molten salts, which have also been investigated for CSP (*9*, *10*). Inorganic nitrate-based molten salts have freezing points of 120°C or greater which is undesirable in a solar energy collector due to the additional thermal expansion, potential for line freezing, and added engineering cost. Some ILs have melting points of -50°C or lower, which provides a distinct advantage to the use of ILs in system design.

Nanofluids

Suspending nanomaterials in common solvents provides useful advantages in industrial fuel systems, including heat transfer fluids (*11*, *12*), magnetic fluids (*13*), and lubricant fluids (*14*). With particular emphasis on heat transfer fluids, nanofluids are traditional HTFs containing nanometer sized solids (metallic or non-metallic) and have heat transfer properties surpassing those of the base fluid. For example, adding carbon nanotubes to ethylene glycol yields a “pronounced increase” in the heat capacity with respect to neat ethylene glycol (*15*).

Nanoparticle Enhanced Ionic Liquids

We have previously shown how the intrinsically high heat capacity associated with nanoscale metals or metal oxides can enhance the properties of ILs (*16*). Here, the chemical and physical properties of a larger series of NEILs containing 0.5-2.5 weight percent Al_2O_3 were measured to determine how the presence of nanoparticles affected the properties. These systems have increased our understanding of the effects of addition of nanoparticles to different ILs.

Experimental

The 1-butyl-3-methylimidazolium bis(trifluoromethylsulfonyl)imide ([C_4mim][Tf_2N]) and 1-butyl-2,3-dimethylimidazolium bis(trifluoromethyl sulfonyl)imide ([C_4mmim][Tf_2]) ILs were used as received from IoLiTec (Tuscaloosa, AL). The 1-butyl-3-methylimidazoliumbis(perfluoroethyl sulfonyl)imide [C_4mim][BETI]) IL was prepared via aqueous metathesis of [C_4mim][Cl] and LiBETI. A 1:1 molar ratio of 1-butyl-3-metylidizolium chloride (Aldrich) and Li bis(perfluoroethylsulfonyl)imide (3M) were mixed together and covered in 300mL of deionized water. The mixture was allowed to stir for 30 minutes after all salts were dissolved. The solution was allowed to settle into two phases. The organic phase was washed with DI water and allowed to settle for thirty minutes. This process was repeated three times. The washed organic phase was then bubbled with dry N_2 for 24 hours to help dry the resulting ionic liquid. The samples were diluted and analyzed for chloride content using a Dionex RFIC-3000 ion chromatography system with the following parameters: IonPac AG-19 4 mm × 50 mm guard column, IonPac AS-19 4 mm × 250 mm analytical column, and a suppressed conductivity detector. Each injection used 50 μL of sample and a 20-40 mmol KOH gradient mobile phase with a 1 mL/min flow rate. Control of the system and data acquisition used Dionex Chromeleon v.6.8 software. No residual chloride was detected for the IL.

All TGA experiments were conducted under a N_2 atmosphere using a Netzsch 209 F1 thermal gravimetric analyzer with single use Al crucibles at a ramp rate of 10°C/minute. The thermal analysis software (Proteus V5.2.0) calculates the thermal onset temperature based on the intersection of the baseline with the tangent, at the inflection point, of the decomposition rate.

The heat capacity of ionic liquid was measured using Differential Scanning Calorimetry (DSC Q200 from TA instruments Inc.). The ionic liquid sample was placed in a standard Tzero hermetic pan and the average sample size was 32 mg. The initial temperature was 25°C and ramp up a rate of 20°C/min up to 350°C. The experiments were repeated four times and uncertainty has been calculated to be ±1.5%.

Viscosity measurements were taken on a Thermo Haake Mars III Rheometer from 25-200°C using a 0.5° Ti cone and plate. The temperature was controlled by electric heaters. Approximately 1 mL of ionic liquid was added to the plate after zeroing and allowed to equilibrate to temperature. Rheometer operation was verified by NIST standards within the viscosity ranges tested and was within 5% experimental error range.

Nanoscale Al_2O_3 was purchased from Sigma Aldrich (#544833). The nanoparticles are less than 50nm in diameter as determined by TEM and have a multi-point BET surface area of 142 m^2/g.

Results

NEIL Characterization

In the present study, NEILs were produced using the three ILs shown in Figure 1.

The density, viscosity, and thermal stability data of the neat ILs is summarized in Table 1. The Tf_2N^- and $BETI^-$ anions were selected for use because they produce ILs with low viscosity. Similarly, ILs containing imidazolium cations were selected since they typically have high thermal stability. The results shown in Table 1 are comparable to the density (*17*), viscosity (*17–19*), and thermal stability (*20*) data for the ILs reported in the literature. To be considered a viable heat transfer fluid, the addition of nanoparticles to ILs should not have a deleterious effect on the physical properties. Thus, 0.5-2.5 wt % nanoparticles were added to ILs and the physical properties are summarized in Table 2.

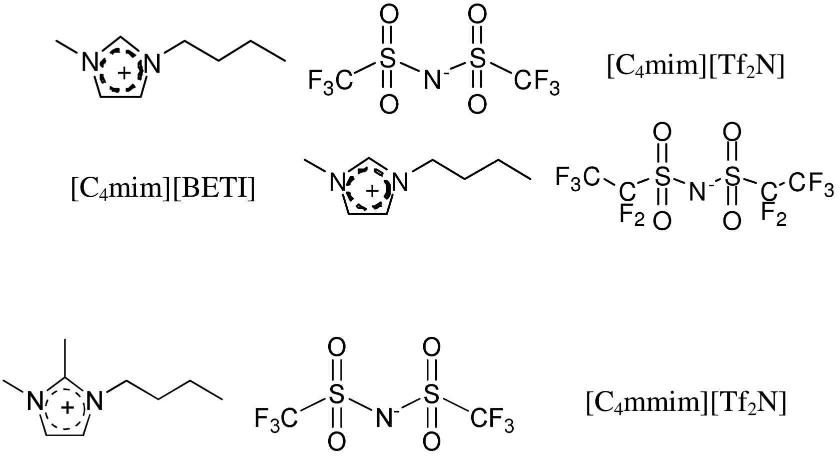

Figure 1. Structure of ILs.

Table 1. Density, Viscosity, and Thermal Stability of Neat ILs

Temperature (°C)	*[C_4mim][Tf_2N]*	*[C_4mmim][Tf_2N]*	*[C_4mim][BETI]*
	Density (g/cm^3)		
20	1.4414	1.4239	1.5177
40	1.4226	1.4052	1.4964
60	1.4026	1.3867	1.4753
	Viscosity (cP)		
25	51.0	105	102
60	15.9	22.1	21.6
100	6.3	7.8	7.4
200	1.9	1.9	0.8
	Thermal Stability		
N/A	413	430	392

The ILs tested here are typically non-coordinating in the sense that the cation and anion are too weakly coordinating and not suitable to dissolve oxides (*21*). However, there is ample evidence in the literature that the nanoparticles interact with the IL cations and anions (*22*), albeit in a fashion that does not impact the stability at elevated temperatures. At room temperature, [BETI] appears to have a much stronger interaction with the Al_2O_3 than [Tf_2N], thereby causing a larger increase in the viscosity. As the temperature increases, the effects are not as pronounced. This trend follows at both 0.5 and 2.5 wt%. Very little heat capacity data for ILs with nanoparticles is available for comparison, although recent experiments with ILs and carbon nanotubes (*23*) have been reported. With 1-1.5 % multiwalled carbon nanotubes in [C_4mim][PF_6], the mixture shows a maximum in heat capacity as a function of temperature. An increase of 8% vs. neat IL was observed, despite increased nanotube loading (*23*).

Table 2. Density, Viscosity, and Thermal Stability of NEILs Containing 0.5 and 2.5 wt % Al_2O_3

Temperature (°C)	*[C_4mim][Tf_2N]*	*[C_4mmim][Tf_2N]*	*[C_4mim][BETI]*
	0.5 wt % Al_2O_3, Density (g/cm^3)		
25	1.485	1.454	1.545
40	1.452	1.426	1.532
60	1.433	1.405	1.497
	0.5 wt % Al_2O_3, Viscosity (cP)		
25	53.0	103.0	120.0
60	15.0	22.8	24.2
100	6.3	8.2	8.4
200	1.9	2.1	2.0
	2.5 wt % Al_2O_3, Viscosity (cP)		
25	61.0	147.3	171.1
60	18.9	43.0	44.6
100	8.9	18.9	20.8
200	3.2	4.7	3.9
	0.5 wt % Al_2O_3, Thermal Stability		
N/A	405	420	394

The most significant impact of adding nanoparticles to ILs is the increased heat capacity relative to the neat IL. As shown in Table 3, the addition of Al_2O_3 to [C_4mmim][NTf_2] increases the heat capacity in comparison to the neat IL.

With 2.5 wt. % Al_2O_3, the heat capacity is temperature dependent and increases up to 28% in comparison to the neat IL. The Al_2O_3-based NEILs exhibit a smooth increase in heat capacity as a function of temperature (*16*).

Table 3. Heat Capacity of Neat IL vs NEIL

	Heat Capacity (J/g.K)	
Sample	*100 °C*	*200 °C*
$[C_4mim][Tf_2N]$	1.65	1.79
$[C_4mmim][Tf_2N]$	1.71	2.09
$[C_4mmim][Tf_2N]$ + 2.5 wt% Al_2O_3	2.25	2.28
$[C_4mim][BETI]$	1.99	2.05
$[C_4mim][BETI]$ + 2.5 wt% Al_2O_3	2.31	2.62

Corrosion

In order to use ILs as HTFs, it is important to consider their compatibility with common construction materials, particularly at elevated temperatures. In general, ILs of $[Tf_2N]$ and [BETI] are considered noncorrosive (*24*) and there have been very limited studies of their behavior at elevated temperatures (*25*). Perissi et al. studied $[C_4mim][Tf_2N]$ at temperatures up to 325°C (*25*). Five different common metals were studied and all showed low corrosion current densities with Inconel 600, an austenitic nickel-chromium superalloy, showing the most corrosion resistance. In all metals, corrosion was a temperature dependent phenomenon.

For this study, $[C_4mmim][Tf_2N]$ was chosen as a surrogate HTF based on it having the most favorable properties of the three ILs previously described. Four metals, Aluminum 2024, Carbon Steel 1018, Copper 110, and Stainless Steel were cut into cubic metal coupons which were 1 cm/side. The coupons were then polished on all sides to a 600 grit finish and weighed, see Figure 2. After polishing, the coupons were immersed in approximately 20mL of IL. The initial water concentration of the ILs was confirmed to be 200ppm by Karl Ficsher titration. Initially the ILs were clear and coupons visibly appeared free of corrosion, see Figure 3. One set of ILs was left out at room temperature and open to the ambient atmosphere. The second set of coupons was placed in an oven at 200°C with an uncontrolled air atmosphere.

The coupons were visually examined and weighed at 49, 108, 179, and 365 days. The coupons that were exposed to 200°C were inadvertently removed from temperature at 108 days, therefore the elevated temperature experiment was terminated at that point. However, the room temperature experiment was allowed to continue for one year.

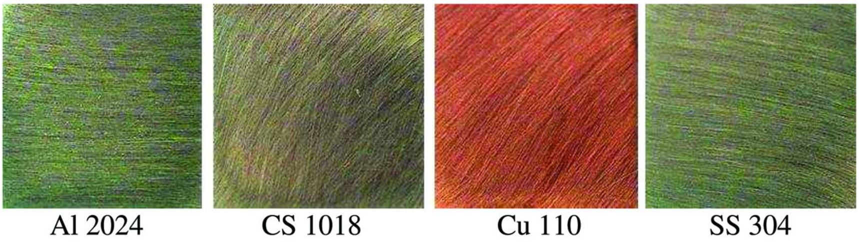

Figure 2. Micrographs of metal coupons before immersion in [C_4mmim][Tf_2N] polished to a 600 grit finish.

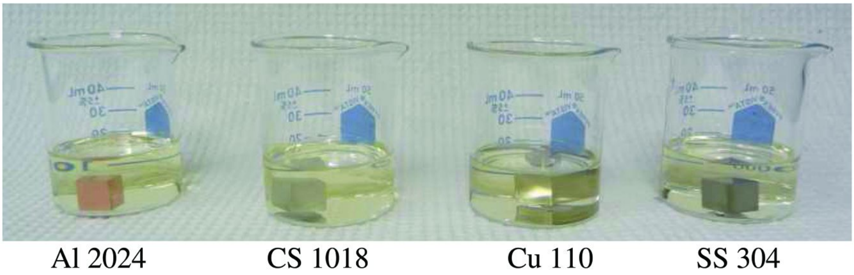

Figure 3. Coupons in IL at the onset of exposure. The IL is clear and the coupons appear free of corrosion.

Figure 4 (top) shows the ILs containing the coupons after 49 days of exposure. The room temperature ILs remain clear for Al and SS, but the Cu takes on a slight yellowish hue and the CS becomes light brown from iron deposits from the coupon. The CS sample shows a weight loss of 0.75%, while no other coupons have a measureable weight loss, see Table 4. This weight loss on the coupon does not change throughout the year, suggesting that a passive layer is formed on the surface where corrosion initially occurred. The final water content of all the IL after one year was approximately 5000ppm suggesting that this is the water saturation limit at room temperature. Even though the water content of the IL increased over time, the corrosion rates of the coupons did not.

Figure 4 (bottom) shows the ILs with coupons that have been exposed to 200°C for 49 days. The IL has dramatically darkened to a reddish/brown color. Cu is the only coupon that had a measureable weight loss of 3.53%. The surface of the Cu coupon is also visible roughened. At 108 days the weight loss jumps to 5.94%. All of the ILs that have been exposed to temperature display slight polymerization or coagulation, even the neat sample that did not contain a metal coupon. Interestingly, the beaker containing the SS coupon had less polymerization occurring than the neat IL.

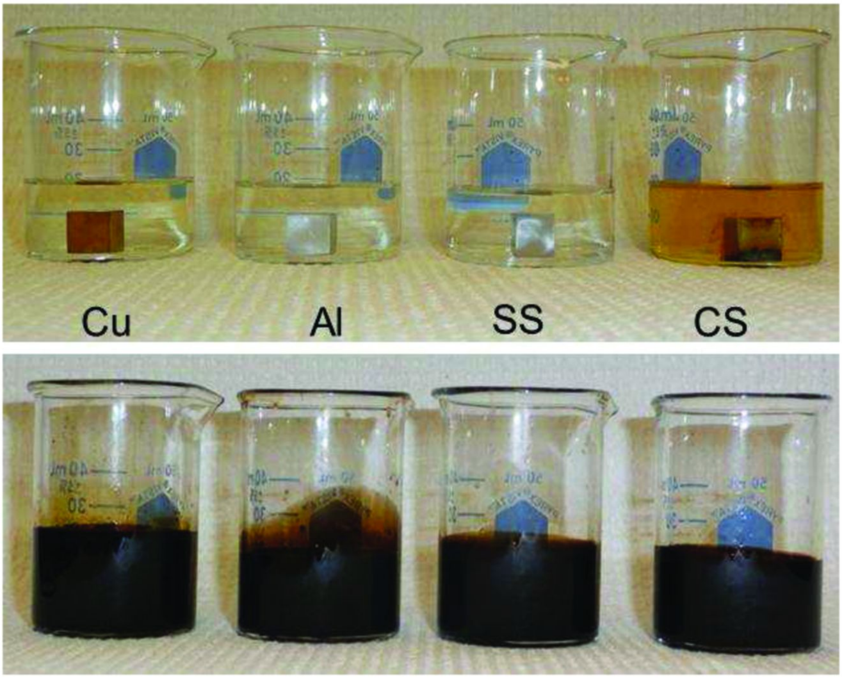

Figure 4. Appearance of ILs after 49 days of coupon exposure. Top: Room temperature and open to the room atmosphere. Bottom: 200°C in a furnace with an air purge.

Table 4. Weight loss percentage from starting weight in coupons over the course of exposure to the IL

	Cu		*Al*		*SS*		*CS*	
Days of Exposure	*24°C*	*200°C*	*24°C*	*200°C*	*24°C*	*200°C*	*24°C*	*200°C*
49	NC	3.53	NC	NC	NC	NC	0.75	NC
108	NC	5.94	NC	NC	NC	NC	0.69	NC
175	NC	*	NC	*	NC	*	0.67	*
365	NC	*	NC	*	NC	*	0.76	*

∗ = not measured. NC = no sample mass change.

When the coupons were examined after removal from the IL, all appeared to have dark deposits on the surface, see Figure 5. This is presumed to be deposition of corrosion byproducts on the surface or possibly from carbon deposition from the IL (*25*). Deposit formation was increased on the CS and Cu samples over the Al and SS, possibly suggesting the more active coupons can catalyze the IL decomposition process. Immediate surface passivation with no mass loss was seed for Al and SS. For CS, the surface experienced some initial corrosion that ended after the passive layer had a chance to build up over 49 days. The Cu sample did not appear to build a corrosion layer that would prevent additional corrosion even after 108 days. The corrosion for the Al, SS, and CS samples were all within acceptable limits. Testing with Cu was discontinued because corrosion passed acceptable limits. Although the corrosion mechanism and any accompanying ionic liquid mechanisms are unknown, it can be theorized that in the CS the deposition layer could assist the inhibition of corrosion offered by the oxide passive layer where on the Cu sample the surface is not passivated but generates more active surface area through pitting.

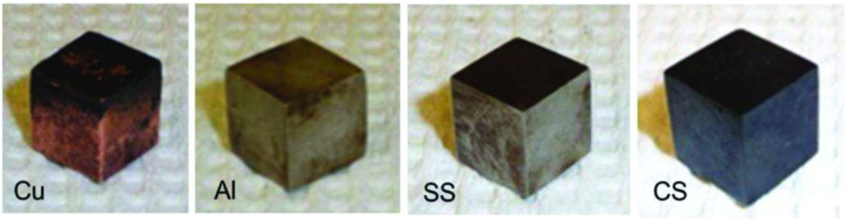

Figure 5. Photograph of coupons after exposure at 200°C for 108 days.

Conclusions

This study demonstrates that the addition of inorganic nanoparticles can improve the heat capacity and increased thermal conductivity of an IL, dependant upon the selection of the nanomaterial. Nanoparticle Enhanced Ionic Liquids (NEILs) were prepared in [C_4mmim][Tf_2N] and show the thermal stability is not compromised upon the addition of up 2.5 weight percent Al_2O_3 nanoparticles, in agreement with the inertness of the nanoparticles and the non-coordinating nature of this IL. The viscosity of the NEILs is highly temperature dependent and only moderately impacts viscocity for these ILs at these weight loadings.

NEILs have thermal properties that make them especially attractive as heat transfer fluids. In comparison to a traditional heat transfer fluid (e.g., Therminol VP-1), the high heat capacities for traditional ILs together with inorganic materials together produce NEILs that are a promising heat transfer fluid for solar concentration systems.

The attractive properties of ILs are further enhanced by the addition of nanoparticles to form a new class of ILs, NEILs, although careful selection of nanoparticle is necessary. The large increase in heat capacity combined with thermal stability suggest NEILs could provide a viable alternative to present heat transfer fluids.

Acknowledgments

The DOE-EERE Solar Energy Technology Program is gratefully acknowledged for funding of this work. The authors wish to thank Jamil Khan and Titan Paul at the University of South Carolina for DSC analysis. Savannah River National Laboratory is managed by Savannah River Nuclear Solutions. This work was prepared under Federal Contract DE-AC09-08SR22470. The United States Government retains, and by accepting the article for publication the publisher acknowledges that the United States Government retains, a non-exclusive, paid-up, irrevocable, worldwide license to publish or reproduce the published form of this work, or allow others to do so, for United States Government purposes.

References

1. SunShot Vision Study, U.S. Department of Energy, 2012. http://www1.eere.energy.gov/solar/pdfs/47927_chapter5.pdf.
2. Moens, L.; Blake, D. *J. Sol. Energy Eng.* **2010**, *132*, 031006-1-4.
3. Earle, M. J.; Esperanca, J. M. S. S.; Gilea, M. A.; Canongia Lopes, J. N.; Rebelo, L. P. N.; Magee, J. W.; Seddon, K. R.; Widegren, J. A. *Nature (London)* **2006**, *439*, 831–834.
4. Holbrey, J. D.; Reichert, W. M.; Reddy, R. G.; Rogers, R. D. In *Ionic Liquids as Green Solvents*; Rogers, R. D., Seddon, K. R., Eds.; ACS Symposium Series 856; American Chemical Society: Washington, DC, 2003, pp 121−133.
5. Zhang, M.; Reddy, R. *ECS Trans.* **2006**, *2*, 27–34.
6. Reddy, R.; Zhang, Z.; Arenas, M.; Blake, D. M. *High Temp. Mater. Processes* **2003**, *22*, 87–94.
7. Anouti, M.; Caillon-Caravanier, M.; Le Floch, C.; Lemordant, D. *J. Phys. Chem. B* **2008**, *112*, 9412–9416.
8. Van Valkenberg, M. E.; Vaughn, R. L.; Williams, M.; Wilkes, J. S. *Thermochim. Acta* **2005**, *425*, 181–188.
9. Blake, D. M.; Moens, L.; Hale, M. J.; Price, H.; Kearney, D.; Hermann, U. *Proceedings of the 11th SolarPACES International Symposium on Concentrating Solar Power and Chemical Energy Technology*, Zurich, Switzerland, September 4−6, 2002.
10. Blake, D. M.; Moens, L.; Rudnicki, D.; Pilath, H. *Proceedings of the 11th SolarPACES International Symposium on Concentrating Solar Power and Chemical Energy Technology*, Zurich, Switzerland, September 4−6, 2002.
11. Liu, M.; Lin, M. C.; Wang, C. *Nanoscale Res. Lett.* **2011**, *6*, 297–310.
12. Shin, D; Banerjee, D. *J. Heat Transfer* **2011**, *133*, 024501/1–024501/4.
13. Lucian, G. *J. Mar. Technol. Environ.* **2011**, 47–50.
14. Ye, P; Jiang, X.; Li, S. *Wear* **2002**, *253*, 572–575.
15. Amrollahi, A.; Hamidi, A. A.; Rashidi, A. M. *Nanotechnology* **2008**, *19*, 315701/1–315701/8.
16. Bridges, N. J.; Visser, A. E.; Fox, E. B. *Energy Fuels* **2011**, *25*, 4862–4864.

17. Pan, Y.; Boyd, L. E.; Kruplak, J. F.; Cleland, W. E.; Wilkes, J. S.; Hussey, C. L. *J. Electrochem. Soc.* **2011**, *158*, F1–F9.
18. Frez, C.; Diebold, G. J.; Tran, C. D.; Yu, S. *J. Chem. Eng. Data* **2006**, *51*, 1250–1255.
19. Raeissi, S.; Peters, C. J. *Green Chem.* **2009**, *11*, 185–192.
20. Zhang, M. M.; Reddy, R. G. *Trans. Inst. Min. Metall., Sect. C* **2010**, *119*, 71–76.
21. Nockmann, P.; Thijs, B.; Pittois, S.; Thoen, J.; Glorieux, C.; Van Hecke, K.; Van Meervelt, L.; Kirchner, B.; Binnemans, K. *J. Phys. Chem. B.* **2004**, *110*, 20978–20992.
22. Neouze, M.-A. *J. Mater. Chem.* **2010**, *20*, 9593–9607.
23. Nieto de Castro, C. A.; Lourenco, M. J. V.; Ribiero, A. P. C.; Langa, E.; Vieira, S. I. C.; Goodrich, P.; Hardacre, C. *J. Chem. Eng. Data* **2010**, *55*, 653–661.
24. Lu, Q.; Wang, H.; Ye, C.; Liu, W.; Xue, Q. *Tribol. Int.* **2004**, *37*, 547–552.
25. Perissi, I.; Bardi, U.; Caporali, S.; Lavacchi, A. *Corros. Sci.* **2006**, *48*, 2349–2362.

Chapter 13

OKE Spectroscopy and Molecular Dynamics Simulations of Nonpolar and Polar Molecules in Ionic Liquids

**Edward L. Quitevis,*,[1] Fehmi Bardak,[1] Dong Xiao,[1]
Larry G. Hines, Jr.,[1] Pillhun Son,[1] Richard A. Bartsch,[1]
Peng Yang,[2] and Gregory A. Voth*,[3]**

**[1]Department of Chemistry & Biochemistry, Texas Tech University,
Lubbock, Texas 79409
[2]Department of Physics & Astronomy, University of Utah,
Salt Lake City, Utah 84112
[3]Department of Chemistry, University of Chicago, Chicago, Illinois 60637
*E-mails: edward.quitevis@ttu.edu (E.L.Q.); gavoth@uchicago.edu (G.A.V.)**

The intermolecular dynamics of mixtures of [C_5mim][NTf_2] with CS_2 and CH_3CN were studied using OKE spectroscopy. To help understand the OKE spectra of these mixtures, MD simulations of these systems were performed. The OKE spectra are interpreted in terms of an additivity model with the spectrum of CS_2 in the IL being narrower and lower in frequency than that of neat CS_2 and the spectrum of CH_3CN in the IL being broader and higher in frequency than that of neat CH_3CN. These results are consistent with the simulations that show the IL to be nanosegregated with CS_2 molecules residing in the nonpolar domains and CH_3CN molecules residing at the interface between the polar and nonpolar domains.

Introduction

Room-temperature ionic liquids (ILs) and high-temperature inorganic molten salts share the trait that they are both characterized by locally charge-ordered structures with alternating cation and anion shells as dictated by Coulombic interactions (*1–3*). In the case of ILs, because of the highly nonspherical nature of the charge distributions in the organic cations and inorganic or organic anions

In Ionic Liquids: Science and Applications; Visser, A., et al.;
ACS Symposium Series; American Chemical Society: Washington, DC, 2012.

of which these materials are comprised, the solvation-shell geometry around the ions often tends to be asymmetric (*4*). Indeed, solvation-shell asymmetry is one of the reasons given for the low melting points of ILs.

Molecular dynamics (MD) simulations (*5–10*) and X-ray scattering measurements (*11–19*) suggest, however, that besides possessing solvation shell asymmetry, ILs can be structurally heterogeneous on a nanoscale. This structural heterogeneity or intermediate-range order (IRO), which was first revealed in MD simulations of ILs based on the 1-alkyl-3-methylimidazolium ($[C_n\text{mim}]^+$) cation with $n = 4$ and longer alkyl chains (*6–10*), is attributed to the segregation of the alkyl chains into nanosized nonpolar domains that grow in size with chain length and are embedded in a polar network formed by the charge-ordering of the imidazolium headgroups and anions.

The presence of a low-Q peak or prepeak in the small-wide angle X-ray scattering (SWAXS) data is commonly presented as evidence for the existence of IRO in ILs. One finds that the length scale associated with this peak, as given by the Bragg relation, $D = 2\pi/Q_{\text{peak}}$, is found to vary linearly with alkyl chain length (*11–19*). Recently, the assignment of the low-Q peak to IRO has been questioned by other researchers who have argued for solvation-shell asymmetry as being the origin of this feature in the SWAXS data (*4*, *20–22*) However, new experimental data pertaining to mixtures of ILs with different chain lengths and chains with polar character (*23*, *24*), as well as a re-analysis of the low-Q peak in terms of nonpolar and polar correlations (*25*), has lent further support for the existence of IRO in ILs (*26*).

MD simulations indicate that this IRO (sometimes referred to as nanostructural organization) in ILs plays an important role in determining the solvation of small solute molecules in ILs (*9*, *27*, *28*) Specifically, solute molecules will tend to be localized in regions of the IL for which the affinity is the greatest – nonpolar solutes, such as hexane, in the nonpolar domains, polar aprotic solutes, such as acetonitrile, at the non-polar/polar interfacial regions, and polar protic solutes, such as water, in the polar domains.

Herein we present results from two recent studies (*29*, *30*) from our laboratories in which the structure and subpicosecond intermolecular dynamics of mixtures of the nonpolar solute CS_2 and the polar aprotic solute CH_3CN in 1-pentyl-3-methylimidazolium bis{(trifluoromethane)sulfonyl}amide ($[C_5\text{mim}][\text{NTf}_2]$) were studied by MD simulations and optical Kerr effect (OKE) spectroscopy. The results from these studies provide further insight into the nature of the interactions of small solute molecules with ILs. The MD simulations show CS_2 molecules to be localized in the nonpolar domains and CH_3CN molecules at the polar-nonpolar interface. The OKE spectra of these binary mixtures are interpreted in terms of an additivity model with a contribution arising from the solute and a contribution arising from the IL. In the case of CS_2/IL mixtures, the CS_2 contribution is lower in frequency and narrower than the OKE spectrum of neat CS_2, which is consistent with CS_2 molecules being in an alkane-like environment. In the case of CH_3CN/IL mixtures, the CH_3CN contribution is higher in frequency and broader than the OKE spectrum of neat CH_3CN, which is consistent with CH_3CN molecules being at the polar-nonpolar interface and interacting with the IL through ion-dipole forces.

Models and Simulation Methodology

Simulations were performed using the DL_POLY 2.19 package (*31*) with periodic boundary conditions and the Amber force field. The force-field parameters for $[C_5mim]^+$ were obtained from the standard Amber force field. The force-field parameters and partial charges for $[NTf_2]^-$ were obtained from the work of Lopes and Padua (*32*). A rigid-body model that only considers van der Waals and Coulombic interactions and takes the parameters from the Amber force field was used to model CS_2 in the liquid state. The partial charges for the cation and CS_2 were calculated from fits of the ab initio electrostatic potentials with the RESP fitting package (*33*). Gaussian 03 (*34*) was used to perform the ab initio calculations. The six-site flexible model developed by Nikitin and Lyubartsev (*35*) was the basis for the force field and partial charges used for CH_3CN in the simulations.

The initial configurations of the two mixture systems were generated by manually positioning the solute molecules within large simulation boxes (Table 1). To obtain a constant volume, configurations were simulated at 300 K at constant NPT for 1-2 ns, equilibrated at 1000 K under constant NVT conditions, and cooled down to 400 K in 200 K increments with each increment equilibrated for 1.2 ns. The final configuration was obtained by running simulations for 8 ns at 298 K under constant NVT conditions.

Table 1. Sizes for Different Simulated Mixtures

Mole percent solute	*Number of ion pairs*	*Number of solute molecules*	*Simulation-cell size (X,Y,Z) [Å]*
$CS_2/[C_5mim][NTf_2]$ Mixtures			
0	64	0	31.4, 31.4, 31.4
5	76	4	33.4, 33.4, 33.4
10	72	8	32.9, 32.9, 32.9
20	64	16	32.0, 32.0, 32.0
50	64	64	33.4, 33.4, 33.4
$CH_3CN/[C_5mim][NTf_2]$ Mixtures			
0	64	0	31.4, 31.4, 31.4
5	76	4	33.4, 33.4, 33.4
10	72	8	32.8, 32.8, 32.8
20	64	16	31.8, 31.8, 31.8
50	64	64	33.1, 33.1, 33.1

The atoms in the mixture systems can be divided into three groups: polar, nonpolar, and solute. The positively charged imidazolium ring and the $[NTf_2]^-$ anion are the polar groups and the entire alkyl chain is the nonpolar group. The center of mass of the imidazolium ring defines the headgroup. The carbon atom (CT) on the terminal methyl group on the alkyl chain defines the tail. The nitrogen atom (NP) in $[NTf_2]^-$ approximately gives the center of mass of the anion. The hydrogen atoms on the imidazolium ring are referred to as H4 and H5. The nitrogen atom in CH_3CN is YN, and the carbon atom in CS_2 is CM. (See Figure 1 for group definitions.)

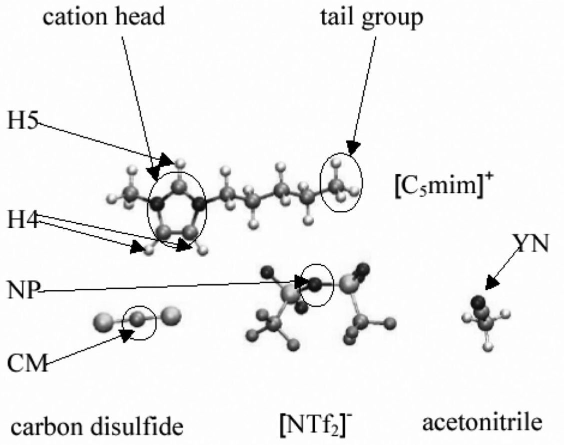

Figure 1. Structures of $[C_5mim]^+$, $[NTf_2]^-$, CS_2, and CH_3CN and group definitions. (adapted with permission from ref. (29), copyright 2011, American Institute of Physics, and from ref. (30), copyright 2012, John Wiley & Sons).

Experimental

The synthesis of $[C_5mim][NTf_2]$ has been previously described (*36*). As determined by Karl Fisher titration, the water content of the IL was < 200 µg/g. Prior to its use the IL was kept in a dessicator. CS_2 and CH_3CN (Aldrich, spectrochemical grade) were used without further purification. Whereas CH_3CN and $[C_5mim][NTf_2]$ are completely miscible, CS_2 and $[C_5mim][NTf_2]$ are miscible up to only 30 mol % CS_2 at room temperature.

In these studies, the variant of OKE spectroscopy known as optical heterodyne-detected Raman-induced Kerr effect spectroscopy (OHD-RIKES) was used. The OHD-RIKES apparatus, procedure, and data analysis have been previously described (*37–39*). Briefly, OHD-RIKES makes use of a femtosecond laser pulse to produce a transient birefringence in a liquid sample (*40*). The birefringence has an instantaneous electronic component (the coherent spike) and a non-instantaneous nuclear component, with the latter being directly related to the derivative of the time-correlation function of the collective-polarizability anisotropy (*41*). The apparatus uses 36-fs pulses from a lab-built, self-modelocked Ti:sapphire laser and a (45°/0°/90°) polarization geometry for the pump, probe and analyzer polarizers with a λ/4-plate in the probe beam (*42*). Stray birefringences, such as from the windows of the sample cell, can be nulled with the λ/4-plate. A slight rotation (±δ°) of the probe polarizer introduces a local-oscillator (LO) field E_{LO} for the signal field E_S (*42*). The difference of signals with in-phase (+δ° and out-of-phase (-δ° local oscillators gives the heterodyne contribution $Re[E_{LO}{\cdot}E_S]$. The samples were contained in sealed 2-mm path-length, UV-grade, fused-silica cells. Temperature control of the sample was achieved by placing the sample cell in a lab-built copper cell holder, whose temperature was regulated and controlled with a thermoelectric heater/cooler system. To save time during data collection, scans were carried out in 10 fs steps for delays between –1 and 4 ps and in 100 fs steps for delays greater than 4 ps.

By use of a Fourier-transform-deconvolution procedure (*43*, *44*) the OHD-RIKES signal can be converted to a spectral density or OKE spectrum, which is directly related to the depolarized Rayleigh/Raman spectrum of the liquid (*45*). The focus of our work to date has been on the part of the OKE spectrum associated with subpicosecond intermolecular dynamics. To obtain this spectrum, the slow (1 ps or longer) orientational contribution is removed from the Kerr transient prior to performing the Fourier-transform-deconvolution procedure, yielding a reduced response comprising the electronic and vibrational contributions. The corresponding spectrum, referred to as the reduced spectral density (RSD), accesses only the 0.01-10 THz region of the OKE spectrum. Application of a Gaussian window function prior to performing this procedure reduces the noise in the RSD without affecting its line shape in the low-frequency (0-200 cm^{-1}) range (*46*). For molecular liquids, such as CS_2 and CH_3CN, the RSD in this range is characterized by a single band with a peak frequency ω_{pk} and a full-width at half-maximum $\Delta\omega$. Because this band in ILs tends be structured, the average frequency as given by the first spectral moment $<\omega>$ is also used to define the band position.

Results and Discussion

Simulations

Figure 2 shows radial distribution functions (RDFs) corresponding to the key interactions in 5, 10, and 20 mol % CS_2/[C_5mim][NTf_2] mixtures with the CM-CT RDF giving the interaction between CS_2 and the terminal methyl group on the alkyl chain, the CM-headgroup RDF giving the interaction between CS_2 and the imidazolium ring, and the CM-NP RDF giving the interaction between CS_2 and [NTf_2]$^-$. As one can see from this figure, the first peak of the CM-CT RDF for these mixtures is greater than that of the CM-headgroup and CM-NP RDFs, indicating that CS_2 molecules are mainly localized in the nonpolar domains.

Figure 3 shows RDFs corresponding to the key interactions in 5, 10, 20, and 50 mol % CH_3CN/[C_5mim][NTf_2] mixtures with the YN-CT RDF giving the interaction between CH_3CN and the terminal methyl group on the alkyl tail, the YN-headgroup RDF giving the interaction between CH_3CN and the imidazolium ring, and the YN-NP RDF giving the interaction between CH_3CN and [NTf_2]$^-$. For the 20 and 50 mol % mixtures, the height of the first peak in the YN-CT

RDF is comparable to that of the first peak in the YN-headgroup and YN-NP RDFs, indicating that CH_3CN molecules are mainly localized at the polar-nonpolar interface.

Note that the height of the first peak of the YN-headgroup and YN-NP RDFs for CH_3CN/IL mixtures is greater than that of the CM-headgroup and CM-NP RDFs for CS_2/IL mixtures, which supports the conclusion that CH_3CN headgroup and CH_3CN-anion interactions are greater than CS_2-headgroup and CS_2-anion interactions. For example, for 5 mol % $CH_3CN/[C_5mim][NTf_2]$, intensities of the first peak in the YN-CT, YN-headgroup, and YN-NP RDFs are 2.09, 2.02, and 1.71, respectively. In contrast, for 5 mol % $CS_2/[C_5mim][NTf_2]$, intensities of the first peak in the CM-CT, CM-headgroup, and CM-NP RDFs are 2.25, 1.48, and 1.66, respectively. Moreover, the simulations show strong hydrogen bonding between the solute and the cation as reflected in the intensity of the first peak of the YN-H4 and YN-H5 RDFs of the $CH_3CN/[C_5mim][NTf_2]$ mixtures depicted in Figure 4. Interestingly, the YN-headgroup RDF for the 50 mol % mixture show two close peaks at 6.1 and 7.2 Å suggesting that that there are two distinct ways by which a CH_3CN molecule can interact with the cation headgroup.

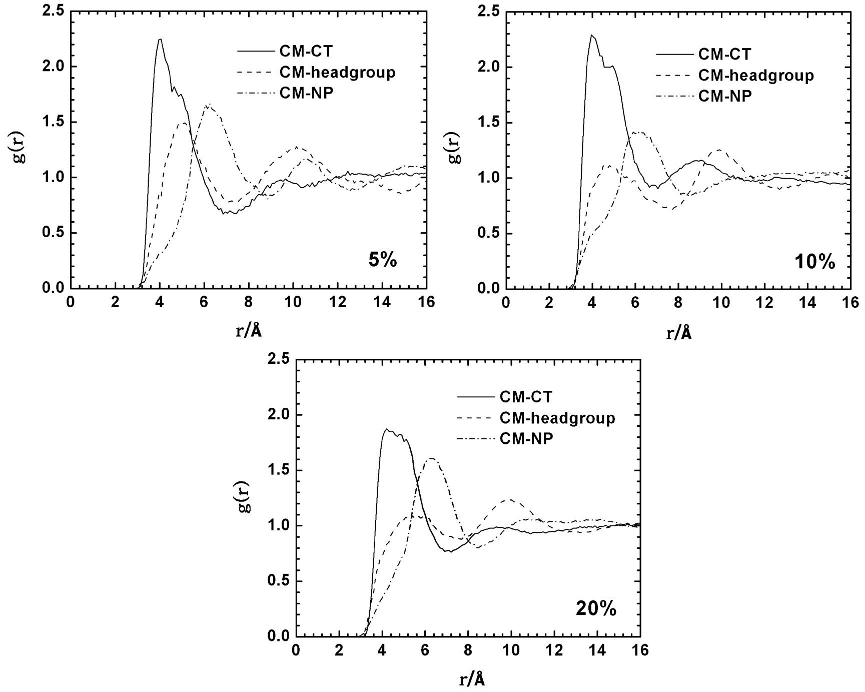

Figure 2. Radial distribution functions for $CS_2/[C_5mim][NTf_2]$ mixtures corresponding to the interactions between CS_2 and various groups of the IL. (adapted with permission from ref. (29), copyright 2011, American Institute of Physics).

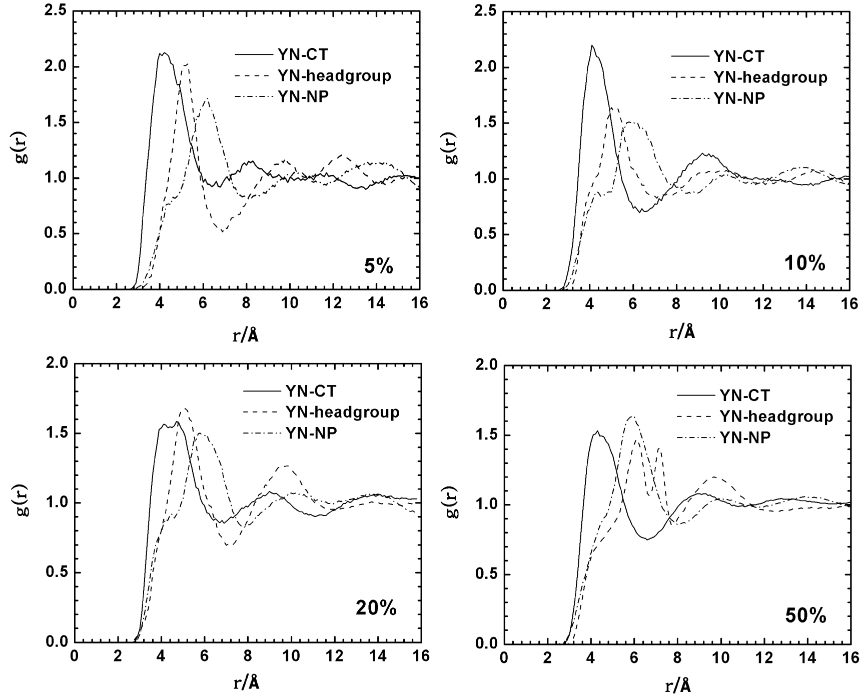

Figure 3. Radial distribution functions for $CH_3CN/[C_5mim][NTf_2]$ mixtures corresponding to the interactions between CH_3CN and various groups of the IL. (adapted with permission from ref. (30), copyright 2012, John Wiley & Sons).

The simulations of CS_2/IL and CH_3CN/IL mixtures also show that at low solute concentrations the ionic network is not strongly affected by the presence of solute molecules. This can readily be seen in Figure 5. This figure depicts the headgroup-NP RDFs for the 5, 10, and 20 mol % CS_2/IL mixtures and for the 5, 10, 20, and 50 mol % CH_3CN/IL mixtures. These RDFs show very little change as the mole fraction of either CS_2 or CH_3CN in these mixtures is increased in the given composition ranges.

Finally, Figure 6 shows snapshots of MD trajectory data during production runs for these two mixture systems at 50 mol %. Although experimentally CS_2 and $[C_5mim][NTf_2]$ are immiscible above 30 mol %, the snapshot at 50 mol % is quite instructive. What is striking about these snapshots is that whereas aggregation of the CS_2 molecules occurs in the CS_2/IL mixture, aggregation does not occur for CH_3CN molecules in the CH_3CN/IL mixture. This difference is consistent with CS_2/IL mixtures being misible only below 30 mol % and CH_3CN/IL mixtures being completely miscible for all compositions. Moreover, the snapshot of the CH_3CN/IL mixture is in agreement with the simulations of Lopes and workers (*27*, *28*) that showed CH_3CN molecules to be aligned with the nitrile groups pointing toward the ionic network.

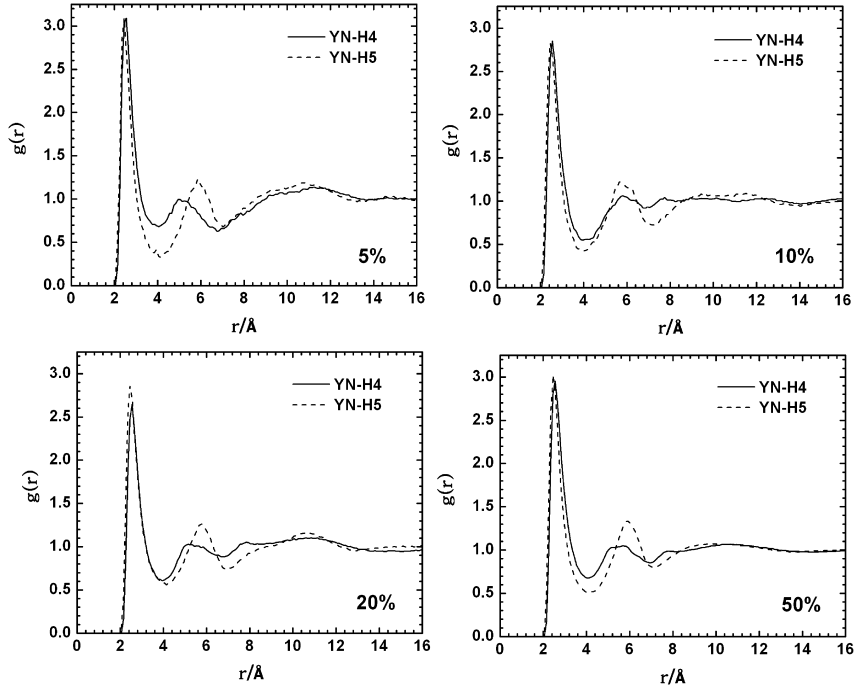

Figure 4. Radial distribution functions between the nitrogen atom (YN) on CH_3CN and the hydrogen atoms (H4 and H5) on the imidazolium ring of the cation in CH_3CN/[C_5mim][NTf_2] mixtures. (adapted with permission from ref. (30), copyright 2012, John Wiley & Sons).

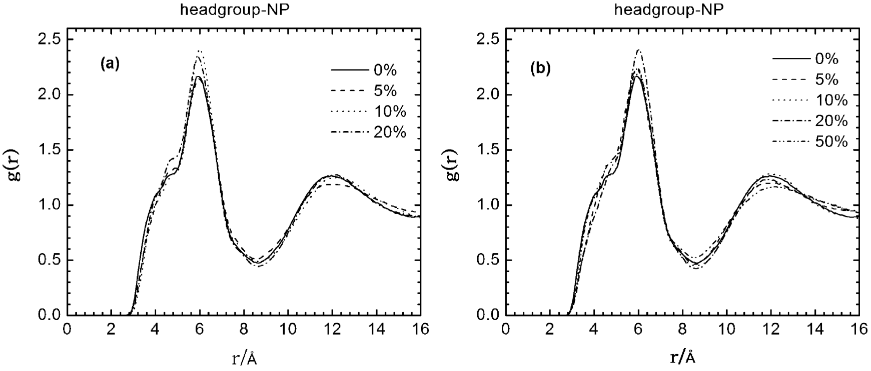

Figure 5. Radial distribution functions between the cation headgroup and anion for (a) CS_2/[C_5mim][NTf_2]mixtures and (b) CH_3CN/[C_5mim][NTf_2] mixtures. ((a) adapted with permission from ref. (29), copyright 2011, American Institute of Physics).

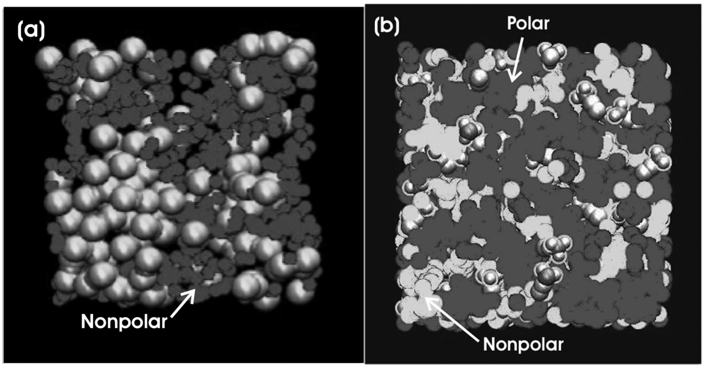

Figure 6. Snapshots of the nanostructural organization in (a) 50 mol % CS_2/[C_5mim][NTf_2] (polar domains not shown for clarity) and (b) 50 mol % CH_3CN/[C_5mim][NTf_2]. Solute molecules are represented by space-filling structures. ((b) adapted with permission from ref. (30), copyright 2012, John Wiley & Sons).

OHD-RIKES Time-Domain Data

Figure 7 shows semilogarithmic plots of the OHD-RIKES signals for the two mixture systems in the 0-4 ps time range at 295 K. Each OHD-RIKES signal is comprised of an instantaneous electronic response at zero time (the coherent spike) and a noninstantaneous nuclear response. The oscillations superimposed on the relaxational part of OHD-RIKES signal are associated with intramolecular vibrations that are coherently excited. The data have been height-normalized at the coherent spike. The long-time part ($t > 1$ ps) of the nuclear response decays exponentially for neat CS_2 and CH_3CN and nonexponentially for the neat IL and the mixtures. (The nonexponential decay in the case of the neat IL is a consequence of the complex-fluid nature of ILs (*47*, *48*).) The data in Figure 7 also shows that as the mole fraction of the solute is increased, the amplitude of the nuclear response relative to that of the electronic response increases.

OKE Spectra

Figure 8 depicts the RSDs in the 0-200 cm^{-1} range obtained by applying the Fourier-transform-deconvolution procedure to the reduced responses associated with the OHD-RIKES signals in Figure 7 (see refs. (*29*) and (*30*) for details of the calculations). The RSDs of neat CS_2 and CH_3CN are characterized by single intermolecular bands. In contrast, the RSD of neat [C_5mim][NTf_2] is comprised of a broad bimodal intermolecular band with peaks at ≈ 25 and 70 cm^{-1} and two smaller intramolecular bands at ≈ 120 and 170 cm^{-1} corresponding to cation/anion intramolecular vibrational modes. Given that the intermolecular dynamics are governed by both Coulombic and van der Waals interactions in the IL and only by van der Waals interactions in CS_2 and by mainly dipole-dipole interactions in

CH_3CN, it is not surprising that the RSD of [C_5mim][NTf_2] is higher in frequency and broader (<ω> ≈ 75 cm^{-1}; Δω ≈ 125 cm^{-1})than that of neat CS_2 (<ω> ≈ 44 cm^{-1}; Δω ≈ 57 cm^{-1}) and neat CH_3CN (<ω> ≈ 67 cm^{-1}; Δω ≈ 95 cm^{-1}).

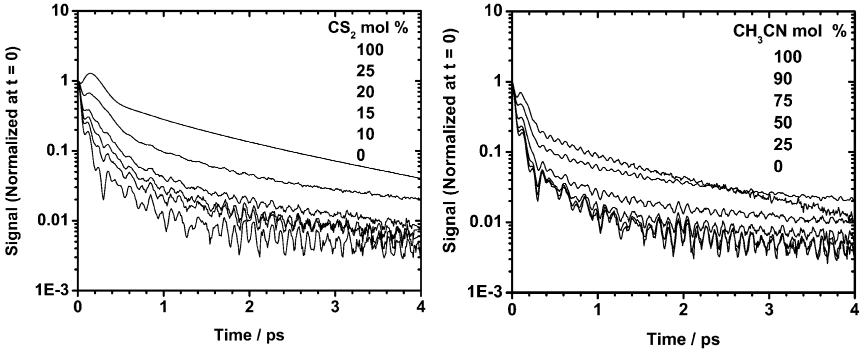

Figure 7. OHD-RIKES signals in 0-4 ps time range for CS_2/[C_5mim][NTf_2] and CH_3CN/[C_5mim][NTf_2] mixtures. (adapted with permission from ref. (29), copyright 2011, American Institute of Physics, and from ref. (30), copyright 2012, John Wiley & Sons, respectively).

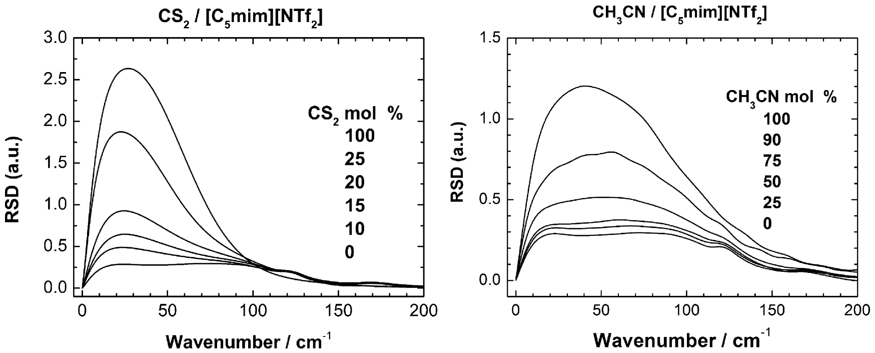

Figure 8. RSDs of CS_2/[C_5mim][NTf_2] and CH_3CN/[C_5mim][NTf_2] mixtures associated with OHD-RIKES signals in Figure 7. (CH_3CN/IL plot adapted with permission from ref. (30), copyright 2012, John Wiley & Sons).

For both CS_2/IL and CH_3CN/IL mixture systems, the RSDs narrow and shift to lower frequency with increasing mole fraction of solute. In addition, the RSDs of the mixtures increase in amplitude relative to that of the neat IL with increasing mole fraction of solute. These spectral changes suggest that the mixture RSDs can be empirically represented by the sum of an IL contribution, $I_{IL}^{mix}(\omega)$, and a solute contribution, $I_{solute}^{mix}(\omega)$:

$$I_{mix}(\omega) = I_{solute}^{mix}(\omega) + I_{IL}^{mix}(\omega) \qquad (1)$$

The implication of eq 1 is that the spectral changes exhibited by the data in Figure 8 are due to an increase in the relative amplitude of the narrower and lower frequency solute contribution to the mixture RSDs with increasing solute concentration.

In principle, the solute contribution should not be same as the RSD of the neat liquid simply because the local environment and therefore intermolecular potential seen by solute molecules in a mixture will be different than in the neat liquid. Similarly, the IL contribution should not be the same as the RSD of the neat IL. However, at low solute concentrations, the MD headgroup-anion RDFs (Figure 5) indicate that the ionic network in the IL is not strongly perturbed by the presence of solute in these mixtures. As shown previously, the RSD of an imidazolium-based IL is largely determined by the intermolecular dynamics of the imidazolium rings in the ionic network (*14*, *49–52*). Under these conditions, the RSD of a mixture can therefore be approximated by

$$I_{mix}(\omega) \approx I^{mix}_{solute}(\omega) + \lambda_{IL} I^{neat}_{IL}(\omega) \qquad (2)$$

where $I^{mix}_{IL}(\omega)$ in eq 1 has been replaced by the RSD of the neat IL, $I^{neat}_{IL}(\omega)$, and λ_{IL} is a parameter that accounts for the relative contribution of the IL to the RSD. The above equation, which we will refer to as the additivity model, basically defines a difference spectrum corresponding to the deviation of a mixture spectrum from that of the neat IL, with the difference being given by the first term in the equation. That the IL term in the additivity model can be approximated by the RSD of the neat IL is justified by the headgroup-anion RDFs not being strongly affected by the presence of the solute molecules (Figure 5) and the intermolecular part of the RSD of the imidazolium-based ILs largely being a reflection of the intermolecular dynamics of imidazolium rings in the ionic network.

To facilitate the analysis of the RSDs of the mixtures, the solute contribution in eq 2 is empirically represented by a multicomponent line shape function with the lowest frequency component given by the Bucaro-Litovitz (BL) function

$$I_{BL}(\omega) = A_{BL}\omega^{a} \exp(-\omega / \omega_{BL}) \qquad (3)$$

and higher frequency components by an antisymmetrized Gaussian (AG) lineshape function

$$I_{AG}(\omega) = A_{AG}\{\exp[-(\omega - \omega_{AG})/2\varepsilon^2] - \exp[-(\omega + \omega_{AG})/2\varepsilon^2]\} \qquad (4)$$

Figure 9 show the results of fits of eq 2 to the RSDs for the 10 and 20 mol % CS_2/IL and for the 25 and 50 mol % CH_3CN/IL (see refs. (*29*) and (*30*) for fit parameters). These spectra were chosen on the basis of the structure of the ionic network not being strongly affected by the presence of solutes molecules as indicated by headgroup-anion RDFs at the corresponding mole fractions (Figure 5). That the amplitude of the solute contribution relative to that of the IL contribution is greater for CS_2/IL mixtures than for CH_3CN/IL mixtures, despite the CS_2 mole fraction being lower than the CH_3CN mole fraction, is attributed to the polarizability of CS_2 being greater than that of CH_3CN.

In Figure 10, the solute contributions obtained from the fits in Figure 9 are compared to the RSDs of the corresponding neat liquids, along with the component bands. In the case of CS_2/IL mixtures, $I_{CS2}^{mix}(\omega)$ is narrower and lower in frequency than the RSD of neat CS_2 (see Table 2) with two component bands (one BL and one AG function) needed to described its line shape. If we assume $I_{CS2}^{mix}(\omega)$ to be associated with intermolecular dynamics of CS_2 in CS_2/IL mixtures, a narrower and lower frequency spectrum indicates that CS_2 molecules see a softer intermolecular potential in CS_2/IL mixtures than in neat CS_2. This behavior is analogous to that of CS_2 in CS_2/alkane mixtures with the RSDs of CS_2/pentane mixtures being narrower and lower in frequency than that of neat CS_2 (*53–58*). The intermolecular spectrum of CS_2 in CS_2/IL mixtures is therefore consistent with the simulations which show CS_2 molecules to be localized in the nonpolar domains.

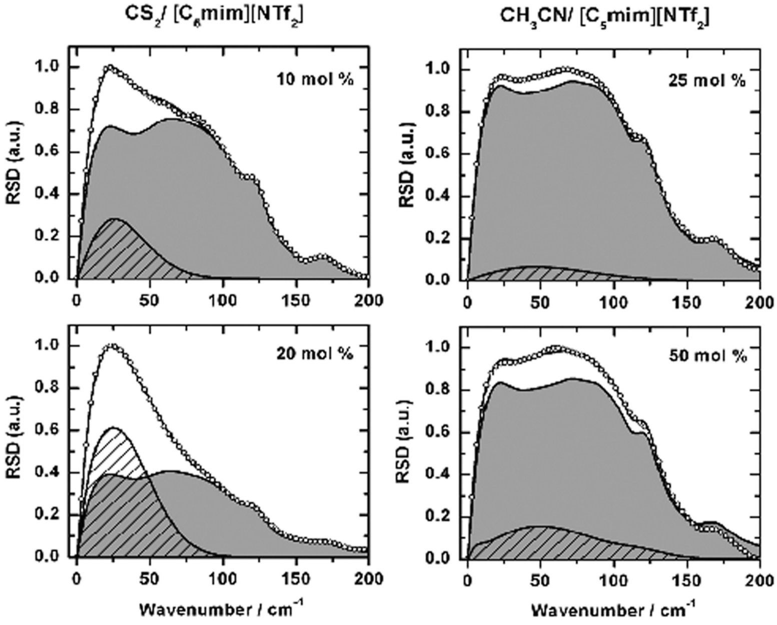

Figure 9. Fits (solid lines) of the RSDs (points) to the additivity model (eq 2) for CS_2/[C_5mim][NTf_2] and CH_3CN/[C_5mim][NTf_2] mixtures with solute (hatched spectra) and IL (gray spectra) contributions. (adapted with permission from ref. (29), copyright 2011, American Institute of Physics, and from ref. (30), copyright 2012, John Wiley & Sons, respectively).

In the case of CH_3CN/IL mixtures, the opposite behavior is observed with $I_{CH3CN}^{mix}(\omega)$ being higher in frequency and broader than the RSD of neat CH_3CN (see Table 2) with three component bands (one BL and two AG functions) needed to describe its line shape. If we assume $I_{CH3CN}^{mix}(\omega)$ to be associated with the intermolecular dynamics of CH_3CN in CH_3CN/IL mixtures, then a broader and higher frequency spectrum indicates that CH_3CN molecules see a stiffer intermolecular potential in CH3CN/IL mixtures than in neat CH3CN. This behavior is expected, given that the simulations show CH3CN molecules to be localized at the polar-nonpolar interface with the ion-dipole force being the dominant interaction between CH3CN and the IL as opposed to the weaker dipole-dipole force between the molecules in neat CH3CN.

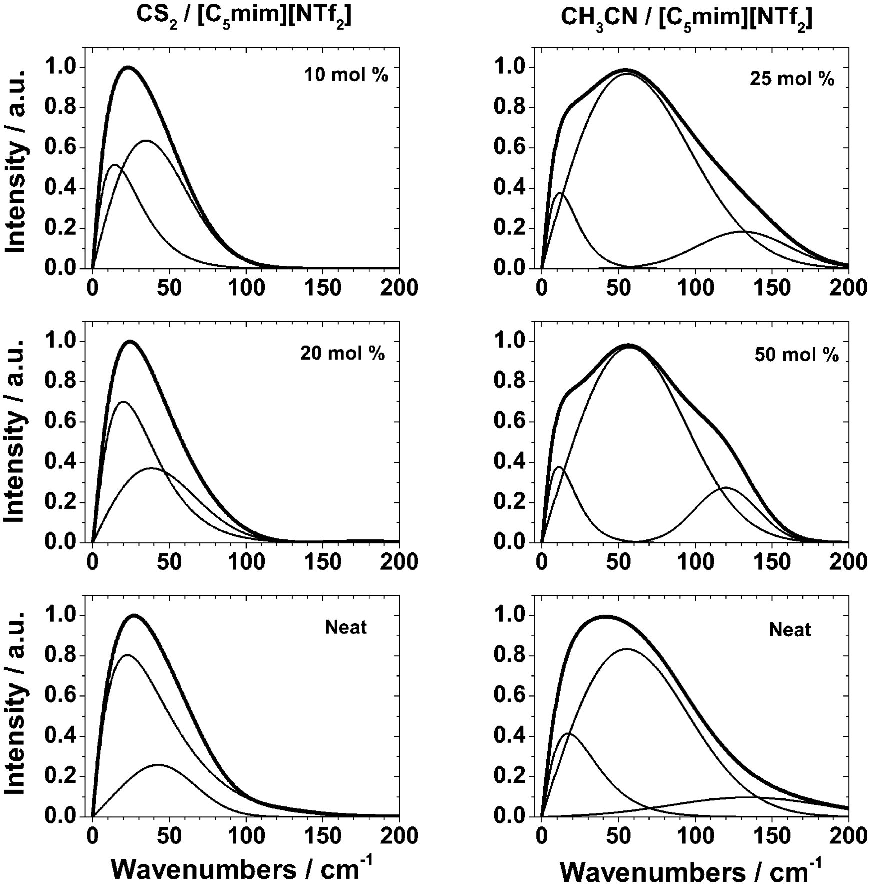

Figure 10. Intermolecular spectra of CS_2 in CS_2/IL mixtures and neat CS_2 and intermolecular spectra of CH_3CN in CH_3CN/IL mixtures and neat CH_3CN with component bands obtained from multicomponent line shape analysis. See Table 2 for spectral parameters. (adapted with permission from ref. (29), copyright 2011, American Institute of Physics, and from ref. (30), copyright 2012, John Wiley & Sons, respectively).

Interestingly, the intermolecular spectrum of CH3CN in the IL is more structured compared to that of neat CH3CN, as evidenced by the enhanced shoulders on the high- and low-frequency sides of the spectrum. This difference is consistent with the CH3CN exhibiting a more complicated interaction with the cation as indicated by the split first peak in the YN-headgroup RDF of the 50 mol % mixture (Figure 3). In contrast, the intermolecular spectrum of CS2 in the IL is characterized by a featureless single band not unlike that of neat CS_2, which is consistent with the lack of fine structure in the RDFs of the CS_2/IL mixtures.

Table 2. Solute Intermolecular Spectral Parameters[a],[b]

Mole percent solute	*Peak frequency, ω_{pk}*	*Full-width-half maximum, $\Delta\omega$*	*First spectral moment, $\langle\omega\rangle$*
CS_2/[C_5mim][NTf_2] Mixtures			
10	23	53	37
20	24	52	40
100	27	57	44
CH_3CN/[C_5mim][NTf_2] Mixtures			
25	53	111	73
50	55	114	69
100	42	95	67

[a] Units of spectral parameters: cm^{-1}. [b] Experimental error: ± 1 cm^{-1}.

Concluding Remarks

The OKE spectra of CS_2/[C_5mim][NTf_2] and CH_3CN/[C_5mim][NTf_2] mixtures provide support for the tendency of solute molecules to reside in regions where the affinity is greatest – nonpolar molecules, such as CS_2, localized in the nonpolar domains; polar aprotic molecules, such as CH_3CN, localized at the polar-nonpolar interface. The solvation environments of CS_2 and CH_3CN is further confirmed by MD simulations of these mixtures. The significance of this work is that specific interactions of the IL with functional groups on a solute molecule often underlie solute-IL interactions. In order to understand, for example, the effect of ILs on reactions, it is therefore important to study the interactions of small solute molecules that mimic the functional groups on larger molecules. Future work in our laboratories will focus on MD simulations and the OKE spectroscopy of other solute/IL mixture systems and testing the additivity model as a means of obtaining a molecular-level understanding of solute-IL interactions in these systems.

Acknowledgments

This research was supported by grants from the National Science Foundation (CHE-0718678) and the American Chemical Society Petroleum Research Fund (47615-AC6) to E.L.Q., The Welch Foundation (D-0775) to R.A.B., and the Air Force Office of Scientific Research to G.A.V. We thank Lianjie Xue for help with some of the OKE measurements.

References

1. Hardacre, C.; Holbrey, J. D.; McMath, S. E. J.; Bowron, D. T.; Soper, A. K. *J. Chem. Phys.* **2003**, *118*, 273–278.
2. Hardacre, C.; McMath, S. E. J.; Nieuwenhuyzen, M.; Bowron, D. T.; Soper, A. K. *J. Phys. Condens. Matter* **2003**, *15*, S159–S166.
3. Deetlefs, M.; Hardacre, C.; Nieuwenhuyzen, M.; Padua, A. A. H.; Sheppard, O.; Soper, A. K. *J. Phys. Chem. B* **2006**, *110*, 12055–12061.
4. Hardacre, C.; Holbrey, J. D.; Mullan, C. L.; Youngs, T. G. A.; Bowron, D. T. *J. Chem. Phys.* **2010**, *133*, 074510.
5. Urahata, S. M.; Ribeiro, M. C. C. *J. Chem. Phys.* **2004**, *120*, 1855–1863.
6. Wang, Y.; Voth, G. A. *J. Am. Chem. Soc.* **2005**, *127*, 12192–12193.
7. Lopes, J. N. A. C.; Padua, A. A. H. *J. Phys. Chem. B* **2006**, *110*, 3330–3335.
8. Wang, Y.; Voth, G. A. *J. Phys. Chem. B* **2006**, *110*, 18601–18608.
9. Jiang, W.; Wang, Y.; Voth, G. A. *J. Phys. Chem. B* **2007**, *111*, 4812–4818.
10. Wang, Y.; Yan, T.; Voth, G. A. *Acc. Chem. Res.* **2007**, *40*, 1193–1199.
11. Triolo, A.; Russina, O.; Bleif, H.-J.; Di Cola, E. *J. Phys. Chem. B* **2007**, *111*, 4641–4644.
12. Atkin, R.; Warr, G. G. *J. Phys. Chem. B* **2008**, *112*, 4164–4166.
13. Xiao, D.; Hines, L. G., Jr.; Li, S.; Bartsch, R. A.; Quitevis, E. L.; Russina, O.; Triolo, A. *J. Phys. Chem. B* **2009**, *113*, 6426–6433.
14. Russina, O.; Triolo, A.; Xiao, D.; Hines, L. G., Jr.; Bartsch, R. A.; Quitevis, E. L.; Gontrani, L.; Caminiti, R.; Plechkova, N. V.; Seddon, K. R. *J. Phys. Condens. Matter* **2009**, *21*, 424121.
15. Triolo, A.; Russina, O.; Fazio, B.; Appetecchi, G. A.; Carewska, M.; Passerini, S. *J. Chem. Phys.* **2009**, *130*, 164521.
16. Pott, T.; Meleard, P. *Phys. Chem. Chem. Phys.* **2009**, *11*, 5469–5475.
17. Russina, M.; Gontrani, L.; Fazio, B.; Lombardo, D.; Triolo, A.; Caminiti, R. *Chem. Phys. Lett.* **2010**, *493*, 259–262.
18. Greaves, T. L.; Kennedy, D. F.; Kirby, N.; Drummond, C. J. *Phys. Chem. Chem. Phys.* **2011**, *13*, 13501–13509.
19. Hayes, R.; Imberti, S.; Warr, G. G.; Atkin, R. *Phys. Chem. Chem. Phys.* **2011**, *13*, 3237–3247.
20. Annapureddy, H. V. R.; Kashyap, H. K.; De Biase, P. M.; Margulis, C. J. *J. Phys. Chem. B* **2010**, *114*, 16838–16846.
21. Santos, C. S.; Annapureddy, H. V. R.; Murthy, N. S.; Kashyap, H. K.; Castner, E. W., Jr; Margulis, C. J. *J. Chem. Phys.* **2011**, *134*, 064501.
22. Kashyap, H. K.; Santos, C. S.; Annapureddy, H. V. R.; Murthy, D. S. N.; Margulis, C. J.; Castner, E. W., Jr *Faraday Discuss.* **2012**, *154*, 133–143.
23. Russina, O.; Triolo, A. *Faraday Discuss.* **2012**, *154*, 97–109.
24. Russina, O.; Triolo, A.; Gontrani, L.; Caminiti, R. *J. Phys. Chem. Lett.* **2012**, *3*, 27–33.
25. Kashyap, H. K.; Hettige, J. J.; Annapureddy, H. V. R.; Margulis, C. J. *Chem. Commun.* **2012**, *48*, 5103–5105.
26. For a synopsis of the controversy concerning the origin of low-*Q* peak, see ref. 30.

27. Lopes, J. N. A. C.; Gomes, M. F. C.; Padua, A. A. H. *J. Phys. Chem. B* **2006**, *110*, 16816–16818.
28. Padua, A. A. H.; Gomes, M. F. C.; Lopes, J. N. A. C. *Acc. Chem. Res.* **2007**, *40*, 1087–1096.
29. Yang, P.; Voth, G. A.; Xiao, D.; Hines, L.; Bartsch, R. A.; Quitevis, E. L. *J. Chem. Phys.* **2011**, *135*, 034502.
30. Bardak, F.; Xiao, D.; Hines, L. G., Jr.; Son, P.; Bartsch, R. A.; Quitevis, E. L.; Yang, P.; Voth, G. A. *ChemPhysChem* **2012**, *13*, 1687–1700.
31. Smith, W.; Forester, T. R. *The DL_POLY_2_USER MANUAL*, 2008.
32. Lopes, J. N. C.; Padua, A. A. H. *J. Phys. Chem. B* **2004**, *108*, 16893–16898.
33. Bayly, C. I.; Cieplak, P.; Cornell, W.; Kollman, P. A. *J. Phys. Chem.* **1993**, *97*, 10269–10280.
34. Frisch, M. J.; Trucks, G. W.; Schlegel, H. B.; Scuseria, G. E.; Robb, M. A.; Cheeseman, J. R.; Montgomery, J., J. A. ; Vreven, T.; Kudin, K. N.; Burant, J. C.; Millam, J. M.; Iyengar, S. S.; Tomasi, J.; Barone, V.; Mennucci, B.; Cossi, M.; Scalmani, G.; Rega, N.; Petersson, G. A.; Nakatsuji, H.; Hada, M.; Ehara, M.; Toyota, K.; Fukuda, R.; Hasegawa, J.; Ishida, M.; Nakajima, T.; Honda, Y.; Kitao, O.; Nakai, H.; Klene, M.; Li, X.; Knox, J. E.; Hratchian, H. P.; Cross, J. B.; Adamo, C.; Jaramillo, J.; Gomperts, R.; Stratmann, R. E.; Yazyev, O.; Austin, A. J.; Cammi, R.; Pomelli, C.; Ochterski, J. W.; Ayala, P. Y.; Morokuma, K.; Voth, G. A.; Salvador, P.; Dannenberg, J. J.; Zakrzewski, V. G.; Dapprich, S.; Daniels, A. D.; Strain, M. C.; Farkas, O.; Malick, D. K.; Rabuck, A. D.; Raghavachari, K.; Foresman, J. B.; Ortiz, J. V.; Cui, Q.; Baboul, A. G.; Clifford, S.; Cioslowski, J.; Stefanov, B. B.; Liu, G.; Liashenko, A.; Piskorz, P.; Komaromi, I.; Martin, R. L.; Fox, D. J.; Keith, T.; Al-Laham, M. A.; Peng, C. Y.; Nanayakkara, A.; Challacombe, M.; Gill, P. M. W.; Johnson, B.; Chen, W.; Wong, M. W.; Gonzalez, C.; Pople, J. A. *Gaussian 03 Revision C.02*; Gaussian, Inc.: Wallingford, CT, 2004.
35. Nikitin, A. M.; Lyubartsev, A. P. *J. Comput. Chem.* **2007**, *28*, 2020–2026.
36. Dzyuba, S. V.; Bartsch, R. A. *ChemPhysChem* **2002**, *3*, 161–166.
37. Quitevis, E. L.; Neelakandan, M. *J. Phys. Chem.* **1996**, *100*, 10005–10014.
38. Neelakandan, M.; Pant, D.; Quitevis, E. L. *J. Phys. Chem. A* **1997**, *101*, 2936–2945.
39. Hyun, B.-R.; Dzyuba, S. V.; Bartsch, R. A.; Quitevis, E. L. *J. Phys. Chem. A* **2002**, *106*, 7579–7585.
40. McMorrow, D.; Lotshaw, W. T.; Kenney-Wallace, G. A. *IEEE J. Quantum Elect.* **1988**, *24*, 443–454.
41. Fourkas, J. T. In *Ultrafast Infrared and Raman Spectroscopy*; Fayer, M. D., Ed.; Marcel Dekker, Inc.: New York, 2001; pp 473−512.
42. Lotshaw, W. T.; McMorrow, D.; Thantu, N.; Melinger, J. S.; Kitchenham, R. *J. Raman Spectrosc.* **1995**, *26*, 571–583.
43. McMorrow, D. *Opt. Commun.* **1991**, *86*, 236–244.
44. McMorrow, D.; Lotshaw, W. T. *J. Phys. Chem.* **1991**, *95*, 10395–10406.
45. Kinoshita, S.; Kai, Y.; Yamaguchi, M.; Yagi, T. *Phys. Rev. Lett.* **1995**, *75*, 148–151.
46. Giraud, G.; Karolin, J.; Wynne, K. *Biophys. J.* **2003**, *85*, 1903–1913.

47. Turton, D. A.; Hunger, J.; Stoppa, A.; Hefter, G.; Thoman, A.; Walther, M.; Buchner, R.; Wynne, K. *J. Am. Chem. Soc.* **2009**, *131*, 11140–11146.
48. Li, J.; Wang, I.; Fruchey, K.; Fayer, M. D. *J. Phys. Chem. A* **2006**, *110*, 10384–10391.
49. Giraud, G.; Gordon, C. M.; Dunkin, I. R.; Wynne, K. *J. Chem. Phys.* **2003**, *119*, 464–477.
50. Xiao, D.; Rajian, J. R.; Li, S.; Bartsch, R. A.; Quitevis, E. L. *J. Phys. Chem. B* **2006**, *110*, 16174–16178.
51. Xiao, D.; Rajian, J. R.; Cady, A.; Li, S.; Bartsch, R. A.; Quitevis, E. L. *J. Phys. Chem. B* **2007**, *111*, 4669–4677.
52. Shirota, H. *ChemPhysChem* **2012**, *13*, 1638–1648.
53. Kalpouzos, C.; McMorrow, D.; Lotshaw, W. T.; Kenney-Wallace, G. A. *Chem. Phys. Lett.* **1988**, *150*, 138–146.
54. Kalpouzos, C.; McMorrow, D.; Lotshaw, W. T.; Kenney-Wallace, G. A. *Chem. Phys. Lett.* **1989**, *155*, 240–242.
55. McMorrow, D.; Thantu, N.; Melinger, J. S.; Kim, S. K.; Lotshaw, W. T. *J. Phys. Chem.* **1996**, *100*, 10389–10399.
56. Steffen, T.; Meinders, N. A. C. M.; Duppen, K. *J. Phys. Chem. A* **1998**, *102*, 4213–4221.
57. Scodinu, A.; Fourkas, J. T. *J. Phys. Chem. B* **2003**, *107*, 44–51.
58. Zhong, Q.; Fourkas, J. T. *J. Phys. Chem. B* **2008**, *112*, 15529–15539.

Chapter 14

Probing the Interface of Charged Surfactants in Ionic Liquids by XPS

Lang G. Chen and Harry Bermudez[*]

**Department of Polymer Science and Engineering,
University of Massachusetts, 120 Governors Drive,
Amherst, Massachusetts 01003
[*]E-mail: bermudez@polysci.umass.edu**

Room-temperature ionic liquids (ILs) are playing increasingly vital roles in many processes of both fundamental and applied natures such as separations and catalysis. It is therefore critical to obtain a better understanding of their interfacial properties such as surface charge and composition. Here we examine the influence of positively-charged surfactants on IL interfaces by X-ray photoelectron spectroscopy (XPS). The roles of surfactant alkyl chain length, concentration, and information depth on interfacial properties are investigated. XPS provides detailed compositional information that is used to calculate properties such as surface activity, composition, and charge. Depending on the chain length and concentration, the surfactants can alter the IL interface to varying extents, highlighting a simple route to manipulate interfacial properties. Our results are a further demonstration of the ability of XPS to give insights into the surface activity and aggregation behavior in multi-component ionic liquid systems.

In Ionic Liquids: Science and Applications; Visser, A., et al.;
ACS Symposium Series; American Chemical Society: Washington, DC, 2012.

Introduction

Room-temperature ionic liquids (ILs), organic salts with a melting point below 100 °C, continue to receive intense attention because of their unusual and diverse properties. The nature of the IL interface is of central importance in applications such as catalysis, chromatography, and fuel cells (*1–5*). The self-assembly of amphiphilic molecules such as surfactants in ILs is also of fundamental interest to the field of colloid and interface science (*6–10*).

Because of the negligible vapor pressure of ILs, ultrahigh vacuum (UHV) techniques can be used to interrogate IL surface and bulk properties (*11–18*). The application of UHV based techniques including X-ray photoelectron spectroscopy (XPS), secondary ion mass spectrometry (SIMS) (*12*), metastable impact electron spectroscopy (MIES) (*19*), direct recoil spectroscopy (*20*), and low-energy ion scattering (LEIS) (*21*), provides insight into both chemistry and surface properties at molecular length scales. Other surface-sensitive methods without UHV conditions include sum frequency generation (SFG) (*22*, *23*), X-ray reflectivity (*23*, *24*), and surface tension measurements (*25–27*). Among all of these techniques, XPS is arguably the most common and prominent UHV-based tool to provide unique information on chemical composition, chemical state identification and even composition depth profiles of the near-surface region. A comprehensive review article was recently published by Lovelock et al. (*28*) on photoelectron spectroscopy applied to IL interfaces. Since the first work on XPS of ILs at the IL-air interface reported by Smith et al. (*11*) and Caporali et al. (*21*) in 2005, there have been many XPS studies on the influence of anions (*15*) and substituents (*16*) on the surface composition of neat ILs. Other XPS studies have sought to reveal the orientation of ions at the interface (*14*), to monitor organic reactions in ILs (*29*) and to characterize novel IL materials such as amino acid based ionic liquids (*30*). XPS has also been used to investigate surface enhancement and solubility of salts dissolved in ILs (*18*, *31*). However, few studies have examined more complex systems such as surfactant-IL mixtures. Through the introduction of (charged) surfactants, the interfacial properties such as surface tension, composition, and charge can be tuned and controlled. More importantly, these properties can be quantitatively characterized by XPS.

This chapter intends to highlight opportunities in colloid and interface science made possible by the unique properties of ionic liquids and the strengths of XPS. While the ability of ILs to solubilize a wide variety of compounds is of clear interest and continues to be studied (*32–38*), mixtures that include ILs have complex phase behavior that is relevant to many potential applications. For example, the formation of microemulsions or other dispersed phases can be facilitated and controlled through the use of amphiphilic molecules (*39*). At a more basic level, ionic liquids provide a window to re-examine our understanding of solubility and aggregation phenomena, which is most often based on our experiences with water, a unique solvent itself. To begin addressing some of these questions, we have used a model hydrophilic ionic liquid, 1-ethyl-3-methylimidazolium ethyl sulfate, more commonly referred to as [EMIM][$EtSO_4$] (see Figure 1). This imidazolium ionic liquid has been widely studied (*12*, *13*, *40–43*) and is miscible with water in all proportions. Alkyltrimethylammonium bromides with different alkyl chain lengths were chosen as model ionic surfactants.

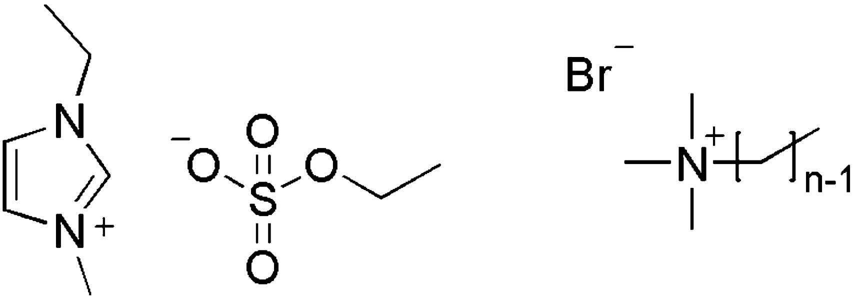

Figure 1. Structures of ionic liquid and surfactants in this study.

Experimental

Materials

[EMIM][EtSO$_4$] was obtained from Sigma (>95%). The ionic liquid was dried by heating at 70°C under vacuum for 2 days. The purity of the neat ionic liquid, and selected surfactants, were assessed by ^{1}H-NMR and did not reveal any impurities. These findings were confirmed by subsequent XPS control experiments (*41*).

Dodecyltrimethylammonium bromide (C$_{12}$TAB) (99%) was purchased from Fisher. Hexyltrimethylammonium bromide (C$_6$TAB) (>98%), octyltrimethylammonium bromide (C$_8$TAB) (>98%), decyltrimethylammonium bromide (C$_{10}$TAB) (>98%), and tetradecyltrimethylammonium bromide (C$_{14}$TAB) (>99%) were purchased from Sigma. All surfactants were used as received.

Tensiometry

Surface tension was measured by the Wilhelmy method using a Micro Trough XS (Kibron, Finland). For room temperature isotherms, the samples of alkyltrimethylammonium bromides were prepared and investigated as described in a previous report (*41*). Briefly, after all surfactants were dissolved in reverse-osmosis water, between 5 and 40μL of aqueous solutions were applied onto the ionic liquid subphase with volume of 300-500μL. We note that although water is introduced in the application of surfactant, it is always less than 12% by volume and does not significantly alter the bare surface tension ($\Delta\gamma < 3\%$), which was also found by Marsh et al (*44*). Surface tensions were measured after an equilibration time of 15 min.

X-ray Photoelectron Spectroscopy

Samples for XPS were prepared and investigated the same way as in a previous report (*41*). 5μL of aqueous surfactant solutions were applied onto the surface of 5μL of IL droplets using (oxygen-plasma-cleaned) silicon wafers as substrates. Samples were dried in a flowing nitrogen environment for 3 days at room temperature prior to conducting XPS measurement. XPS data were recorded using a Physical Electronics Quantum 2000 Microprobe instrument with monochromatic Al X-rays at 50 W, and a 200 μm spot area. Atomic compositions were obtained by using known sensitivity factors for the instrument and setup. To determine molecular compositions, atomic mass balances were performed using the chemical formulas of each species (for details see Chen et al. (*41*)). Importantly, the purity of the neat IL and the negligible influence of water and nitrogen introduced during preparation were confirmed by several different XPS control experiments (*41*).

Results and Discussion

The phase behavior of ionic surfactants is complex and depends on the solvent, concentration, and temperature. For example, micellization only occurs above a critical concentration and critical temperature, referred to as the critical micelle concentration (cmc) and Krafft temperature (T_k), respectively. We have recently shown that Krafft temperatures for ionic surfactants in ILs are generally much higher than room temperature (*43*). As a consequence, surface tension measurements at room temperature do not entirely reflect the phase behavior of surfactants, in particular at high concentrations (Figure 2). Because our XPS measurements were conducted at room temperature, these results are not complicated by the potential appearance of micelles. Of course, at sufficiently high surfactant concentrations, a separate solid phase will appear in equilibrium with the liquid phase. At low surfactant concentrations, interfacial properties will not be substantially altered – at least until a surface monolayer has been established. Indeed, as was first noted by Rayleigh (*45*) the first break in plots of surface tension vs. concentration (i.e., isotherms) marks the onset of this condensed phase (Figure 2). Here we denote this transition concentration as C_a, and it furthermore provides a useful reference point. For example, using a relative concentration $C^{*} \approx 10C_a$ allows us to compare surfactants of different chain lengths in a more meaningful way than on an absolute basis (e.g., Figure 3).

Table 1 lists both the transition concentrations (C_a) and critical micelle concentrations (cmc) of C_nTAB in [EMIM][EtSO$_4$] and in water. As noted earlier, the cmc can only be attained above the Krafft temperature. Although the C_a is a function of temperature, the values reported here are at room temperature to facilitate interpretation of the XPS measurements. Our own cmc determinations in water are consistent with literature values (*46*, *47*) and these cmc are generally lower than those in ionic liquids, indicating the well-known behavior of greater solubility in ionic liquids.

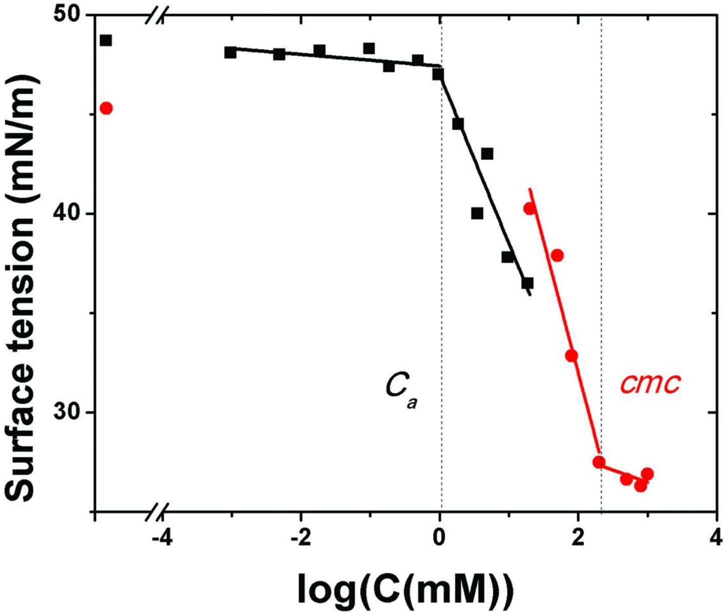

Figure 2. Isotherms of C_{14}TAB in [EMIM][EtSO$_4$] at different temperatures: 20°C (squares) and 90°C (circles). The surface tensions of neat IL at different temperatures are shown as the first points before the break. The Krafft temperature for this system is T_k = 75°C (43).

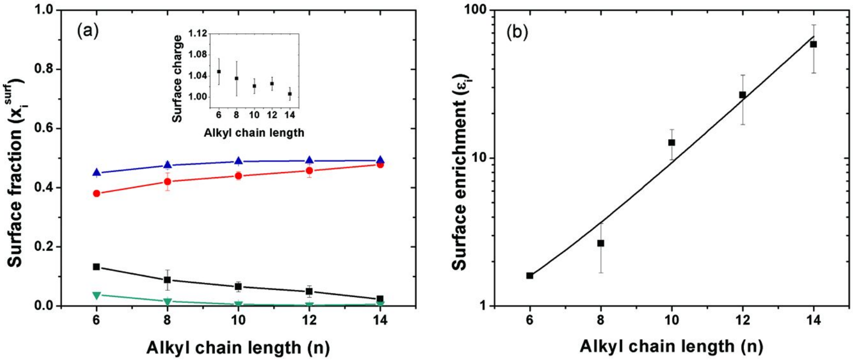

Figure 3. (a) Surface fractions, x_i^{surf}, (C_nTA^+ (squares), $[EMIM]^+$ (circles), $[EtSO_4]^-$ (top triangles), and Br^- (bottom triangles) and overall surface charge ratios (inset) and (b) surface enrichment of C_nTAB on [EMIM][EtSO$_4$]. Overall surface charge is defined as the ratio of total surface cations to total surface anions. Surface enrichment is defined as the ratio $\varepsilon_i = x_i^{surf} / x_i^{bulk}$, where x_i^{surf} are taken over the XPS information depth $d \approx 3.2$ nm.

Table 1. Alkyltrimethylammonium Bromide Transition Concentrations and Critical Micelle Concentrations, in mM, Determined by Tensiometry

Chain length	*[EMIM][EtSO$_4$]*		*water*		
	C_a (90°C)	*cmc_{exp} (90°C)*	*C_a (20°C)*	*cmc_{exp} (20°C)*	*cmc_{ref} (25°C)*
6	70	5100	/	/	990 (*46*)
8	33	3300	43	380	261 (*46*)
10	6.0	2000	4.3	69	64.6 (*47*)
12	1.4	510	2.2	14.8	14.2 (*47*)
14	0.6	190	0.03	3.1	3.6 (*47*)

Chain Length Effect

Analysis of XPS data typically involves decoupling signal peaks into contributions from particular elemental types based on their respective binding energies (*12–15*). However, this process is complicated in our systems due to the increased number of species: two ions from the IL and two ions from the surfactant. We therefore analyzed the elemental composition data by means of atomic mass balances (*48*, *49*), which only rely on the presence of one or more unique atomic species (e.g., nitrogen or sulfur). In essence, this approach simply accounts for the relative amounts of a given element within each molecular species (*41*). Once the compositions of all molecular species are determined, numerous additional quantities may be calculated. The mole fractions of each species x_i^{surf} gives an effective surface concentration averaged over the information depth $d \approx 3.2$ nm (based on an emission angle of 45°) which is greater than the molecular lengths of the ions and surfactants (*50*, *51*). Figure 3(a) shows the surface fractions of each species in the C_nTAB / [EMIM][EtSO$_4$] mixtures. It can be seen that the IL components always remain the major surface species, which is likely due to the relatively low overall concentration of surfactants. As mentioned earlier, the *bulk* concentration for each mixture is fixed at $C^* \approx 10C_a$. In spite of this normalized concentration, the shorter chain length surfactants are more abundant near the surface than their longer counterparts are.

To more carefully consider the effect of surfactant chain length, we define "surface enrichment" as the ratio of surface fraction to bulk fraction, $\varepsilon_i = x_i^{surf}/x_i^{bulk}$, which provides a measure of the relative tendency of a species to segregate to the interface (i.e., for an ideal mixture $\varepsilon_i = 1$). We find that all C_nTA^+ surfactants exhibit surface enrichments $\varepsilon \gg 1$, confirming their surface activity at the IL interface (Figure 3(b)). Therefore, XPS can be used as a direct measure of surface activity even in mixtures, which may prove advantageous in situations where tensiometry is either not possible or inconvenient. Furthermore, ε increases exponentially with chain length, which we presume to be due to IL solvatophobicity, analogous to the hydrophobic effect in water (*50*). A key result of Figure 3 is that while the surface fraction of longer surfactants (e.g., $C_{14}TA^+$) is not particularly large, they are partitioning to the interface much more efficiently than shorter surfactants. We also note that the surfactant $Br^–$ counterions are undetectable (below 0.1 atomic %) at the interface for longer surfactants, suggestive of nearly complete dissociation. This situation is in stark contrast to C_nTAB behavior in water, where a significant fraction of $Br^–$ counterions remains bound to the surfactant (or micelle) (*52*). Our observation of $Br^–$ dissociation is consistent with earlier studies reporting the dissociation of halides in ILs (e.g., $Cl^–$ from $[Pt(NH_3)_4]Cl_2$ in $[EMIM][EtSO_4]$) (*18*, *20*). The surface enrichment of C_nTA^+ and simultaneous dissociation of $Br^–$ indicate a complex interplay among the various charged species. Previous work from our group (*41*) with anionic surfactants shows similar surface fraction and enrichment effects which suggest that this behavior does not depend on the specific chemical identity of the ionic surfactant. We are currently exploring the importance of counterions more carefully through the examination of zwitterionic and catanionic surfactants.

Another quantity that is directly determined from the XPS compositional data is the overall surface charge, defined here as the ratio of total cations to total anions. We again emphasize that this property is defined over the information depth $d \approx 3$ nm. This ratio is expected to be unity due to the condition of electroneutrality and we find that the surface charge ratio is 1.01±0.03 for neat $[EMIM][EtSO_4]$ ($N = 27$), which implies a slight net positive charge of the IL. However, considering the relative error of the XPS experiments, the overall surface charge is indeed close to electroneutrality. As shown in the inset of Figure 3(a), the surface charge ratio shows significant overlap with that of the neat $[EMIM][EtSO_4]$ for all surfactant chain lengths. If we recall that $C^* \approx 10C_a$, it seems plausible to interpret this effect to be a result of both IL ions being the majority species at the interface.

Concentration Effects

To further examine the influence of surfactants on IL interfacial properties, we varied the surfactant concentration for two specific chain lengths: n=8 and n=14. With increasing C_8TAB surfactant concentration, the fractions of $[EMIM]^+$ and $[EtSO_4]^-$ both decrease, while the fractions of C_8TA^+ and its counterion Br^- both increase (Figure 4(a)). This trend reflects a dynamic ion exchange process near the interface, where one cation type progressively exchanges with the other. A similar trend is observed for the anions. This exchange of ions does not continue indefinitely, since the C_8TA^+ and Br^- fractions appear to reach a plateau at high concentrations. Such behavior suggests that even below the Krafft temperature, the interface achieves complete saturation with C_8TA^+ at a concentration near the cmc. This scenario would be consistent with surface tension-concentration isotherms carried out *above* the Krafft temperature, where the cmc can be clearly identified. However, since the XPS experiments were conducted at room temperature, a second solid phase must appear at high surfactant concentrations, and certainly before the cmc. We are led to conclude that the solid phase of C_8TA^+ is minimally surface-active in $[EMIM][EtSO_4]$.

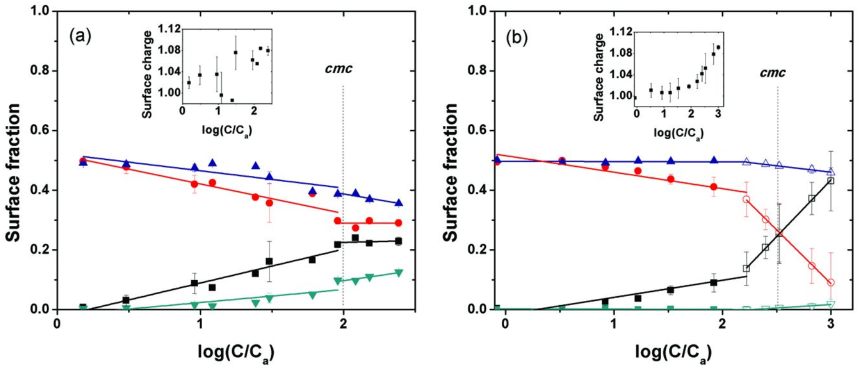

Figure 4. Surface fractions (C_nTA^+ (squares), $[EMIM]^+$ (circles), $[EtSO_4]^-$ (top triangles), and Br^- (bottom triangles) and surface charge ratios (inset) of (a) C_8TAB and (b) $C_{14}TAB$ in $[EMIM][EtSO_4]$. The open symbols represent samples that exhibit a semi-solid surface film.

For the longer $C_{14}TAB$ surfactant, the fraction of $C_{14}TA^+$ increases with concentration and appears to cross a transition point, beyond which it increases more steeply (Figure 4(b)). In this second regime the ion exchange of the two cations ($C_{14}TA^+$ and $[EMIM]^+$) reaches completeness, that is, their fractions become equal. Curiously, this point of equality coincides almost exactly with the cmc, even though once again the system is below the Krafft temperature. The fractions of both anions (Br^- and $[EtSO_4]^-$) remain more or less constant irrespective of the surfactant concentration. Therefore, in contrast to the situation with C_8TAB, for $C_{14}TAB$ there are fewer species are participating in the ion exchange process. The concentration-dependent differences in behavior for C_8TAB and $C_{14}TAB$ might due to several reasons, possibly including that $C_{14}TA^+$ is substantially more surface active than C_8TA^+ (Figure 3(b)). Furthermore, at high $C_{14}TAB$ concentrations we observed the formation of semi-solid surface layer, which is suggestive of a multilayer film (the open symbols in Figure 4(b) are used in this case). This type of film would be possible if $C_{14}TA^+$ retains significant surface activity below its Krafft temperature, but further investigation is needed to clarify the nature of this interface.

Even at high $C_{14}TAB$ concentrations, the Br^- counterion is minimally present while the $[EtSO_4]^-$ anion is about half of the total surface fraction. A possible reason for this behavior is that the intermolecular attraction between $C_{14}TA^+$ and $[EtSO_4]^-$ is stronger than that between $C_{14}TA^+$ and Br^-. The former interaction would clearly contain a van der Waals contribution whereas the latter would be primarily of an electrostatic nature. Results from our own previous work and that of others have indicated the possibility of highly effective charge screening within ILs (*53*–*55*), which would support an interaction between C_nTA^+ and $[EtSO_4]^-$ that increases with chain length due to van der Waals attraction. While the low polarizability of halides could also explain the low Br^- surface fraction (*18*), this effect would be independent of the surfactant.

At low surfactant concentrations, the surface charge remains close to that of the neat IL (insets in Figure 4). However, for both surfactants there is an increasing trend with concentration, ultimately crossing into the positive charge regime. In the case of C_{14}TAB, this elevated positive surface charge may reflect the presumed formation of a multilayer at the interface. We note that other effects, such as the strength of ion-pairing between the IL ions (*53*, *54*, *56*), or local heterogeneities within the IL (*57–60*), may be important factors in determining whether surface charge can be altered by surfactants. Indeed, angle-resolved studies have revealed surface layering of ions, which leads to a composition profile that oscillates with depth (*24*, *61*).

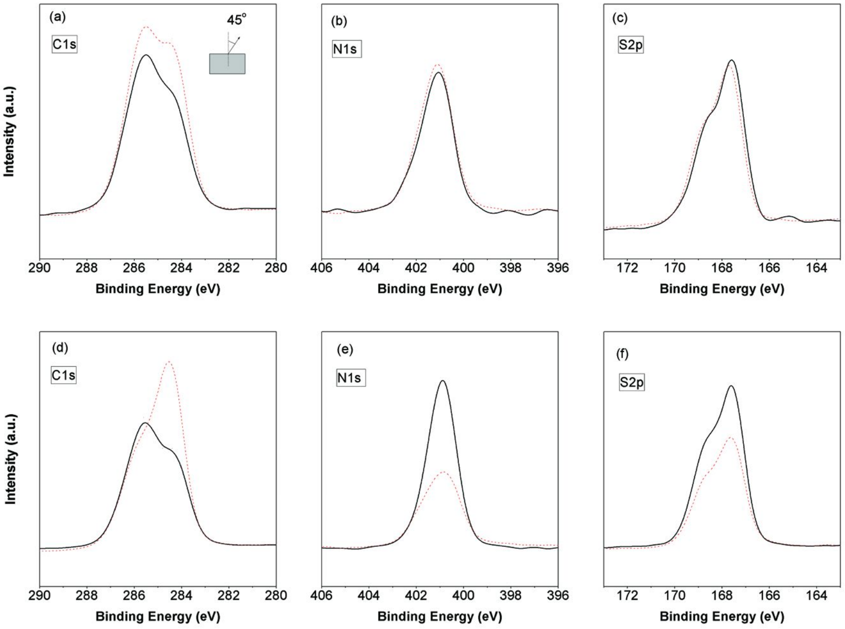

Figure 5. Detailed X-ray photoelectron spectra of (a, b, c) C_8TAB and (d, e, f) C_{14}TAB in [EMIM][EtSO$_4$] at two different surfactant concentrations. The solid lines represent $C \approx 30C_a$ < cmc, while the dashed lines represent C > cmc. The spectra were taken with an emission angle of 45° (information depth $d \approx 3.2$ nm).

In Figure 5, selected X-ray photoelectron spectra of C1s, N1s, and S2p are presented to illustrate the effects of chain length and concentration. For both C_8TAB and C_{14}TAB surfactants, the C1s peak intensity increases with concentration (Figure 5(a) and 5(d)), suggesting the adsorption of surfactant molecules at the interface. Furthermore, the C1s peaks can be deconvoluted into two distinct peaks with binding energies of approximately 286 eV and 284 eV. These two contributions represent carbon atoms bonded to heteroatoms (nitrogen or oxygen, 286 eV) denoted by C_{hetero}, and carbon atoms only bonded to other carbons and hydrogen, denoted by C_{alkyl} (*16*). Even without performing peak-fitting calculations (for a detailed discussion of this procedure and its assumptions, see Lovelock et al. (*28*)), the intensity ratio of C_{alkyl}/C_{hetero} increases with concentration for both surfactants, confirming that adsorption at the interface is due to the surfactant. The changes in C1s peak intensity and C_{alkyl}/C_{hetero} ratio with concentration are more obvious for $C_{14}TAB$, which is probably due to the high surface activity of this longer chain surfactant. Consequently, the decreases in peak intensity for N1s and S2p signals (Figure 5(b), (c), (e), (f)) are also more pronounced for $C_{14}TAB$, with the latter decrease clearly attributable to the surfactant. These qualitative results that are obtained directly from the X-ray photoelectron spectra further support our above discussions.

Information Depth Effects

As mentioned previously, the various quantities calculated from the XPS data are spatial averages over an information depth that is determined by the emission angle. Here we define this angle to be between the detector and the surface normal, but we note that other conventions are sometimes used. The relationship between the emission angle θ and the information depth d is given by the expression $d \approx 3\lambda \cos\theta$ (*41*), where λ is the electron mean free path. Since λ varies with the element being considered, we take an average over C1s, N1s, and S2p to arrive at $\lambda = 1.50$ nm. By using a larger XPS emission angle, the information depth is reduced and hence we expect to observe a larger surface fraction of surfactant. However, using *too small an information depth is undesirable* because the resultant length scales would be less than the size of the surfactants and rule out the use of both atomic mass balance analysis *and* peak-fitting deconvolution. Therefore, we examined emission angles of 75°, 45°, and 30°, which correspond to information depths of 1.2 nm, 3.2 nm, and 3.9 nm, respectively. We note that the unit length of surfactant alkyl chain is 0.126 nm (*50*) so the fully extended surfactant chain length is between 0.63 nm (n=6) and 1.64 nm (n=14). The true chain dimensions will be somewhat smaller than the full extensions due to chain conformational flexibility and hence are expected to be within our information depths. In this regard, we emphasize once more that emission angles greater than 75° are not used since the information depth would be smaller than the thickness of surfactant monolayer at the interface.

In Figure 6, we use the difference in cation surface fractions $\Delta x^+ = C_nTA^+ - [EMIM]^+$ to summarize changes with concentration at various information depths. Both smaller and larger d show that with increasing surfactant concentration, the cation surface fraction difference Δx^+ is also increasing. This increase in Δx^+ is due to the fraction of C_nTA^+ increasing while the surface fraction of $[EMIM]^+$ is decreasing (see Figure 4). The value $\Delta x^+ = 0$ indicates the concentration corresponding to complete cation exchange. Clearly, this concentration shifts higher when larger d are used. On the other hand, at the smallest d studied, the larger surface fraction differences confirm that the surfactants are prone to stay close to the liquid-vapor interface.

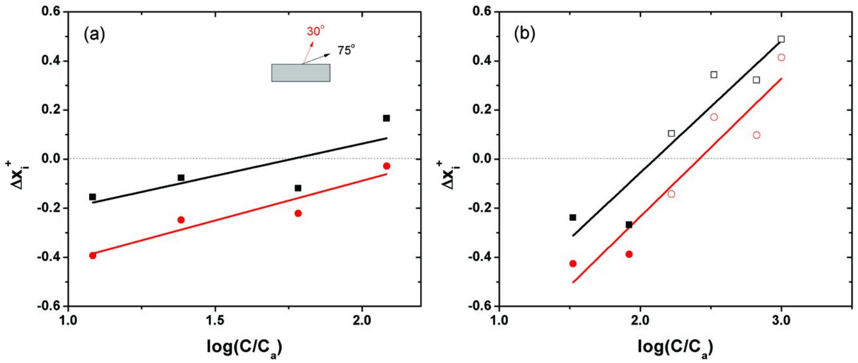

Figure 6. Surface fraction difference of cations $\Delta x^+ = C_nTA^+ - [EMIM]^+$, for (a) C_8TAB and (b) $C_{14}TAB$ in $[EMIM][EtSO_4]$. The emission angles of 75° (squares) and 30° (circles) correspond to information depths d of 1.2 nm and 3.9 nm, respectively. The open symbols represent samples that exhibit a semi-solid surface film.

Conclusions

In this work we examined the influence of charged surfactants in ionic liquids by XPS. Interfacial properties such as surface composition, charge, and enrichment were studied in terms of the surfactant alkyl chain length, concentration, and XPS information depth. Consistent with conventional tensiometry, our XPS results directly establish the surface activity of the surfactants and show that this quantity increases with alkyl chain length. We also find that an ion exchange process between like-charged surfactant and IL ions occurs at the interface, progressively increasing with surfactant concentration. Thus, surfactants can appreciably alter the interfacial properties of IL systems. By varying the XPS information depth *d*, we find that the effective surface activity increases inversely with *d*, confirming the tendency of the surfactant to remain close to the interface. Finally, we note that many opportunities remain to be explored with surfactant-IL mixtures, such as the role of counterions, nanoscale clustering in the bulk phase, and influences on layering near the interface. Although we have not done so here, careful angle-resolved XPS studies may show evidence of surfactant-induced surface layering that is distinct from the neat IL.

Acknowledgments

This work was financially supported by an NSF CAREER Award (DMR-0847558) to H.B., and by the NSF Materials Research Science and Engineering Center (DMR-0820506).

References

1. Welton, T. *Chem. Rev.* **1999**, *99*, 2071–2083.
2. Wasserscheid, P.; Keim, W. *Angew. Chem., Int. Ed.* **2000**, *39*, 3772–3789.
3. Yao, C.; Pitner, W. R.; Anderson, J. L. *Anal. Chem.* **2009**, *81*, 5054–5063.
4. Greaves, T. L.; Drummond, C. J. *Chem. Rev.* **2008**, *108*, 206–237.
5. Aliaga, C.; Santos, C. S.; Baldelli, S. *Phys. Chem. Chem. Phys.* **2007**, *9*, 3683–3700.
6. Fletcher, K. A.; Pandey, S. *Langmuir* **2004**, *20*, 33–36.
7. Zheng, L. Q.; Li, N.; Zhang, S. H.; Wu, J. P.; Li, X. W.; Yu, L. *J. Phys. Chem. B* **2008**, *112*, 12453–12460.
8. Li, N.; Zhang, S. H.; Zheng, L. Q.; Dong, B.; Li, X. W.; Yu, L. *Phys. Chem. Chem. Phys.* **2008**, *10*, 4375–4377.
9. Ogino, K.; Kakihara, T.; Abe, M. *Colloid Polym. Sci.* **1987**, *265*, 604–612.
10. Patrascu, C.; Gauffre, F.; Nallet, F.; Bordes, R.; Oberdisse, J.; de Lauth-Viguerie, N.; Mingotaud, C. *ChemPhysChem* **2006**, *7*, 99–101.
11. Smith, E. F.; Villar Garcia, I. J.; Briggs, D.; Licence, P. *Chem. Commun.* **2005**, 5633–5635.
12. Smith, E. F.; Rutten, F. J. M.; Villar-Garcia, I. J.; Briggs, D.; Licence, P. *Langmuir* **2006**, *22*, 9386–9392.
13. Gottfried, J. M.; Maier, F.; Rossa, J.; Gerhard, D.; Schulz, P. S.; Wasserscheid, P.; Steinruck, H. P. *Z. Phys. Chem.* **2006**, *220*, 1439–1453.
14. Lockett, V.; Sedev, R.; Bassell, C.; Ralston, J. *Phys. Chem. Chem. Phys.* **2008**, *10*, 1330–1335.
15. Kolbeck, C.; Cremer, T.; Lovelock, K. R. J.; Paape, N.; Schulz, P. S.; Wasserscheid, P.; Maier, F.; Steinruck, H. P. *J. Phys. Chem. B* **2009**, *113*, 8682–8688.
16. Lovelock, K. R. J.; Kolbeck, C.; Cremer, T.; Paape, N.; Schulz, P. S.; Wasserscheid, P.; Maier, F.; Steinruck, H. P. *J. Phys. Chem. B* **2009**, *113*, 2854–2864.
17. Maier, F.; Cremer, T.; Kolbeck, C.; Lovelock, K. R. J.; Paape, N.; Schulz, P. S.; Wasserscheidc, P.; Steinrueck, H.-P. *Phys. Chem. Chem. Phys.* **2010**, *12*, 1905–1915.
18. Maier, F.; Gottfried, J. M.; Rossa, J.; Gerhard, D.; Schulz, P. S.; Schwieger, W.; Wasserscheid, P.; Steinruck, H. P. *Angew. Chem., Int. Ed.* **2006**, *45*, 7778–7780.
19. Hofft, O.; Bahr, S.; Himmerlich, M.; Krischok, S.; Schaefer, J. A.; Kempter, V. *Langmuir* **2006**, *22*, 7120–7123.
20. Law, G.; Watson, P. R.; Carmichael, A. J.; Seddon, K. R.; Seddon, B. *Phys. Chem. Chem. Phys.* **2001**, *3*, 2879–2885.
21. Caporali, S.; Bardi, U.; Lavacchi, A. *J. Electron Spectrosc.* **2006**, *151*, 4–8.
22. Romero, C.; Baldelli, S. *J. Phys. Chem. B* **2006**, *110*, 6213–6223.
23. Jeon, Y.; Sung, J.; Bu, W.; Vaknin, D.; Ouchi, Y.; Kim, D. *J. Phys. Chem. C* **2008**, *112*, 19649–19654.
24. Solutskin, E.; Ocko, B. M.; Taman, L.; Kuzmenko, I.; Gog, T.; Deutsch, M. *J. Am. Chem. Soc.* **2005**, *127*, 7796–7804.
25. Law, G.; Watson, P. R. *Langmuir* **2001**, *17*, 6138–6141.

26. Carvalho, P. J.; Freire, M. G.; Marrucho, I. M.; Queimada, A. J.; Coutinho, J. A. P. *J. Chem. Eng. Data* **2008**, *53*, 1346–1350.
27. Ghatee, M. H.; Zolghadr, A. R. *Fluid Phase Equilibr.* **2008**, *263*, 168–175.
28. Lovelock, K. R. J.; Villar-Garcia, I. J.; Maier, F.; Steinruck, H. P.; Licence, P. *Chem. Rev.* **2010**, *110*, 5158–5190.
29. Niedermaier, I.; Kolbeck, C.; Taccardi, N.; Schulz, P. S.; Li, J.; Drewello, T.; Wasserscheid, P.; Steinruck, H. P.; Maier, F. *ChemPhysChem* **2012**, *13*, 1725–1735.
30. Hurisso, B. B.; Lovelock, K. R. J.; Licence, P. *Phys. Chem. Chem. Phys.* **2011**, *13*, 17737–17748.
31. Silvester, D. S.; Broder, T. L.; Aldous, L.; Hardacre, C.; Crossley, A.; Compton, R. G. *Analyst* **2007**, *132*, 196–198.
32. Liu, Q. B.; Janssen, M. H. A.; van Rantwijk, F.; Sheldon, R. A. *Green Chem.* **2005**, *7*, 39–42.
33. Wasserscheid, P.; Keim, W. *Angew. Chem., Int. Ed.* **2000**, *39*, 3772–3789.
34. Jacquemin, J.; Husson, P.; Majer, V.; Padua, A. A. H.; Gomes, M. F. C. *Green Chem.* **2008**, *10*, 944–950.
35. Domanska, U. *Pure Appl Chem* **2005**, *77*, 543–557.
36. Swatloski, R. P.; Spear, S. K.; Holbrey, J. D.; Rogers, R. D. *J. Am. Chem. Soc.* **2002**, *124*, 4974–4975.
37. Blesic, M.; Lopes, J. N. C.; Gomes, M. F. C.; Rebelo, L. P. N. *Phys. Chem. Chem. Phys.* **2010**, *12*, 9685–9692.
38. Roscioli, J. R.; Nesbitt, D. J. *J. Phys. Chem. Lett.* **2010**, *1*, 674–678.
39. Jones, R. A. L. *Soft Condensed Matter*; Oxford University Press: Oxford, 2002.
40. Fernandez, A.; Torrecilla, J. S.; Garcia, J.; Rodriguez, F. *J. Chem. Eng. Data* **2007**, *52*, 1979–1983.
41. Chen, L. G.; Lerum, R. V.; Aranda-Espinoza, H.; Bermudez, H. *J. Phys. Chem. B* **2010**, *114*, 11502–11508.
42. Sarkar, S.; Pramanik, R.; Ghatak, C.; Setua, P.; Sarkar, N. *J. Phys. Chem. B* **2010**, *114*, 2779–2789.
43. Chen, L. G.; Bermudez, H. *Langmuir* **2012**, *28*, 1157–1162.
44. Marsh, K. N.; Boxall, J. A.; Lichtenthaler, R. *Fluid Phase Equilibr.* **2004**, *219*, 93–98.
45. Strutt, J. W. *Philos. Mag.* **1899**, 321–337.
46. Gomez-Diaz, D.; Navaza, J. M.; Sanjurjo, B. *J. Chem. Eng. Data* **2007**, *52*, 889–891.
47. Mukerjee P, M. K. *Critical Micellar Concentration of Aqueous Surfactant Systems*; National Bureau of Standards: Washington, DC, 1971.
48. Hougen, O. A. *Chemical Process Principles*; Wiley: New York, 1954.
49. Felder, R. M.; Rousseau, R. W. *Elementary Principles of Chemical Processes*; John Wiley: New York, 1999.
50. Israelachvili, J. N. *Intermolecular and Surface forces*; Academic Press: San Diego, 1992.
51. Rebelo, L. P. N.; Lopes, J. N. C.; Esperanca, J. M. S. S.; Guedes, H. J. R.; Lachwa, J.; Najdanovic-Visak, V.; Visak, Z. P. *Accounts Chem. Res.* **2007**, *40*, 1114–1121.

52. Mosquera, V.; del Rio, J. M.; Attwood, D.; Garcia, M.; Jones, M. N.; Prieto, G.; Suarez, M. J.; Sarmiento, F. *J. Colloid. Interf. Sci.* **1998**, *206*, 66–76.
53. Lynden-Bell, R. M. *Phys. Chem. Chem. Phys.* **2010**, *12*, 1733–1740.
54. Ueno, K.; Tokuda, H.; Watanabe, M. *Phys. Chem. Chem. Phys.* **2010**, *12*, 15133–15134.
55. Ueno, K.; Inaba, A.; Kondoh, M.; Watanabe, M. *Langmuir* **2008**, *24*, 5253–5259.
56. Angell, C. A.; Byrne, N.; Belieres, J. P. *Acc. Chem. Res.* **2007**, *40*, 1228–1236.
57. Wang, Y. T.; Voth, G. A. *J. Am. Chem. Soc.* **2005**, *127*, 12192–12193.
58. Wang, Y.; Jiang, W.; Yan, T.; Voth, G. A. *Acc. Chem. Res.* **2007**, *40*, 1193–1199.
59. Lynden-Bell, R. M.; Del Popolo, M. G.; Youngs, T. G. A.; Kohanoff, J.; Hanke, C. G.; Harper, J. B.; Pinilla, C. C. *Acc. Chem. Res.* **2007**, *40*, 1138–1145.
60. Triolo, A.; Russina, O.; Bleif, H. J.; Di Cola, E. *J. Phys. Chem. B* **2007**, *111*, 4641–4644.
61. Bhargava, B. L.; Balasubramanian, S. *J. Am. Chem. Soc.* **2006**, *128*, 10073–10078.

Subject Index

A

- AFC. *See* alkaline fuel cells (AFC)
- Alginic acid, 167
  - solubility, 170
- Alkaline fuel cells (AFC)
  - IL incorporation, 137
    - conductivity testing, 140, 141*f*
    - difficulty, 137
    - ex-situ electrochemical testing, 139, 140*f*
    - membrane preparation, 138
    - PBI polymer synthesis, 137, 138*f*
  - ionic liquid characterization, 132
    - bulk conductivity, 133, 134*f*
    - synthesis, 132, 133*f*
    - thermogravimetric analysis, 135, 135*f*, 136*t*, 137*f*
  - overview, 129
  - schematic diagram, 131*f*
- Alkyldicyanmides, 20*s*
- Alkyltrimethylammonium bromide
  - transition concentrations, 294*t*
- Anions, lithium batteries, 74*f*, 92*t*
- Aprotic IL reactivity, 8

B

- Biopolymer composite materials
  - alginic acid, 168*f*
    - solubility, 170
  - 1-butyl-3-methylimidazolium chloride, 169*f*
  - characterization methods, 172
  - composite material preparation, 172
  - materials, 169
  - MCC, 171*f*
    - fibers, 175*f*
  - MCC:AA fibers, 176*f*, 177*f*, 179*f*, 180*f*, 181*f*, 182*f*, 183*f*, 184*t*
  - overview, 167
  - spinning solution preparation, 170
  - standard powder mixture, 170
- 1-Butyl-3-methylimidazolium chloride, 169*f*

C

- Cations, lithium batteries, 74*f*, 92*t*
- Charged surfactant probing, XPS
  - alkyltrimethylammonium bromide
    - transition concentrations, 294*t*
  - chain length effect, 294
  - concentration effect, 295
  - C_{14}TAB isotherms, 293*f*, 297*f*
  - information depth effects, 298
  - materials, 291
  - overview, 289
  - structures, 291*f*
  - surface fractions, 293*f*, 296*f*, 299*f*
  - tensiometry, 291
- Chemical propulsion
  - alkyldicyanmides, 20*s*
  - ammonium-based IL dicyanamides, 4, 5*s*, 6*t*
  - aprotic IL reactivity, 8
  - cyanoureate anion, 21*s*
  - diaminoguanidinium azide, 15*s*
  - dicyanamides
    - aminated guanidinium, 14*s*
    - cyclization reactions, 9*s*
    - guanidinium, 14*s*, 14*t*, 15*t*
    - 1-(2-hydroxyethyl)-4-amino-1,2,4-triazolium, 9*s*
    - hydroxylammonium dicyanamide cyclization, 10*s*
    - reaction, 20*s*, 21*s*
  - drop test, 2*f*
    - reliability, 11
    - reproducibility, 11
  - higher density dicyanamides, 13, 13*s*
  - hydrazidinium cations, 17*s*
  - hydrogen-bond network, 7*f*, 10*f*, 16*f*
  - hypergolic fuels, 22*s*
  - hypergolic ignition, 8*t*
  - ignition tests, 16*t*, 18*t*
  - IL mixtures as fuels, 12
  - ion formation, nitric acid, 19*s*
  - ionic azides reaction, 3*s*
  - molecular structure, 7*f*, 10*f*, 11*f*, 16*f*
  - nitric acid autodissociation, 18*s*
  - nitrocyanamide, 20*s*
  - overview, 1
  - protic IL reactivity, 6*f*, 8
  - TGA isothermal, 7*f*
  - trimethylazidoethyl nitrocyanamide, 12*s*
  - X-ray crystal structure, 13*f*, 14*f*, 17*f*, 18*f*, 21*f*, 22*f*

Downloaded by UNIV OF ALABAMA BIRMINGHAM on December 19, 2012 | http://pubs.acs.org
Publication Date (Web): December 18, 2012 | doi: 10.1021/bk-2012-1117.ix002

Downloaded by UNIV OF ALABAMA BIRMINGHAM on December 19, 2012 | http://pubs.acs.org
Publication Date (Web): December 18, 2012 | doi: 10.1021/bk-2012-1117.ix002

Chitin degradation
  Benedict's test, 194
  HPLC measurements, 194, 197*f*
  hydrolysis, 190*f*
  ionic liquids acid catalyst synthesis, 192, 192*f*
  materials, 192
  1-methyl-3-(alkylsulfonic acid)imidazolium acid catalyst synthesis, 193*f*
  overview, 189
  reaction experiment, 193
  reducing sugars, 195*f*, 196*f*
Cotton, NFW, 149*f*, 154*f*, 155*f*, 158*f*, 160*f*, 163*f*
Cyanoureate anion, 21*s*
Cycling performance, lithium batteries, 108*f*, 109*t*, 110*t*

D

Deintercalation capacity, lithium batteries, 99*t*, 100*t*
Delivered capacity, lithium batteries, 106*t*
Diaminoguanidinium azide, 15*s*
Dicyanamides
  aminated guanidinium, 14*s*
  ammonium-based IL, 4, 5*s*, 6*t*
  cyclization reactions, 9*s*
  guanidinium, 14*s*, 14*t*, 15*t*
  higher density, 13, 13*s*
  1-(2-hydroxyethyl)-4-amino-1,2,4-triazolium, 9*s*
  hydroxylammonium dicyanamide cyclization, 10*s*
  reaction, 20*s*, 21*s*
Discharge capacity, lithium batteries, 102*t*, 104*f*, 105*t*, 106*f*, 111*t*, 112*t*, 117*t*, 118*t*, 119*t*, 120*t*
Drop test, IL, 2*f*
  reliability, 11
  reproducibility, 11

E

Electrospray propulsion systems
  capillary emitter, 30*f*
  cation mass spectra, 41*f*
  electrospray space propulsion, 29
  1-ethyl-3-methylimidazolium bis(trifluoromethylsulfonyl)imide, 33, 34*f*
  HEH^+ cation, 39*f*
  2-hydroxyethylhydrazinium nitrate, 38
  ion current density, 40*f*
  ion energy, 42*f*
  MD simulations, 35*f*
  needle emitter, 30*f*
  NO_3- anion, 39*f*
  overview, 27
  trajectory dissociation, 36*f*, 37*f*
Ethanol/water extractive distillation
  chemicals, 242*t*
  $[C_2mim]N(CN)_2$, 251, 252*f*, 253*f*, 254*f*
  composition, 248*f*
  energy requirement, 253, 254*f*
  ethylene glycol, 250, 250*f*
  IL selection, 243
  ionic liquid recovery techniques, 251
  operational conditions, 248*t*
  overview, 239
  pilot plant experiments, 244, 245*t*, 246*f*
  process, 240*f*, 242*f*
  product purity, 249*t*
  reflux ratio, 249*t*
  Sulzer Mellapak™ 750 Y, 245*f*
  temperature, 248*f*, 249*f*
  volatilities, 243*f*
  water content, 249*t*
1-Ethyl-3-methylimidazolium bis(trifluoromethylsulfonyl)imide, 33, 34*f*

F

Fatty acids, lipid-inspired ionic liquids, 201, 202*s*, 204*t*, 205*f*
Flammability tests, lithium batteries, 72*f*

G

Gas solubility
  overview, 217
  simultaneous solubility, two gases, 218, 220*f*
  single gas, binary liquid mixture, 223, 224*f*, 225*f*, 226*f*, 227*f*, 229*f*, 230*f*, 233*f*, 234*f*
Gene transfection agents, 206
Graphite, negative electrodes, 91, 92*t*, 94*f*, 95*t*, 96*t*, 97*t*
Graphite reversible capacity, lithium batteries, 92*t*, 94*f*, 95*t*, 96*t*, 97*t*

Downloaded by UNIV OF ALABAMA BIRMINGHAM on December 19, 2012 | http://pubs.acs.org
Publication Date (Web): December 18, 2012 | doi: 10.1021/bk-2012-1117.ix002

H

Heating tests, lithium batteries, 73*f*
Hydrazidinium cations, 17*s*
Hydrophobic lithium batteries, 79*f*
2-Hydroxyethylhydrazinium nitrate, 38
Hypergolic fuels, 22*s*
Hypergolic ignition, 8*t*

I

Ignition tests, IL, 16*t*, 18*t*
Ionic azides reaction, 3*s*
Ionic conductivity, lithium batteries, 80*f*, 81*f*, 83*f*
Ionic liquid electrolytes
  lithium batteries, 68, 68*f*
    anions, 74*f*, 92*t*
    capacity, 88*t*
    cations, 74*f*, 92*t*
    cycling performance, 108*f*, 109*t*, 110*t*
    deintercalation capacity, 99*t*, 100*t*
    delivered capacity, 106*t*
    discharge capacity, 102*t*, 104*f*, 105*t*, 106*f*, 111*t*, 112*t*, 117*t*, 118*t*, 119*t*, 120*t*
    ESW, 84*f*
    flammability tests, 72*f*
    graphite reversible capacity, 92*t*, 94*f*, 95*t*, 96*t*, 97*t*
    heating tests, 73*f*
    hydrophobic, 79*f*
    ionic conductivity, 80*f*, 81*f*, 83*f*
    LFP cathodes, 112*f*, 113*t*, 114*t*
    LiTFSI-PYR$_3$TFSI electrolytes, 102*t*
    LiTFSI-PYR$_{14}$TFSI electrolytes, 101*t*, 120*f*
    LiTFSI-TMHATFSI electrolytes, 104*t*
    lithium-ion cells, 116
    LMO cathodes, 106*f*, 106*t*
    melting point, 75*t*
    negative electrodes, 89
    operating window, 71*f*
    performance, 116*t*
    physicochemical properties, 75*t*, 85*t*
    positive electrodes, 102
    PYR$_{13}$FSI, 79*f*
    room temperature electrochemical performance, 121*t*
    safety drawbacks, 69
    thermal runaway, 71*f*
    thermal stability, 75*t*
    use, 88
    viable ionic liquids, 71
    viscosity, 75*t*
  overview, 67

L

LFP cathodes, lithium batteries, 112*f*, 113*t*, 114*t*
Lipid-inspired ionic liquids
  alkyl chain length, 202*f*
  cation structures, 207*s*
  cationic, 209*t*
  fatty acids, 201, 202*s*, 204*t*, 205*f*
  gene transfection agents, 206
  lipofection, 206
  oleic acid, 203*s*
  overview, 199
  putative anion-induced transformation, 209*f*
  thiol substituents, 211, 213*s*, 214*s*
Lipofection, 206
LiTFSI-PYR$_3$TFSI electrolytes, 102*t*
LiTFSI-PYR$_{14}$TFSI electrolytes, 101*t*, 120*f*
LiTFSI-TMHATFSI electrolytes, 104*t*
Lithium batteries, IL electrolytes, 68, 68*f*
  anions, 74*f*, 92*t*
  capacity, 88*t*
  cations, 74*f*, 92*t*
  cycling performance, 108*f*, 109*t*, 110*t*
  deintercalation capacity, 99*t*, 100*t*
  delivered capacity, 106*t*
  discharge capacity, 102*t*, 104*f*, 105*t*, 106*f*, 111*t*, 112*t*, 117*t*, 118*t*, 119*t*, 120*t*
  ESW, 84*f*
  flammability tests, 72*f*
  graphite reversible capacity, 92*t*, 94*f*, 95*t*, 96*t*, 97*t*
  heating tests, 73*f*
  hydrophobic, 79*f*
  ionic conductivity, 80*f*, 81*f*, 83*f*
  LFP cathodes, 112*f*, 113*t*, 114*t*
  LiTFSI-PYR$_3$TFSI electrolytes, 102*t*
  LiTFSI-PYR$_{14}$TFSI electrolytes, 101*t*, 120*f*
  LiTFSI-TMHATFSI electrolytes, 104*t*
  lithium-ion cells, 116
  LMO cathodes, 106*f*, 106*t*
  melting point, 75*t*
  negative electrodes, 89
  operating window, 71*f*
  performance, 116*t*
  physicochemical properties, 75*t*, 85*t*
  positive electrodes, 102
  PYR$_{13}$FSI, 79*f*

Downloaded by UNIV OF ALABAMA BIRMINGHAM on December 19, 2012 | http://pubs.acs.org
Publication Date (Web): December 18, 2012 | doi: 10.1021/bk-2012-1117.ix002

  room temperature electrochemical performance, 121*t*
  safety drawbacks, 69
  thermal runaway, 71*f*
  thermal stability, 75*t*
  use, 88
  viable ionic liquids, 71
  viscosity, 75*t*
Lithium cobalt oxide, positive electrodes, 102, 102*t*, 104*f*, 104*t*, 105*t*
Lithium iron phosphate, positive electrodes, 109, 110*t*, 111*t*, 112*f*, 112*t*, 113*t*, 114*t*
Lithium manganese oxide, positive electrodes, 105, 106*f*, 106*t*
Lithium metal, negative electrodes, 89, 90*f*
Lithium-alloys, negative electrodes, 100
Lithium-ion cells, 116
LMO cathodes, lithium batteries, 106*f*, 106*t*

M

MCC. *See* microcrystalline cellulose (MCC)
MCC:AA fibers, 176*f*, 177*f*, 179*f*, 180*f*, 181*f*, 182*f*, 183*f*, 184*t*
Melting point, lithium batteries, 75*t*
Microcrystalline cellulose (MCC), 171*f*
  fibers, 175*f*
Molecular dynamics simulations
  intermolecular spectra, 283*f*
  methodology, 273
  models, 273
  nanostructural organization, 279*f*
  OHD-RIKES time-domain data, 279, 280*f*
  overview, 271
  radial distribution functions, 276*f*, 277*f*, 278*f*
  reduced spectral density, 280*f*, 282*f*
  simulated mixture sizes, 273*t*
  solute intermolecular spectral parameters, 284*t*

N

Nanoparticle enhanced ionic liquids (NEIL)
  characterization, 262, 263*f*
  corrosion, 265, 266*f*, 267*f*, 267*t*, 268*f*
  density, 263*t*, 264*t*
  heat capacity, 265*t*
  heat transfer fluids, 260
  nanofluids, 261
  overview, 259
  thermal stability, 263*t*, 264*t*
  viscosity, 263*t*, 264*t*
Natural fiber welding (NFW)
  chemical transformations, 159
  composite characterization protocols, 151
  cotton, 149*f*, 154*f*, 155*f*, 158*f*, 160*f*, 163*f*
  instrumentation, 151
  materials, 151
  overview, 145
  physical transformations, 152
  properties, 146*t*
  protocols, 151
  schematics, 150*f*
  silk, 148*f*, 156*f*
Negative electrodes, lithium batteries, 89
  graphite, 91, 92*t*, 94*f*, 95*t*, 96*t*, 97*t*
  lithium metal, 89, 90*f*
  lithium-alloys, 100
  titanium oxides, 98, 99*t*, 100*t*
NEIL. *See* nanoparticle enhanced ionic liquids (NEIL)
NFW. *See* natural fiber welding (NFW)
Nitric acid
  autodissociation, 18*s*
  ion formation, 19*s*
Nitrocyanamide, 20*s*

O

OKE Spectra, 279
Operating window, lithium batteries, 71*f*

P

Performance, lithium batteries, 116*t*
Physicochemical properties, lithium batteries, 75*t*, 85*t*
Positive electrodes, lithium batteries, 102
  lithium cobalt oxide, 102, 102*t*, 104*f*, 104*t*, 105*t*
  lithium iron phosphate, 109, 110*t*, 111*t*, 112*f*, 112*t*, 113*t*, 114*t*
  lithium manganese oxide, 105, 106*f*, 106*t*
Protic IL reactivity, 6*f*, 8
$PYR_{13}FSI$, 79*f*

Downloaded by UNIV OF ALABAMA BIRMINGHAM on December 19, 2012 | http://pubs.acs.org
Publication Date (Web): December 18, 2012 | doi: 10.1021/bk-2012-1117.ix002

R

Room temperature electrochemical performance, lithium batteries, 121*t*

S

Safety drawbacks, lithium batteries, 69
Silk, NFW, 148*f*, 156*f*
Sulzer Mellapak™ 750 Y, 245*f*

T

Thermal runaway, lithium batteries, 71*f*
Thermal stability, lithium batteries, 75*t*
Titanium oxides, negative electrodes, 98, 99*t*, 100*t*
TMEDA•8HNO_3
  burn rate, 60*f*
  combustion, 58, 59*f*, 60*f*
  confined rapid thermolysis, 57
  hypergolic droplet-on-pool impingement, 53*f*
  ignition, 60*f*
  molecular structure, 52*f*
  overview, 51
  oxidation, 64*f*
  preparation, 54
  rapid thermolysis, 60, 62*f*, 63*f*
  self-accelerating decomposition, 56*f*
  strand burner, 56, 57*f*
Trimethylazidoethyl nitrocyanamide, 12*s*

V

Viable ionic liquids, lithium batteries, 71
Viscosity, lithium batteries, 75*t*